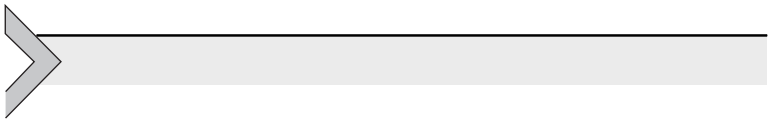

ENERGETIC NANOMATERIALS

Synthesis, Characterization, and Application

Edited by

VLADIMIR E. ZARKO
Voevodsky Institute of Chemical Kinetics and Combustion, Siberian Branch of the Russian Academy of Sciences, Novosibirsk, Russia
Tomsk State University, Tomsk, Russia

ALEXANDER A. GROMOV
Technical University Georg-Simon-Ohm, Nürnberg, Germany
Fraunhofer Institute of Chemical Technology, Pfinztal, Germany
Tomsk Polytechnic University, Tomsk, Russia
Semenov Institute of Chemical Physics, Russian Academy of Science, Moscow, Russia

ELSEVIER

Amsterdam • Boston • Heidelberg • London
New York • Oxford • Paris • San Diego
San Francisco • Singapore • Sydney • Tokyo

Elsevier
Radarweg 29, PO Box 211, 1000 AE Amsterdam, Netherlands
The Boulevard, Langford Lane, Kidlington, Oxford OX5 1GB, UK
50 Hampshire Street, 5th Floor, Cambridge, MA 02139, USA

Notices

Knowledge and best practice in this field are constantly changing. As new research and experience broaden our understanding, changes in research methods, professional practices, or medical treatment may become necessary.

Practitioners and researchers must always rely on their own experience and knowledge in evaluating and using any information, methods, compounds, or experiments described herein. In using such information or methods they should be mindful of their own safety and the safety of others, including parties for whom they have a professional responsibility.

To the fullest extent of the law, neither the Publisher nor the authors, contributors, or editors, assume any liability for any injury and/or damage to persons or property as a matter of products liability, negligence or otherwise, or from any use or operation of any methods, products, instructions, or ideas contained in the material herein.

ISBN: 978-0-12-802710-3

British Library Cataloguing in Publication Data
A catalogue record for this book is available from the British Library

Library of Congress Cataloging-in-Publication Data
A catalog record for this book is available from the Library of Congress

DEDICATION

To the Russian scientists Yu. Kondratyuk and F. Tsander, who in the 1920s suggested using the metals as energetic material in propulsion systems.

LIST OF CONTRIBUTORS

Ting An
Science and Technology on Combustion and Explosion Laboratory, Xi'an Modern Chemistry Research Institute, Xi'an, China

Vladimir A. Arkhipov
Tomsk State University, Tomsk, Russia

Giovanni Colombo
Space Propulsion Laboratory, Department of Aerospace Science and Technology, Politecnico di Milano, Milan, Italy

Luigi T. DeLuca
Space Propulsion Laboratory, Department of Aerospace Science and Technology, Politecnico di Milano, Milan, Italy

Stefano Dossi
Space Propulsion Laboratory, Department of Aerospace Science and Technology, Politecnico di Milano, Milan, Italy

G.C. Egan
Department of Chemical and Biomolecular Engineering and Department of Chemistry and Biochemistry, University of Maryland, College Park, Maryland, United States

Igor V. Fomenkov
Zelinsky Institute of Organic Chemistry, Moscow, Russia

Luciano Galfetti
Space Propulsion Laboratory, Department of Aerospace Science and Technology, Politecnico di Milano, Milan, Italy

Alon Gany
Technion – Israel Institute of Technology, Haifa, Israel

Oleg G. Glotov
Voevodsky Institute of Chemical Kinetics and Combustion, Siberian Branch of the Russian Academy of Sciences, Novosibirsk, Russia

Alexander A. Gromov
Technical University Georg-Simon-Ohm, Nürnberg, Germany; Fraunhofer Institute of Chemical Technology, Pfinztal, Germany; Tomsk Polytechnic University, Tomsk, Russia; Semenov Institute of Chemical Physics, Russian Academy of Science, Moscow, Russia

L.J. Groven
South Dakota School of Mines & Technology, Rapid City, SD, USA

I.E. Gunduz
Purdue University, West Lafayette, IN, USA

Xiao-de Guo
National Special Superfine Powder Engineering Research Center, Nanjing University of Science and Technology, Nanjing, China

Ga-zi Hao
National Special Superfine Powder Engineering Research Center, Nanjing University of Science and Technology, Nanjing, China

Wei-liang Hong
School of Chemistry and Chemical Engineering, Shenzhen University, Shenzhen, China

Yan Hu
Micro-Nano Energetic Device Join Laboratory, School of Chemical Engineering, Nanjing University of Science and Technology, Nanjing, Jiangsu, China

A. Il'in
Tomsk Polytechnic University, Tomsk, Russia

S. Isert
Purdue University, West Lafayette, IN, USA

Wei Jiang
National Special Superfine Powder Engineering Research Center, Nanjing University of Science and Technology, Nanjing, China

Keerti Kappagantula
Department of Mechanical Engineering, Ohio University, Athens, OH, USA

Alexander G. Korotkikh
Tomsk Polytechnic University, Tomsk, Russia; Tomsk State University, Tomsk, Russia

Feng-sheng Li
National Special Superfine Powder Engineering Research Center, Nanjing University of Science and Technology, Nanjing, China

Jie Liu
National Special Superfine Powder Engineering Research Center, Nanjing University of Science and Technology, Nanjing, China

Filippo Maggi
Space Propulsion Laboratory, Department of Aerospace Science and Technology, Politecnico di Milano, Milan, Italy

Gianluigi Marra
Centro Ricerche ENI per le Energie Rinnovabili e l'Ambiente – Istituto ENI Donegani, Novara, Italy

Konstantin A. Monogarov
Semenov Institute of Chemical Physics, Russian Academy of Science, Moscow, Russia

Alexander S. Mukasyan
University of Notre Dame, Notre Dame, IN, USA

Nikita V. Muravyev
Semenov Institute of Chemical Physics, Russian Academy of Science, Moscow, Russia

Michelle Pantoya
Mechanical Engineering Department, Texas Tech University, Lubbock, TX, USA

Christian Paravan
Space Propulsion Laboratory, Department of Aerospace Science and Technology, Politecnico di Milano, Milan, Italy

Alla N. Pivkina
Semenov Institute of Chemical Physics, Russian Academy of Science, Moscow, Russia

Zhao Qin
Micro-Nano Energetic Device Join Laboratory, School of Chemical Engineering, Nanjing University of Science and Technology, Nanjing, Jiangsu, China

Alexander S. Rogachev
Institute of Structural Macrokinetics and Materials Science, RAS, Chernogolovka, Russia; National University of Science and Technology "MISIS", Moscow, Russia

Valery Rosenband
Technion – Israel Institute of Technology, Haifa, Israel

J. Schoonman
Department of Chemical Engineering (ChemE), Delft University of Technology, Delft, The Netherlands

Ruiqi Shen
Micro-Nano Energetic Device Join Laboratory, School of Chemical Engineering, Nanjing University of Science and Technology, Nanjing, Jiangsu, China

T.R. Sippel
Iowa State University, Ames, IA, USA

S.F. Son
Purdue University, West Lafayette, IN, USA

Ulrich Teipel
Technical University Georg-Simon-Ohm, Nürnberg, Germany; Fraunhofer Institute of Chemical Technology, Pfinztal, Germany

B.C. Terry
Purdue University, West Lafayette, IN, USA

Yu-jiao Wang
National Special Superfine Powder Engineering Research Center, Nanjing University of Science and Technology, Nanjing, China

Lizhi Wu
Micro-Nano Energetic Device Join Laboratory, School of Chemical Engineering, Nanjing University of Science and Technology, Nanjing, Jiangsu, China

Yan-jing Yang
Science and Technology on Combustion and Explosion Laboratory, Xi'an Modern Chemistry Research Institute, Xi'an, China

Yinghua Ye
Micro-Nano Energetic Device Join Laboratory, School of Chemical Engineering, Nanjing University of Science and Technology, Nanjing, Jiangsu, China

Jian-hua Yi
Science and Technology on Combustion and Explosion Laboratory, Xi'an Modern Chemistry Research Institute, Xi'an, China

M.R. Zachariah
Department of Chemical and Biomolecular Engineering and Department of Chemistry and Biochemistry, University of Maryland, College Park, Maryland, United States

Vladimir E. Zarko
Voevodsky Institute of Chemical Kinetics and Combustion, Siberian Branch of the Russian Academy of Sciences, Novosibirsk, Russia; Tomsk State University, Tomsk, Russia

Feng-qi Zhao
Science and Technology on Combustion and Explosion Laboratory, Xi'an Modern Chemistry Research Institute, Xi'an, China

Peng Zhu
Micro-Nano Energetic Device Join Laboratory, School of Chemical Engineering, Nanjing University of Science and Technology, Nanjing, Jiangsu, China

PREFACE

This book presents reviews of the results of studying the transformations in nanoenergetic materials. The term *nanoenergetic materials* is used here to characterize the energetic materials or energetic systems, containing or consisting of nanocomponents. This is a relatively young but very promising field of research, and expected results could lead to breakthroughs in the development of advanced explosives, propellants, and microenergetic devices. Common advantages of nanoenergetic materials are their great reactivity and ability of very fast chemical transformations.

From the beginning, the most developed nanoenergetic materials were based on nanometals. Those materials are produced now by different methods in several countries and their production reached a relative maturity. Another direction of research is based on studying the nano-oxides, which have found wide application as catalysts in solid propellants as well as in pyrotechnic compositions. Those compositions may demonstrate extremely high combustion propagation rates comprising few km/s. Energetic nanocomposites can find also wide application in mini rocket motors and in different types of microchips.

Evidently, efficient realization of unique properties of energetic nanomaterials can be performed only based on studying the intrinsic mechanisms of the reactions in solids at the atomistic level. To acquire such knowledge, one needs to explore those mechanisms with use of advanced techniques and sophisticated approaches. Intense work in this direction is underway in many countries.

This book summarizes the recent achievements (since $\sim$2005) of the leading scientific groups working in the field of energetic nanomaterials in China, Germany, Israel, Italy, Russia, and the United States.

Chapter 1 presents a comprehensive review of the modern achievements in nanomaterials synthesis and application, emphasizing that the research in nanochemistry opened a bottom-up approach in the architecture of matter on a different spatial scale. This approach may provide effective tools for understanding the mechanisms governing the nanoenergetic materials properties, which would allow creating new energetic substances with well-tailored chemical and physical properties.

Chapter 2 focuses on developing a better understanding of fundamental reaction dynamics associated with particulate media. New strategies for designing aluminum fuel particles with greater reactivity and faster reacting formulations are presented. In addition to synthesis, several combustion characterization techniques are examined to quantify the combustion performance.

A survey of nanometals (mostly produced by electrical explosion of wires) usage in different energetic systems with the focus on nanometals combustion efficiency is

presented in Chapter 3. The chemically reacting systems containing nanoaluminum exhibit improved kinetic characteristics in ignition and burning rate behavior for propellants, explosives, and thermites.

In Chapter 4, the authors provide an overview of the three main components of the combustion of aluminum nanoparticle-based energetic materials: heat transfer mechanism, effect of the oxide shell, and reaction pathway. They note many experimental challenges that limit the understanding of the reaction mechanisms and give some recommendations for the future research activities.

Nanocatalysts, including metal nanoparticles (Ni, Cu, Al), metallic oxide nanoparticles (Fe_2O_3, CuO, Co_2O_3), and nanoparticles of hydrides (LiH, MgH_2, Mg_2NiH_4, Mg_2CuH_3), are discussed in Chapter 5. The catalytic impact of nanocatalysts on the thermal decomposition of AP and AP/HTPB as well on the combustion performance of AP/HTPB propellant is examined in detail.

The characteristics of coating aluminum particles by nanometric layers of nickel or iron are considered in Chapter 6. Coated particles ignite at a much lower temperature and exhibit shorter ignition times than uncoated ones due to exothermic intermetallic reaction between the aluminum and the coating metal and due to formation of a molten eutectic layer. Coated aluminum particles produce smaller size agglomerates than regular aluminum in combustion of metallized solid propellants.

In Chapter 7, research progress is reported on the synthesis, characterization, and energetic chip performance of multidimensional nanostructured energetic materials, including carbon nanotubes/KNO_3, CuO nanowires/Al, Ni nanorods/Al, Co_3O_4 nanowires/Al, Al/Ti multilayer film, Al/Ni multilayer film, CuO/Al multilayer film, porous copper/NH_4ClO_4, and porous copper/$NaClO_4$, 3D Fe_2O_3.

The characteristics of gasless metal–nonmetal and metal–metal nanostructured composite particles, prepared by high-energy ball milling, as well as of thermite-like metal–metal oxide mixtures of nanopowders are discussed in Chapter 8. Those reactive systems demonstrate extremely low ignition temperatures and very high reaction front propagation velocities that can be as high as 10^3 m/s. Efforts are made to explain the observed phenomena.

The catalytic effect of nano-oxides of Ti, Al, Fe, and Si on HMX thermolysis and combustion is discussed in Chapter 9. The point defects in the catalyst material are considered in the interfacial catalysis mechanism and it is shown that the presence of acidic or basic surface groups influences the space charges and thus the catalytic efficiency of listed nano-oxides.

Chapter 10 reports the data on the properties of carbon nanotubes (CNTs) supported metal (Pb, Ag, Pd, Ni) or metal oxide (PbO, CuO, Bi_2O_3, NiO) catalysts and their effect on thermal decomposition and burning rate of single, double-base, and composite modified double-base propellants. The synergistic impact of CNTs and metal oxide nanoparticles on the decomposition and combustion behavior of energetic materials is responsible for significantly enhanced combustion performance of those materials that makes them promising candidates for application in solid propellants.

The characteristics of oxide nanoparticles formed in combustion of aluminum and titanium microparticles are discussed in Chapter 11. Despite the distinctions in the mechanism of aluminum and titanium combustion, their oxide nanoparticles are of almost the same dimensions and display similar morphological and charge properties. The charging of metal nanoparticles due to thermoelectron emission plays a key role in oxide nanoparticles formation. The evolution of oxide aerosol particles is described, and some unresolved problems in studying the mechanism of nanoparticles growth are formulated.

Chapter 12 summarizes the recent efforts to incorporate the benefits of nanoscale materials to propellants without the drawbacks due to sintering the nanoparticles and increasing the viscosity of propellant slurry. One of the effective approaches is encapsulation of nanoscale materials into crystalline particles that for nanoscale catalysts show improved performance over direct physical mixing. Another approach is encapsulating the inclusion materials into metals, like aluminum, that may facilitate the ignition of metal particles and formation of smaller size combustion products since the particles fragment when heated.

Chapter 13 describes the advanced techniques and approaches for precharacterization of nanoparticles of Al used in condensed energetic systems. Different properties of various powders (passivated by air or organic compounds and coated by hydrocarbons and fluorohydrocarbons) are investigated. The presented results provide some insight into the relationships between nanosized additives' morphology/structure, oxidative reactivity, and propellant/fuel rheological behavior.

Each chapter was carefully edited according to the procedures employed by archival publications. Thus, the book can be considered as supplemental reading for students, researchers, and engineers in research centers and in industries dealing with energetic materials production, characterization, and applications.

Classification of the material presented in various chapters appears in the table.

Vladimir E. Zarko
Alexander A. Gromov
July 31, 2015

	Chapter												
Material or process	**1**	**2**	**3**	**4**	**5**	**6**	**7**	**8**	**9**	**10**	**11**	**12**	**13**
Nanoaluminum	+	+	+	+	+	+	+	+				+	+
Nanoaluminized propellants	+		+	+	+	+				+		+	+
Nanocomposites	+	+			+		+	+	+	+	+	+	+
Nanoexplosives	+		+						+				
Nanothermites	+	+	+	+	+	+	+	+					
Performance characterization	+	+	+	+	+	+	+	+	+	+	+		+
Synthesis of nanomaterials	+	+				+	+	+		+	+	+	

CHAPTER ONE

Nanoenergetic Materials: A New Era in Combustion and Propulsion

Vladimir E. Zarko
Voevodsky Institute of Chemical Kinetics and Combustion, Siberian Branch of the Russian Academy of Sciences, Novosibirsk, Russia; Tomsk State University, Tomsk, Russia

1. INTRODUCTION

The nanoworld corresponds to the place where self-arrangement of atoms leads to formation of chemical substances. The "nano" concept, which includes nanoscience and nanotechnology, was introduced in the middle of the twentieth century. The Nobel Prize winner Richard Feynman declared (in 1959) in a lecture entitled "There is plenty of room at the bottom" that no law of physics forbids the devices construction of few atoms size. However, to be correct, mankind actually had deal with nanomaterials many centuries earlier. Examples are the Lycurgus Cup (British Museum, London, 400 AD), church windows made of molten glass with embedded gold nanoparticles ($\sim$500 AD), daguerreotype photography (1839), etc.

In recent years, new nanomaterials have been intentionally fabricated, novel nanotools have been developed and old ones industrially implemented, and novel properties of matter at the nanoscale level have been discovered. For these reasons, nanoscience and nanotechnology should not be seen as entirely new but rather as "work-in-progress science." Nanotechnology should be seen rather as an evolution, not a revolution.

The definition of nanomaterials is somewhat arbitrary and can be based on different criteria. First of all, it involves a scaling measure and usually corresponds to submicron sizes. Normally, in different fields of science and technology various subdivisions of length are used to define coarse and fine particles. Typically, 100 nm is accepted as a boundary between the fine and nano size particles [1]. However, one may define this boundary as corresponding to sharply changing the physical properties, e.g., melting temperature. Such a boundary depends on the nature of the substance, and for aluminum (Al) it is about 15 nm, for gold (Au) about 50 nm, etc. Another approach can be based on the changes in reactive properties; for energetic materials, the nanoscale typically starts at 100 nm, at which the noticeable acceleration of ignition and combustion reactions is realized [2]. Thus, when discussing the issues about nanoparticles properties and their behavior, one has to consider a particular definition of nanoscale.

Energetic Nanomaterials
ISBN 978-0-12-802710-3, http://dx.doi.org/10.1016/B978-0-12-802710-3.00001-5

Nanotechnology manipulates matter for the deliberate fabrication of nanosized materials. Therefore, the definition of nanotechnology generally includes "intentionally made nanomaterials," with the nanomaterials being the objects that have at least one dimension in the nanometer scale. It has been underscored in a comment by S. Pearton [3], that nanotechnology, as any new innovation, is developing in a typical manner while passing through different periods, including pre-buzz, buzz, rave reviews, saturations, overhyped, backlash, and backlash-to-the-backlash. This can be depicted as a prognostication diagram having a sine form with the first maximum at saturation point and minimum in backlash point. Various technologies have their own situation according to this "Florida law of original prognostication," and in the case of biomaterials, it seems that they are at the initial peak of their potential. The situation with nanoenergetic materials has been ingeniously described recently by M. Zachariah [4]. He underlined that the interest in these materials lies in fundamental thermodynamic limitations obtained from using traditional CHNO systems. Researchers and engineers have a clear understanding that typical CHNO-based chemical systems are near the limit of stored chemical energy. Potential benefits of using nanoenergetic materials are their high volumetric energy density and the capability to produce environmentally benign products as well as controlled rate of energy release and reduced sensitivity. This made reactive nanocomposites an attractive material for wide applications, including environmentally clean primers, detonators, improved rocket propellants and explosives, thermal batteries, and many others.

In the past, there was great expectation of the probable presence of significant excess energy associated with high compressive forces in small size particles. Later it was revealed theoretically and experimentally that there is no noticeable advantage to the nanoscale that corresponds to practical applications (30–100 nm). At the same time, there was the expectation that the close proximity (a few angstroms) between the fuel and oxidizer components in energetic material would result in a strong acceleration of chemical reaction rate that could be called "nanoenergetics." These expectations have been justified, but only partly, because the experimentally observed effects were less than expected. As stated in Ref. [4], "we still do not have a good conceptual grasp of many of the initiation and propagation processes in such systems, which are significantly more heterogeneous than the molecular counterparts." Therefore, the community must pay attention to elaboration of fundamentals of the above processes in order to get answers to the question, how to make a good nanoenergetic composite?

There are some unique examples of obtaining nanoenergetic materials with an extremely fast burning rate that can be used in different applications. For example, a burn rate reaching a value of over 3000 m/s was achieved in samples of porous silicon films impregnating in nanoscale pores with sodium perchlorate [5].

It is also necessary to note that nanoenergetics, as any modern technology, gave birth to fears related to negative and dangerous consequences of its application, which

were discussed in a special issue (#12, 2011) of the Proceedings of the French Academy of Sciences entitled "Nanosciences and nanotechnologies: hopes and concerns." Even if not considering different social aspects of such technology applications, it is worth mentioning that nanoparticles have to be processed with certain precautions because of their toxicity and great ability to penetrate living bodies (carbon nanotubes have been found in the brains of exposed mice), as well as of enhanced pyrophoric and energy impact sensitivity [6,7]. It is important to emphasize that until now, at least in Europe, legal texts dedicated to specific fields of objects of nanoscience and nanotechnologies do not exist. One of the reasons is that scientific knowledge about professional risks in many cases is uncertain. According to the European definition, nanoscience "concerns the study of phenomena and manipulation of materials at atomic, molecular and macromolecular scales, where properties differ significantly from those at larger scale."

Risk aspects have to be taken into account when establishing new legislation for nanotechnology and they have be the basis for any definition used for regulatory purposes [8]. There were some discussions in this respect related to the question whether there is a potential release of nano-objects that are the subject of investigation in nano safety research. From a regulatory point of view, the materials where the nanoscale structure does not result from discrete particles and when no risk exists if nano-objects could be released should not be considered as nanomaterials. Definitions of nanomaterials have to reflect this difference when formulating new nanotechnology legislation. Actually, regulation of nanomaterials should focus on nano-objects as concluded in the report by the European Commission Joint Research Center [9].

Nanostructured energetic materials have nanoscale structures at least in one dimension. Small critical diameter, high reaction rate, and great released heat allow those materials to fit well for explosive chips. Physical modeling and simulation in the area of nanoscale composite energetic materials is continuously under process. The situation is permanently improving, and the methods of preparation and characterization of energetic nanomaterials have become more and more sophisticated and efficient. This chapter discusses some recent developments in this area as well as possibilities for future research. The peculiarities of ignition and combustion mechanisms of individual metal particles as well as composite nanosystems and some methods of preparing the compositions with unique properties are of great interest.

Several authors have stated that the exact physical mechanism for nano-Al particles ignition is currently unclear. The main reason is the lack of available commercial experimental techniques because it is difficult to design experiments to record physical changes occurring with particles of nanosizes at heating rates reaching $10^6 \div 10^8$ K/s. Additionally, while use of tiny particles increases specific surface area and reduces length scales between fuel and oxidizers, it also limits the ability of probing reactions at the scale on which they occur.

Along with the detailed research on Al-based reactive nanomaterials, essential progress has also been made in creating improved quality high explosive materials. It was recently shown that explosives' sensitivity to external stimuli decreases with decreasing crystal size. This gave a start to work on the synthesis of nanocrystals of different explosives (like RDX, HMX, CL-20, TATB) by using evaporation-assisted and sol–gel techniques.

The following materials are only introductory and illustrative in character and are not meant to be exhaustive. A large volume of information can be found in several reviews published recently [10–13]. In addition, some fresh information appears in the present volume. It must be mentioned that the usage of nanoenergetic materials has some advantages as well as drawbacks. The latter relate mostly to the problems of nanomaterials handling and preparation of the mixtures on their basis. These are briefly listed in the following sections. Prospective applications and possibilities for future research are also discussed.

2. COMBUSTION OF Al NANOPARTICLES

2.1 Heat Transfer of Nanoparticles

Recent studies of nanoaluminum particles combustion [14] revealed some peculiarities of heat transfer indicating the overestimation of heat losses from nanoparticles in surrounding gas during combustion. For nanoscale particles, the Knudsen number ($\mathrm{Kn} = 2\lambda/d$, where λ is the mean free path of the molecules in the gas and d is the particle size) effects have to be taken into consideration when this number becomes $\mathrm{Kn} > 10$. In such conditions the noncontinuum heat transfer expressions must be used to describe heat losses from particle to ambient gas. However, it was found that the formal application of these expressions gives the burning time values, which are two orders of magnitude shorter than experimentally observed. This finding means that for correct description of heat transfer of nanoparticles it is necessary to use proper energy accommodation coefficient and reasonably low values of sticking probability for collision of oxygen molecules in reaction with the aluminum surface. For example, in the shock tube experiments [14] with nanoaluminum particles of 80 nm size, the measured burning time was found to comprise 124 μs instead of 1 μs estimated by formal calculations. To fit with a theoretical estimate, the authors used the value of energy accommodation coefficient equal to 0.0035 and sticking probability equal to 0.0009. They concluded that at high ambient temperatures existing in the shock tube experiments, the nanosized metal particles experience a sort of thermal isolation from the surrounding gas. This effect has to be taken into account when modeling metal nanoparticle combustion.

2.2 Effect of Oxide Layer

It is well known that the presence of an oxide layer significantly reduces the amount of active metal in nanoparticles. For example, in the case of a 3 nm thick oxide layer, the content of active metal equals 99.9% for 30 μm size particles and only 51% for 30 nm size particles. That is why numerous efforts were directed in recent years toward the development of methods to synthesize metal particles without a passivating oxide layer. An advanced method for protecting active metal against oxidation in air might be use of organic self-assembling monolayers, which are densely packed organic films organized on a material surface via chemisorption of a molecular amphiphile [15]. It was expected that in the case of one organic molecule thick layer "the contamination" of metal particle would be extremely small. However, in practice the content of active aluminum in the particles of 80–100 nm size passivated by perfluoroalkyl carboxylic acid ($C_{13}F_{27}COOH$) became equal to 23–25% only [16,17]. This is despite the total absence of oxide layer on the metal particle that resulted from using a wet chemistry technique with coating of metal in solution.

Another method of passivating nanometal particles has been suggested in Refs [18] and [19]. The original nano-Al particles of 50 nm size were produced by Gen–Miller flow-levitation installation [20] via metal evaporation and following condensation in a mixture of hexamethyldisilazane vapors with argon. This resulted in formation of trimethylsiloxane coating on Al nanoparticles with a small change in particle size—from 48 to 54 nm. Surprisingly, the content of active Al was found to increase only to a very small extent—from 72.5% for oxide coated to 74.5% for polymer coated. This small difference in active Al content remained in both types of particles after 60 days storage (64.4% for oxide coated and 66.6% for polymer coated).

The above information demonstrates great technical difficulties in passivating the surface of metal particles without loss of the content of active metal.

2.3 Effect on the Burn Rate and Performance of Solid Propellants

One of the first applications of nanometal particles as energetic material was using them in solid propellants. It was expected that the replacement of micron-sized Al in propellant formulation would result not only in enhancement of burning rate but also in decreasing the dependency of the burning rate on pressure. Pioneering data obtained in the 1960s at the Institute of Chemical Physics (Moscow) demonstrated that the burning rate of composite propellants based on ammonium perchlorate and bitumen binder with total replacement of 13 or 31% of 15 μm Al by nano-Al (Gen–Miller type, 90 nm) was really increased by about 50%, but the pressure exponent in the burning law was also increased by about 10% [21]. In the following years when obtaining first the electroexploded nano-Al particles, the researchers assumed the presence of additional

heat of formation contained in submicron metal particles that can be employed for enhancement of the energy content of propellant. The idea of the existence of energy excess (up to 400 cal/g) in aluminum nanoparticles was proposed in Ref. [22]. Later on, this effect was studied in detail in Ref. [23]. It was revealed in differential thermal analysis experiments that for Al (50–100 nm) nanoparticles produced by the wire electroexplosion method and aged for 0.5–1.5 years, any effect of stored energy could not be detected. The recorded weak exothermic peak at 580 °C is associated with the oxidation of the particles due to the presence of small amounts of oxygen impurities in the purge gas (argon or helium), and also with the possible effect of adsorbed air. It has to be noted that the effect of stored energy should be manifested in the value of the specific impulse of the solid propellant. However, an increased amount of oxide in nanosized Al particles can reduce and mask this effect. Therefore, its detection requires specialized detailed measurements that can be performed in the future.

Another expectation related to using the ultrafine Al particles was decreasing the pressure exponent in the propellant burning law. Numerous previous attempts to realize decreasing pressure exponent in experiments with partially replaced micron-sized Al in solid propellants failed [24–26]. Those experiments established that the heat release in the condensed phase in fact becomes significantly higher in the presence of nano-Al particles, which results in increasing the magnitude of the burning rate but does not decrease its pressure exponent. Note that when replacing micron-sized Al with the oxide-coating nano-Al, the total energy content in solid propellant decreases due to enhanced content of Al_2O_3 in nanoparticles (the smaller particle size, the higher oxide fraction). This leads to decreasing the performance efficiency of solid propellant. By calculation, in the case of model propellant formulation (70% ammonium perchlorate and 15% energetic binder) containing 15% Al, the replacement of ordinary 15 μm size Al (99.5% of active metal) by 80 nm Al (82.3% of active metal) should lead to decrease in the value of specific impulse from Isp (15% Al) = 266.6 s to Isp (12.3% Al) = 260.6 s. These values are estimated for the chamber pressure 40 atm and nozzle exit pressure 1 atm.

A specific drawback of using the nanometal particles is that due to their large specific surface, the viscosity of propellant slurry at the particles contents exceeding 10% weight becomes too high and prevents application of casting technology in production of solid propellants. Studies of the rheological characteristics of HTPB-based suspensions filled with aluminum nanoparticles of Alex type (80–100 nm) have shown that the viscosity of the suspension $\eta_{\mathrm{rel,Alex}}$ is related to the volume concentration C_v of the solid additive as follows [27]:

$$\eta_{\mathrm{rel,Alex}} = \eta_{\mathrm{suspension}}/\eta_{\mathrm{HTPB}} = 1 + 5.5\,C_v - 31.4\,C_v^2 + 74.5\,C_v^3$$

This equation is valid for volume concentrations of metal nanoparticles $C_v < 50\%$.

2.4 Effect of Nanosized Particles Sintering

Some fresh results obtained experimentally and theoretically [28,29] demonstrate the fact of fast sintering of particles aggregates into bulk alumina in conditions of fast heating rate. Thus, questions are raised about "effective" particle size during ignition and combustion of ensemble of nano-Al particles. The reactive molecular dynamics calculations carried out in Ref. [30] showed that upon rapid heating of aluminum core/oxide shell particles the melted core Al atoms diffuse outward into the oxide shell, which is driven by an induced built-in electric field. It leads to the melting of oxide shell at temperatures much lower than the oxide melting point and to sintering of the particles due to action of surface tension forces. Importantly, the characteristic sintering time according to calculations is even shorter than the reaction time. This may qualitatively explain why the experiment does not give an extremely short burning time for very small Al particles.

3. COMBUSTION OF NANOTHERMITE COMPOSITIONS

Nanopowders are often used to produce so-called metastable intermolecular composites (MICs). These are mixtures of nanosized reagents that are stable under normal conditions and capable of interacting with each other with the release of large amounts of energy after activation by a triggering stimulus (thermal, mechanical, or electrical). Examples of such MICs are mixtures of nanoparticles of metals such as Al, Mg, Zr, Hf, etc., and nanoparticles of metal oxides (Fe_2O_3, MoO_3, Cr_2O_3, MnO_4, CuO, Bi_2O_3, and WO_3). It is known that in the case of classical thermites, the combustion reaction is slow due to the relatively slow diffusion process. When the reagents are in the nanoscale, the diffusion path is much shorter and the reaction rate is increased significantly as compared with the reaction rate of conventional thermites. Additives of polymer materials or binders or gas-generating agents to metal and metal oxide–based MICs are able to provide the necessary working body during combustion. An area of particular interest is the use of MICs in microscale motors. This is related to the development of microscale propulsion systems and the use of these energetic materials in micromotors and even small spacecraft. Supposedly, such mixtures could find application as the gas-generating compositions. They can combine high-energy characteristics with unprecedented stability, safety, and an opportunity to precisely control the burning rate in a wide range through the regulation of granulometric composition. In the case of nanothermites, due to fast reactions the energy losses to the combustor wall are negligible. For example, the burning rate of MoO_3–Al nanothermite, prepared by mechanical mixing of 79 nm aluminum particles and 30×200 nm MoO_3 flakes reaches 790 m/s in a metal tube of 0.5 mm diameter. This composition is considered a promising base for microscale rocket propellants [31]. Other possible applications of nanoscale MICs are ammunition primers and electric matches [32].

3.1 Methods of Preparing MICs

There are several advanced technologies for mixing nanoenergetic materials, such as ink-jetting, vapor deposition processes, cold spraying, etc. Three technological approaches to producing different MICs are widely used: mechanical stirring, arrested reactive mixing, and sol–gel technology. The first approach is the simplest and most common method of production of nanothermites. Nanopowders of metal oxides and a fuel are mixed in a volatile inert liquid (to reduce the static charge) and treated with ultrasound to ensure an even distribution of the components and their deagglomeration. After evaporation of the liquid, the thermite is ready to use. The technology of mechanical mixing is suitable for almost all thermite systems, and its simplicity makes it widely used. Its main drawback is the need to use nanoscale starting materials.

Arrested reactive milling is based on the use of ball mills and vibratory ball mills. The method involves co-milling of the metal oxide and aluminum. The component particles may be both nanosized and micrometer sized. In the course of milling, the particles are mixed to form nanocomposite particles in which fuel and oxidizer are contained in the same particle. The particles produced by that technology are in the size range of 1–50 nm and consist of layers of metal (e.g., Al) and oxidizer, about 10 nm thick. Particle size is a function of the milling time, but because of the high reactivity of the mixture, after some time of treatment (depending on the initial particle size, type of the components, and the milling medium) when the particles are reduced below a certain size, the ignition of the mixture may occur. The term *arrested reactive milling* implies that grinding is stopped before the moment of ignition of the mixture. Advantages of this method are: the possibility of using initial micrometer-sized particles; production of nanocomposite particles with density approaching the theoretical value; highly reduced presence of metal oxide because of the effect of encapsulation of the metal in the particle matrix; and precise control of the degree of mixing and, hence, reactivity by changing the milling time. The main disadvantage of the method is that only a few thermite mixtures can be prepared by this method as most mixtures are too sensitive and ignite before sufficient mixing is achieved.

The sol–gel method of obtaining nanostructured materials implies the processes where reactive precursors (monomers) are mixed into solution in which polymerization occurs, leading to the formation of a three-dimensional highly cross-linked solid network that results in a gel. The gel is then dried using supercritical extraction to produce samples of highly porous low-density aerogel or to produce xerogel by controlled slow evaporation. Energetic materials can be incorporated during the formation of the solution or during the gel stage of the process. The composition and size of the primary particles, the time of gel formation, surface area, and density may be tailored and controlled by methods of solution chemistry. An important area of application of the sol–gel methods is the synthesis of nanostructured metal oxides,

which are used for obtaining different MICs (mainly metal/metal oxide nanothermites). These methods can be used to synthesize nanostructured oxides of various metals and metalloids: Fe, Cr, Al, Ga, In, Hf, Sn, Zr, Mo, Ti, V, Co, Ni, Cu, Y, Ta, W, Pb, B, Nb, Ge, Pr, U, Ce, Er, and Nb [33]. To obtain energetic nanocomposites containing metal oxide and metal, powdered metallic fuel needs to be introduced into the sol before the beginning of gelation, when the viscosity starts to increase rapidly. In this way, it is possible to obtain a metal oxide gel matrix with uniformly distributed Al particles. When other substances are used as the fuel, agglomeration of the particles can be prevented by ultrasonic agitation. The advantage of sol–gel methods is the broad range of materials used and relatively high productivity.

3.2 Understanding the MICs Reactive Mechanisms

Over the last three decades there has been significant growth in understanding the ignition and combustion mechanisms of nanothermites and other nanoenergetic materials. However, there is still much that is unknown about the physics and processes that control these highly exothermic reactions. The role of metal oxide oxygen release in the phenomenon of nanothermites ignition was discussed in Ref. [34]. In that work, the advanced experimental approach was used, which included simultaneous use of time-of-flight mass spectrometer, optical emission, and T-jump heating units at heating rates up to 10^5 K/s. The reactions of type $2Al + 3MO \rightarrow Al_2O_3 + 3M + \Delta Q$ were studied (MO = metal oxide). It was found that the oxygen produced by decomposition of MO particles plays an active role in the reaction. Experiments with different oxides like CuO, Fe_2O_3, and ZnO showed that the reactivity of the Al/MO pair directly depends on the capability of oxygen release from oxide particles. Therefore, higher reactivity of Al/CuO mixture can be attributed to the higher oxygen release rate as compared with the lower release rates for Fe_2O_3 and especially ZnO. Time-resolved mass spectrometry records of formation of Al suboxides (AlO and Al_2O) show that the reaction of Al oxidation does not follow thermal equilibrium calculations, indicating that the system is far from equilibrium. Supplementary records by high-speed X-ray movie (135,000 fps) confirm that the oxygen releases prior to the ignition instant, indicated by temperature measurements. Actually, ignition temperature definitely correlates to instant of oxygen release from MO. At the same time, an original observation was made in experiments with Bi_2O_3. In the system Al/Bi_2O_3 it was clearly recognized that nanothermite reaction starts before the oxygen is released from the neat Bi_2O_3. It suggests the condensed phase reaction of liquid Al with oxygen ions formed in melted Bi_2O_3 and then transported to the surface of Al particles. It is stressed that these reactions may play a more significant role than it was previously expected. Later on, the same authors' team published an article in a special issue of *Combustion and Flame* [35] that generalized the experimental data regarding the mechanism of condensed-phase

reactions of Al with different metal oxides, which proceed simultaneously with the reactive sintering. As was mentioned in an editorial comment to this issue [36], the results suggest that condensed-phase reactions may be more prominent than previously thought. Additional evidence of the presence of developed condensed-phase reactions in ignition and combustion of nanothermite materials were presented recently in Refs [37] and [38]. The comprehensive review of state-of-the-art formulation of the reaction mechanism of nanothermites is presented in the Chapter 4 by M. Zachariah and G. C. Egan in this volume.

4. COMBUSTION OF NANOEXPLOSIVES

4.1 Carbon Nanotube Supported Explosives

Nanostructured energetic materials are a new concept composite powder, which can dramatically improve the performance of gunpowder and explosives. The combination of nanocrystals of explosives and nanoporous substrates makes the composite products possess original properties and unique parameters. Following are some examples of recently reported research results obtained in experiments with nanoexplosives.

One of the first attempts to control the combustion properties of a high explosive in the nanostate is reported in Ref. [39]. A porous chromium(III) oxide matrix was impregnated by RDX (hexahydro-1,3,5-trinitro-1,3,5-triazine). The reactivity and sensitivity of Cr_2O_3/RDX nanocomposites were studied by impact and friction tests, differential scanning calorimetry, and time-resolved cinematography. It was found that the size of RDX nanoparticles and their distribution in the Cr_2O_3 matrix have an important influence on their reactivity, which differs significantly from those of micron-sized RDX. In particular, in the nanocomposites with the RDX contents between 6.2% and 80%, the decomposition starts before the melting point of RDX. This means that the thermal decomposition of nanometric RDX proceeds with decreased activation energy. It was also found that for an RDX content of 14.3–42.0%, the nanocomposites are less sensitive to impact than pure RDX. Note that in this case the explosive layer is not continuously distributed on the Cr_2O_3 surface, while with higher RDX content (42.0–95.0 wt%) it covers all Cr_2O_3 surface that results in increased sensitivity as compared with pure RDX. However, at highest RDX content (>95%), the same as RDX impact sensitivity has been detected. The combustion of nanocomposites with relatively low RDX content (14.3% and 25.0%) is very irregular, and it stops when cutting the laser irradiation. Self-sustained combustion after laser cut-off is realized for the RDX-rich nanocomposites (40–95%). The burning rate decreases when RDX content increases.

Observed RDX reactivity behavior correlates well with the morphology of explosive material distribution in Cr_2O_3 matrix. At low RDX contents (<10 wt%), the

resulting RDX particles are separated from one another and are typically of 10 nm size. The decomposition proceeds in one step, and the composition is very insensitive to impact and friction stress. With increased RDX content (10–40 wt%), the deposited explosive particles are on the surface of the chromium oxide rods but they are still discontinuous and nanometric size. The decomposition proceeds in two exothermic stages before an RDX melting. The combustion is not self-sustaining, and there is no transition to detonation. At RDX content between 40% and about 75%, the surface of the oxide pores is totally covered with an explosive layer. The composition undergoes a self-sustained combustion, and it can detonate in a confined space. Finally, for RDX content higher than 75%, the explosive layer surrounds the Cr_2O_3 core, and the properties of composition approach those of pure RDX.

Another example of unique properties of nanostructured EMs was described recently in Ref. [40]. It was demonstrated that a self-propagating reactive wave moving faster than 2 m/s can be realized using 7 nm RDX annular shell around a multiwalled carbon nanotube (CNT). This burning rate exceeds more than 10^3 times the value for bulk RDX at atmospheric pressure. It was found that the burning rate increment depends on the structure of carbon nanotube. The effect is higher in the case of 10 walls nanotube (22 nm tube diameter) as compared with that for 9 walls nanotube (13 nm).The reaction also evolves an anisotropic pressure wave of high total impulse per mass (300 N-s/kg) and produces a concomitant electrical pulse as large as 7 kW/kg. The physical reason for unusual combustion behavior of coated CNTs is extremely high thermal conductivity of CNT, which may reach the value of 3500 W/m-K at room temperature that is more than 80 times larger than that for the best conductor Ag (430 W/m-K).

Unfortunately, there are great problems with scaling of discovered effects. Actually, with larger system size the effects become much less and special efforts have to be undertaken in order to provide practical feasibility of new phenomena. There are also some technology issues because of heterogeneities in the thickness of carbon nanotubes as well as the RDX coating, leading to irregular performance along axial position of the composites.

The continuation and further development of this direction of research was made with single-walled CNT coated with chemically bonded energetic material [41]. Using diazonium chemistry, a series of nitrophenyl-decorated CNT composites have been synthesized. The intention was to explore coated CNT, which may release energy in a controllable manner, and to investigate the effect of thermal conductivity of CNT on the rate of explosive reactions. It was established that diazonium chemistry is an efficient scheme to attach energetic molecules (Nitrobenzenes) onto CNT surface homogeneously with high density. It was found that chemically bonded composites release energy at low temperatures over physically mixed ones (T_{max} heat release = 373.6 °C

against 280.3 °C) and the composites with highly conductive CNT exhibit explosive behavior at lower temperatures. In addition, it was concluded that the better performance is demonstrated when composites are made in vertically arrayed structures with "metallic" conductivity CNT.

The original attempts of using multiwalled carbon nanotubes as support for incorporating the polynitrogen, N_8, were made in Refs [42] and [43]. The N_8 possesses giant heat of formation, $H_f = +3630$ cal/g, exceeding greatly that of the best explosives (HMX ~ +91 cal/g). It is a known fact that pure polynitrogen systems are metastable, but advanced theoretical studies showed that when a polymeric nitrogen chain is encapsulated in a carbon nanotube, it can be stable at ambient pressure and room temperature, which makes such composites promising nanoscale energetic material. Actually, clear evidence of polynitrogen atoms presence in carbon nanotubes has not yet been found. According to experimental data of Ref. [43], the content of nitrogen atoms in carbon nanotubes can vary in the range 1.7–4.0%, and nitrogen exists in the form of pyridine-like, graphite-like, oxidized nitrogen and nitrogen physisorption layer. The results of experimental studies state that it is possible to obtain nitrogen-doped carbon nanotubes with controlled concentration and structure. This may provide the development of novel nanoenergetic materials.

4.2 Porous Silicon Impregnated Composites

Porous silicon (PSi) was discovered first as a reactive material when it was tested in combustion studies being immersed in nitric acid [44]. The electrochemical etching of bulk silicon in solutions containing fluoride (e.g., HF) can be used to produce PSi. It allows adjusting the pore sizes in the range from 2 to 1000 nm by selecting suitable etching parameters. Then the nanopores can be filled with a liquid oxidizer ($Ca(ClO_4)_2$, $KClO_4$, $NaClO_4$, etc.). The potentialities of PSi as fast-burning energetic material were well established in Ref. [5], when ~65–95 μm thick PSi films composed of pores with diameter less than 3 nm were fabricated using a galvanic etching approach. The nanoenergetic composite was then created by impregnating the nanoscale pores with sodium perchlorate ($NaClO_4$). The combustion propagation speed was measured using specially fabricated diagnostic tools in conjunction with high-speed optical imaging up to 930,000 fps. For PSi films with specific surface area of ~840 m^2/g and porosities of 65–67%, the measured burning rate reached 3050 m/s.

Even faster propagation speed up to 3660 m/s, which is at present the highest reported flame speed for available nanoenergetic systems, was recorded in specially fabricated channeled porous silicon [45]. It was found that the mechanism of enhancement of flame propagation rate in channeled porous silicon is different from the convectively controlled combustion in original porous silicon. The aim of the study was to relate the speed of sound to events where a flame jumped ahead of the primary, visible reaction front. Supposedly, there exist acoustically aided reactions in porous silicon

channel combustion and the channels more readily ignite compared to original porous silicon. It is believed that acoustic waves traveling through the porous silicon film can carry enough energy to ignite the sensitive PSi channel structures and propagate the reaction.

Detailed study of the mechanism of propagating the reactive waves through porous silicon-sodium perchlorate composites was undertaken in Ref. [46]. The speeds of propagation were varied by changing specific surface area (SSA) of the samples. The samples with relatively low SSA ($\sim$300 m^2/g) normally exhibited baseline speeds of $\sim$1 m/s while samples with high SSA ($\sim$700 m^2/g) exhibited fast reactive wave speed propagations of $\sim$1000 m/s. To study the effect of microscale structures on the reactive wave propagation, specially prepared samples were used consisting of an unpatterned and a patterned section. The patterned section contained micron-sized square pillars and microchannels. The samples were ignited in the unpatterned PSi section and the reactive wave propagated into the patterned PSi. Shadowgraph records showed that upstream permeation of hot gaseous combustion products was responsible for a two order of magnitude enhancement in the reactive wave propagation speed obtained by the presence of organized microscale patterns on PSi. It was also taken into account that the oxidation of silicon atoms in the nanoporous structure results in a volume expansion, which can initiate cracks formation. The experiments indicated that a combination of conductive and convective burning, possibly assisted by fast crack propagation within the silicon porous silicon substrate, was responsible for the observed difference in propagation speeds and was the mechanism by which the reactive wave propagated with the speed on the order of a km/s within the porous layers.

The very specific application of energetic nanocrystalline porous silicon was demonstrated in Ref. [47]. It was shown that upon igniting the impregnated porous silicon by an electrical current passing through 100 nm thick aluminum film deposited on the unpolished side of the wafer, the ignited sample causes strong explosion, which destroys the explosive chip into small fragments. Use of such a system allows obtaining the explosion impulse, which may reach about 140 mN-s. In fact, this value is two orders of magnitude larger of impulse produced by conventional propellants [48] (about 0.1–6 mN-s for conventional propellants such as lead styphnate or ammonium perchlorate). Moreover, via stacking three porous silicon chips together, it becomes possible to get an explosion impulse of 0.25 N-s, which allows propelling a 30 g object up to 3 m high.

5. EXPERIMENTAL METHODS TO CHARACTERIZE NANOENERGETIC SYSTEMS PERFORMANCE

A wide set of advanced experimental methods and tools are used in characterization of nanoenergetic systems. These include fast video and X-ray filming, time-of-flight mass

spectrometry, optical emission measurement, ion-focused tomography, etc. An important feature of listed methods is extremely high space and time resolution. Some examples of contemporary approaches are presented herein.

The exploration of structural properties of explosive materials takes using methods with the length scales spanning several orders of magnitude, from just under 10 nm to at least 10 μm. Those methods can be used for determining the sizes of nano- and microparticles as well as the sizes of pores and total porosity of the samples. In Ref. [49], a rich combination of the methods has been employed to characterize triaminotrinitrobenzene (TATB)-based explosives. It included ultra-small angle X-ray scattering, ultra-small angle neutron scattering, and X-ray computed tomography. Ultra-small angle X-ray scattering (USAXS) allows determining structural inhomogeneities from a few nanometers to a few microns scale. Ultra-small angle neutron scattering (USANS) bridges the gap between USAXS and imaging techniques, and extends the sensitivity of scattering to about 10 μm. Synchrotron-based X-ray microtomography allows imaging the low-z materials with reasonable contrast from a few microns to about 1 cm. In particular, USAXS explored the smallest voids including hot-spot voids from hundreds of nanometers to a few microns, and it was found that upon temperature cycling the number of these voids increases and size distribution shifts toward larger sizes. These derived data give important information used for better understanding of microstructural mechanisms affecting the mechanical properties of explosives and can be used as empirical input to computational models of detonation. The goal of such research is to determine the relationship between the voids and microstructure and their effect on detonation properties.

Similar information about the porosity and pores size distribution has been obtained in Ref. [50] with use of computer-aided X-ray microtomography. These data were used to correlate the laser initiation thresholds with microstructure of samples of furazanotetrazine dioxide and dinitrodiazapentane mixture, which depended on the conditions of crystallization of samples and mass ratio of components.

In Ref. [51], when studying the sensitivity of nanocomposite granules containing small RDX crystals, the method of focused ion beam (FIB) nanotomography with spatial resolution about 10 nm has been successfully employed. Using the estimates of theoretical maximum density, it was shown that most of the porosity comes from the voids with sizes less than 100 nm. It was stated that the low shock sensitivity is primarily due to the absence of large voids.

Original nanocalorimetry technique has been demonstrated in Ref. [52]. This technique allows measuring thermal effects upon heating with extremely high heating rate of the individual crystals of explosives of a few nanograms mass. Thermal sensitivity of the device comprises 10 microW, the maximal heating rate reaches 1 million K/s. The device can measure the heat of phase transitions and decomposition. The

preliminary tests were conducted with the single crystals of RDX, PETN, and CL-20 with mass of 7–30 ng at heating rates up to 2500 °C. The tests showed very peculiar thermal behavior of listed explosives at high heating rates, which will need to be examined in detail in the future.

6. CONCLUSION

Research in nanochemistry opened a bottom-up approach in the architecture of matter, from the atom to millimeter scale. The main idea in energetics is to enhance the surface area and intimacy between reactive components in order to increase the reaction rate and decrease the ignition delay. Existing lack of understanding of the underlying mechanisms stems from the difficulty of experimental observation of the nanoscale changes occurring in nanoenergetic materials in the very brief time scales associated with the rapid heating rates and high temperatures intrinsic to the reaction and combustion dynamics.

Obviously, the experiments in a vacuum, which prevent any significant heterogeneous gas-condensed phase reaction, can capture the interfacial condensed phase interaction of the nanoparticle systems without the convoluting effects of gas phase chemistry. The possible effects of gas phase chemistry and difficulties of interpretation of experimental data can be demonstrated in examples of measuring the displacement of the luminescent front in the plastic tubes filled with energetic material. It was shown in experiments [53] with loosely packed aluminum/copper oxide (Al/CuO) thermites in an acrylic burn tube, composed of fully and partially filled sections, that the velocity of the luminous front in unfilled regions approached 1000 m/s and was about 600 m/s in the filled region. In partially filled regions, the intermediate and product species expanded forward and completely filled the tube being heated to a temperature of about 3000 K. In the filled region, the temperature first increased to the value of 3200 K and then remained at 3000 K even after the front exited the end of tube. These results suggest that the luminous front may not represent the ignition of new material but rather that some reacting material part is propelled forward through the tube.

Qualitatively similar findings were obtained earlier in the burn tube experiments [54] with MoO_3/Al system. In the case of low-density samples of loosely packed nanoenergetic material, the high "burning rate" reaching 1000 m/s was experimentally recorded while for densely packed samples a moderate rate was recorded comprising $\approx$1 m/s, which was also typical of the systems with micron-sized powders. The results indicate that observed very high velocities of luminescent front propagation during combustion of nanoenergetic systems in thin channels are probably caused by the hot gas exhaustion and not by the kinetics of heterogeneous chemical reactions in

nanosystems. This shows that the question about significant differences (few orders of magnitude) in the reaction kinetics of nano- and microthermite systems remains open.

Note that extremely fast burning rates exceeding 3 km/s recorded in combustion of impregnated porous silicon materials may have objective meaning, but the controlling parameters of this process are not yet known in detail. Establishing the real reaction mechanism for nanoenergetic materials takes designing special experimental conditions and techniques. Recently, for the first time clear evidence of the fact that the major part of heat release in nano-Al-based thermite reactions is contributed by a condensed phase mechanism were obtained in very detailed studies [37] when various nanothermite combinations were ignited using rapidly heated fine wire. At the same time, practically the first direct evidence of the contribution of gas-phase oxygen on the ignition and combustion of nano-Al formulations was obtained in Ref. [55]. This work tested stoichiometric mixtures of nano-Al (50 nm) as fuel and nanoparticles of periodates (KIO_4, $NaIO_4$) sized 50–300 nm as oxidizer. The periodate particles were prepared by atomization of aqueous solutions with subsequent solvent evaporation. Analysis of experimental data on thermal analysis and temperature-jump wire heating showed that exothermic decomposition of periodate salts contributes to the low ignition temperature of nanoenergetic formulations. It was shown that the reaction mechanism of periodate salt-based nanoenergetic formulations differs from those of metal oxide nanothermites and provides higher rates of gas release and maximum pressure in the combustion cell as compared with traditional nanothermite (Al/CuO) and Al/$KMnO_4$ mixture. It was concluded that the gas phase oxygen released in decomposition of periodate salt is critical to the ignition and combustion of periodate nanoenergetic formulations.

When dealing with nanoenergetic materials, the question arises how to obtain the advantages of nanoscale compositions without the drawbacks related to technology limitations. One of the promising options might be use of micrometer-scale particles with nanoscale features. As an example, such materials were prepared by self-assembling the energetic compounds in mesoporous substrate [56,57]. For that, HNIW (CL-20) was first dissolved in acetone and entered the mesopores of linearly ordered mesoporous material SBA-15 by capillary forces. Then, with the evaporation of acetone, HNIW was self-assembled in mesopores via host–guest hydrogen bonds. The sizes of both the nanopores and nanocrystals of HNIW were of the order of 10 nm. The maximum content of HNIW comprised about 70 wt%. The thermal properties of nanocomposites were measured by DSC analysis. Compared with pure HNIW and a physical components mixture, the decomposition peak temperature of the confined crystals decreased by 11 °C, while the total amount of heat released slightly increased. Additional experiments showed that mesoporous carbons (like FDU-15) may also play a role of potential host. When FDU-15 is used, 2,4,6-trinitrophenol (TNP) can also self-assemble in mesoporous carbon nanochannels to form nanocomposites. The weight percent of TNP in nanocomposites can reach 66%. Such nanocomposites may have

great potential to be used in different applications as energetic fillings in various gas-generating propellants, in microexplosive devices, etc.

Original realization of idea of engineering the molecularly built energetic materials employing deoxyribonucleic acid (DNA), Al, and CuO has been demonstrated in Ref. [58]. The authors used the DNA "sticky properties" to graft strands of DNA onto nanoscopic beads of aluminum and of copper oxide and then mixed together the two types of nanoparticles coated with DNA strands. As a result, they obtained compact, solid material that spontaneously ignites when heated to 410 °C and releases heat up to 1.8 MJ/kg.

The above examples of creating new energetic materials with unique properties do not cover all fields of their application but clearly show the potential for utilization in various devices and installations. Due to high energy density and micro-electromechanical systems compatible fabrication methods, on-chip porous silicon compounds have considerable promise as an energetic material.

The nanoenergetic composites could also find applications as gas igniters in internal combustion engines or as fuel in aircrafts and space rockets, miniature detonators, on-site welding tools, as additives to propellants in rocket engines, etc.

There are still a number of unsolved problems in preparation and application of nanoenergetic materials. These relate, in particular, to the questions what is the role of the interface between reacting components and how to predict the reactive behavior in dependency of ignition method, and what is the relationship between nanoparticles size and the composites performance? To get answers, the results of the experimental studies have to be presented in a detailed and concise manner allowing comparison of materials prepared using different manufacturing approaches. Based on critical assessment of available information, it will be possible to construct ignition and combustion models and make reliable predictions of combustion and operational behavior.

The elaborated "bottom-up" approaches must provide efficient tools for better understanding the structural mechanisms governing nanoenergetic materials thermal properties. Such knowledge will allow the ability to create molecularly manipulated energetic substances and formulations having well-tailored chemical and physical properties.

ACKNOWLEDGMENTS

The work was partially financially supported from the Ministry of Education and Science of the Russian Federation within the framework of the Federal Target Program. Agreement No. 14.578.21.0034 (RFMEFI57814X0034).

REFERENCES

[1] G.P. Sutton, O. Biblarz, Rocket Propulsion Elements: An Introduction to the Engineering of Rockets, seventh ed., John Wiley & Sons, USA, 2001, 739 pp.
[2] S.S. Son, R.A. Yetter, V. Yang, Introduction: nanoscale energetic materials, J. Prop. Power 23 (4) (2007) 643–644.

[3] S. Pearton, The shifting tide of expectations, Mater. Today 10 (10) (2007) 6.
[4] M. Zachariah, Nanoenergetics: hype, reality and future, Propell. Exlos. Pyrotech. 38 (2013) 7.
[5] C.R. Becker, S. Apperson, C.J. Morris, et al., Galvanic porous silicon composites for high-velocity nanoenergetics, Nano Lett. 11 (2) (2011) 803–807, http://dx.doi.org/10.1021/nl104115u.
[6] J.-L. Pautrat, Nanosciences: evolution or revolution? C.R. Phys. 12 (2011) 605–613, http://dx.doi.org/10.1016/j.crhy.2011.06.003.
[7] S. Lacour, A legal version of the nanoworld, C.R. Phys. 12 (2011) 693–701.
[8] N. Muellera, B. van der Bruggenb, V. Keuterc, et al., Nanofiltration and nanostructured membranes – should they be considered nanotechnology or not? J. Hazard. Mater. 211–212 (2012) 275–280.
[9] G. Lövestam, H. Rauscher, G. Roebben, et al., Considerations on a Definition of Nanomaterial for Regulatory Purposes, JRC Joint Research Center, 2010, ISBN 978-92-79-16014-1.
[10] C. Rossi, K. Zhang, D. Estive, et al., Nanoenergetic materials for MEMS: a review, J. Microelectromech. Syst. 16 (4) (2007) 919–931.
[11] R.A. Yetter, G.A. Risha, S.F. Son, Metal particle combustion and nanotechnology, Proc. Comb. Inst. 32 (2009) 1819–1838.
[12] E.L. Dreizin, Metal-based reactive nanomaterials, Prog. Energy Combust. Sci. 35 (2009) 141–167.
[13] M.K. Berner, V.E. Zarko, M.B. Talawar, Nanoparticles of energetic materials: synthesis and properties (Review), Combust. Explos. Shock Waves 49 (6) (2013) 1–23.
[14] D. Allen, H. Krier, N. Glumac, Heat transfer effects in nano-aluminum combustion at high temperatures, Comb. Flame 161 (2014) 259–302.
[15] G. Smidt, Clusters and Colloids: From Theory to Applications, VCH, New York, 1994.
[16] L.H. Dubois, R.G. Nuzzo, Annu. Rev. Phys. Chem. 43 (1992) 437–463.
[17] R.J. Jouet, A.D. Warren, D.M. Rosenberg, et al., Surface passivation of bare aluminum nanoparticles using perfouroalkyl carboxyl acids, Chem. Mater. 17 (2005) 2987–2996.
[18] A.N. Zhigach, I.O. Leipunskii, A.N. Pivkina, et al., Aluminum/HMX nanocomposites: syntheses, microstructure, and combustion, Combust. Explos. Shock Waves 51 (1) (2015) 100–106.
[19] A.N. Zhigach, M.L. Kuskov, I.O. Leipunskii, et al., Preparation of ultrafine powders of metals, alloys, and metal compounds by the Gen-Miller method: history, current status, and prospects, Ros. Nanoteknolog 7 (3–4) (2012) 28–37.
[20] M.Y. Gen, M.S. Ziskin, Y.I. Petrov, Research of dispersion of aerosols of aluminum depending on conditions of their formation, USSR Acad. Sci. Proc. 127 (2) (1959) 366–368. See also, http://nanorf.ru/events.aspx?cat_id=223&d_no=4188.
[21] P.F. Pokhil, A.F. Belyaev, Y.V. Frolov, et al., Combustion of Powdered Metals in Active Environments, M:Science, 1972, pp. 238–251.
[22] G.V. Ivanov, F. Tepper, Activated aluminium as a stored energy source for propellants, in: Proc. 4th Int. Symp. Spec. Topics Chem. Propulsion, Stockholm, Sweden, May 27–28, 1996, pp. 636–644.
[23] M.M. Mench, C.L. Yeh, K.K. Kuo, Propellant burning rate enhancement and thermal behavior of ultra-fine. Aluminum powders (ALEX), in: Proceedings of the 29th International Annual Conference of Insitut of Chemische Techologie(ICT), Karlsruhe, Germany, 1998, pp. 30.1–30.15.
[24] A. Dokhan, D.T. Bui, E.W. Price, et al., A detailed comparison of the burn rates and oxide products of ultra-fine al in AP based solid propellants, in: 34th Int. Annual Conference of ICT, 2003. Paper 28.
[25] D.T. Bui, A.I. Atwood, T.M. Atienza, Effect of aluminum particle size on combustion behavior of aluminized propellants in PCP binder, in: 35th Ann. Conference of ICT, 2004. Paper 27.
[26] L. Galfetti, L.T. DeLuca, F. Severini, et al., Pre and post-burning analysis of nano-aluminized solid rocket propellants, Aerosp. Sci. Technol. 11 (2007) 26–32.
[27] U. Teipel, Energetic Materials. Particle Processing and Characterization, Wiley-VCH, Weinheim, 2005.
[28] K.T. Sullivan, W.-T. Chiou, R. Fiore, M.R. Zachariah, Appl. Phys. Lett. 97 (13) (2010) 133104.
[29] P. Chakraborty, M.R. Zachariah, Do nanoenergetic particles remain nano-sized during combustion? Comb. Flame 161 (2014) 1408–1416.
[30] S. Chung, E. Gulians, C. Bunker, et al., J. Phys. Chem. Solids 72 (6) (2011) 719–724, http://dx.doi.org/10.1016/j.pcs.2011.02.021.
[31] T.M. Klapotke, Chemistry of High-Energy Materials, Walter de Gruyter, Berlin, 2011.

[32] A. Gibson, L.D. Haws, J.H. Mohler, Integral Low-Energy Thermite Igniter, 1984. US Patent No. 4464989.
[33] T.M. Tillotson, R.L. Simpson, L.W. Hrubesh, Metal-Oxide-Based Energetic Materials and Synthesis There, 2006. US Patent No. 6986819.
[34] L. Zhou, N. Piekel, S. Chowdhury, M.R. Zachariah, The Role of Metal Oxide Oxygen Release on the Ignition of Nanothermities, Proc. 42 Annual Conference of ICT 4 (1) (2011).
[35] K.T. Sullivan, et al., Reactive sintering: an important component in the combustion of nanocomposite thermites, Combust. Flame 159 (2012) 2–15.
[36] P. Dagaut, F.N. Egolfopoulos, Editorial comment, Combust. Flame 159 (2012) 1, http://dx.doi.org/10.1016/j.combustflame.2011.10.026.
[37] R.J. Jacob, G.Q. Jian, P.M. Guerieri, M.R. Zachariah, Energy release pathways in nanothermites follow through the condensed state, Combust. Flame 162 (2015) 258–264, http://dx.doi.org/10.1016/j.combustflame.2014.07.002.
[38] G.C. Egan, T. LaGrange, M.R. Zachariah, Time-resolved nanosecond imaging of nanoscale condensed phase reaction, J. Phys. Chem. C 119 (5) (2015) 2792–2797, http://dx.doi.org/10.1021/jp5084746.
[39] M. Comet, B. Siegert, V. Pichot, et al., Preparation of explosive nanoparticles in a porous chromium(III) oxide matrix: a first attempt to control the reactivity of explosives, Nanotechnology 19 (2008) 285716, http://dx.doi.org/10.1088/0957-4484/19/28/285716, 9 pp.
[40] W. Choi, S. Hong, J.T. Abrahamson, et al., Chemically driven carbon-nanotube-guided thermopower waves, Nat. Mater. (2010), http://dx.doi.org/10.1038/nmat2714.
[41] C.H. Lee, S. Haam, H. Choi, et al., Synthesis of energetic material using single-walled carbon nanotube, in: 2013 Insensitive Munitions & Energetic Materials Technology Symposium, 2013. http://www.dtic.mil/ndia/2013IMEM/T16100_Lee.pdf. See also H. Choi, W.-J. Kim, C.H. Lee, H. Seungjoo, Synthesis of energetic material using single-walled carbon nanotube, in: 44th ICT-Conference, Paper V4(1–9).
[42] H. Abou-Rachid, A. Hu, V. Timoshevskii, et al., Nanoscale high energetic materials: a polymeric nitrogen chain N8 confined inside a carbon nanotube, Phys. Rev. Lett. 100 (2008) 196401. See also H. Abou-Rachid, A. Hu, D. Arato, et al. Novel nanoscale high energetic materials: nanostructure polymeric nitrogen and polynitrogen, in: Abstracts of "7th Int. Symp. on Special Topics in Chem. Propulsion", Kyoto, Japan, 2007.
[43] H. Liua, Y. Zhanga, R. Lia, H. Abou-Rachid, et al. Uniform and High Yield Carbon Nanotubes with Modulated Nitrogen Concentration for Promising Nanoscale Energetic Materials. http://www.eng.uwo.ca/people/asun/Paper/Uniform%20and%20High%20Yield%20Carbon%20Nanotubes%20with%20Modulated%20Nitrogen%20Concentration%20for%20Promising%20Nanoscale%20Energetic%20Materials.pdf.
[44] P. McCord, S.L. Yau, A.J. Bard, Chemiluminescence of anodized and etched silicon: evidence for a luminescent siloxene-like layer on porous silicon, Science 257 (5066) (1992) 68.
[45] N.W. Piekiel, C.J. Morris, L.J. Currano, D.M. Lunking, et al., Enhancement of on-chip combustion via nanoporous silicon microchannels, Combust. Flame 161 (5) (2014) 1417–1424, http://dx.doi.org/10.1016/j.combustflame.2013.11.004.
[46] V.S. Parimi, S.A. Tadigadapa, R.A. Yetter, Reactive wave propagation mechanisms in energetic porous silicon composites, Combust. Sci. Technol. 187 (1–2) (2014) 249–268, http://dx.doi.org/10.1080/00102202.2014.973493.
[47] V.C. Nguyen, K. Pita, C.H. Kam, et al., Giant and tunable mechanical impulse of energetic nanocrystalline porous silicon, J. Propul. Power 31 (2) (2015) 694–698, http://dx.doi.org/10.2514/1.B35274.
[48] E. Zakar, Technology Challenges in Solid Energetic Materials for Micro Propulsion Applications, U.S. Army Research Lab. Rept. ARL-TR-5035, 2009.
[49] T.M. Willey, G.E. Overturf, Towards next generation TATB-based explosives by understanding voids and microstructure from 10 nm to 1 cm, in: 40 International Annual Conference of ICT, vol. 19, FRG, Karlsruhe, 2009, pp. 1–12.

[50] V.E. Zarko, A.A. Kvasov, V.N. Simonenko, et al., Laser initiation thresholds for FTDO/DNP crystalized mixtures, in: 42nd International Annual Conference of the ICT, vol. 23, 2011, pp. 1–9 (Karlsruhe, Germany).
[51] H. Qiu, V. Stepanov, T. Chou, et al., Preparation and characterization of an insensitive RDX-based nanocomposite explosive, in: 2011 MRS Fall Meeting & Exhibit. Abstracts – Symposium Y: Advances in Energetic Materials Research, 2011. Y1.2, http://www.mrs.org/f11-abstracts-y/.
[52] N. Piazzon, A. Bondar, D. Anokhin, et al., Thermal signatures of explosives studied by nano-calorimetry, in: 42nd International Annual Conference, ICT, vol. 7, 2011, pp. 1–8 (Karlsruhe, Germany).
[53] J.M. Densmore, K.T. Sullivan, A.E. Gash, J.D. Kuntz, Expansion behavior and temperature mapping of thermites in burn tubes as a function of fill length, Propel. Explos. Pyrotech. 39 (3) (2014) 416–422, http://dx.doi.org/10.1002/prep.201400024.
[54] M.L. Pantoya, J.J. Granier, Combustion behavior of highly energetic thermites: nano versus micron composites, Propel. Explos. Pyrotech. 30 (1) (2005) 53–62.
[55] G. Jian, J. Feng, R.J. Jacob, et al., Super-reactive nanoenergetic gas generators based on periodate salts, Angew. Chem. Int. Ed. 52 (2013) 9743–9746, http://dx.doi.org/10.1002/anie.201303545.
[56] H. Cai, R. Yang, G. Yang, et al., Host–guest energetic nanocomposites based on self-assembly of multi-nitro organic molecules in nanochannels of mesoporous materials, Nanotechnology 22 (2011) 305602, http://dx.doi.org/10.1088/0957-4484/22/30/305602.
[57] H. Cai, H. Huang, Design and preparation of host-guest energetic nanocomposites by self-assembly of energetic compounds in mesoporous materials, in: 43rd International Annual Conference, ICT, vol. 41, 2012, pp. 1–10 (Karlsruhe, Germany).
[58] F. Séverac, P. Alphonse, A. Estève, et al., High energy Al/CuO nanocomposites obtained by DNA-directed assembly, Adv. Funct. Mater. XX (2011) 1–7. http://phys.org/news/2011-11-explosive-composite-based-nanoparticles-dna.html#jCp.

CHAPTER TWO

Fast-Reacting Nanocomposite Energetic Materials: Synthesis and Combustion Characterization

Keerti Kappagantula[1] **and Michelle Pantoya**[2]
[1]Department of Mechanical Engineering, Ohio University, Athens, OH, USA
[2]Mechanical Engineering Department, Texas Tech University, Lubbock, TX, USA

1. INTRODUCTION

Combustion can be defined as a rapid chemical reaction that produces heat and light. For composite energetic materials the reacting materials consist of a fuel and an oxidizer. Once the reactive materials come together, if there is enough energy to initiate the reaction, combustion occurs. When one of the reactants (i.e., either fuel or oxidizer) has nanoscale dimensions, the composite is referred to as a nanocomposite energetic material. If the energy obtained from combustion is more than necessary to sustain the reaction, energy spreads to the surrounding reactants. As the energy of the surrounding reactants also reaches a threshold, continued combustion is initiated and energy transfers, thus propagating the combustion [1].

For a combustion reaction to be initiated, the participating reactants should possess energy beyond a certain threshold, called *activation energy*, a term coined by Svante Arrhenius. He defined a relationship between activation energy and reaction rate $k(T)$ according to Eqn (1):

$$k(T) = A \cdot \exp\left(-\frac{E_a}{\mathrm{R}T}\right) \tag{1}$$

where A is the preexponential factor, R is the gas constant, and T is the absolute temperature. The activation energy of an exothermic reaction as a function of the reaction path is depicted in Figure 1. The initiation of a combustion reaction is commonly referred to as ignition. Reactants can be ignited using several approaches, such as thermal, mechanical, electrical, shock, optical, chemical, or acoustic stimuli. Each method gives rise to unique combustion characteristics depending on the state of the reactants and the heating rate among other factors.

After reactants are ignited, since combustion is exothermic by nature, the chemical reaction generates enough energy to drive the surrounding reactants to their activation

Energetic Nanomaterials
ISBN 978-0-12-802710-3, http://dx.doi.org/10.1016/B978-0-12-802710-3.00002-7

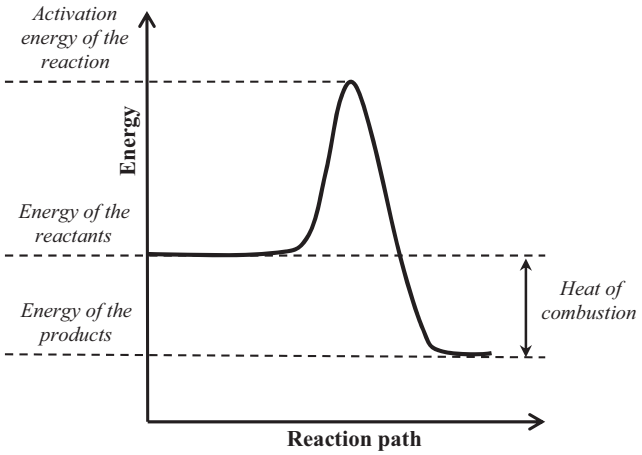

Figure 1 Plot showing energy as a function of reaction path during an exothermic combustion reaction.

energy and, thus, ignition. The cycle of ignition and energy transfer then repeats consequently throughout the reactants and is physically manifested as a flame. A thorough review of the different theories available in the literature discussing ignition and propagation in combustion of composites is provided by Farley et al. [2].

Energetic materials are broadly classified into homogeneous and heterogeneous materials. Homogeneous reactive materials, sometimes referred to as monomolecular energetics or explosives (like TNT, HMX, RDX, PETN, etc.), include fuel (i.e., carbon and hydrogen) and oxidizer (i.e., oxygen, fluorine, and nitrogen) bonded within the same molecule. Combustion occurs when the activation energy barrier is reached through external stimuli and the bonds in the homogeneous reactive material are broken. What follows is a very quick release of energy. Since the time scale for energy release is small because the controlling mechanism is bond breaking, the power delivered from these materials is high. However, by the very nature of being monomolecular, they often have an imperfect fuel–oxidizer ratio and thus, low energy density.

Heterogeneous reactive materials, also called energetic composites, consist of physical mixtures of fuel and oxidizer components. The fuels in physical contact with oxidizer undergo combustion at the points of contact. Figure 2 shows a particulate composite mixture of magnesium (Mg) fuel combined with manganese oxide (MnO). Rates of reaction are limited by the diffusion of particles and are comparatively lower. But, compared to monomolecular explosives, energy density is very high (i.e., $\sim$16,736 J/g for aluminum and molybdenum trioxide ($Al + MoO_3$) compared with 2094 J/g for TNT). Homogeneity of the fuel–oxidizer mixture and the size of the particles become important factors in determining the rate of energy release and therefore the power available from reaction. Energetic composites offer versatility in many parameters to

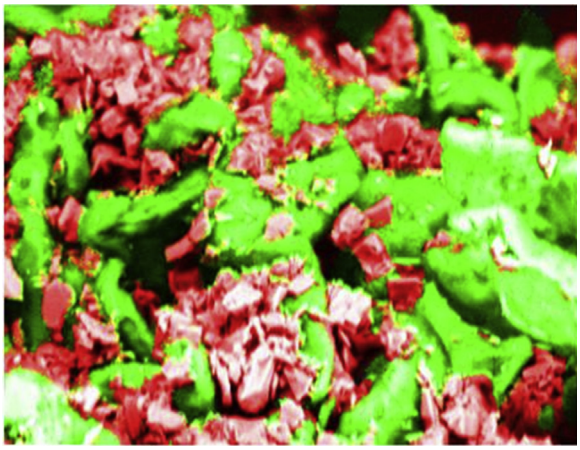

Figure 2 Scanning electron microscopy (SEM) with color mapping to show magnesium particles in red (dark gray in print versions) and manganese oxide particles in green (light gray in print versions).

control reactivity including, particle size, formulation, composition, number of reactants, fuel–oxidizer ratios, to name a few. In this way, energetic composites may be tailored for specific applications that require increased reliability, controlled reaction rates, and tailored sensitivity, and hence enable multifunctionality.

Conventional energetic composites contain particles ranging in size between 1 and 100 μm. Since classical combustion theory suggests that these reactions are diffusion controlled, decreasing the size of the reactant particles decreases the transport distance and thus enhances the operative mechanism, thereby increasing reaction velocity. Decreasing the particle size from micron- to nanoscale considerably increases the surface area-to-volume ratio. A larger ratio will imply decreased diffusion distances between the particles, increased number of contact points between the reactants, and subsequently, greater reactivity. Nanoscale energetic composites are thus known to exhibit greater reaction velocities than their micron-scale counterparts, although the energy density of the bulk materials remains identical.

Brown et al. decreased the particle size of the $Sb/KMnO_4$ system from 14 to 2 μm and found that the burn rate increased from 2–8 mm/s to 2–28 mm/s [3]. Shimizu et al. showed that an increased number of contact points between the fuel and oxidizer in the Fe_2O_3/V_2O_5 system increased the reaction rate of the components [4]. Aumann et al. examined nano-aluminum in the loose powdered media and suggested that aluminum thermite mixtures with an average particle size 20–50 nm reacted almost 1000 times more than conventional thermites because of the reduced diffusion distance between the individual reactants [5]. Bockmon et al. showed that when the size of the reactants is reduced from micron to nanoscale, reaction velocities increase by up to 1000 times for loosely packed powders [6].

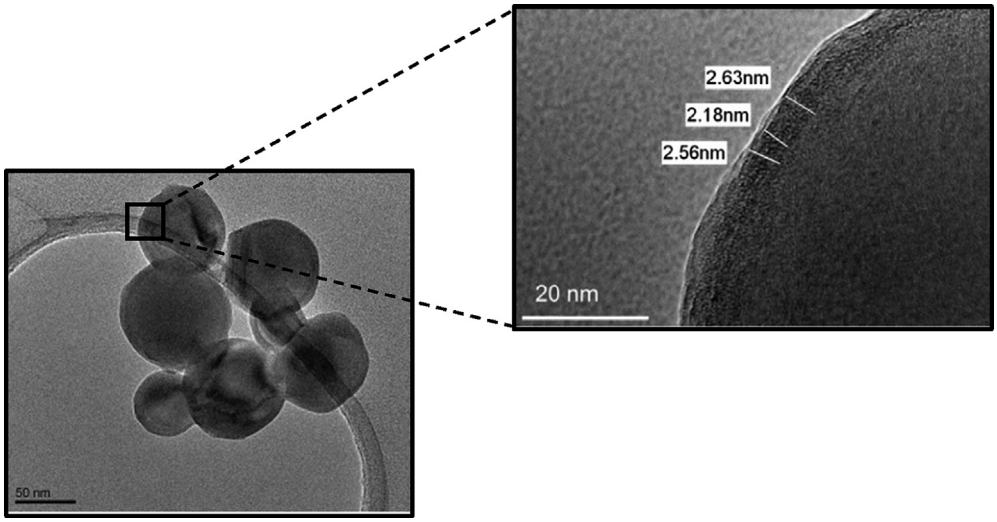

Figure 3 Transmission electron microscopy images of aluminum nanoparticles with aluminum oxide shell [8].

Aluminum (Al) has been a preferred fuel in nanoenergetic composites, finding extensive use in ordnance and industrial applications, because of its high heat of combustion (~32 kJ/g) [7]. An aluminum oxide (Al_2O_3) or alumina shell of 2–4 nm thickness forms a barrier between the pure Al core and available oxygen and reduces the spontaneous pyrophoric nature of the fuel, making aluminum particles stable and easy to work with. Figure 3 shows transmission electron microscopy images of Al particles, with the alumina shell.

For micron-size Al particles, the alumina shell accounts for about 1% of the particle weight. On the other hand, for nanoscale Al particles, depending on the diameter, the Al_2O_3 shell forms 20–45% of the total weight, which is a substantial part of the particle. However, the alumina shell typically does not participate in combustion and acts more like a heat sink. It also forms a barrier between the oxidizer and active Al core, hindering the particle's oxidation. Depending on the size of the Al particles, reaction takes place when the fuel or oxidizer diffuses through the alumina shell. Thus, alumina behaves both as a barrier to Al oxidation and a heat sink at elevated temperatures.

Fluorine (F) is one of the few elements strong enough to react with alumina and the aluminum–fluorine bond is one of the strongest in nature (665 kJ/mol). In fact, fluorine is the most reactive element and is often called a material of extremes [9] because it is the most electronegative. Since it is so reactive, fluorine gas is not commercially used as a reactant. However, fluorine also forms an extremely strong bond with carbon (536 kJ/mol). French chemists Dumas and Peligot are credited for displaying the stability of the C–F bond [10]. The discovery of polytetrafluoroethylene (PTFE) by Roy Plunkett of Dupont in 1938,

when he was experimenting with tetrafluoroethylene (TFE) to create a safe refrigerant, was the beginning of the fluoropolymer era in earnest [11].

Shortly after PTFE was manufactured commercially, the use of fluoropolymers in energetic composites began [12]. Since then, fluropolymers have found widespread use in the energetic community as favored oxidizers and/or reactive binders [13,14]. Combinations of PTFE with strong electropositive metals such as Al, magnesium (Mg), and silicon (Si) dominate the literature as examples of PTFE-based energetic composites [15–21]. Fluoropolymers are also known for their thermal stability and chemical resistance, which is welcomed in the field of energetics where safety is always a primary concern.

To better understand the oxidizing nature of fluoropolymers and their highly exothermic reaction with electropositive metal, it is helpful to understand the decomposition mechanism of the fluoropolymer into its reactive components. Thermal degradation of PTFE occurs exothermically around 460–610 °C and depends greatly on the environment. Heating PTFE in air leads to the formation of its monomer, TFE (C_2F_4), and carbonyl fluoride (COF_2). The monomer, TFE, can further decompose into difluorocarbene ($:CF_2$). On the other hand, in a vacuum or inert environment, decomposition of PTFE is endothermic, forming TFE and a mixture of fluorocarbons, including cyclic fluorocarbons [12,22].

The mechanism for the reaction between Al and F is an area of intense focus within the energetics community [16,23,24]. Osborne et al. investigated the reaction between the alumina shell on Al particles and PTFE and found that an exothermic preignition reaction (PIR) occurs involving the fluorination of Al_2O_3 by PTFE before the oxidation of the active Al core. This was the first time the alumina shell surrounding the aluminum core was found to exothermically contribute to the overall reaction energy. The idea of using alumina as a catalyst bed to excite exothermic reaction that contributes to the overall exothermicity of the reaction was born [25]. The first studies exploring this surface reactivity showed that the exothermicity of the PIR was highly dependent on the surface area-to-volume ratio of the fuel particles [25]. They also showed the PIR was constant regardless of fuel-to-oxidizer ratio. Figure 4 is a heat flow curve from a differential scanning calorimeter analysis of Al + PTFE for varied fuel-to-oxidizer ratio. The PIR is constant for fuel lean to fuel rich formulations. The PIR is especially large for nanoaluminum particles because the high surface area-to-volume ratio promotes more surface exothermic chemistry than micron-scale particles.

Watson et al. [23] studied the influence of the gases released during the burning of an energetic composite made of Al, PTFE, and molybdenum trioxide (MoO_3). Mixtures of Al/PTFE and Al/PTFE/MoO_3 were burnt in open and confined setups. Results showed that confinement had a dramatic effect on the burn velocities of Al/PTFE, leading to a 200-fold increase. They suggested that without confinement, the gases decomposed from PTFE did not fully react with Al as the products diffused away. Confining the

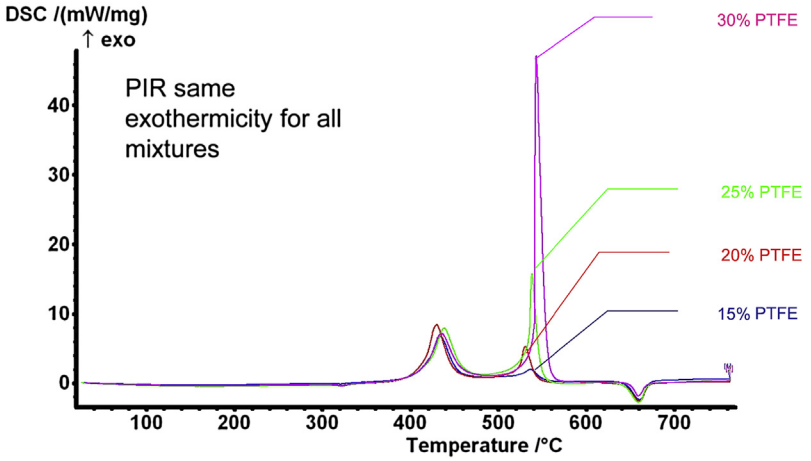

Figure 4 Heat flux as a function of temperature in an argon environment for nanoparticles of Al and PTFE as a function of fuel-to-oxidizer ratio (in terms of PTFE weight percent concentration). Initial exothermic peak is the preignition reaction (PIR).

reactants enhanced reaction dynamics, effectively forcing the fluorine from decomposing PTFE to react with the alumina shell surrounding Al particles thereby activating Al oxidation and thus producing higher burn velocities. Table 1 shows the dramatic difference between flame speeds in the open and confined configuration [23]. Surface exothermic reaction kinetics between fluorine from PTFE and the alumina surface may contribute to promoting high flame speeds, especially when coupled with MoO_3.

Yarrington et al. studied the combustion characteristics of loose powder and pressed pellets of mixtures of Al, PTFE (trade name Teflon®) and a binder,

Table 1 50 nm Al particles combined with polytetrafluoroethylene (PTFE) and/or molybdenum trioxide (MoO_3).

	Burn velocity (m/s)					
	Open burning configuration			Confined burning configuration		
Wt% Al	Al/PTFE	Al/MoO_3/PTFE	Al/MoO_3	Al/PTFE	Al/MoO_3/PTFE	Al/MoO_3
10	0.00	0.00	2	0.00	0.00	88
20	0.14	11	23	0.01	351	557
30	1.6	356	435	299	690	901
40	3.2	410	456	837	957	960
50	4.2	230	201	752	816	756
60	2.6	76	31	562	272	393
70	2.3	9	3	386	72	160
80	1.3	1	0.8	79	8	0.00
90	0.00	0.30	0.06	0.00	0.00	0.00

See Ref. [23].

poly(hexafluoropropylene-co-vinylidene fluoride) (HFP-VF trade name Viton®), known as AlTV. Chemical equilibrium codes were used to identify the fuel-to-oxidizer ratios, dominant products, reaction temperatures and pressures. Burn velocities of the pellets increased with increasing Al content, and optimized speeds were obtained at 58% wt, far beyond the stoichiometric condition of 28% wt observed during the flame tube studies. The researchers suggested that the AlTV reactions occur in both condensed and gas phases.

For high-speed reactions, PTFE dominates the energetic composite research as the most common source of fluorine that produces flame speeds on the order of 1000 m/s. But, there are other fluoropolymers experimented upon. Graphitic fluoride $(-CF-)_n$ has been shown to outperform PTFE as an oxidizer in energetic formulations, yielding higher combustion temperatures [26]. Cudzilo et al. [27] reported highly exothermic and self-sustaining reactions between $(-CF-)_n$ and several fuel particles including silicon (Si) and Al-Si alloys. They showed that exfoliated graphite is the dominant product produced despite the fuel used.

Iacono et al. explored the use of perfluoropolyether (PFPE), fluorinated polyurethanes and copolymers of the two, as fluorinated matrices for the preparation of energetic composites with Al fuels in different structural forms like pellets, fibers, and cylindrical "pucks" [15,28–30]. As opposed to PTFE, PFPE is a liquid, paste-like oligomer that wets the surface of Al particles, effectively coating them.

Fluoropolymers have been used as binders in energetic composites. HFP-VF has been applied as a reactive binder in the place of hydrocarbons such as hydroxyl terminated polybutadiene (HTPB). Nandagopal et al. [14] coated ammonium perchlorate (AP) particles with HFP-VF in propellant formulations and showed that Al/HTPB/AP had increased thermal stability compared to control energetic composites without the HFP-VF binder, thereby providing a safer and easier-to-handle solid rocket propellant.

This chapter will focus on exploring synthesis approaches to activating Al fuel particles in order to produce fast-reacting formulations. The goal is to improve Al reactivity by exploiting exothermic surface chemistry inherent in the alumina shell. At one time, the alumina shell was considered dead weight in the reaction: (1) a barrier to Al oxidation, limiting Al reactivity; and, (2) a heat sink during the production of liberated chemical energy. However, alumina is an active catalyst and exploiting catalytic reactions on the alumina surface to effectively enhance Al oxidation toward production of fast-reacting mixtures is an important avenue for future energetic materials development.

2. EFFECT OF FUEL AND OXIDIZER PROXIMITY ON COMBUSTION

Although decrease in the reactant size enhances reactivity, there are several problems associated with nanoscale reactants. The higher surface energy of the nanoparticles leads to greater particle aggregation (in order to minimize the free energy of the

system), which makes homogenizing the composite very difficult [31]. Another issue associated with the high surface area of the nanoparticles is the increased amount of viscosity when the nanoparticles are introduced into a solvent during composite preparation, which can lead to unwanted friction generation during particle mixing and increased composite agglomeration [32]. Apart from these, however, one of the biggest problems is excessive oxidation of the fuel particle (Al) before combustion [33]. In general, nano-Al particles have a passivating alumina (Al_2O_3) shell with an average thickness of 1.7–6.0 nm [34], which accounts for almost 25–40% of the entire volume, depending on the particle size. Although the oxide layer is an inert coating, prolonged exposure to air or moisture will further oxidize the Al particle, thus depleting the active Al content over time, thereby aging the fuel.

One technique to counter these problems is chemical functionalization of the nanoparticle surface. In general, surface functionalization refers to the process of encompassing the nanoparticles in an organic corona. Because the Al particles have a surrounding Al_2O_3 shell, the material used for surface functionalization should be capable of interacting either physically or chemically with the alumina shell. Under standard atmospheric conditions, the Al_2O_3 shell can become partially hydroxylated [35], providing an additional route for surface functionalization. Ample literature is available about the chemical functionalization of Al_2O_3 oxide on bulk Al particles using the condensation of carboxylic acids to surface-bound hydroxyls in order to form self-assembled monolayers (SAMs) [36–38]. Successful functionalization of alumina with silanes [39], phosphoric acids [40], and hydroxamic acids [41] has been demonstrated. Research shows that the physical properties of these nanoparticles are functions of the physical and chemical compositions of the surface corona to a great extent [42,43].

Developing new Al-based nanocomposite systems that possess energetic properties tailored for a desired application often requires the use of very large particle loadings. This has been achieved by using perfluoroalkyl carboxylic acids [32], silanes [44], and glycols [45] among others. It was seen that the combustion performance of such Al nanocomposites was affected by the presence of functional groups on these particles; combustion velocities of such nanocomposites decreased with the presence of hydroxyl groups [46].

Surface functionalization of Al nanoparticles without the alumina shell was also achieved [32]. However, flame propagation studies of energetic nanocomposites made with such Al particles showed that their burn velocity was very low compared to energetic nanocomposites consisting of Al with alumina shell and no surface functionalization [46]. In addition, the method of preparation of such perfluoroalkyl carboxylic acid–coated Al particles without the alumina shell was deemed unfit for mass production because partial fluorine passivation led to an extremely pyrophoric material. Perfluoroalkyl acids are particularly interesting as coatings over Al particles because using fluorinated compounds offers an added increase in energy content of the system during combustion because fluorine can act as an oxidizer for aluminum. In fact, the formation

of AlF_3 releases 55.67 kJ/g of Al, which is a significant increase over the formation of Al_2O_3 (30.96 kJ/g) [47]. In an effort to capitalize on this potential, nano-Al particles with an Al_2O_3 shell were coated with perfluoroalkyl tetradecanoic (PFTD) acid in an effort to improve their reaction kinetics [48].

Aluminum particles with and without surface functionalization were synthesized and combined with molybdenum trioxide, and their flame propagation characteristics were measured and analyzed. Potential factors relating the burn velocity of the energetic composites and their chemical makeup are identified in order to improve the understanding of fast-reacting energetic nanocomposite systems [49].

2.1 Materials and Sample Preparation

Aluminum particles with 80 nm average particle diameter were used as fuels in this study. All the Al particles were encapsulated in an alumina (Al_2O_3) passivation shell with an average thickness of 2.7 nm with an active Al content of 86% by volume. Surface functionalization of the Al results in a 5 nm thick layer (35% by weight) of PFTD bonded to the Al–Al_2O_3 core–shell particle. The detailed preparation method for the acid-coated Al particles may be obtained elsewhere [48]. The second type of Al particles had an alumina passivation shell without acid coating and will be referred to as Al. Molybdenum trioxide (MoO_3) is used as the principal oxidizer and has a flake-like morphology with 44 nm average flake thickness.

The three different composites, identified as Al/MoO_3/PFTD, Al-PFTD/MoO_3, and Al/MoO_3, were prepared for the flame propagation experiments. The Al/MoO_3/PFTD is a physical mixture of discretely separated powders of Al, PFTD powder, and MoO_3. In contrast, the Al-PFTD/MoO_3 includes MoO_3 and Al particles coated with PFTD chains. This sample has Al chemically bonded to PFTD. The Al/MoO_3 consists of Al and MoO_3 alone. The redox reactions between Al, the PFTD functionalization, and MoO_3 are complex; hence, the reactant concentrations are expressed in terms of mass percentages and not equivalence ratios. Dikici et al. [46] showed that similar Al-PFTD/MoO_3 combinations with 70.6% by mass MoO_3 have the highest burn velocity, and the same Al-PFTD/MoO_3 ratio was adopted here. Since the Al-PFTD particles had 35% by mass of PFTD, the PFTD content accounted for 10.36% of the total Al-PFTD/MoO_3. This implied that the active Al and the Al_2O_3 content in Al-PFTD accounted for 19.06% of the total composite mass. The same mass percentages were also assumed for preparing the Al/MoO_3/PFTD composite in order to keep the chemistry of the reaction constant and vary only the proximity of the PFTD to the Al in order to study its effects on the burn velocity of the composites. The mass percentages of fuel and oxidizers present in the three different composites prepared are given in Table 2.

Measured quantities of reactants required for preparing each composite were suspended in hexanes. The suspension was then sonicated using a Misonix Sonic wand for 120 s in 10 s intervals to break agglomerates and improve homogeneity of the composite.

Table 2 Fuel and oxidizer reactants, along with their masses in the composites prepared.

				Wt% reactants		
Sample name	**Fuel**	**Ox 1**	**Ox 2**	**Fuel**	**Ox 1**	**Ox 2**
Al/MoO_3/PFTD	Al	PFTD powder	MoO_3	19.04	10.36	70.6
Al-PFTD/MoO_3	Al-PFTD	PFTD coating	MoO_3	19.04	10.36	70.6
Al/MoO_3	Al	MoO_3	—	21.24	78.76	—

The hexane suspension was transferred to a Pyrex dish and heated to a temperature of 45 °C to facilitate the evaporation of hexane. Once the powder mixture dried, it was reclaimed for further experimentation. This is a standard procedure for combining solid particle reactants.

2.2 Flame Propagation Experiments

The prepared composites were subjected to flame propagation experiments. A schematic of the experimental setup is shown in Figure 5. It consists of a quartz tube, 110 mm long, with an inner diameter of 3 mm and an outer diameter of 8 mm. Each composite was loaded into the quartz tube and placed on a vibrating block for 5 s to reduce local density gradients. Each tube contained approximately 470 ± 10 mg of composite resulting in a loose powder fill estimated to be 7% of the theoretical maximum density. Once prepared, the tube was placed in a steel combustion chamber with viewing ports for diagnostics. Three quartz tubes were prepared for each composite allowing for an estimate of the repeatability and uncertainty in the measurement.

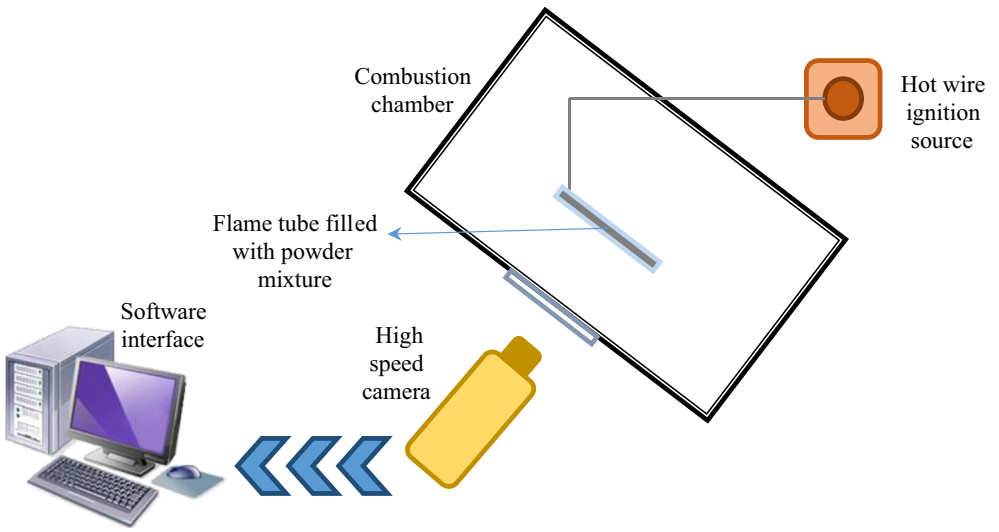

Figure 5 Schematic illustrating camera position relative for powder-filled flame tube and ignition source.

Figure 6 Sequential images of the flame propagating along the tube.

Ignition was achieved via thermal stimulus provided by a Nichrome wire connected to an external voltage supply. A Phantom v7 (Vision Research, Inc., Wayne, NJ) with a Nikon AF Nikkor 52 mm 1:2.8 lens was used to record ignition and flame propagation. The camera captured images of the reacting composite, perpendicular to the direction of flame propagation, at a speed of 160,000 frames per second, with a resolution of 256×128 pixels. Vision Research software was used to postprocess the recorded photographic data. When a reference length is established, the software determines speed based on a distance between sequential time frames. Using a "find-edge" image filter that identifies preset variations in pixel intensity, the flame front location (the region of the flame with the maximum radiance) is identified and marked for speed measurements. Figure 6 shows representative sequential images from high-speed imaging of flame propagation through this tube apparatus filled with powder energetic composite.

2.3 Results

Figure 7 shows a representative plot for the distance traversed by the flame front as a function of time. The initial portion of the curve shows unsteadiness as the flame progresses down the quartz tube. Flame speed is measured when propagation attains steady-state behavior seen in the latter portion of the tube represented by linearity in the distance versus time plot. The slope of the linear region represents burn velocity.

The steady-state burn velocities are compared in Figure 8 with bars representing standard deviations. The burn velocity of the acid-coated aluminum (Al-PFTD/MoO_3) is 366% faster than the physical mixture of aluminum and perfluorotetradecanoic acid (Al/MoO_3/PFTD). The burn velocity of the composite with the acid-coated aluminum, Al-PFTD/MoO_3, is almost double that of nontreated nano-aluminum

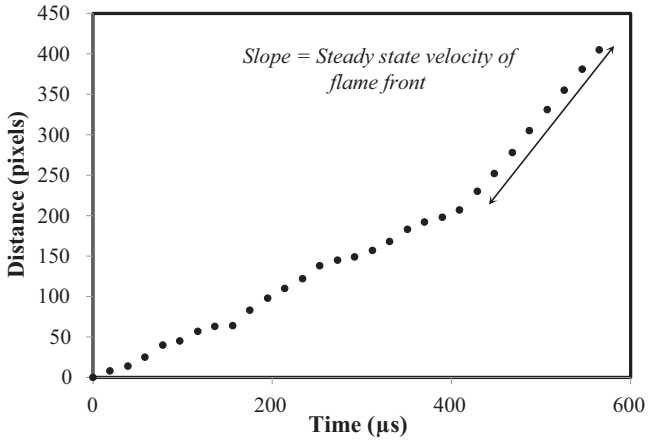

Figure 7 Distance traveled by the flame front in the burn tube for Al/MoO_3 composite as a function of time.

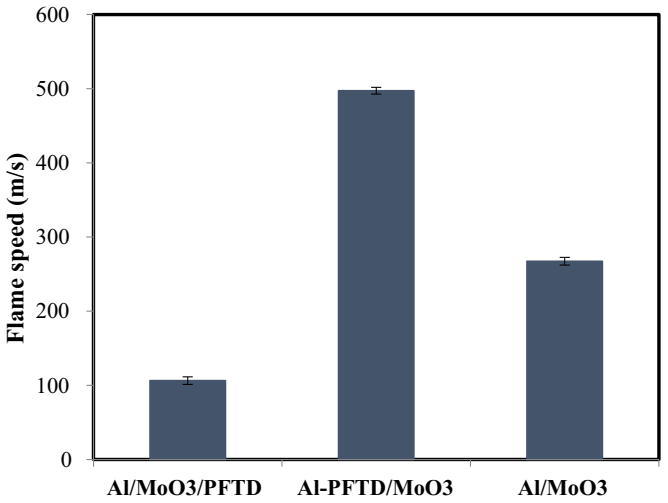

Figure 8 Burn velocity of Al/MoO_3/PFTD, Al-PFTD/MoO_3, and Al/MoO_3 with uncertainty measurements.

composite, Al/MoO_3. Interestingly, the composite containing the surface-functionalized Al, Al-PFTD/MoO_3, had the highest burn velocity in the study, while the physically mixed composite, Al/MoO_3/PFTD, had the lowest burn velocity.

The increase in the burn velocity of Al-PFTD/MoO_3 may be attributed to the bonding of the oxidizing PFTD to the Al fuel. During the combustion of the acid-coated aluminum, the reaction is hypothesized to progress in two distinct stages. In Stage 1, the PFTD chains on the surface of the Al fuel particles react with the Al_2O_3 shell to form AlF_3. Fluorination of the alumina shell is identified as a rate-determining step for

Al reactions with fluoropolymers [25]. This interaction makes the Al core readily available for further reactions. The proximity of the PFTD chains in the surface functionalized Al enhances the rate of the fluorination reaction when compared to the unbonded PFTD. Subsequently, in Stage 2, the aluminum core undergoes rapid oxidization by the fluorine from the PFTD, MoO_3, and air.

In the case of Al/MoO_3/PFTD composite, the PFTD particles are not bonded to the Al nanoparticle. The diffusion distance between Al and PFTD particles is therefore greater and the fluorination reaction may take longer. As a result, the burn velocity of Al/MoO_3/PFTD is significantly less than Al-PFTD/MoO_3.

The burn velocity of the physically mixed composite, Al/MoO_3/PFTD, is lower than the simple Al/MoO_3 composite. In the case of Al/MoO_3/PFTD, there are two competing reactions progressing during combustion: Al reacting with PFTD and Al reacting with MoO_3. The primary oxidizing component of PFTD is fluorine, which reacts with Al_2O_3 and Al. This reaction is similar to Al reacting with PTFE since the PFTD chains resemble PTFE polymer chains after their initial decarboxylation during reaction. PFTD may start reacting with Al before the MoO_3 does due to its proximity to the Al. Watson et al. [23] showed that the burn velocity of Al with PTFE is lower than with MoO_3. They also showed that the burn velocity of Al with PTFE and MoO_3 combined is lower than Al/MoO_3. Similar trends are mirrored in the results from the current study. Fluorine separation from PFTD may be the rate-determining step to reaction with Al and decrease Al's availability to react with MoO_3, making the Al-PFTD the primary reaction. If the slower reaction becomes the primary reaction, then the burn velocity of the entire ternary composite would be less than that of the binary composite, Al/MoO_3. Similar results were observed by Prentice et al. [50] when they performed flame propagation studies with Al mixed with varying compositions of silicon dioxide (SiO_2) and iron oxide (Fe_2O_3). They showed that Al/SiO_2 had the lowest burn velocity and Al/Fe_2O_3 had the highest, whereas the burn velocities of all composites with increasing percentages of SiO_2 added to Al/Fe_2O_3 had correspondingly decreasing burn velocity. Prentice et al. [50] showed that for ternary composites, competing reactions with Al tend reduce the burn velocity over the highest binary reaction burn velocity when the mixtures are physically mixed and diffusion limited.

3. TUNING COMBUSTION PERFORMANCE OF ENERGETIC NANOCOMPOSITES THROUGH SURFACE FUNCTIONALIZATION OF THE FUELS

Flame propagation studies of energetic composites made of PFTD functionalized and nonfunctionalized Al nanoparticles (Al-PFTD and Al, respectively) combined with molybdenum trioxide (MoO_3) demonstrated that the PFTD actively participates in the reaction and contributes to the enhanced flame speed of Al-PFTD/MoO_3 compared to

Al/MoO_3. However, functionalizing Al particles with PFTD only leads to increased burn velocity. The greater goal is on achieving process control and tailorability of Al particles by studying the flame propagation of Al nanoparticles functionalized with perfluorocarboxylic acids such that the burn velocity of the corresponding energetic composite will decrease. Thermites are ideal energetic composites because of their tailorability based on manipulating reactant properties. To this effect, a shorter, more sterically hindered organic acid, perfluorosebacic acid (PFS) was used to functionalize Al nanoparticles according to the procedure in reference in [48]. Experiments were performed to study the thermoequilibrium and nonequilibrium combustion behaviors, using differential scanning calorimetry and flame propagation experiments. Activation energy (E_a) and burn velocity of the energetic composites were evaluated and the relationship between the structure of the acid coating and the combustion behaviors was investigated [51].

3.1 Material Synthesis

Three different types of Al with 80 nm average particle diameter were used as fuels. All the Al particles were encapsulated in an alumina (Al_2O_3) passivation shell with an average thickness of 2.7 nm. Al-PFTD particles had a 5 nm thick layer of PFTD over the Al_2O_3 shell. Similarly, particles referred to as Al-PFS henceforth, had a 5 nm thick layer of PFS over the Al_2O_3 shell. It is noted that these acids bond to the alumina shell through the surface hydroxylation. The third type of Al particles had an alumina passivation shell without any acid coating and will be referred to as Al. The structures of PFTD and PFSs are shown in Figure 9.

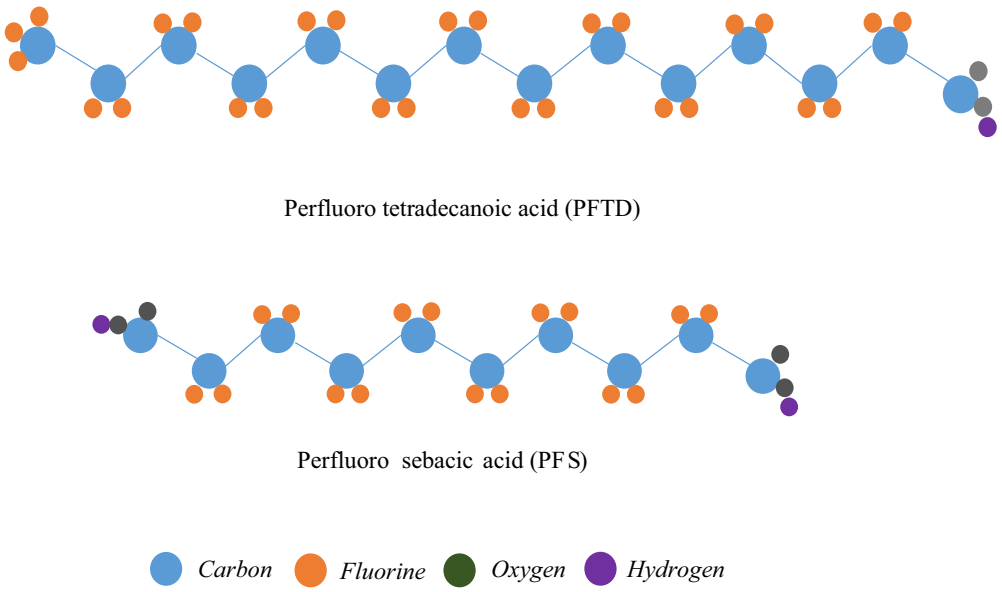

Figure 9 Schematic representation of the chemical structure of the PFTD and PFSs, respectively.

The Al nanoparticles used throughout this study were procured from Nova Centrix Corp. Austin, TX, USA. These Al particles were coated with PFTD to obtain Al-PFTD and with PFS to obtain Al-PFS, respectively in slurry of diethyl ether. The powder product was washed three times in diethyl ether to remove any acid that was not bonded to the alumina shell. The end result was Al particles with a perfluoroalkyl acid self-assembled monolayer surrounding the Al_2O_3 shell. The detailed preparation method for these acid-coated Al particles may be obtained elsewhere [48]. It was proposed that the perfluoroalkyl acids, PFTD and PFS, bond to the alumina through the carboxylic functional group [32]. The oxidizer comprised of MoO_3 was procured from Mach I, USA. The MoO_3 particles have an average thickness of 44 nm with rectangular plate-like morphology, whereas the Al particles are all spherical.

For preparing the energetic composites, requisite amounts of Al fuel (with and without SAMs) and MoO_3 oxidizer were measured and suspended in hexanes. The suspension was then sonicated as described in Section 2.1 following standard mixing procedures for reactive powder preparation. Three energetic composites were prepared corresponding to the three different Al fuels.

3.2 Flame Propagation Experiments

Flame propagation experiments were conducted using the three energetic composites to determine the burn velocity. The flame tube apparatus was used and reported extensively in flame propagation experiments [6,46,52–54]. Each energetic composite was loaded into the tube and placed on a vibrating block for 5 s to reduce local density gradients. Each tube contained about 468 ± 10 mg of energetic composite resulting in a loose powder fill estimated to be 7% of the theoretical maximum density. Once prepared, the tube was placed in a steel combustion chamber; the experimental setup is schematically represented in Figure 6. In these experiments, the camera captured images of the reacting composite, perpendicular to the direction of flame propagation, at a speed of 160,000 frames per second, with a resolution of 256×128 pixels. Vision Research software was used to postprocess the recorded photographic data.

3.3 Thermal Equilibrium Experiments

Activation energy was found using a thermoequilibrium isoconversion method. Samples of approximately 6 mg were loaded into a Neztsch STA 409 differential scanning calorimeter (DSC) and thermogravimetric analyzer (TGA) and heated to 1273 K at 2, 5, or 10 K/min in a 1:3 (by volume) oxygen-argon environment. Within the DSC/TGA, the sample crucible is compared to an empty reference crucible in order to obtain the net energy and mass change. Also, the sample carrier was mounted on a microscale (i.e., TGA) allowing for mass change measurements that relay phase change (i.e., gas production) information as a function of equilibrium temperature.

The slope of the DSC curve changes when the reaction within the DSC/TGA produces enough energy to become noticeable within the natural noise of the machine. The area under the DSC curve corresponds with the net exothermic behavior. The activation energies were then calculated using Eqn (2) from the Type B-1.95 peak method as described by M. J. Starink [55]:

$$\frac{B}{T_p^{1.95}} = A \exp\left(-\frac{E_a}{R T_p}\right) \tag{2}$$

In Eqn (2), B is the heating rate, A is the preexponential factor, E_a is the activation energy, R is the universal gas constant, and T_p is the temperature at the exothermic peak of the reaction. Reaction rate is approximated by $B/T_p^{1.95}$. Taking the natural log yields Eqn (3):

$$\ln\left(\frac{B}{T_p^{1.95}}\right) = -\frac{E_a}{R T_p} + \ln A \tag{3}$$

By plotting $\ln(B/T_p^{1.95})$ as a function of $(1/RT_p)$ for the different heating rates, E_a (kJ/mol) can be found as the slope of the trend line.

3.4 Results of Flame Speeds

The activation energy for these samples as well as their burn velocity is shown in Table 3. The burn velocity of Al-PFTD/MoO_3 is 86% faster than the burn velocity of Al/MoO_3, whereas the burn velocity of Al-PFS/MoO_3 is almost half of Al/MoO_3.

Figures 10–12 show the DSC/TGA plots of the three energetic composites as a function of temperature at three different heating rates: 2, 5, and 10 K/min.

Al-PFTD/MoO_3 and Al-PFS/MoO_3 reactions show a smaller exotherm before the bigger one whereas the same is not seen in the Al/MoO_3 reaction plot. On the other hand, the Al/MoO_3 plot shows a two-stage exotherm signifying two reactions occurring at two different temperatures. Also, two small endotherms are to be noted on the DSC plots of the energetic composites with acid-coated fuels at about 650–660 °C. This temperature corresponds to the melting point of Al, which might mean that the endotherm may represent the melting of some excess Al left over after it reacts with the MoO_3 present.

Table 3 Burn velocity and activation energy results.

Energetic composite	Activation energy E_a (kJ/mol)	Average flame speed (m/s)
Al/MoO_3	252	267
Al-PFTD/MoO_3	185	497
Al-PFS/MoO_3	553	138

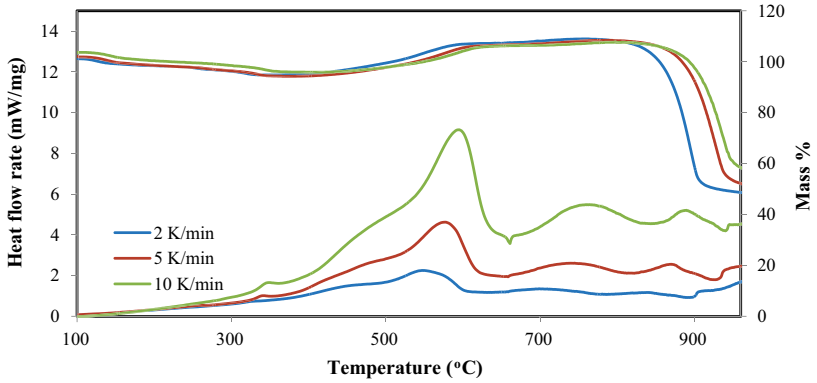

Figure 10 DSC (three plots on the bottom)/TGA (three plots on the top) of Al-PFTD/MoO_3 reaction at different heating rates. Note that mass loss results from the TGA analysis corresponding to the top three curves.

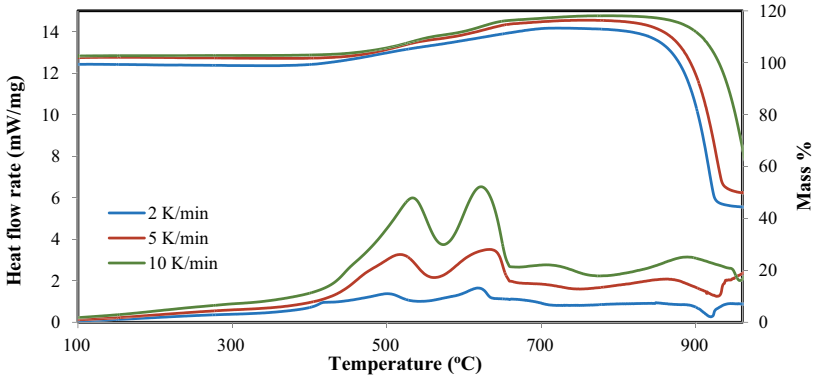

Figure 11 DSC (three plots on the bottom)/TGA (three plots on the top) of Al/MoO_3 reaction at different heating rates.

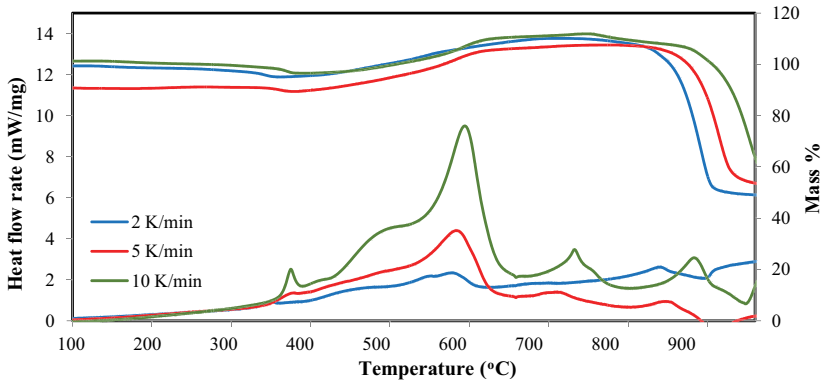

Figure 12 Heat flow from DSC (three plots on the bottom) and mass loss from TGA (three plots on the top) of Al-PFS/MoO_3 reaction at different heating rates of 2, 5, and 10 K per minute.

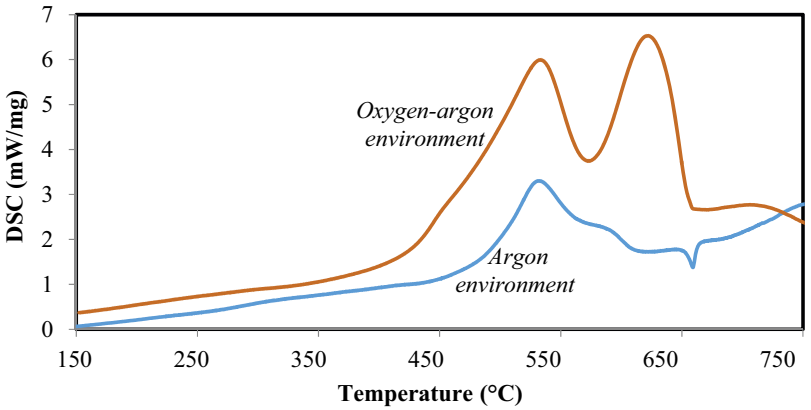

Figure 13 Heat flux curve of Al/MoO_3 energetic composite as a function of temperature for a constant 10 K/min heating rate.

Such an endotherm is not present in the Al/MoO_3 DSC plots; there is, however, a second endotherm present in the Al/MoO_3 plot. It may be concluded that the first peak corresponds to the oxidation of Al with MoO_3 particles, which is known to occur at around 540 °C [56]. In order to understand the second peak of the heat curve, a DSC run of the same energetic composite was performed with the identical sample size and heating rate in an exclusively argon (Ar) environment. The resultant heat curve is shown in Figure 13.

The Al/MoO_3 combustion in an Ar environment shows an endothermic dip at about 660 °C (corresponding to unburned Al melting). Comparing this to the heat curve initially observed for Al/MoO_3 (Figure 13) combustion in an oxygen-argon environment, it may be seen that the second exothermic peak corresponds with the Al melt endotherm. In an entirely argon environment, the only oxidizer available during the reaction would be MoO_3. Once all the MoO_3 is used by the Al fuel present in the redox reaction, any leftover Al particles cannot react with any other oxidizer and hence melt when heated further. On the other hand, in a 1:3 (by volume) oxygen-argon environment, the Al particles have two oxidizers to react with: the MoO_3 mixed in the energetic composite and the oxygen in the reaction environment. Therefore, any Al left behind after the entire amount of MoO_3 is consumed in the redox reaction may be oxidized in the oxygen environment on further heating. This oxidation of Al by oxygen will result in an exotherm. Therefore, it may be concluded that the second exothermic peak in the heat curve of Al/MoO_3 is due to the unburned Al particles being oxidized by oxygen in the reaction environment. For better comparison, the DSC plots of all the energetic composites for a constant 10 K/min heating rate are provided together in Figure 14.

Figure 14 shows that the first exotherm on DSC plot of Al-PFTD/MoO_3 occurs at a lower temperature than the first exotherm on the Al-PFS/MoO_3 plot. The analysis in

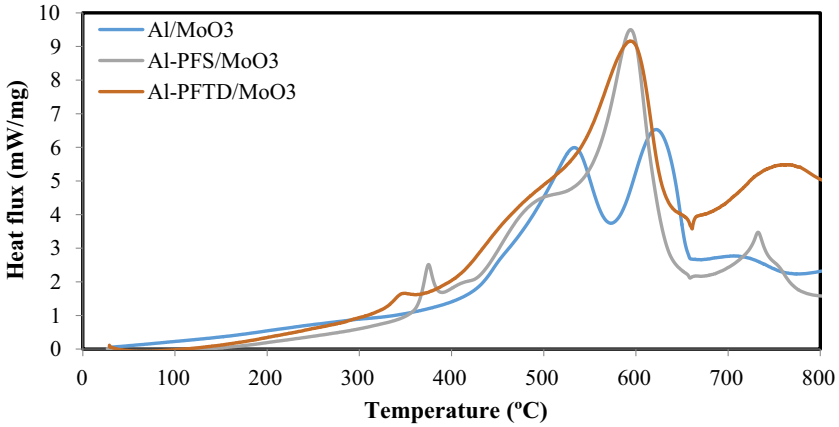

Figure 14 Heat flux DSC curve of each energetic composite as a function of temperature for a constant 10 K/min heating rate.

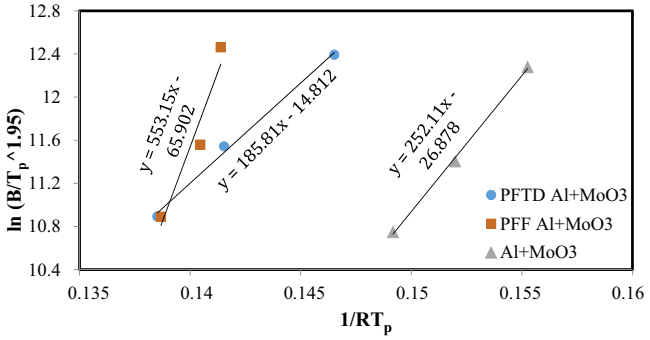

Figure 15 Trend lines showing the activation energy of the energetic composite compositions.

Figure 14 is extended to lower heating rates in order to measure the isoconversion temperature corresponding to a continuous transition. Using the values for peak temperature at various heating rates (i.e., 2, 5, and 10 K/min), the $\ln(B/T_p^{1.95})$ as a function of $(1/RT_p)$ for each energetic composite was plotted, and results are shown in Figure 15.

The slopes of the trend lines in Figure 15 are the activation energies (E_a) of the compositions reported in Table 3 and show that the E_a of Al/MoO_3 is 252 kJ/mol, corresponding to the E_a values of the energetic composite as found in literature [57,58]. The interesting point to note is that the activation energy trend is opposite to that of the burn velocity values, i.e., compositions with low burn velocity have high E_a and vice versa. Since all the parameters like flame tube diameter, length, Al and MoO_3 concentration, TMD, and stimulus voltage were maintained constant for all the tests, the contributing factor for the difference in the burn velocity may be the chemical composition and kinetics of the acid shell.

Osborne and Pantoya [25] showed that when Al reacts with PTFE, the fluorine reacts with the Al_2O_3 shell at elevated temperatures leading to the formation of aluminum fluoride (AlF_3). This interaction occurs during a preignition reaction around 400 °C. They postulated that the formation of AlF_3 serves to degrade Al_2O_3 leaving the Al core exposed for further reaction. The acid coatings used here contain a large percentage of fluorine in their alkyl chains terminating in carboxylic groups as illustrated in Figure 9. PFTD contains 72% fluorine by weight whereas PFS has 62% fluorine be weight. At elevated temperatures, the fluorine radicals from the acid coating may react with Al_2O_3 (similar to fluorine radicals from PTFE molecules) degrading the alumina shell and exposing the Al core for further oxidation. This can be seen in Figure 14 when comparing the heat flow curves for the two acid-coated energetic composites. Al-PFTD/MoO_3 exhibits a PIR onset at 320 °C and peak at 342 °C while the Al-PFS/MoO_3 exhibits a PIR onset at 350 °C and peak at 374 °C. After the PIR in Figures 10 and 12, the heat flow curves appear similar and there is no further indication of discrepancies in the equilibrium kinetics that account for the differences in burn velocity seen in Table 3 (86% increase over Al/MoO_3 in case of Al-PFTD/MoO_3 and 48% decrease in case of Al-PFS/MoO_3).

An interesting interpretation from Figure 10 and Table 3 is that the acid coating may be tailored to sensitize or desensitize the energetic composite. In the case of PFTD, the coating appears to enhance ignition sensitivity by the following:

1. reducing the onset of the PIR,
2. having lower activation energy; and,
3. promoting higher flame speeds.

The PFTD has a longer $-CF_2-$ chain compared to PFS (Figure 9). Longer chains are less stable and faster to react because they more readily form radicals compared to acids with smaller chains [59]. Also, PFTD contains higher fluorine wt% (72% compared to 62% in PFS), which is a highly electronegative oxidizer. Dean et al. [20] showed that the Al-F PIR is directly correlated with fluorine concentration and the specific surface area of the Al particle. Higher fluorine concentrations and specific surface areas lead to a lower PIR onset. This is also seen in Figure 15 with a 30 °C reduction in onset PIR with PFTD compared with PFS. Reducing the onset for the PIR may accelerate the Al oxidation and explain the observation of increased burn velocity of Al-PFTD/MoO_3 compared to Al-PFS/MoO_3. Controlling the PIR onset may be a key to controlling the reactivity of the acid-coated Al energetic composite.

Furthermore, PFS is a more symmetrically stable molecule compared to PFTD. Therefore, bond breaking and radical formation from PFS requires more energy than PFTD, resulting in higher E_a. Also, oxygen and hydrogen from PFS carboxylic group may bond with fluorine radicals at the reaction front, further decreasing the concentration of fluorine available, consequently inhibiting Al oxidation and decreasing the burn velocity of the Al-PFS/MoO_3. Also, PFS molecules have an extra carboxylic acid

functional group, consisting of a π bond between carbon and oxygen. Although the −C−F− is one of the strongest single bonds with a bond dissociation energy (BDE) of 490 kJ/mol, the −C═O− is a π bond with a higher BDE of about 799–802 kJ/mol [59]. This means that almost twice the amount of energy required to cleave a −C−F− bond is necessary to cleave a −C═O− bond, which may also account for the higher E_a of Al-PFS/MoO_3. Thadani et al. [60] showed that for solid-state reactants, a reduced onset temperature would imply a higher reaction rate. It is very interesting to note that results from this study are consistent with Thadani et al. such that the onset temperature for Al-PFTD/MoO_3 is lower than Al-PFS/MoO_3, and the burn velocity and E_a are similarly correlated.

The burn velocity and E_a have an inverse relationship for the three energetic composites (Table 3). Activation energy measured here is apparent activation energy because the measurement considers influences beyond fuel-to-oxidizer ratio. The apparent activation energy quantifies the energy barrier needed to be overcome in order for a chemical reaction to occur. Reactants having high activation energy require greater energy input compared to reactants with lower activation energy.

Combustion of an energetic composite in a flame tube proceeds along the lateral axis of the flame tube. Given that the diameter of the flame tube (i.e., 3 mm) is smaller than its length (i.e., 10 cm) by an order of magnitude, heat transfer during the reaction may be approximated as one dimensional along the axis of propagation. Thermal stimulus via Nichrome wire heats up the portion of energetic composite in its vicinity, increasing the energy of the reactants above their activation energy. An exothermic reaction starts during the oxidation of the fuel. Energy released during this oxidation reaction heats the energetic composite adjacent to the reaction zone. Once the adjacent reactants obtain energy greater than its activation energy, the fuel and oxidizer particles start reacting exothermally. Thus, the reaction propagates in a flame tube. This progression of the reaction manifests itself as a fast-moving flame front that can be observed visually. Energetic composites with low activation energy require comparatively less energy to overcome the E_a barrier. This implies that energy is more readily transferred to (rather than consumed by) unreacted energetic composite, and the result is faster propagation of the reaction and higher burn velocity. On the other hand, energetic composites with comparatively higher E_a consume more energy at the reaction site and result in lower burn velocity. This is exactly mirrored in the results as can be seen from Table 3.

4. CONCLUSIONS

The analysis of an approach to particle synthesis by functionalizing aluminum fuel particles led to characterizations of reaction kinetics and combustion performance of aluminum–fluoropolymer reactions. Experiments were performed to alter key parameters

of the reaction, namely flame speeds. Results show that enhanced outcome control and reaction tailorability may be achieved by simply altering the additive components.

Nanoscale aluminum particles were functionalized using PFTD bonded to the alumina passivation shell around Al. Three different energetic composites were created using molybdenum trioxide: Al functionalized with PFTD and MoO_3; non-functionalized Al with MoO_3 and individual PFTD particles; and nonfunctionalized Al with MoO_3 alone. Their flame speeds were measured in order to understand the effects of surface functionalization on aluminum reactivity. Results show that the surface-functionalized Al composite (Al-PFTD/MoO_3) has a reaction rate twice that of Al/MoO_3 and three and a half times of Al/MoO_3/PFTD. The drastic change in the flame propagation and burn velocity was attributed to the proximity of the PFTD to the Al particles and, hence, enhanced reaction kinetics.

Functionalization was further explored to tailor reactivity. Thermal equilibrium and flame propagation experiments were performed of three energetic composites each containing 80 nm average diameter Al particles combined with MoO_3, but two energetic composites contained Al-coated particles with different acids, and an uncoated Al energetic composite was used as a baseline for comparison. The acids were self-assembled monolayers of PFTD and PFS such that the energetic composites were labeled: Al-PFTD/MoO_3, Al-PFS/MoO_3, and Al/MoO_3. Results showed that Al-PFTD/MoO_3 had the highest velocity and almost double that of Al/MoO_3. On the other hand, Al-PFS/MoO_3 had the lowest velocity and 48% of Al/MoO_3. Equilibrium analyses revealed that the PFTD promoted a lower onset for a preignition reaction that may be spurred by reduced structural stability of the acid molecular chain. The lower onset for the fluorine aluminum preignition reaction was the only difference in the heat flow trends for the two different acid coatings and may be an indication of the key to increasing or decreasing the reactivity of the acid-coated Al energetic composites.

Activation energy (E_a) showed a completely inverse trend with velocity, with highest velocity associated with the lowest E_a. This finding was anticipated because propagation velocity can be described as a series of ignition sites such that lower activation energy correlates with higher propagation velocity for the similar energetic composites examined here.

These findings are impactful because they suggest that the structure of the acid coating can be tailored to enhance or reduce the reactivity of the energetic composite. Results suggest that because the PFTD coating is less stable and contains a higher concentration of fluorine, these factors promote an earlier onset of a preignition reaction that enhances energetic composite reactivity (results in higher velocity and lower activation energy). On the other hand, PFS is more stable, requires greater bond energy for dissociation, and results in a delayed onset for the PIR, higher activation energy, and lower flame speeds, reducing the overall energetic composite reactivity.

REFERENCES

[1] S.R. Turns, An Introduction to Combustion: Concepts and Applications, third ed., vol. 3, McGraw Hill, New York, 2012.

[2] C. Farley, Reactions of Aluminum with Halogen Containing Oxides, Dissertation. Lubbock, TX, May 2013.

[3] M. Brown, S. Taylor, M. Tribelhom, Fuel oxidant particle contact in binary pyrotechnic reactions, Propell. Explos. Pyrotech. 23 (1998) 320–327.

[4] A. Shimizu, J. Saitou, Effect of contact points between particles on the reaction rate in the Fe_2O_3-W_2O_5 system, Solid State Ionics 38 (1990) 261–269.

[5] C. Aumann, G. Skofronick, J. Martin, Oxidation behavior of aluminum nanopawders, J. Vac. Sci. Technol. 13 (3) (1995) 1178–1183.

[6] B.S. Bockmon, M.L. Pantoya, S.F. Son, B.W. Asay, J.T. Mang, Combustion velocities and propagation mechanisms of metastable interstitial composites, J. Appl. Phys. 98 (6) (2005) 064903–064907.

[7] S.H. Fischer, M.C. Grubelich, Theoretical energy release of thermites, intermetallics and combustible metals, in: 24th International Pyrotechnics Seminar. Monterey, CA, 1998.

[8] J. Gesner, M. Pantoya, V. Levitas, Effect of oxide shell growth on nano-aluminum thermite propagation rates, Combustion and Flame 159 (2012) 3448–3453.

[9] K. Johns, G. Stead, Fluoroproducts – the extremophiles, J. Fluorine Chem. 104 (2000) 5–14.

[10] P. Kirsch, Modern Fluoroorganic Chemistry: Synthesis, Reactivity, Applications, John Wiley and Sons, Hoboken, NJ, 2004.

[11] L. McKeen, Fluorinated Coatings and Finishes Handbook: The Definitive Users Guide, William Andrew, 2006.

[12] E. Koch, Metal-fluorocarbon pyrolants: III. Development and application of magnesium/teflon/viton (MTV), Propell. Explos. Pyrotech. 27 (5) (2002) 262–266.

[13] E. Koch, Metal-fluorocarbon pyrolants IV: thermochemical and combustion behavior of magnesium/teflon/viton (MTV), Propell. Explos. Pyrotech. 27 (6) (2002) 340–351.

[14] S. Nandagopal, M. Mehilal, M. Tapaswi, S. Jawalkar, K. Radhakrishnan, B. Bhattacharya, Effect of coating of ammonium perchlorate with fluorocarbon on ballistic and sensitivity properties of AP/Al/HTPB, Propell. Explos. Pyrotech. 34 (6) (2009) 526–531.

[15] N. Clayton, K. Kappagantula, M. Pantoya, S. Kettwich, S. Iacono, Fabrication, characterization and energetic properties of metalized fibers, ACS Appl. Mater. Interfaces. 6 (2014) 6049.

[16] E. Dreizin, Metal based nanoreactive materials: a review article, Prog. Energy Combust. Sci. 35 (2) (2009) 141–167.

[17] K. Kappagantula, M. Pantoya, Experimentally measured themal transport properties of aluminum-polytetrafluoroethylene nanocomposites with graphene and carbon nanotube additives, Int. J. Heat Mass Transfer 55 (4) (2012) 817–824.

[18] K. Kappagantula, M. Pantoya, E. Hunt. Impact ignition of aluminim-teflon based energetic materials impregnated with nano-structured carbon additives, J. Appl. Phys. 112 (2) (n.d.) 024902–024908

[19] S. Kettwich, K. Kappagantula, B. Kusel, E. Avijan, S. Danielson, Thermal investigations of nanoaluminum/perfluoropolyether core-shell impregnated composites for structural energetics, Thermochim. Acta 591 (2014) 45–50.

[20] M. Pantoya, S. Dean, The influence of alumina passivation on nano-Al/Teflon reactions, Thermochim. Acta 493 (2009) 109–110.

[21] C. Yarrington, S. Son, T. Foley, Combustion of silicon/teflon/viton and aluminum/teflon/iton energetic composites, J. Propul. Power 26 (4) (2010) 734–743.

[22] S. Moldoveanu, Analytical Properties of Synthetic Organic Polymers, Elsevier, Amsterdam, 2005.

[23] K. Watson, M. Pantoya, V. Levitas, Fast reactions with nano- and micrometer aluminum: a study on oxidation versus fluorination, Combust. Flame 155 (4) (2008) 619–634.

[24] R. Yetter, G. Risha, S. Son, Metal combustion and nanotechnology, Proc. Combust. Inst. 32 (2) (2009) 1819–1838.

[25] D. Osborne, M. Pantoya, Effect of Al particle size on the thermal degradation of Al/Teflon mixtures, Combust. Sci. Technol. 179 (8) (2007) 1467–1480.

[26] E. Koch, Metal-fluorocarbon pyrolants: V. Theoretical evaluation of the combustion performance of metal-fluorocarbon pyrolants based on strained fluorocarbons, Propell. Explos. Pyrotech. 29 (1) (2004) 9–18.
[27] S. Cudzilo, M. Szala, A. Huczko, M. Bystrzejewski, Combustion reactions of poly carbon monofluoride with different reductants and characterization of the products, Propell. Explos. Pyrotech. 32 (2) (2007) 149–154.
[28] S. Danielson, et al., Metastable Metalized Perfluoropolyether Functionalized Composites, American Chemical Society, New Orleans, LA, 2013.
[29] R. Fantasia, S. Pierson, C. Hawkins, S. Iacono, S. Kettwich, Facile Route Towards Perfluoropolyether Segmented Polyurethanes, American Chemical Society, Denver, CO, 2011.
[30] S. Pierson, D. Richard, C. Lindsay, S. Iacono, S. Kettwich, Synthesis and Characterization of Aluminum Perfluoropolyether Blended Materials, American Chemical Society, Anaheim, CA, 2011.
[31] J. Brege, C. Hamilton, C. Crouse, A. Barron, Ultrasmall carbon nanoparticles from a hydrophobically immobilized surfactant template, Nano Lett. (2009) 2239–2242.
[32] R.J. Jouet, A. Warren, D.M. Rosenberg, V.J. Bellito, K. Park, M. Zachariah, Surface passivation of bare aluminum nanopaticles using perfluoroalkyl carbozylic acids, Chem. Mater. 17 (2005) 2987–2996.
[33] R. Brewer, P. Dixon, S. Ford, K. Higa, R. Jones, Lead free Electric Primer, Final, Naval Air Warfare Center, WEapoms Division, China Lake, CA, 2006.
[34] D. Pesiri, C. Aumann, L. Bilger, D. Booth, R. Carpenter, R. Dye, E. O'Neill, D. Shelton, K. Walter, Industrial scale nano aluminum powder manufacturing, J. Pyrotech. 19 (2004) 19–32.
[35] K. Wefers, C. Misa, Oxides and Hydroxides of Aluminum, Alcoa Technical Paper 19, 1988.
[36] K. Oberg, P. Persson, A. Shchukarev, B. Eliasson, Comparison of monolayer films of stearicacid and methyl stearate on an, Thin Solid Films 397 (2001) 102–108.
[37] M. Lee, K. Feng, X. Chen, N. Wu, A. Raman, J. Nightingale, E. Gawalt, D. Korakakis, L. Hornak, A. Tiperman, Adsorption and desorption of stearic acid on self-assembled monolayers on aluminum oxide, Langmuir (2007) 2444–2452.
[38] M.E. Karaman, D.A. Antelmi, R.M. Pashley, The production of stable hydrophobic surfaces by the adsorption of hydrocarbon and fluorocarbon carboxylic acids onto alumina substrates, Colloids Surf. A Physicochem. Eng. Asp. 182 (1–3) (2001) 285–298.
[39] M. Abela, J. Wattsa, R. Digby, The adsorption of alkoxysilanes on oxidised aluminium substrates, Int. J. Adhes. Adhes. (1998) 179–192.
[40] I. Liakosa, E. McAlpineb, X. Chen, R. Newmand, M.R. Alexander, Assembly of octadecyl phosphonic acid on the α-Al_2O_3 (0 0 0 1) surface of air annealed alumina: evidence for termination dependent adsorption, Appl. Surf. Sci. 255 (5) (2008) 3276–3282.
[41] J. Folkers, C. Gorman, P. Laibinis, S. Buchholz, G. Whitesides, R. Nuzzo, Self-assembled monolayers of long-chain hydroxamic acids on the native oxide of metals, Langmuir (1995) 813–824.
[42] C. Crouse, C. Pierce, J. Spowart, Influencing solvent miscibility and aqueous stability of aluminum nanoparticles through surface functionalization with acrylic monomers, ACS Appl. Mater. Interfaces 2 (2010) 2560–2569.
[43] D. Weibel, A. Michels, A. Feil, L. Amaral, S. Teixeria, F. Horowitz, Adjustable hydrophobicity of Al substrates by chemical surface functionalization of nano/microstructures, J Phys. Chem. C (2010) 13219–13224.
[44] S. Valliappan, J. Swiatkiewicz, J.A. Puszynski, Reactivity of aluminum nanopowders with metal oxides, Powder Technol. 156 (2005) 164–169.
[45] R. Thiruvengadathan, A. Bezmelnitsyn, S. Apperson, C. Staley, P. Redner, W. Balas, S. Nicolich, D. Kapoor, K. Gangopadhyaya, S. Gangopadhyay, Combustion characteristics of novel hybrid nanoenergetic formulations, Combust. Flame 158 (2011) 964–978.
[46] B. Dickiki, S. Dean, M. Pantpya, V. Levitas, J. Jouet, Influence of aluminum passivation on reaction mechanism: flame propagation studies, Energy Fuels 23 (2009) 4231–4235.
[47] CRC Handbook of Chemistry and Physics, vol. 71, CRC Press, Boca Raton, FL, 1991.
[48] J. Horn, J. Lightstone, J. Carney, J. Jouet, Preparation and characterization of functionalized aluminum nanoparticles, in: Shock Compression of Condensed Matter – 2011: Proceedings of the Conference of the American Physical Society Topical Group on Shock Compression of Condensed Matter. Chicago, Illinois, 2011.

[49] K. Kappagantula, M. Pantoya, J. Horn, Effect of surface coatings on aluminum fuel particles toward nanocomposite combustion, Surf. Coat. Technol. 237 (2013) 456–459.
[50] D. Prentice, M. Pantoya, B. Clapsaddle, Effect of nanocomposite synthesis on the combustion performance of a ternary thermite, J. Phys. Chem. B 109 (43) (2005) 20180–20185.
[51] K. Kappagantula, C. Farley, M. Pantoya, J. Horn, Tuning energetic material reactivity using surface functionalization of aluminum fuels, J. Phys. Chem. C 116 (46) (2012) 24469–24475.
[52] C. Yarrington, S. Son, T. Foley, S. Obrey, A. Pacheo, Nano aluminum energetics: the effect of synthesis method on morphology and combustion performance, Propell. Explos. Pyrotech. 36 (6) (2011) 551–557.
[53] K. Kappagantula, B. Clark, M. Pantoya, K. Kappagantula, Flame propagation experiments of non gas generating nanocomposite reactive materials, Energy Fuels 25 (2) (2011) 640–646.
[54] M. Weismiller, J. Malchi, J. Lee, R. Yetter, T. Foley, Effects of fuel and oxidizer particle dimensions on the propagation of aluminum containing thermites, Proc. Combust. Inst. 33 (2) (2011) 1989–1996.
[55] M.J. Starnik, Analysis of aluminum based alloys by calorimetry: quantitative analysis of reactions and reaction kinetics, Int. Mater. Rev. 49 (3) (2004) 191–226.
[56] J.H. Bae, D.K. Kim, T.H. Jeong, H.J. Kim, Crystallization of amorphous Si thin films by the reaction of MoO_3/Al, Thin Solid Films 518 (2010) 6205–6209.
[57] D. Stamatis, E.L. Dreizen, K. Higa, Thermal initiation of al-MoO3 nanocomposite materials prepared by different methods, J. Propul. Power 27 (2011) 1079–1087.
[58] J. Sun, M. Pantoya, S. Simona, Dependence of size and size distribution on reactivity of aluminum, Thermochim. Acta 444 (2006) 117–127.
[59] T.W. Graham Solomons, C. Fryhle, Organic Chemistry, Wiley, 2011.
[60] N. Thadhani, S. Namjoshi, K. Vandersall, X. Xu, Thermal analysis Instrumentation for the Kinetics of Shocked Materials, Final report, Storming Media, Atlanta, 1999.

CHAPTER THREE

Nanometals: Synthesis and Application in Energetic Systems

Alexander A. Gromov[1,3,4,5], Alexander G. Korotkikh[4,6], A. Il'in[4], Luigi T. DeLuca[2], Vladimir A. Arkhipov[6], Konstantin A. Monogarov[5] and Ulrich Teipel[1,3]

[1]Technical University Georg-Simon-Ohm, Nürnberg, Germany
[2]Space Propulsion Laboratory, Department of Aerospace Science and Technology, Politecnico di Milano, Milan, Italy
[3]Fraunhofer Institute of Chemical Technology, Pfinztal, Germany
[4]Tomsk Polytechnic University, Tomsk, Russia
[5]Semenov Institute of Chemical Physics, Russian Academy of Science, Moscow, Russia
[6]Tomsk State University, Tomsk, Russia

1. INTRODUCTION

Specific surface could be viewed as an effective operational parameter for low-dimension structures (characteristic size less than ~100 nm) along with temperature, pressure, concentration of reactants, and so on. The fundamental physical characteristics for nanostructures are normally displaced to low-temperature and low-energy field (melting temperature, oxidation temperature, red-ox potential, etc.) [1]. Some thermodynamic properties of two-dimensional (2D) nanomaterials have abnormal values, e.g., the extremely high thermal conductivity of graphene (5000 W/m⋆K) with the specific surface area S_{sp} ~1000 m^2/g exceeds those of metals by a factor of 10 [2]. The advantage of high specific surface of nanometals in catalysis, ignition, oxidation, and combustion of energetic systems (ES) results in high rates of heterogeneous reactions. The existing models in macrophysical chemistry are little applicable for the analysis of the combustion processes of ES with metal nanopowders or nanometals (*n*Me; mean surface particle diameter $d \sim 50–500$ nm) [3]. An example of such ES is the composition *n*Al/*n*MoO_3 with a burning rate of about 1 km/s [4].

Historically, the technology of *n*Me application to thermal nuclear engineering progressed in the United States (US), while at the same time *n*Me applications were developed in the Soviet Union for energetics since World War II. The results of Soviet works on nanometals were primarily published in Morokhov's book in 1977 [5]. In Western Europe and the US, the term *nanocrystalline material* became well known after Gleiter's published work in 1989 [6], but engineering works on *n*Me applications started about 30 years earlier than the term *nano* appeared. The terms *superfine*, *ultrafine*, *ultradispersed*, and *submicrocrystalline* powders exist along with *nano* up to now in periodicals [1,3,5,6]. The discussion on the exact definition of "what is really nano?" continues today.

Energetic Nanomaterials
ISBN 978-0-12-802710-3, http://dx.doi.org/10.1016/B978-0-12-802710-3.00003-9

Possibilities of using powdery metals as additives to ES began to be intensively studied after the discovery by two Russian aerospace scientists, Kondratyuk and Tsander, in 1910 [7]. Several review books were published from 1960–1970 [8,9] where the very basic laws of combustion for micron-sized metal powders (μMe, $d \sim 5$–500 μm) under high-temperature oxidizing environments were discussed. The drawbacks of μMe as a fuel were detected during the very first tests of metalized propellants in the 1940s: the clustering of particles (especially for aluminum); a low degree of metal reaction completion in the gas phase (incomplete combustion, up to 50% of unburned metal); significant two-phase flow losses of specific impulse (15% for the compositions containing 25 mass% of μAl) [10]. Zeldovich et al., in the 1970s [10] showed one of the approaches to reduce these losses by using ultrafine metal particles for fuels and combustion catalysts, in particular *n*Me. The recent efforts of several teams in Russia, Italy, France, Germany, US, and China are focusing more or less on the realization of those ideas in the modern nanoenergetic science.

2. NANOMETALS IN ENERGETIC SYSTEMS

Nowadays, tons of rather cheap *n*Me are produced in several countries for different technological applications, while the problems of their standardization, storage, handling, toxicity, and correct application for ES are still under discussion [1]. The modern energetic materials community demands the truthful picture of *n*Me properties and, consequently, their application avenues. The "romantic atmosphere" of the 1990s around *n*Me and myths about their "excess energy" should be changed by clear frames and conditions of *n*Me application for energetic purposes. Nanopowders, especially *n*Me, still remain rather "capricious" technological raw materials with metastable physical and chemical properties. In many cases because *n*Me, in addition to small particle size, show very high reducing properties: *n*Cu chemically reacts like a massive Zn (displaces H_2 from acids); *n*Al shows the properties of bulk Na and K: it reacts with water at room temperature; *n*Ti and *n*Zr are self-exploding by contact with air, etc.

The current circle of scientific and engineering applications of *n*Al in ES is shown on Figure 1. Some basic energetic applications of *n*Al as well as the analysis of the combustion regimes, the content of intermediate and final burning products, and proposals for future work in this field are reviewed.

2.1 Nanometals Production, Passivation, and Properties

Gas condensation using different vaporization methods, such as thermal evaporation, laser ablation, microwave plasma processes, chemical vapor deposition, and pyrolysis of salts are the most known among the methods of *n*Me production by massive metals dispersion and particles synthesis from atoms [11–13]. The electrical explosion of wires (EEW) method [14] is the most efficient among the existing methods for *n*Me production [3].

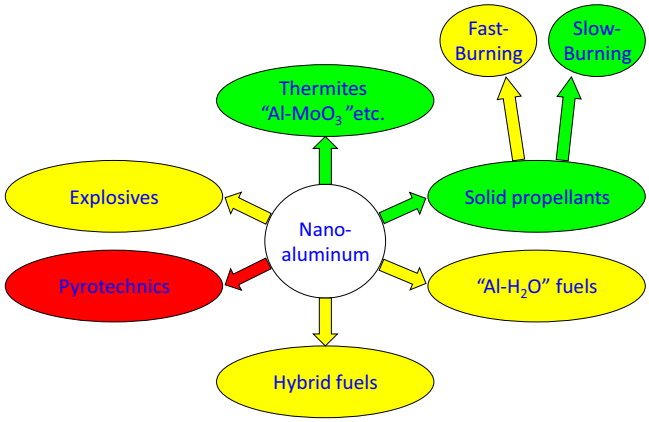

Figure 1 *n*Al applications to energetic systems (green (dark gray in print versions) arrows—developed areas; yellow (light gray in print versions) arrows—in development; red (black in print versions) arrow—limited application so far).

The material of the wire transforms into nanoparticles at high temperature and pressure by EEW. The entered energy is comparable with metal sublimation enthalpy and can be high enough to disperse metal wires to nanoparticles. EEW *n*Me have a high active metal content (85–95 mass%) in comparison with *n*Me obtained by other methods [3]. The particle size and active metal content in the powder could be regulated by changing the parameters of electric explosion. Selection of the conditions of passivation provides the control of the physical and chemical properties of *n*Me [15,16]. One of the most difficult and still unsolved problems for EEW *n*Me is their wide particle size distribution: sometimes powder could have a three-modal particle size distribution [3]. The number of nanosized particles can reach 90% of the total number of particles produced by EEW. But the major part of powder by mass can consist of micron-sized particles, which are only a small percentage of the total number of all particles. For example, the mass of the fraction of micron-sized particles (1–3 μm) was ~68% of the total mass for *n*Al sample with $S_{sp} = 12\ m^2/g$ produced by EEW [17]. However, the number of micron-sized particles was only 2% of the total number of the particles [17]. Thus, the problem of the *n*Me production with narrow particle size distribution is still actual. Another problem of the *n*Me is the clustering during production caused by liquid particles collision and its further storage. Clustering provide the right part of the size distribution curves for *n*Me (Figure 2). Active *n*Me with the particle sizes less than ~30 nm are normally unstable to oxidation, sintering, and clustering. The *n*Me particles of such size are easily sintered at room temperature even under an inert atmosphere. Their interaction is accompanied by thermal explosion during heating in chemically reactive media.

The *n*Al particles, obtained in inert gas media (argon, argon + hydrogen, argon + nitrogen) by any of existing methods, are normally pyrophoric in air because the amount

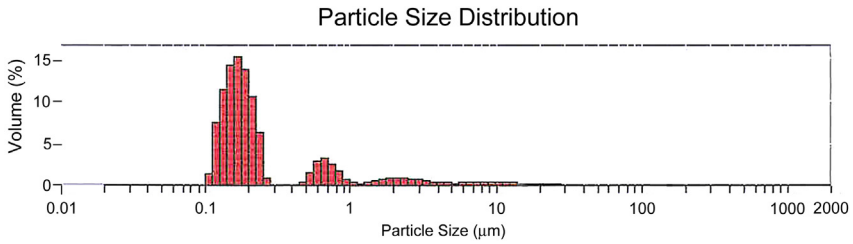

Figure 2 Particle size distribution of *n*(Cu-6% Ni) produced by EEW.

and the rate of heat release from the oxidation reaction at room temperature is high enough to heat the nanoparticle to the ignition temperature (~400 °C for 100 nm *n*Al) [18]. That is why the particle surface should be passivated by a protective layer between metal and reactive gas (air) for the particle stabilization. The passivation quality defines the chemical stability of *n*Me and its reactivity in the further oxidation processes. The traditional method of μAl passivation is coating with hydrocarbons. For example, industrial μAl with flake particles coated by ~2 mass% of paraffin.

The oxide-passivated layers are formed on the *n*Al particles at slow oxidation rates by air during the passivation process (Figure 3). EEW *n*Al particles have amorphous oxide layers that crystallize at the definite thickness of 7–8 nm during a storage period of two to three years at room temperature. The metal content in the powder substantially reduces (down to 30–50 mass%) if the *n*Al particle size decreases down to ~30 nm. As a rule, smaller particle diameters result in lower metal content, and the metal content is

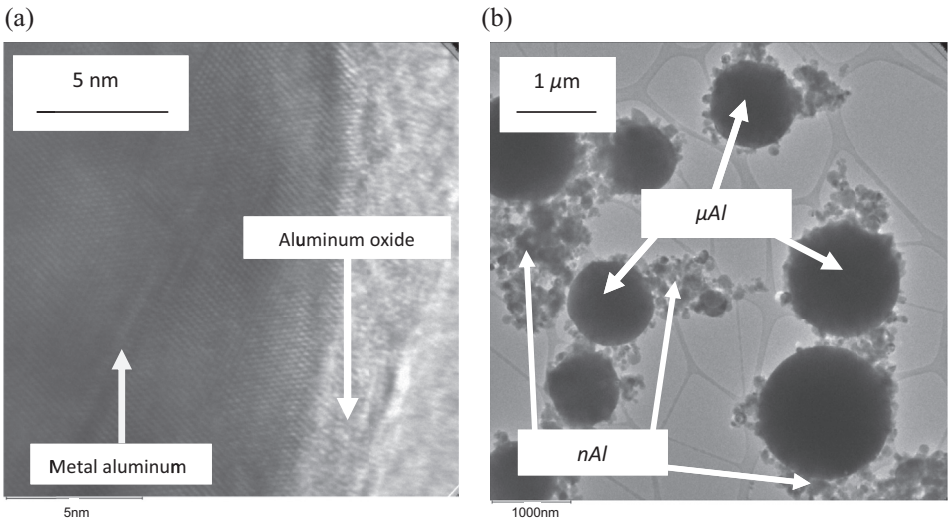

Figure 3 Transmission electron microscopy images of air-passivated *n*Al: (a) individual particle, and (b) mixture of *n*Al and μAl.

~30 mass% for the particle size of ~10 nm. The average aluminum content is 70–90 mass% in *n*Al stabilized with organic reagents [19]. However, all existing passivation approaches do not allow reaching metal content of 98 mass% for *n*Al and from this viewpoint they will never achieve the best μAl values (97–99.8 mass%).

2.1.1 Nanoaluminum Thermal Characterization

The most convenient method for *n*Al thermal characterization is the identification of *reactivity parameters* of the certain powder based on the nonisothermal oxidation curves (by differential thermal analysis (DTA), differential scanning calorimetry (DSC), thermogravimetry (TGA)) [20]. The basic results of *n*Al thermal characterization by DTA/DSC/TGA in the first decade of the 2000s are expressed by the works of several actively published scientific groups since the 1990s (Ivanov et al., Il'in et al., Russia; Eisenreich et al., Germany; Pantoya et al., Dreizin et al., US; Turcotte et al., Canada; and others). Powders with different particle diameters (mostly from 10 to 500 nm), surface characteristics (passivation layers, coatings), and oxidation under various heating rates (from 0.5 to 500 K/min) and oxidizing environments (Ar + additives, N_2, Air, O_2) are discussed. If the *n*Al oxidizes in air with a low rate, the final oxidation product is nano-α–Al_2O_3 ($T \geq 1200$ °C) [21]. For EEW *n*Al the formation of nano-γ–Al_2O_3 with the $S_{sp} = 450$ m^2/g by slow oxidation (0.5–20.0 K/min) occurs at rather low temperatures ($T = 400$–600 °C).

The most common *reactivity parameters* for *n*Al characterization can be determined by thermal analysis (DTA/DSC/TGA) curves (Figure 4) [20]:

- oxidation onset temperature (T_{on}), °C;
- heat release over a certain temperature range (ΔH), J/g (at T_{on}, °C);
- degree of oxidation $Al \rightarrow Al_2O_3$ at the given temperature $\alpha_{Al \rightarrow Al_2O_3}(T) = +\Delta m/(Al^{\circ} \cdot 0.89)$, %
- max oxidation rate, g/°C or g/s.

However, the thermal characteristics of *n*Al emerging from the DTA/DSC/TGA dataset appear often contradictory because of several reasons:

1. the *n*Al metastable physical and chemical properties;
2. the different *n*Al production technologies and storage conditions;
3. the speculative interpretation of the thermal data because of the poor characterization of *n*Al and lack of complete information on powder properties (particle size and shape, size distribution function, specific surface, metal content, etc.).

The third one is the most critical point, since a detailed statistical analysis of the published experimental data is difficult to accomplish due to the very wide scatter in powder characteristics. For example, the scatter for T_{on} data taken from the DTA/TGA data for different samples of *n*Al, produced by EEW, is up to ±80 °C for particles with $d \sim 80$–380 nm [18,22]. Anyway, the heating rates by thermal characterization are much lower than those met in solid propellant and other energetic applications.

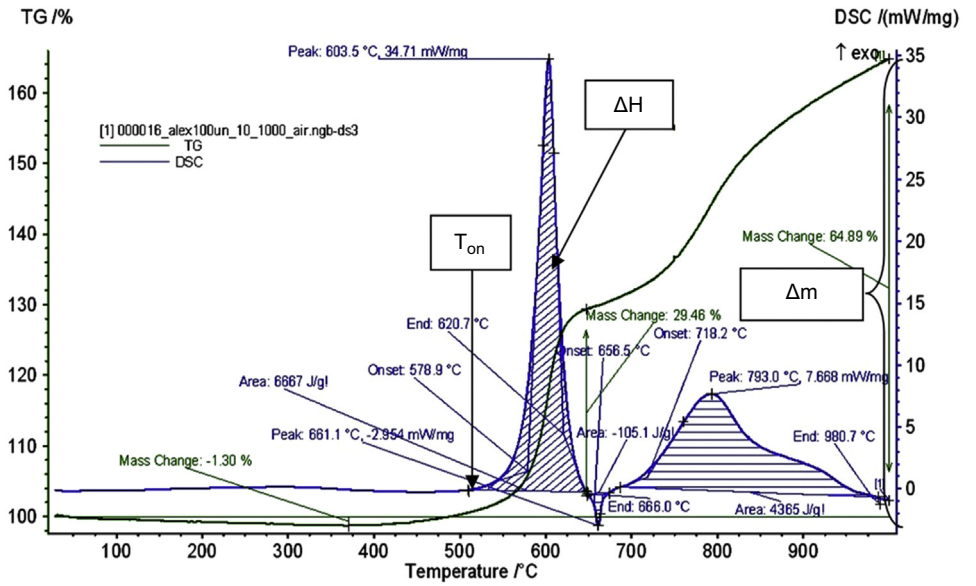

Figure 4 Reactivity parameters taken from DSC/TGA data for typical *n*Al powder: oxidation onset temperature (T_{on}), °C; heat release before Al melting (ΔH_{ox}), J/g; mass gain ($+\Delta m$), %.

2.1.2 Nanometals' Effect on Energetic Materials Decomposition

The decomposition temperature for a wide class of EM can be lowered thanks to the catalytic effects associated with *n*Me [23,24]. One of the most convenient methods for the study of the catalysis in *n*Me/EM systems is DSC/TGA. The catalytic activity of *n*Al, *n*Fe, *n*W, *n*Ni, *n*Cu, and *n*(Cu–Ni) mixed with energetic materials (AP, AN, and HMX) as well as with μAl were studied in Ref. [18]. Experiments were performed in nitrogen to avoid *n*Me/air interaction (sample weight 10 mg, heating rate 10 K/min). Nitrogen proved to be an inert gas for *n*Me except for *n*Al [21]. Particles of *n*Fe, *n*W, *n*Ni, *n*Cu, and *n*(Cu–Ni) were negligibly nitrided, after heating in nitrogen up to 600 °C. Thus, the DSC/TGA study of the mixes *n*Me/EM showed interactions only in binary systems, excepting reaction of components with nitrogen. The mixes (*n*Me/50 mass% EM) were suspended in ethanol, dried in air, and then analyzed by DSC/TGA. The size of energetic materials particles (HMX, AP, and AN) was larger than *n*Me by a factor of 1000 and equal to ~100 μm.

2.1.2.1 *n*Me/HMX

The T_{on} for the HMX mixture with *n*Al was 242 °C (Table 1), that is 46 °C lower than for pure HMX ($T_d = 288$ °C). Hence, *n*Al initiated the decomposition of HMX at a lower temperature. Particles of *n*Fe, *n*Cu, *n*(Cu-45% Ni) and *n*(Cu-6% Ni) strongly affect the HMX decomposition. For *n*(Cu-45% Ni) and *n*(Cu-6% Ni) this strong effect (see temperature decrease, ΔT, Table 1) could be caused by a catalytic process.

Table 1 Catalytic effect (+), i.e., high values of ΔT, for *n*Me on EM by DSC/TGA in N_2.

		HMX (T_d = 288 °C)			AP (T_d = 307 °C)			AN (T_d = 166 °C)		
No	Metal (alloy)	T_{on}, °C	ΔT[a], °C	Effect	T_{on}, °C	ΔT[a], °C	Effect	T_{on}, °C	ΔT[a], °C	Effect
1.	μAl	270	18		n.a.	n.a.	n.a.	n.a.	n.a.	n.a.
2.	*n*Al	242	46	+	320	13		n.a.	n.a.	n.a.
3.	*n*W	284	4		311	4		155	11	
4.	*n*Ni	283	5		291	16		149	17	
5.	*n*Fe	192	96	+	244	63	+	161	5	
6.	*n*Cu	228	60	+	146	161	+	132	34	+
7.	*n*(Cu-6% Ni)	193	95	+	246	61	+	84	82	+
8.	*n*(Cu-45% Ni)	196	92	+	277	30	+	87	79	+

[a]$\Delta T = T_d - T_{on}$, °C.

The decomposition temperature of HMX was 96 °C lower as a result of the *n*Fe interaction with HMX. Neither *n*Ni nor *n*W decreased the T_d of HMX significantly. The main products of HMX decomposition (gaseous carbon oxides and nitrogen oxides [25]) appeared at temperatures higher than 250 °C and could not promote reaction "solid HMX/solid *n*Me."

2.1.2.2 *n*Me/AP

The parameters of AP decomposition were practically unchanged for mixtures with *n*Al. For other *n*Me, AP affected their oxidation (not vice versa) because AP had a higher T_d than all of the studied mixtures of AP with metals and AP released oxidative gases by its own decomposition.

2.1.2.3 *n*Me/AN

Except *n*Fe and *n*W, other metals started to intensively react with AN only by the third polymorph transformation of AN. The oxidation of *n*Me was carried out simultaneously with the AN decomposition. The exceptions are *n*Cu and *n*(Cu-Ni) for decomposition of mixtures with AN and AP.

For the studied energetic materials, *n*Me particles significantly decrease the T_{on} by nonisothermal heating: *n*Cu, *n*(Cu-Ni) for AN (*n*Al, *n*Fe, *n*W, and *n*Ni have no effect); *n*(Cu-Ni), *n*Cu, and *n*Fe for AP (*n*Al, *n*W, and *n*Ni have no effect); *n*(Cu-Ni), *n*Cu, and *n*Fe for HMX (*n*W and *n*Ni have no effect), while *n*Al reacts chemically.

3. IGNITION OF ENERGETIC SYSTEMS CONTAINING NANOALUMINUM

It is possible to increase the magnitude of stationary burning rate of ES by changing the composition of ES, in particular, the percentage of *n*Al powder in it.

However, increasing the aluminum content in ES with the same component compositions and particle size of oxidizers could increase the size of the agglomerated particles of alumina in the combustion products and reduce the energy performance of ES [26–29]. Replacing μAl by nAl in the ES increases the acoustic conductivity in the combustion chamber [30–32].

According to [8], Al_2O_3 on the surface of Al particles significantly affects their combustion process by having a melting point substantially above the melting point of aluminum. It was found [30] that the thickness of the oxide shell for the nAl with the $d_{43} = 0.18$ μm is less by a factor of ~3 than the oxide shell thickness for μAl with the $d_{43} = 7.34$ μm. Furthermore, the thickness of the oxide shell increases during heating the Al particles in an oxidizing environment [33]. Combustion of Al particles occurred at the high temperature gradient near the burning surface of ES with the appearance of cracks and destruction of the oxide shell, resulting in intense oxidation of metal. The diffusion mechanism of combustion for micron-sized Al powder was observed at relatively low heating rates [8,34]. A melt-dispersion mechanism [35,36] is associated with the destruction of the Al_2O_3 shell and the initial crushing of nanosized Al particles to clusters of ~3–20 nm at high heating rates (more than 10^6 K/s).

The most common experimental setups for the ignition of ES are:

1. direct contact of the heated gas or solid igniter with the cold sample of ES (conductive ignition);
2. heat transfer radiation from the hot gas or solid particle (radiant ignition);
3. heat transfer by convection from the hot gas (convective ignition).

The results of studying of the ignition process of aluminized ES with radiant and conductive heating are presented below.

3.1 Ignition by Radiation Heat Flux

There are three different operating modes under the ES heating: ignition, flame quenching, and thermal explosion depending on the rate of heat release and heat losses.

A lab setup with the radiant power ~600 W (Xenon lamp) and emission spectrum $\lambda = 0.25-1.85$ μm [37] was used for studying the ignition process of aluminized ES. The ignition times of ES were determined at different values of the radiant flux density. The formal kinetics of investigated compositions was studied.

The tested ES formulations were based on ammonium perchlorate (AP), butyl rubber BKL, and Al powders. The samples had the cylindrical shape of 10 mm in diameter and 5 mm in height. The ignition time t_{ign} was determined by the appearance of the flame detected by photodiode and ionization gauge.

The dependence of the ES ignition time on radiant flux density $t_{ign}(q)$ is shown in Figure 5. The ignition time is reduced by a factor 1.6 at $q = 60$ W/cm^2 and by a factor 2.6 at $q = 250$ W/cm^2 under the complete replacement of μAl by nAl in ES.

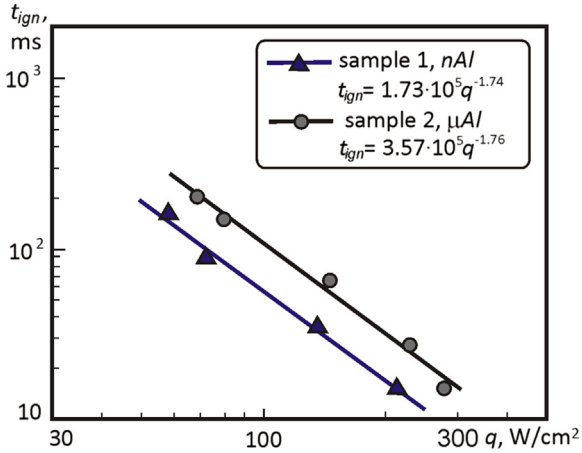

Figure 5 The ignition time of ES containing 72 mass% AP, 18 mass% BKL, 10 mass% Al versus radiant flux density.

Replacement of μAl by nAl (Table 2) leads to reduction of the temperature of intensive oxidation and ignition time (Table 3). This is caused by the enhanced chemical reactivity of nAl, which have higher specific surface as compared with μAl (Table 2).

Ignition of aluminized ES by monochromatic radiant flux was carried out using the setup based on CO_2 laser with a wavelength of radiation 10.6 μm and a maximum power

Table 2 Characteristics for the studied Al powders.

Al powder	d_{10}, μm	d_{20}, μm	d_{30}, μm	d_{32}, μm	d_{43}, μm	Size distribution function, μm^{-1}	C_{Al}, mass %	$\delta_{Al_2O_3}$, nm	ρ_b, g/cm³
μAl	1.47	1.98	2.67	4.85	8.05	$g(d) = 0.064d^{1.21}\exp(-0.303d)$	98.7	10.8	1.06
nAl	0.11	0.12	0.13	0.15	0.17	$f(d) = 28.7\cdot10^6 d^{4.49}\exp(-46.8d)$	86.0	3.1	0.15

Note: d_{10}, d_{20}, d_{30}, d_{32}, d_{43}, the average diameters; $g(d)$, $f(d)$, the weight and counting distribution function; C_{Al}, Al metal content; $\delta_{Al_2O_3}$, the calculated thickness of oxide layer; ρ_b, the apparent (loose) density of powder.

Table 3 Reactivity parameters of the studied Al powders.

Al powder	T_{ox}, °C	α_{ox} (660 °C), %	α_{ox} (1000 °C), %	v_{ox}, mg/s (at T, °C)
μAl	820	2.5	41.8	0.05 (970–980)
nAl	548	39.4	65.0	0.25 (541–554)

Note: T_{ox}, the temperature of intensive oxidation onset; α_{ox}, the degree of oxidation; v_{ox}, the average rate of oxidation on the most intensive stage.
From DTA/TGA.

of 100 W [38]. The ES ignition time is determined by the appearance of flame by a photodiode signal.

The influence of Al powders on the ES ignitability was studied for two basic formulations of ES. The first formulation (sample A) contained 24 mass% of energetic binder of MPVT-LD type, 56 mass% of mixed oxidizer (AN/HMX in 50/50 ratio), and 20 mass% of Al powder. The second formulation (sample B) contained 12 mass% of inert binder (butyl rubber SKDM-80), 73 mass% of mixed oxidizer (AN/HMX/AP in 40/40/20 ratio), and 15 mass% of Al powder. Replacement of μAl by *n*Al generally reduces the ignition time of ES for both samples A and B at the radiant flux densities lower than 150 W/cm^2 (Figure 6).

The thermal imager Jade J 530 SB was used to determine the surface temperature of the reaction layer of ES at CO_2 laser ignition. The flame appearance for the sample A3 containing *n*Al occurred at ~550 °C. The flame appearance of sample A1 containing μAl occurred at ~710 °C. The heating and ignition times are substantially greater in the case of the sample A1 at the same values of the heat flux density.

Partial (50%) μAl → *n*Al replacement in the composition A (sample A2) reduced the average surface temperature of the reaction layer to ~660 °C at flame appearance.

The flame appearance for samples B1–B3 occurred at the average temperature ~470 °C, which is determined by the reactions in the gas phase at low temperature decomposition of oxidizers and combustible binder and does not depend on the Al oxidation and particle size. The heating time of the reaction layer for the sample B1 based on the inert binder was much lower than for the sample A1 on the basis of energetic binder containing μAl. In accordance with the solid phase ignition model, the calculated

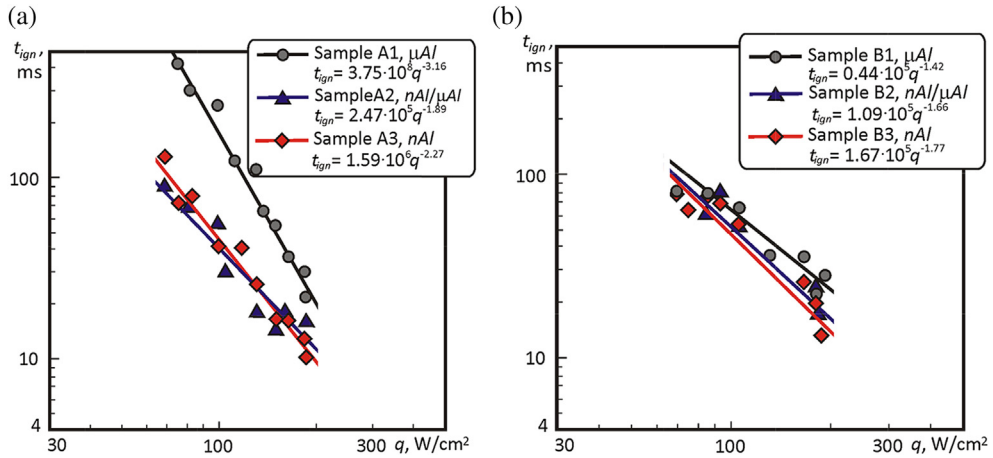

Figure 6 The ignition time of ES versus the flux density of laser radiation: (a) sample A: AN, HMX, MPVT-LD, and μAl or *n*Al; (b) sample B: AN, HMX, AP, SKDM-80, and μAl or *n*Al.

values of activation energy for ES composition B changed from 78 to 226 kJ/mol for increasing Al particle size [38] at the radiant fluxes 60–200 W/cm^2.

Thus, the ignition time of ES is dependent on the formulation, the type of binder, and the size of metal particles under the same pressure.

3.2 Ignition by Conductive Heat Flux

The ignition study of the ES based on 62 mass% AP, 18 mass% HTPB, 20 mass% Al (sample A) and 72 mass% AP, 18 mass% BKL, 10 mass% Al (sample B) on a heated body (conductive heating by a hot metal plate) [39] was conducted in air, at 0.1 MPa and within a temperature range 350–440 °C. The purpose was to estimate the temperature of the reaction layer of ES at ignition and the effect of burning rate control reaction in the condensed phase.

The ignition time of ES were reduced with the temperature of the plate surface increasing. Partial (50%) μAl → *n*Al replacement reduces the ignition time of ES based on AP and inert binder (Figure 7). The ratio of ignition time of ES by μAl → *n*Al replacement is increased from 1.2 to 1.8 when the temperature of the plate surface increases from 350 to 400 °C for samples A and from 1.2 to 1.5 when the temperature increases from 390 to 440 °C for samples B based on AP and BKL.

The mechanism of the *n*Al influence on the ignition process of ES is determined by the intensive oxidation of Al nanoparticles on the surface reaction layer. "Explosive ignitions" accompanied by cracking of the sample and loud sound effects [39] at the oxidation of Al nanoparticles in the reaction layer were observed. The two-stage oxidation is characteristic for *n*Al when a hot plate temperature is about 400 °C. Low-temperature oxidation proceeds with a rapid rise in temperature up to 2000 °C [21]. Thus, the more active the oxidizer and heat resistance of the binder, the more likely the "explosive ignition" mode occurs.

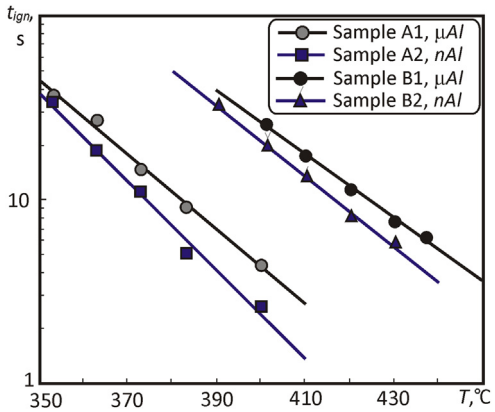

Figure 7 The ignition time of ES samples versus the temperature of hot plate: sample A: AP, HTPB and *m*Al or *n*Al; sample B: AP, BKL and *m*Al or *n*Al.

4. NANOALUMINUM COMBUSTION IN SOLID PROPELLANTS

The *n*Al improves the ballistics of solid propellants (SP). The presence of condensed combustion products (CCPs) upon firing the aluminized SP is very effective in damping the acoustic rocket motor instabilities, but CCPs also reduce the specific impulse and cause nozzle erosion. Two phase losses are a peculiar negative aspect of the combustion processes influenced by μAl powders. In addition, a significant amount of Al_2O_3 slag can accumulate in the chamber space close to the nozzle. Al_2O_3 accumulation may have important consequences on specific impulse, thermal insulation behavior, and thrust vectoring. The US space shuttle solid rocket boosters in static tests produce up to 1400 kg of alumina slag [25].

The usage of *n*Al is an effective method of minimization for some of the above-mentioned losses of aluminized propellants performance. Literature data concerning the burning rate of *n*Al-loaded SP formulations are summarized in Table 4. In the presented data summary, the *n*Al effects on the burning rate r_b are evaluated by the coefficient $K = r_{b,n\mathrm{Al}}/r_{b,\mu\mathrm{Al}}$ (ratio of the burning rate of *n*Al-loaded SP formulation and the burning rate of the corresponding SP formulation with μAl). The latter parameter has been determined for a reference combustion chamber pressure $p = 3.0$ MPa. For the particle size range 20–363 nm, the achieved r_b increase with respect to baseline value was from 25% to 421% for different binders and *n*Al content (see Table 4).

The possible scatter in the ballistic data could be due to the poor *n*Al dispersion in the polymer matrix and different ingredients used. The lab scale samples of few cm sizes also

Table 4 Overview of literature data on burning rate of *n*Al-loaded solid propellants.

Particle size of *n*Al, *d*, nm	*n*Al (Production technique/passivation or coating)	Solid propellant formulation (AP/Al/Binder), mass%	*K* (at $p = 3.0$ MPa)	References
145−154	EEW[d]/Al_2O_3	68/**15**/17 (HTPB)	1.73−1.76[c]	[40]
363	PC[e]/Hydrocarbon		1.25[c]	
100[a]	EEW/Al_2O_3	71/**18**/11 (PBAN)	5.21	[41]
145−154	EEW/Al_2O_3	68/**15**/17 (HTPB)	1.80−1.77	[42]
20−80[a]	n.a.	51/**15**/34 (HTPB)	1.60[b]	[43]
30−100[a]			1.42[b]	
202	EEW/Al_2O_3	68/**14**/18 (HTPB)	1.78−1.52	[44]
202	EEW/1% HTPB		2.03	
127−136	EEW/Al_2O_3	68/**15**/17 (HTPB)	2.08−1.83	[45]
363	PC/Hydrocarbon		1.68	

[a]Given by the producer.
[b]Baseline formulation loaded with μAl spherical particles ($d = 34$ μm).
[c]Baseline formulation loaded with μAl flake particles ($d = 50$ μm).
[d]Electrical explosion of wires.
[e]Plasma condensation.

Table 5 The catalyst burning rate efficiency (K_{cat}) of metallized in air at atmospheric pressure, depending on the catalyst type and content.

Catalyst content in SP	K_{cat}
0% (no catalyst)	1.00
1% *n*Fe	1.15
1% *n*Cu	1.47
1% *n*Ni	0.10
4% *n*Fe	1.24
4% μFe	1.11

could be a source of errors. The small additives of *n*Al (2.5–5.0 mass%) to standard μAl-loaded SP result in 10–360% burning rate increasing at 4 MPa [46].

The catalytic effect of the EEW *n*Me additives to the SP formulations was evaluated by the coefficient $K_{cat} = r_{b,cat}/r_{b,0}$ [47]. The results are shown in Table 5. The studies were conducted in air at 0.1 MPa. The formulations included 10 mass% of 10 μm Al powder as the metal fuel. The burning rate increases in the catalyzed compositions by 10–47% due to the metal additives action.

5. NANOALUMINUM USAGE IN THERMITES

Nanothermites exhibit a reduced ignition time with respect to conventional, micron-sized compositions due to their enhanced reactivity demonstrated by DSC and laser ignition tests [48]. The nonisothermal heating of Al/MoO_3 thermite was investigated by DSC in Ar for two different Al particle sizes [48]. The tested μAl ($d = 10$–14 μm) exhibited exothermic reaction at $T = 959$ °C, after Al melting. And *n*Al ($d = 40$ nm) presents a marked exothermic effect at $T = 476$ °C. Addition of *n*Al to μAl can reduce ignition time of thermite formulations [49]. Performance of a thermite formulation depends on several factors: particle size of reagents, equivalence ratio, fuel/oxidizer particle size distributions, and actual density (free packed powders or pressed pellets).

Fuel-rich formulations exhibit shortened ignition time and higher burning rate [50,51] independently on the environment oxidizers (O_2, CO_2, H_2O). Combustion tests on low-density samples of *n*Al/*n*MoO_3 at ambient pressure and under vacuum conditions (~3.3 Pa) were described in Ref. [51]. There was no significant difference between burning rates in atmospheric and vacuum tests. This suggests that the environment oxidizers do not influence thermite combustion. Maximum burning rate is usually associated with fuel-rich conditions for the thermites of *n*Al with MoO_3 and CuO [50].

6. NANOALUMINUM IN EXPLOSIVES

Aluminum powders are added to explosives to enhance air blast, raise reaction temperatures, and increase bubble energies in underwater weapons. In explosives, as well as in solid composite propellants, it is generally assumed that the combustion of μAl particles occurs behind the reaction front, during the expansion of gaseous detonation products. Particles act as inert ingredients and are not oxidized in the reaction zone [24]. *n*Al powders are known to react faster than μAl in propellant and explosive compositions, and *n*Al particles are small enough to participate in the detonation reaction zone. The usage of EEW *n*Al in explosives was first investigated in Ref. [52]. The velocity of detonation for *n*Al/ADN mixtures increased by a factor of 2 [53]. The mechanism of *n*Al reactions in explosives is not yet clear and needs to be further studied.

7. CONCLUSION

Several classes of ES loaded with *n*Al have been analyzed. Many new ES like *n*Al/ice [54], SP with *n*Me as catalysts [39,47] require emphasis and very detailed results analyses. It is clear that aging [55] and aggregation/agglomeration problems for *n*Al as well as the problem of their low metal content will be hardly solved because they are connected with the physical and chemical state of those metastable nanoproducts. The limiting key factor of the *n*Al efficiency for SP technology is the adhesion of *n*Al particle surface to binder. However, for solid (hybrid) fuels the adhesion in *n*Al/binder pair is not critical, therefore such *n*Al-loaded ES are the most promising. They are mostly based on inert binders (HTPB, paraffin, etc.) and thus, aluminum content in powders will not be affected by storage. Still a lot of research activity has to be done in order to understand and to control the effects of *n*Me in explosives and SP with active binders (fast reactions). Thus, the fundamental question of *n*Al application—how to use the high specific surface of *n*Al with maximum efficiency—is still open for discussion.

ACKNOWLEDGMENT

The work was financed by the Alexander-von-Humboldt Foundation (Germany) and Ministry of Education and Science of Russian Federation (via Tomsk Polytechnic University, Federal Target Program contract RFMEFI58114X0001).

REFERENCES

[1] D. Vollath, Nanomaterials, second ed., Wiley-VCH, Weinheim, 2014.
[2] J.H. Seo, I. Jo, A.L. Moore, L. Lindsay, Z.H. Aitken, M.T. Pettes, X. Li, Z. Yao, R. Huang, D. Broido, N. Mingo, R.S. Ruoff, L. Shi, Two-dimensional phonon transport in supported graphene, Science 328 (5975) (2010) 213–216.
[3] A. Gromov, U. Teipel (Eds.), Metal Nanopowders: Production, Characterization, and Energetic Applications, Wiley-VCH, Weinheim, 2014.

[4] B.S. Bockmon, M.L. Pantoya, S.F. Son, B.W. Asay, Burn rate measurements in nanocomposite thermites, in: Proc. of Am. Inst. Aeronaut. Astronaut. Aerosp. Sci. Meeting, 2003. Paper No. AIAA-2003-0241.
[5] I.D. Morokhov, L.I. Trusov, S.P. Chizhik, Ultradispersed Metal Medium, Atomizdat, Moscow, 1977.
[6] H. Gleiter, Nanocrystalline materials, Progr. Mater. Sci. 33 (4) (1989) 223–315.
[7] K.A. Gilzin, Rocket Engines, Oborongiz, Moscow, 1950.
[8] P.F. Pokhil, A.F. Belyaev, YuV. Frolov, V.S. Logachev, A.I. Korotkov, Combustion of Powdered Metals in Active Media, Science, Moscow, 1972.
[9] M. Summerfield (Ed.), Solid Propellant Rocket Research, Academic Press, New York, 1960.
[10] Y.B. Zeldovich, O.I. Leipunsky, V.B. Librovich, Theory of Non-stationary Combustion of Powders, Science, Moscow, 1975.
[11] A.A. Rempel, A.I. Gusev, Nanocrystalline Materials, International Science Publishing, Cambridge, 2004.
[12] G.B. Sergeev, Nanochemistry, Elsevier, Amsterdam, 2006.
[13] M. Suryanarayana, Mechanical alloying and ball milling, Progr. Mater. Sci. 46 (2001) 1–184.
[14] W.G. Chase, H.K. Moore (Eds.), Exploding Wires, Plenum, New York, 1962.
[15] Y.S. Kwon, A.A. Gromov, A.P. Ilyin, G.H. Rim, Passivation process for superfine aluminum powders obtained by electrical explosion of wires, Appl. Surf. Sci. 211 (2003) 57–67.
[16] Y.S. Kwon, A.A. Gromov, A.P. Ilyin, A.A. Ditts, J.S. Kim, S.H. Park, M.H. Hong, Features of passivation, oxidation and combustion of tungsten nanopowders by air, Int. J. Refract. Metal. Hard Mat. 22 (6) (2004) 235–241.
[17] A.V. Korshunov, Influence of dispersion aluminum powders on the regularities of their interaction with nitrogen, Rus. J. Phys. Chem. A 85 (7) (2011) 1202–1210.
[18] A. Gromov, Y. Strokova, A. Kabardin, A. Vorozhtsov, Experimental study of the effect of metal nanopowders on the decomposition of HMX, AP and AN, Propell. Explos. Pyrotech. 34 (2009) 506–512.
[19] A. Sossi, E. Duranti, M. Manzoni, C. Paravan, L.T. DeLuca, A.B. Vorozhtsov, M.I. Lerner, N.G. Rodkevich, A.A. Gromov, N. Savin, Combustion of HTPB-based solid fuels loaded with coated nanoaluminum, Comb. Sci. Tech. 185 (1) (2013) 17–36.
[20] A.P. Il'in, A.A. Gromov, G.V. Yablunovskii, Reactivity of aluminum powders, Combust. Explos. Shock Waves 37 (4) (2001) 418–422.
[21] A.A. Gromov, A.P. Il'in, U. Foerter-Barth, U. Teipel, Effect of the passivating coating type, particle size, and storage time on oxidation and nitridation of aluminum powders, Combust. Explos. Shock Waves 42 (2) (2006) 177–184.
[22] Y.S. Kwon, A.A. Gromov, A.P. Ilyin, Reactivity of superfine aluminum powder stabilized by aluminum diboride, Comb. Flame 131 (2002) 349–352.
[23] L. Liu, F. Li, T. Linghua, M. Li, Y. Yang, Effects of nanometer Ni, Cu, Al and NiCu powders on the Thermal decomposition of ammonium perchlorate, Propell. Explos. Pyrotech. 29 (2004) 34–38.
[24] N. Kubota, Propellants and Explosives: Thermochemical Aspects of Combustion, Wiley-VCH, Weinheim, 2001.
[25] J. Duterque, Experimental studies of aluminum agglomeration in solid rocket motors, Int. J. Energ. Mat. Chem. Propuls. 4 (1997) 693–705.
[26] O.G. Glotov, V.E. Zarko, V.N. Simonenko, D.A. Yagodnikov, V.S. Vorob'ev, Ignition, combustion, and agglomeration of encapsulated aluminum particles in a composite solid propellant. II. Experimental studies of agglomeration, Combust. Explos. Shock Waves 43 (3) (2007) 320–333.
[27] V. Babuk, I. Dolotkazin, A. Gamsov, A. Glebov, L.T. DeLuca, L. Galfetti, Nanoaluminum as a solid propellant fuel, J. Propul. Power 25 (2) (2009) 482–489.
[28] G.V. Sakovich, V.A. Arkhipov, A.B. Vorozhtsov, A.G. Korotkikh, B.V. Pevchenko, N.I. Popok, L.A. Savel′eva, Burning rate control of metal nanopowder-based high-energy materials, in: Proc. Of IV Internat. Workshop "High Energy Materials: Demilitarization, Antiterrorism and Civil Application «HEMs−2008", Biysk, Russia, FSUE FR&PC ALTAI, 2008, pp. 130–131.
[29] G.V. Sakovich, V.A. Arkhipov, A.B. Vorozhtsov, A.G. Korotkikh, Solid propellants on basis of double oxidizer containing aluminum ultra-fine powder, Bull. Tomsk Polytechnic Univ. 314 (3) (2009) 18–22.

[30] V.A. Arkhipov, S.S. Bondarchuk, A.G. Korotkikh, V.T. Kuznetsov, A.A. Gromov, S.A. Volkov, L.N. Revyagin, Influence of aluminum particle size on ignition and nonstationary combustion of heterogeneous condensed systems, Combust. Explos. Shock Waves 48 (5) (2012) 625–635.
[31] V.A. Arkhipov, S.S. Bondarchuk, A.G. Korotkikh, Comparative analysis of methods for measuring the transient burning rate. II. Research results, Combust. Explos. Shock Waves 46 (5) (2010) 570–577.
[32] V.A. Arkhipov, S.S. Bondarchuk, A.G. Korotkikh, A.B. Vorozhtsov, A. Bandera, L. Galfetti, L.T. DeLuca, G. Colombo, Nonsteady effects of the combustion of high-energy nanocomposites, Russ. Phys. J. 50 (9/2) (2007) 3–12.
[33] V.V. Pomerantsev, Fundamentals of Practical Combustion Theory, Energoatomizdat, Leningrad, 1986.
[34] T. Bazyn, H. Krier, N. Glumac, Evidence for the transition from the diffusion-limit in aluminum particle Combustion, Proc. Comb. Inst. 31 (2) (2007) 2021–2028.
[35] V.I. Levitas, Burn time of aluminum nanoparticles: strong effect of the heating rate and melt-dispersion mechanism, Comb. Flame 156 (2) (2009) 543–546.
[36] Y. Ohkura, P.M. Rao, X. Zheng, Flash ignition of Al nanoparticles: mechanism and application, Comb. Flame 158 (12) (2011) 2544–2548.
[37] A.G. Korotkikh, V.T. Kuznetsov, V.A. Arkhipov, I.A. Evseenko, The influence of radiation spectral composition on the ignition characteristics of composite solid propellants, Khimicheskaya Fizika i mezoskopiya 14 (2) (2012) 186–192.
[38] V.A. Arkhipov, A.G. Korotkikh, The influence of aluminum powder dispersity on composite solid propellants ignitability by laser radiation, Comb. Flame 159 (1) (2012) 409–415.
[39] V.A. Arkhipov, A.G. Korotkikh, V.T. Kuznetsov, E.S. Sinogina, Influence of metal powders dispersity on the characteristics of conductive and radiant ignition of mixed compositions, Khim. Fiz. 26 (6) (2007) 58–67.
[40] L.T. DeLuca, L. Galfetti, G. Colombo, F. Maggi, A. Bandera, V.A. Babuk, V.P. Sindistkii, Microstructure effects in aluminized solid rocket propellants, J. Propul. Power 26 (4) (2010) 724–732.
[41] Dokhan, E.W. Price, J.M. Seitzman, R.K. Sigman, The effects of bimodal aluminum with ultrafine aluminum on the burning rates of solid propellants, Proc. Comb. Inst. 29 (2) (2002) 2939–2946.
[42] L.T. DeLuca, L. Galfetti, F. Severini, L. Meda, G. Marra, A.B. Vorozhtsov, V.S. Sedoi, V.A. Babuk, Burning of nano-aluminized composite rocket propellants, Combust. Explos. Shock Waves 41 (6) (2005) 680–692.
[43] K. Jayaraman, K.V. Anand, S.R. Chakravarty, R. Sarathi, Effect of nano-aluminium in plateau-burning and catalyzed composite solid propellant combustion, Combust. Flame 156 (8) (2009) 1662–1673.
[44] A. Reina, Nano-metal Fuels for Hybrid and Solid Propulsion (Ph.D. thesis), Politecnico di Milano, 2013.
[45] A. Conti, Steady Burning and Ignition Properties of Aluminized Solid Rocket Propellants, Politecnico di Milano, 2007 (M.Sc. thesis).
[46] E.M. Popenko, A.A. Gromov, Y.Y. Shamina, A.P. Il'in, A.V. Sergienko, N.I. Popok, Effect of the addition of ultrafine aluminum powders on the rheological properties and burning rate of energetic condensed systems, Combust. Explos. Shock Waves 43 (1) (2007) 46–50.
[47] V.A. Arkhipov, A.G. Korotkikh, V.T. Kuznetsov, L.A. Savel'eva, Influence of dispersivity of metal additions on combustion rate of mixture compositions, Khimicheskaya Fizika 23 (9) (2004) 18–22.
[48] M.L. Pantoya, J.J. Granier, Combustion behavior of highly energetic thermites: nano versus micron composites, Propell. Explos. Pyrotech. 30 (1) (2005) 53–62.
[49] K. Moore, M.L. Pantoya, S.F. Son, Combustion behaviors resulting from bimodal aluminum size distributions in thermites, J. Propul. Power 23 (1) (2007) 181–185.
[50] V.E. Sanders, B.W. Asay, T.J. Foley, B.C. Tappan, A.N. Pacheco, S.F. Son, Reaction propagation of four nanoscale energetic composites (Al/MoO_3, Al/WO_3, Al/CuO, and Bi_2O_3), J. Propul. Power 23 (4) (2007) 707–714.
[51] B.W. Asay, S.F. Son, J.R. Busse, B.S. Jorgensen, B. Bockman, M.L. Pantoya, Ignition characteristics of metastable intermolecular composites, Propell. Explos. Pyrotech 29 (4) (2004) 216–219.

[52] A.A. Reshetov, V.B. Shneider, N.A. Yassvorovsky, Ultra Dispersed Aluminum's Influence on the Speed of Detonation of Hexogen, in: First All-Union Symposium on Macroscopic Kinetic and Chemical Gas-Dynamics, vol. 1, 1984.
[53] P.J. Miller, C.D. Bedford, J.J. Davis, Effect of metal particle size on the detonation properties of various metallized explosives, in: Eleventh International Symposium on Detonation, 1998, pp. 214–220.
[54] D.S. Sundaram, V. Yang, T.L. Connell Jr., G.A. Risha, R.A. Yetter, Flame propagation of nano/micron-sized aluminum particles and ice (ALICE) mixtures, Proc. Comb. Inst. 34 (2) (2013) 2221–2228.
[55] S. Cerri, M.A. Bohn, K. Menke, L. Galfetti, Ageing behaviour of HTPB rocket propellant formulation, Centr. Eur. J. Energ. Mater. 6 (2009) 149–165.

CHAPTER FOUR

Mechanisms and Microphysics of Energy Release Pathways in Nanoenergetic Materials

M.R. Zachariah and G.C. Egan
Department of Chemical and Biomolecular Engineering and Department of Chemistry and Biochemistry, University of Maryland, College Park, Maryland, United States

1. INTRODUCTION

As with any other new class of materials, a critical step on the path to optimization and control is establishing a deep understanding of the physics and chemistry involved in its processes. This allows for the creation of models that can drive and guide the further development of these systems. However, for the case of nanoenergetic materials, several experimental challenges have until recently limited our understanding of the fundamental physical processes that control reaction and propagation. In many ways, these challenges are direct consequences of the advantages gained by moving from traditional energetics to nanoscale materials. For example, the high reaction rates that make these materials so desirable also demand that the diagnostic tools used be capable of fast response and high temporal resolution. Additionally, while using smaller particles increases specific surface area and reduces length scales between fuel and oxidizers, which increase reactivity, this also limits our ability to directly probe reaction at the scale on which it occurs. The small sizes of these materials also lead to the formation of fractal aggregates during synthesis and handling as can be seen in Figure 1. These complex morphologies promote coalescence and sintering that reduces surface area and destroys nanostructure on time scales faster or comparable to reaction [1–3]. Further, the high temperatures that are one of the most significant benefits of metal-based nanoenergetics create complex multiphase and nonequilibrium environments during combustion, which significantly complicates interpretation of results.

More challenges arise from the reactive nature of the metallic fuels often used, typically aluminum (Al), which causes a 2–5 nm shell of oxide material to form on the nanoparticles and serves as a barrier to reaction [4,5]. This shell is perhaps also one of the reasons that nanoaluminum has been shown to have combustion behavior that is highly heating rate dependent [6,7]. This dependence places further constraints on experimental techniques with the need to reproduce the high heating rates (estimated at

Energetic Nanomaterials
ISBN 978-0-12-802710-3, http://dx.doi.org/10.1016/B978-0-12-802710-3.00004-0

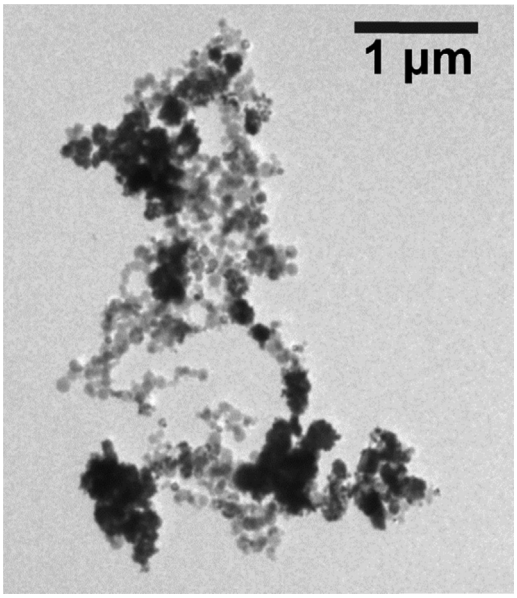

Figure 1 An example of the complex structures that can occur in nanomaterials. This is a transmission electron microscope (TEM) image of Al/CuO nanothermite mixed with ultrasonication in ethanol. The lighter spherical material is Al and the dark, more irregular shapes are CuO.

10^5–10^8 K/s) found during combustion [3,7]. While there is still significant value to slow heating rate techniques (e.g., DSC, TGA), any theories of mechanistic behavior must be validated with experiments reproducing these high heating rate conditions [8].

The compounded impact of all these challenges has prevented the development of a cohesive theory for the physics that control nanoenergetic reaction. Indeed there are still several conflicting theories for the underlying mechanism [3,5,9–11]. All of this discussion is exemplified with one of the most prevalent experiments in the nano-energetic community: burn tubes (see Figure 2) [12]. These experiments are comprised of loading a tube with energetic material, igniting from one end, and observing the propagation of the luminous front with high speed video and/or the pressure wave with a series of pressure transducers to determine a flame speed [12,13]. Such experiments are good examples of high speed diagnostics and feature the high heating rates of free combustion, which has led to their results being used as the basis for many of the theories and models of nanoenergetic combustion [5,14,15]. However, even the straightforward and exceedingly prevalent measurement (flame speed) has been shown to be significantly complicated by the challenging nature of these materials. Recent work by Densmore et al. has helped illuminate how much is still unknown about this widespread technique [16]. While the luminous front has long been taken as the reaction front, the authors showed that this front propagates even faster through unfilled tube, which suggests that it

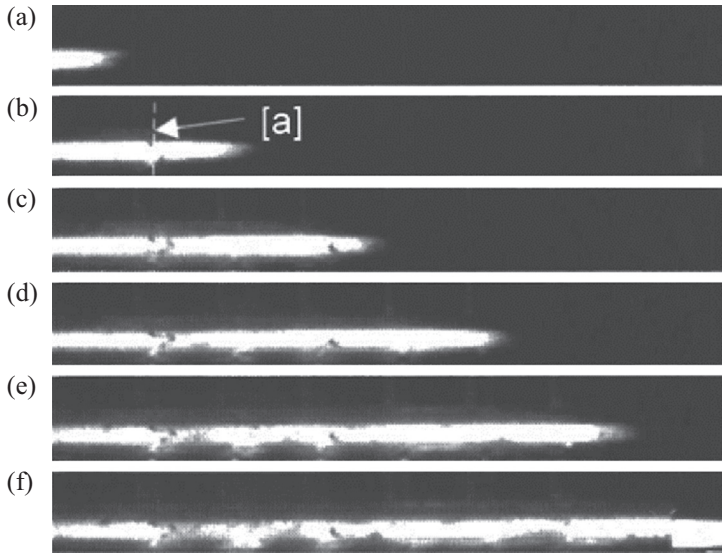

Figure 2 An example of a burn tube experiment involving Al/MoO_3. Parts (a–f) show sequential frames from a high speed camera taken ~20 μs apart, with frame (f) taken 100 μs after frame (a). Point [a] represents the location of a sensor. *Reprinted with permission from Ref. [12]. Copyright 2005, AIP Publishing LLC.*

does not represent the ignition of new material but rather already combusting material being propelled forward through the tube. Further, they showed that the materials remain hot and bright long after the luminous front passed, which implies that significant unreacted material exists and continues to burn far outside the initial passage of the luminous front. For these reasons and despite being one of the most prevalent measurements found in the field of nanoenergetics, the actual physical meaning of flame speed is far from understood.

Even with all these complications and challenges, significant progress has been made in understanding the mechanism of aluminum-based nanoenergetics by using novel experimental setups and advanced diagnostics. In this chapter we will provide the latest and best understanding of the microphysics that control nanoenergetic combustion, focusing on Al-based nanocomposites, which are referred to as nanothermites and metastable intermolecular composites (MICs). The overall process of reaction propagation can be divided into two components: heat transfer and reaction. Heat transfer is generally better understood than the reaction mechanisms but includes some processes more complex than a simple categorization as conduction, convection, or radiation. This will be the first topic discussed in this chapter. Before considering reaction, some discussion on the passivating effect of the oxide shell is needed. This layer serves as a barrier to reaction and must be overcome before or during the combustion process. This can be achieved through a simple diffusion of reactive ions through the barrier or a

physical deterioration of the shell through fracturing or softening. The physics and evidence for these different processes as well as their potential impact on reaction mechanism will be discussed.

For the possible reaction mechanism, we will discuss the three major pathways that have been proposed and considered throughout the literature: gas-condensed heterogeneous reaction, condensed phase interfacial reaction, and melt dispersion mechanism (MDM). The first is a two-step process with the solid oxidizer decomposing to produce gaseous oxygen, which then reacts heterogeneously with the solid or molten fuel. The second involves the transport of reacting species through the condensed phase and across the intercomponent interfaces [1,3,10]. Lastly, MDM has been theorized to occur for high heating rates of aluminum nanoparticles, where pressure buildup from the melting of the core causes violent rupture of the oxide shell and spallation of the Al core into small droplets that burn at high rates [7,11,17]. While multiple pathways could contribute to the overall reaction process, one will be the dominant process, although it is possible that which one dominates could change depending on combustion conditions.

2. HEAT TRANSFER

One thing that is certain from the burn tube experiments is that nanoenergetic reaction can produce hot material that moves very fast [16]. We also know that these waves of hot material coincide or slightly precede high pressure waves, even in materials that are not expected to produce significant gas [13,18]. This suggests that the primary means of heat transport is a convective process, which has been supported by a variety of studies [13,14,19,20]. The key evidence from these studies is that the highest flame speeds coincided with low packing densities, high gas production, low initial pressure, and confinement, which are all the conditions that are most conducive to moving gases and material. In comparison, condensed phase conduction would be oppositely affected or insensitive to those parameters. Convection is further supported by the high specific surface area and small sizes intrinsic to nanoparticles, which yields a very low thermal relaxation time, meaning that in a hot gas they will quickly equilibrate to that temperature [21].

Outside of experiments, it can also be established that a convective mechanism is dominant, through a process of elimination based on some simple order of magnitude calculations [22]. To make these calculations simpler, we will use the same base system of Al/CuO in a 3.2 mm inner diameter burn tube with a packing density of 6% theoretical maximum density (TMD), which is similar to a variety of experimental setups used in the literature [13]. In terms of heat transfer, the key value will be the energy needed to heat room temperature reactants to the point of ignition. For this point we will use 1300 K, which is the point at which Al has been found to be significantly mobile and

Table 1 Parameters used in the calculations and estimations made in this section. Those values in bold were chosen based on the experiments in Ref. [13]. The other values were calculated based on those parameters.

Burn tube calculation parameters	
Material system	**Al/CuO**
Tube inner diameter	**3.2 mm**
Packing density	**6% TMD**
Assumed ignition temperature	**1300 K**
Mass of material present	2.4 mg/mm
Energy needed for reactants to reach ignition temperature	2 J/mm

comparable to typical ignition temperatures of Al/CuO at high heating rates [2,23]. We will assume that no exothermic reaction happens below this ignition point, which is reasonable considering the fast timescales ($<<1$ ms) discussed. From the stated parameters, this burn tube will contain 2.4 mg of Al/CuO for each mm of packed tube. Using enthalpy data from the NIST Webbook, it would take $\sim$2 J to heat each mm of material to 1300 K. All of these parameters are summarized in Table 1 for easy reference. The following calculations can also be found in more detail in Ref. [22].

With those numbers in mind, we shall consider conduction through the powder media. While temperature gradients inside burn tubes have not been well characterized, the ignition front thickness was estimated by Asay et al. to be $\sim$10 mm based on pressure rise times and flame speed, which lines up reasonably well with recent temperature measurements [16,20]. Other measurements made with pyrometry have suggested even thicker temperature rise zones of $\sim$40 mm [24]. As we want upper bound estimates for heat transfer speed, we assume the smaller reaction zone for this calculation. Taking a thermal gradient from 3000 to 300 K over 10 mm along with the bulk thermal conductivity of Al (237 W/m-K), Fourier's law gives a heat flux of 6.4×10^7 W/m^2. Based on the assumed tube diameter, this corresponds to a heat flow of 510 W. Now if we consider all this energy to be delivered to the 1 mm of reactants discussed above, it would take 0.004 s to reach 1300 K. Dividing that considered distance by that time yields a flame speed of just 0.25 m/s, which is orders of magnitude less that those measured in burn tubes and open tray experiments [25]. It should be noted that this calculation stands as a strong overestimation of conductivity, as the thermal conductivity of Al is the highest in the system and we made the calculation based on fully dense material. In comparison, the effective conductivity of a porous nanoparticle bed can be an order of magnitude less than bulk [26,27].

We can give a similar treatment to radiative heat transfer. Nanoparticles have high specific surface area, which does support a radiative process. However, in the burn tube, the only radiation that will transfer heat to the unreacted materials is that which passes through the circular cross-section of the tube. Based on this, we can sum the

contribution of the many particles and simplify the system into two black body cylinders of material, one hot (3000 K) and one cold (300 K). Here the radiative heat transfer occurs through the presenting ends of the cylinders. Thus, from the Stefan–Boltzmann law, $\dot{Q}_{\text{rad}} = \sigma A(T_1^4 - T_2^4)$, where σ is the Stefan–Boltzmann constant and A is the cross-sectional area of the tube. For our problem, this yields radiative heat flow of 36 W, which is an order of magnitude less than what we found for conduction and corresponds to flame speed of 0.018 m/s. Again, this calculation serves as an overestimation of heat flow, particularly because, in practice, the local temperature difference will not be so extreme.

By ruling out the conduction and radiation, only heat transfer based on the flow of hot material remains. Yet despite the consensus in literature on the dominance of this mechanism, there is still much that is unknown regarding the physics of this process. The key question that remains is, exactly what species and materials are being advected forward to the unreacted zones? The high pressure wave found for nanothermite systems and the fast thermal relaxation time seem to suggest that hot gases would play a significant role in the transportation of heat. However, the amount of gases present in these systems is unlikely to be able to account for the amount of heat needed, as can be easily illustrated with some further simple calculations.

Returning to our example Al/CuO burn tube, experimental results have shown temperatures of ~3000 K and pressures of ~1900 psi [13,16]. Using the 3.2 mm inner diameter and considering a 1 mm section of tube, the ideal gas law yields only about 4×10^{-6} mol of gaseous species in that volume at these conditions. If we assume the movement of gases is responsible for heat transfer, the idealized scenario and upper bounds for the amount of heat transferred would be taking 100% of the hot gases produced from reaction and moving them into an equal volume cell of unreacted material. These gases would equilibrate with this material by cooling down and heating the reactants. However, the process of cooling the calculated amount of perfect gas ($c_p = 5/2$ R) from 3000 to 1300 K would only add 0.15 J to the reactants or only 7% of the 2 J needed to ignite 1 mm of reactant.

We can also consider that the gas could be in part formed from vaporized metals that could condense to release additional energy, but even that cannot produce the amount of energy needed. For Al/CuO at equilibrium, the amount of copper gas expected is 4 mol per kg of reactant, which is 9.6×10^{-6} mol for the 2.4 mg considered [13]. The heat of vaporization of copper is 300 kJ/mol, thus the energy liberated by condensing this amount of copper would be 2.9 J, which is 145% of the energy needed to reach ignition. However, despite theoretically providing sufficient energy, for several reasons it is unlikely that this mechanism is responsible for the significant portion of heat transport.

First, that concentration of copper gas was calculated at 1 atm constant pressure, which is not good representation of experimental conditions. Many experiments have shown that nanothermites can produce high pressures, which means that the reactions

produce gases faster than they can dissipate [13,28]. Thus, a constant volume approximation may be more accurate. In this case the confined volume would lead to higher pressures (as observed experimentally) and the vaporization of copper would be suppressed upon reaching the vapor pressure of Cu. Based on Cheetah equilibrium code calculations, Al/CuO at 10% TMD would only produce 0.18 mol of copper gas per kg of reactant, the condensation of which would only liberate 6.5% of the needed energy for ignition.

Second, copper vaporization (boiling point ~2840 K) is the final step of the reaction process and serves as a heat sink, which limits the flame temperature, which means that the potential 4 mol/kg of Cu gas will only exist when the reaction is near 100% complete. Therefore, this gas will only be available to participate in the heat transfer process if the reaction is sufficiently faster than the heat transport. However, nanothermites have been found to burn on the order of 0.1–3 ms, while even the slowest flame speeds are ~10 m/s, which means that they cover 1 mm in 0.1 ms [25,28,29]. A 1000 m/s flame would cover that distance in just 1 μs. This indicates that heat transfer is faster than or at least comparable to the overall reaction timescale, which indicates that much of the Cu gas will not participate in the process.

Finally, we must consider nonenclosed scenarios, where much of the gas produced will escape to the environment and will not contribute to the heat transfer process. While the exact percent of gas that is propelled forward rather than away from the propagation direction will depend on the experimental conditions and is not well defined, if even 30% of the 4 mol/kg of Cu gas is lost, there will no longer be enough energy to reach the ignition threshold. For all these reasons, we can conclude that the movement and condensation of Cu gas is likely not entirely responsible for the transfer of heat during propagation.

While there will be differences depending on the materials used, these calculation results will be similar as Al/CuO is one of the highest gas-producing thermites in terms of moles of gas produced [30]. So if the movement of gases does not control heat transfer, then there must be significant hot condensed phase material that is advected into the unreacted zones. Such a physical response is not surprising given the high flow velocities, pressure gradients, and low mass of nanoparticles found in these systems, which are conditions that would lead to the aerosolization of materials [29]. Indeed evidence of rapid gas release leading to hot material being rapidly thrown can be seen in high speed video of many combustion experiments. An example of this is Figure 3, which shows fuel-rich Al/CuO ignited by a wire heated at a high rate [23]. Hot, light-emitting species can clearly be seen to leave the wire at high velocity as a result of reaction. Large-scale effects of such behavior have been observed in the burning of unconfined lines of nanothermite, where hot material was propelled forward and caused a discontinuous jump in reaction front [25]. This has been explained as part of a pressure buildup and unloading model detailed in Ref. [31]. Assuming that the hot material being thrown

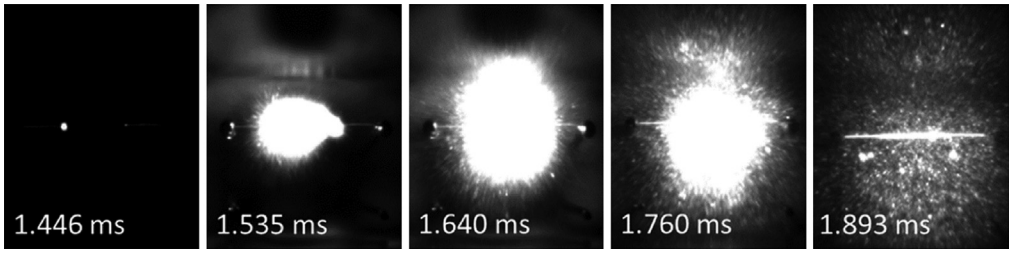

Figure 3 Frames taken from high speed video of fuel rich Al/CuO ignited by a temperature jump (T-Jump) wire experiment at heating rates of $\sim 5 \times 10^5$ K/s. All the material starts on the wire, but reaction and rapid gas production drives material away at high rates. For scale, the fully bright wire in the final frame has a length of 10 mm. *Reprinted with permission from Ref. [23]. Copyright 2012, American Chemical Society.*

would likely be molten, it would transfer its heat rapidly once in contact with unreacted material, leading to a very fast, if complex, form of heat transport. Advective behavior is also predicted by the melt dispersion mechanism, as the molten aluminum droplets produced would be propelled at high rates and would react as soon as they come into contact with an oxidizer [11,17].

3. PHYSICAL RESPONSE OF THE OXIDE SHELL

For any given sample of reactive metal, a 2–5 nm oxide shell is expected to form upon exposure to air (see Figure 4) [4,9,32]. Given the small length scales of nanomaterials, this thin layer can represent a significant portion of the mass leading to a large amount of dead weight. With aluminum, this passivating layer (Al_2O_3) has a melting temperature of 2345 K, which is much higher than the ignition temperatures typically found for aluminum-based nanoenergetics [19,33,34]. Therefore, through ignition, and potentially a significant portion of reaction, the shell is expected to be a barrier to reaction.

The simplest answer for how reaction occurs with respect to the shell would be a diffusion model where Al^+ diffuses out and O^- diffuses in. If oxygen diffused faster than the aluminum, this would produce a "shrinking core" scenario where the thickness of the shell increases inward, leading to a smaller and smaller metallic core [35–37]. Alternatively, if the outward diffusion of metallic ions is the faster process, then a thick, hollow oxide structure could result [38]. However, a hurdle to viability of this behavior is that self-diffusion coefficients for bulk Al_2O_3 are too low to account for the timescale measured in combustion experiments [17]. For example at $\sim$2000 K, Ref. [39] gives values of $\sim 10^{-15}$ and $\sim 10^{-17}$ m^2/s for Al and O in alumina. So given even a 2 nm oxide shell, one can expect a characteristic diffusion time $\left(\frac{l^2}{D}\right)$ of 4 ms, which is much

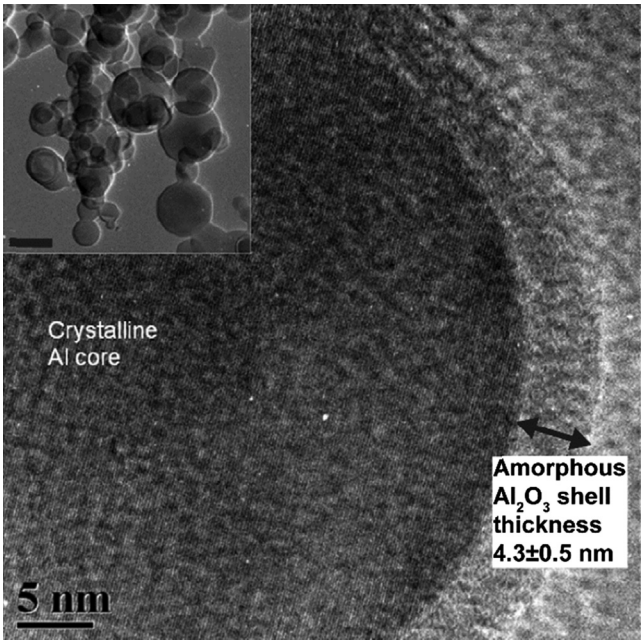

Figure 4 A high resolution transmission electron microscope (HR-TEM) image of an Al-NP and its amorphous oxide shell. The inset image is a lower magnification (scale bar = 100 nm) image of the same particle. *Adapted with permission from Ref. [32]. Copyright 2012, American Chemical Society.*

slower than the burn times and timescales found for Al-NP and nanothermite combustion, which have shown responses on the order of 10–50 μs. This suggests that cross-barrier diffusion may only be viable under slow heating rate conditions [17,28,40]. However, the kinetics of this process could be significantly enhanced by other mechanisms, such as an intrinsic electric field to support enhanced diffusion with a Cabrera–Mott mechanism as has been shown in molecular dynamics (MD) simulations and used in other models [41,42]. It is also possible that an initial diffusion step occurs during ignition, which then creates high temperatures and alternate pathways. This could explain the ignition delay observed in some systems [9].

The alternative to a diffusive process is one that involves the mechanical breakdown of the oxide shell. This would allow for a molten Al core to quickly diffuse through the produced cracks or, if associated with a large pressure buildup, potentially lead to violent spallation into molten drops as predicted by MDM [17,43]. There are several different manners in which the impact of the shell could be reduced or removed through physical processes. For example, the breakdown of the shell has been modeled based on the density changes caused by crystallization from its initially amorphous state, which has been shown to occur at temperatures below the melting point of Al [4]. An illustration of this process is shown in Figure 5. Heterogeneous crystallization and localized fracturing

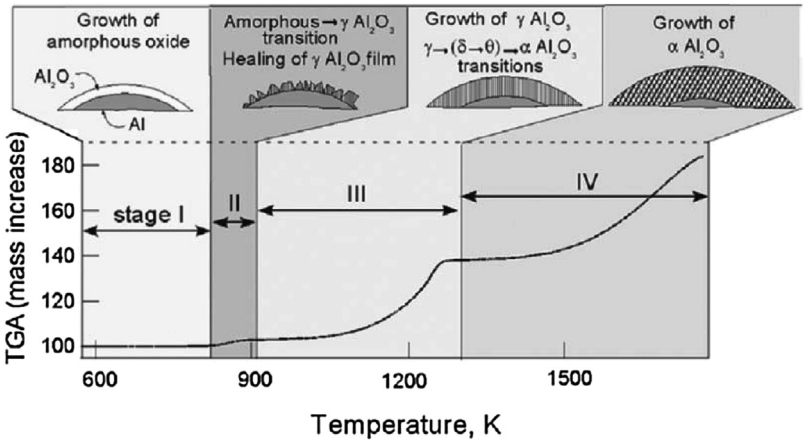

Figure 5 A schematic illustration of a proposed mechanism for aluminum oxidation based on the crystallization of the oxide shell. *Reprinted with permission from Ref. [4]. Copyright 2006, Taylor & Francis.*

in the oxide shell has also been observed with in situ transmission electron microscopy (TEM) experiments [32]. However, both of these observations were made from slow heating rate (<40 K/min) experiments, so it is not clear if the heat rate dependencies discussed above would impact the kinetics of the observed processes at the higher heating rates of combustion. Alternatively, a variety of MD simulations have shown a softening process in the oxide shell caused by interdiffusion between core and shell creating a metastable lower melting reduced oxide of Al [44–47]. Similar behavior was also observed in Ref. [32] with swelling of the oxide without an oxidizing environment. In addition, some high heating rate ($\sim 5 \times 10^5$ K/s) mass spectrometry has shown evidence of a decreased melting temperature of the shell [23]. One final option is the rupture and cracking of the shell from stresses induced by the melting of the aluminum core at 933 K. Upon melting, Al will expand by an estimated 6% while the oxide shell remains relatively static [17,43]. For nanoparticles this could lead to a pressure buildup, which could drive the fracturing of the shell.

Experimentally validating any of these possible mechanisms is a challenging proposition because of the nanoscale of the behavior and the necessity to produce high heating rates. One approach is to heat Al-NPs at high heating rates ex situ and analyze them after the fact with TEM. Both flash heating and T-Jump wire heating of Al-NPs in inert environments have shown the creation of hollow oxide structures that imply the escape of Al from the oxide shell, but it was not consistent for every nanoparticle [23,48]. Recent advances in the field of in situ electron microscopy have enabled direct imaging of morphological changes. High heating rate ($\sim 10^6$ K/s) hot stage studies have shown that heating Al-NPs above their melting points does not necessarily lead to the breakdown of the oxide shell as can be seen in Figure 6. Here the aggregate (Figure 6(a) and (b)) was

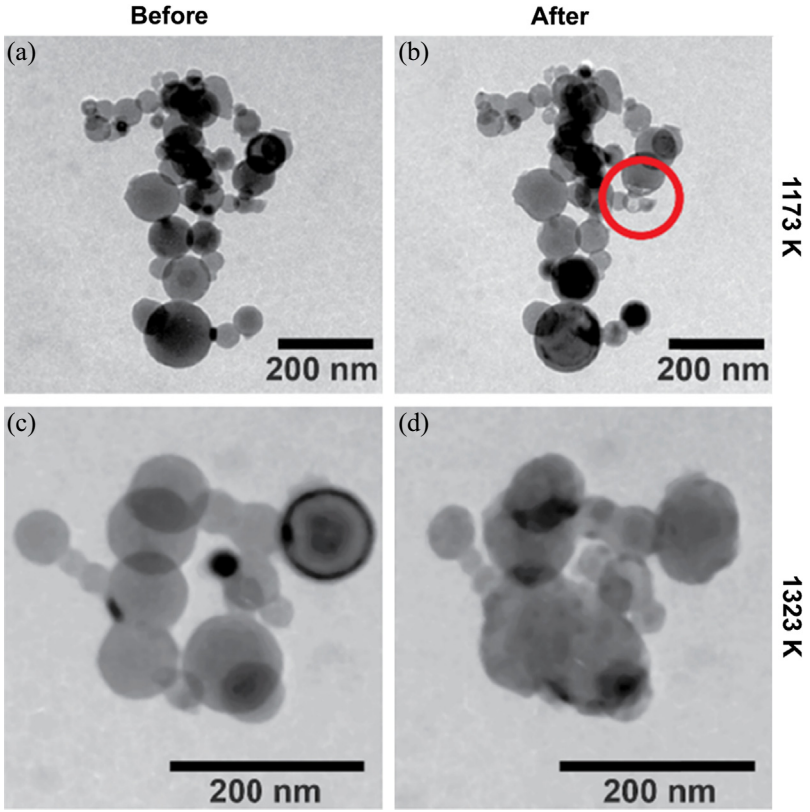

Figure 6 TEM images of Al-NPs heated in situ on a hot stage capable of $\sim 10^6$ K/s. Images (a) and (c) are the aggregates before heating to 1173 and 1323 K, respectively; (b) and (d) are the respective after images. *Adapted with permission from Ref. [2]. Copyright 2014, AIP Publishing LLC.*

heated above the melting point of Al but showed no significant rupture or morphological change except for the circled location where a small fracture may have occurred. However, the change in contrast between the before and after images does imply that melting occurred. In comparison, the aggregate heated above 1300 K (Figure 6(c) and (d)) exhibited significant morphological change. It is interesting to note that the coalescence process that occurred did not include any hollow ruptured shells as in the ex situ experiments discussed above and neither was there any violent rupturing like predicted by MDM. Instead it appears that the oxide shell flowed with the molten core, which suggests either a softening behavior as in the MD simulations or fracturing into pieces small enough to be carried with the Al. This latter process could be aided by the crystallization of the shell [4,32]. The same study also employed in situ laser heating to achieve higher heating rates (10^{11} K/s) and higher temperatures, which also allowed for nanosecond, time-resolved imaging with dynamic transmission electron microscopy (DTEM) [2]. As

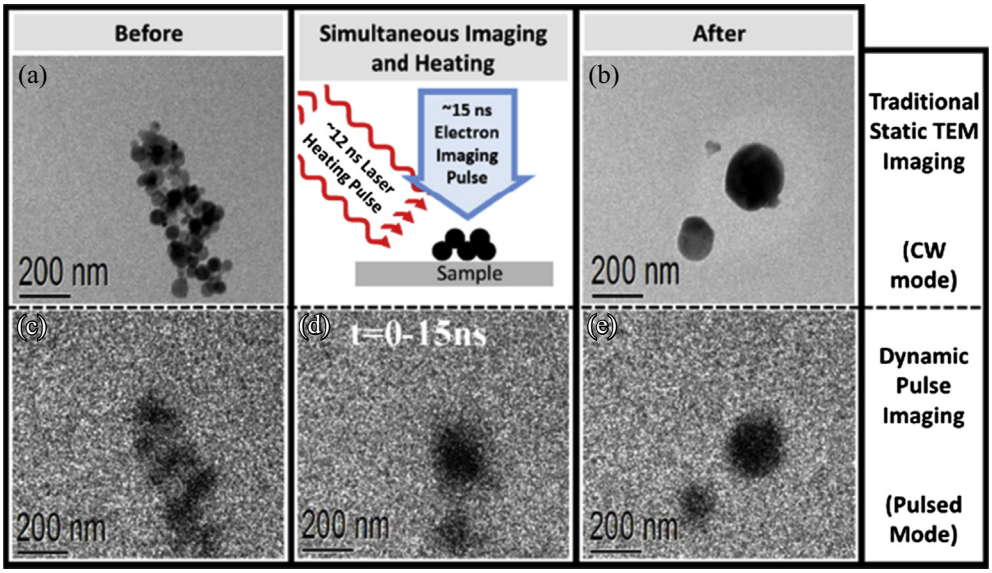

Figure 7 Example results from dynamic transmission electron microscopy (DTEM) experiments on Al-NPs. Images (a) and (b) were taken with traditional TEM imaging and show, respectively, the sample before and after heating by a 12 ns long 1064 nm wavelength heating pulse. Images (c–e) were taken using pulsed electrons, which allow for ~15 ns resolved images. *Reprinted with permission from Ref. [2]. Copyright 2014, AIP Publishing LLC.*

can be seen from the example in Figure 7, the Al-NPs exhibited similar physical response under these heating conditions, with apparent unrestrained flow of aluminum during coalescence. The time-resolved images taken during the laser heating pulse (Figure 7(d)) reveal that the process can occur on the order of ~15 ns. The coalescence observed is important for two reasons. First, it is dependent upon, and indicative of, overcoming the alumina barrier. Therefore at the temperatures and conditions at which coalescence can occur, reaction can proceed on timescales faster than the limited ones discussed for cross-barrier diffusion. This is supported by the short diffusion timescale observed in Figure 7. Second, the coalescence represents the loss of both surface area and nanostructure, which together provide some of the key benefits of using nanomaterials. This point will be addressed in more detail later in this chapter.

From all the results discussed in this section, it can be concluded that a significant step to nanoenergetic combustion is the breakdown of the passivating metal oxide layer. However, cross-barrier diffusion still could be important as a determining factor for ignition delays or as a mechanism responsible for weakening of the oxide shell. The exact nature of the overcoming of the shell is not yet well understood, but it has been observed in a variety of experiments. The breakdown exposes elemental aluminum that can be readily reacted through the mechanisms to be discussed below.

4. REACTION MECHANISMS

4.1 Gas-Condensed Heterogeneous Reaction

Unlike with heat transfer, there has been little consensus on the reaction mechanism of nanoenergetics. As discussed earlier, the possible physics can be fit into three broad categories. The first is the gas-condensed heterogeneous reaction mechanism, which has developed in response to the observation that many of the nanoparticle oxidizers used for nanoenergetics decompose to release oxygen at elevated temperatures [28,33,49]. This decomposition typically involves the reduction to a stable reduced phase (e.g., $CuO \rightarrow Cu_2O$, $Fe_2O_3 \rightarrow Fe_3O_4$, $Co_3O_4 \rightarrow CoO$, $WO_3 \rightarrow WO_2$). High heating rate mass spectrometry of these oxides and the corresponding thermites has shown that this reduction process often occurs at temperatures comparable to ignition and that significant gaseous oxygen is present during reaction [33,49]. This is all in accordance with the gas-condensed heterogeneous reaction mechanism, which is based on the burning of the fuel in the high-pressure O_2 environment created by the decomposition of these oxides. Part of the attraction of this mechanism is its relative simplicity, as it can be treated as almost a one-component system. The limiting step is either the reduction of the oxide to produce oxygen or the reaction of the fuel with the gas. As these two processes likely have very different kinetics, the overall reaction rate can be reduced to the slower of the two. Focusing on reaction, the problem of spheres burning in gases is a long-studied and well-understood one [50]. So even allowing for the role of the shell or the potential loss of nanostructure, this mechanism is conducive to relatively straightforward models. Further, it also has the advantage that burning of metallic nanoparticles in oxidizing environments can be studied directly in a wide array of different experiments [51–53]. Such studies provide a valuable metric in assessing the viability of the gas-condensed reaction mechanism as the timescales for the two forms of combustion can be compared.

To make this comparison, it is important to establish a timescale for nanothermite combustion, which is not a straightforward task. From burn tubes, velocities of $\sim$1 km/s and a reaction front width of 10 mm have been reported [20]. This suggests a characteristic time of $\sim$10 μs, but as discussed above, the exact nature of this front is not well understood. Constant volume pressure cell tests of the fastest nanocomposites suggest two rather distinct timescales, as can be seen in Figure 8. The pressure signal reaches its peak values in $\sim$10 μs, which is comparable to the burn tube experiments. On the other hand, the optical signal does not reach its maximum until $\sim$100 μs and has a full width at half maximum (FWHM) value of more than twice that. This order of magnitude difference in timescales suggests a two-step process that could be indicative of initial reaction, which heats up and reduces the oxidizer followed by heterogeneous burning in the released O_2 [28]. For the material ignited by wire in Figure 3, the visible process takes place over 400 μs, making it comparable to the optical signal in the pressure cell.

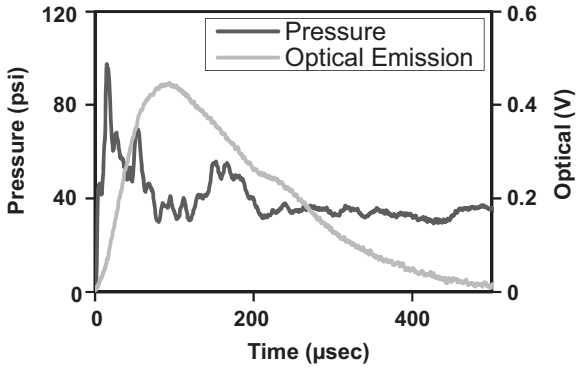

Figure 8 Results from Al/CuO nanothermite combustion in a constant volume pressure cell (25 mg of reactant in a 13 cc cell). Note that there is a considerable difference in the time to peak for the optical and pressure signals. *For details of the experimental setup, see Ref. [26].*

The challenge in interpreting these timescales is that it is not clear how the measured values relate to the overall reaction progress of these materials.

For Al-NPs burning in oxidizing environments the key measurement is burn time. One setup used to make this measurement is Bunsen burner–type experiments where aerosolized Al is burned and the flame produced is observed [53,54]. For particles smaller than 100 nm, burn times range from 10 ms down to 200 μs depending on temperature and oxidizing environment. The fastest of these timescales lines up well with the slower timescales of the nanocomposites. Even faster burn times have been found in shock tube experiments, which use a reflected shock to ignite materials at a variety of temperatures and elevated pressures [37,40,52]. Here Al-NPs were found to burn on a timescale of 50–500 μs. While that lower value is approaching the fast timescale for the nanothermites, the trend observed suggests 50 μs is the lower limit for burn time even at extreme pressures (32 atm) and temperature (>2000 K) [40]. Therefore, it seems unlikely that gas-condensed heterogeneous reaction could be responsible for the ~10 μs timescale but could be responsible for a slower burning that occurs after the initial fast reaction.

Another reason why this mechanism is unlikely to play the dominant role in determining reaction rate is that the decomposition properties of the oxidizer are not a good indicator of performance. With regard to ignition, there are some oxidizers (e.g., CuO, Fe_2O_3, $AgIO_3$) that show a correlation between the release of O_2 and the ignition with Al as shown in Figure 9 [49]. However, there are many more that show no similar trends. Indeed, Bi_2O_3, WO_3, MO_3, and SnO_2 have all been shown to ignite without any O_2 present. This suggests that for many cases, a gas-condensed heterogeneous reaction is not responsible for ignition.

Further, if gaseous oxygen was critical to the reaction, it would follow that the materials that release very little oxygen or decompose only at high temperatures would

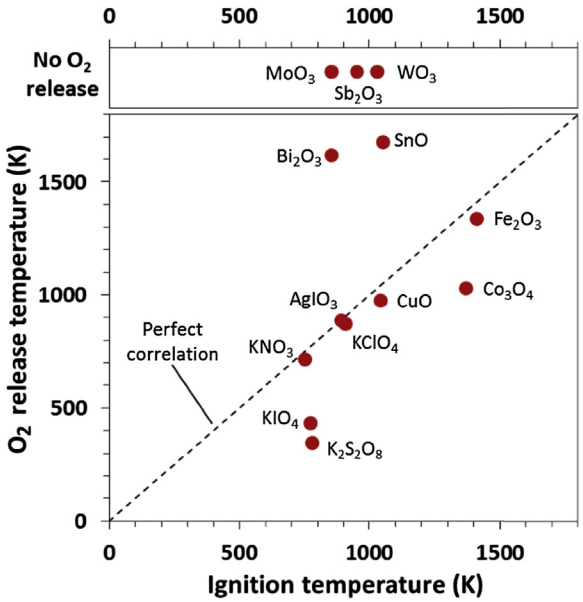

Figure 9 Data from high heating rate (~5 × 10^5 K/s) T-Jump TOF-MS experiments such as those in Ref. [47]. This figure shows the temperature at which O_2 was first observed during heating of the oxidizer alone (Y-axis) versus the ignition temperature of the oxidizer when mixed stoichiometrically with Al-NPs (X-axis). The oxidizers that were found to not release O_2 below the experimental limit (1700 K) are plotted separately at the top of the figure.

perform significantly worse than the O_2 producers. However, we can compare Figure 10 and Table 2 to see that this is not the case. Figure 10 shows the oxygen release profiles for various oxides during 3 ms heating pulses of ~5 × 10^5 K/s. It is clear that CuO produces the most oxygen, earliest, followed by Fe_2O_3, Bi_2O_3, and then SnO_2. Note that the time that the O_2 signal first rises is proportional to the O_2 release temperatures plotted in Figure 9. If the presence of gaseous oxygen was important to the overall reaction process, it would follow that CuO would perform the best in combustion tests with Fe_2O_3, Bi_2O_3, and SnO_2 performing comparably but with Fe_2O_3 being the best of that bunch. Looking at Table 2, we find that this is not the case. The pressurization rate, which correlates to flame speed in a burn tube and is indicative of overall performance, is similar for CuO, Bi_2O_3, and SnO_2 [55]. Only Fe_2O_3 is a significantly worse performer, with a pressurization rate two orders of magnitude slower. Similarly, MoO_3, which does not release O_2 below 1700 K, will also react in the TOF-MS with aluminum without the presence of detectable O_2 during reaction [33]. Thus, again, if gaseous oxygen was critical to the reaction mechanism, MoO_3 would be expected to be a terrible performer, but burn tube studies have found it to be one of the best [13].

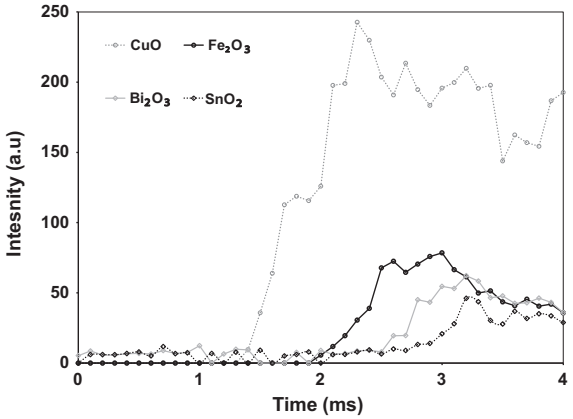

Figure 10 The O_2 release profiles from various oxidizers as measure by T-Jump TOF-MS. Each sample was heated with a similar 3 ms long heating pulse of $\sim 5 \times 10^5$ K/s. The lines represent a smoothing of the data point to guide the eye.

Table 2 Experimental pressure cell results for various thermites.

	Peak pressure, psi	Pressurization rate, psi/μs	FWHM burn time, μs
Al/SnO_2	80	7.7	210
Al/Bi_2O_3	123	12	193
Al/CuO	108	11	185
Al/Fe_2O_3	13	0.017	936

Data taken with setup discussed in Ref. [26].

4.2 Condensed Phase Interfacial Reaction and the Loss of Nanostructure

As an alternative to the previously discussed mechanism, this one assumes that oxidation occurs directly between the condensed phase (i.e., solid or molten) fuel and the condensed phase oxidizer. While this has often been considered as a possible and viable pathway for reaction of nanoenergetics, the underlying properties and processes have not been very well developed. This is in part because it is a far more challenging problem to conceptualize and model in comparison to particles burning in a gas. Consider the complex aggregate morphology shown in Figure 1. How would a condensed phase reaction progress for this case? By definition it must occur across interfaces between the materials, but in this initial configuration the amount of interfacial area is only the points of contact between adjacent nanoparticle spheres of differing components. These very limited interfaces would severely limit the flux of reacting species and lead to very slow kinetics. However, if there is some degree of mobility in either the fuel or the oxidizer, it can coalesce toward the opposite component and thereby increase the amount of

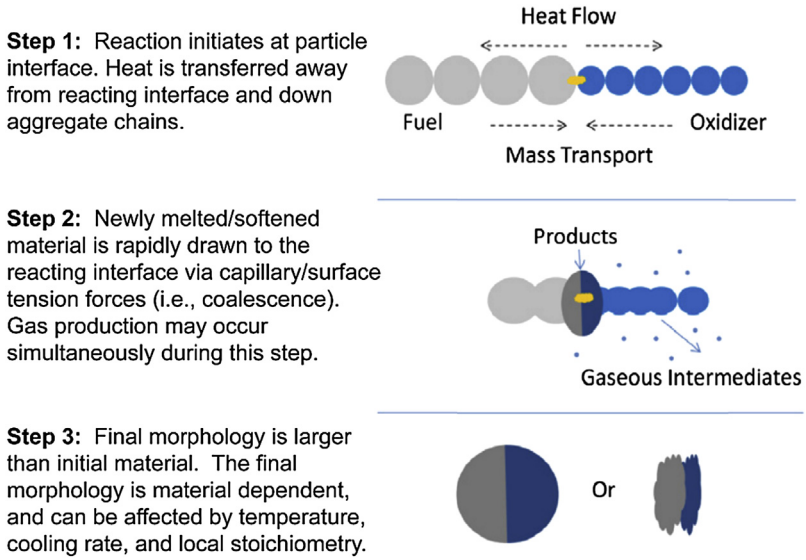

Figure 11 A schematic representation of the reactive sintering process. *Adapted from Ref. [3], Copyright 2012, with permission from Elsevier.*

contact. The increased interfacial area will increase reaction rates, which will generate heat, which will drive further coalescence leading to a feedback loop of sorts. This general process, which is illustrated schematically in Figure 11, has been dubbed reactive sintering [3].

Even with this general conception for the mechanism, the details and information needed to derive models are far from clear. For example, this process is dependent on the loss of original nanostructure, which means the initial configurations and morphologies will be lost prior to the bulk of reaction. How then will the length scale and total interfacial area develop? And how, if at all, will this process be related to that initial configuration? However, before we delve into such complicated processes, we will assess the viability of this proposed mechanism.

To do so, we will first consider a system that vastly simplifies the problem of reaction to a question of one-dimensional diffusion. Reactive multilayers or nanolaminates are fully dense planar structures made up of alternating layers of fuel and oxidizer (Al/CuO example shown in Figure 12) or two metals that can combine to form an intermetallic phase [56–59]. Typically, they are created by physical vapor deposition. Being fully dense limits reaction to the condensed phase, and the planar geometry means that the interfaces and diffusion distances are well defined. For Al/CuO nanolaminates, speeds have been measured up to $\sim$80 m/s, which is comparable to values found for nanoparticle thermites in similar open configuration experiments [19,25,58]. This indicates that condensed phase reaction could be fast enough to account for the high reaction rates in

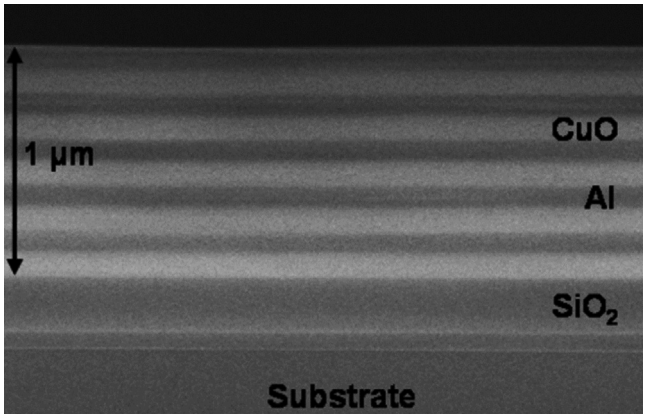

Figure 12 An example of an Al/CuO reactive multilayer that was sputter deposited onto an oxidized silicon substrate. *Reprinted with permission from M. Petrantoni, C. Rossi, L. Salvagnac, V. Conedera, A. Esteve, C. Tenailleau, P. Alphonse, Y. J. Chabal, J. Appl. Phys. 108 (2010). Copyright 2010, AIP Publishing LLC.*

nanothermites if there is sufficient interfacial area. To estimate if this amount of contact is reasonable, we consider that ~80 m/s was achieved with bilayers that were 150 nm thick and comprised of 18% Al by weight. For a single bilayer there will be a single interface between components, and the area of this interface on a per mass basis can be calculated as $\frac{A}{At_b\rho} = \frac{1}{t_b\rho}$, where A is the interfacial area (width of film times length), t_b is the bilayer thickness, and ρ is the average density. Therefore, for the 80 m/s case there is 1.3 m^2/g of interfacial area. As bilayers are stacked, there will be additional interfaces between the bilayers, so with an infinite number of bilayers there will be two interfaces per bilayer, which would mean 2.6 m^2/g of interfacial area. Given that the nanoparticles typically used in nanothermites have specific surface areas an order of magnitude higher (27.7 m^2/g for 80 nm spherical Al-NPs), it seems reasonable that comparable interfacial area could be achieved even after considerable loss of nanostructure [13].

Another example of thermite material that is restricted to reacting through the condensed phase is material produced through arrested reactive milling (ARM) [36,60–63]. This procedure typically involves ball milling powders into full dense micron-scale materials that contain both fuel and oxidizer as nanoscale inclusions, as is shown in Figure 13. As with the nanolaminates, the fully dense nature of the materials limits the role of any gas-based reaction mechanism, although the geometry here is far less simple to model and the amount of interfacial area is not as well known. However, we can still take away the fact that these materials have been found to burn very quickly, with reaction initiated through electrostatic shock and flyer plates shown to have burn times <100 μs [61]. This is very similar to the timescales discussed in the previous section for loose powder nanothermites, which again suggests that condensed phase reaction kinetics are fast enough to explain combustion.

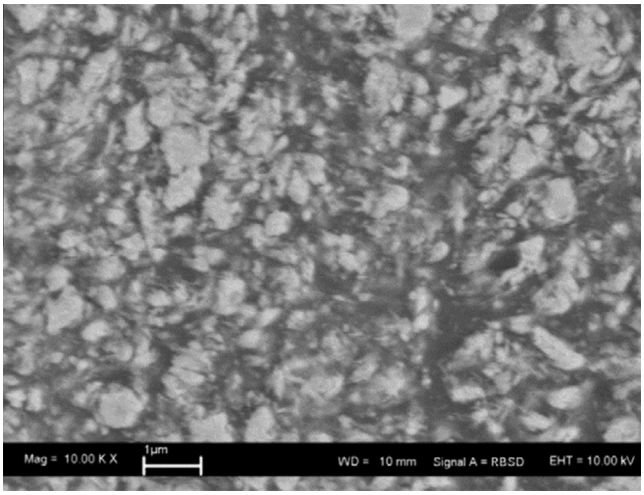

Figure 13 An example cross-section of a fully dense Al/CuO nanocomposite produced with ARM. Note the scale bar represents 1 μm. *Reprinted from Ref. [60]. Copyright 2011, with permission from Elsevier.*

For an even better study of the viability of this process in loose powder nanothermites, recent developments in the field of time-resolved electron microscopy allow for the timescale of this mechanism to be measured experimentally. Movie mode dynamic transmission electron microscopy (MM-DTEM) allows for the direct observation of nanometer-scale morphological change with nanosecond temporal resolution [1,64–66]. This technique uses short (~15 ns) electron pulses with high enough intensity that one pulse can generate an image. These imaging pulses are timed with respect to laser heating (~12 ns pulse, 10^{11} K/s heating rate) in order to determine the temporal evolution of the material. More details of this technique can be found in Refs [65,67,68]. Given that DTEM experiments occur in vacuum and with very small sample size, any effect of gas phase species will be greatly reduced, which makes the technique ideal for probing the condensed phase reaction process.

When applied to Al/CuO, DTEM studies showed morphological progression like that described above for condensed phase reaction, with melting and coalescence leading to the formation of large intercomponent interfaces. This behavior was found to occur on the order of hundreds of nanoseconds as shown in Figure 14. The final morphology of the DTEM products was consistently phase separated and EDS line scans confirmed that reaction had occurred with all of the oxygen located in the aluminum phase [1]. Further interaction was also found to have occurred with some cases of alloying to form Al_xCu_y phases. The time to completion was found to vary depending on the size of the aggregates observed, but generally ranged from ~0.5 to 5 μs. This lines up well with the ~10 μs discussed above as the defining value of fast nanoenergetic combustion.

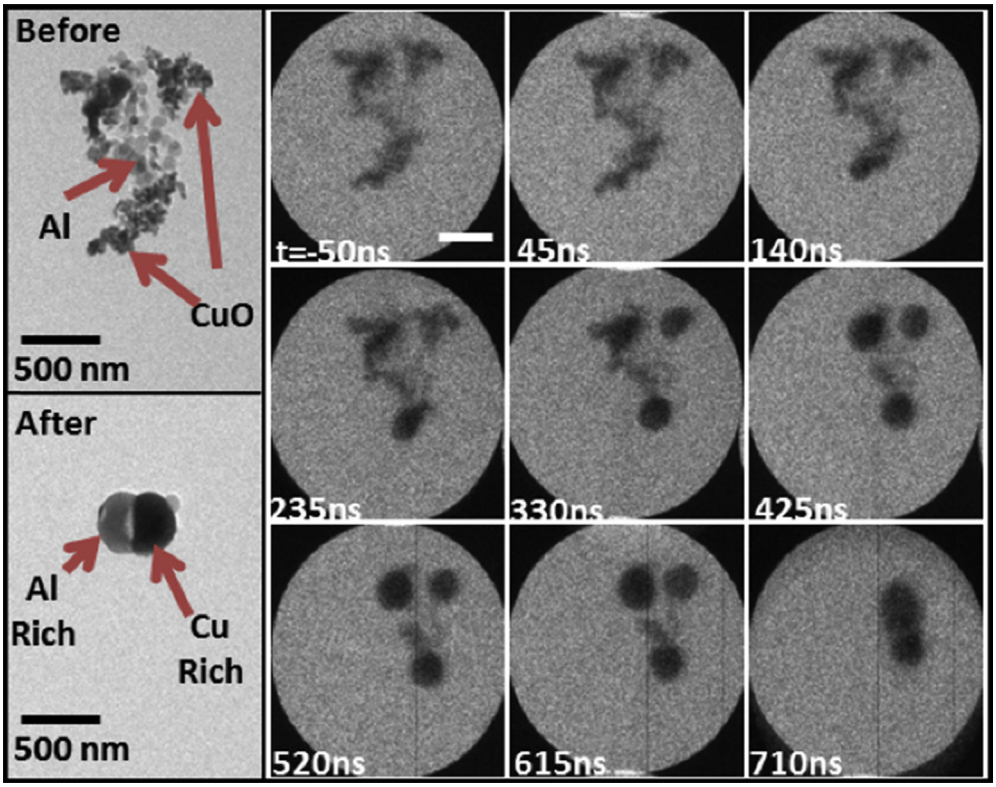

Figure 14 Results from an MM-DTEM experiment performed on Al/CuO nanothermite. The images on the left-hand side were taken with traditional TEM imaging and show the aggregate before and after reaction. The nine images to the right were taken with electron pulses spaced 95 ns apart. The listed times are with respect to the peak of the 12 ns heating pulse. More on this work can be found in Ref. [1].

Given that the kinetics of this condensed phase reaction appear to be sufficiently fast, the next step is to determine if it actually occurs during combustion. One of the defining properties of the condensed phase reaction mechanism as discussed so far is the loss of nanostructure and increase in particle size. Therefore, the products that result from such a reaction will be easily identifiable by significant interfaces and large sizes relative to the initial nanoscale reactants. Indeed there have been several different studies that have involved the capture of nanoenergetic material from a variety of experimental setups that have shown this type of product [10,25,69,70]. All these products exhibit resulting morphologies that were larger than 1 μm and contained both fuel and oxide elements within one particle as an alloy or in adjoining phases as shown in Figure 15(a). In their experimental setup, Jacob et al. were able to measure the time at which the product was collected relative to the point of ignition. From this they were able to determine that the

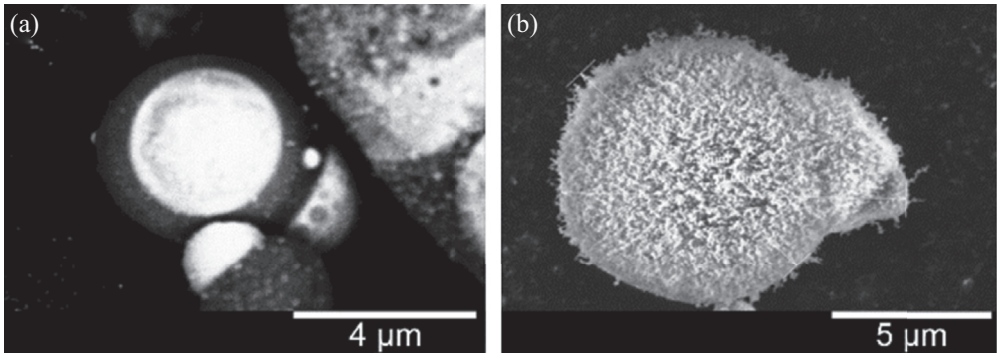

Figure 15 Product captured from a T-Jump ignition experiment (like the one shown in Figure 3) of Al/CuO nanothermite. The material in (a) was captured ~90 μs after ignition and was imaged using back-scattered electrons (BSE), which makes the heavier elements (Cu) appear brighter. The material in (b) was captured further out at a time of ~350 μs and does not use BSE. *Reprinted from Ref. [10]. Copyright 2015, with permission from Elsevier.*

products could not have formed from the vapor phase because not enough time had elapsed to form such large products. Thus, these large products must have formed directly in the condensed phase. The authors also noticed a large number of nanosized products that can be seen decorating the micron-scale particle in Figure 15(b). These averaged ~50 nm in diameter and were consistent with homogenous nucleation from the vapor phase. However, volume analysis indicated that this nanomaterial represented <15% of the total mass of the product [10].

The results of these studies fully support that condensed phase reaction occurs and is the dominant mechanism for nanothermite combustion. The significant loss of nanostructure that occurs in the formation of the large particles effectively closes off the possibility of gas-condensed heterogeneous reaction as the kinetics of that mechanism are highly size dependent [53]. Further, the large mass percent that these products represent suggests that they will be most responsible for generating heat. However, there were some inconsistencies between results that must be addressed before this mechanism can be taken for granted. In particular, the work with Al/Bi_2O_3 in Refs [10] and [69] both showed the formation of micron-scale particles from coalescence but showed differences in composition. Jacob et al. exhibited particles that contained both Al and Bi, while Poda et al. presented particles that were primarily Bi with the Al existing primary as nanoscale Al_2O_3. It is unclear why the two different combustion techniques (wire heating vs constant volume bomb cell) would produce such differences. Additionally, some authors have reported the opposite trend, with final product morphologies being considerably smaller [11,48]. In these cases it may be possible that the observed particles were from the vapor phase as discussed above and that sampling technique minimized the capture of large particles. So while there is significant evidence for condensed phase reaction being an important mechanism, future work is needed to explore these issues.

The general processes of condensed phase reaction raise some further questions about the effect that nanoscale features have on reactions. In particular, if we lose so much of our nanostructure prior to and during combustion, what then are the advantages to using nanomaterial? This is a fundamental question to the discussion of nanoenergetics, and we will address it several ways.

First, we would like to point out that several studies have shown diminished returns in performance as particle size is reduced through the nano regime. Take for example the data reproduced in Figure 16, which show burn tube flame speeds with varied particle fuel size [21]. Note the marked difference in trends after sizes are reduced to less than 3.5 μm, as well as the large spread in nanoparticle data. Another example is burn times of Al-NPs in gaseous oxidizers, which are expected to scale linearly with diameter under kinetically controlled burning [50]. However, studies have shown much lower dependence with a scaling law closer to $d^{0.3}$ instead [53]. In both these cases, the diminished returns through further reduction in size can be explained by the loss of nanostructure, with the small initial particles coalescing into large particles. If this happens prior to significant combustion, the material will have the kinetics of the larger particles. Such a process is likely as recent results have shown that the timescales for coalescence and sintering are much faster than those for combustion. This was found in part using molecular dynamic simulations, an example of which is shown in Figure 17. Here, 8 nm particles were found to coalesce in 0.7 ns [47]. This value can be extrapolated to more complex aggregates of larger sizes based on a modified Frenkel law [71]. Doing so yields a time of 50 ns for an aggregate of 100 particles with 50 nm diameters. This value lines up very well with the Al-NPs DTEM results discussed earlier and shown in Figure 7 [2]. This timescale is orders of magnitude faster than any of those discussed for reaction of aluminum-based nanoenergetics, the shortest of which was 10 μs.

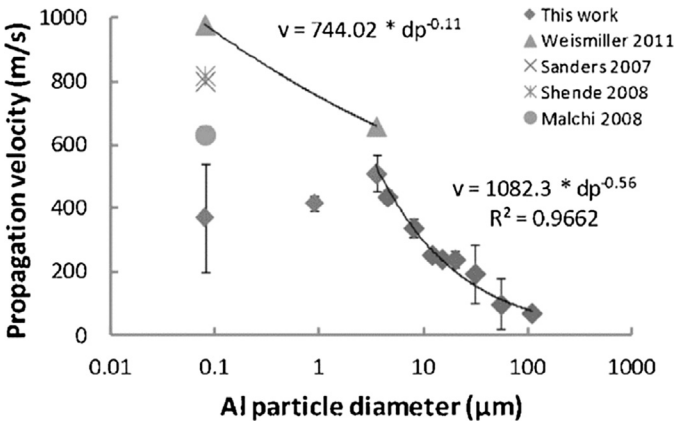

Figure 16 The effect of fuel particle size on combustion performance in a burn tube. *Reprinted from Ref. [21]. Copyright 2014, with permission from John Wiley and Sons.*

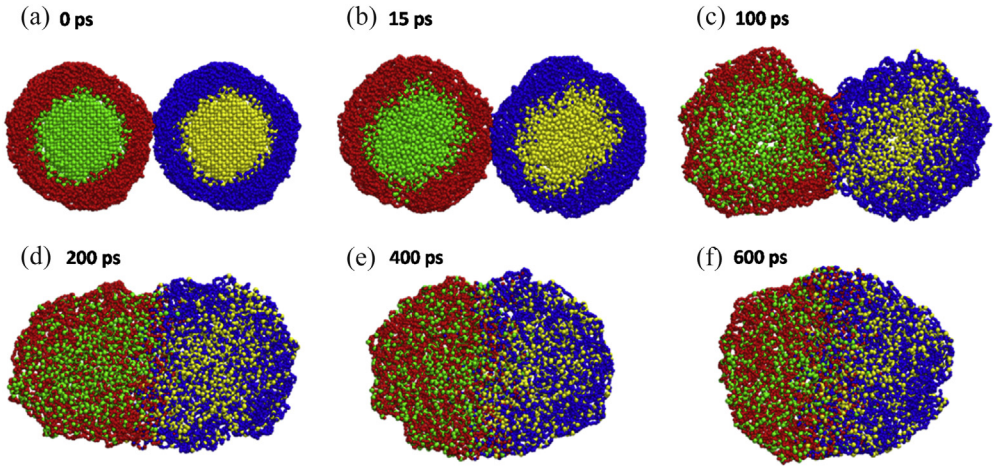

Figure 17 Molecular dynamics simulation of two 8 nm Al-NPs with oxide shells that were rapidly heated (0–15 ps) to 2000 K and held there. The system starts as two distinct particles in (a) that coalesce into a single particle over the course of 600 ps as shown sequentially in (c–f). The different colors represent the different designations for each oxide as either shell (oxide) or core (aluminum). *More details can be found in Ref. [45].*

Second, we want to point out that there are other potential advantages gained by using nanoparticles even if significant nanostructure is lost. One example is that nanomaterials allow for far more intimate mixing of fuel and oxidizer compared to larger composites. While it has been shown that the initial configuration of the material is quickly lost, the number of intercomponent interfaces during the early stages of reaction will still be dependent on the degree of segregation and the distances between components. Indeed, it has been shown that nanothermites are highly sensitive to mixing, although quantification of how this relates to intercomponent distances has not been well characterized [72–74]. The initial nanoscale may also aid in heat transfer as the loss of nanostructure is not expected until temperatures are comparable to ignition. Thus, the majority of the heating will occur prior to that process and when the material retains its small thermal mass and short thermal relaxation time. Additionally, the nanoscale could play a significant role in the breakdown of the oxide shell because the pressure buildup that could occur upon melting of the core would be size dependent [17,43]. Also, the added surface energy of nanoparticles will drive coalescence, leading the molten Al to escape the shell as well as move toward reaction interfaces. In this way the loss of nanostructure process could be beneficial to some degree.

Third, if we are indeed losing a significant portion of the benefits of nanostructure to the coalescence intrinsic to this condensed phase mechanism, material design approaches can account for this and minimize the effect. This will be discussed further in the final section.

As a final point of discussion for this section, we want to address the future work that is needed to fully understand the condensed phase mechanism. There is still much that is unknown about this process and how it relates to the overall propagation of reaction. The nature of the interfaces between the two components as the particle size grows is of particular interest. Many of the product particles were shown to contain elements from both fuel and oxidizers, so how does one define an interface in this case? Does the possibility of such alloying enhance the kinetics? These are the types of questions that must be addressed. The goal of gaining this understanding is to develop a model that can capture the appropriate physics and relate that to a reaction rate. However, the complex and dynamic morphologies intrinsic to this process make this a significant challenge. From the work so far, it seems that capturing the loss of nanostructure process will be a critical step in future developments. We speculate that this could be in part modeled based on a modified Frenkel law touched on above [47,71,75]. This could give the total amount of interfacial area over which reaction could occur, which could then be coupled with kinetics derived from nanolaminate studies.

4.3 Melt Dispersion Mechanism

The final of the possible reaction mechanisms to be discussed is the melt dispersion mechanism (MDM) [11,17,43]. As described briefly above, the premise of this reaction pathway is the violent rupture of the oxide shell that coats Al-NPs, as shown schematically in Figure 18. This event has been theorized to be caused by volumetric expansion of the metallic core upon melting, which would lead to a high stress buildup in the still solid oxide shell. It follows that for high heating rates, sufficient pressure would cause spallation of the core and shell. This material would be propelled forward and the Al would be readily able to react, which would drive high propagation rates. Considerable calculation and experimental analysis have been done to support this theory, much

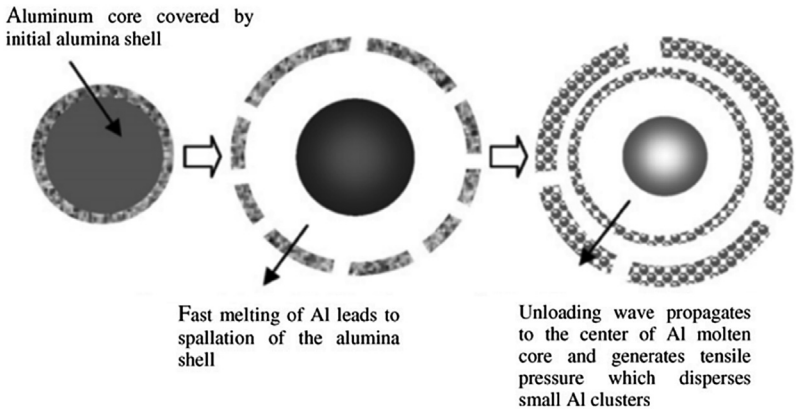

Figure 18 A schematic of the melt dispersion mechanism. *Reprinted from Ref. [7]. Copyright 2009, with permission from Elsevier.*

of which can be found in Ref. [76] and is summarized in a recent review article, Ref. [43]. This includes a model used to calculate the amount of melt in the core needed to fracture the shell, which was found to predict experimental flame speeds. Given these resources, we will not go into much further detail on the theory.

While this mechanism is fundamentally very different from the condensed phase discussed above, the two are not necessarily mutually exclusive. It is possible that MDM occurs when one set of experimental parameters is met and a condensed phase mechanism occurs under other parameters. Alternatively, both could occur simultaneously, but with one dominating the overall process. For example, in the sample collection experiment by Jacob et al. discussed in the previous section, there were two size regimes for products [10]. It could be that the micron-sized particles were the result of condensed phase interfacial reaction, while the smaller nanoscale products resulted from MDM. Even if this small particle population only represents a small portion of the overall combustion, with MDM it could still be significant because of the high burn rate suggested by the theory. However, we would like to point to DTEM experiments of both Al-NPs and Al/CuO nanocomposite, which have shown that coalescence and condensed phase reaction occur very fast without MDM. The fast kinetics observed there and discussed in the previous section are important because MDM was developed in part to explain the high flame speeds that were not compatible with simple diffusion across an oxide shell [1,2,43]. Further, despite the high heating rates in the DTEM experiments, there was no evidence of spallation occurring. For these reasons and the wide support found for it, we find the condensed phase interfacial reaction mechanism to be a more likely controller of reaction propagation than MDM.

Ultimately, more work is needed to determine what role, if any, MDM plays in the overall reaction of nanoenergetics. In particular, we would like to see more tests outside of burn tubes, which we have touched on as not being fully understood in terms of the kinetics of reaction [16]. And as this theory mostly focuses on the behavior of the fuel, we would like to see more on the effect of other factors, such as oxidizer material choice and size, have on determining flame rate.

5. CONCLUSION AND FUTURE DIRECTIONS

Throughout this chapter we have continually referred to how complex the reactions and mechanisms of nanoenergetic materials are and to the many experimental challenges that have limited our understanding of them. Despite this, the energetic community has been able to establish a solid knowledge base, in part with the aid of new high speed diagnostics and novel experimental setups. So while there is still much work to be done, the mechanisms of aluminum nanoenergetic reaction and propagation can be reasonably explained. Based on the discussion in the preceding sections, we can describe the overall process of combustion as follows. Heat is transferred through a convective process driven by high pressure buildup in the material. This pressure drives hot solid and

molten material forward into the unreacted zone. The heated metal escapes its shell through fracture or softening. It then begins to coalesce with the particles around it, which creates an interface with the oxidizer. Reaction then occurs across this interface with potentially significant alloying and intermixing speeding up this process. Throughout the reaction, gases are generated from the surfaces of these large particles, which propels more material forward and propagates the reaction. Behind this front, reaction continues with any O_2 generated earlier by reduction of the oxide. It is this step that likely accounts for the slower, secondary timescale found for some nanocomposites.

From this rough framework for the combustion process, we can anticipate what type of materials will form the basis of future nanoenergetics. For example, one issue to be overcome is the loss of nanostructure that occurs during condensed phase reaction. While to a certain extent this is necessary to increase the amount of intercomponent interfacial area, it can reach a point where the increased size and decreased surface area negatively impact kinetics. This effect can be minimized by keeping the aggregates as small as possible during reaction, which can be achieved with microstructured materials that incorporate gas generators [70]. Wang et al. were able to use electrospray to assemble Al/CuO nanothermite into microspheres (~5 μm) bound with nitrocellulose (NC), which would quickly generate gas at low temperature. The authors found that these mesoparticles significantly outperformed traditional Al/CuO as well as Al/CuO/NC that was physically mixed rather than assembled. The increased performance was found to correlate with product that was significantly smaller, as shown in Figure 19. It follows that the assembly and gas generation kept the Al/CuO nanoparticles from becoming

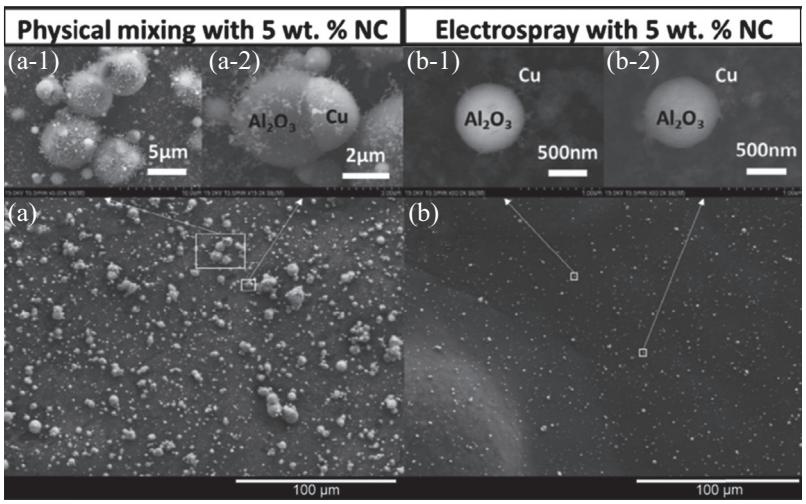

Figure 19 Product collected from the combustion of Al/CuO/NC nanoenergetics. The material for (a) was produced using a traditional nanothermite mixing technique (ultrasonication). Electrospray synthesis was used to form mesoparticles, which had increased overall performance and led to much smaller product as shown in (b). *Reprinted from Ref. [70]. Copyright 2014, with permission from Elsevier.*

too aggregated. As a result, the material retained more of its specific surface area as it coalesced, which would increase the overall reaction rate. This strategy has also been employed and shown promise in propellants, which further suggests its viability in the future [77].

Another approach for the future may be to design microstructure that can enhance and control the transport of energy. An example of this has been found to be effective for porous silicon-based energetics, where pillars were fabricated into the reaction pathway [78]. This addition caused a two order of magnitude increase in flame speed. The groundwork for similar structures has been laid for nanothermites as well. Researchers at Lawrence Livermore National Laboratory have used three-dimensional printed silver structures as an electrode, which is then coated with thermite using electrophoretic deposition [25,79]. With this tool, the goal will be to create well-designed architecture that can better direct the energy of reaction forward to enhance reactivity, as has been shown for microconfinement [80]. Such designs could take advantage of the properties of convective heat transfer discussed in Section 2. For this reason, something similar to pillars could be a good choice for thermites as well. In such a configuration, the hot material responsible for much of the energy transport could be thrown forward from one pillar to be caught by another.

In order to support the design of these new structures and materials, the development of new models will be critical. So while the exact nature of the next generation of nanoenergetics is not clear, we can be sure that they will be built with a further understanding of the mechanisms discussed above.

REFERENCES

[1] G.C. Egan, T. LaGrange, M.R. Zachariah, Time resolved nanosecond imaging of nanoscale condensed phase reaction, J. Phys. Chem. C 119 (5) (2015) 2792–2797.
[2] G.C. Egan, K.T. Sullivan, T. LaGrange, B.W. Reed, M.R. Zachariah, In situ imaging of ultra-fast loss of nanostructure in nanoparticle aggregates, J. Appl. Phys. 115 (8) (2014).
[3] K.T. Sullivan, N.W. Piekiel, C. Wu, S. Chowdhury, S.T. Kelly, T.C. Hufnagel, K. Fezzaa, M.R. Zachariah, Reactive sintering: an important component in the combustion of nanocomposite thermites, Combust. Flame 159 (1) (2012) 2–15.
[4] M.A. Trunov, M. Schoenitz, E.L. Dreizin, Effect of polymorphic phase transformations in alumina layer on ignition of aluminium particles, Combust. Theory Model. 10 (4) (2006) 603–623.
[5] V.I. Levitas, M.L. Pantoya, B. Dikici, Melt dispersion versus diffusive oxidation mechanism for aluminum nanoparticles: critical experiments and controlling parameters, Appl. Phys. Lett. 92 (1) (2008).
[6] M.L. Pantoya, J.J. Granier, The effect of slow heating rates on the reaction mechanisms of nano and micron composite thermite reactions, J. Thermal Anal. Calorim. 85 (1) (2006) 37–43.
[7] V.I. Levitas, Burn time of aluminum nanoparticles: Strong effect of the heating rate and melt-dispersion mechanism, Combust. Flame 156 (2) (2009) 543–546.
[8] E.L. Dreizin, Metal-based reactive nanomaterials, Prog. Energ. Combust. Sci. 35 (2) (2009) 141–167.
[9] S. Chowdhury, K. Sullivan, N. Piekiel, L. Zhou, M.R. Zachariah, Diffusive vs explosive reaction at the nanoscale, J. Phys. Chem. C 114 (20) (2010) 9191–9195.
[10] R.J. Jacob, G.Q. Jian, P.M. Guerieri, M.R. Zachariah, Energy release pathways in nanothermites follow through the condensed state, Combust. Flame 162 (1) (2015) 258–264.
[11] V.I. Levitas, M.L. Pantoya, S. Dean, Melt dispersion mechanism for fast reaction of aluminum nano- and micron-scale particles: flame propagation and SEM studies, Combust. Flame 161 (6) (2014) 1668–1677.

[12] B.S. Bockmon, M.L. Pantoya, S.F. Son, B.W. Asay, J.T. Mang, Combustion velocities and propagation mechanisms of metastable interstitial composites, J Appl. Phys. 98 (6) (2005).
[13] V.E. Sanders, B.W. Asay, T.J. Foley, B.C. Tappan, A.N. Pacheco, S.F. Son, Reaction propagation of four nanoscale energetic composites (Al/MoO_3, Al/WO_3, Al/CuO, and Bi_2O_3), J. Propuls. Power 23 (4) (2007) 707–714.
[14] M.R. Weismiller, J.Y. Malchi, R.A. Yetter, T.J. Foley, Dependence of flame propagation on pressure and pressurizing gas for an Al/CuO nanoscale thermite, Proc. Combust. Inst. 32 (2009) 1895–1903.
[15] B.D. Shaw, M.L. Pantoya, B. Dikici, Detonation models of fast combustion waves in nanoscale Al-MoO_3 bulk powder media, Combust. Theory Model. 17 (1) (2013) 25–39.
[16] J.M. Densmore, K.T. Sullivan, A.E. Gash, J.D. Kuntz, Expansion behavior and temperature mapping of thermites in burn tubes as a function of fill length, Propell. Explos. Pyrotech. 39 (3) (2014) 416–422.
[17] V.I. Levitas, B.W. Asay, S.F. Son, M. Pantoya, Melt dispersion mechanism for fast reaction of nanothermites, Appl. Phys. Lett. 89 (7) (2006).
[18] S.W. Dean, M.L. Pantoya, A.E. Gash, S.C. Stacy, L.J. Hope-Weeks, Enhanced convective heat transfer in nongas generating nanoparticle thermites, J. Heat Transfer Trans. ASME 132 (11) (2010).
[19] M.L. Pantoya, J.J. Granier, Combustion behavior of highly energetic thermites: nano versus micron composites, Propell. Explos. Pyrotech. 30 (1) (2005) 53–62.
[20] B.W. Asay, S.E. Son, J.R. Busse, D.M. Oschwald, Ignition characteristics of metastable intermolecular composites, Propell. Explos. Pyrotech. 29 (4) (2004) 216–219.
[21] K.T. Sullivan, J.D. Kuntz, A.E. Gash, The role of fuel particle size on flame propagation velocity in thermites with a nanoscale oxidizer, Propell. Explos. Pyrotech. 39 (3) (2014) 407–415.
[22] G.C. Egan, M.R. Zachariah, Commentary on the heat transfer mechanisms controlling propagation in nanothermites, Combust. Flame 162 (7) (2015) 2959–2961.
[23] G. Jian, N.W. Piekiel, M.R. Zachariah, Time-resolved mass spectrometry of nano-al and nano-Al/CuO thermite under rapid heating: a mechanistic study, J. Phys. Chem. C 116 (51) (2012) 26881–26887.
[24] M.R. Weismiller, J.G. Lee, R.A. Yetter, Temperature measurements of Al containing nano-thermite reactions using multi-wavelength pyrometry, Proc. Combust. Inst. 33 (2011) 1933–1940.
[25] K.T. Sullivan, J.D. Kuntz, A.E. Gash, Electrophoretic deposition and mechanistic studies of nano-Al/Cuo thermites, J. Appl. Phys. 112 (2) (2012).
[26] R. Prasher, Ultralow thermal conductivity of a packed bed of crystalline nanoparticles: a theoretical study, Phys. Rev. B 74 (16) (2006).
[27] X.J. Hu, R. Prasher, K. Lofgreen, Ultralow Thermal conductivity of nanoparticle packed bed, Appl. Phys. Lett. 91 (20) (2007).
[28] K. Sullivan, M.R. Zachariah, Simultaneous pressure and optical measurements of nanoaluminum thermites: investigating the reaction mechanism, J. Propuls. Power 26 (3) (2010) 467–472.
[29] K.T. Sullivan, O. Cervantes, J.M. Densmore, J.D. Kuntz, A.E. Gash, J.D. Molitoris, Quantifying dynamic processes of reactive materials: an extended burn tube test, Propell. Explos. Pyrotech. 40 (3) (2015) 394–401.
[30] S.H. Fishcer, M.C. Grubelich, A survey of combustible metals, thermites, and intermetallics for pyrotechnic applications, in: 32nd AIAA/ASME/SAE/ASEE Joint Propulsion Conference, Sandia National Laboratories: Lake Buena Vista, FL, 1996.
[31] K.T. Sullivan, S. Bastea, J.D. Kuntz, A.E. Gash, A pressure-driven flow analysis of gas trapping behavior in nanocomposite thermite films, J. Appl. Phys. 114 (16) (2013).
[32] D.A. Firmansyah, K. Sullivan, K.S. Lee, Y.H. Kim, R. Zahaf, M.R. Zachariah, D. Lee, Micro-structural behavior of the alumina shell and aluminum core before and after melting of aluminum nanoparticles, J. Phys. Chem. C 116 (1) (2012) 404–411.
[33] G. Jian, S. Chowdhury, K. Sullivan, M.R. Zachariah, Nanothermite reactions: is gas phase oxygen generation from the oxygen carrier an essential prerequisite to ignition? Combust. Flame 160 (2) (2013) 432–437.
[34] C.E. Aumann, G.L. Skofronick, J.A. Martin, Oxidation behavior of aluminum nanopowders, J. Vac. Sci. Technol. B 13 (3) (1995) 1178–1183.

[35] K. Park, D. Lee, A. Rai, D. Mukherjee, M.R. Zachariah, Size-resolved kinetic measurements of aluminum nanoparticle oxidation with single particle mass spectrometry, J. Phys. Chem. B 109 (15) (2005) 7290–7299.
[36] A. Ermoline, E.L. Dreizin, Equations for the Cabrera-Mott kinetics of oxidation for spherical nanoparticles, Chem. Phys. Lett. 505 (1–3) (2011) 47–50.
[37] P. Lynch, G. Fiore, H. Krier, N. Glumac, Gas-phase reaction in nanoaluminum combustion, Combust. Sci. Technol. 182 (7) (2010) 842–857.
[38] A. Rai, K. Park, L. Zhou, M.R. Zachariah, Understanding the mechanism of aluminium nanoparticle oxidation, Combust. Theory Model. 10 (5) (2006) 843–859.
[39] W.D. Kingery, H.K. Bowen, D.R. Uhlmann, Introduction to Ceramics, Wiley, 1976.
[40] T. Bazyn, H. Krier, N. Glumac, Combustion of nanoaluminum at elevated pressure and temperature behind reflected shock waves, Combust. Flame 145 (4) (2006) 703–713.
[41] B.J. Henz, T. Hawa, M.R. Zachariah, On the role of built-in electric Fields on the ignition of oxide coated nanoaluminum: ion mobility versus Fickian diffusion, J. Appl. Phys. 107 (2) (2010).
[42] D. Stamatis, A. Ermoline, E.L. Dreizin, A multi-step reaction model for ignition of fully-dense Al-CuO nanocomposite powders, Combust. Theory Model. 16 (6) (2012) 1011–1028.
[43] V.I. Levitas, Mechanochemical mechanism for reaction of aluminium nano- and micrometre-scale particles, Phil. Trans. R. Soc. A-Math. Phys. Eng. Sci. 2013 (371) (2003).
[44] Y. Li, R.K. Kalia, A. Nakano, P. Vashishta, Size effect on the oxidation of aluminum nanoparticle: multimillion-atom reactive molecular dynamics simulations, J. Appl. Phys. 114 (13) (2013).
[45] W.Q. Wang, R. Clark, A. Nakano, R.K. Kalia, P. Vashishta, Fast reaction mechanism of a core(Al)-shell (Al2O3) nanoparticle in oxygen, Appl. Phys. Lett. 95 (26) (2009).
[46] A. Shekhar, W.Q. Wang, R. Clark, R.K. Kalia, A. Nakano, P. Vashishta, Collective oxidation behavior of aluminum nanoparticle aggregate, Appl. Phys. Lett. 102 (22) (2013).
[47] P. Chakraborty, M.R. Zachariah, Do nanoenergetic particles remain nano-sized during combustion? Combust. Flame 161 (5) (2014) 1408–1416.
[48] Y. Ohkura, P.M. Rao, X.L. Zheng, Flash ignition of Al nanoparticles: mechanism and applications, Combust. Flame 158 (12) (2011) 2544–2548.
[49] L. Zhou, N. Piekiel, S. Chowdhury, M.R. Zachariah, Time-resolved mass spectrometry of the exothermic reaction between nanoaluminum and metal oxides: the role of oxygen release, J. Phys. Chem. C 114 (33) (2010) 14269–14275.
[50] R.A. Yetter, F.L. Dryer, Metal Particle Combustion and Classification. Microgravity Combustion: Fire in Free Fall, 2001, 419–478.
[51] P. Lynch, H. Krier, N. Glumac, A correlation for burn time of aluminum particles in the transition regime, Proc. Combust. Inst. 32 (2009) 1887–1893.
[52] T. Bazyn, H. Krier, N. Glumac, Evidence for the transition from the diffusion-limit in aluminum particle combustion, Proc. Combust. Inst. 31 (2007).
[53] Y. Huang, G.A. Risha, V. Yang, R.A. Yetter, Combustion of bimodal nano/micron-sized aluminum particle dust in air, Proc. Combust. Inst. 31 (2007) 2001–2009.
[54] C. Kong, Q. Yao, D. Yu, S. Li, Combustion characteristics of well-dispersed aluminum nanoparticle streams in Post flame environment, Proc. Combust. Inst. 35 (2) (2014) 2479–2486.
[55] S.F. Son, J.R. Busse, B.W. Asay, P.D. Peterson, J.T. Mang, B. Bockmon, M. Pantoya, Propagation Studies of Metastable Intermolecular Composites (MIC), Los Alamos National Laboratory, 2002. No. LA-UR-02-2954.
[56] T.P. Weihs, Fabrication and characterization of reactive multilayer films and foils, in: K. Barmak, K. Coffey (Eds.), Metallic Films for Electronic, Optical and Magnetic Applications: Structure, Processing and Properties, 2014, pp. 160–243.
[57] E.J. Mily, A. oni, J.M. LeBeau, Y. Liu, H.J. Brown-Shaklee, J.F. Ihlefeld, J.P. Maria, The role of terminal oxide structure and properties in nanothermite reactions, Thin Solid Films 562 (2014) 405–410.
[58] K.J. Blobaum, M.E. Reiss, J.M.P. Lawrence, T.P. Weihs, Deposition and characterization of a self-propagating CuO_x/Al thermite reaction in a multilayer foil geometry, J. Appl. Phys. 94 (5) (2003) 2915–2922.

[59] M. Bahrami, G. Taton, V. Conedera, L. Salvagnac, C. Tenailleau, P. Alphonse, C. Rossi, Magnetron sputtered Al-CuO nanolaminates: effect of stoichiometry and layers thickness on energy release and burning rate, Propell. Explos. Pyrotech. 39 (3) (2014) 365–373.
[60] A. Ermoline, M. Schoenitz, E.L. Dreizin, Reactions leading to ignition in fully dense nanocomposite al-oxide systems, Combust. Flame 158 (6) (2011) 1076–1083.
[61] M. Schoenitz, T.S. Ward, E.L. Dreizin, Fully dense nano-composite energetic powders prepared by arrested reactive milling, Proc. Combust. Inst. 30 (2005) 2071–2078.
[62] D. Stamatis, Z. Jiang, V.K. Hoffmann, M. Schoenitz, E.L. Dreizin, Fully dense, aluminum-rich Al-CuO nanocomposite powders for energetic formulations, Combust. Sci. Technol. 181 (1) (2009) 97–116.
[63] W.L. Shaw, D.D. Dlott, R.A. Williams, E.L. Dreizin, Ignition of nanocomposite thermites by electric spark and shock wave, Propell. Explos. Pyrotech. 39 (3) (2014) 444–453.
[64] M.R. Armstrong, K. Boyden, N.D. Browning, G.H. Campbell, J.D. Colvin, W.J. DeHope, A.M. Frank, D.J. Gibson, F. Hartemann, J.S. Kim, W.E. King, T.B. LaGrange, B.J. Pyke, B.W. Reed, R.M. Shuttlesworth, B.C. Stuart, B.R. Torralva, Practical considerations for high spatial and temporal resolution dynamic transmission electron microscopy, Ultramicroscopy 107 (4–5) (2007) 356–367.
[65] M.K. Santala, B.W. Reed, T. Topuria, S. Raoux, S. Meister, Y. Cui, T. LaGrange, G.H. Campbell, N.D. Browning, Nanosecond in situ transmission electron microscope studies of the reversible $Ge_2Sb_2Te_5$ crystalline double left right arrow amorphous phase transformation, J. Appl. Phys. 111 (2) (2012) 024309.
[66] B.W. Reed, M.R. Armstrong, N.D. Browning, G.H. Campbell, J.E. Evans, T. LaGrange, D.J. Masiel, The evolution of ultrafast electron microscope instrumentation, Microsc. Microanal. 15 (4) (2009) 272–281.
[67] T. LaGrange, B.W. Reed, M.K. Santala, J.T. McKeown, A. Kulovits, J.M.K. Wiezorek, L. Nikolova, F. Rosei, B.J. Siwick, G.H. Campbell, Approaches for ultrafast imaging of transient materials processes in the transmission electron microscope, Micron 43 (11) (2012) 1108–1120.
[68] T. LaGrange, G.H. Campbell, B. Reed, M. Taheri, J.B. Pesavento, J.S. Kim, N.D. Browning, Nanosecond time-resolved investigations using the in situ of dynamic transmission electron microscope (DTEM), Ultramicroscopy 108 (11) (2008) 1441–1449.
[69] A. Poda, R. Moser, M. Cuddy, Z. Doorenbos, B. Lafferty, C. Weiss, A. Harmon, M. Chappell, J. Steevens, Nano-aluminum thermite formulations: characterizing the fate properties of a nanotechnology during use, Nanomater. Mol. Nanotechnol. 2 (1) (2013) 1000105.
[70] H. Wang, G. Jian, G.C. Egan, M.R. Zachariah, Assembly and reactive properties of Al/CuO based nanothermite microparticles, Combust. Flame 161 (8) (2014) 2203–2208.
[71] T. Hawa, M.R. Zachariah, Development of a phenomenological scaling law for fractal aggregate sintering from molecular dynamics simulation, J. Aerosol. Sci. 38 (8) (2007) 793–806.
[72] K.S. Martirosyan, L. Wang, A. Vicent, D. Luss, Synthesis and performance of bismuth trioxide nanoparticles for high energy gas generator use, Nanotechnology 20 (40) (2009).
[73] R.R. Nellums, B.C. Terry, B.C. Tappan, S.F. Son, L.J. Groven, Effect of solids loading on resonant mixed Al-Bi_2O_3 nanothermite powders, Propell. Explos. Pyrotech. 38 (5) (2013) 605–610.
[74] F. Severac, P. Alphonse, A. Esteve, A. Bancaud, C. Rossi, High-energy Al/CuO nanocomposites obtained by DNA-directed assembly, Adv. Funct. Mater. 22 (2) (2012) 323–329.
[75] S.K. Friedlander, Smoke, Dust, and Haze, vol. 198, Oxford University Press New York, 2000.
[76] V.I. Levitas, B.W. Asay, S.F. Son, M. Pantoya, Mechanochemical mechanism for fast reaction of metastable intermolecular composites based on dispersion of liquid metal, J. Appl. Phys. 101 (8) (2007).
[77] T.R. Sippel, S.F. Son, L.J. Groven, Aluminum agglomeration reduction in a composite propellant using tailored Al/PTFE particles, Combust. Flame 161 (1) (2014) 311–321.
[78] V.S. Parimi, S.A. Tadigadapa, R.A. Yetter, Control of nanoenergetics through organized microstructures, J. Micromech. Microeng. 22 (5) (2012).
[79] K.T. Sullivan, C. Zhu, D.J. Tanaka, J.D. Kuntz, E.B. Duoss, A.E. Gash, Electrophoretic deposition of thermites onto micro-engineered electrodes prepared by direct-ink writing, J. Phys. Chem. B 117 (6) (2013) 1686–1693.
[80] G. Dutro, S. Son, A. Tappan, in: The Effect of Microscale Confinement Diameter on the Combustion of an Al/MoO_3 Thermite, 44th AIAA/ASME/SAE/ASEE Joint Propulsion Conference & Exhibit, 2008.

CHAPTER FIVE

Applications of Nanocatalysts in Solid Rocket Propellants

Feng-sheng Li, Wei Jiang, Jie Liu, Xiao-de Guo, Yu-jiao Wang and Ga-zi Hao
National Special Superfine Powder Engineering Research Center, Nanjing University of Science and Technology, Nanjing, China

1. INTRODUCTION

The solid rocket should have high capability and reliability, as required by modern high technology. This makes it urgent for technology to improve the integral performance of rocket propellant. At present, nanotechnology has gotten extensive worldwide attention and it has been natural for scientists to utilize the characteristics of nanoparticles to improve the performance of propellant. Many promising results have been achieved.

Ammonium perchlorate (AP) was for a long time the most commonly used oxidizer in the composite propellants, e.g., in hydroxyl-terminated polybutadiene (HTPB)-based propellants. The main effects of AP usage are as follows: (1) Provision of oxygen in the combustion of propellant to ensure enough amount of released energy. (2) Filler of binder matrix to improve mechanical integrity of propellant. (3) Control of the burning rate of propellant through the granularity of AP. The AP fraction in typical propellants comprises 60–90%. Thus one can understand that the thermal decomposition of AP directly affects the combustion performance of propellant, which can be predicted and evaluated on the basis of results of studying the thermal decomposition of AP and AP/HTPB.

In this chapter, the impact of metal nanoparticles (Ni, Cu, Al), metallic oxide nanoparticles (Fe_2O_3, CuO, Co_2O_3), and hydrogen-storage nanoparticles (LiH, MgH_2, Mg_2NiH_4, Mg_2CuH_3) on the thermal decomposition of AP, the impact of the metal and hydrogen-storage nanoparticles on the thermal decomposition of AP/HTPB, as well as the impact of nitrogen nanoparticles (nano-Ni), copper nanoparticles (nano-Cu), aluminum nanoparticles (nano-Al) and nano-Fe_2O_3 on the combustion performance of AP/HTPB propellants are discussed in detail.

Energetic Nanomaterials
ISBN 978-0-12-802710-3, http://dx.doi.org/10.1016/B978-0-12-802710-3.00005-2

2. IMPACT OF NANOCATALYSTS ON THE THERMAL DECOMPOSITION OF AMMONIUM PERCHLORATE AS OXIDIZER IN SOLID PROPELLANTS [1,2]

2.1 Thermal Decomposition Characteristics of Ammonium Perchlorate

To investigate the effects of metal powders on the thermal decomposition of AP, the thermal decomposition characteristics of AP itself should be studied first. In this chapter, the used AP particles were produced by Dalian North Chlorate Company of China with an average particle size of 60 μm. Numerous investigations on the thermal decomposition characteristics of AP have been carried out by experts and scholars worldwide [3,4], and some coherent results were obtained. AP is represented by relatively stable white color orthorhombic crystals, which begin to dissociate, sublime, and decompose when the temperature is higher than 150 °C. The thermal behavior of AP at atmospheric pressure upon increase of temperature has the following stages: (1) At 240−250 °C it transforms from orthorhombic phase to cubic crystal system, and this process is endothermic with the heat of crystal transformation −9.622 kJ/mol. (2) With further increased temperature, the minor thermal decomposition (low temperature decomposition) occurs at 330−350 °C accompanied by the dissociation and sublimation. The low temperature decomposition of AP is exothermic. This process ceases when about 30% of AP is decomposed. The remaining AP transforms into relatively stable porous form. (3) With the temperature continuing to increase, the major decomposition (high temperature decomposition) proceeds at 450−480 °C. In this stage, AP decomposes, completely releasing a substantial amount of heat. The typical differential scanning calorimetry (DSC) curve of AP thermal decomposition at the heating rate of 20 °C/min is shown in Figure 1.

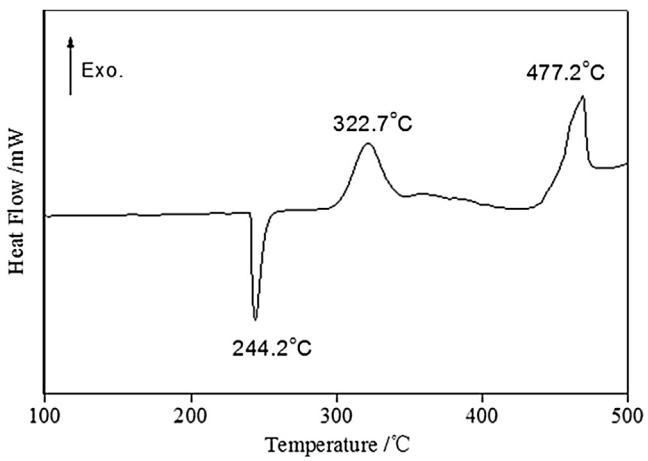

Figure 1 Differential scanning calorimetry (DSC) curve of AP.

3. IMPACT OF METAL NANOPARTICLES ON THE THERMAL DECOMPOSITION OF AP

3.1 Special Performance of Metal Nanoparticles

After the metals and alloys were prepared in the form of nanoparticles, they would have the common characteristics of nanoparticles such as the small scale effect, surface and interface effect, quantum size effect, and so on, which make metal nanoparticles exhibiting brand-new physical and chemical properties and having extensive application foreground.

1. Thermal properties.
   The melting point and crystallization temperature are both much lower for those of bulk powder materials. Because of the small size, high surface energy, and high specific surface atom density, nanoparticles require smaller energy to melt, resulting in the noticeable decrement of the melting point of nanoparticles.
2. Magnetic properties.
   Metal nanoparticles may have fascinating magnetic properties, sometimes showing superparamagnetism or high coercive force.
3. Surface activity and catalytic properties.
   In the case of metal nanoparticles the surface bonds and electron forms are dramatically different from those in the bulk of material, and there are a large number of unsaturated bonds caused by coordinately unsaturated surface atoms. All these contribute to the high surface activity of metal nanoparticles. The smaller the particle size, the bigger the surface atoms fraction, the larger the specific surface area, and the better the catalytic properties. In addition, much improved high adsorption ability is favorable for improving the catalytic properties.

3.2 Preparation of Nanoparticle/AP Composites

The preparation method of nanoparticle/AP composites would obviously affect the catalytic impact of nanoparticles on the thermal decomposition of AP. In order to disperse nanoparticles homogeneously into AP, we prepared nanoparticles and AP composite mixtures through careful grinding. This technique enables nanoparticles to disperse uniformly in AP. The preparation approach of nanoparticle/AP composites is generally as follows:

1. Sonicating freshly prepared metal nanoparticles in diethyl ether for several minutes and separately grinding the AP for finite time in agate mortar.
2. Placing the sonicated metal nanoparticles slurry into AP powder, then carefully grinding the mixture by hand until most of the ether is volatilized.
3. Placing the ground metal nanoparticle/AP composites in the vacuum-drying oven at room temperature for 30 min, then slightly grinding the metal nanoparticle/AP composites by hand to smash the agglomerates.

All of the above operations must be undertaken using serious precautions in order to avoid explosion of the mixture.

3.3 Effect of Ni Nanoparticles

According to numerous research reports, the addition of Ni nanoparticles into solid rocket propellant improves the combustion efficiency and increases the combustion velocity [5—7]. The effect of Ni nanoparticles on the thermal decomposition of AP is discussed below. The micron-sized Ni particles are produced by Jianghui Metal Powder Co., Ltd. in Botou city of China; they are used as the raw material to produce nanometer Ni particles with an average particle size of 50 nm using high frequency inductively coupled plasma technology.

3.3.1 Comparison of the Effects of Ni Nanoparticles and Micron-Sized Ni Particles on the Thermal Decomposition of AP

The DSC curves of the composites of nano-Ni/AP and micron-Ni/AP at the heating rate of 20 °C/min are shown in Figure 2. Curve 1 is the DSC signal of AP. Curves 2 and 3 are the DSC signals of the composites of micron-sized nanoparticles (micron-Ni) with different granularity and AP. The DSC signal of the composites of nano-Ni and AP is shown in Curve 4. The content of all Ni powders in the composites was 2 wt%. Table 1 presents the DSC data of the Ni/AP composites.

As shown in Figure 2, after adding Ni powders, the endothermic peak temperature of AP representing the transformation of rhombic to cubic form showed no change, indicating that Ni powders had no effect on the AP crystalline phase transformation. However, the exothermic peak temperatures of AP showed an obvious change.

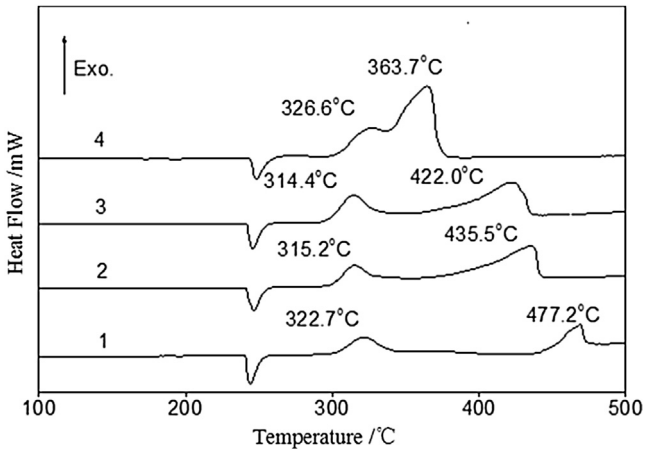

Figure 2 DSC curves of AP and Ni/AP, 1: AP, 2: 30 μm Ni/AP, 3: 20 μm Ni/AP, 4: 50 nm Ni/AP.

Table 1 DSC data on decomposition of AP and Ni/AP.

Sample	T_L, °C	T_H, °C	H, kJ/g
AP	322.7	477.2	0.436
30 μm AP/Ni	315.2	435.5	0.646
20 μm AP/Ni	314.4	422.0	0.727
50 nm AP/Ni	326.6	363.7	1.320

The exothermic peaks shifted to the lower temperature and became higher and wider, suggesting that Ni powders had a distinct effect on the exothermic decomposition of AP.

The stronger effect of nano-Ni is clearly demonstrated. The high exothermic peak temperatures (T_H) of pure AP and the composites of nano-Ni/AP were, respectively, 477.2 and 363.7 °C, showing that nano-Ni decreased the T_H of AP by 113.5 °C. In addition, nano-Ni slightly increased the low exothermic peak temperature (T_L) of AP, by 4 °C, and the decomposition heat (H) was increased from 0.436 to 1.320 kJ/g.

The kinetic parameters of the thermal decomposition of pure AP and Ni/AP composites are shown in Table 2. When nano-Ni was applied as the catalyst, the activation energy of high temperature decomposition (E_{0H}) of AP was decreased from 177 to 168 kJ/mol. At the same time, the activation energy of low temperature decomposition (E_{0L}) of AP was increased from 100 to 108 kJ/mol. Furthermore, the pre-exponential factor of high temperature decomposition (A_H) and low temperature decomposition (A_L) were both increased by the order of magnitude.

3.3.2 Effect of Nano-Ni Content

The DSC data of nano-Ni/AP composites with different content of Ni nanoparticles are shown in Table 3. The contents of nano-Ni in the composites were 0, 1, 2, 5, and 10 wt %, respectively. As can be seen in Table 3, with the contents of nano-Ni increasing from 0% to 10%, the corresponding T_H decreased from 477.2 to 350.5 °C. When the nano-Ni content was 1%, the low exothermic peak temperature of nano-Ni/AP composites was 317.5 °C, which was a bit lower than that of pure AP, indicating a weak catalytic effect of nano-Ni on the low temperature decomposition of AP. However, when nano-Ni content reached or exceeded 2%, the low exothermic peak temperature of nano-Ni/AP composite became a bit higher than that of pure AP. When the content

Table 2 Thermal decomposition dynamics parameters of AP and Ni/AP.

Sample	E_{0L}, kJ/mol	E_{0H}, kJ/mol	A_L	A_H
AP	100	177	6.92×10^6	2.68×10^{10}
30 μm AP/Ni	100	225	8.83×10^6	7.01×10^{14}
20 μm AP/Ni	101	175	1.23×10^7	2.06×10^{11}
50 nm AP/Ni	108	168	5.80×10^7	8.07×10^{11}

Table 3 DSC data on AP decomposition with different nano-Ni contents.

Content, %	T_L, °C	T_H, °C	H, kJ/g
0	322.7	477.2	0.436
1	317.5	388.0	1.230
2	326.6	363.7	1.320
5	328.6	361.3	1.380
10	350.5	350.5	1.470

of nano-Ni reached 10 wt%, the high and low temperature exothermic peaks of AP merged into a large exothermic peak with the peak temperature of 350.5 °C. At the same time, the H of nano-Ni/AP composites was increased from 0.436 to 1.470 kJ/g at 10 wt% of nano-Ni.

The above results show that 50-nm nano-Ni has remarkable effect on the thermal decomposition of AP, which is pronouncedly stronger than that of micron-Ni. When nano-Ni is added in AP, the high exothermic peak temperature is decreased. The higher the nano-Ni content, the lower T_H and the larger H.

3.4 Effect of Cu Nanoparticles

The effect of Cu nanoparticles on the thermal decomposition of AP is discussed in detail as follows [8—10]. The micron-sized Cu particles with an average particle size of 26 μm are produced by Tong Ling Copper Base Powder Co., Ltd. of China, and these particles are used as the raw material to produce nanometer Cu particles with an average particle size of 20 nm using high frequency inductively coupled plasma technology.

3.4.1 Comparison of the Effects of Cu Nanoparticles and Micron-Sized Cu Particles on the Thermal Decomposition of AP

The DSC curves of Cu/AP composites at the heating rate of 20 °C/min are shown in Figure 3, and the corresponding data are presented in Table 4. The contents of micron-sized Cu (micron-Cu) and nano-Cu in the composites were both 5 wt%.

As shown in Figure 3 and Table 4, the addition of micron-Cu or nano-Cu had no effect on the crystal form transformation of AP but had a clear effect on the high temperature exothermic decomposition of AP, enlarging the exothermic peak significantly.

The low and high exothermic peak temperatures for nano-Cu/AP composites were 287.6 and 347.0 °C, which was by 35.1 and 130.2 °C lower than those of pure AP, respectively, demonstrating enhanced, as compared with micron-sized Cu, catalytic effects of nano-Cu on the low and high temperature decomposition of AP. Furthermore, when Cu nanoparticles were added in AP, the decomposition heat was obviously increased from 0.436 to 1.300 kJ/g.

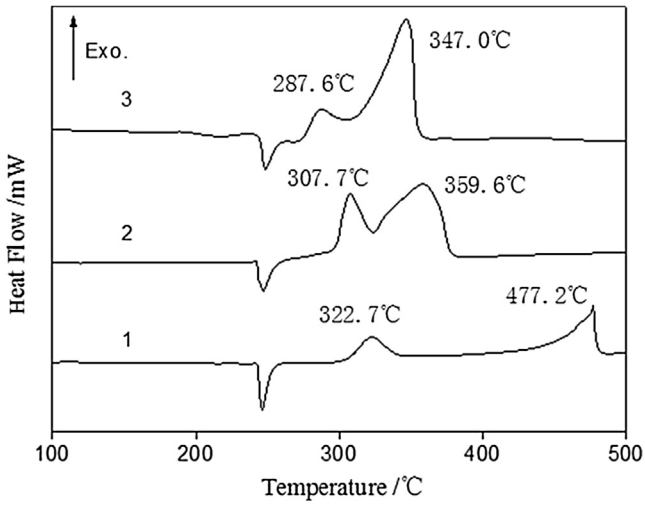

Figure 3 DSC curves of AP and Cu/AP, 1: AP, 2: 26-μm Cu/AP, 3: 20-nm Cu/AP.

Table 4 DSC data on decomposition of AP and Cu/AP.

Sample	T_L, °C	T_H, °C	H, kJ/g
AP	322.7	477.2	0.436
26 μm Cu/AP	307.7	359.6	1.290
20 nm Cu/AP	287.6	347.0	1.300

As seen from Table 5, when nano-Cu was added in AP, the activation energies of high and low temperature decomposition of AP were decreased by 7 and 22 kJ/mol, respectively. These decrements of E_{0L} and E_{0H} were larger than those of micron-Cu/AP composites. The results are consistent with the observations that nano-Cu provided strong catalytic effects on both the low and high temperature thermal decomposition of AP. The preexponential factors of low temperature thermal decomposition were practically unchanged when micron-Cu or nano-Cu were added in AP. However, the preexponential factors of high temperature thermal decomposition were enhanced by almost an order of magnitude.

Table 5 Thermal decomposition kinetics parameters of AP and Cu/AP.

Sample	E_{0L}, kJ/mol	E_{0H}, kJ/mol	A_L	A_H
AP	100	177	6.92×10^6	2.68×10^{10}
26 μm Cu/AP	98	160	7.60×10^6	2.61×10^{11}
20 nm Cu/AP	93	155	5.65×10^6	1.85×10^{11}

Table 6 DSC data on AP decomposition with different nano-Cu contents.

Content, %	T_L, °C	T_H, °C	H, kJ/g
0	322.7	477.2	0.436
1	293.4	367.1	1.170
5	287.6	347.0	1.300
10	303.4	342.7	1.300

3.4.2 Effect of Nano-Cu Content

Table 6 shows the DSC data of nano-Cu/AP composite with various amounts of nano-Cu addition. The contents of nano-Cu in AP were 0, 1, 5, and 10 wt%, respectively. As shown in Table 6, when the nano-Cu content was increased step by step, the corresponding low exothermic peak temperatures were 322.7, 293.4, 287.6, and 303.4 °C, showing first the decreasing trend with nano-Cu content increase up to 5% and then the increasing trend at higher nano-Cu content. However, all the low exothermic peak temperatures of nano-Cu/AP composites were evidently lower than those of pure AP. This suggested the noticeable effect of nano-Cu on the low temperature thermal decomposition of AP. On the other hand, with the nano-Cu increasing, the high exothermic peak temperature decreased gradually. When nano-Cu content was increased to 10%, the T_H decreased by 134.5 to become 342.7 °C. In addition, the decomposition heat was evidently increasing with nano-Cu content at least up to 5 wt%. At higher nano-Cu content, the decomposition heat remained unchanged.

Thus, the nano-Cu (20 nm) exhibited better catalytic effectivity in AP decomposition than that of micron-Cu (26 μm). The higher the nano-Cu content, the lower T_H and the larger H.

3.5 Effect of Al Nanoparticles [5,11]

Aluminum powders have a high calorific value and are widely used as energetic additives in solid propellants, the ammunition industry, and different energetic materials [12]. Generally, the particle size of Al particles in the propellants is around 30 μm. Aluminum particles should have large specific surface area and small average particle size to enhance their activity in solid propellants. Aluminum nanoparticles have a large specific surface area so that they may serve as a catalyst in solid propellant. The effect of Al nanoparticles on the thermal decomposition of AP is discussed below. The micron-sized Al particles with an average particle size of 25 μm are produced by ChangYuan County MingYu Aluminum Co., Ltd. of China. These particles were employed as the raw material to produce nanometer Al particles with an average particle size of 30 nm using high frequency inductively coupled plasma technology.

3.5.1 Comparison of the Effects of Aluminum Nanoparticles and Micron-Sized Aluminum Particles on the Thermal Decomposition of AP

The DSC curves of Cu/AP at the heating rate of 20 °C/min are shown in Figure 4, and the corresponding DSC data are shown in Table 7. The contents of Al in both composites were 5 wt%. The T_H of nano-Al/AP composite was by 51.8 °C lower than that of pure AP, which indicated good performance of nano-Al in the course of high temperature thermal decomposition of AP. However, the low exothermic peak temperature of nano-Al/AP composite was by 5.9 °C higher than that of pure AP. When the micron-sized Al was used, the T_L and the T_H of AP were decreased by 3.8 and 7.7 °C, respectively. At the same time, the decomposition heat (H) was significantly increased by 0.903 kJ/g from 0.436 to 1.339 kJ/g when nano-Al was added in AP.

3.5.2 Effect of Nano-Al Content

Table 8 shows the DSC data of nano-Al/AP composites with different contents of nano-Al in the mixtures. The contents of nano-Al were 0, 1, 5, and 10 wt%, respectively. As can be seen, the high exothermic peak temperature of AP was gradually decreasing

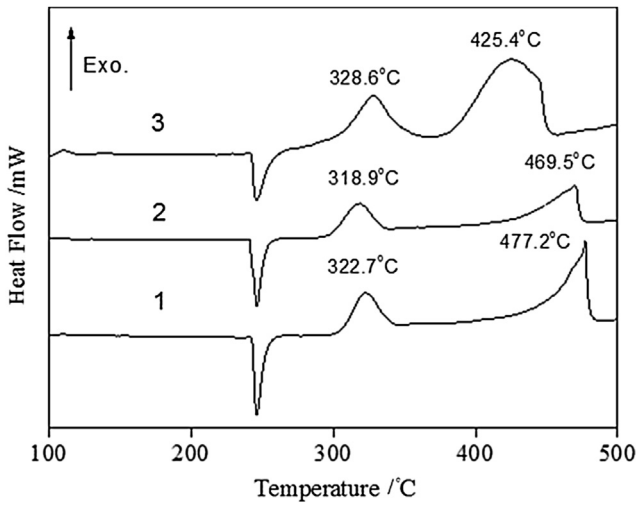

Figure 4 DSC curves of AP and 5 wt% Al/AP. 1: AP, 2: 25-μm Al/AP, 3: 30-nm Al/AP.

Table 7 DSC data on decomposition of AP and Al/AP.

Sample	T_L, °C	T_H, °C	H, kJ/g
AP	322.7	477.2	0.436
25-μm Al/AP	318.9	469.5	0.738
30-nm Al/AP	328.6	425.4	1.339

Table 8 DSC data on AP decomposition with different nano-Al contents.

Content, wt%	T_L, °C	T_H, °C	H, kJ/g
0	322.7	477.2	0.436
1	317.1	439.4	0.937
5	328.6	425.4	1.339
10	329.6	420.7	1.436

with the nano-Al content. When the content of nano-Al was 1%, the low exothermic peak temperature was lower than that of pure AP, and the decomposition heat was increased by 0.501 kJ/g. Its value was lower than those of 5% nano-Al/AP and 10% nano-Al/AP.

According to the above results, the nano-Al (30 nm) demonstrated better catalytic effect than that of the micron-sized aluminum (micron-Al; 25 μm) remarkably increasing H and decreasing T_H values.

The common feature of decomposition behavior of AP doped with nanometals is decreasing T_L at low metal content and then increasing T_L with metal content remaining lower than the T_L for pure AP. The T_H value decreases and H increases gradually for all three metals studied.

For the above three metal nanoparticles, nano-Cu (20 nm) exhibited the best catalytic effect on the high temperature thermal decomposition of AP, followed by nano-Ni (50 nm) and nano-Al (30 nm). However, nano-Ni/AP generated the largest decomposition heat, followed by nano-Al/AP and nano-Cu/AP.

4. IMPACT OF METALLIC OXIDE NANOPARTICLES ON THE THERMAL DECOMPOSITION OF AP

Several universities and research institutes have done extensive research on nanometer oxide catalysis in solid propellants since the 1950s. Results have shown that the metal oxides used in solid propellants can provide improved propellant combustion properties. In this section, the catalytic properties and impact of nano-Fe_2O_3, CuO nanoparticles (nano-CuO), and nano-Co_2O_3 on the thermal decomposition of AP are discussed [13,14].

The micron-sized Fe_2O_3 particles are produced by WenAn County TianYuan Chemical Co. Ltd. of China, the micron-sized CuO particles are produced by ZhiYuan Chemical Product Co. Ltd. in Zhengzhou City of China, and the micron-sized Co_2O_3 particles are produced by HuaYi Chemical Co. Ltd. in Zhangjiagang city of China. These three metallic oxide materials were used to obtain metallic oxide nanoparticles.

Table 9 The DSC data on AP decomposition with different nano-Fe_2O_3 contents.

Sample	T_H, °C
AP	477.2
1% Fe_2O_3 + AP	439.0
2% Fe_2O_3 + AP	435.1
2.5% Fe_2O_3 + AP	420.8
5% Fe_2O_3 + AP	406.6

4.1 Effect of Fe_2O_3 Nanoparticles

Table 9 shows the DSC data about the effect of different contents of 12-nm nano-Fe_2O_3 on high temperature thermal decomposition of AP.

As shown in Table 9, the effect of nano-Fe_2O_3 content on the high temperature thermal decomposition of AP is evident. The T_H was gradually decreasing with the nano-Fe_2O_3 content. When the nano-Fe_2O_3 content was 5 wt%, the T_H of AP decreased by 70.6 from 477.2 to 406.6 °C.

4.2 Effect of CuO Nanoparticles [15]

Table 10 shows the DSC data on the noticeable effect of 15-nm nano-CuO different contents on the thermal decomposition of AP. When 1 wt% nano-CuO was added, the high exothermic peak temperature decreased by 95.8 from 477.2 to 381.4 °C. With the catalyst content increasing, the high decomposition temperature was continuously and gradually decreasing.

4.3 Effect of Co_2O_3 Nanoparticles

Table 11 shows the DSC data about the remarkable effect of 10-nm Co_2O_3 nanoparticles (nano-Co_2O_3) of different contents on the thermal decomposition of AP. When the 1% nano-Co_2O_3 was added, the high decomposition temperature decreased by 130.1, from 477.2 to 347.1 °C. When the catalyst content was increased, the high decomposition temperature gradually decreased. When 4% nano-Co_2O_3 was added, the T_H decreased

Table 10 DSC data on AP decomposition with different nano-CuO contents.

Sample	T_H, °C
AP	477.2
1% nano-CuO + AP	381.4
1.5% nano-CuO + AP	378.2
2% nano-CuO + AP	376.9
4% nano-CuO + AP	376.1

Table 11 DSC data on AP decomposition with different nano-Co_2O_3 contents.

Sample	T_H, °C
AP	477.2
1% nano-Co_2O_3 + AP	347.1
1.5% nano-Co_2O_3 + AP	344.4
4% nano-Co_2O_3 + AP	330.1

by 147.1 °C, which suggested that Co_2O_3 nanoparticles have a strong catalytic effect on the thermal decomposition of AP.

As follows from the data in Table 11, among the studied three metallic oxide nanoparticles the nano-Co_3O_2 (10 nm) exhibits the strongest catalytic effect on the high temperature thermal decomposition of AP, and then are nano-CuO (15 nm) and nano-Fe_2O_3 (12 nm). With the contents of these metallic oxide nanoparticles increasing, the T_H shows a gradual decreasing trend.

5. IMPACT OF HYDROGEN-STORAGE NANOPARTICLES ON THE THERMAL DECOMPOSITION OF AP

Hydrogen is a kind of new clean energy source that has high energy density and is getting increasing research attention. The micron-sized hydrogen-storage materials such as LiH, MgH_2, Mg_2NiH_4, and Mg_2CuH_3 are produced by the Institute of Metal Research, Chinese Academy of Sciences. These micron-sized materials are employed to prepare nanometer particles. The effect of the nanoparticles, including LiH, MgH_2, Mg_2NiH_4, and Mg_2CuH_3, on the thermal decomposition of AP is summarized below.

5.1 Effect of LiH nanoparticles (nano-LiH)

LiH is an important hydrogen-storage composite containing Li; it plays a very important role in the nuclear chemistry and national economy fields. In LiH, the hydrogen content is 12.6%. It has the best hydrogen storage capacity and is more stable than other hydrogen-storage materials. It can be promising material in the new energy development fields.

LiH is prepared by direct reaction of Li and H. LiH is usually in the form of crystals, which are white or light-gray. It doesn't react with oxygen, chlorine, and chlorides at room temperature. It can decompose quickly into LiOH and H_2 when in contact with water. Because of the high hydrogen content, LiH is potentially an ideal fuel in rocket propellant.

Table 12 DSC data on AP decomposition with different nano-LiH contents.

Content, %	T_H, °C	*H*, kJ/g
0	477.2	0.436
2	405.2	0.819
5	401.5	1.102
10	369.7	1.185

Table 12 shows the DSC data of AP composites with different contents of 25-nm LiH nanoparticles (nano-LiH). When the nano-LiH contents were 2, 5, and 10 wt%, the high temperature exothermic peak of AP decreased by 72.0, 75.7, and 107.5 °C, respectively. Additionally, the decomposition heat of nano-LiH/AP was higher than that of pure AP, and the *H* increased with the nano-LiH content. When 10% nano-LiH was added, the *H* increased by 0.749 kJ/g.

5.2 Effect of MgH_2 Nanoparticles

Table 13 shows the DSC data for AP composites with different content of 30-nm MgH_2 nanoparticles (nano-MgH_2). It is seen that nano-MgH_2 has a noticeable catalytic effect on the high temperature thermal decomposition of AP. When the nano-MgH_2 content was 2%, the T_H of AP was decreased by 88.7, from 477.2 to 388.5 °C. When the nano-MgH_2 content was 5%, the T_H was further decreased to 366.1 °C. However, when the nano-MgH_2 content was increased to 10%, the T_H became only a bit lower than that of 5% nano-MgH_2/AP particles. The *H* of AP composite particles was gradually increasing with the content of nano-MgH_2. When the nano-MgH_2 content was increased up to 10%, the *H* increased by 0.893 kJ/g from 0.436 to 1.329 kJ/g.

5.3 Effect of Mg_2NiH_4 nanoparticles [16–18]

Table 14 shows the DSC data for AP composites with different content of 20-nm Mg_2NiH_4 nanoparticles (nano-Mg_2NiH_4). It can be seen that nano-Mg_2NiH_4 demonstrates similar to nano-MgH_2 effect on the high temperature thermal decomposition of AP. When 2% nano-Mg_2NiH_4 was added in AP, the T_H decreased by 84.2 °C to

Table 13 DSC data on AP decomposition with different nano-MgH_2 contents.

Content, %	T_H, °C	*H*, kJ/g
0	477.2	0.436
2	388.5	1.111
5	366.1	1.232
10	361.8	1.329

Table 14 DSC data on AP decomposition with different nano-Mg_2NiH_4 contents.

Content, %	T_H, °C	H, kJ/g
0	477.2	0.436
2	393.0	1.174
5	392.8	1.269
10	366.6	1.379

393.0 °C, and the H increased from 0.436 kJ/g to 1.174 kJ/g. With further increase in the nano-Mg_2NiH_4 content, the T_H decreased to 366.6 °C at 10% content, and the H increased to 1.379 kJ/g.

5.4 Effect of Mg_2CuH_3 Nanoparticles

Table 15 shows the DSC data on AP decomposition with different contents of 25-nm Mg_2CuH_3 nanoparticles (nano-Mg_2CuH_3). When the nano-Mg_2CuH_3 content in AP was 2%, the T_H sharply decreased by 108.5 to 368.7 °C, and the H remarkably increased by 0.928 kJ/g to 1.364 kJ/g. With further nano-Mg_2CuH_3 content increasing, the T_H was gradually decreasing and the H slightly increasing. These results showed that the effect of increase in the Mg_2CuH_3 content on the thermal decomposition of AP was not significant.

Among the above four hydrogen-storage nanoparticles, the 25-nm nano-Mg_2CuH_3 exhibits the best catalytic effect on the AP high temperature thermal decomposition peak, followed by 30-nm nano-MgH_2, 20-nm nano-Mg_2NiH_4, and 25-nm nano-LiH. Nano-Mg_2CuH_3/AP generates as well the largest decomposition heat, followed by nano-Mg_2NiH_4/AP, nano-MgH_2/AP, and nano-LiH/AP.

Summarizing the results of this section, the catalytic effect of metallic oxide nanoparticles on the high temperature thermal decomposition peak of AP is relatively stronger than those for metal nanoparticles and hydrogen-storage nanoparticles. In terms of AP thermal decomposition heat, the effect of metal nanoparticles is relatively higher than that for hydrogen-storage nanoparticles and metallic oxide nanoparticles.

Table 15 DSC data on AP decomposition with different nano-Mg_2CuH_3 contents.

Content, %	T_H, °C	H, kJ/g
0	477.2	0.436
2	368.7	1.364
5	363.4	1.391
10	361.4	1.405

6. IMPACT OF NANOCATALYSTS ON THE THERMAL DECOMPOSITION OF AP/HTPB PROPELLANT

6.1 Thermal Decomposition Characteristics of AP/HTPB

Solid propellants prepared on the basis of HTPB have excellent technological and mechanical properties and they are well-developed propellants all over the world.

Before studying the effects of metal nanoparticles on thermal decomposition of AP/HTPB solid propellant, one should examine the thermal decomposition properties of propellant itself. Figure 5 shows the DSC curve at the heating rate of 20 °C/min for basic AP/HTPB propellant comprising 75% AP and 25% HTPB.

Due to the high AP percent (75%), the thermal decomposition properties of AP/HTPB propellant are mostly affected by those of AP. As one can see from Figure 5, there are one endothermic peak and two exothermic peaks in the DSC curve, which correspond to the crystal form transition and the thermal decomposition of AP.

1. The endothermic temperature peak of propellant is almost the same as that of AP, and the thermal effects mainly are caused by the crystal transition.
2. The temperature of the first exothermic peak of AP/HTPB propellant is 335.9 °C, which is slightly higher than that of pure AP (322.7 °C). This is because the HTPB binder begins melting during the low-temperature exothermic stage, which delays the temperature of the first exothermic peak of AP/HTPB propellant.
3. The temperature of the second exothermic peak of AP/HTPB propellant has a value of 405.8 °C, which is lower than that of AP (477.2 °C). In this stage, HTPB binder decomposes along with the high temperature decomposition of AP. The high temperature products of HTPB react with the decomposed products of AP, and these

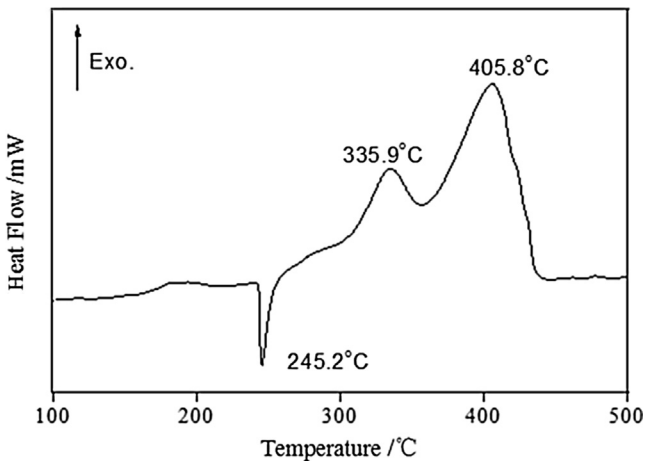

Figure 5 DSC curve of AP(75)/HTPB(25) propellant.

thermal effects accelerate the decomposition of AP. That is why the second exothermic peak temperature of AP/HTPB propellant decomposition is decreased significantly.

When nanocatalysts are added in AP/HTPB, the samples are comprised of 75% AP, 20% HTPB, and 5% nanocatalysts.

7. IMPACT OF METAL NANOPARTICLES ON THE THERMAL DECOMPOSITION OF AP/HTPB [19]

7.1 Effect of Nano-Ni

The DSC curves and data of AP/HTPB and nano-Ni-AP/HPTB at the heating rate of 20 °C/min are shown in Figure 6 and Table 16. As can be seen, when 50-nm nano-Ni was added, the two exothermic peaks merged, and the formed single exothermic peak has a narrower and higher shape indicating that nano-Ni has a noticeable catalytic effect on the thermal decomposition of AP/HTPB. The thermal decomposition peak temperature equals 382.3 °C, the decomposition heat is greatly increased by 1.43 kJ/g from 1.94 to 3.37 kJ/g.

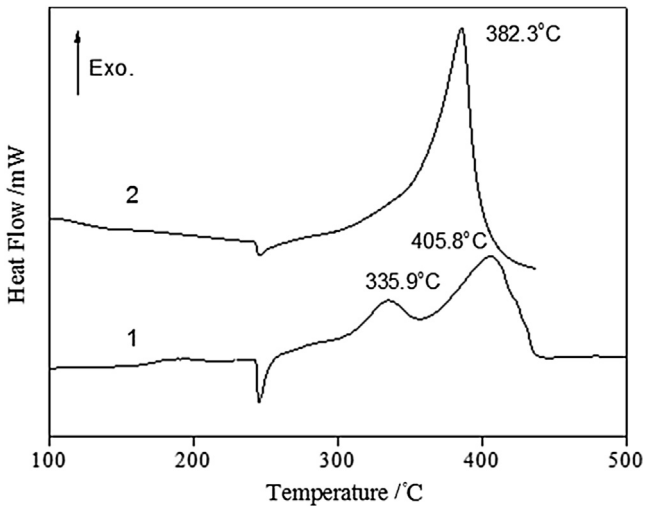

Figure 6 DSC curves of AP/HTPB and 5% nano-Ni-AP/HTPB, 1: AP/HTPB, 2: 5% nano-Ni-AP/HTPB.

Table 16 DSC data on decomposition of AP/HTPB and 5% nano-Ni-AP/HTPB.

Sample	T_L, °C	T_H, °C	H, kJ/g
AP/HTPB	335.9	405.8	1.94
AP/HTPB + 5% nano-Ni	—	382.3	3.37

7.2 Effect of Nano-Cu

Figure 7 and Table 17 present the DSC curves and data of AP/HTPB and nano-Cu-AP/HTPB at the heating rate of 20 °C/min. It can be seen that when 20-nm nano-Cu was added, the major exothermic peak became narrower and higher indicating that nano-Cu has a noticeable catalytic effect on the thermal decomposition of AP/HTPB. The T_L and T_H were 284.3 and 372.2 °C, which were by 51.6 and 33.6 °C lower than those of AP/HTPB, respectively. The decomposition heat was evidently increased by 1.21 kJ/g from 1.94 to 3.15 kJ/g.

7.3 Effect of Nano-Al

DSC curves and data of AP/HTPB and nano-Al-AP/HTPB at the heating rate of 20 °C/min are presented in Figure 8 and Table 18.

As shown in Figure 8 and Table 18, when micron-Al (25 μm) particles were added in AP/HTPB, the temperatures of the two exothermic peaks were slightly decreased (by 2.9 and 13.5 °C, respectively), and the decomposition heat was increased by 0.74 kJ/g. When 30-nm nano-Al was added in AP/HTPB, the high temperature exothermic peak

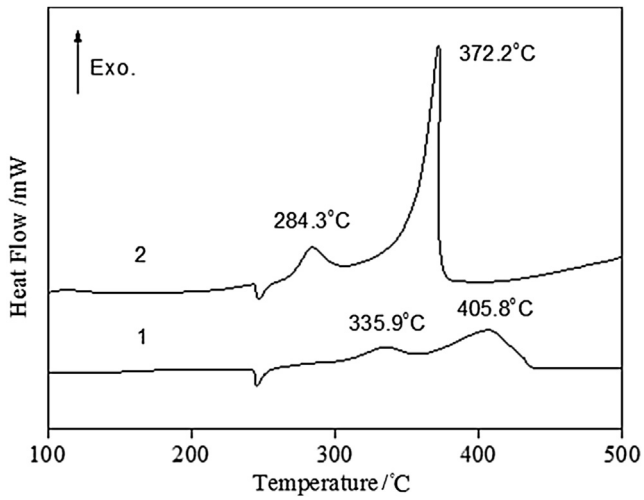

Figure 7 DSC curves of AP/HTPB and 5% nano-Cu-AP/HTPB, 1: AP/HTPB, 2: 5% nano-Cu-AP/HTPB.

Table 17 DSC data of AP/HTPB and 5% nano-Cu-AP/HTPB.

Sample	T_L, °C	T_H, °C	H, kJ/g
AP/HTPB	335.9	405.8	1.94
AP/HTPB + 5% nano-Cu	284.3	372.2	3.15

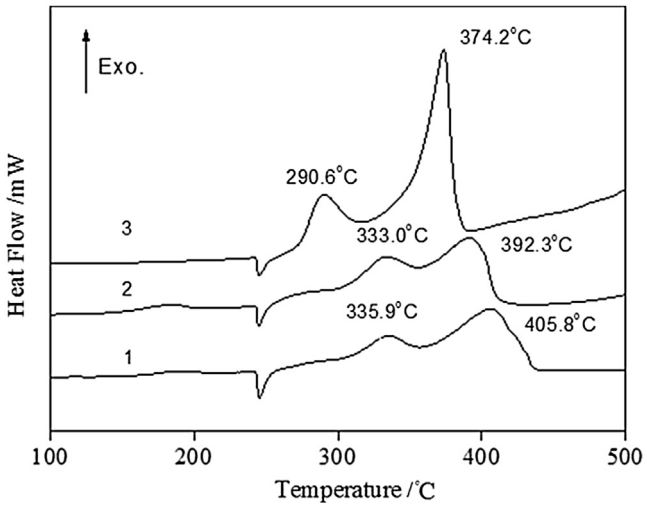

Figure 8 DSC curves of AP/HTPB and 5% Al-AP/HTPB, 1: AP/HTPB, 2: 5% micron-Al-AP/HTPB, 3: 5% nano-Al-AP/HTPB.

Table 18 DSC data of AP/HTPB and 5% Al-AP/HTPB.

Sample	T_L, °C	T_H, °C	H, kJ/g
AP/HTPB	335.9	405.8	1.94
AP/HTPB + 5% micron-Al	333.0	392.3	2.68
AP/HTPB + 5% nano-Al	290.6	374.2	3.39

became higher and narrower, and the temperatures of the two exothermic peaks decreased by 45.3 and 31.6 °C, respectively. Additionally, the decomposition heat was essentially increased by 1.45 kJ/g from 1.94 to 3.39 kJ/g. These results showed good catalytic effect of nano-Al on the thermal decomposition of AP/HTPB.

The results obtained for the above three metal nanoparticles show that the best catalytic effect on the high temperature thermal decomposition peak of AP/HTPB was exhibited by 20-nm nano-Cu. Similar effect was exhibited by 30-nm nano-Al and a lower effect by 50-nm nano-Ni. The results on affecting the AP/HTPB decomposition behavior by nano-Cu and nano-Al additives were similar to those obtained in decomposition of pure AP. In the case of nano-Ni the low and high temperature decomposition peaks merged indicating the specific role of binder transformations on AP/HTPB decomposition in presence of this additive. The largest decomposition heat was recorded in the case of the nano-Al addition; a similar effect was demonstrated by nano-Ni and a lower effect by nano-Cu.

8. IMPACT OF HYDROGEN-STORAGE NANOPARTICLES ON THE THERMAL DECOMPOSITION OF AP/HTPB

8.1 Effect of Nano-LiH

Figure 9 and Table 19 show the DSC curves and data on decomposition of AP/HTPB and nano-LiH-AP/HTPB at the heating rate of 20 °C/min. It can be seen that when 25-nm nano-LiH was added, both exothermic peaks were obviously changed. The T_L and T_H were decreased by 13.1 and 24.5 °C to be 322.8 and 381.3 °C, respectively. In addition, the decomposition heat was evidently increased by 1.89 kJ/g from 1.94 to 3.83 kJ/g.

8.2 Effect of MgH_2 Nanoparticles

Figure 10 and Table 20 show the DSC curves and data on decomposition of AP/HTPB and nano-MgH_2-AP/HTPB at the heating rate of 20 °C/min. It can be seen from the curves that after 30-nm nano-MgH_2 was added, the two exothermic peaks merged into one wide and high peak. The T_H was decreased by 17.5 to 388.3 °C. In addition, the decomposition heat was essentially increased by 2.34 kJ/g from 1.94 to 4.28 kJ/g.

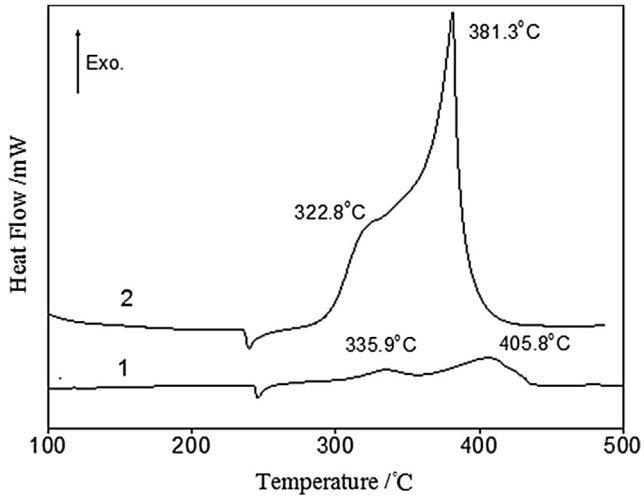

Figure 9 DSC curves of AP/HTPB and 5% nano-LiH-AP/HTPB, 1: AP/HTPB, 2: 5% nano-LiH-AP/HTPB.

Table 19 DSC data on decomposition of AP/HTPB and 5% nano-LiH-AP/HTPB.

Sample	T_L, °C	T_H, °C	H, kJ/g
AP/HTPB	335.9	405.8	1.94
AP/HTPB + 5% nano-LiH	322.8	381.3	3.83

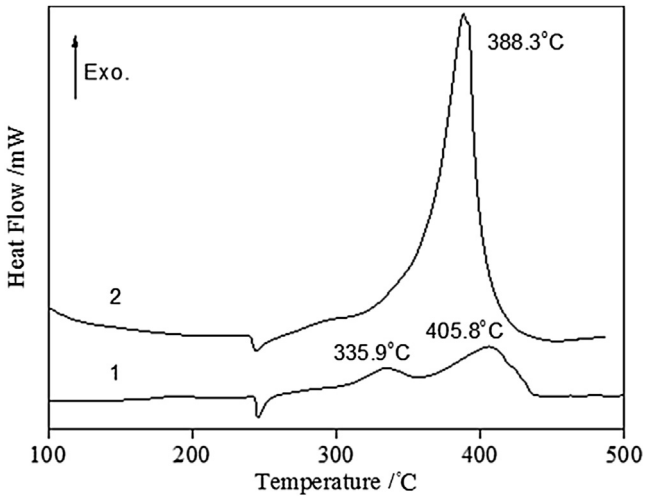

Figure 10 DSC curves of AP/HTPB and 5% nano-MgH_2-AP/HTPB, 1: AP/HTPB, 2: 5% nano-MgH_2-AP/HTPB.

Table 20 DSC data of AP/HTPB and 5% nano-MgH_2-AP/HTPB.

Sample	T_L, °C	T_H, °C	H, kJ/g
AP/HTPB	335.9	405.8	1.94
AP/HTPB + 5% nano-MgH_2	—	388.3	4.28

8.3 Effect of Mg_2NiH_4 Nanoparticles

Figure 11 and Table 21 show the DSC curves and data on decomposition of AP/HTPB and nano-Mg_2NiH_4-AP/HTPB at the heating rate of 20 °C/min. It can be seen from the curves that after 20 nm nano-Mg_2NiH_4 was added, the two exothermic peaks were combined into practically one wide and high peak. The T_H was decreased by 9.6 to 396.2 °C. In addition, the decomposition heat was evidently increased by 1.92 kJ/g from 1.94 to 3.86 kJ/g.

8.4 Effect of Mg_2CuH_3 Nanoparticles

Figure 12 and Table 22 show the DSC curves and data on decomposition of AP/HTPB and nano-Mg_2CuH_3-AP/HTPB at the heating rate of 20 °C/min. It can be seen from the curves that after 25-nm nano-Mg_2CuH_3 was added, the T_L and T_H were decreased by 6.5 and 41.7 °C. In addition, the decomposition heat was evidently increased by 1.60 kJ/g from 1.94 to 3.54 kJ/g.

For the above four hydrogen-storage nanoparticles, the best catalytic effect on the high temperature thermal decomposition peak of AP/HTPB demonstrates

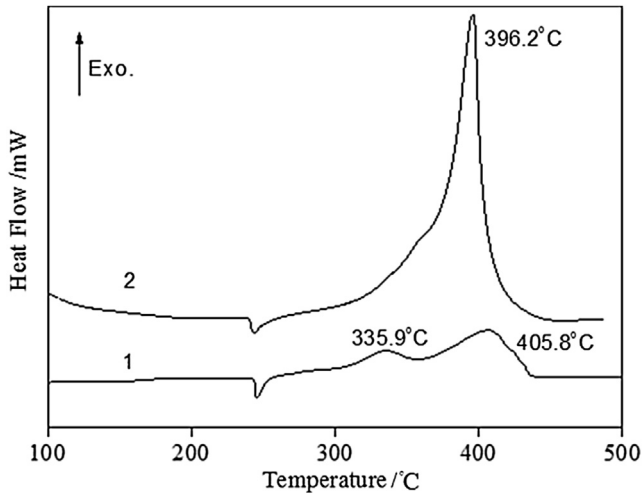

Figure 11 DSC curves of AP/HTPB and 5% nano-Mg_2NiH_4-AP/HTPB, 1: AP/HTPB, 2: 5% nano-Mg_2NiH_4-AP/HTPB.

Table 21 DSC data on decomposition of AP/HTPB and 5% nano-Mg_2NiH_4-AP/HTPB.

Sample	T_L, °C	T_H, °C	H, kJ/g
AP/HTPB	335.9	405.8	1.94
AP/HTPB + 5% nano-Mg_2NiH_4	—	396.2	3.86

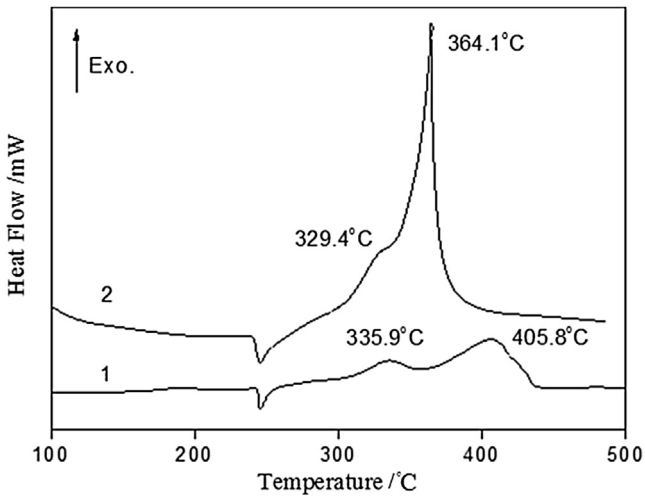

Figure 12 DSC curves of AP/HTPB and 5% nano-Mg_2CuH_3-AP/HTPB, 1: AP/HTPB, 2: 5% nano-Mg_2CuH_3-AP/HTPB.

Table 22 DSC data of AP/HTPB and 5% nano-Mg_2CuH_3-AP/HTPB.

Sample	T_L, °C	T_H, °C	H, kJ/g
AP/HTPB	335.9	405.8	1.94
AP/HTPB + 5% nano-Mg_2CuH_3	329.4	364.1	3.54

nano-Mg_2CuH_3 (25 nm), followed by nano-LiH (25 nm), nano-MgH_2 (30 nm), and nano-Mg_2NiH_4 (20 nm). The largest decomposition heat is generated by the mixture nano-MgH_2-AP/HTPB, followed by nano-Mg_2NiH_4-AP/HTPB, nano-LiH-AP/HTPB, and nano-Mg_2CuH_3-AP/HTPB.

In summary, for the investigated metal and hydrogen-storage nanoparticles, the value of the catalytic effect on the high temperature thermal decomposition peak of AP/HTPB obeys the following order: nano-Mg_2CuH_3 > nano-Cu > nano-Al > LiH > nano-Ni > nano-MgH_2 > nano-Mg_2NiH_4. For the effect on the decomposition heat, the above nanoparticles obey the following order: nano-MgH_2 > nano-Mg_2NiH_4 > LiH > nano-Mg_2CuH_3 > nano-Al > nano-Ni > nano-Cu.

9. IMPACT OF NANOCATALYSTS ON THE COMBUSTION PERFORMANCE OF AP/HTPB PROPELLANT

9.1 Impact of Nano-Ni

When the burning rates of propellants were tested, the samples consisted of 75% AP, 20% HTPB, and 5% nano-Ni. The results are shown in Table 23.

As shown in Table 23, when the micron-Ni was added in AP/HTPB, the burning rate at 9.8 MPa was obviously increased from 8 to 20 mm/s, and the pressure exponent was decreased by 0.09 from 0.58 to 0.49 ranging in 4.0—20 MPa. When the nano-Ni was added in AP/HTPB, the burning rate at 9.8 MPa was significantly enhanced to 30 mm/s, and the pressure exponent ranging in 4.0—20 MPa was reduced to 0.41. That is, the burning rate was increased by about 270% and the pressure exponent was reduced by about 29%, correspondingly. The results clearly demonstrate that the Ni particles, especially the Ni nanoparticles, can noticeably improve the combustion performance of AP/HTPB.

Table 23 The burning rate and pressure exponent of Ni particles added propellant.

Propellant sample	Burning rate/mm/s (9.8 MPa)	Pressure exponent (4.0—20 MPa)
AP/HTPB	8	0.58
AP/HTPB-30 μm Ni	20	0.49
AP/HTPB-50 nm Ni	30	0.41

9.2 Impact of Nano-Cu

When the burning rates of propellants were tested, the samples comprised 75% AP, 20% HTPB, and 5% Cu nanoparticles. The results are shown in Table 24.

As shown in Table 24, when the nano-Cu was added in AP/HTPB, the burning rate at 9.8 MPa was significantly enhanced to 33 mm/s, and the pressure exponent ranging in 4.0—20 MPa was reduced to only 0.32. That is, the burning rate was increased by about 310%, and the pressure exponent was reduced by about 45%, correspondingly. These results clearly demonstrate significant impact of the Cu nanoparticles on the combustion performance of AP/HTPB.

9.3 Impact of Nano-Al

When the burning rates of propellants were tested, the samples comprised 75% AP, 20% HTPB, and 5% Al nanoparticles. The results are shown in Table 25.

As shown in Table 25, when the nano-Al was added in AP/HTPB, the burning rate at 9.8 MPa was increased to 23 mm/s, and the pressure exponent ranging in 4.0—20 MPa was reduced to 0.49. Thus, the burning rate was increased by about 100%, and the pressure exponent was reduced by about 16%, correspondingly. These results demonstrate rather moderate effect of nano-Al particles on the burning law of AP/HTPB propellant.

9.4 Impact of Nano-Fe_2O_3

When the burning rates of propellants were tested, the samples comprised 75% AP, 22% HTPB, and 3% Fe_2O_3 nanoparticles. The results are shown in Table 26.

Table 24 The burning rate and pressure exponent of Cu particles added propellant.

Propellant sample	Burning rate/mm/s (9.8 MPa)	Pressure exponent (4.0—20 MPa)
AP/HTPB	8	0.58
AP/HTPB-26 μm Cu	25	0.45
AP/HTPB-20 nm Cu	33	0.32

Table 25 The burning rate and pressure exponent of Al particles added propellant.

Propellant sample	Burning rate/mm/s (9.8 MPa)	Pressure exponent (4.0—20 MPa)
AP/HTPB	8	0.58
AP/HTPB-25 μm Al	16	0.55
AP/HTPB-30 nm Al	23	0.49

Table 26 The burning rate and pressure exponent of Fe_2O_3 particles added propellant.

Propellant sample	Burning rate/mm/s (9.8 MPa)	Pressure exponent (4.0—20 MPa)
AP/HTPB	8	0.58
AP/HTPB-12 nm Fe_2O_3	15	0.29

As shown in Table 26, when the nano-Al was added in AP/HTPB, the burning rate at 9.8 MPa was enhanced to only 15 mm/s and the pressure exponent ranging in 4.0—20 MPa was reduced to 0.29. That is, the burning rate was increased by about 87% but the pressure exponent was reduced significantly, by about 50%.

According to the above results, when the content of metal nanoparticles in AP/HTPB propellant was 5%, the highest burning rate and the lowest pressure exponent was demonstrated by the nano-Cu-AP/HTPB propellant while the nano-Al-AP/HTPB propellant had the lowest burning rate and highest pressure exponent. When 3 wt% nano-Fe_2O_3 was added in AP/HTPB propellant, the pressure exponent became much lower than that of the studied metal nanoparticle-AP/HTPB propellants (0.29!). However, the burning rate of nano-Fe_2O_3—AP/HTPB propellant was much lower than that of the metal nanoparticle-AP/HTPB propellants.

10. CONCLUSIONS

The nanocatalysts, such as metal nanoparticles, metallic oxide nanoparticles, and hydrogen-storage nanoparticles, have obvious impacts on the thermal decomposition of AP and AP/HTPB, which are higher than those of the micron particles. When nanocatalysts are added in AP and AP/HTPB, the high exothermic decomposition temperature peak (T_H) is evidently decreasing, and the decomposition heat (H) is remarkably increasing. The T_H and H changes are greater when the nanocatalyst contents are higher. The comparison between the magnitudes of the effects could not at this time be made very precisely because the characteristic sizes of used nanoparticles varied in the range of 12—50 nm. However, a crude estimation can be made on the basis of data obtained.

For the value of catalytic effect on the high temperature thermal decomposition peak of AP, the nanoparticles obey the following order: nano-Co_3O_2 > nano-Cu > nano-Ni > nano-Mg_2CuH_3 > nano-MgH_2 > nano-CuO > nano-Mg_2NiH_4 > LiH > nano-Fe_2O_3 > nano-Al. For the impact on the AP thermal decomposition heat, the above nanoparticles obey the following order: nano-Ni > nano-Mg_2CuH_3 > nano-Al > nano-Cu > nano-Mg_2NiH_4 > nano-MgH_2 > LiH >metallic oxide nanoparticles.

For the catalytic effect on the high temperature thermal decomposition peak of AP/HTPB propellant, the above nanoparticles obey the following order: nano-Mg_2CuH_3 > nano-Cu > nano-Al > LiH > nano-Ni > nano-MgH_2 > nano-Mg_2NiH_4. The decomposition heat of hydrogen-storage nanoparticles-AP/HTPB is relatively larger than that of metal nanoparticles-AP/HTPB propellant. For the impact on the AP/HTPB propellant thermal decomposition heat, the above nanoparticles obey the following order: nano-MgH_2 > nano-Mg_2NiH_4 > LiH > nano-Mg_2CuH_3 > nano-Al > nano-Ni > nanoCu.

The burning rates of AP/HTPB-based propellants are essentially increasing and the pressure exponents remarkably decreasing when studied nanocatalysts are applied, which clearly demonstrates that those nanoparticles significantly improve the combustion performance of AP/HTPB. When the content of metal nanoparticles in AP/HTPB propellant was 5%, the nano-Cu-AP/HTPB propellant demonstrated the highest burning rate and the lowest pressure exponent, while the nano-Al-AP/HTPB propellant had the lowest burning rate and highest pressure exponent. With 3 wt% nano-Fe_2O_3 added AP/HTPB propellant, the pressure exponent became much lower than that for the metal nanoparticles-AP/HTPB propellant, reaching the value of 0.29. However, the burning rate of this propellant was almost twice lower than that of the other metal nanoparticle-AP/HTPB propellants.

In future work, the effects of metal and metallic oxide nanoparticles as well as hydrogen-storage nanoparticles on the propellant combustion performance characteristics such as burning rate and pressure exponent must be researched in detail, paying special attention to studying the intrinsic mechanism of combustion. In particular, it will be necessary to conduct measurement of temperature and species concentration profiles in the combustion wave. These results will further promote the applications of nanocatalysts in solid propellants.

REFERENCES

[1] F.S. Li, Superfine Powder Technology, National Defense Industry Press, Beijing, 2000.
[2] F.S. Li, Y. Yang, Nano/Micron Composite Technology and Applications, National Defense Industry Press, Beijing, 2002.
[3] Z.R. Liu, C.M. Yin, Y.H. Kong, F.Q. Zhao, Y. Luo, H. Xiang, The thermal decomposition of ammonium perchlorate, Chin. J. Energ. Mater. 8 (2000) 75–79.
[4] R.P. Fitzgerald, M.Q. Brewster, Flame and surface structure of laminate propellants with coarse and fine ammonium perchlorate, Combustion Flame 136 (2004) 313–326.
[5] L.L. Liu, F.S. Li, L.H. Tan, M. Li, Y. Yi, Effects of nanometer Ni, Cu, Al and NiCu powders on the thermal decomposition of ammonium perchlorate, Propellants Explosives Pyrotechnics 29 (2004) 34–38.
[6] L.H. Tan, Q.H. Li, Y. Yang, F.S. Li, L.L. Liu, M. Li, Study on the preparation and catalytic characteristics of nano-nickel powder, J. Solid Rocket Technol. 27 (2004), 198–200, 232.
[7] T.A. Andrzejak, E. Shafirovich, A. Varma, Ignition mechanism of nickel-coated aluminum particles, Combustion Flame 150 (2007) 60–70.

[8] F.Q. Zhao, P. Chen, D. Yang, S.W. Li, C.M. Yin, Effects of nanometer metal powders on thermal decomposition characteristics of RDX, J. Nanjing Univ. Sci. Technol. 25 (2001) 420–423.
[9] Z. Jiang, F.S. Li, F.Q. Zhao, P. Chen, C.M. Yin, S.W. Li, Effect of nano metal powder on the thermal decomposition characteristics of HMX, J. Propuls. Technol. 23 (2002) 258–261.
[10] L.L. Liu, F.S. Li, Y. Yang, L.H. Tan, Q.S. Zhang, Effect of nanometer Cu powder on thermal decomposition of ammonium perchlorate, Chin. J. Inorg. Chem. 21 (2005) 1525–1530.
[11] Z.Y. Ma, F.S. Li, A.S. Chen, H.C. Song, Preparation and characterization of composite particles of Al/ammonium perchlorate, J. Propuls. Technol. 25 (2004) 373–376.
[12] A. Gromov, Y. Strokova, A. Kabardin, A. Vorozhtsov, U. Teipel, Experimental study of the effect of metal nanopowders on the decomposition of HMX, AP and AN, Propellants Explosives Pyrotechnics 34 (2009) 506–512.
[13] Y. Yang, H.Y. Liu, F.S. Li, X.Y. Zhang, J.X. Liu, Nanometer transition metal oxide and rare earth oxide catalysis on AP thermal decomposition, J. Propuls. Technol. 27 (2006) 92–96.
[14] Z.Y. Ma, F.S. Li, A.S. Chen, H.P. Bai, Preparation and thermal decomposition behavior of Fe_2O_3/ammonium perchlorate composite nanoparticles, Acta Chimica Sinica 62 (2004) 1252–1255.
[15] A.S. Chen, F.S. Li, Z.Y. Ma, H.Y. Liu, Research on the preparation and catalytic function of nano-CuO/AP composite particles, J. Solid Rocket Technol. 27 (2004), 123–125,140.
[16] L.L. Liu, F.S. Li, C.L. Zhi, H.C. Song, Y. Yang, Synthesis of magnesium-copper hydrogen storage alloy and its effect on the thermal decomposition of ammonium perchlorate, Acta Chimica Sinica 66 (2008) 1424–1428.
[17] L.L. Liu, F.S. Li, C.L. Zhi, L.H. Tan, Y. Yang, Q.S. Zhang, Effect of Mg_2NiH_4 on the thermal decomposition of ammonium perchlorate, Chem. J. Chin. Univ. 28 (2007) 1420–1423.
[18] C.L. Zhi, H.C. Song, F.S. Li, L.L. Liu, H.Y. Liu, L.H. Tan, Preparation of Mg_2NiH_4 and its catalytic characteristics of thermal decomposition of ammonium perchlorate, J. Industrial Eng. Chem. 58 (2007) 2793–2797.
[19] L.L. Liu, F.S. Li, L.H. Tan, M. Li, Y. Yang, Effects of metal and composite metal nanopowders on the thermal decomposition of ammonium perchlorate (AP) and the ammonium perchlorate/hydroxyterminated polybutadiene (AP/HTPB) composite solid propellant, Chin. J. Chem. Eng. 12 (2004) 595–598.

CHAPTER SIX

Nanocoating for Activation of Energetic Metals

Valery Rosenband and Alon Gany
Technion – Israel Institute of Technology, Haifa, Israel

1. INTRODUCTION

Metal powders are used as fuel components in solid propellants because of their high heat of combustion and high energy density. At present, mainly aluminum powder has been widely used for rocket motor applications. However, the addition of aluminum implies some disadvantages, which depend significantly on its combustion characteristics. Particle agglomeration is one of the characteristic phenomena taking place during the combustion of aluminized solid propellants. Aluminum particles seem to accumulate and often agglomerate on or near the propellant burning surface. Agglomeration of aluminum particles leads to lower combustion efficiency, slag accumulation, and higher two-phase flow losses, as the combustion products are accelerated through the rocket nozzle. Rocket motor studies have shown that a significant increase in motor performance can be obtained by improvement of aluminum particles' combustion efficiency.

Previous investigations [1,2] showed that one of the main phenomena leading to aluminum particles agglomeration is disruption of the protective oxide film around the particles under stresses appearing during aluminum melting (because of the volume increase by about 6%). Liquid metal, penetrating through cracks in the oxide layer, causes bonding of adjacent particles besides forming large droplets. To prevent agglomeration, a thin nickel or iron coating on the aluminum particles surface can be used. In this case, aluminum particles agglomeration on the burning propellant surface may be prevented [3] by improvement of the aluminum particles ignition and a possible elastic or plastic deformation because of the relatively small Young's modulus of nickel and iron compared to that of aluminum oxide.

A method for production of aluminum powder coated by a nickel or iron layer, based on thermochemical deposition of nickel or iron on the aluminum particles, was developed. This method allows for the production of coated aluminum powder with controlled weight content of nickel or iron, and with a different thickness of nickel or iron layer on the aluminum particle surface. For the production of coated aluminum

Energetic Nanomaterials
ISBN 978-0-12-802710-3, http://dx.doi.org/10.1016/B978-0-12-802710-3.00006-4

particles, it is not necessary to remove the initial aluminum oxide film existing on the aluminum particles' surface.

2. NICKEL-COATED ALUMINUM PARTICLES

Samples of aluminum particles coated by a thin layer of nickel were prepared and characterized. Atomized aluminum powders, produced by Metal Powder Company, Ltd., Madurai, India, were used in all experiments. The nickel content in the coated aluminum particles was 1–16 wt%.

The calculated amount of nickel in the powder and the average thickness of nickel layer plated on the aluminum particle surfaces are presented in Table 1. The data on the nickel-coated aluminum particles have been provided by Rosenband and Gany [4]. The Table also presents the nickel weight percent in the coated aluminum, measured by atomic adsorption spectroscopy method. It can be seen that the calculated and measured amounts of nickel are in good agreement.

Volume particle size distribution of the uncoated (as-received) and nickel-coated (5 wt% of nickel) aluminum powders, determined by laser diffraction using LS 230 Coulter Particle Size Analyzer, is presented in Table 2. The specific surface area of the powders, measured by BET method in a Coulter SA 3100 device, is also listed in this table.

The particle sizes of initial (as-received) and coated aluminum particles are practically the same, indicating no noticeable aggregation of the particles due to the nickel coating.

The average nickel coating thickness ranges from about 16 nm for 1% nickel to 160 nm for 9% nickel. On the other hand, as indicated by Table 2, the surface area of the nickel-coated Al particles increases significantly (more than fourfold). Scanning electron microscope (SEM) photographs of the regular and nickel-coated aluminum powders (Figure 1) can give a good explanation, revealing structural details of initial (regular) and nickel-coated (5 wt%) Al particles and their surfaces.

As can be seen in Figure 1, the regular Al particle surface is relatively smooth, whereas the surface of the nickel-coated Al particles is covered by what looks like numerous small (100–200 nm) nickel humps, which compose the coating layer and cause the increase in the surface area (see details in Figure 2).

Table 1 Weight percent of Ni in the coated aluminum particles.

Initial wt% of Ni	Measured wt% of Ni	Calculated thickness of Ni layer, nm
0.99	0.93	16
1.96	1.87	33
2.91	3.11	50
4.76	4.33	81
9.09	9.10	162

Table 2 Volume particle size distribution of uncoated and coated aluminum powders.

Sample	D_{10}, μm	D_{25}, μm	D_{50}, μm	D_{75}, μm	D_{90}, μm	Surface area, m^2/g
Initial Al powder	10.88	18.39	29.16	41.00	53.55	0.29
Ni-coated Al powder	9.41	18.08	29.42	42.00	54.87	1.33

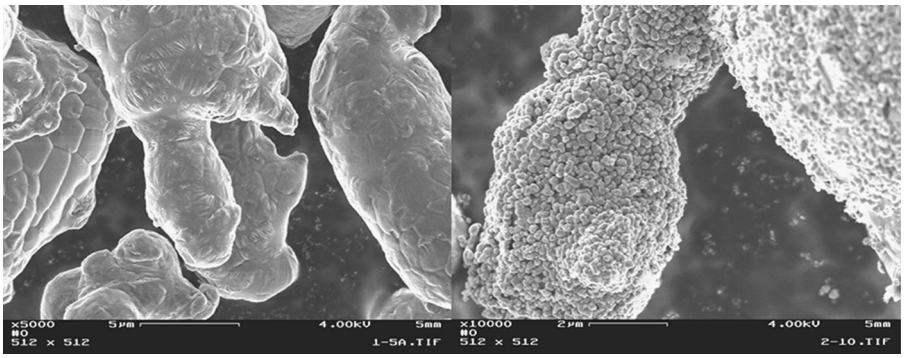

Figure 1 Scanning electron microscope (SEM) photographs of regular aluminum particles (left) and aluminum particles coated by 5 wt% of nickel (right) [4].

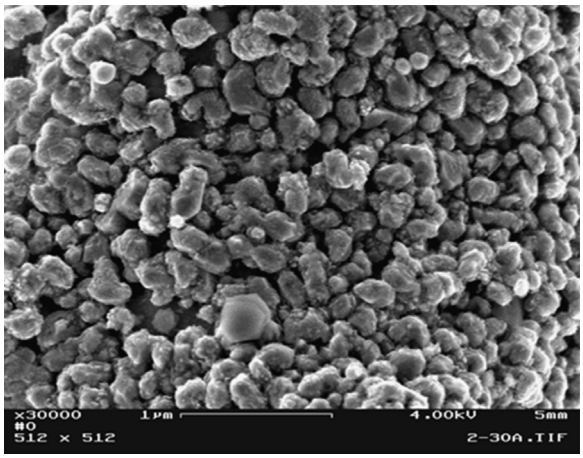

Figure 2 Detailed SEM photograph of the surface of a single nickel-coated aluminum particle.

Results of Auger spectroscopy analysis of an aluminum particle coated by a nickel layer (with nickel content of 5 wt%) are shown in Figure 3. The Auger profile reveals dominant existence of nickel within a surface layer of a few tens of nanometer thickness, in agreement with the calculated average nickel coating thickness.

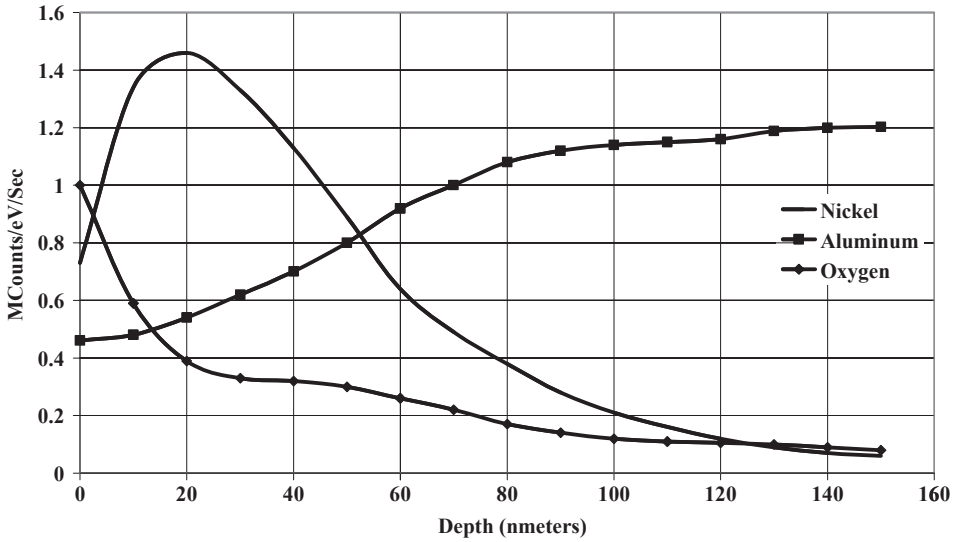

Figure 3 Auger depth profiling of a 30 μm mean particle size nickel-coated aluminum particle [4].

Aluminum particles coated with nickel were heated in air to 800 °C. No particle accumulation or agglomeration was observed after powder cooling. It was shown that even very thin nickel coating on the aluminum particle surface (calculated thickness of 16 nm, weight content of nickel of 1%) already successfully prevents the accumulation and agglomeration of aluminum particles, whereas, after heating/cooling stages of regular aluminum particles, agglomerates in the form of large drops of molten metal were observed (Figure 4).

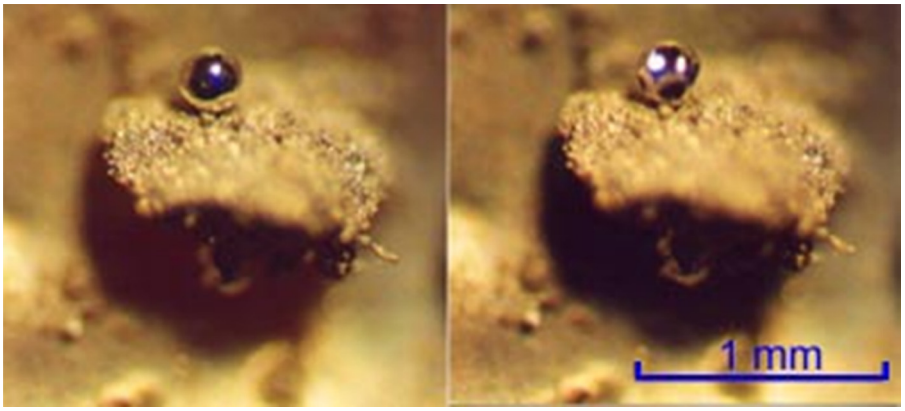

Figure 4 A large liquid drop of melted aluminum on the sample surface: T = 850 °C (left photograph). The buckling and wrinkling of a surface oxide shell on following rapid cooling of a drop (right photograph) [2].

Hence, nickel coating of aluminum particles seems to be a promising approach for the reduction of their agglomeration.

3. THERMOANALYTICAL TESTS

Thermoanalytical investigation of the behavior of initial (regular) and coated aluminum particles during their heating was conducted using STA 449C NETZSCH Simultaneous TG-DSC Apparatus. Heating of the aluminum powders up to 1200 °C at a rate of 10 °C/min was carried out in nitrogen and air flow. The main goal was to investigate how the above-described nickel coating of aluminum particles affects their flammability.

Figure 5 shows that, under the test conditions, regular Al particles do not react with N_2, whereas similar particles coated by Ni (5 wt%) demonstrate fast reaction whose onset indicates ignition. Results for nitridation of nickel-coated Al particles with different Ni contents are shown in Figure 6. One can see substantial mass gain due to nitridation (typically 40–50%, while a complete reaction between aluminum and nitrogen would theoretically yield 51% mass gain), with a relatively small effect of the nickel content within the range tested (between 1% and 16% Ni). Nevertheless, nickel content was found to have a more significant effect on ignition temperature—the higher the content of nickel, the lower the ignition temperature (e.g., 1100 °C for 1 wt% Ni and 850 °C for

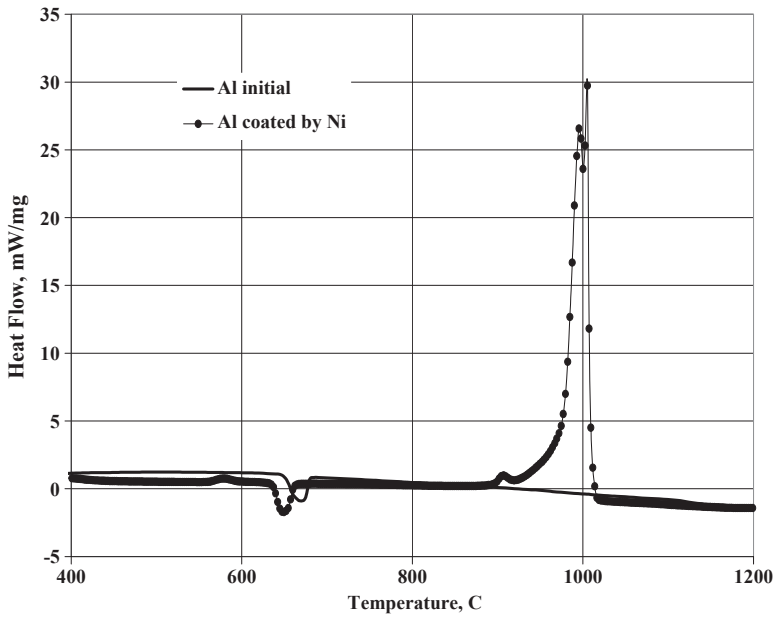

Figure 5 Behavior of regular Al particles and Al particles coated by Ni (5 wt%) during heating in nitrogen.

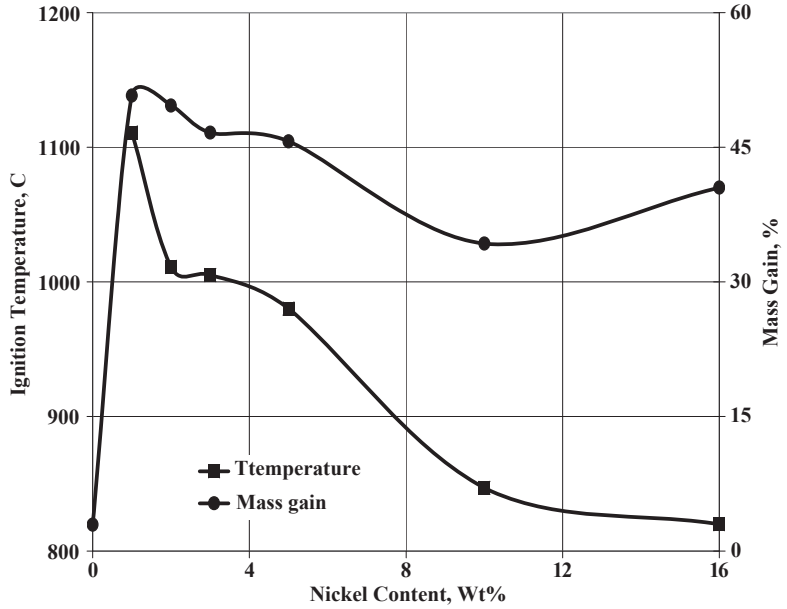

Figure 6 Ignition temperature and mass gain during nitridation of Ni-coated Al particles versus Ni content.

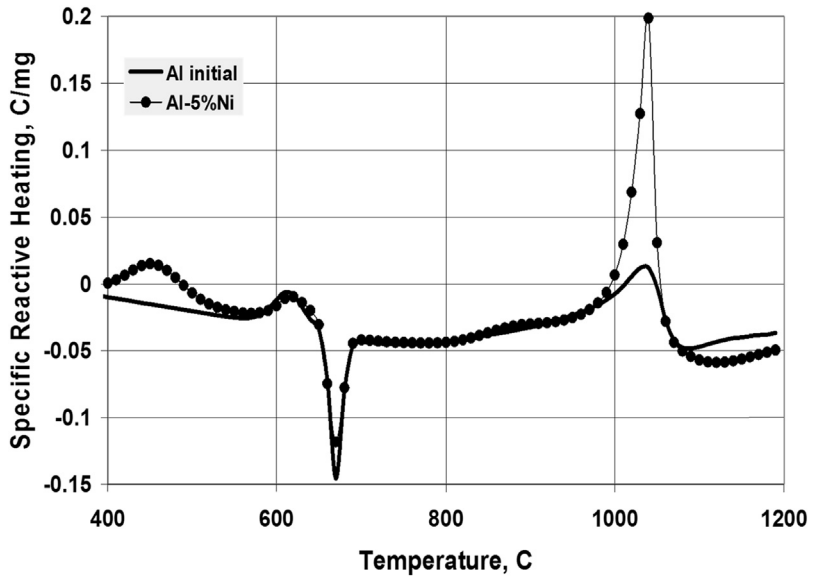

Figure 7 Behavior of initial (regular) Al particles and Al particles coated by Ni (5 wt%) during heating in air.

10 wt% Ni). Thermal analysis results clearly reveal that coating of Al particles by Ni increases their flammability in nitrogen.

Similar results were received from thermoanalytical study of oxidation of regular and nickel-coated aluminum powders in air (Figure 7). As can be seen, the reactive heat due to aluminum oxidation in air is much higher for nickel-coated aluminum powder than for the regular aluminum powder. One may conclude once again that coating of Al particles by Ni increases their reactivity both in nitrogen and in air.

4. IGNITION TESTS

To study ignition characteristics of nickel-coated aluminum particles compared with regular aluminum particles, Rosenband and Gany [5] placed aluminum powders on an electrically heated canthal ribbon in air. The powder temperature was measured by a thermocouple embedded in the powder. Experiments revealed that regular aluminum powders did not ignite upon heating up to the maximum temperature provided by this device (about 1200 °C), whereas nickel-coated (5 wt%) aluminum powders do ignite at temperature range of about 800–1000 °C (Figure 8).

Figure 9 shows the temperature history of regular and nickel-coated aluminum particles during heating in a heated-tape experiment. It can be seen that under the specific test conditions the maximum temperature of the regular aluminum powder reaches only 800 °C (as a result of the electrical heating), whereas for the nickel-coated aluminum powder a temperature of 1200 °C is attained due to occurrence of highly exothermic oxidation reaction.

Experiments were done not only with aluminum powders consisting of spherical or nearly spherical particles but also with different types of aluminum flakes. Aluminum flakes are flat or of scale-like shape whose thickness is small compared with the other dimensions (Figure 10). Two types of aluminum flakes with a specific surface area of 4.02 and 6.46 m^2/g were used in the experiments. Ignition delay of regular aluminum flakes, as well as of nickel-coated aluminum flakes (5 wt% of Ni), was measured in the

Figure 8 Behavior of regular (left) and nickel-coated (right) aluminum particles during heating in air. Regular aluminum powder exhibits no ignition, whereas nickel-coated aluminum powder ignites and burns violently [5].

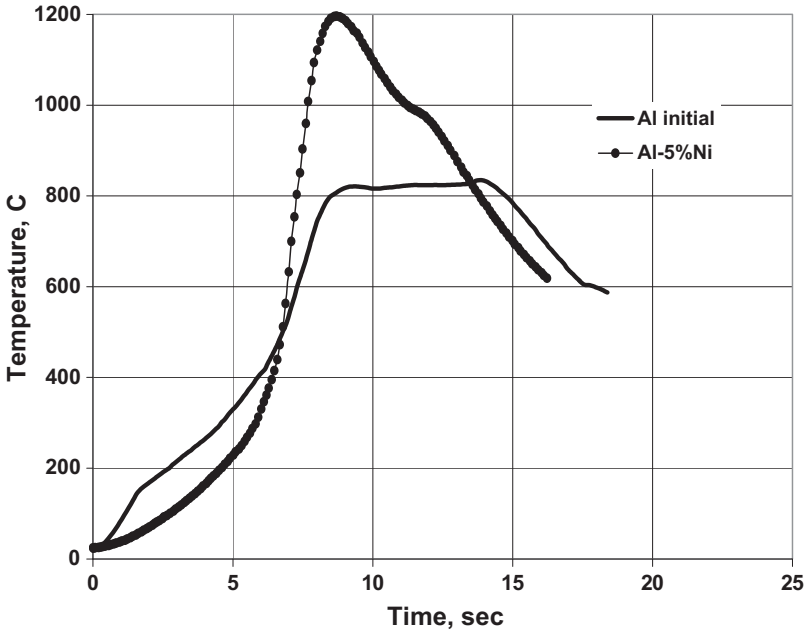

Figure 9 Temperature history of regular and nickel-coated aluminum powders when placed on an electrically heated ribbon.

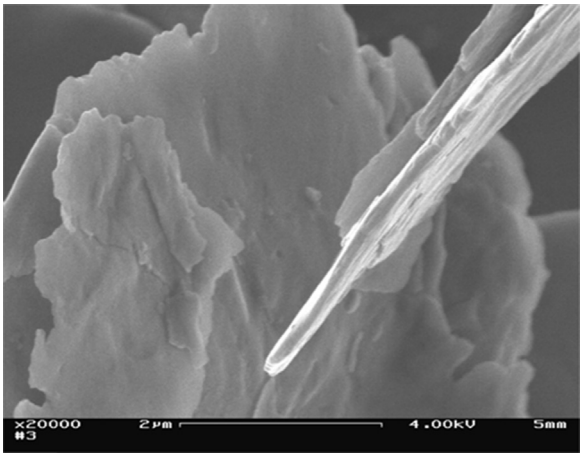

Figure 10 SEM photograph of as-received aluminum flakes.

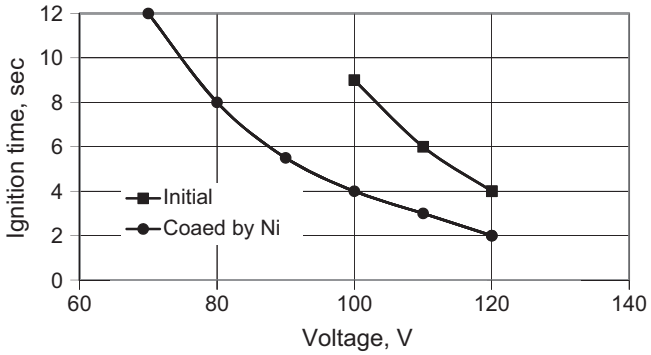

Figure 11 Dependency of ignition time on the voltage supplied to the heating tape for as-received aluminum flakes and nickel-coated aluminum flakes.

heated-tape experiments in air for different heating rates, controlled by the electrical voltage applied at the canthal tape. The experiments revealed a noticeable improvement of the ignition of the nickel-coated aluminum flake powder, as compared to initial, as-received aluminum flake powder.

Dependency of the ignition time of regular (specific surface area 6.46 m^2/g) and nickel-coated aluminum flakes on the electrical power supplied to the heating tape is presented in Figure 11. Ignition of the nickel-coated aluminum flakes was recorded for a much lower electrical heating power and at about half of the time than in the case of the initial (as-received) aluminum flakes.

As in the case of aluminum particles, temperatures measured in the aluminum flake experiments are substantially higher for the nickel-coated aluminum flakes as compared with initial aluminum flakes (Figure 12), indicating the existence of an exothermic oxidation or Ni–Al reaction in the former and no reaction in the latter case.

The improved ignition of nickel-coated aluminum particles is supported by Shafirovich et al. [6] who observed a fourfold reduction in ignition time for the coated particles in their laser-heated particle levitation experiments (Figure 13).

Combustion of nickel-coated aluminum and pure aluminum powders was characterized using a 9.2 L explosion (CVE) apparatus [7]. A cloud of powder was produced in a spherical vessel filled with air, and the cloud was ignited at its center by electrically heated tungsten wire. The estimated total electrical energy supplied to the igniter was 30 J. The powder charge was introduced to the explosion vessel with a gas blast from the air reservoir through a solenoid valve. A pressure transducer was used to record the pressure pulse produced by the propagating flame. The maximum pressure achieved in this experiment is proportional to the total energy released in combustion, whereas the rate of pressure rise is indicative of the reaction rate. The CVE experiment is well suited

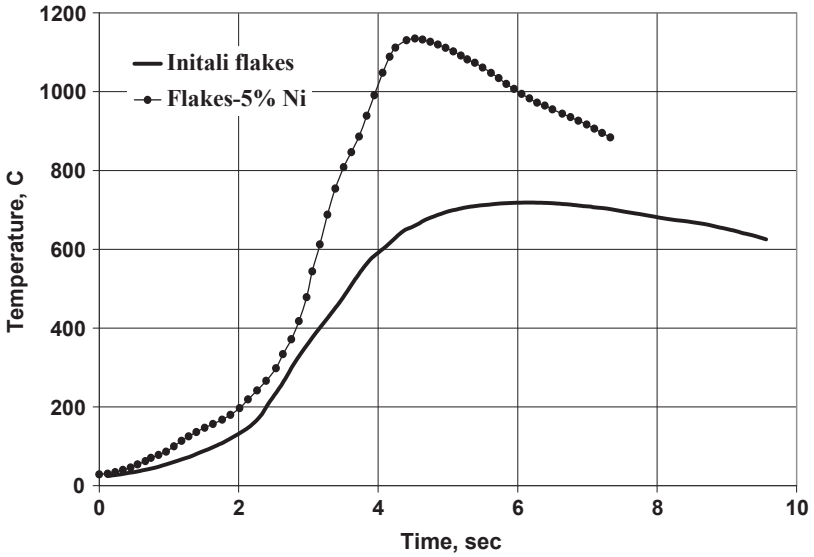

Figure 12 Temperature history of the regular and nickel-coated aluminum flakes.

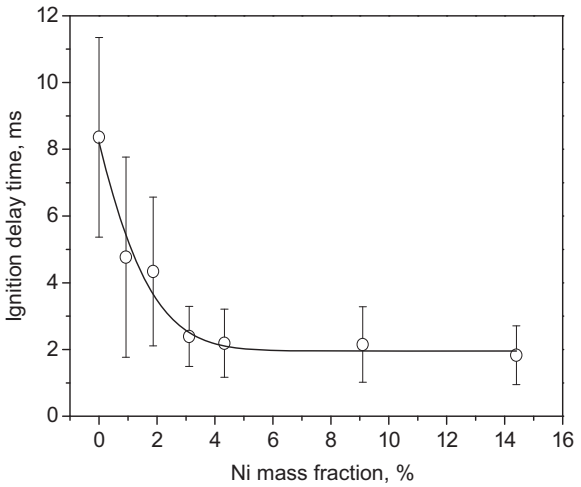

Figure 13 Ignition delay time of Ni-coated Al particles in air as a function of Ni mass fraction, using a 50 W CO_2 laser beam as the energy source [6].

for the comparison of combustion characteristics for different materials. In this particular case the combustion behavior of coated and uncoated Al powders was compared.

Characteristic pressure traces recorded for the combustion of nickel-coated aluminum and pure aluminum powders in a constant volume vessel are shown in

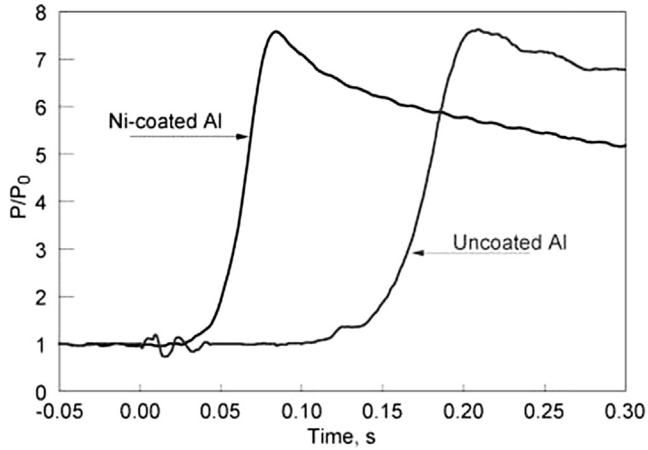

Figure 14 Pressure traces (presented as ratio of the measured pressure over the initial pressure in the combustion vessel) obtained from the constant volume explosion experiments for the Ni-coated and uncoated aluminum powders [7].

Figure 14. Both powders ignite and burn producing similar maximum pressures and exhibiting generally similar rates of pressure rise. Thus, the differences in the overall combustion energy released in constant volume explosion tests are negligible for the coated and uncoated powders. The main difference between the two materials appears to be in the induction period, which is the time after the igniter was initiated and until a substantial pressure increase was observed. A substantial difference (at the same concentration of dust) is observed for the induction period, which is about three times shorter for the Ni-coated material. Hence, the ignition temperature of the nickel-coated aluminum powders is noticeably lower than that for the uncoated aluminum particles.

One may propose some explanation for the reasons for increasing ignitability of aluminum particles due to nickel coating. The specific intermetallic reaction and phase formation between nickel and aluminum at elevated temperature seem to play a role in the process of the aluminum particles ignition (Figure 15) [8].

Aluminum and nickel can undergo an exothermic intermetallic reaction, enhancing the heating rate of the particle. It is believed that initial exothermic reaction, followed by fast temperature growth, takes place at temperature close to the aluminum melting point (660 °C). According to the phase diagram of aluminum-nickel system [8], an intermetallic Al_3Ni phase is formed due to this exothermic reaction. As a result, the particle is coated by a layer of this solid intermetallic compound. However, during further heating to 854 °C, a peritectoid reaction, Al_3Ni = Liquid + Al_3Ni_2, takes place, which proceeds with a liquid phase formation. Appearance of a liquid surface coating causes a much more intensive diffusion of oxygen to the metal surface. As a result, a fast and highly

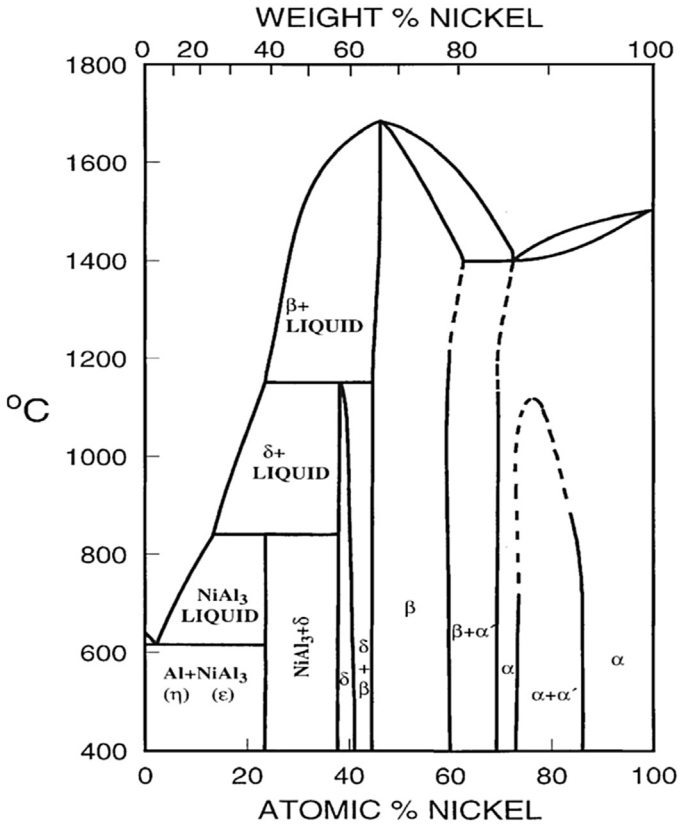

Figure 15 Binary Al-Ni phase diagram [8].

exothermic reaction of aluminum oxidation can take place, followed by the particle ignition.

It was suggested [9] that reduced agglomeration can be achieved by improving the aluminum particle ignition characteristics and shortening the time of ignition. Because a substantial decrease in ignition temperature and delay time for the nickel-coated aluminum when compared to the regular aluminum, one can expect reduced agglomeration resulting from the nickel coating of the aluminum particles in solid propellants.

Special experiments were done to check the impact of the nickel coating on agglomeration of aluminum particles during solid propellant combustion [10]. The experiments were conducted with model propellants composed of 15% aluminum, 55–65% AP, and 30–20% HTPB, respectively (on a weight basis). The aluminum particles used have diameters of 6 μm and 25 μm, and the AP particles were of 20 or 200 μm. Propellants containing regular (as-received) or nickel-coated aluminum were compared. The propellants were of the same composition, prepared at the same time,

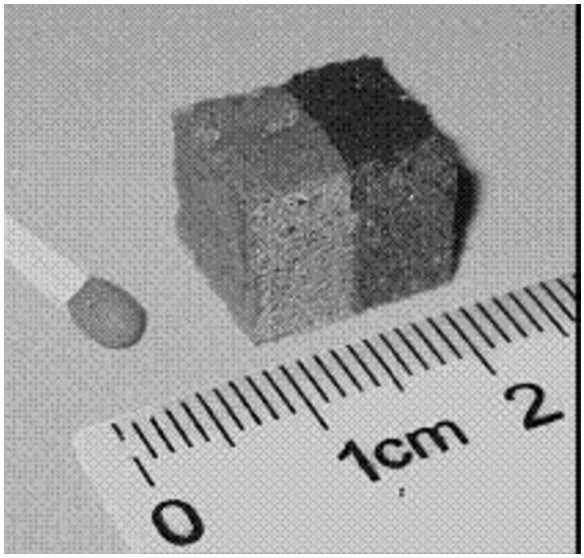

Figure 16 An isometric view of a double-strand propellant sample (front and upper surfaces are visible). The dark strand (on the right) is the nickel-coated Al propellant [10].

and under the same conditions. Experiments have been conducted in air both in pressurized (up to 32 atm) and atmospheric environments. In the experiments, two almost identical propellant strands were glued together with epoxy, as shown in Figure 16. They differed only by their aluminum component, which was either regular or with nickel coating. The glued strands were ignited simultaneously, in order to better observe and notice the effect of the nickel coating.

Observations of the burning strands revealed that the use of nickel-coated aluminum leads to a decreased diameter of ejected aluminum agglomerates. Figure 17 demonstrates well the phenomenon, showing large agglomerates ejected from the propellant containing regular aluminum (left), and smaller particles at higher flux from the propellant containing nickel-coated aluminum (right).

In each experiment, a median particle diameter was calculated, for which half of the particles' volume is concentrated in larger particles and the other half is concentrated in smaller particles. It was found that the diameter of agglomerates resulting from nickel-coated aluminum is around 60% of the diameter of agglomerates resulting from regular aluminum, with only little effect of pressure on the diameter ratio. This finding is very important when the mass reduction is taken into consideration; the "reduced" agglomerate constitutes approximately 20% mass of the "original" one. This reduction is expected to lead to more complete combustion of aluminum particles within the solid rocket motor as well as to reduction of slag accumulation.

Figure 17 Large agglomerates are observed for the propellant containing regular (uncoated) aluminum (left side). More intense flow of smaller particles is observed for the propellant containing coated aluminum (right side) [10].

5. IRON-COATED ALUMINUM PARTICLES

Coating of aluminum particles by a nanometric layer of iron for improvement of ignition and combustion characteristics of aluminum powders has been studied by Rosenband and Gany [11]. Similar studies have been done, for instance by Yagodnikov and Voronetskij [12] and Babuk et al. [13].

For the iron-coated particles study, Rosenband and Gany [11] prepared and characterized samples of aluminum particles coated with a thin iron layer. It was possible to obtain iron coating with controlled mass fraction of iron and mean thickness of the iron layer. Atomized aluminum powder with an average particle size of 25 μm, produced by Metal Powder Company, Ltd. was used in the experiments. Scanning electron microscope (SEM) image of received iron-coated aluminum particles is presented in Figure 18. As can be seen, the iron-coated Al particles are covered with numerous small (100–200 nm) bonded iron or iron oxide humps.

Thermoanalytical study of oxidation of produced iron-coated aluminum powders in air at heating rate of 20 K/min was done. DTA curves of iron-coated, nickel-coated, and regular aluminum powders are presented in Figure 19.

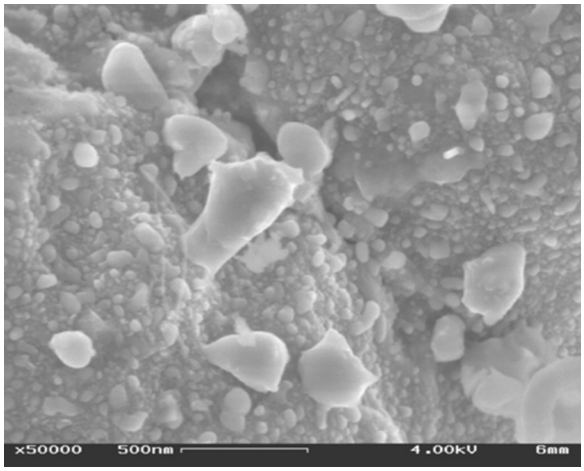

Figure 18 SEM photograph of aluminum particles coated by 5 wt% of iron [11].

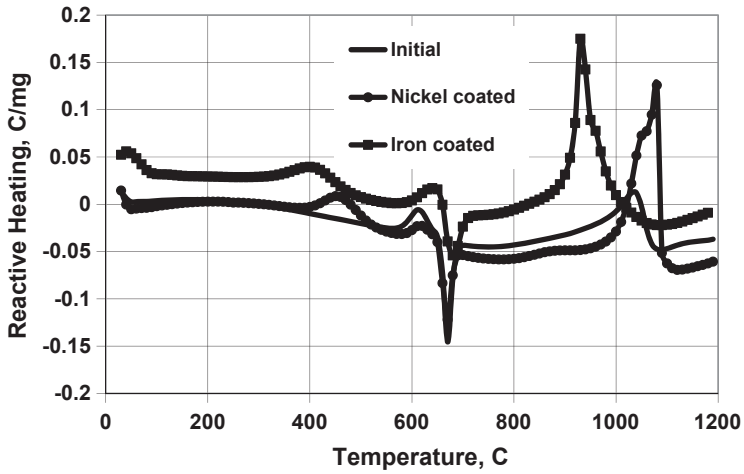

Figure 19 Behavior of initial (regular) Al particles and Al particles coated by Ni (5 wt%) and Fe (5 wt%) during heating in air.

As can be seen, similarly to nickel-coated aluminum, iron-coated aluminum particles oxidizing in air releases much more heat than regular aluminum powder. One may conclude once again that coating of Al particles by iron increases their reactivity in air. As well, oxidation of the iron-coated aluminum particles begins at the temperatures lower than these for the nickel-coated aluminum particles and proceeds with a higher rate.

A noticeable difference exists between the behaviors at the heating of Fe- and Ni-coated aluminum particles. For Ni coatings, intermetallic reactions do not appreciably influence the heating rate until the melting of $NiAl_3$ on peritectic reaction at 854 °C,

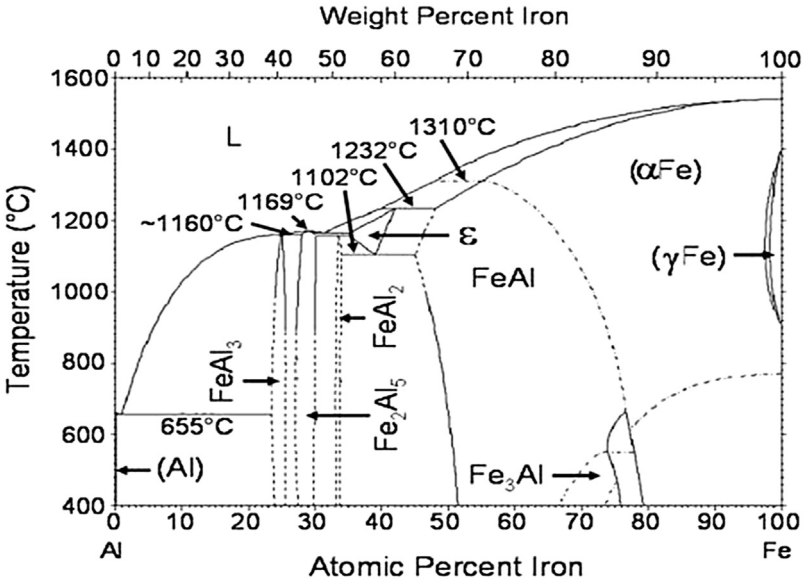

Figure 20 Binary Al-Fe phase diagram [8].

and as a result, this temperature was determined to be critical for particle ignition. For Fe-coated Al particles, as can be seen from the Al-Fe phase diagram (Figure 20) [8], Fe-Al intermetallic reactions contribute significantly to the heating rate upon Al melting at 660 °C. The lower temperature required for thermal contributions from intermetallic reactions as compared with Ni-coated particles may explain the more favorable influence of Fe coatings on ignition and prohibited agglomeration of aluminum particles during propellant combustion, as was observed in reference [3].

6. CONCLUSIONS

A method for activation of aluminum particles by coating with a thin (nanometric scale) nickel or iron layer has been developed and tested. Comparative thermoanalytical and ignition experiments have revealed substantial improvement of ignition of the nickel-coated and iron-coated aluminum particles compared to regular, as-received aluminum particles. The conclusion is that nickel and iron coating of aluminum particles shortens the ignition time of these particles, probably due to the formation of liquid phases at low temperatures (as compared to aluminum oxide) in nickel and iron aluminide and via Ni–Al and Fe-Al exothermic reactions, or thermite reaction between Al and oxides of nickel and iron.

Experiments also show that metal-coated aluminum particles produce smaller size agglomerates than regular aluminum in combustion of metallized solid propellants. The shorter ignition time causes a decrease in aluminum accumulation at the propellant

surface layer prior to ignition, leading to reduction of the agglomeration phenomenon and to ejection of smaller aluminum agglomerates.

REFERENCES

[1] V. Rosenband, A. Gany, Testing of metal powders behavior in a hot stage microscope, Int. J. Energ. Mater. Chem. Propuls. 5 (Issue 1–6) (2002) 377–383.
[2] V. Rosenband, A. Gany, A microscopic and analytic study of aluminum particles agglomeration, Combust. Sci. Technol. 166 (2001) 91–108.
[3] A.L. Breiter, V.M. Mal'tsev, E.I. Popov, Means of modifying metallic fuel in condensed systems, Combust. Explos. Shock Waves 26 (1988) 86–92.
[4] V. Rosenband, A. Gany, Agglomeration and ignition of aluminum particles coated by nickel, Int. J. Energ. Mater. Chem. Propuls. 6 (Issue 2) (2007) 143–152.
[5] V. Rosenband, A. Gany, Activated metal powder as potential energetic materials, Int. J. Energ. Mater. Chem. Propuls. 8 (Issue 4) (2009) 291–307.
[6] E. Shafirovich, P.E. Bocanegra, C. Chanvean, I. Gokalp, U. Goldshleger, V. Rosenband, A. Gany, Ignition of single nickel-coated aluminum particles, Proc. Combust. Inst. 30 (2005) 2055–2062.
[7] S.L. Vummidi, Y. Aly, M. Schoenitz, E.L. Dreizin, Characterization of fine nickel-coated aluminum powder as potential fuel additive, J. Propuls. Power 26 (3) (2010) 454–460.
[8] T.B. Massalski (Editor-in-Chief), Binary Alloy Phase Diagrams, American Society for Metals, Metal Park, OH, 1992.
[9] A. Gany, L.H. Caveny, Agglomeration and ignition mechanism of aluminum particles in solid propellants, in: Proc. of the 17th Symposium (International) on Combustion, The Combustion Institute, 1978, pp. 1453–1461.
[10] Y. Yavor, V. Rosenband, A. Gany, Reduced agglomeration resulting from nickel coating of aluminum particles in solid propellants, Int. J. Energ. Mater. Chem. Propuls. 9 (6) (2010) 477–492.
[11] V. Rosenband, A. Gany, High reactivity aluminum powders, Int. J. Energ. Mater. Chem. Propuls. 10 (1) (2011) 19–32.
[12] D.A. Yagodnikov, A.V. Voronetskij, Experimental and theoretical study of the ignition and combustion of an aerosol of encapsulated aluminum particles, Combust. Explos. Shock Waves 33 (1) (1997) 49–55.
[13] V.A. Babuk, V.A. Vassiliev, V.V. Sviridov, Propellant formulation factors and metal agglomeration in combustion of aluminized solid rocket propellant, Combust. Sci. Technol. 163 (1) (2001) 261–289.

CHAPTER SEVEN

Nanostructured Energetic Materials and Energetic Chips

Ruiqi Shen, Yinghua Ye, Peng Zhu, Yan Hu, Lizhi Wu and Zhao Qin
Micro-Nano Energetic Device Join Laboratory, School of Chemical Engineering, Nanjing University of Science and Technology, Nanjing, Jiangsu, China

1. INTRODUCTION

Nanostructured energetic materials (NSEMs) have nanoscale objects at least in one dimension. These are oxides embedded in carbon nanotube (1D), Al/CuO multilayer films (2D) and oxides embedded in porous silicon or porous copper (3D). The performances of NSEMs are very different from that of microstructured energetic materials in terms of released heat and reaction rate. Small critical diameter, high reaction rate, and high released heat allow NSEMs to fit very well for energetic chips (or energetic microchips, energetic MEMS chips). In the applications, energetic microchips and energetic bridges are very useful to facilitate ignition; they can even directly initiate high explosives. Because of microcharacteristics, research of nanostructured energetic materials and energetic microchips has been a hotspot for over 10 years. Great progress in the synthesis, the energetic microchip fabrication, and the energetic bridge application with NSEMs has been made. In this chapter, the progress of researchers at the Nanjing University of Science and Technology (NUST) on the synthesis, the energetic chip fabrication, and the explosion performance of NSEMs is analyzed and summarized.

2. 1D NSEMs AND ENERGETIC CHIPS

Several one-dimensional (1D) structure materials such as carbon nanotube, CuO nanowire, Co_3O_4 nanowire, and Ni nanorod are studied to fabricate energetic chips.

2.1 Energetic Carbon Nanotubes

Research motivation on energetic carbon nanotubes (CNTs) is to find a way to obtain an energetic material with nanometer critical diameter. It was found that the KNO_3-embedded carbon nanotube (KNO_3@CNTs) material can facilitate ignition when it was deposited on the conventional bridge [1,2].

The feasible synthesis technology of KNO_3@CNTs is as follows. Samples of carbon nanotubes were suspended in concentrated HNO_3 and saturated solution of KNO_3,

Energetic Nanomaterials
ISBN 978-0-12-802710-3, http://dx.doi.org/10.1016/B978-0-12-802710-3.00007-6

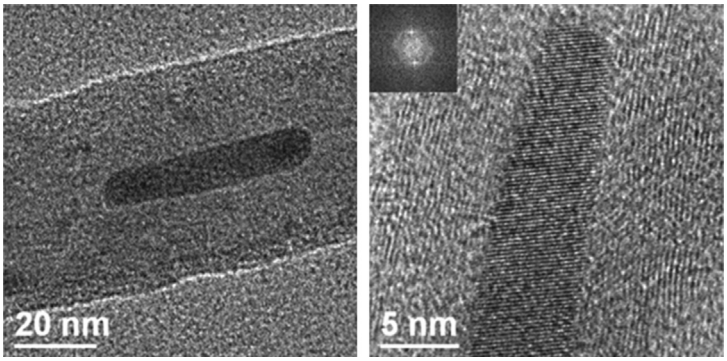

Figure 1 TEM of KNO_3@CNTs.

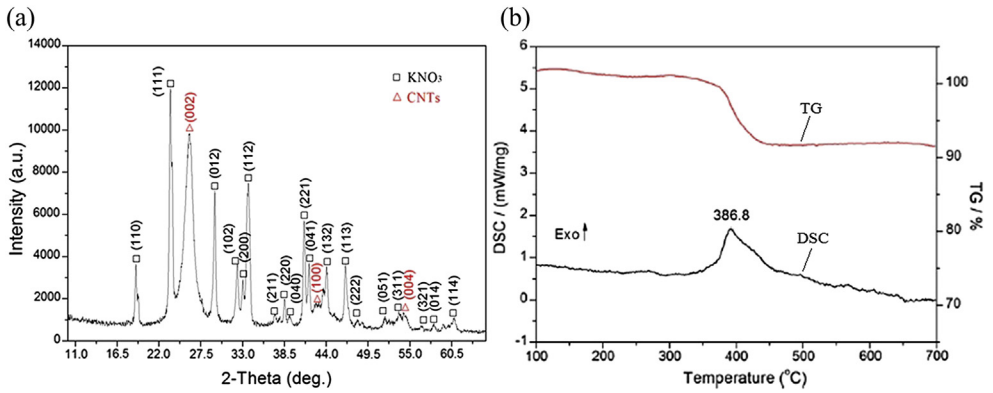

Figure 2 XRD pattern (a) and DSC/TG cures at heating rate of 5 °C/min (b) of KNO_3@CNTs.

and stirred at 140 °C for 24h. After cooling to the ambient temperature, the black residue was completely rinsed with deionised water and then dried in vacuum at 60 °C overnight KNO_3@CNTs is analyzed by transmission electron microscopy (TEM), X-ray diffraction (XRD), and differential scanning calorimetry/thermogravimetric analysis (DSC/TG). The results are shown in Figures 1 and 2, respectively.

TEM analysis results show that only part of KNO_3 is filled into CNTs; see Figure 1. XRD results verify that KNO_3 crystallizes in CNTs. DSC/TG results (Figure 2) show that KNO_3@CNTs decomposition has a single exothermic peak. The released heat equals 876.1 J/g at the heating rate of 5 °C/min and corresponds to the temperature peak value of 386.8 °C, and the mass loss of 8.6% proceeds in the range from 373.3 °C to 429.8 °C. The KNO_3@CNTs energetic chip is fabricated by electrophoresis. The fabrication process is shown in Figure 3. KNO_3@CNTs is deposited on a Cu bridge to get the thickness of the Cu thin film 0.76 μm and that of KNO_3@CNTs film 1.45 μm; see Figure 4.

The KNO_3@CNTs energetic chip and Cu bridge were ignited by 100 μF capacity discharge, and their exploding temperatures are shown in Figures 5 and 6, respectively.

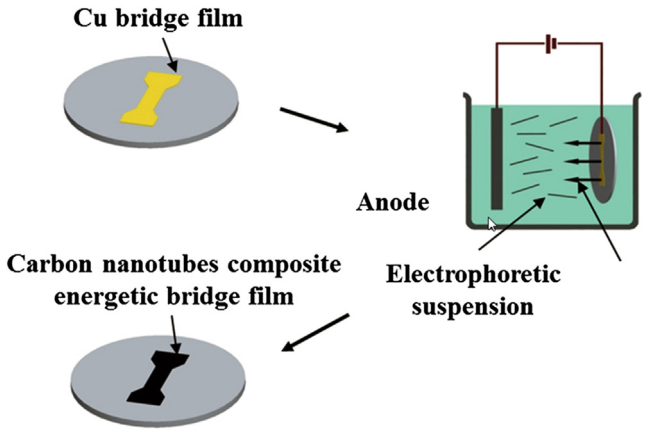

Figure 3 Schematic of fabricating process of KNO_3@CNTs energetic chip.

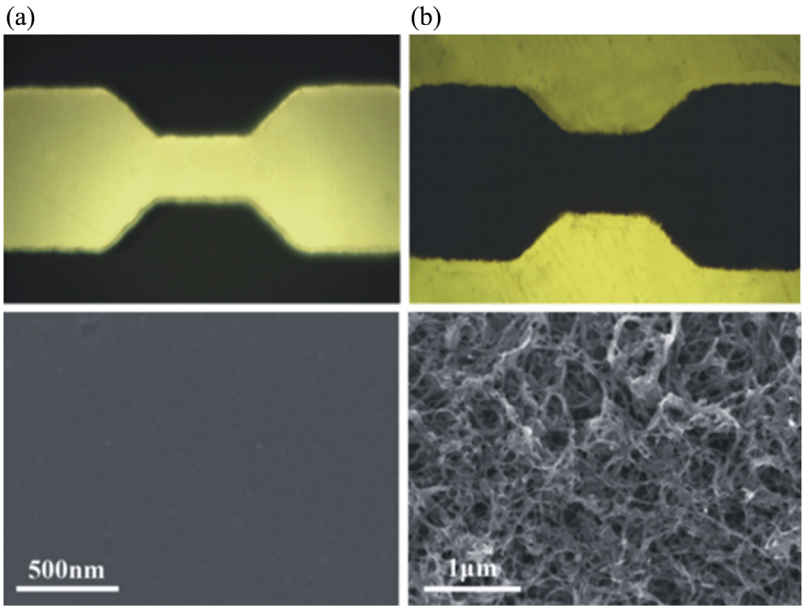

Figure 4 The Cu bridge film (a) and the carbon nanotubes composite energetic bridge film (b).

Figure 5 Electrical explosion phenomena of Cu bridge (left) and KNO_3@CNTs-Cu bridge (right) at 20,000 fps.

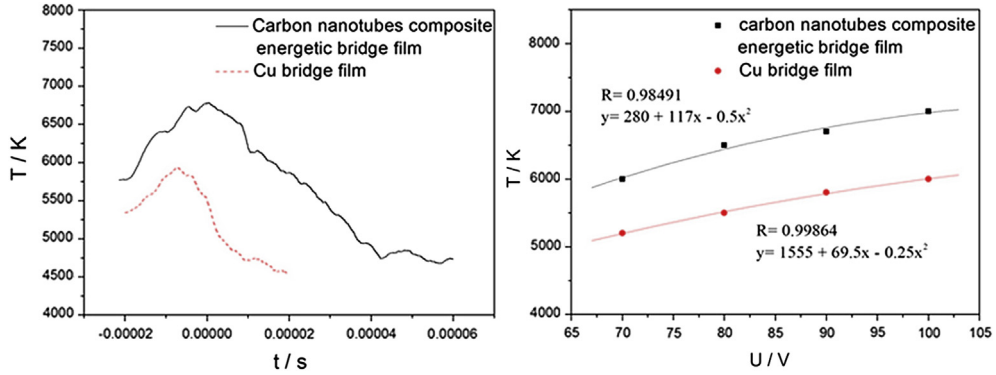

Figure 6 Exploding temperatures of KNO_3@CNTs bridge and Cu bridge ignited by 100 μF capacity charge.

With deposited KNO_3@CNTs film, the Cu bridge becomes an energetic chip. From the high-speed photography experiment results, the electrical explosion durations of the Cu thin film and the energetic chip are about 0.45 and 0.7 ms, respectively. Compared with the Cu thin-film microbridge, the electrical explosion phenomenon of the energetic chip is more intense and its duration is longer. This indicates that chemical reactions are involved in the electrical explosion process of the energetic chip, accompanied by higher heat release [1].

2.2 Al/CuO Nanowires

Zhang et al. early synthesized Al/CuO nanowires and fabricated Al/CuO nanowire energetic chip, in which the micro Cu film was deposited on Si substrate by vacuum thermal evaporation [3,4]. The synthesis process of CuO nanowire film is shown in Figure 7. The Ti film is deposited onto the silicon substrate as the intermediate layer by magnetron sputtering to prevent copper thin film cracking during thermal oxidation [5].

Heating of the Cu film at 400 °C during 4 h optimizes the process conditions to synthesize CuO nanowires. This process is shown in Figure 8.

The selected area electron diffraction (SAED) and XRD analysis results are shown in Figure 9. The nanowires consist of CuO and Cu_2O.

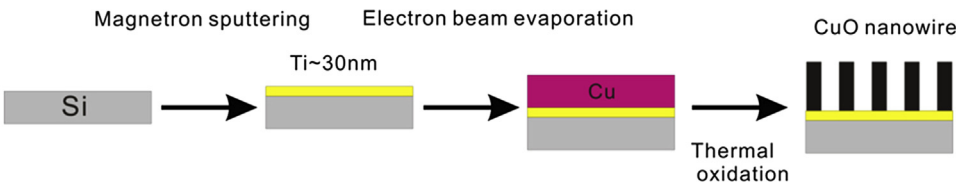

Figure 7 Schematic of fabricating process of CuO nanowires process.

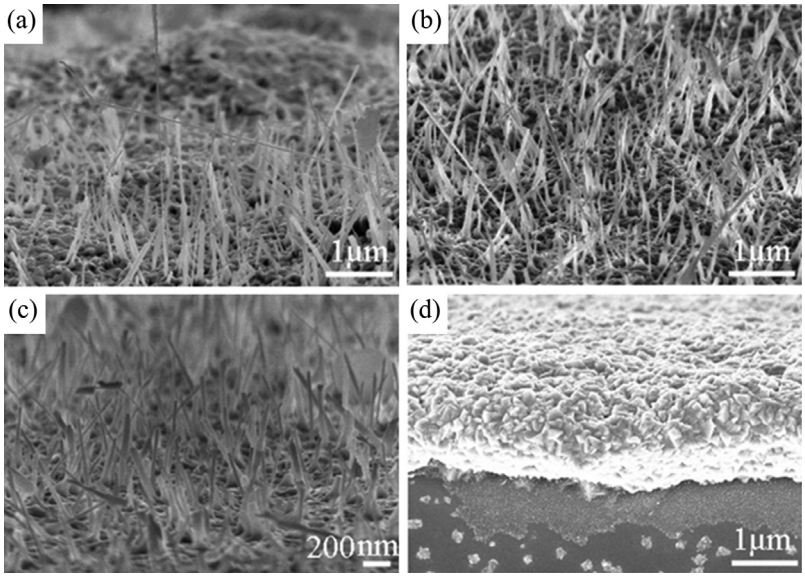

Figure 8 SEM cross-sectional images of 1 μm thick copper films annealed at 400 °C in air for different annealing time: (a) 2 h, (b) 4 h, (c) 5 h, and (d) 6 h.

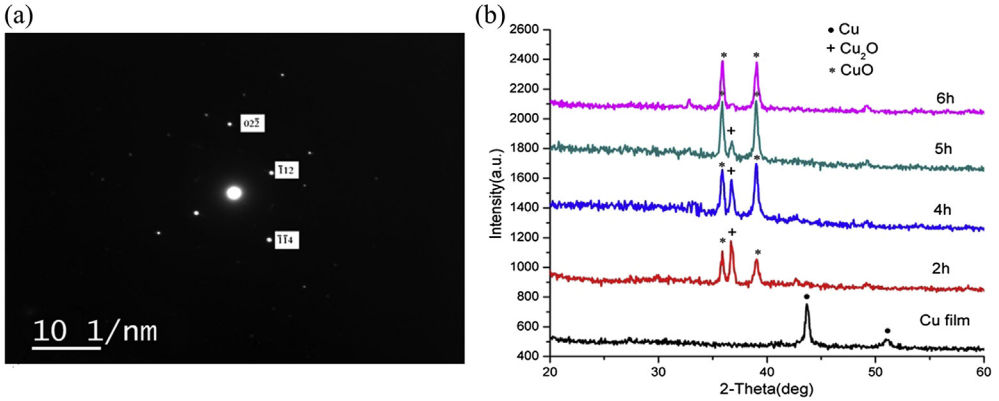

Figure 9 SAED pattern from a single nanowire (a) and XRD patterns of the copper film in air at 400 °C for 2 h, 4 h, 5 h, and 6 h (b).

Energetic core/shell nanowires of Al/CuO nanowires are synthesized by sputtering Al on CuO nanowires, in which CuO nanowires are synthesized by heating Cu film at 400–500 °C in the air, as shown in Figure 10. The exothermal reaction heat of the CuO/Al is 1263 J/g at the onset temperature of 450 °C determined by DSC analysis, which is below the melting temperature of Al (660 °C).

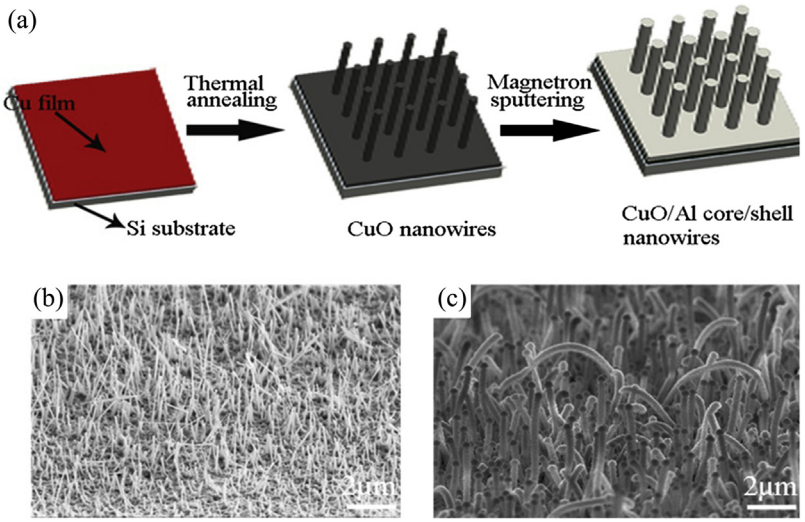

Figure 10 Schematic of fabricating process of CuO nanowires (a), SEM image of CuO nanowires (b), and SEM image of CuO/Al core/shell nanowires (c).

2.3 Al/Ni Nanorods

Due to the large contact area and rigid substrate, Al/Ni nanorod energetic chip can be fabricated by sputtering Al on the free-standing silicon substrate Ni nanorods [6]. Ni nanorods are synthesized by anodization, electric-chemical deposition, and porous alumina membrane (PAM) methods. The fabrication process of Al/Ni nanorods is shown in Figure 11. The microstructures of Ni nanorods and Al/Ni nanorods are shown in Figure 12.

DSC analysis results show that Al/Ni nanorods have one released heat peak at onset temperature of about 600 °C, as shown in Figure 13. The released heat depends on the amount of coated Al and sputtering time. Sputtering Al for 30, 45, and 60 min increases

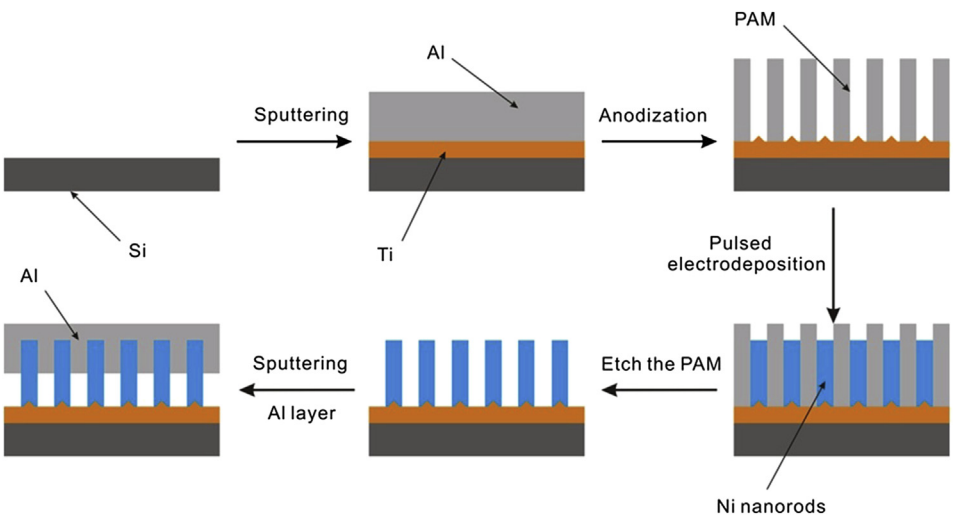

Figure 11 Schematic of fabricating process of Al/Ni nanorods.

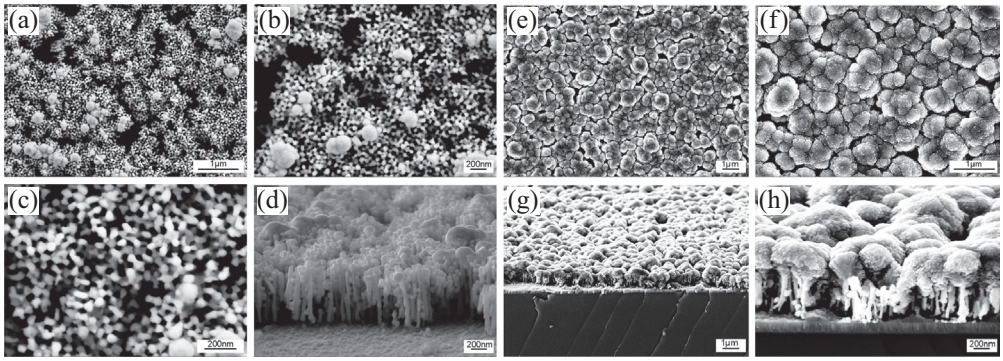

Figure 12 EM images of Ni nanorods and Al/Ni nanorods: (a), (b), and (c) are surface view of Ni nanorods, with magnification of 5000, 10,000, and 20,000, respectively; (d) is 90° visual angle view of Ni nanorods; (e) and (f) are surface view of Al/Ni nanorods, with magnification of 20,000 and 50,000; (g) and (h) are 90° visual angle view of Al/Ni nanorods, with magnification of 20,000 and 50,000.

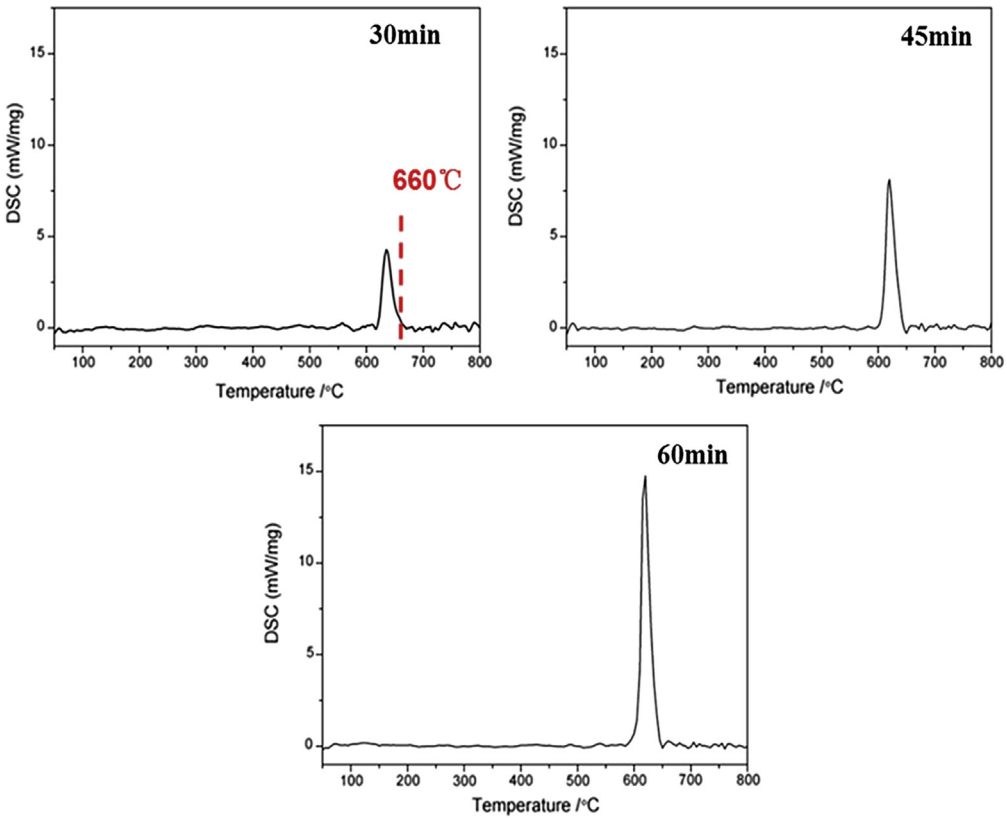

Figure 13 DSC analysis results of Al/Ni nanorods at different sputtering time of Al.

the released heat of Al/Ni nanorods up to 350.7 J/g (60 min), which is far less than the theoretical value 1381.4 J/g. The difference between practical and theoretical heat release could be due to two possible reasons. First, it is nearly impossible to synthesize the stoichiometric ratio multilayer films because of the complex deposition process. Second, the boundary layer of multilayer films is inactive due to prereaction of reactants.

2.4 Al/Co_3O_4 Nanowires

Co_3O_4 nanowires can be synthesized by ammonia-evaporation-induced synthetic method (in $Co(NO_3)_2$ and NH_3 solution); this is a hydrothermal process. Co_3O_4 has been used to prepare Al/Co_3O_4 based nanoenergetic materials by magnetron sputtering of coating nano-Al to Co_3O_4 nanorods [7]. The synthesis process of Al/Co_3O_4 nanowires is shown in Figure 14.

Field emission scanning electron microscope (FESEM), XRD, and Fourier transform infrared spectroscopy (FTIR) are used to characterize the prepared samples and analyze the components. FESEM analysis results show that the Si substrate consists of vertically aligned nanowires with diameter of about 400 nm; see Figure 15. The Al is integrated

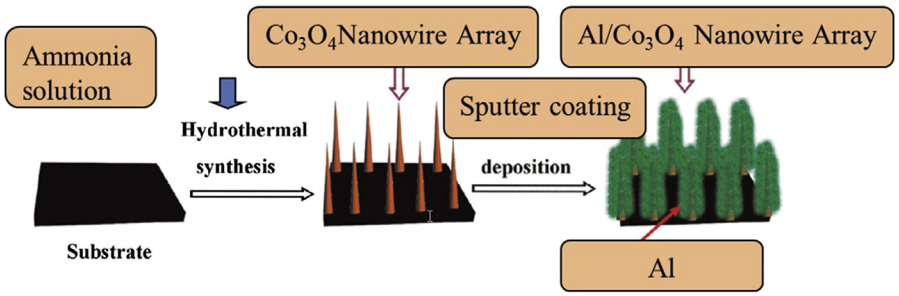

Figure 14 Schematic of fabricating process of Al/Co_3O_4 nanowires.

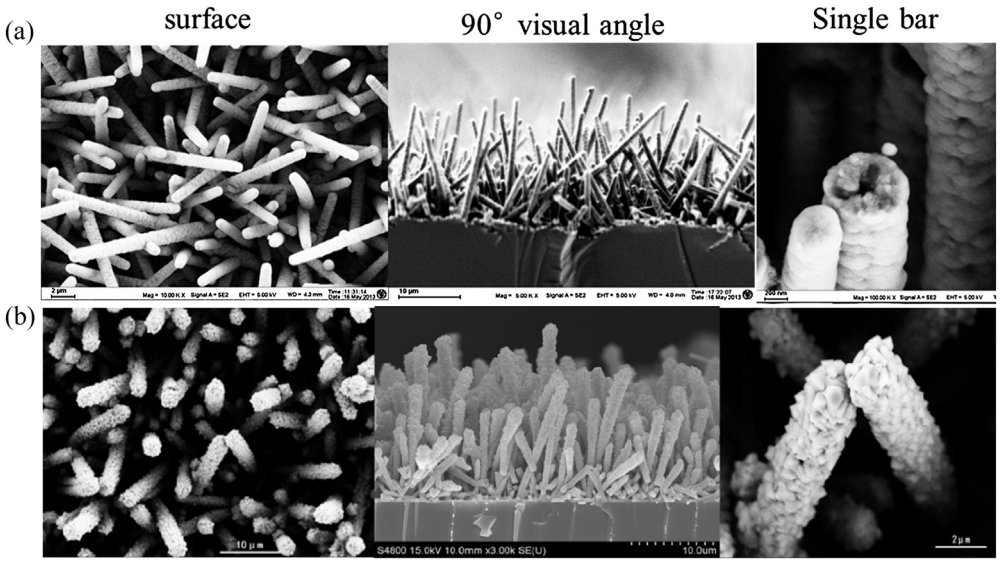

Figure 15 FESEM of Co_3O_4 nanowires (a) and Al/Co_3O_4 nanowires (b).

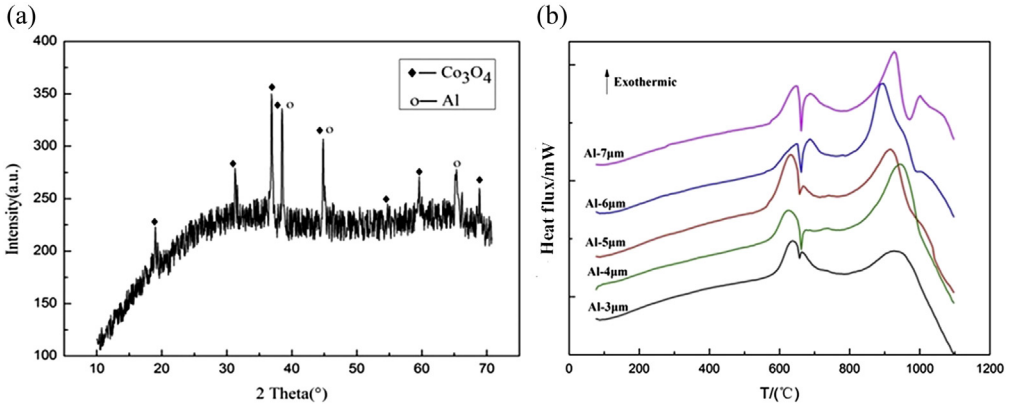

Figure 16 XRD analysis result (a) and DSC analysis results at different thickness of Al (b).

around the Co_3O_4 nanowires to form a core–shell nanoenergetic material nanostructure. XRD analysis results show that only diffraction lines for Al (JCPDS-652869) and Co_3O_4 (JCPDS-431003) are identified and there is no peak for Co, as shown in Figure 16(a). This means that Co_3O_4 and Al do not react very much in the high vacuum evaporator, which is mostly due to the low substrate temperature during the evaporation of Al. The reaction between Al and Co_3O_4 has a high theoretical heat of reaction of 4232 J/g. DSC analysis results show that the heats of reaction of 3, 4, 5, 6, and 7 μm Al thickness composites are about 1198.2 J/g, 1274.1 J/g, 2254.6 J/g, 1489.9 J/g, and 1326.5 J/g, respectively. These follow from the integration of major exothermic peak, as shown in Figure 16(b). When the content of Al is low, the reaction is not complete, and when the content of Al is high, the melting endothermic peak of Al appears; both lead to low heat release. Therefore, Al film with thickness of 5 μm is more appropriate for preparing the Al/Co_3O_4 energetic composites.

Co_3O_4 nanowires are easier to form on a silicon surface than on a gold surface, so Co_3O_4 nanowires are suitable to fabricate Al/Co_3O_4 reactive semiconductor bridge (Al/Co_3O_4-RSCB), as shown in Figure 17.

The electrical explosion performance of Al/Co_3O_4-RSCB is researched by 47 μF capacity discharge, as shown in Figure 18. The higher the charging voltage, the shorter

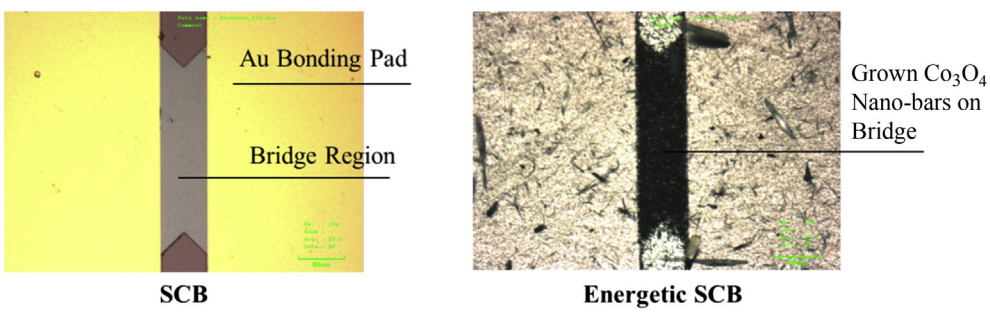

Figure 17 Al/Co_3O_4 reactivity semiconductor bridge.

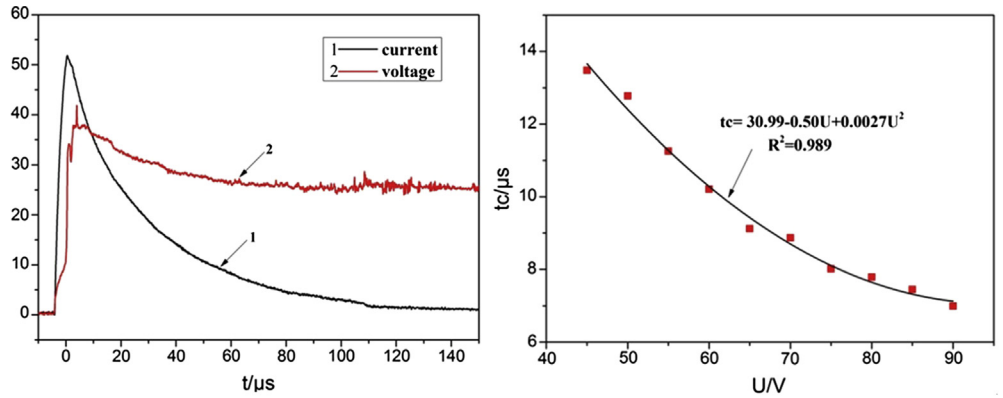

Figure 18 Volt-current characteristics (left), and exploding rise time (right) of Al/Co_3O_4-SCB by capacity discharge of 47 μF.

the ignition delay time. The critical ignition energy is in the range of 8.75–9.10 mJ, and the flame length and the flame duration of Al/Co_3O_4-RSCB are longer than that in performance of conventional semiconductor bridge (SCB).

3. TWO-DIMENSIONAL NSEMs AND ENERGETIC CHIPS

A large group of nanostructured reaction systems can release a high reaction heat. The calculated heat of reaction systems is listed in Table 1. The reactants of reaction systems can be sputtered alternatively to multilayer films to obtain two-dimensional nanostructured energetic materials (2D NSEMs), which are deposited on metal or semiconductor bridges to fabricate energetic chips or energetic ignition bridges.

Table 1 Reactivity systems for nanostructured energetic materials.

Constituents	Heat of reaction, cal/g	Constituents	Heat of reaction, cal/g
$2Al + 3CuO$	974	$8Al + 3Co_3O_4$	1012
$2Al + MoO_3$	1124	$4\,Mg + Fe_3O_4$	1033
$2Al + 3MnO_2$	1159	$3\,Mg + Fe_2O_3$	1110
$2Al + Ni_2O_3$	1292	$2\,Mg + MnO_2$	256
$2B + Ti$	1320	$3Si + 5Ti$	1322
$2B + Al$	742	$B + V$	536
$2B + V$	650	$Al + Ni$	330
$2Si + V$	700	$Al + Ti$	314

3.1 Al/Ti Multilayer Film

The cross-section structure of Al/Ti multilayer film is roughly 2 μm in total thickness produced by sputtering 75 nm Al layer and 25 nm Ti layer for each bilayer (the components thickness ratio is 3:1). The film image is shown in Figure 19(a). DSC analysis results of the film show that Al/Ti multilayer film has three exothermic peaks (340～430 °C, 620～700 °C, 780～930 °C, see Figure 19(b)), and the sum of released heat is 918.36 J/g, which is about 80.7% of theoretical value.

The released heat of Al/Ti depends on the thickness and the layers number of reactants. The sum of heat is smaller than the theoretical value, and the sum of heat of the thin layer is smaller than that of the thick layer due to prediffusion reaction at the contacted surface [8]; see Table 2.

The results of XRD analysis of the initial and the reacted Al/Ti nanoenergetic multilayer films (nEMFs) are shown in Figure 20.

The diffraction peaks of initial Al/Ti nEMFs are assigned to Al (111), Al (222), Ti (100), Ti (110), and AlTi (111). After reaction, the results of XRD analysis of the reacted Al/Ti nRMFs show that the compositions are AlTi (001), AlTi (111), AlTi (002), AlTi (200), AlTi (202), AlTi (220), AlTi (311), and AlTi (222), in which AlTi (111) is the main reaction product.

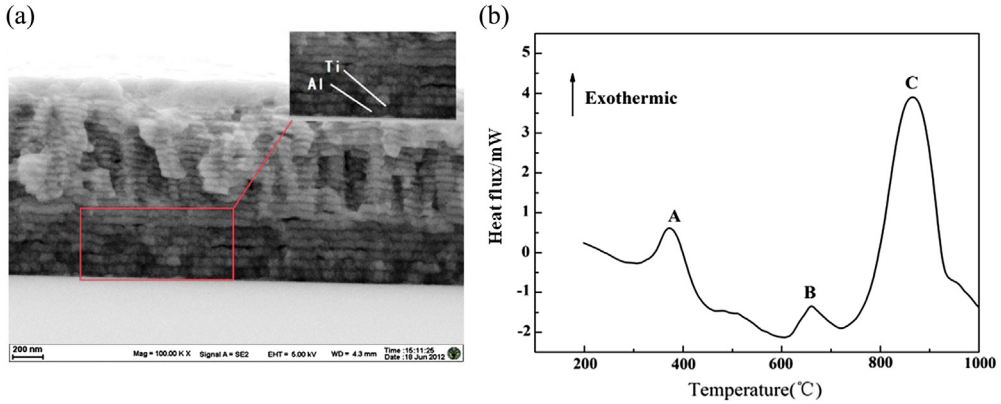

Figure 19 Cross-sectional image (a) and DSC analysis result (b) of Al/Ti film.

Table 2 Released heats of Al/Ti multilayer film at different bilayer cycles.

Al thickness, nm	Ti thickness, nm	Bilayer thickness, nm	Total layer thickness, μm	Sum of heat, J/g
25	25	50	2	458.0
50	50	100	2	493.4
100	100	200	2	696.8

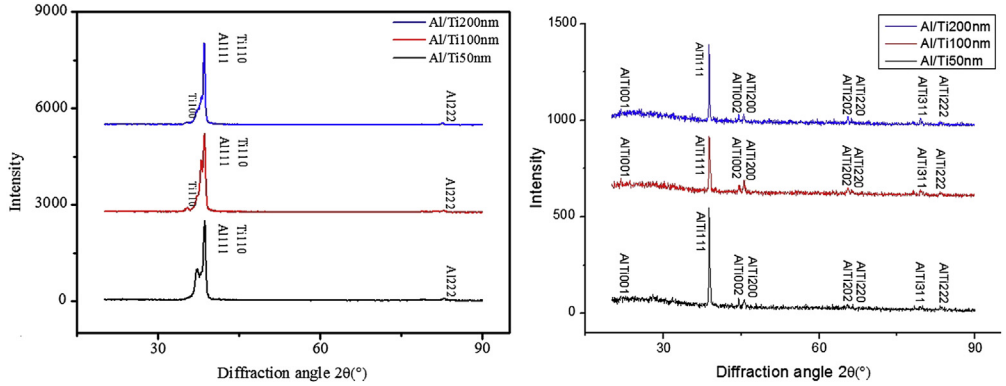

Figure 20 XRD spectra of initial Al/Ti (left) and reacted Al/Ti nEMFs (right) at different bilayers.

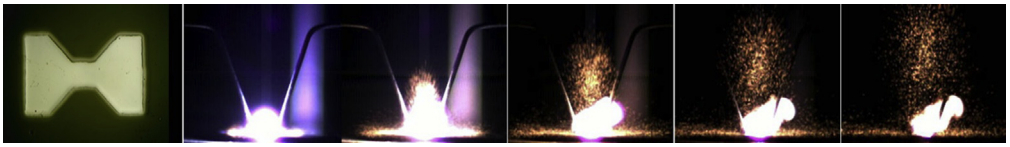

Figure 21 Al/Ti multilayer bridge and its electrical explosion at 100 cycles, capacity 100 μF, and charge voltage 140 V.

Al/Ti multilayer film has been used to fabricate an energetic bridge of 1 mm length and 1 mm width. It is ignited by the 100 μF capacity discharge with the charge voltage of 140 V; see Figure 21.

3.2 Al/Ni Multilayer Film

Al and Ni layers with bilayer thicknesses of 50, 100, and 200 nm were prepared by radio frequency magnetron sputtering. In each bilayer, the thickness ratio of Al to Ni was maintained at 3:2 ratio [9]. The cross-section structures of Al/Ni multilayer film with 60 nm Al layer and 40 nm Ni layer are shown in Figure 22(a). DSC analysis results show that Al/Ni multilayer film has three exothermic peaks (230～250 °C, 280～370 °C, 380～460 °C), as shown in Figure 22(b). DSC curves indicate that the released heat of Al/Ni multilayer films with bilayer thicknesses of 50, 100, and 200 nm are 389.4, 396.7, and 409.9 J/g, respectively. The released heat of Al/Ni multilayer film at different deposition cycles is listed in Table 3.

XRD analysis results of initial Al/Ni and reacted Al/Ni nEMFs are shown in Figure 23.

Before reaction, the compositions Al/Ni nEMFs XRD spectra comprise Al (111), Al (222), Ni (111), and Ni (200) peaks, but the diffraction peak of Al_xNi_y(AlNi (110)) is

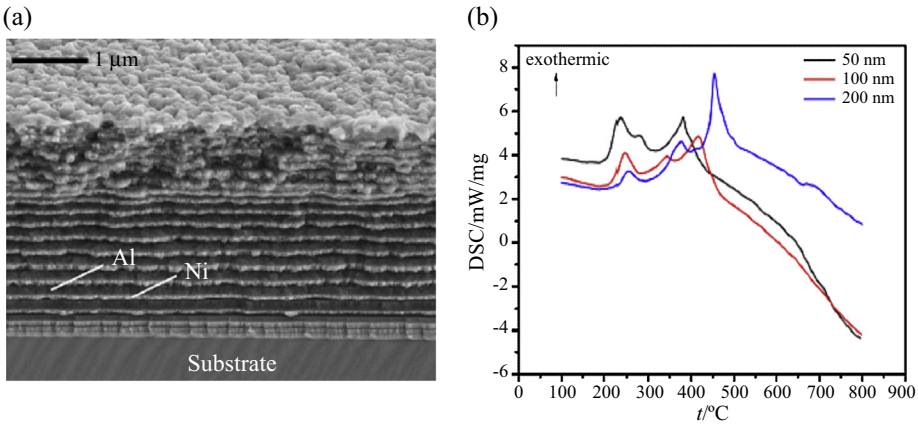

Figure 22 Cross-sectional image (a) and DSC analysis result (b) of Al/Ni multilayer film.

Table 3 Released heats of Al/Ni multilayer film at different deposition cycles.

Al thickness, nm	Ni thickness, nm	Bilayer thickness, nm	Total layer thickness, μm	Sum of heat J/g
30	20	50	2	389.4
60	40	100	2	396.7
120	80	200	2	409.9

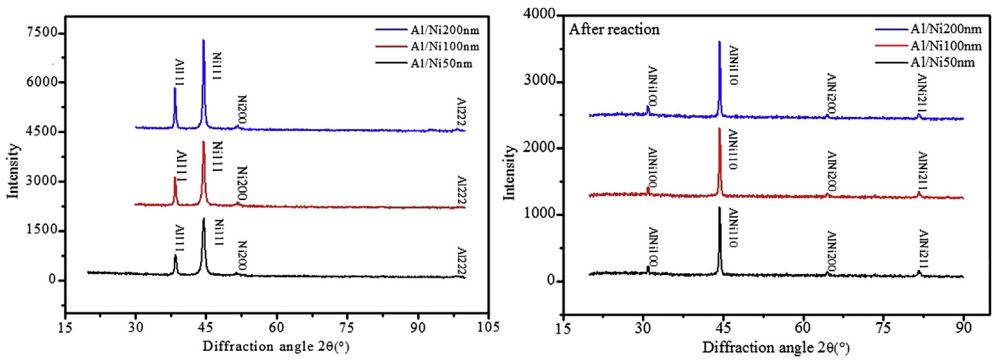

Figure 23 XRD spectra of initial Al/Ni (left) and reacted Al/Ni nEMFs (right) at different bilayers.

not confirmed since it overlaps the diffraction peak of Ni (111). After reaction, the spectra comprise AlNi (100), AlNi (110), AlNi (200), and AlNi (211) peaks.

Al/Ni multilayer film is used to fabricate an energetic bridge of 1 mm length and 1 mm width. The ignition capacity charge is the same as for the Al/Ti multilayer film.

The exploding temperatures show that not only the temperature of Al/Ni is higher than that of pure Al or Ni explosion, by about 2000 K, but also the area of the exploding field is stronger than Al and Ni bridges; see Figure 24.

The Al/Ni multilayer film is deposited on a conventional semiconductor bridge to fabricate a reactive semiconductor bridge (Al/Ni-RSCB) [10], as shown in Figure 25.

The electrical explosion performance of Al/Ni-RSCB was tested by capacity discharge of 47 μF, as shown in Figure 26. The higher the charging voltage, the shorter

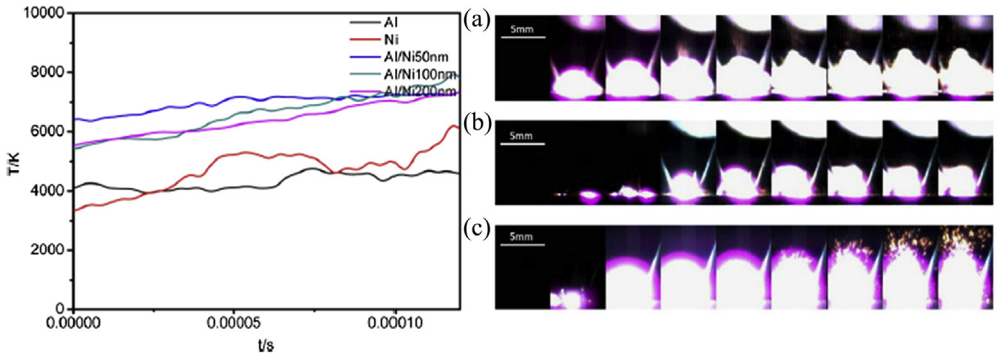

Figure 24 Exploding temperatures (left) and exploding fields (right) of Al (a), Ni (b), and Al/Ni (c).

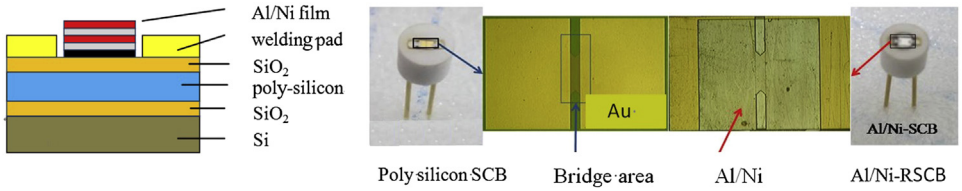

Figure 25 Structure and samples of Al/Ni reactivity semiconductor bridge.

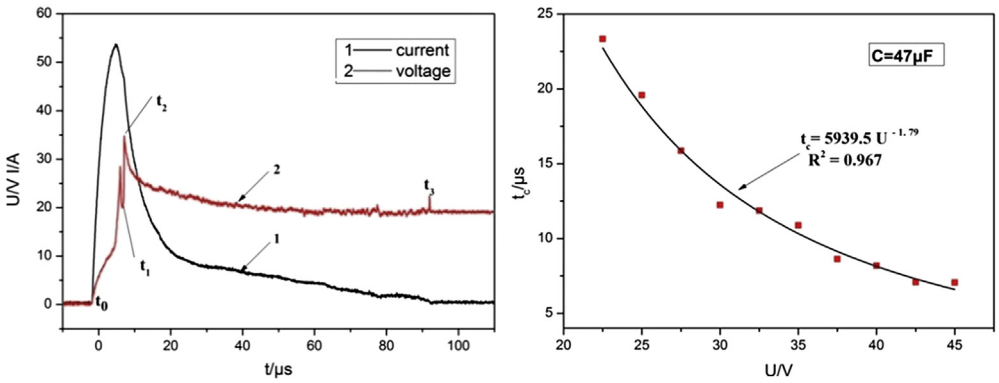

Figure 26 Volt-current characteristics (left), exploding rise time tc (right) of Al/Ni-RSCB by capacity discharge of 47 μF.

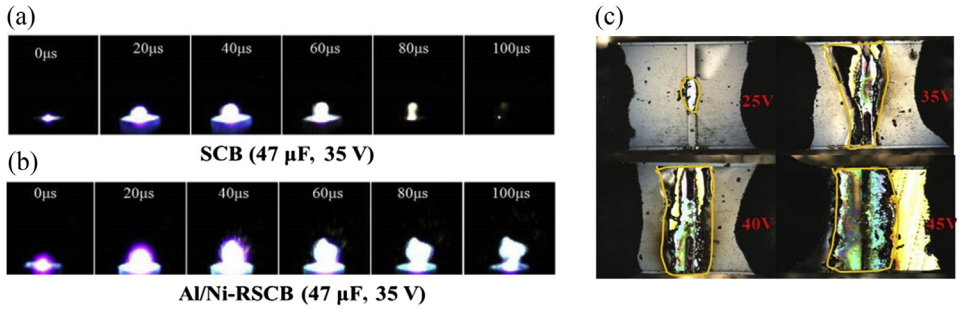

Figure 27 Electrical explosion images of (a) SCB and (b) Al/Ni-RSCB at 20,000 fps and (c) bridge area of ignited Al/Ni-RSCB at different voltage.

the ignition delay time. The critical ignition energy is in the range of 4.0–4.7 mJ, and the flame length and the flame duration of Al/Ni-RSCB are longer than that of SCB; see Figure 27.

The output energy can be calculated according to burned area of Al/Ni film, and the sum of released heat can be obtained by DSC analysis. The output energy of Al/Ni-RSCB is 15.94 mJ at 47 μF, 35 V, and this value is about four times higher of input energy (4.48 mJ).

3.3 Al/CuO Multilayer Film

Al/CuO multilayer films are the best nanostructured energetic materials and have been researched for many years due to their high energy, easy fabrication to energetic microchips, and compatibility with many materials or MEMS process. The cross-section structure of Al/CuO multilayer film and its energetic chip fabricated by sputtering as well as the DSC analysis results are shown in Figure 28.

The thicknesses of Al and CuO layers are controlled in the range of 20–40 nm. DSC analysis results show that there are two exothermic peaks at onset temperatures of 550

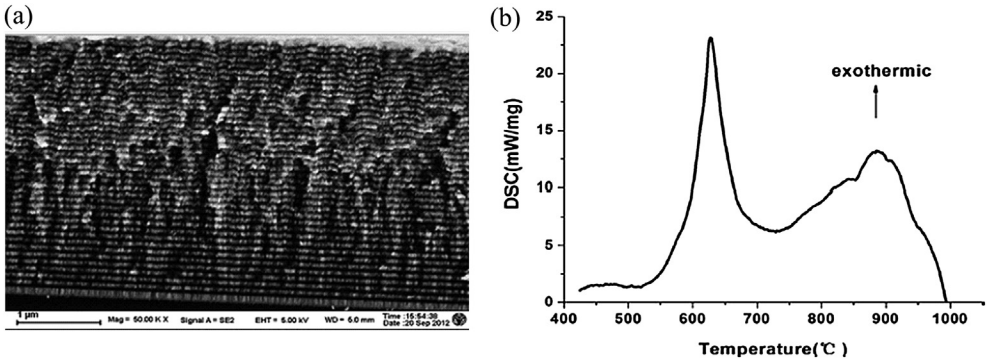

Figure 28 Cross-sectional structure of Al/CuO multilayer film and its DSC analysis result.

and 750 °C. The sum of released heat is about 2024 J/g. It is less than the theoretical value (4079 J/g) due to the prereaction between CuO and Al layers.

Different Al/CuO-RSCB have been researched. Al/CuO multilayer film is used to fabricate reactive semiconductor bridge by depositing Al/CuO multilayer film on metal bridge or on semiconductor bridge. The structures of typical reactive semiconductor bridges are shown in Figure 29.

The tested Al/CuO-RSCB (Figure 29(a)) has two V-type angles (90°) and 380 μm (width) × 80 μm (length) × 2.5 μm (thickness) dimensions. The Al/CuO multilayer film size is 1 mm (width) × 1 mm (length) × 3 μm (thickness) and the resistance of SCB is 1.3 Ω. When the Al/CuO-RSCB is ignited by capacitor discharge (47 μF, 30 V), the exploding temperature of Al/CuO-RSCB is higher than that of SCB by about 40%, reaching about 7000 K (measured by the double line of atomic emission spectroscopy) [11]. The voltage–current (U-I) characteristic is very similar to that of conventional SCB, as shown in Figure 30 [12].

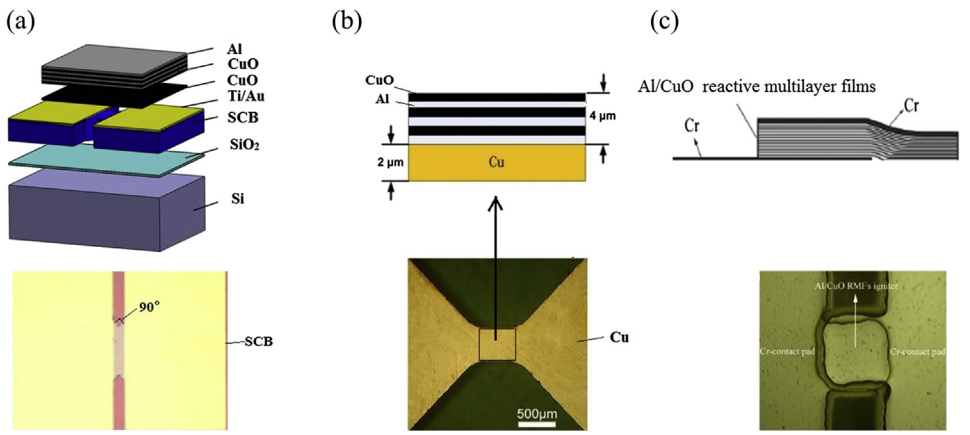

Figure 29 Al/CuO reactive multilayer films, (a) Al/CuO-SCB, (b) Al/CuO-Cu bridge, (c) Al/CuO-dielectric bridge.

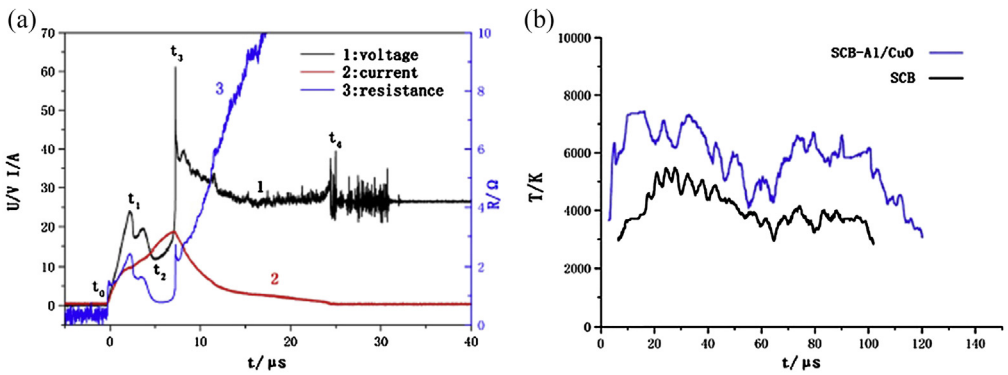

Figure 30 Exploding characteristics of Al/CuO-RSCB (a) exploding voltage-current resistance and (b) exploding temperature.

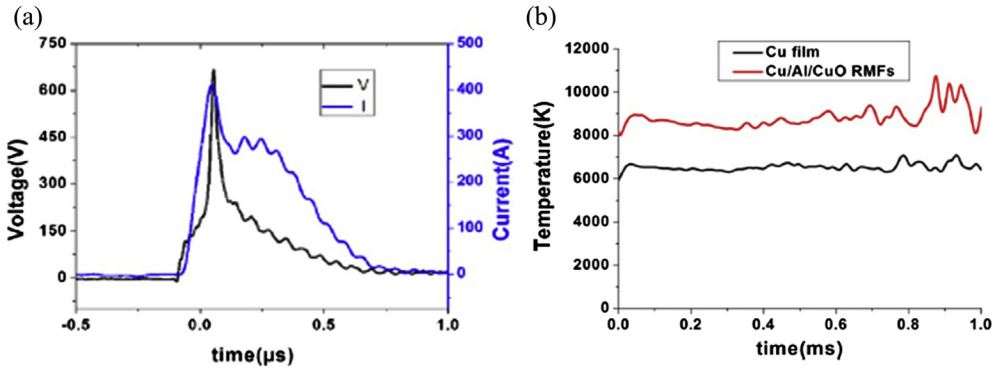

Figure 31 Exploding characteristics of Al/CuO-dielectric energetic bridge (a) exploding volt-current and (b) exploding temperature.

The tested Al/CuO-Cu chip (Figure 29(b)) consists of a Cu bridge of 0.45 mm × 0.45 mm bridge area size with a resistance of 200–250 mΩ and a deposited Al/CuO multilayer film of 4 μm thickness (150 nm bilayer). The exploding temperatures of Cu bridge and Al/CuO-Cu bridge are about 7000 and 9000 K at capacitor charge of 0.22 μF and 600 V, respectively, as shown in Figure 31 [13].

The tested Al/CuO dielectric bridge (Figure 29(c)) consists of three layers: the top and bottom layers are 1000 × 1000 × 2 μm joining with Cr contact pad, and the middle layer is 1000 × 1000 × 7.2 μm Al/CuO multilayer layer. The Al/CuO multilayer includes six Al/CuO bilayers, and each Al/CuO bilayer is 1.2 μm (0.38 μm thickness of Al layer and 0.82 μm thickness of CuO). When the Al/CuO dielectric bridge is ignited, the Al/CuO multilayer is broken down by an electric field, and the current transfers from one side of Cr film to its another side. The exploding temperature of Al/CuO-dielectric bridge is about 3773 K (measured by atomic emission spectroscopy) at 40 V DC voltage source, as shown in Figure 32 [14].

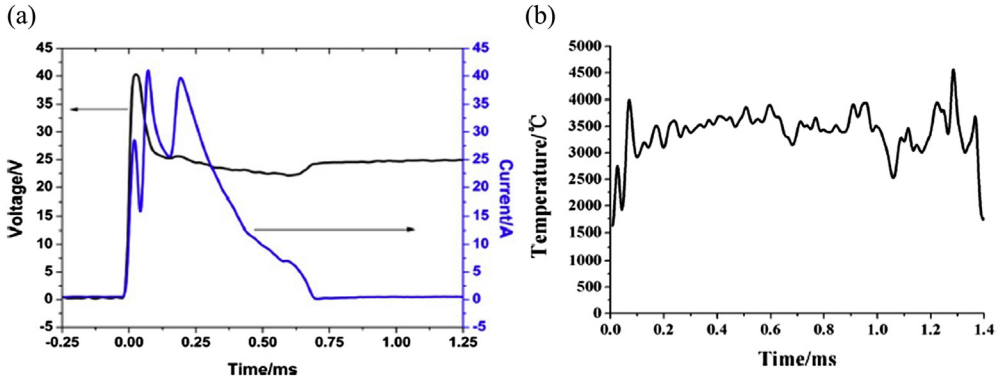

Figure 32 Exploding characteristics of Al/CuO-Cu bridge (a) exploding volt-current and (b) exploding temperature.

4. THREE-DIMENSIONAL NSEMs AND ENERGETIC CHIPS

The promising three-dimensional (3D) structured materials, such as porous copper, porous silicon, and 3D Fe_2O_3, have been researched to fabricate energetic chips [15]. When porous copper, porous silicon, and 3D Fe_2O_3 are deposited by metal fuels or oxidants in situ reaction, they will become a group of energetic materials.

4.1 Energetic Porous Copper

Energetic porous copper samples can be synthesized by depositing oxidants into porous copper or by in situ azido reaction in gaseous hydrazoic acid environment, in which the porous copper can be synthesized by electrodeposition in $CuSO_4$ (0.2 mol/L)/H_2SO_4 (1.0 mol/L)/NH_4Cl (10.0 mol/L) solution [16]. The structures of porous copper and $NaClO_4$-porous copper are shown in Figure 33(a) and (b). $NaClO_4$-porous copper is prepared by absorbing and drying processes of $NaClO_4$/ethanol solution, as shown in Figure 33(c).

The low-temperature and high-temperature exothermic peaks due to the thermal decomposition of $NaClO_4$ can be noticed at the DSC curves shown in Figure 34: these are listed in Table 4. The TG curve shows fast weight loss near the second exothermic peak (Figure 34). Note that the onset temperatures increase with the heating rate as well as the released heat.

The results show the two exothermic reactions, in which the first step reaction is solid phase reaction between porous copper and $NaClO_4$ ($4Cu + NaClO_4 \rightarrow NaCl + 4CuO$) and the second step reaction is decomposition reaction ($NaClO_4 \rightarrow NaCl + 2O_2\uparrow$).

4.2 Energetic Porous Silicon

Porous silicon is widely used to fabricate energetic chips [17,18]. Oxidants are imbedded into structure of porous silicon via submerging the silicon into the oxidant acetone

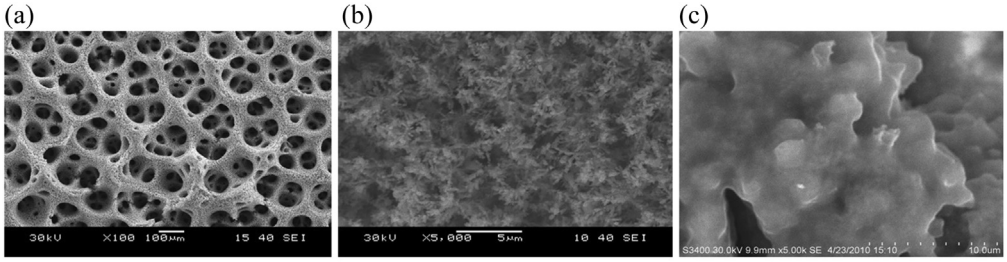

Figure 33 Structure of porous copper and of $NaClO_4$ impregnated porous copper.

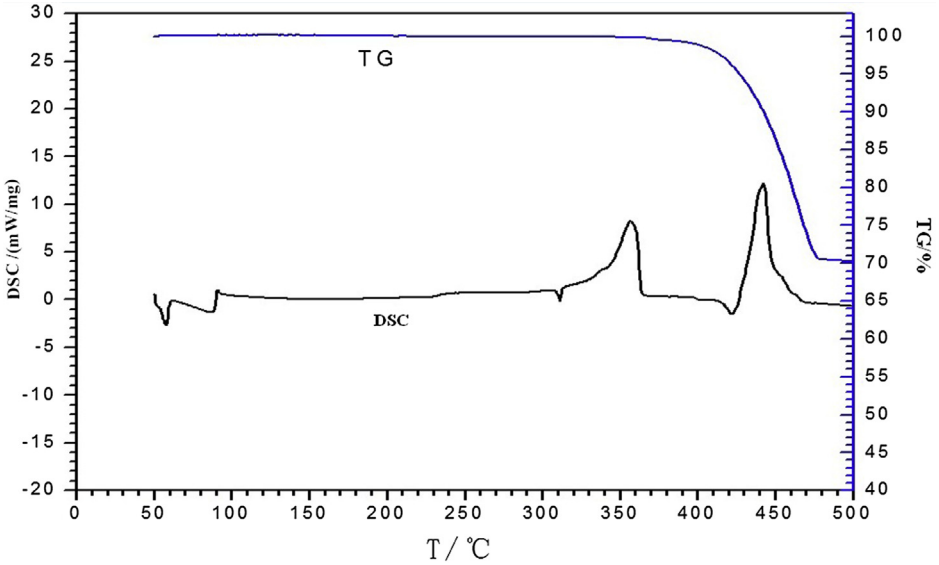

Figure 34 DSC and TG analysis of $NaClO_4$ impregnated porous copper.

Table 4 Onset temperatures and heat of $NaClO_4$-porous copper exothermic peaks.

Heating rate, °C/min	First onset, °C	First exothermic heat, J/g	Second onset, °C	Second exothermic heat, J/g
5	319	100.6	423	213.0
10	333	107.0	433	221.0
15	343	108.2	439	212.7
20	350	101.9	442	293.9

solution under ultrasonic treatment. Porous silicon can be synthesized by electrochemical etching in 30–35% HF acid solution at 0.1–0.5 A.

The porous silicon and its energetic chips are shown in Figure 35. The process of porous silicon energetic chip preparation can be described as follows: fabricating the porous silicon chip array on silicon wafer by lithography and electrochemical corrosion, fabricating the Cr bridges on the porous chip array, and imbedding oxidants into porous silicon chip array.

The results of DSC and TG thermal analysis of porous silicon-NH_4ClO_4 and porous silicon-$NaClO_4$ show only one exothermic peak (Figure 36). $NaClO_4$-porous silicon has onset temperature of 309.8 °C, peak temperature of 393.3 °C, and the released heat

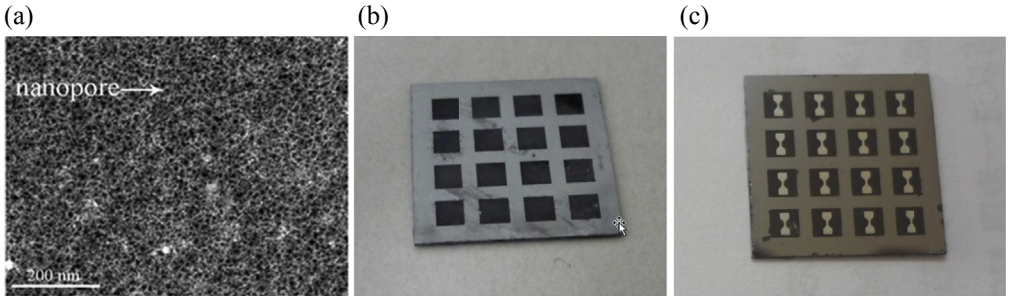

Figure 35 Structure of porous silicon (a), its porous silicon array (b), and energetic porous silicon chip array (c).

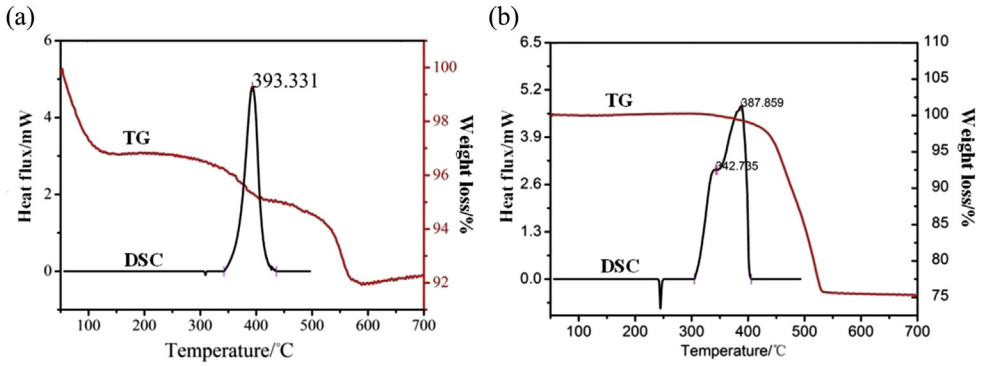

Figure 36 DSC and TG analysis results of $NaClO_4$-porous silicon (a) and NH_4ClO_4-porous silicon (b).

of 488.1 J/g. NH_4ClO_4-porous silicon has onset temperature of 305.0 °C and peak temperature of 387.7 °C, and the released heat of 1046.3 J/g. The loss weights of $NaClO_4$-porous silicon and NH_4ClO_4-porous silicon comprise 4.51% and 24.76%; this may be due to different filling extent of silicon or due to incomplete decomposition of energetic substance. In accordance with the released heat values, the NH_4ClO_4-porous silicon is more efficient than $NaClO_4$-porous silicon.

The igniting performances have been researched in the conditions of capacitor (100 μF) discharge ignition. The ignition characteristics of NH_4ClO_4-porous silicon chip at different charge voltage are presented in Table 5. The micro Cr bridge of 0.5 mm (width) × 1.0 mm (length) is fabricated on the porous silicon substrate. The high-speed images of ignition processes of NH_4ClO_4-porous silicon chips are shown in Figure 37.

The results show that the plasma excited by higher voltages has stronger ignition ability in ignition of NH_4ClO_4-porous silicon, and the delay time to ignite NH_4ClO_4-porous silicon is shorter at 140 V than at 20 V. The electronic exploding temperature of the bridge is about 7500 °C at the charging voltage of 110 V.

Table 5 Explosion characteristics of NH_4ClO_4-porous silicon chips.

Ignition voltage, V	Ignition energy, mJ	Explosion duration time, s	
		Micro Cr exploding	NH_4ClO_4 porous silicon exploding
80	0.240	8.9×10^{-5}	1.1×10^{-4}
90	0.153	2.4×10^{-5}	8.0×10^{-5}
140	0.286	2.7×10^{-6}	8.0×10^{-5}

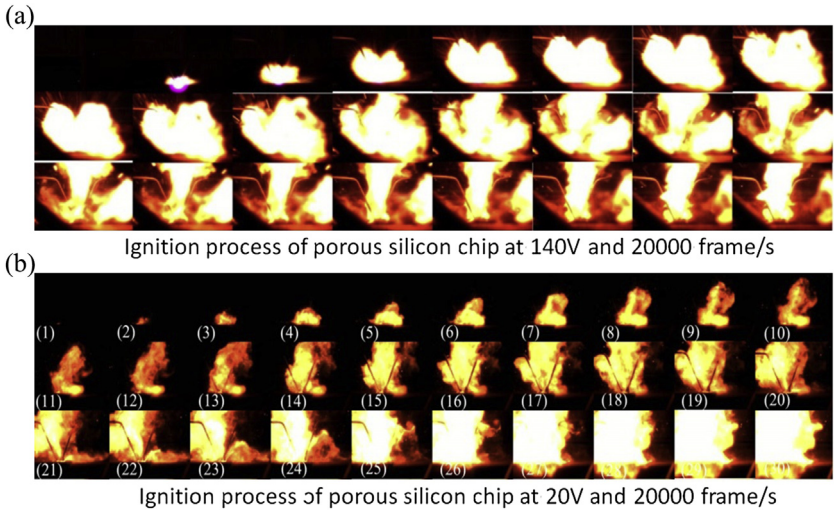

Figure 37 Ignition processes of NH_4ClO_4-porous silicon chips.

4.3 Three-Dimensional Fe_2O_3 Nanoenergetic Materials

A new nanostructured material, Fe_2O_3/Al, has been synthesized by template method and sputtering process [19]. The synthesis process of 3D Fe_2O_3/Al is shown in Figure 38. Polystyrene spheres are assembled on the substrate to synthesize polystyrene sphere template. $Fe(NO_3)_3$ solution fills in the polystyrene colloidal template and the 3D Fe_2O_3 film is synthesized via calcination of a polystyrene spheres template. The 3D Fe_2O_3/Al film is synthesized by sputtering Al on the 3D Fe_2O_3 film. The images of samples in different steps are shown in Figure 39. DSC thermal analysis results and thermal explosion of 3D Fe_2O_3/Al are shown in Figure 40. The DSC thermal analysis of Fe_2O_3/Al film is conducted in a temperature range of 100–900 °C with a heating rate of 20 °C/min under 30.0 ml/min N_2 flow. The first exotherm develops slowly with a peak temperature at 548 °C. This means that the nanoscale Fe_2O_3/Al membrane can react mildly below the melting point of Al, 660 °C. The second exotherm develops more abruptly with a peak temperature at 770 °C. This suggests that the Fe_2O_3/Al film has a faster heat release rate when Al has melted.

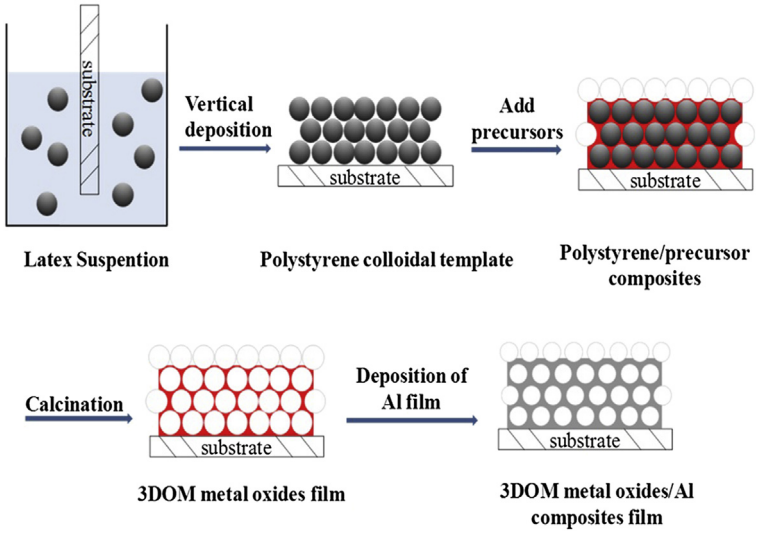

Figure 38 Schematic of the synthesis procedure for 3D nanothermite film.

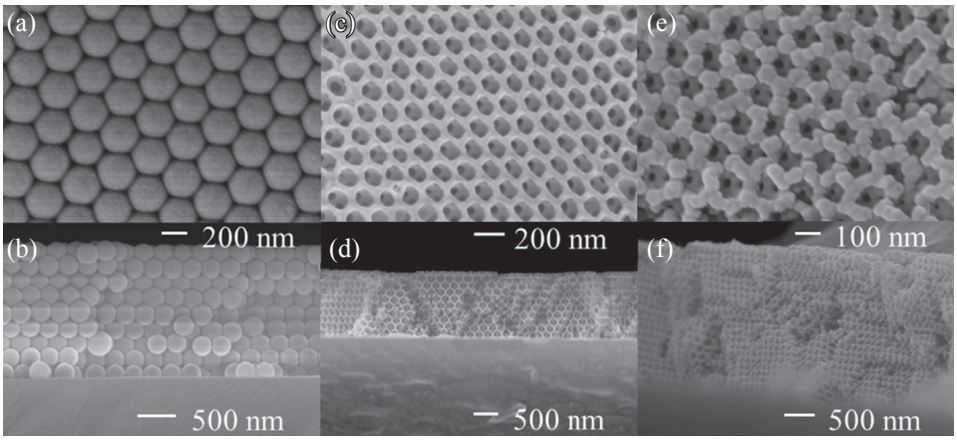

Figure 39 SEM images of polystyrene spheres template (a, b), 3D α-Fe_2O_3 membrane (c, d), and Fe_2O_3/Al membrane after Al deposition (e, f).

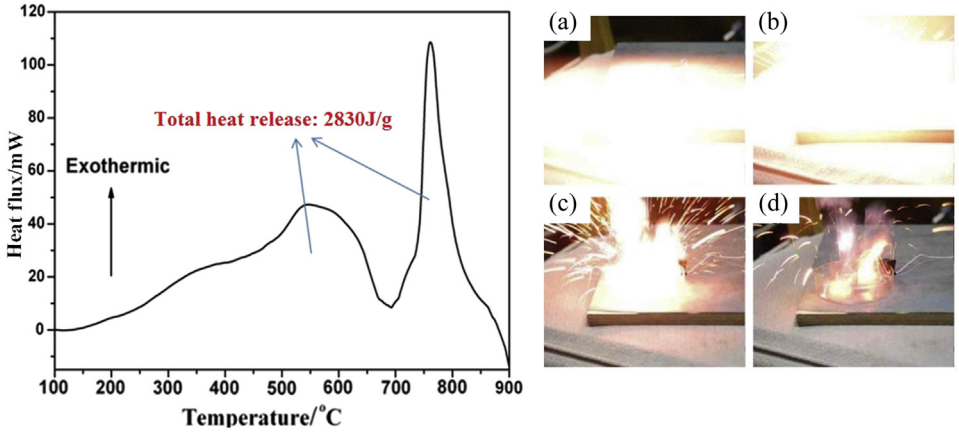

Figure 40 DSC curve of Fe_2O_3/Al membrane obtained and thermal explosion phenomena: (a) 0.00s; (b) 0.04s; (c) 0.08s; (d) 0.12s.

5. CONCLUSIONS

Nanostructured energetic materials are an important group of innovative energetic materials. Because of their nanoscale structure, the NSEMs can release reaction heat fast enough to replace traditional energetic materials. The thermal analysis results show the scale effect in reactions of NSEMs, in which the released heat is lower than theoretical value, but the reaction rate is high in the small scale.

Because the synthesis processes are compatible with the fabrication processes of MEMS, NSEMs are suitable for fabricating energetic chips or pyro-MEMS such as energetic ignition bridge, micropropulsion charge, microexplosive train and microchip packaging. The energetic igniting bridges can be fabricated by composing NSEMs on the surface of conventional igniting bridges (such as Cr bridge and semiconductor bridge), or can be fabricated directly (such as Al/Ni bridge and Al/CuO bridge). The tested results of energetic igniting bridges show that the NSEMs augment output energy and igniting ability of igniting bridges. Upon initiating, the energetic igniting bridges produce higher temperature and longer duration flame than that of conventional igniting bridge.

Because of broad market application prospects, NSEMs are the subject of continuing and active academic research. The syntheses, properties characterizations, and applications of NSEMs are beyond existing theoretical research. Detailed mechanisms of interfacial reactions and the scale effects of NSEMs performance are still unknown, therefore, the fundamental research of NSEMs will focus on these in future.

ACKNOWLEDGMENTS

Our thanks to professor Kaili Zhang, City University of Hong Kong, who gave great assistance to us, and also thanks to our graduate students, whose hard work and creativity helped our research progress to go fast. We also thank Dr Wei Zhang for carefully revising the manuscript.

REFERENCES

[1] R. Guo, Y. Hu, R. Shen, Y. Ye, L. Wu, A micro initiator realized by integrating KNO_3@CNTs nanoenergetic materials with a Cu microbridge, Chem. Eng. J. 211–212 (2012) 31–36.
[2] Y. Hu, R. Guo, Y. Ye, R. Shen, L. Wu, P. Zhu, Fabrication and electro-explosive performance of carbon nanotube energetic Igniter, Sci. Technol. Energ. Mater. 73 (4) (2012) 115–122.
[3] K. Zhang, C. Rossi, G. Rodriguez, et al., Development of a nano-Al/CuO based energetic material on silicon substrate, Appl. Phys. Lett. 91 (11) (2007) 113117.
[4] K. Zhang, C. Rossi, M. Petrantoni, N. Mauran, A nano initiator realized by integrating Al/CuO-based nanoenergetic materials with a Au/Pt/Cr microheater, J. Microelectromech. Syst. 17 (4) (2008) 832.
[5] Y. Wang, R. Shen, X. Jin, P. Zhu, Y. Ye, Y. Hu, Formation of CuO nanowires by thermal annealing copper film deposited on Ti/Si substrate, Appl. Surf. Sci. 258 (1) (2011) 201–206.
[6] X. Jin, Y. Hu, Y. Wang, R. Shen, Y. Ye, L. Wu, S. Wang, Template-based synthesis of Ni nanorods on silicon substrate, Appl. Surf. Sci. 258 (7) (2012) 2977–2981.

[7] D. Xu, Y. Yang, H. Cheng, et al., Integration of nano-Al with Co_3O_4 nanorods to realize high-exothermic core-shell nanoenergetic materials on a silicon substrate, Combust. Flame 159 (6) (2012) 2202–2209.
[8] D. Li, P. Zhu, S. Fu, R. Shen, Y. Ye, T. Hua, Fabrication and characterization of Al/Ni and Al/Ti multilayer nanofilms, Chin. J. Energ. Mater. 21 (6) (2014) 749–753.
[9] C. Yang, Y. Hu, R. Shen, Y. Ye, S. Wang, T. Hua, Fabrication and performance characterization of Al/Ni multilayer energetic films, Appl. Phys. A 114 (2) (2014) 459–464.
[10] P. Zhu, D. Li, S. Fu, B. Hu, R. Shen, Y. Ye, Improving reliability of SCB initiator based on Al/Ni multilayer nanofilm, Eur. Phys. J. Appl. Phys. 63 (1) (2013) 10302.
[11] P. Zhu, R. Shen, Y. Ye, S. Fu, D. Li, Characterization of Al/CuO nanoenergetic multilayer films integrated with semiconductor bridge for initiator applications, J. Appl. Phys. 113 (18) (2013) 184505.
[12] P. Zhu, R. Shen, Y. Ye, X. Zhou, Y. Hu, L. Wu, Fabrication and electrical explosion of igniters based on Al/CuO reactive multilayer films, Sci. Technol. Energ. Mater. 73 (5) (2012) 127–131.
[13] X. Zhou, R. Shen, Y. Ye, P. Zhu, Y. Hu, Influence of Al/CuO reactive multilayer films additives on exploding foil initiator, J. Appl. Phys. 110 (9) (2011) 095505.
[14] P. Zhu, R. Shen, Y. Ye, X. Zhou, Y. Hu, Energetic igniter realized by integrating Al/CuO reactive multilayer films with Cr films, J. Appl. Phys. 110 (7) (2011) 074513.
[15] H. Zhang, Y. Ye, R. Shen, C. Ru, Y. Hu, Effect of bubble behavior on the morphology of foamed porous copper prepared via electrodeposition, J. Electrochem. Soc. 160 (10) (2013) D441–D445.
[16] C. Wang, H. Zhang, Y. Ye, R. Shen, Y. Hu, Effect of nanostructured foamed porous copper on the thermal decomposition of ammonium Perchlorate, Thermochim. Acta 568 (2013) 161–164.
[17] S. Wang, R. Shen, Y. Ye, Y. Hu, An investigation into the fabrication and combustion performance of porous silicon nanoenergetic array chips, Nanotechnology 23 (43) (2012) 435701.
[18] S. Wang, R. Shen, Y. Chen, Y. Ye, Y. Hu, X. Li, Fabrication, characterization and application in nanoenergetic materials of uncracked nano porous silicon thick films, Appl. Surf. Sci. 265 (2013) 4–9.
[19] W. Zhang, B. Yin, R. Shen, J. Ye, J. Thomas, Y. Chao, Significantly enhanced energy output from 3D ordered macroporous structured Fe_2O_3/Al nanothermite film, ACS Appl. Mater. Interfaces 5 (2) (2012) 239–242.

CHAPTER EIGHT

Combustion Behavior of Nanocomposite Energetic Materials

Alexander S. Mukasyan[1] and Alexander S. Rogachev[2,3]
[1]University of Notre Dame, Notre Dame, IN, USA
[2]Institute of Structural Macrokinetics and Materials Science, RAS, Chernogolovka, Russia
[3]National University of Science and Technology "MISIS", Moscow, Russia

1. INTRODUCTION

Nanocomposite energetic materials, which consist of nanosized particles or nanolayers of fuel and oxidizer, possess unique combustion features including low ignition temperatures and high velocity of reaction front propagation. Such materials can be produced using different approaches such as convectional mixing of nano-dispersed powders; mechanical treatment of the microdispersed powders of the fuel and oxidizer in high-energy planetary ball mills; sol–gel technology; and other methods. Two types of nanoenergetic materials are the focus of this chapter: gasless metal–nonmetal or metal–metal nanostructured composite particles and thermite-like metal–metal oxide mixtures of nanopowders. Based on a literature analysis as well as original experimental data, in such systems we consider the behavior of the combustion wave at both the macroscopic and microscopic scales. The gasless nanosystems have unusually low reaction onset temperatures, as compared to micron-scale mixtures, however, moderate combustion propagation velocity is typically less than 1 m/s. It has been shown that the process retardation occurs due to the relatively low rate of heat transfer at the boundaries between composite particles. Various routes for controlling the combustion wave velocity by modification of the thermal properties of the interparticle boundaries are also discussed. On the other hand, nanothermites possess extremely high ignition sensitivity and demonstrate extremely high combustion velocities (e.g., $\geq$1 km/s). The current opinion is that such high velocities occur due to the convection of hot gaseous species in confined environments, which rapidly preheats the reactive media ahead of the front. However, it is not yet clear what intrinsic kinetic mechanisms can permit the supersonic propagation of the reaction front without forming a shock wave. This issue will be addressed by examining different reaction mechanisms suggested in the literature. Current and prospective applications of nanocomposite energetic materials, including those for solid propellants, igniters, and joining of materials, are also discussed.

Energetic Nanomaterials
ISBN 978-0-12-802710-3, http://dx.doi.org/10.1016/B978-0-12-802710-3.00008-8

2. NANOSTRUCTURED COMPOSITE HIGH-ENERGY-DENSITY MATERIALS

At first glance, the fabrication of the nanocomposite energetic materials by mechanical treatment appears to be a simple and effective technological approach. Indeed, we just need to mix two or more relatively coarse (usually ~1–100 μm) powders until the components are milled to nanoscale sizes. Various well-known methods of mechanical grinding can be applied, including processing in high-speed planetary ball or vibrational mills, where the particles of the mixture are subjected to mechanical impacts with force sufficient to break down the brittle components and plastically deform the viscous ones [1]. Thus brittle components are milled into finer particles, whereas plastic components (typically, metals) are subjected to multiple flattening collisions. The combined effect is the formation of layered composites in which layer thickness decreases as milling duration increases. Small fragments of brittle components are often found inside the particles of plastic component due to the cold-welding process. As a result, such treatment not only decreases the particle size of reactants but also increases the contact surface area between them. These new contact surfaces, formed under severe milling conditions in an inert atmosphere, are typically oxygen free and involve high concentrations of defects. All these factors enhance the chemical activity of the prepared reactive media [2,3]. For this reason, the process of high-energy ball milling (HEBM) is also commonly referred to as "mechanical activation" (MA).

Despite the apparent simplicity, HEBM of reactive mixtures raises many questions. For example, what size of the reactive elements can be reached before the reagents start to chemically react with each other? Indeed, it is well known that the HEBM process may cause dissolution of one reagent in the other (mechanical doping or mechanical alloying); or the components of the mixture may react to cause the formation of a new compound (synthesis). If the components of the mixture are immiscible, or for some kinetic reason cannot react, then HEBM can result in the formation of nanocomposites with the size of structural components (phases) in the range of 10–100 nm. However, in reactive systems the duration of HEBM cannot surpass some critical value beyond which the reaction is self-initiated by the local impact or friction occurring during the milling process.

Examples of the dependence of self-ignition temperature (T_i) for mixtures subjected to HEBM as a function of the milling time (t_m) are shown in Figure 1 [4]. Analysis of these experimental data allows us to outline two qualitatively different types of dependences. For Ti + Ni, Ti + Al, Ti + Si mixtures, T_i monotonically decreases with increase of duration of the HEBM, and after some critical milling time the mixtures become noncombustible. The Ti-BN and Ti-SiC-C mixtures demonstrate another type of behavior, i.e., T_i first decreases and then slowly increases with increasing MA time. It

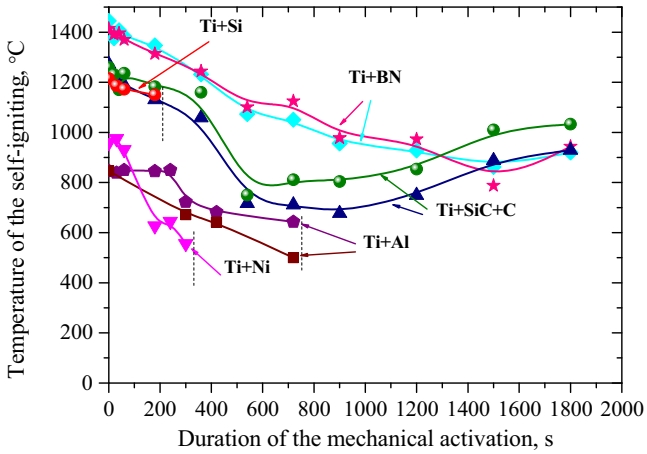

Figure 1 Dependences of self-ignition temperature on activation time for some reactive mixtures prepared in argon [4].

was suggested [4] that in the first case, self-sustained reactions quickly occur during the milling, while in the second case, the reactions proceed slowly in the mixing jar. This assumption was proved by X-ray diffraction (XRD) analysis of the particles obtained after HEBM. For the Ti-Ni, Ti-Al, and Ti-Si systems, the stoichiometric phases, i.e., TiNi, TiAl, and TiSi, were the only ones detected when MA time exceeded the corresponding critical values. In the case of Ti-BN and Ti-SiC-C systems, product phases such as TiB_2, TiN, and TiC, partially appeared after some specific milling time, and their amounts gradually increased with additional milling. The first group of reactive mixtures, which possess the sharp decrease in self-ignition temperatures, is of the most interest for combustion applications due to their high rates of heat release. Indeed if milling is terminated just before the critical time, reactive mixtures with low self-ignition temperature and essentially fully preserved heat of reaction can be obtained. This method, known as arrested reactive milling (ARM), is currently widely used in the fabrication of nanocomposite energetic materials [5].

It has been proved for many systems that MA leads to a drastic decrease in the self-ignition temperature. For example, the self-ignition temperature of the Ti-C system decreases from 1600 K for nonactivated mixtures to 770 K after low-energy activation during 5–10 h milling [6]; the corresponding decrease in the Ti-Si system was found to be from 1670 to 870 K after several hours of activation [7]. For the 3Ti-Si-2C system, the self-ignition temperature decreases from 1190 to 430 K for 90 min of activation, but spontaneous ignition occurs directly in the milling jar at a temperature of approximately 340 K for 106 min of treatment [8].

The critical duration of HEBM, minimum self-ignition temperature, and combustion parameters of the mixtures strongly depend on the intensity of mechanical

treatment. Analysis of recent publications shows that the "effectiveness" of the MA process depends on many parameters, including the velocity, acceleration, mass, size, and shape of the milling bodies, the geometric size of the mill, the mass ratio of the milling bodies (balls) to the activated mixture, the medium in which the activation is performed (air, inert gas, vacuum, or liquid), and many others [9]. However, it is possible to identify three main parameters that reflect the physical (not engineering) aspect of the process: the energy of one impact (collision between balls or between a ball and the wall), collision frequency, and activation time. Using these parameters, one can obtain the total energy involved in activation. It is worth noting that this does not mean that all this energy is "stored" in the activated mixture, because the majority of the energy is converted to heat. Nevertheless, these three parameters and their product can be used as a physical basis for comparison of the obtained results. It is important that the reported data fall into two clearly distinguished groups in terms of the impact energy. The first group can be called low-energy activation, where the impact energy is 0.1–0.2 J, and the activation time ranges from minutes to tens of hours (note that the authors of these publications often speak about high-energy treatment, but we refer to these processes as low-energy activation). The combustion velocities and temperatures for this group are shown in Figure 2 as functions of milling time [6,10–13]. The second group of data is associated with high-energy activation, where the impact energy is 1–2 J or greater, and the activation time ranges from several seconds to minutes; the combustion parameters of this group are presented in Figure 3 [14–17].

In the case of low energy of activation (Figure 2), the combustion velocity and maximum temperature of the mixtures typically gradually increases with increasing milling time. The thermodynamic calculation of the adiabatic combustion temperature yields the following values: $T_{ad} = 3290$ K for the Ti-C composition, 1870 K for Nb-2Si, 2290 K for 5Nb-3Si, 1690 K for Ti-2Si, and 2400 K for 5Ti-3Si. It seems logical to assume that an increase in the reaction rate owing to mechanical activation for these compositions decreases the heat losses and thus increases the degree of conversion in the combustion wave, which in turn would lead to an increase in the measured maximum temperature. It can be seen that for these systems the maximum combustion temperature (T_{max}) gradually approaches the T_{ad} but never reaches the full value ($T_{max} < T_{ad}$).

For other systems, the T_{max} appeared to be higher than the adiabatic temperature (Figure 2). These systems include Ta-2Si ($T_{ad} = 1794$ K), 5Ta-3Si ($T_{ad} = 1823$ K), and Si-C ($T_{ad} = 1873$ K). Based on the experimental data, one may conclude that these superadiabatic values occur due to the excess energy accumulated by the crystal lattices of reagents during mechanical processing. In our opinion, this conclusion is premature. There are at least three sources of errors in the comparison between T_{ad} and T_{max}: (1) error in thermodynamic calculations due to inaccuracies in the thermodynamic functions for the considered systems at high temperatures; (2) inaccuracy of temperature measurements, especially with the use of pyrometry [11]; (3) uncertainty of the initial

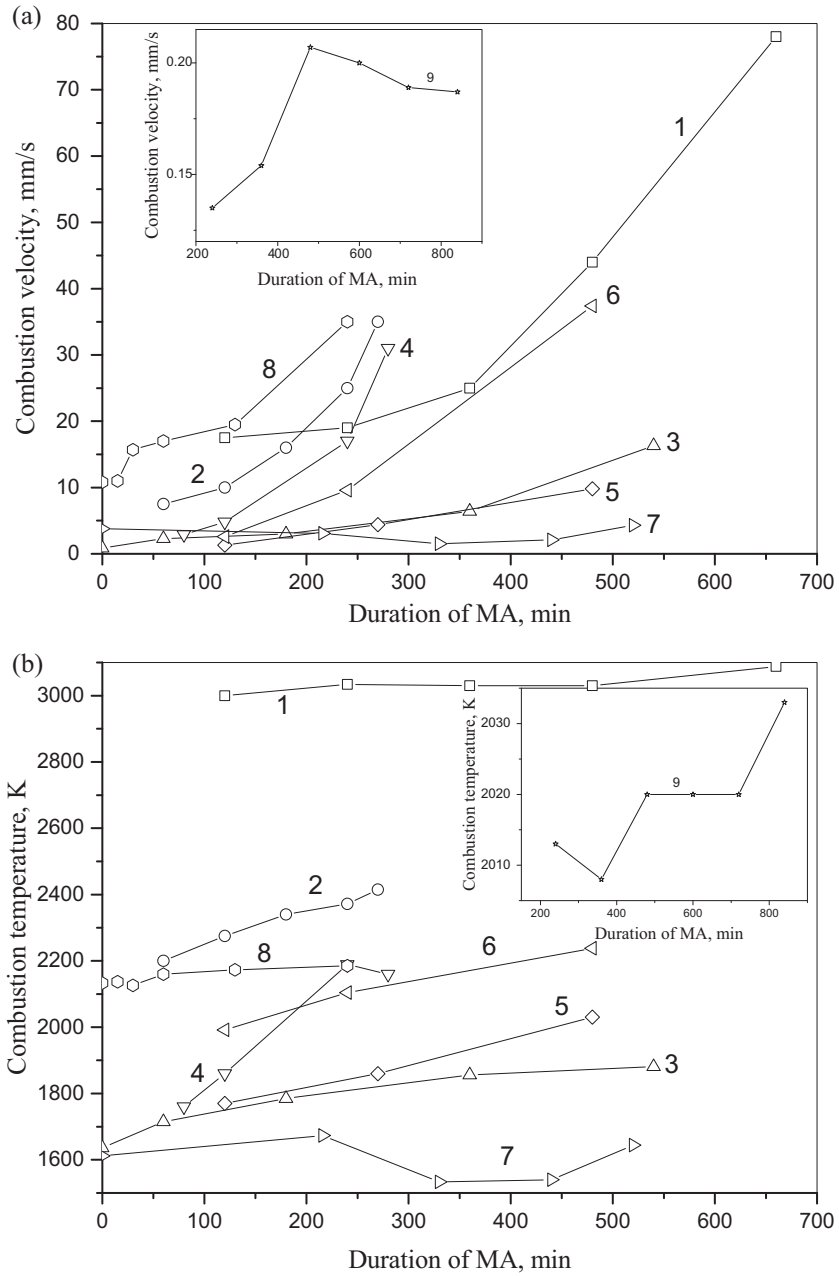

Figure 2 Combustion parameters of MA compositions (low-energy MA): 1: Ti-C [6]; 2: Ti-0.43C [6]; 3: Nb-2Si [10]; 4: 5Nb-3Si [10]; 5: Ta-Si [11]; 6: 5Ta-3Si [11]; 7: Ti-Si [12]; 8: 5Ti-3Si [12]; 9: Si-C [13].

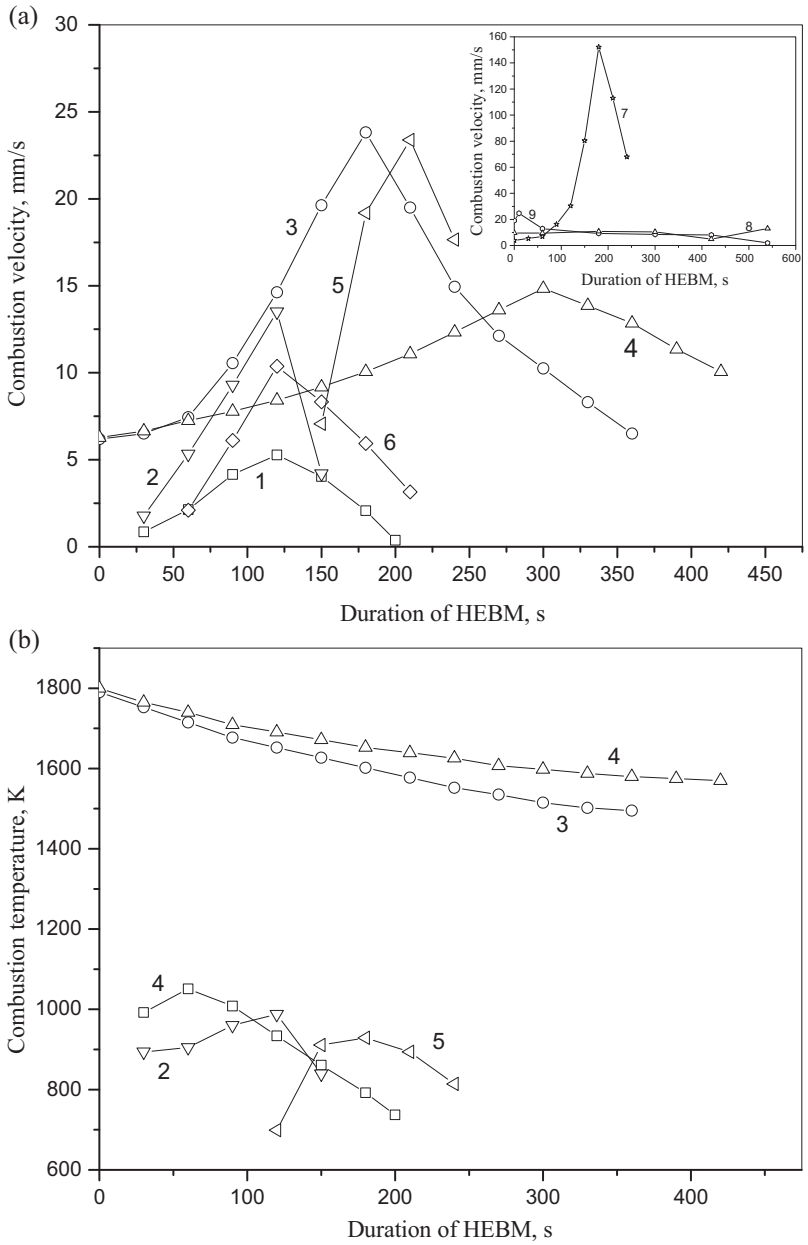

Figure 3 Combustion parameters of MA compositions (high-energy MA) 1: 3Ni-Al [14]; 2: 3Ni-Al [16]; 3: (Ti-2.1B)-60% Cu, 60 g [15]; 4: (Ti-2.1B)-60% Cu, 40 g [15]; 5: Ti-Ni [16]; 6: 4Ni-Si [16]; 7: Ni-Al [16]; 8: Ni-Al, MA in air [17]; 9: Ni-Al, MA in argon [17].

temperature along the media. The latter error could appear because cylindrical samples 8 mm in diameter and 10 mm height were ignited by a hot spiral located at a distance of 1 mm from the upper surface of the cylinder [11]. Since there was not direct contact between the spiral and the sample, the surface could be heated relatively slowly, which allowed heat to penetrate into the volume of the sample to a considerable depth, thereby increasing the initial temperature. Therefore, additional investigations are necessary to make a validated conclusion about the influence of energy stored in solid components during ball milling on the combustion temperature. Finally, for the systems where the product phase appears gradually during the mechanical treatment, the decrease in self-ignition temperature is accompanied by a decrease in the combustion temperature. For example, low-energy MA of the 5Ti-3Si mixture for up to 6 h resulted in depression of the ignition temperature from 1250 to 1700 K, with a simultaneous decrease of the combustion temperature from 2170 to 1620 K [17].

It can be seen that the dependences obtained after high-energy activation (HEBM) are qualitatively different (Figure 3). The combustion velocities typically have maximums at some activation time in the range of 100–300 s. The decrease in the combustion velocity at longer times is usually explained by the formation of reaction products at the stage of activation. The temperature curves for some systems also have maximums. It is interesting that for the same composition the milling time at which T_{max} is observed can be different from the time of the maximum combustion velocity. A monotonic decrease in the combustion temperature was observed for Ti-B-Cu compositions. In all cases, the maximum combustion temperature measured by thermocouples was lower than the corresponding adiabatic value. It is worth noting that an increase in the combustion velocity is observed for compositions with low thermal effect (curves 1–6) or low density (curve 7). In those cases where the initial mixture corresponds to stoichiometry with the high heat release and was pressed to the optimal density (insert in Figure 3: curves 8 and 9), an increase in combustion velocity was not observed [18]. Mechanical activation of weakly exothermal compositions makes it possible to increase the degree of conversion and to decrease the amount of secondary phases in the final product [19].

Mechanical activation was also applied to thermite-type compositions. For the thermite-type systems, most of the results related to mechanical activation deal with the initiation of the reaction and less data are available on the combustion propagation velocity. An overview of the mechanical and thermal activation of various thermites was made in Refs [21] and [22]. Thermite systems usually burn vigorously, with considerable heat release, and do not require additional activation to obtain a self-sustained reaction. Mechanical activation is used for these systems to obtain either fine-grain (nanocrystalline) products (e.g., the Al_3Ni-Al_2O_3 nanocomposite [23]), or a superactive thermite composition [23–27]. For this purpose, first, the critical time of self-ignition for the Me_1-Me_2O_x system during mechanical mixing is determined (usually, tens of minutes). Next, mechanical activation is "arrested" at approximately half of the defined

critical time in order to obtain an intermediate product in the form of micron-sized composite particles with small (beginning from several nanometers) size crystallites. This intermediate product depends heavily on the mechanical activation conditions.

For example, the arrested reaction milling of Al-CuO thermite was performed in the shaker mill, with 5 mm steel balls and a small amount of hexane as a process control agent, for a time range of 2–60 min [20]. It was shown that the ignition temperature decreases from 850–900 °C to 650–750 °C when MA time is increased from 16 to 60 min. The decrease in ignition temperature was attributed to a higher degree of structural refinement achieved with longer milling time [20]. An increase in the combustion velocity for mechanically activated compositions was reported, and fairly moderate combustion velocities ($\sim$0.5 m/s for Al-Fe_2O_3 [25]) were found. The activation energies of ignition were determined to be 150 kJ/mol for the Al-MoO_3 nanothermite and 170 kJ/mol for Al-Fe_2O_3. These values are close to the activation energies of ignition for nonactivated thermites (e.g., $E_{apparent} \sim 170$ kJ/mol for the Al-Fe_2O_3 system [28]).

Another important research direction is fabrication of pore-free energetic materials. Two steps should be distinguished: (1) preparation of dense nanocomposite powders and (2) compaction of these powders into dense macroscopic items. Formation of dense lamellar particles in metal–metal systems has been described in many works, starting from the early publications on the HEBM/MA of SHS mixtures, e.g., [2,3,17], dense thermite-type particles were described in Ref. [23]. It was found by means of high-speed video recording that propagation of the reaction along the composite particle occurs at a much higher rate than the measured average macroscopic combustion velocity [29].

However, only recently has a method been developed to consolidate the nanocomposite particles, thus producing pore-free energetic material. A technique known as the "cold gas dynamic spray" process (CGDS) was used to deposit a dense layer of the reactive composite particles onto a metal substrate [30]. The particles were injected via the high-speed gas flow (helium) and consolidated via plastic deformation upon impact with the Al substrate. The porosity of the media was reduced to approximately $1.0 \pm 0.5\%$. The 99% dense Ni-Al mechanically activated samples possess combustion propagation velocities of $\sim$20 cm/s, which is higher than that (5 cm/s) of the 75% dense cold-pressed samples prepared from similar composite particles. It should be noted that the preliminary mechanical activation is a significant stage in the technique, because the Ni-Al dense material deposited by CDGS from individual Ni and Al powder particles was not ignitable [30]. Some microstructure transformations taking place in the Ni-Al systems during the CGDS deposition were discussed in Ref. [31].

This consolidation method was also applied to the Al-CuO thermite mixture, yielding formation of fully dense material [32]. However, the reduction of the porosity of the Al-CuO energetic material resulted in a decrease of combustion propagation velocity from 140 cm/s at 20% density down to 15 cm/s at 100% density. This effect was

explained by assuming that there is a transition from convection mechanism of energy transfer at high porosity, to heat conduction mechanism at low porosity, when gas infiltration is essentially eliminated [32].

Increased sensitivity of reactive compositions after HEBM allows initiation of some activated gasless energetic materials by mechanical impact [33–35]. Comparison of the HEBM Ni-Al submicron composites with the mixture of Ni and Al nanoparticles revealed noticeable differences [34]. Exothermic reaction activation energy was found to equal 230 ± 21 kJ/mol for the nanopowders mixture and 117 ± 8 kJ/mol for the HEBM composites. Thus, the HEBM samples were more sensitive to thermal initiation due to lower reaction activation energy, while the nanopowders mixtures were more sensitive to mechanical impact initiation due to high contact stresses between nanoparticles during impact. The impact ignition threshold energy for the Ni-Al energetic material decreases from $\sim$500 J down to $\sim$50 J after HEBM [35].

Summarizing published experimental results, we can conclude that mechanical activation leads to the following effects: (1) decreases the self-ignition temperature; (2) expands the flammability limits; (3) favors a more complete reaction; (4) in some cases, increases the combustion wave propagation velocity, and (5) makes mixtures more sensitive to mechanical impact initiation. Mechanisms of these effects usually relate to the micro- and nanostructure transformations caused by HEBM/MA. Let us briefly consider some such relationships discussed in the literature.

The first effect is related to the formation of the mechanically induced reactive media with nanoscale heterogeneity, which enhances the reactivity of these systems. For example, most researchers observed broadening of X-ray diffraction peaks and interpret this broadening as evidence of the diminishing of the crystalline size. Some authors present more direct TEM or STEM observation of the nanostructures [17,36–40]. These results confirm the presence of nanosized particles or crystallites in mechanically treated powders. An example of STEM data on nanostructured Ni-Al energetic material is presented in Figure 4 [37]. It was found that a thin (50–100 nm) intermediate layer forms along the Ni/Al boundary, where nanoparticles of Ni are immersed in the Al matrix. Formation of such layers results in a significant increase of the reactivity and makes possible the "solid flame" phenomenon when solely solid-state reactions are responsible for the thermal explosion in gasless energetic systems [37].

A direct relationship between microstructure and reactivity was revealed also for the HEBM Ti + C mixtures [38]. Self-ignition temperature decreases from $\sim$1900 K down to $\sim$600 K after short-term HEBM. It was proved that a combination of several factors is responsible for increasing reactivity, with the carbon playing a key role in the first stage of HEBM through formation of layers that provide high surface area contacts between the reagents.

The second effect involves the formation of unstable solid solutions. For example, the reactive mixture Al-3Ti was prepared in stearic acid ($CH_3(CH_2)_{16}COOH$), which was

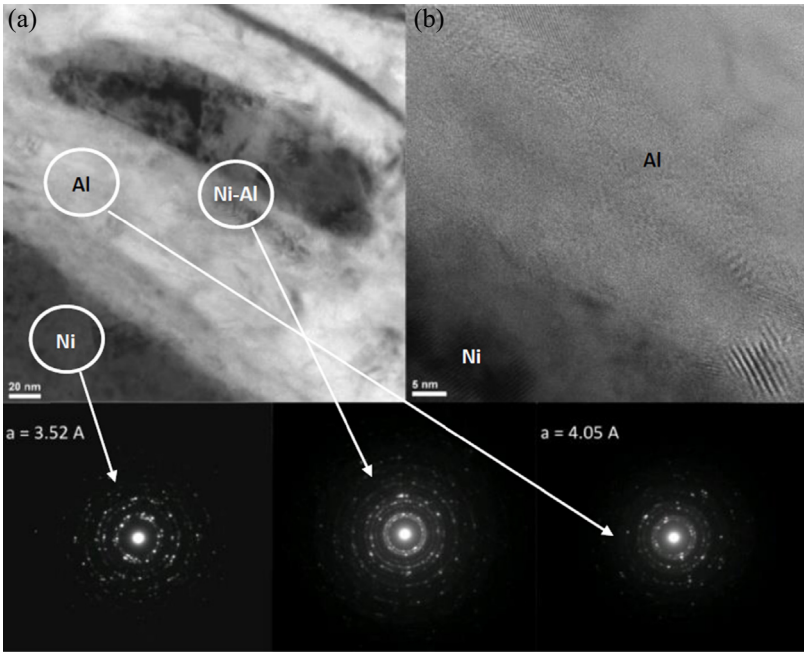

Figure 4 STEM micrograph showing nanoscale Ni particles embedded in Al matrix near interface surface (a) and the lack of defects in some regions (b). Electron diffraction patterns indicate only Ni ($a = 4.52$ A), Al ($a = 4.05$ A), and unreacted mixture of Ni and Al (center). *Adapted from [37].*

used as a controlling agent to prevent cold welding of metal particles, and subjected to low-energy mechanical activation in an argon medium [41]. After 100 h of mechanical activation, the X-ray diffraction analysis revealed the appearance of a new phase, which was identified as an oversaturated solid solution of titanium in the FCC lattice of aluminum. The size of crystallites in this phase, which was determined by the Scherrer formula, was extremely small (3.8 nm). Moreover, such solutions cannot exist in accordance with the equilibrium phase diagram. A TEM analysis of particles confirmed the formation of such a nonequilibrium solution with nanosized crystallites. It is important that these particles turned out to be highly reactive: exposure to an electron beam with a current density of ≈ 20 pA/cm^2 for 1 s was sufficient for "self-ignition" of the solution, with formation of the equilibrium Al_3Ti phase with the particle size of several nanometers. Thus, it was demonstrated that mechanical activation can lead to the formation of nonequilibrium oversaturated solutions with small-sized crystallites, which can possess unique reactive properties owing to structural changes. Based on these results, the parameters of ignition and combustion of such nonequilibrium oversaturated nanocrystalline solutions in various oxidizing media (air, oxygen) were further investigated [42–45]. For example, a nonequilibrium solution of Mg-Al (10–50% Mg) prepared

by ball milling has an ignition temperature ≈1000 K, substantially lower than that for aluminum (≈2300 K) [42]. Qualitatively similar results were obtained in Al-Ti, Al-Li, and Al-Zr systems [43–45].

Finally, many authors also indicate that mechanical deformation ensures a clean (oxygen-free) contact surface between the reagents, free from oxides and contamination, which enhances the reactivity of the mixtures. This hypothesis requires further experimental validation and quantification.

A mathematical model has been developed for combustion of activated mixtures that accounts for the following three factors: pumping in an excess of energy into the mixture; increased contact surface area (fragmentation of the reagents); and changes in the activation energy of the chemical reaction [46]. This model was later extended by including the heat of phase transitions [47]. As a whole, these models yield reasonable and predictable results, e.g., an increase in the combustion velocity. Some features of propagation of gasless combustion waves in mechanically activated (structured) systems, especially at the microscopic level, are successfully explained by the microheterogeneous (discrete) model [29]. The discrepancies between the experimental results and the theories are still too large to allow precise quantitative modeling of the process. Additional experimental data on the HEBM processes, as well as on microstructure and properties of the mechanically activated mixtures, must be obtained in order to create a basis for adequate theoretical description of the mechanically produced nanostructured energetic materials.

3. NANOTHERMITES

Thermite by definition is a pyrotechnic heterogeneous mixture of metal and metal oxide powders that produces an exothermic oxidation–reduction reaction. The thermite reactions in which Al and/or Mg are used as the reducing agents to purify ores have been known for almost two centuries. Such reactions have been adapted to obtain many metals including pure uranium [48]. The development of combustion synthesis (CS) as a novel methodology for production of materials significantly broadened the application of thermite systems allowing synthesis not only of metals but also much more complex compositions, including ceramics, cermets, and composites [49]. An example of this type of CS is:

$$B_2O_3{}^{(s)} + 3Mg^{(s)} + Ti^{(s)} = 3MgO^{(l)} + TiB_2{}^{(s,l)} + 700\ \text{kJ/mol},$$

where TiB_2 is the desired product (cermet), while MgO can be easily removed by leaching in acid solutions. The reduction-CS method with additives, which is known as alkali metal molten salt-assisted CS, is widely used for the production of nanopowders including metals (Ti, Ta, W) and metal carbides (TiC, TaC, WC) [50].

The progress in nanotechnologies for production of relatively low-cost nanopowders allows engineering of the nanoenergetic materials with desired structures and properties. The main idea in energetics is to enhance the contact surface area between reactive components in order to increase the reaction rate and decrease the ignition delay time [51]. While the range of available nanopowders is rather wide and includes metals (aluminum, nickel, cooper), nonmetals (boron, carbon, silicon), and a variety of oxides, a review of published works shows that during the last decade the main research interest has focused on so-called nanothermites or superthermites.

The uniqueness of nanothermites, as compared to the micron-scale reactive mixtures, is their extremely high ignition sensitivity, both by thermal and mechanical means; record high reaction rates; and, for some systems, extremely rapid rate of gas evolution [52]. Thus, the nanothermites have been proposed for use as igniters and lead-free primers for ammunition [53], as a replacement for toxic substances like lead and mercury salts. Again, the capability of nanothermite composites to produce reaction propagation rates similar to those of conventional primary explosives, with pressure levels well below that of solid explosives, makes them a promising candidate for fast-impulse microthruster applications [54]. The nanothermite composite is capable of producing shock waves with Mach numbers up to 2.44 in an air-filled tube [55], which can be used for production of nanomaterials such as nanodiamonds [56]. The micro- and nanoelectromechanical systems and sensors are also extremely promising fields for nanothermites [57]. Finally, their specific application is related to gas generators [58]. In this chapter, we primarily focus on the combustion characteristics of the nanothermites, which are critical for the different applications of these nanoenergetic materials.

3.1. Nanothermite Systems: Types and Method of Preparation

The data on the chemical compositions and particle sizes of the reagents for some investigated superthermite systems are summarized in Table 1. The parameter φ determines the composition of the initial mixtures:

$$\varphi = (m_f/m_{ox})_{exp}/(m_f/m_{ox})_{st},$$

where $(m_f/m_{ox})_{st}$ is the stoichiometric ratio of the fuel to oxidizer mass and $(m_f/m_{ox})_{exp}$ is the ratio used in experiments. It can be seen that the research has been focused primarily on thermite nanosystems with nano-Al (nAl) being used as the reducing element. Thus it is important to account for the morphological and microstructural aspects of such nanoparticles.

The aluminum particle always has a thin layer of alumina on its surface. The Al nanoparticles (nAl) are typically stored under nitrogen (99.9 vol.% N_2 with 50 ppm O_2) atmosphere in a glove box to prevent further oxidation and contamination. TEM images of (nAl) with different exposure time in air (0–90 min) are shown in Figure 5(a–d) [69].

Table 1 Some parameters of the investigated superthermites.

System	Composition φ	Al particle size, nm	Oxide particle size and morphology	References
Al-MoO_3	0.5–4.5	17, 25, 30, 40, 53, 76, 100, 108, 160, 200	10 μm/10 nm plates	[59,60]
	1.2	50, 80, 120	10 μm–10 nm	[61]
	1–1.45	44, 80, 120	1 μm–20 nm	[62]
	1	44	15.5 nm	[63]
	1.2–1.4	30, 45, 140, 170	BET = 66 m^2/g	[64]
	0.65–1.6	80	30–200 nm	[65]
Al-WO_3	1–1.5	80	20–100 nm	[66]
Al-Bi_2O_3	1–1.5	80	2–25 μm, fibers	[66]
	1	40, 100	40, 108, 321, 416 nm	[67]
Al-CuO	1–1.5	80	20–100 nm	[66]
Al-Fe_2O_3	0.9–4	52	BET = 50–300 m^2/g	[68]

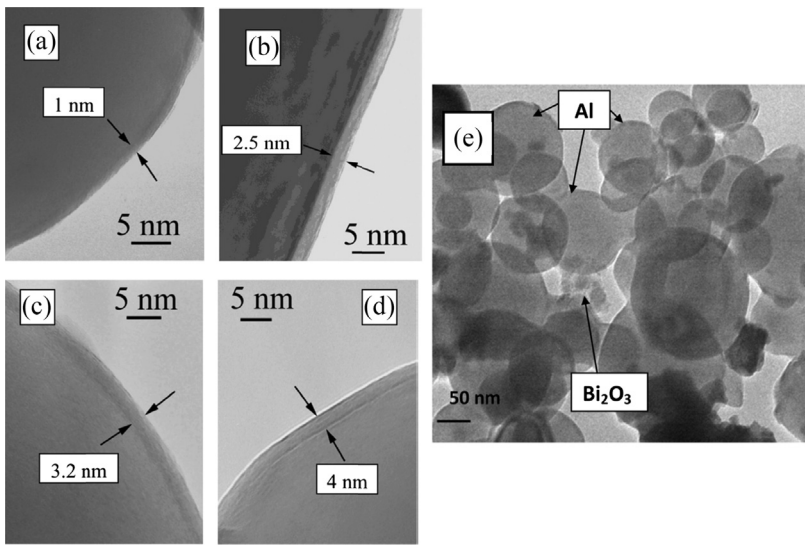

Figure 5 TEM images of Al nanoparticles oxide layer following different exposure times in air: (a) 0 min; (b) 5 min; (c) 20 min; (d) 90 min; and (e) Bi_2O_3 + nAl mixture. *Adapted from Ref. [69]*

It can be seen that the layer thickness is about 1 nm before exposure in air and reached an asymptotic value of about 4 nm after 30 min.

The next issue that one must account for is the amount of active metal in nAl particles, which depends on the size of the powder and the method of its production. Two nano aluminum powders manufactured by Argonide Corp. and Novacentrix are widely used by researchers. Argonide aluminum is produced by an exploding wire

Table 2 Some properties of nAl powders.

Powder	% of active metal	Nominal particle size, nm	BET, m^2/g	Supplier
Novacentrix Al	79	80	28	Novacentrix
ALEX	86	100	13	Argonide Corp

process and is commonly referred to as ALEX aluminum. Novacentrix aluminum is manufactured using the inert gas condensation method following plasma heating. The Argonide aluminum consists of many fused spheres of nanoaluminum mixed with some even larger micron-scale particles, while Novacentrix nAl consists of spherical particles with narrow particle size distribution. The properties of these powders are shown in Table 2. It was demonstrated that such different characteristics lead to different optimum ratios between Al and the oxidizer, from the standpoint of degree of conversion, and thus results in different reactions rates [70]. Thus, parameters such as the amount of active metal inside the particle, which is typically not recognized in micron-scaled systems, becomes an important issue in the case of combustion synthesis of materials in reactive nanomixtures.

The following nanothermite systems have attracted the most attention—Al-MoO_3, Al-CuO, Al-Fe_2O_3, Al-Bi_2O_3, Al-WO_3—among which the widest range of metal nanoparticles was provided in experiments with the Al-CuO and Al-MoO_3 mixtures. The studies with nanothermite systems led to the development of novel approaches for the preparation of reactive mixtures. A wide variety of methods, like conventional mechanical and ultrasonic mixing, high energy ball milling, and the sol–gel approach, have been used to achieve uniform mixing of nanopowders with a high contact surface area between the reagents. However, each of these method exhibits some disadvantages. For example, physical methods, such as ultrasonic mixing and HEBM, produce nanomixtures with a random distribution of the oxidizer and fuel particles on the nanometer scale. The sol–gel approach provides better control over the reagents' dispersion of the solid, however, typically results in the presence of undesired phases, e.g., Al_2O_3 (from dissolved $AlCl_3$ salt) or SiO_2 (from added silicon alkoxide). To overcome these limitations, a surfactant self-assembly method has been developed to produce nanostructured reactive mixtures (e.g., Al metal fuel and Fe_2O_3 oxidizer) with molecular-level mixing [71]. This process involves several steps: (1) coating of Fe_2O_3 nanotubes with a surfactant, e.g., polyvinylpyrrolidone (PVP) by ultrasonicating in 2-propanol for 4 h; (2) removal of the residual surfactant by repeated cycles of centrifugation; (3) drying of the extracted powder at 65 °C for 12 h; (4) ultrasonication of the PVP-coated nanotubes with nAl; and (5) drying of the obtained mixture at 65 °C for 12 h prior to the characterization. The morphology and microstructure of the as-prepared mixtures obtained by two different techniques, i.e., self-assembly and conventional physical mixing, are shown in

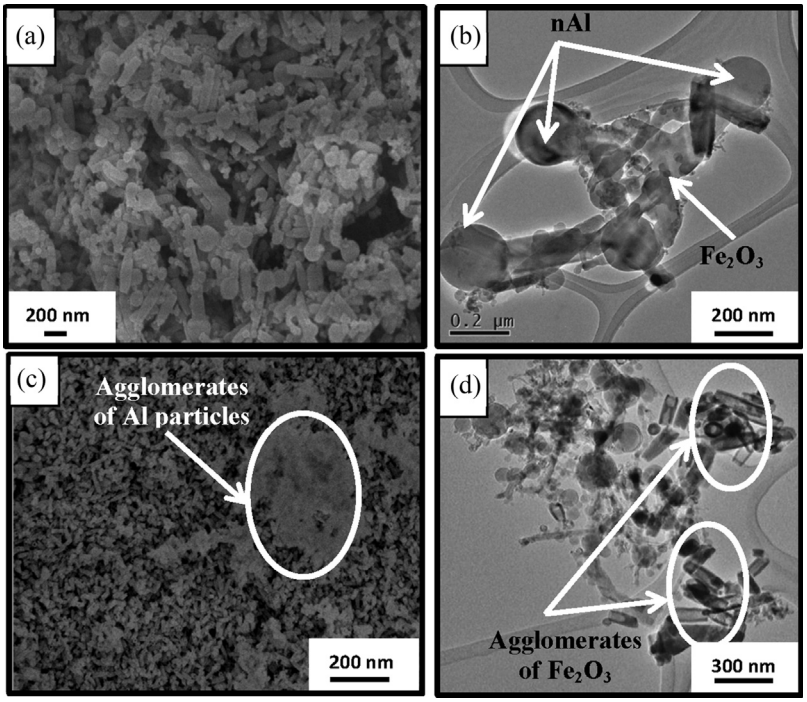

Figure 6 FESEM (a,c) and TEM (b,d) images of Fe_2O_3-nAl reactive mixtures prepared by self-assembled (a,b) and physical solvent mixing (c,d) methods. *Adapted from Ref. [71].*

Figure 6. The self-assembled Al-Fe_2O_3 system (Figure 6(a) and (b)) clearly showed the achievement of high interfacial contacts between the Fe_2O_3 nanotubes and nAl particles. On the other hand, distinct segregated agglomerations of Al clusters were observed throughout the sample prepared by physical mixing (Figure 6(b) and (c)).

For example, when the Al + Fe_2O_3 nanothermite system is prepared by self-assembly approach, it exhibited significant enhancement in reaction kinetics as compared to nanoscale thermite samples prepared by simple physical solvent mixing [72]. Increasing the contact surface area between the fuel and oxidizer by self-assembly significantly enhanced solid-state diffusion between the reactants. It was also construed that the interfacial contact area was more important than the reactant size, as revealed by the reduced thermal reactivity of physically mixed nanosized reactants in contrast to those prepared by self-assembly. The latter conclusion is of vital importance for the different applications of the superthermites.

3.2. Combustion Characteristics

The initiation parameters such as ignition temperature and delay time, as well as combustion parameters, i.e., burning rate and temperature profiles, were measured in most

reported works. It is important to note that the burning rate was determined in three different experimental configurations: (1) for confined mixtures, e.g., in tubes opened at one end; (2) for loose mixtures on an open plane or in a channel open over its entire length; and (3) for freely standing compacted samples. The ignition and combustion processes were usually registered by a set of photodiodes or by high-speed video cameras (e.g., Phantom).

Ignition parameters. In general, it was shown that nanothermites have a lower ignition temperature (T_{ig}) and time delay (t_d) when compared to the same compositions with microscale heterogeneity. For example, in the Al-MoO_3 system, the thermocouple measurements of the temperature-time history (Figure 7) of different samples preheated by laser demonstrate this effect [59]. In these experiments, a 50 W CO_2 laser is focused into a beam (2 mm in diameter) on the flat end surface of a cylindrical sample. It can be seen that a nanothermite with particle sizes ranging from 17 to 200 nm is ignited approximately within 20 ms, while a thermite of the same composition but with micron-sized particles (3.5–20 μm) has an ignition time delay in the range of 1–5 s. The results of differential thermal analysis (DTA) confirm that the reaction initiation temperatures for nanothermites are lower as compared to similar microscale systems. For instance, the main exothermal peak appears in the MoO_3-Al system at a temperature of ~950 °C if the Al particle size is 10 μm and ~500 °C if the Al particle size is 40 nm [60]. It is worth noting that these values differ significantly from those of thermocouple measurements (see Figure 7), but the qualitative conclusion is the same—micron-sized powders exhibit

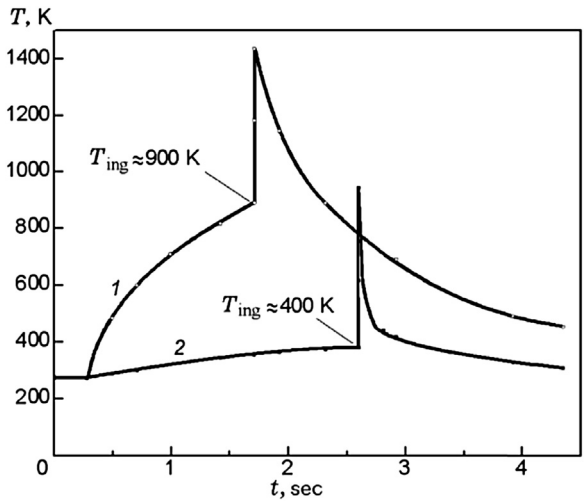

Figure 7 Temperature curves (measurements by a C-type thermocouple 75 μm thick on the pellet surface) of heating and ignition of the Al-MoO_3 thermite with the aluminum particle size of 3–4 μm (curve 1) and 55 nm (curve 2). The mixture is ignited by laser radiation with a power of 15 (1) and 5 W (2). Based on the results of Ref. [59].

intense interaction when the melting point of aluminum is reached, whereas nanopowders are active in solid-phase reactions. Pantoya and Granier also studied this problem by means of DTA for different heating rates [61]. An approximately linear dependence of the reaction initiation temperature on the precursor particle size and a weak dependence on the heating rate were obtained.

Puszinski et al. [67] studied the parameters of initiation in a Bi_2O_3/Al nanothermite system. Particular attention was paid to searching for effective inhibitors that would allow mixing of aluminum and bismuth oxide in water without significant changes in the chemical composition of the reactive mixture. In particular, it was shown that ammonia dihydrophosphate ($NH_4H_2PO_4$) is the best inhibitor—by forming a coating on the aluminum nanoparticle surface, it allows mixing of Al and Bi_2O_3 powders in water and the attainment of mixtures with a highly homogeneous composition. The sensitivity of superthermite systems in terms of ignition under the action of an electrostatic discharge was examined. The Bi_2O_3/Al system was demonstrated to be the most sensitive because its ignition requires only $\sim$0.1 μJ of energy (the corresponding values for Al-MoO_3 and Al-Fe_2O_3 systems are $\sim$50 and $\sim$1 μJ). The use of such an inhibitor as oleic acid leads to a significant (greater than an order of magnitude) increase in energy necessary for self-ignition of the system under the same conditions. This study also illustrates the importance of safety aspects in operations with superthermites because of their extremely high ignition sensitivity.

Combustion velocity. Figure 8(a) shows the generalized data for the burning rate U of nanothermites under confined conditions, i.e., in closed channels or tubes, with the

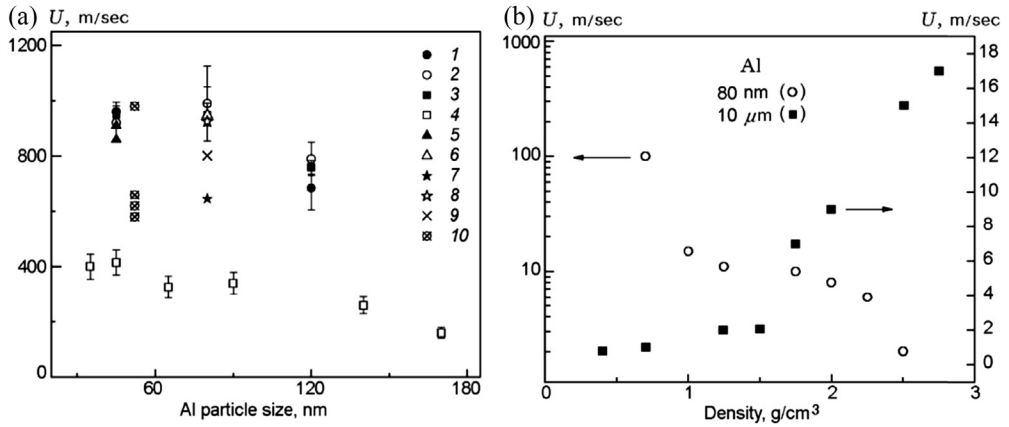

Figure 8 Summary of the burning rates of aluminum–metal oxides nanosystems in closed channels or tubes with low relative densities of the mixture (a) and burning rate of the MoO_3-Al thermite versus the density of the reactive medium for nano- and microheterogeneous mixtures [59] (b) MoO_3-Al [62] (1–3), MoO_3-Al [63] (4), MoO_3-Al [64] (5), MoO_3-Al [66] (6), Bi2O3-Al [66] (7), WO3-Al [66] (8), CuO-Al [66] (9), and Fe2O3-Al [68] (10).

mixture density close to the loose density. Though the values are distributed in a wide range, i.e., from several hundreds of meters to 1 km per second, all of them are much higher than the mean burning rates of heterogeneous systems with micron-sized particles.

Bockmom et al. [62] used substantially longer samples (about 10 cm with a diameter of 3 mm) to study the dependence of burning rate on the metal particle size (Al powders with 45, 80, and 120 nm). In all experiments, powders with a loose density (relative density equal to 5–10% of the theoretical value) were placed into long acrylic tubes and ignited from the closed end, while the other end of the tube remained open. The burning rate was estimated on the basis of frame-by-frame analysis of high-speed video recordings of the process and measurements of changes in the gas pressure along the tube after reaction initiation. Extremely high burning rates were obtained (600–1000 m/s), which exceed those given for the same compositions in Refs [59] and [60] by a factor of hundreds.

Record high combustion velocity was reported for the bismuth trioxide (Bi_2O_3) nanoparticles, which were prepared by solution combustion synthesis using bismuth nitrate and glycine [72,73]. The microstructure of the reaction mixture, which contains the synthesized Bi_2O_3 nanoparticles and fresh nAl powders with an average particle size of 100 nm, is presented in Figure 5(e). It was observed that such a system can burn with the glowing front propagation velocity equal to 2500 m/s with an extremely rapid ($\sim$10 μs) gas pressure rise in the reactor. It was demonstrated [72] that the thickness of the Al_2O_3 layer significantly influences the reaction kinetics, and thus again it was concluded that the microstructural characteristics of the metal particles should be accounted for when nAl is used as a reducing element in thermite systems. *Therefore, the second specific feature of nanothermites is very high velocity of the combustion front propagation.*

Dependence on media density. The result of comparison between the dependences of the burning rate versus the reactive medium density in the MoO3-Al system for micro- and nanoscale heterogeneous mixtures was obtained by Pantoya and Granier [59,60] (see Figure 8(b)). It was shown that the burning rate in micron-sized powders increases with increasing density of the reactive medium (which is associated with the increase in thermal diffusivity of the mixture). The opposite effect was found in nano-mixtures—high burning rates ($\approx$1000 m/s) for samples with a comparatively low density and moderate burning rates ($\approx$1 m/s) for dense samples, which is commensurable with data obtained for micron-sized powders. These results indicate that the extremely high velocities of luminescent front propagation during combustion of superthermites in thin channels are caused by the macrokinetics of hot gas exhaustion rather than by the kinetics of chemical reactions in nanosystems. The conclusion that the *burning rate in nanothermites increases with increasing of media porosity* was also supported by observations of the combustion velocities obtained under different experimental conditions.

Dependence upon experimental configuration. For example, Sanders et al. [66] studied the burning rate as a function of the composition and density of the reactive mixture for four thermite systems: Al/WO_3, Al/MoO_3, Al/Bi_2O_3, and Al/CuO. In all cases, Al powder with a particle size of 80 nm was used, whereas the oxide powders were different: WO_3 (100 × 20 nm) and MoO_3 (200 × 30 nm) flakes, CuO (20 × 100 nm) nanocolumns, and micron-sized (2 μm) Bi_2O_3 particles. Combustion of these compositions was studied under three different conditions: in a closed reactor (the dynamics of pressure was measured), on an open substrate (loose density), and in long thin (≈3.5 mm) acrylic tubes closed on one end (with relative density of 47%). Two main results should be noted. First, the burning rate for all compositions on the substrate turned out to be substantially lower than for those in the tube: 365/925 m/s for WO_3, 320/950 m/s for MoO_3, 525/800 m/s for CuO, and 425/645 m/s for Bi_2O_3. Second, *the burning rate of the packed mixtures in acrylic tubes was much lower than that in loose mixtures*. Son et al. [65] studied combustion in even thinner microchannels (inner diameter 0.48, 1.01, and 1.85 mm). Consecutive frames of the process are shown in Figure 9(a). As in Ref. [62], extremely high burning rates (400–1000 m/s) were registered, despite the small diameters of the samples. The burning rate decreased with decreasing channel diameter (Figure 9(b)), which was attributed to higher heat losses.

In recent work [74] it was again shown that in the Al_2O_3-Al system the combustion velocity under confined conditions is ∼960 m/s, while for open geometry it is 12 m/s. Qualitatively similar trends were observed for other nanothermites.

Dependence on particle size of precursors. In Ref. [59] it was shown that the ignition delay time in Al-Mo_2O_3 system does not depend on the size of Al particles in the range of 17–200 nm. It was also shown [60] that the combustion rate is also weakly dependent on the size of nano-Al (Figure 10(a)). Some decrease (Figure 10(b)) in velocity of the

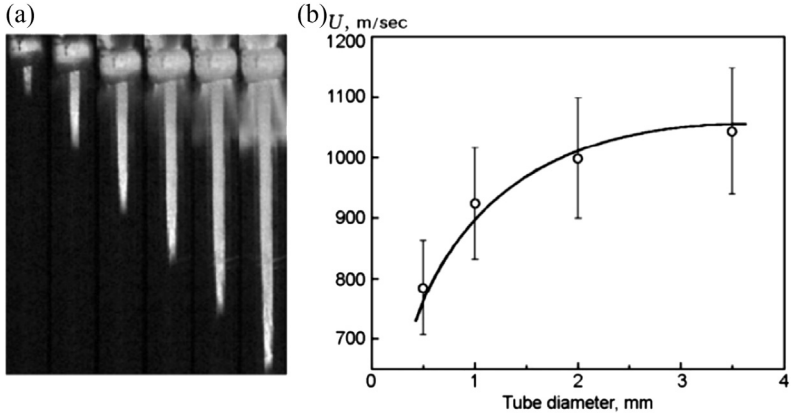

Figure 9 Consecutive frames (with an interval of 13.8 μs) of combustion in an acrylic tube (inner diameter 2 mm) (a) and burning rate as a function of the tube diameter (b) [65].

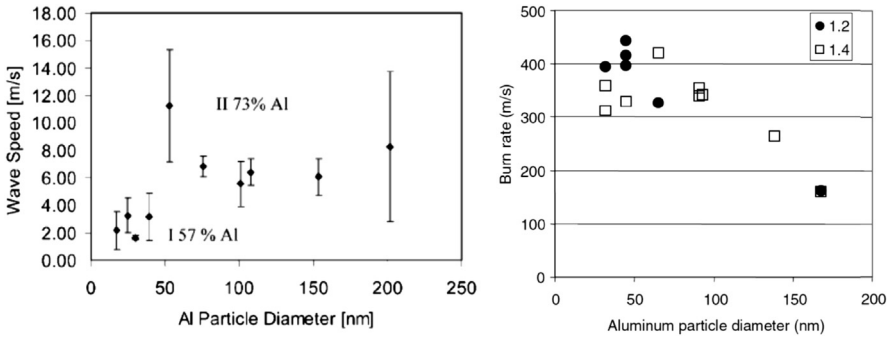

Figure 10 Typical dependence of burning rate as a function of nAl particle size in Al-MoO_3 thermite system [59,64].

reaction propagation in the same system was observed in [64]. However, in general, analysis of the literature shows that the burning *rate weakly depends on the Al size in the range from* 20 *to* 200 nm.

To understand these results, we must consider the specific features of the experiments as well as the combustion mechanism of nanothermite compositions.

3.3. Reaction Mechanism

The range of the burning rates in nanothermite systems is really remarkable. As discussed above different authors report that the combustion wave velocities exceed 1 km/s, which is close to the speed of sound in the reactive medium, while the absence of detonation is clearly outlined. In our opinion, these data require both experimental validation and, possibly, revision of the interpretation of the results obtained. Indeed, all previously reported data on combustion velocities in micron-scale thermite systems (cf. [49]) are in the range 1–100 cm/s. None of the known kinetics models [75] can predict such a large increase in U_c by just accounting for the size effect of the precursors. In addition, the maximum observed values for combustion velocities in nanofoils [76] do not exceed 100 m/s. It is worth noting that in the nanofoils, the sizes (10–50 nm) of the reagents are even smaller than those for typical nanothermite systems, and their thermal conductivities are much higher when compared to the thermal conductivity of porous mixtures of nanopowders. Based on all the above discussions, it can be concluded that the measured values of the hot spot propagation in the nanothermite system are not related to the classical definition of the combustion velocity, but instead are the result of the combined effect of high temperature, gasification, and gas flow in the constrained environment.

Understanding the role of the gas phase in the process investigated, Bockmom et al. [62] proposed a convective combustion mechanism that involves the transport of hot melted Al and gasified MoO_3 species by the gas flow to the cold zone of unreacted

precursors. This mechanism agrees with the previous conclusion based on the analysis of the model experiments [63]. In this case, "barriers," i.e., sapphire disk (0.4 mm thick and 4.4 mm in diameter) and "inert" porous plug (with thickness of several mm) made of metal oxide powder were placed in the reaction media in the way of combustion wave propagation for the loose mixture of Al (44 nm) and MoO_3 (15 nm) nanopowders placed into long acrylic tubes. It was shown that the transparent for radiation heat transfer disk stopped the propagation of the reaction front. At the same time, the front "jumped" through the inert porous plug. The results of pressure measurements at the open end of the tube showed that the main increase in pressure was observed ~7 mm ahead of the luminescent front and the pressure reached a maximum value (~250 atm) in a time span of ~10 μs, while the velocity of the luminescent front was ~900 m/s. Based on these measurements, the authors estimated the total width of the preheating and combustion zones to be 10 mm. If this is the case, then the rough estimate of the characteristic reaction time is 1 μs.

The mechanism suggested in Ref. [65] is also based on the leading role of the hot gaseous species (in their case sublimated aluminum oxide), which "pushes" the melted molybdenum into the nonreacted medium, leading to rapid heating and reaction of the latter. The model was formulated based on the results of thermodynamic calculations, which predict an extremely high adiabatic combustion temperature (>2900 K), which is above the sublimation temperatures of aluminum oxide and the melting point of molybdenum.

As concerns intrinsic chemical kinetics, the literature analysis suggests that there are currently three main mechanisms used to describe and interpret the reaction of nano-Al particles in an oxidizing atmosphere, including nanothermites. In all of them, the layer of alumina on the surface of the Al metal particles plays a key role. It is worth noting that basic physical ideas for nano-Al oxidation are close to those formulated for the micron-sized metal particles [77,78], where different mechanisms for the internal strains in the metal particle cladded by oxide layer have been discussed. The strain may lead to the rupture of the oxide layer, leading to the direct contact between metal and the oxidizer and thus accelerating the reaction. However, these ideas were reformulated for the conditions of nanoscale dimensions and high heating rates. The main features of these models are briefly described next.

First is known as the **diffusive oxidation mechanism** under internal pressure gradient, which was first justified experimentally [79] and then developed into a model [80]. The bottom line is that at high heating rates, $\sim 10^3$ K/s, and temperatures above the melting point of Al (660 °C) large pressure gradients are present in the oxide shell of the nanoparticles (Figure 11). If the coating thickness is less than 1 nm, then the maximum negative pressure is in the middle of the shell (Figure 11(a)). If the oxide thickness has grown significantly (thickness $>>1$ nm), then a relatively wide region exists along the oxide shell (Figure 11(b)) with a constant large negative pressure

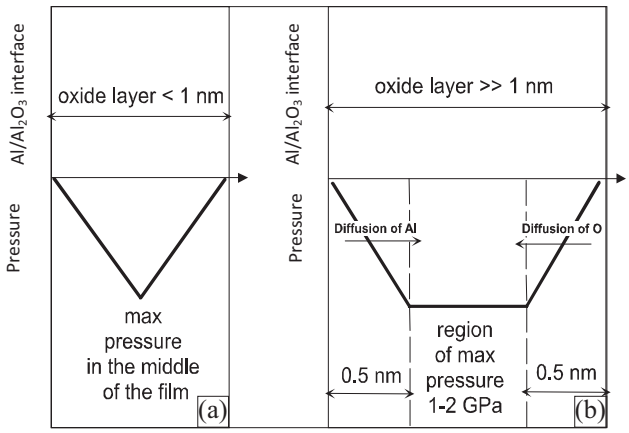

Figure 11 Pressure profile inside an oxide-coated nano-Al particle: (a) with oxide coating thickness <1 nm; (b) while the right side is for particle (b) with coating thickness $>>$ 1 nm. *Adapted from Ref. [80].*

($\sim$1–2 GPa). A natural effect of this pressure gradient will be the motion of atoms in the direction of decreasing pressure, which occurs in addition to the diffusive transport within the oxide shell. Thus, the pressure effect can be thought of as an effective convective flux of oxygen and aluminum ions in addition to the diffusive flux due to concentration. Oxygen will diffuse from the outer surface of the particle to the reaction surface gradient (see Figure 11(b)), while aluminum will diffuse from the metal/metal oxide interface to the reaction surface, leading to the formation of hollow alumina particles.

It was found that under the suggested model the kinetics law can be presented in the following form:

$$t \propto r^{1.6\pm0.1} \tag{1}$$

where t is the time required for a particle to react to a degree of conversion (e.g., 50%) and r is the initial radius of the particle. If this process was just a surface reaction in the free molecular regime, one would expect a linear relationship, but here diffusion of species through the aluminum oxide shell is the rate-limiting step and hence it is not purely a surface process. If we have diffusion of either only aluminum or only oxygen through the oxide shell and without any pressure gradients, then the power law obtained is $t \propto r^2$ and is in agreement with the shrinking core model in the absence of pressure gradients. It is noted that this rapid diffusion process may be enhanced by the rupture and thinning of the oxide shell.

Second is a **melt-dispersion mechanism** (Figure 12), which as it is stated works at temperature above the melting point of Al and at very high heating rates, $>10^6$ K/s

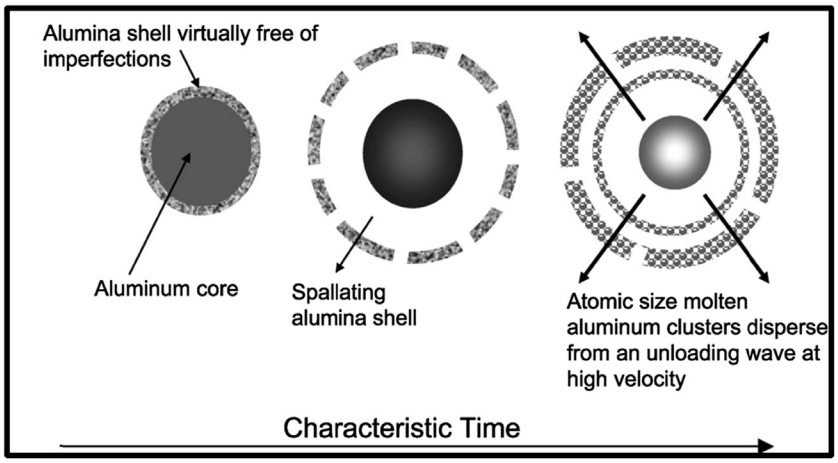

Figure 12 Schematic representation of the how nAl particles may react via a melt-dispersion mechanism. Initially melting of Al creates internal pressures followed by spallation of the oxide shell, exposing the molten core and generating a pressure wave, which disperses small Al clusters. *Adapted from Ref. [83].*

[81,82]. It was shown that at fast heating rates, the alumina shell of nanoparticles does not break until Al melts. The main geometric parameter that determines stresses in the Al core–shell system is the ratio of Al core radius R to oxide thickness δ, $M = R/\delta$. It was found [81–83] that for $M < 19$, the entire Al particle melts before the oxide shell fractures. Melting of Al is accompanied by a 6% volume expansion, which creates high dynamic pressures (1–3 GPa) in the liquid core. Pressure of such magnitude overloads the alumina shell with the hoop stresses σ_h that exceed the ultimate strength of alumina σ_u and cause the shell's dynamic fracture and spallation. After oxide spallation, pressure within the liquid Al remains unchanged while at the bare Al surface the pressure is on the order of 10 MPa only due to surrounding gas pressure and surface tension. An unloading wave then propagates from the surface to the center of the particle and creates a tensile pressure at the particle center of 3–8 GPa. Such a pressure exceeds the strength (cavitation limit) of molten Al and disperses the liquid Al into small bare clusters, which travel at high velocity (100–250 m/s). Oxidation of these clusters is not limited by diffusion through the initial oxide shell.

Based on the experimental results obtained by conventional thermogravimetric analysis (TGA), the third mechanism, **a diffusion-type oxidation model**, was established that accounts for the phase transformations in the alumina shell [84,85]. The characteristic sequence of changes in the alumina-scale growth on the particle surface is shown in Figure 13. It was suggested that the entire oxidation process can be divided into four stages, and the specific processes occurring during each stage are illustrated schematically. The natural amorphous alumina layer covering the particle initially grows

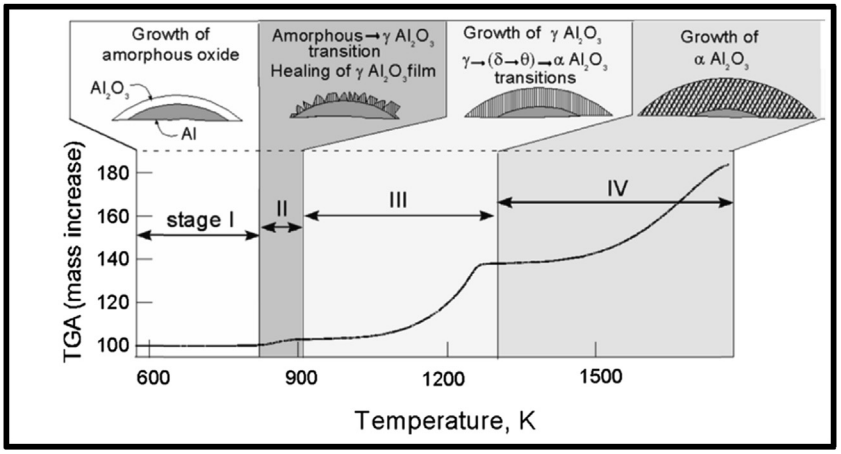

Figure 13 Change in mass of the micron-sized aluminum powder under nonisothermal oxidation. Different stages of oxidation are indicated, and the respective changes in the growing alumina scale are shown schematically [85].

slowly during the low-temperature oxidation stage I. The energy of the oxide–metal interface stabilizes the amorphous oxide only up to a critical thickness of about 5 nm. When the critical thickness is approached or when the temperature becomes sufficiently high, the amorphous oxide transforms to γ-alumina. The density of γ-alumina exceeds that of amorphous alumina, and the smallest γ-alumina crystallites have a size of about 5 nm. Thus, if prior to the phase change the thickness of the amorphous layer was less than 5 nm, the newly formed γ-Al_2O_3 crystallites no longer form a continuous layer covering the aluminum surface. As a result, the rate of oxidation increases rapidly at the beginning of stage II as shown in Figure 13. As the openings in the oxide coating heal, the rate of oxidation decreases. Eventually, a regular polycrystalline layer of γ-Al_2O_3 forms by the end of stage II. The growth of γ-Al_2O_3 continues in stage III, during which the oxidation rate is limited by the inward grain boundary diffusion of oxygen anions. When high temperature destabilizes the transition of alumina polymorphs, stage III ends. The stable and denser α-alumina polymorph starts forming by the end of stage III, and when the oxide is completely transformed to α-alumina, stage IV is considered to have started. By the end of stage III, when the first individual α-Al_2O_3 crystallites begin to form, the thickness of the γ-Al_2O_3 layer decreases and the oxidation rate abruptly increases. Grain boundary diffusion slows down, and the oxidation rate decreases rapidly once most of the oxide layer is transformed to coarse and dense α-Al_2O_3 crystallites, resulting in continuous polycrystalline coverage.

At high heating rates, the thickness of γ-Al_2O_3 layer may be smaller than some critical value, which then forms a discontinuous oxide layer with no diffusion resistance. In this case, the rate of diffusion was controlled by the parent oxide layer, i.e., amorphous

or γ-oxide, for stages II and III, respectively. However, for practically interesting high heating rates, the parent oxide may disappear completely before the layer of the new polycrystalline phase becomes continuous—that is, before the limiting thickness is reached a portion of the aluminum surface becomes directly exposed to the oxidizing gas environment.

To describe extremely rapid burning rates in the nanothermite systems, all of the above models, which have some similarity, but in general lead to different kinetic laws were used. However, the question is: which of them describes the real nature of the reduction type combustion in nanoscale heterogeneous media? In our opinion each of these mechanisms has some strong points as well as weaknesses. Indeed, cracking of the Al_2O_3 layer, which is the conceptual idea of the second model and a possibility mentioned in the first one, looks reasonable. For example, it explains the rapid reaction in the system where one of the nano-precursors (Al) has very thick layer of oxide. However, all models suggested that rupture mechanisms can work at temperatures equal to or above aluminum's melting point (912 K). In this case, the big question is how to explain the values of the ignition temperature for such systems which are typically much lower than 912 K? (Ref. [59]). One more unresolved question is if the oxygen free "fresh" surface of solid (or liquid) nanoscale Al particles is exposed to an oxidizing atmosphere, what will the rate of chemical interaction be? It was reported that self-ignition temperature for oxygen-free titanium particles in air is equal to room temperature and combustion occurs with very high velocity (~m/s) [86].

In addition, we suppose that it is vital to include the phase transformation aspects in the combustion mechanism, as suggested in the third model. However, for extremely high heating rates in the combustion front and very short reaction time, questions arise regarding the kinetics of these phase transformations. Is there enough time in the reaction front to follow all of these equilibrium routes? We strongly believe that without using extremely high diffusion coefficients, which are experimentally unproved, none of the models, which are based on diffusion through the layers, can explain observed extremely low onset temperatures and high rates of combustion wave propagation. We discussed these issues in our recent review [9] and concluded that more in situ experiments are required in order to define with enough confidence the characteristic reaction time (rates) for nanothermite reactions.

4. CONCLUSIONS

Breakthroughs in nanotechnology have allowed the design and fabrication of a new type of material with high-energy density per volume, so-called nanostructured composite particles and nano- or superthermites. In both systems, the scale of heterogeneity of the medium is in the range 10–100 nm. Such significant decrease of the characteristic scale leads to new features associated with the reactivity of the materials.

Indeed, for the same systems but with micron-scale heterogeneity, the self-ignition temperature is typically equal to or above the melting point of the less refractory compounds, while for the corresponding nanosystems it can be well below this value. More importantly, one can tune up this parameter by changing the system nanostructure. For the composite mechanically induced nanostructured particles, this effect is attributed to the oxygen-layer-free, extremely high contact surface area between the reactants, which is formed during high-energy ball milling. The answer for the nanothermite system is not so obvious, and in addition to low scale of heterogeneity it can be associated with the presence of impurities, e.g., in nanoaluminum [87]. A similar situation occurs with the observed values of the combustion velocity. In the mechanically fabricated nanostructured composite particles, while the rate of reaction propagation along each particle is relatively high (up to m/s), the overall velocity of the reaction front propagation along the media is controlled by the rate of heat conduction between the particles. For nanothermites to explain extremely high values (km/s) of the front propagation, one has to admit the convective mechanism of heat transport, which may involve different gaseous species.

Taking into account the various applications of such systems, ranging from rocket propellants to material science, where the precise control of the reaction kinetics is vital, we have to conclude that much more effort, both experimental and theoretical, is required to clarify the reaction mechanisms in nanostructured high-energy-density materials.

ACKNOWLEDGMENTS

The authors gratefully acknowledge the financial support of the Ministry of Education and Science of the Russian Federation in the framework of Increase Competitiveness Program of NUST (No. K2-2014-001). This study is also partially supported by the Department of Energy, National Nuclear Security Administration, under award number DE-NA0002377. Funding from the Defense Threat Reduction Agency (DTRA), grant number HDTRA1-10-1-0119. Counter-WMD basic research program, Dr. Suhithi M. Peiris (program director), is also acknowledged.

REFERENCES

[1] T.F. Grigorieva, A.P. Barinova, N.Z. Lyakhov, Mechanochemical synthesis of intermetallic compounds, Usp. Khim. 70 (2001) 52–71.
[2] T. Grigorieva, M. Korchagin, N. Lyakhov, Combination of SHS and mechanochemical synthesis for nanopowder technologies, KONA Powder and Particle 20 (2002) 144–158.
[3] F. Bernard, E. Gaffet, Mechanical alloying in the SHS research, Int. J. Self Propag. High Temp. Synth. 10 (2001) 109–132.
[4] A.S. Rogachev, N.F. Shkodich, S.G. Vadchenko, F. Baras, R. Chassagnon, N.V. Sachkova, O.D. Boyarchenko, Reactivity of mechanically activated powder blends: role of micro and nano structures, Int. J. Self Propag. High Temp. Synth. 22 (2013) 210–216.
[5] E.L. Dreizin, M. Schoenitz, Nano-composite Energetic Powders Prepared by Arrested Reactive Milling, US Patent No.7.524.355 B2, 28 April, 2009.
[6] F. Maglia, U. Anselmi-Tamburini, C. Deidda, F. Delogu, G. Cocco, Z.A. Munir, Role of mechanical activation in SHS synthesis of TiC, J. Mater. Sci. 39 (2004) 5227–5230.

[7] U. Anselmi-Tamburini, F. Maglia, S. Doppiu, M. Monagheddu, G. Cocco, Z.A. Munir, Ignition mechanism of mechanically activated Me-Si (Me = Ti, Nb, Mo) mixtures, J. Mater. Res. 19 (2005) 1558–1566.
[8] D.P. Riley, E.H. Kisi, D. Phelan, SHS of Ti_3SiC_2: ignition temperature depression by mechanical activation, J. Euro. Ceram. Soc. 26 (2006) 1051–1058.
[9] A.S. Rogachev, A.S. Mukasyan, Combustion of heterogeneous nanostructural systems (Review), Combust. Explos. Shock Waves 46 (2010) 243–266.
[10] F. Maglia, C. Milanese, U. Anselmi-Tamburini, Combustion synthesis of mechanically activated powders in the Nb-Si system, J. Mater. Res. 17 (2002) 1992–1999.
[11] F. Maglia, C. Milanese, U. Anselmi-Tamburini, S. Doppiu, G. Cocco, Z.A. Munir, Combustion synthesis of mechanically activated powders in the Ta-Si system, J. Alloys Compd. 385 (2004) 269–275.
[12] F. Maglia, U. Anselmi-Tamburini, G. Cocco, M. Monagheddu, N. Bertolino, Z.A. Munir, Combustion synthesis of mechanically activated powders in the Ti-Si system, J. Mater. Res. 16 (2001) 1074–1082.
[13] Y. Yang, Z.-M. Lin, J.-T. Li, Synthesis of SiC by silicon and carbon combustion in air, J. Euro. Ceram. Soc. 29 (2009) 175–180.
[14] M.A. Korchagin, N.Z. Lyakhov, Self-propagating high-temperature synthesis in mechanoactivated compositions, Russ. J. Phys. Chem. B 2 (2008) 77–82.
[15] M.A. Korchagin, D.V. Dudina, Application of self-propagating high-temperature synthesis and mechanical activation for obtaining nanocomposites, Combust. Explos. Shock Waves 43 (2007) 176–187.
[16] M.A. Korchagin, T.F. Grigorieva, A.P. Barinova, N.Z. Lyakhov, The effect of mechanical treatment on the rate and limits of combustion in SHS processes, Int. J. Self Propag. High Temp. Synth. 9 (2000) 307–320.
[17] K. Kasraee, A. Tayebifard, S. Salahi, Investigation of pre-milling effect on synthesis of Ti_5Si_3 prepared by MASHS, SHS and MA, J. Mater. Eng. Perform. 22 (2013) 3742–3748.
[18] N.F. Shkodich, N.A. Kochetov, A.S. Rogachev, et al., Effect of mechanical activation on SHS compositions Ni-Al and Ti-Al, Izv. Vyssh. Ucheb. Zaved. Tsvet. Metallurg 5 (2006) 44–50.
[19] M. Zakeri, R. Yazdani-Rad, M.H. Enayati, M.R. Rahimipour, Synthesis of nanocrystalline $MoSi_2$ by mechanical alloying, J. Alloys Compd. 403 (2005) 258–261.
[20] S.M. Umbrajkar, M. Shoenitz, E.L. Dreizin, Exothermic reactions in Al-CuO nanocomposites, Thermochim. Acta 451 (2006) 34–43.
[21] B.S.B. Reddy, K. Das, S. Das, A review on the synthesis of in situ aluminum based composites by thermal, mechanical and mechanical-thermal activation of chemical reactions, J. Mater. Sci. 42 (2007) 9366–9378.
[22] X. Zhou, M. Torabi, J. Lu, R. Shen, K. Zhang, Nanostructured energetic composites: synthesis, ignition, combustion modeling and applications, ACS Appl. Mater. Interfaces 6 (2014) 3058–3074.
[23] M. Schoenitz, T. Ward, E.L. Dreizin, Preparation of energetic metastable nano-composite materials by arrested reactive milling, Mater. Res. Soc. Symp. Proc. 800 (2004). AA2.6.1.
[24] B.S.B. Reddy, K. Rajasekhar, M. Venu, et al., Mechanical activation—assisted solid-state combustion synthesis of in situ aluminum matrix hybrid (Al_3Ni/Al_3O_2) nanocomposites, J. Alloys Compd. 465 (2008) 97–105.
[25] M. Schoenitz, T.S. Ward, E.L. Dreizin, Fully dense nano-composite energetic powders prepared by arrested reactive milling, Proc. Combust. Inst. 30 (2005) 2071–2078.
[26] S.M. Umbrajkar, M. Schoenitz, E.L. Dreizin, Control of structural refinement and composition in Al-MoO_3 Nanocomposites prepared by arrested reactive milling, Propell. Explos. Pyrotech. 31 (2006) 382–389.
[27] S.M. Umbrajkar, S. Seshadri, M. Schoenitz, V.K. Hoffmann, E.L. Dreizin, Aluminum-rich Al–MoO_3 nanocomposite powders prepared by arrested reactive milling, J. Propuls. Power 24 (2008) 192–198.
[28] E.I. Maksimov, A.G. Merzhanov, V.M. Shkiro, Spontaneous ignition of thermite compositions, Russ. J. Phys. Chem. 40 (1966) 251–253.

[29] A.S. Rogachev, N.A. Kochetov, V.V. Kurbatkina, E.A. Levashov, P.S. Grinchuk, O.S. Rabinovich, N.V. Sachkova, F. Bernard, Microstructural aspects of gasless combustion of mechanically activated mixtures. I. High-speed microvideorecording of the Ni + Al composition, Combust. Explos. Shock Waves 42 (2006) 421–429.
[30] A. Bacciochini, M.I. Radulescu, Y. Charron-Tousignant, J. Van Dyke, M. Nganbe, M. Yandouzi, J.J. Lee, B. Jodoin, Enhanced reactivity of mechanically-activated nanoscale gasless reactive materials consolidated by cold spray, Surf. Coat. Technol. 206 (2012) 4343–4348.
[31] A. Bacciochini, S. Bourdon-Lafleur, C. Poupart, M. Radulescu, B. Jodoin, Ni-Al nanoscale energetic materials: phenomena involved during the manufacturing of bulk samples by cold spray, J. Ther. Spray Technol. 23 (2014) 1142–1148.
[32] A. Bacciochini, M.I. Radulescu, M. Yandouzi, G. Maines, J.J. Lee, B. Jodoin, Reactive structural materials consolidated by cold spray: Al-CuO thermite, Surf. Coat. Technol. 226 (2013) 60–67.
[33] I.V. Saikov, L.B. Pervukhin, O.L. Pervukhina, A.V. Poletaev, A.S. Rogachev, H.E. Grigoryan, Initiation of SHS reaction by shock wave. Book of abstracts, X International Symposium on Self-propagating High-temperature Synthesis, Tsakhkadzor, 6–11 July, 2009, Armenia, p. 221.
[34] R.V. Reeves, A.S. Mukasyan, S.F. Son, Thermal and impact initiation in Ni/Al heterogeneous reactive systems, J.Phys. Chem. C 114 (2010) 14772–14780.
[35] D.F. Mason, L.J. Groven, S.F. Son, The role of microstructure refinement on the impact ignition and combustion behavior of mechanically activated Ni/Al reactive composites, J. Appl. Phys. 114 (2013), 113501 (1–7).
[36] G. Cabouro, S. Chevalier, E. Gaffet, Yu Grin, F. Bernard, Reactive sintering of molybdenum disilicide by spark plasma sintering from mechanically activated powder mixtures: processing parameters and properties, J. Alloys Compd. 465 (2008) 344–355.
[37] A.S. Mukasyan, B.B. Khina, R.V. Reeves, S.F. Son, Mechanical activation and gasless explosion: nanostructural aspects, Chem. Eng. J. 174 (2011) 677–686.
[38] K.V. Manukyan, Y.-C. Lin, S. Rouvimov, P.J. McGinn, Microstructure-reactivity relationship of Ti+C reactive nanomaterials, J. Appl. Phys. 113 (2013), 024302 (1-10).
[39] A.S. Rogachev, S.G. Vadchenko, F. Baras, O. Politano, S. Rouvimov, N.V. Sachkova, A.S. Mukasyan, Structure evolution and reaction mechanism in the Ni/Al reactive multilayer nanofoils, Acta Mater. 66 (2014) 86–96.
[40] A.S. Rogachev, N.F. Shkodich, S.G. Vadchenko, F. Baras, D.Yu Kovalev, S. Rouvimov, A.A. Nepapushev, A.S. Mukasyan, Influence of the high energy ball milling on structure and reactivity of the Ni + Al powder mixture, J. Alloys Compd. 577 (2013) 600–605.
[41] C.E. Wen, K. Kobayashi, A. Sugiyama, T. Nishio, A. Matsumoto, Synthesis of nanocrystallite by mechanical alloying and in situ observation of their combustion phase transformation in Al_3Ti, J. Mat. Sci. 35 (2000) 2099–2105.
[42] Y. Shoshin, R. Mudryy, E. Dreizin, Preparation and characterization of energetic Al-Mg mechanical alloy powders, Combust. Flame 128 (2002) 259–269.
[43] M. Schoenitz, E. Dreizin, E. Shtessel, Constant volume explosions of aerosols of metallic mechanical alloys and powder blends, J. Propuls. Power 19 (2003) 405–412.
[44] Y. Shoshin, E. Dreizin, Laminar lifted flame speed measurements for aerosols of metals and mechanical alloys, AIAA J. 42 (2004) 1416–1426.
[45] M. Schoenitz, X. Zhu, E.L. Dreizin, Mechanical alloys in the Al-richpartofthe Al-Ti binary system, J. Metast. Nanocryst. Mater. 20–21 (2004) 455–461.
[46] V.K. Smolyakov, Combustion of mechanically activated heterogeneous systems, Combust. Explos. Shock Waves 41 (2005) 319–325.
[47] L.G. Abdulkarimova, T.A. Ketegenov, Z.A. Mansurov, O.V. Lapshin, V.G. Prokofiev, V.K. Smolyakov, Effect of phase transformation on nonisothermal synthesis in mechanically activated heterogeneous systems, Combust. Explos. Shock Waves 45 (2009) 48–58.
[48] H. Frank Spedding, A. Harley Wilhelm, H. Wayne Keller, Production of Uranium, US Patent No. 2830894, April 15, 1958.
[49] A. Varma, A.S. Rogachev, A.S. Mukasyan, S. Hwang, Combustion synthesis of advanced materials: principles and applications, in: J. Wei (Ed.), Advances in Chemical Engineering, vol. 24, Academic Press, New York, 1998, pp. 79–226.

[50] S.T. Aruna, A.S. Mukasyan, Combustion synthesis and Nonmaterial's, Curr. Opin. Solid State Mater. Sci. 12 (2008) 44–50.
[51] C. Rossi, Two decades of research on nano-energetic materials, Propell. Explos. Pyrotech. 39 (2014) 323–327.
[52] A.S. Rogachev, A.S. Mukasyan, Combustion of heterogeneous nanostructural systems, Combust. Explos. Shock Waves 46 (2010) 21–28.
[53] K.T. Higa, Journal of energetic nanocomposite lead-free electric primers, J. Propuls. Power 23 (2007) 722–727.
[54] S.J. Apperson, A.V. Bezmelnitsyn, R. Thiruvengadathan, K. Gangopadhyay, S. Gangopadhyay, W.A. Balas, P.E. Anderson, S.M. Nicolich, Characterization of nanothermite material for solid-fuel microthruster applications, J. Propuls. Power 25 (2009) 1086–1091.
[55] S. Apperson, R. Shende, S. Subramanian, D. Tappmeyer, S. Gangopadhyay, Z. Chen, et al., Generation of fast propagating combustion and shock waves with copperoxide/aluminum nanothermite composites, Appl. Phys. Lett. 91 (2007) 243109.
[56] C. Rossi, K. Zhang, D. Esteve, P. Alphonse, P. Tailhades, C.J. Vahlas, Nanoenergetic materials for MEMS: a review, Microelectromech. Syst. 16 (2007) 919–931.
[57] V. Pichot, M. Comet, E. Fousson, C. Baras, A. Senger, F. Le Normand, D. Spitzer, An efficient purification method for detonation nanodiamonds, Diam. Relat. Mater. 17 (2008) 13–22.
[58] K.S. Martirosyan, L. Wang, A. Vicent, D. Luss, Nanoenergetic gas-generators: design and performance, Propell. Explos. Pyrotech. 34 (2009) 532–538.
[59] J.J. Granier, M.L. Pantoya, Laser ignition of nanocomposite thermites, Combust. Flame 138 (2004) 373–383.
[60] M.L. Pantoya, J.J. Granier, Combustion behavior of highly energetic thermites: nano versus micron composites, Propell. Explos. Pyrotech. 30 (2005) 53–62.
[61] M.L. Pantoya, J.J. Granier, The effect of slow heating rates on the reaction mechanism of nano and micro composite thermite reactions, J. Therm. Anal. Calorim. 85 (2006) 37–43.
[62] B.S. Bockmom, M.L. Pantoya, S.F. Son, et al., Combustion velocities and propagation mechanisms of metastable interstitial composites, Appl. Phys. 98 (2005) 064903.
[63] B.W. Asay, S.F. Son, J.R. Busse, D.M. Oschwald, Ignition characteristics of metastable intermolecular composites, Propell. Explos. Pyrotech. 29 (2004) 216–219.
[64] K.C. Walter, D.R. Pesiri, D.E. Wilson, Manufacturing and performance of nanometric Al/MoO_3 energetic materials, J. Propuls. Power 23 (2007) 645–650.
[65] S.F. Son, B.W. Asay, T.J. Foley, et al., Combustion of nanoscale Al/MoO_3 thermite in microchannels, J. Propul. Power 23 (2007) 715–721.
[66] V.E. Sanders, B.W. Asay, T.J. Foley, et al., Reaction propagation in four nanoscale energetic composites (Al/MoO_3, Al/WO_3, Al/CuO, and Bi_2O_3), J. Propul. Power 23 (2007) 707–714.
[67] J.A. Puszinski, C.J. Bulian, J.J. Swiatkiewicz, Processing and ignition characteristics of aluminum–bismuth trioxide nanothermic system, J. Propul. Power 23 (2007) 698–706.
[68] K.B. Plantier, M.L. Pantoya, A.E. Gash, Combustion wave speeds of nanocomposite Al/Fe_2O_3: the effect of Fe_2O_3 particle synthesis technique, Combust. Flame 140 (2005) 299–309.
[69] L. Wang, D. Luss, K.S. Martirosyan, The behavior of nanothermite reaction based on Bi_2O_3/Al, J. Appl. Phys. 110 (2011) 074311.
[70] C.D. Yarrington, S.F. Son, T.J. Foley, S.J. Obrey, A.N. Pacheco, Nano aluminum energetics: the effect of synthesis method on morphology and combustion performance, Propell. Explos. Pyrotech. 36 (2011) 551–557.
[71] J.L. Cheng, H.H. Hng, H.Y. Ng, P.C. Soon, Y.W. Lee, Synthesis and characterization of self-assembled nanoenergetic Al-Fe_2O_3 thermite system, J. Phys. Chem. Solids 71 (2) (2010) 90–94.
[72] J.L. Cheng, H.H. Hng, Y.W. Lee, S.W. Du, N.N. Thadhani, Kinetic study of thermal- and impact-initiated reactions in Al-Fe_2O_3 nanothermite, Combust. Flame 157 (2010) 2241–2249.
[73] K.S. Martirosyan, L. Wang, A. Vicent, D. Luss, Synthesis and performance of bismuth trioxide nanoparticles for high energy gas generator use, Nanotechnology 20 (2009) 405609.
[74] V.I. Levitas, M.L. Pantoya, S. Dean, Melt dispersion mechanism for fast reaction of aluminum nano- and micron-scale particles: flame propagation and SEM studies, Combust. Flame 161 (2014) 1668–1677.

[75] A.S. Rogachev, A.S. Mukasyan, Discrete reaction waves: gasless combustion of solid powder mixtures, J. Prog. Energ. Combust. Sci. 34 (2008) 377–416.
[76] A.S. Rogachev, Exothermic reaction waves in multilayer nano-films, Russ. Chem. Rev. 77 (2008) 21–37.
[77] V.I. Rozenband, N.I. Vaganova, A strength model of heterogeneous ignition of metal particles, Combust. Flame 88 (1992) 113–118.
[78] V.I. Rosenband, Thermo-mechanical aspects of the heterogeneous ignition of metals, Combust. Flame 137 (2004) 366–375.
[79] K. Park, D. Lee, A. Rai, D. Mukherjee, M.R. Zachariah, Size-resolved kinetic measurements of aluminum nanoparticle oxidation with single particle mass spectrometry, J. Phys. Chem. B 109 (2005) 7290–7299.
[80] A. Rai, K. Park, L. Zhou, M.R. Zachariah, Understanding the mechanism of aluminium nanoparticle oxidation, Combust. Theory Model. 10 (2006) 843–859.
[81] V.I. Levitas, B.W. Asay, S.F. Son, M.L. Pantoya, Mechanochemical mechanism for fast reaction of metastable intermolecular composites based on dispersion of liquid metal, J. Appl. Phys. 101 (2007) 083524.
[82] V.I. Levitas, M.L. Pantoya, K.W. Watson, Melt-dispersion mechanism for fast reaction of aluminum particles: extension for micron scale particles and fluorination, Appl. Phys. Lett. 92 (2008) 201917.
[83] K.W. Watson, M.L. Pantoya, V.I. Levitas, Fast reactions with nano- and micrometer aluminum: a study on oxidation versus fluorination, Combust. Flame 155 (2008) 619–634.
[84] M.A. Trunov, M. Schoenitz, E.L. Dreizin, Effect of polymorphic phase transformations in alumina layer on ignition of aluminium particles, Combust. Theory Model. 10 (2006) 603–623.
[85] M.A. Trunov, S.M. Umbrajkar, M. Schoenitz, J.T. Mang, E.L. Dreizin, Oxidation and melting of aluminum nanopowders, J. Phys. Chem. B 110 (2006) 13094–13099.
[86] A.S. Mukasyan, V.A. Shugaev, N.B. Kiryakov, The influence of gaseous fluid phase on combustion of titanium in air, Combust. Explos. Shock Waves 29 (1993) 7–11.
[87] A.A. Gromov, Y.I. Pautova, A.M. Lider, A.G. Korokikh, U. Teipel, E.V. Chaplina, Interaction of powdery Al, Zr and Ti with atmospheric nitrogen and subsequent nitride formation under the metal powder combustion in air, Powder Technol. 214 (2011) 229–236.

CHAPTER NINE

Catalysis of HMX Decomposition and Combustion: Defect Chemistry Approach

Alla N. Pivkina[1], Nikita V. Muravyev[1], Konstantin A. Monogarov[1], Igor V. Fomenkov[2] and J. Schoonman[3]

[1]Semenov Institute of Chemical Physics, Russian Academy of Science, Moscow, Russia
[2]Zelinsky Institute of Organic Chemistry, Moscow, Russia
[3]Department of Chemical Engineering (ChemE), Delft University of Technology, Delft, The Netherlands

1. INTRODUCTION

HMX, also known as cyclotetramethylene-tetranitramine or octogen, is a nitramine explosive with high density and high thermal stability. However, HMX-based compositions have some serious drawbacks. One of them is a relatively low burning rate along with high pressure exponent ($\nu \approx 0.8$ for HMX monopropellant and systems with significant nitramine content [1]), whereas the desired pressure exponent value, as a rule, has to be in the range of 0.2–0.6 [2]. Another drawback is a well-known HMX "insensitivity" to the catalysts, which are effective for other formulations.

There are several ways to control the combustion of energetic condensed systems; the most useful are *particle size variation*, *surface coating*, and *addition of catalyst*. Varying the oxidizer particle size is very efficient for changing the burning rate of the ammonium perchlorate-based formulations, but almost ineffective for compositions without ammonium perchlorate (AP) or with high HMX content [3,4]. The main goals of oxidizer surface coating are lowering of their decomposition temperature, enlarging the adhesion between HMX and binder, and lowering the sensitivity to external stimulus. Examples of the HMX coatings are *trans*-1,4,5,8-tetranitroso-1,4,5,8-tetraazadecalin [5], isocyanate, tetramethylammonium [6], ammonium perchlorate [7], 1,3,5-triamino-2,4,6-trinitrobenzene TATB [5,6], and 2,4,6-trinitrotoluene TNT [8].

Despite the advances in modeling and significant progress in experimental techniques, there is still no reliable theory to predict the effect of a given compound on the combustion and decomposition of formulations. In practice, the older well-known techniques are mostly used: for double-base systems the additives of lead- or copper-containing compounds; and for AP-based compositions, iron-containing species.

Addition of double-base propellant catalysts to HMX/active binder formulations can enhance the burning rate. However, with an increase of HMX content or replacement

Energetic Nanomaterials
ISBN 978-0-12-802710-3, http://dx.doi.org/10.1016/B978-0-12-802710-3.00009-X

of an energetic binder with an inert one, the catalytic effect disappears, proving that a catalyst affects only an active binder [9].

The addition of compounds with high redox potential (ZnO_2, I_2O_5) substantially increases the HMX decomposition rate [10]. Lithium and magnesium perchlorates significantly reduce the peak temperature of the nitramine exothermic decomposition; guanidine nitrate has a smaller effect, but also lowers the peak temperature [10]. Brill investigated the influence of gaseous environment on the HMX decomposition under high heating rates. The experiments in H_2, CO, O_2, or NO environments revealed no changes in the primary decomposition products, whereas in the NH_3 environment significant changes were observed [11]. Indeed, the addition of compounds that generate NH_3, i.e., carbamide, aminoguanidine, aminoguanidine nitrate, reveals lowering of the decomposition peak temperature [9]. Contradictory results were obtained for the HMX thermolysis with ammonium salts, which produces NH_3 during decomposition: NH_4Cl and NH_4Br reduce the HMX decomposition temperature, but $(NH_4)_2CO_3$ and $(NH_4)_2CrO_4$, which are decomposing at 170 and 200 °C, respectively, have no influence on it. Finally, all the studied salts have no impact on the HMX-monopropellant burning rate [12]. Metal cupferronates ($Me(C_6H_5N_2O_2)_x$), formiates ($Me(HCOO)_x$), oxalates ($Me_xC_2O_4$), and salts of propionitrile nitramine ($Me(NCCH_2CH_2NNO_2)_x$) decrease the HMX decomposition temperature [13–16]. The water vapor, which is also evolving during the decomposition of these salts, has an inhibiting effect on the HMX thermolysis [13].

Thermal decomposition and combustion processes are characterized by heating rates, which differ in several orders of magnitude. This difference has a great impact on the catalytic performance—some additives that are able to catalyze HMX decomposition do not affect the combustion of nitramine [17,18]. The attempt to capsulate the HMX crystals by incorporation of compounds with low melting points (acetamide, anthracene, diphenyl sulfone, hydrochinon) has no effect on HMX combustion velocity [19].

Currently, some catalytic additives are known to affect HMX combustion. For example, borohydrides decrease the ignition delay time and the burning rate of HMX-based formulations ($NaBH_4$ $LiBH_4$ [20,21]), and reduce the pressure exponent from 0.9 to 0.6 ($NaBH_4$, methylamine monoborane [22]). Drawbacks of borohydrides include high hygroscopicity, instability in the presence of moisture, toxicity, incompatibility with active binder, and high sensitivity to electrostatic discharge [20,22]. The addition of lead stearate ($C_{36}H_{70}O_4Pb$) to HMX/polyether binder formulation, and lead citrate ($C_{12}H_{10}O_{14}Pb_3$) to HMX/active binder formulation, enhances the burning rate [12,23]. The main drawback limiting the use of lead compounds is their high toxicity [24].

The catalytic influence of nanosized metal oxides on combustion and thermolysis of ammonium perchlorate [25], CL-20 [26], and aminonitrobenzodifuroxan [27] already have been demonstrated. The onset temperature of HMX decomposition was shown to be lowered by the addition of nanosized perovskite-structured powders [28,29]. Possible

reasons for the observed effect are: (a) the hydrogen abstraction from the HMX molecule; (b) the typical for perovskites catalytic influence on interaction of CO with NO_x [30]. The addition of a considerable amount of nanosized metal powders (up to 40–50 wt%) decreases the decomposition temperature and enlarges the amount of heat release in the condensed phase during decomposition [31,32]. The maximal effect was observed for the nano-copper and nano-Cu/Ni alloys due to: (a) interaction of metal with nitro groups of HMX molecule with formation of complexes and, as a result, weakening of the N—N bond; (b) the NO reduction by copper; and (c) formation of the "hot spots."

It has been shown that micron-sized titanium dioxide has no effect on combustion rate and thermal decomposition of HMX-based systems [19] but decreases the critical pressure at which the burning rate-pressure dependence changes [33]. The addition of micron-sized titania results in plateau formation on the curve $U_b(P)$ [34] and reduction of the temperature coefficient in the burning rate dependency on the initial temperature [35]. In our previous work strong catalytic effect has been found for HMX with nanostructured TiO_2, which resulted in the onset of decomposition temperature lowering, combustion rate increase, and pressure exponent decrease [36]. These effects were found to be exclusively specific for the nanosized titanium oxide powder, enhancing with decreasing of the particle size and vanishing with ones growing up to the micron size.

This study aimed to find effective catalysts of HMX-based formulation combustion among several micron-sized and nanostructured oxides, i.e., TiO_2, Fe_2O_3, Al_2O_3, and SiO_2. The comparison of different nanomaterials cannot be performed without knowing their bulk and surface properties. In our present work, several techniques were used, i.e., low-temperature gas sorption, laser diffractometry, scanning electron, atomic force, and X-ray photoelectron spectroscopy techniques along with X-ray diffractometry and Fourier transform infrared spectroscopy (FTIR) to characterize the nanosized powders. Thermal behavior was studied with differential scanning calorimetry (DSC) and thermogravimetric analysis (TGA) coupled with the evolved gas analysis via mass spectrometer.

The model with the leading reaction in the condensed phase can adequately represent the HMX combustion process; therefore, the finding of a compound to affect the HMX thermal decomposition is a key point to control the ballistic parameters of HMX-based compositions [37]. Based on the theoretical calculations and referring to the above literature data, two main "ways" to affect the HMX thermolysis can be distinguished: via the hydrogen atom abstraction with the subsequent heterocycle ring cleavage, and via the influence on the reactive species behavior during nitramine decomposition (i.e., on NO_2).

Hydroxyl radicals have been identified as one of the most active H atom abstractors (e.g., $ROH + \cdot OH \rightarrow RO\cdot$) [38]. Depending on the nature of the hydroxyl radicals,

they are surface-bound [39] or diffused species [40]. The amount of surface-bound hydroxyl groups of nanocatalysts has been determined by thermogravimetric technique.

The surface acidity of the nanosized titania particles was found to be important for the catalytic effect on HMX thermolysis, and was altered by corresponding treatment with acid and base solutions.

Nanosized materials have a high surface-to-volume ratio, which is very beneficial for catalytic solid–gas and solid–liquid interfacial reactions. In addition, the nanosized state leads to appearing of space charge regions at the interfaces of the solid catalyst material with an increased spatially dependent concentration of one of the intrinsic point defects in the pure material, depending on the surface charge. In addition, acidic or basic surface groups of the catalyst material will influence the defect structure of the space charge. Here, we have presented the defect chemistry of pure and doped TiO_2 and proposed the position dependence of the concentrations of intrinsic and extrinsic point defects in nanostructured TiO_2.

Finally, we propose a physicochemical model (scenario) of the decomposition and combustion of the HMX/TiO_2 mixtures.

2. EXPERIMENTAL

2.1 Materials

We have studied different oxide powders with variation of particle size and crystal phase, as listed in Table 1.

The literature shows that Degussa P25 titanium oxide has been widely studied in literature (e.g., Refs [41–44]), and represents the mixture of two titania crystal phases, i.e., anatase and rutile. Nanosized titanium oxide Hombitan Anatas also known as Hombikat (trademark) was studied in [41]. In addition to commercially available TiO_2, some of the laboratory-synthesized samples were investigated. Mesoporous titanium oxide has been synthesized at the Department of Materials Science, Moscow State University, via template synthesis technique; details can be found elsewhere [45].

Nanosized iron oxide γ-Fe_2O_3 has been synthesized at Semenov Institute of Chemical Physics via thermolysis of the $Fe(CO)_5$ solution in dioctyl ester with the controlling oxidation of thus-formed iron nanoclusters by trimethylamine N-oxide [46].

The microstructure of γ-Al_2O_3 and α-Fe_2O_3 nano-oxides was explored by atomic force microscopy, indicating both powders to have the spherical shape of nanosized particles. Silicon oxide with the high specific surface (641 ± 13 m^2/g) has been fabricated by milling of silica gel in agate mortar, and nanopowder α-Cr_2O_3 was produced by potassium bichromate burning in air. Both samples had broad particle-size distribution, high porosity, and high specific surface.

HMX powders used in this work were feedstock material, β-phase polymorph, with the average particle size of 50 μm.

Table 1 Investigated metal oxide powders.

#	Size[a]	Metal oxide powders	Manufacturer (synthesis method)	S_{BET}[b], m^2/g	XRD phase
TiO_2					
1	m	Reagent grade	LLC "Reakhim"	4.0 ± 0.1	–
2	n	Degussa P25	Evonik	52 ± 1	A85%/R15%[c]
3	n	**TKP** 102	Tayka	110 ± 3	A > 90%
4	n	FINNTi-S140	Kemira	165 ± 3	A88%/amorphous $Ti(OH)_4$
5	n	Hombitan Anatas	Sachtleben	227 ± 5	A100%
6	n	TiO_2	ICP RAS (hydrothermal synthesis)	120 ± 2	–
7	c	Hombitan Rutile	Sachtleben	92 ± 2	R > 90%/amorphous phase
8	c	Mesoporous TiO_2	MSU (template synthesis)	181 ± 4	Amorphous
9	c	Mesoporous TiO_2 doped with 3%Cr	MSU (template synthesis)	157 ± 3	Amorphous
Fe_2O_3					
10	m	Reagent grade	LLC "Reakhim"	24.2 ± 0.5	α-Fe_2O_3
11	n	Fe_2O_3	ICP RAS	12.8 ± 0.3	α-Fe_2O_3
12	n	Fe_2O_3	ICP RAS (decomposition of $Fe(CO)_5$)	161 ± 3	γ-Fe_2O_3
Al_2O_3					
12	m	Practical grade	LLC "Khimmed"	45.5 ± 0.9	α-Al_2O_3
13	n	Al_2O_3	LLC "Zond"	34.6 ± 0.7	γ-Al_2O_3
SiO_2					
14	m	Reagent grade	LLC "Laverna"	217 ± 4	–
15	c	Highly porous SiO_2	ICP RAS (milling of silica gel)	641 ± 13	–
16	n	AEROSIL® 255	AEROSIL®	249 ± 5	–
Cr_2O_3					
17	m	Reagent grade	LLC "Laverna"	3.5 ± 0.1	–
18	c	Highly porous Cr_2O_3	ICP RAS (combustion product of $K_2Cr_2O_7$)	44 ± 1	α-Cr_2O_3

[a]m, micron-sized particles; n, nanosized; c, micron-sized conglomerates of nano- and ultrafine particles.
[b]S_{BET} obtained after outgassing at 120 °C for 2 h.
[c]A, anatase; R, rutile.

2.2 Methods

Purity and crystallinity of TiO_2 nanoparticles was determined by X-ray diffraction (XRD) using advanced X-ray diffractometer (Bruker AXSD8 advance) with Cu K_α ($\lambda = 1.5418$ Å) radiation. Specific surface area was determined by low-temperature gas sorption analysis (BET) with FlowSorb III 2305 (Micromeritics). The morphology and particle size distribution for powders were investigated with laser diffractometer Analysette 22 MicroTec Plus (Fritsch), scanning electron microscope QUANTA 3D Philips SEM-515 (FEI), and atomic force microscope Ntegra Prima (NT-MDT). X-ray photoelectron spectrometry (XPS) was used to identify the chemical composition of the subsurface layer of oxide particles with PHI 5500 ESCA (Perkin Elmer), whereas the chemical composition of the adsorbed species on the surface was identified by FTIR spectrometry with Alpha Bruker.

The TGA and DSC curves of HMX with and without TiO_2 nanoparticles (by mixing in different ratios) were recorded using STA 449 F3 thermal analyzer (Netzsch). The sample with mass ~1 mg was placed in a closed alumina pan with a pinhole lid and then heated up to 500 °C with the rate 10 K/min under argon flow (70 mL/min). During DSC/TGA analysis, the evolved gases were detected online with mass spectrometer QMS 403 D Aeolos (Netzsch). At the first step the preliminary tests were conducted with registration of all the mass lines with $m/e = 4$–100, because the most important gaseous species lie within this range [47–50]. Then the 30 most changing lines were selected and tracked with reduced spectra collection time. Finally, selected mass lines were attributed to gaseous species according to literature data, including NIST database [51].

Nonisothermal experimental mass loss curves (TGA) at low heating rates (0.5–2 K/min) were processed with software Thermokinetics™ (Netzsch) using model-free methods (Kissinger, Ozawa-Flynn-Wall, Friedman) and formal kinetic modeling [52].

2.2.1 Determination of Hydroxyl Groups Concentration on the Surface of Metal Oxides

Hydroxyl groups cover the surface of metal oxides (Figure 1) and can determine various properties of powders. For example, the concentration of OH groups on the surface of TiO_2 affects the adsorption properties and correlates with the photocatalytic efficiency [41]. High hydroxyl groups' content can reduce the flow rate and cause aggregation of the powder [43]. The amount of OH groups on the surface of nanopowders depends on the synthesis method and storage conditions.

There are various methods of identifying surface functional groups in powdered materials. Some of them, such as FTIR and XPS spectroscopy, perform only qualitative analysis. Among the quantitative methods several approaches can be distinguished: method of isotopic exchange, thermogravimetry, and chemical

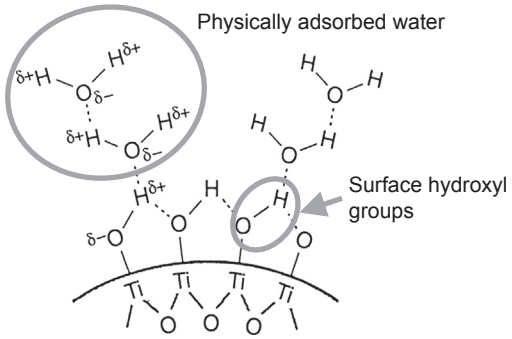

Figure 1 Diffused and surface-bounded hydroxyl groups on the titanium oxide surface.

techniques. The thermogravimetric method is relatively simple and is based on determination of the mass loss during dehydroxylation of the sample.

To determine the OH-group concentration on the surface of nano-oxide powders, the known thermogravimetric method [44] has been refined. The sample was heated with constant heating rate of 10 K/min from 30 to 120 °C to remove the diffused hydroxyl groups (dehydration), followed by isothermal heating during 30 min at $T_1 = 120$ °C. Then powder was heated up with the rate 10 K/min to the final temperature T_2, leading to dehydroxylation of the surface-bounded groups. The mass loss, corresponding to removal of the surface-bounded hydroxyl groups M_{OH} (%), was registered, and the concentration of these functional groups on the surface was calculated as follows:

$$N_{OH} = \alpha \cdot \frac{2 \cdot (m(T_1) - m(T_2)) \cdot N_A}{S_{BET} \cdot m(T_1) \cdot M_{H_2O}}, \quad (1)$$

where α is the calibration coefficient, S_{BET} is the specific surface area value, M_{H_2O} is the molar mass of water, N_A is Avogadro's number, $m(T)$ is the mass of the sample at temperature T. The final temperature T_2 for the TiO_2 heating was chosen to be 650 °C because the full dehydroxylation of titanium oxide occurs at a temperature above 500–600 °C [53]; for other oxides $T_2 = 800$ °C. Multiplier «2» in Formula (1) comes from the fact that in order to form one water molecule two OH-groups are necessary. Formula (1) ignores the lowering of the specific surface area under heating connected with particles sintering, and thus represents the lower estimation of the concentration of the OH groups on the surface.

Prior to the N_{OH} values measurements, we have estimated the role of different experimental factors, i.e., the preliminary evacuation, the sample mass, and selection of T_1 and T_2. It was found that the preliminary evacuation lowers the mass loss at the first heating stage (30–120 °C) but does not change the resulting value of $[m(T_1) - m(T_2)]$.

Table 2 Comparison of the obtained OH-group concentration with literature data.

	N_{OH}, OH/nm^2	
Sample	**Present work**	**Literature data**
TiO_2 No. 2 (*nano, Degussa P25*)	4.7 ± 0.4	4.6 (manufacturer data), 4.8; 4.9 [44]; 4.5 [41]
SiO_2 (*nano, Aerosil*)	3.0 ± 0.2	2–3 (manufacturer data), 3.2–3.5; 2.8–3.2; 2.8 [44]
SiO_2 (*micro, A.C.S.*)	5.4 ± 0.3	5.0 ± 0.8 [54]

This fact reveals that the dehydration and dehydroxylation processes are separated and not overlapped. To enhance the measurement accuracy, the special TGA sample holder was used, allowing us to increase the analyzed oxide mass from 10 mg for the common DSC/TGA holder to 30–100 mg. Calibration coefficient α was calculated by adjusting experimental results to the literature data and was found to be 0.46 (Table 2).

Applying the elaborated technique, we have determined the mass fraction of hydroxyls M_{OH} (%) and concentration N_{OH} (OH/nm^2) for studied titanium oxide powders.

2.2.2 The Catalytic Activity Evaluation for HMX Thermolysis with Nano-oxides

The catalytic activity of metal oxides in HMX thermolysis was calculated based on the HMX conversion degree at temperature 275 °C (Figure 2):

$$\alpha_{275} = 1 - m_{275}/m_{30}, \tag{2}$$

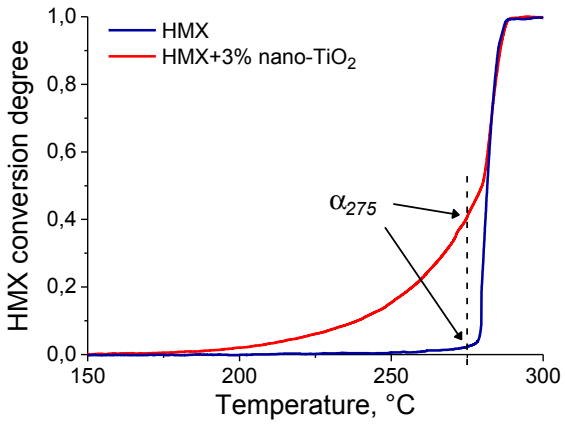

Figure 2 HMX conversion degree versus temperature for neat HMX (blue (black in print versions) curve) and HMX with catalyst (red (gray in print versions)).

where m_{275} and m_{30} are sample masses at temperatures 275 °C and 30 °C, respectively. For investigated samples, the α_{275} values have been derived from experimental TGA data at constant heating rate, i.e., 10 K/min. Temperature point 275 °C was chosen as preceding the HMX melting and decomposition. For neat HMX $\alpha_{275} = 0.03$, whereas for the HMX with catalytic additives this parameter was found to be higher.

2.2.3 Burning Rate Measurements

Constant pressure bomb (Crawford bomb) was used for combustion tests. The burning rate U_b was determined under different pressures of nitrogen (0.1–12 MPa) by two techniques, i.e., (1) by pressure-time curves, and (2) by video registration with the rate of 1200 fps. The relative error of the U_b determination did not exceed 5%.

Samples of HMX monopropellant and HMX with nano-TiO_2 were compacted from powders into pellets, applying the pressure load of 300 MPa during 3 min. To increase the mechanical strength of the samples, one or two droplets of acetone were added before pressing [5]. The lateral surface of samples was covered with epoxy "Poxipol." The sample diameter was selected on the basis of preliminary tests to provide the minimal increase in pressure inside the bomb during combustion (ΔP) at initial pressure (P_0). For most of the experiments the ratio $\Delta P/P_0$ did not exceed 10%, assuring independence of the burning rate data on the sample diameter. Finally, the sample diameter of 6 mm was chosen because U_b values for 6-, 8-, and 10-mm-diameter charges coincide within the measurement accuracy.

Impact of additives on HMX burning rate was estimated via parameter Z:

$$Z = U_{cat}/U_0, \tag{3}$$

where U_{cat} and U_0 are the burning rate values for formulations with additive and for HMX monopropellant, respectively. Subscription of introduced parameter (e.g., Z_2) corresponds to pressure (in MPa), under which it was determined. The accuracy of determined Z values was estimated to be less than 0.06.

3. RESULTS AND DISCUSSION

3.1 Nano-oxides Characterization

Composition, crystal phases, and BET specific surface area for the investigated samples are presented in Table 1.

Mesoporous titanium oxides consist of highly porous particles with the effective size of about 10 μm (Figure 3(a) and (b)). Hombitan Rutile powder has at least two-level hierarchy complex morphology, i.e., spherical agglomerates of about 10 μm in diameter (Figure 3) are consisting of ultrafine and nanosized particles (Figure 3(c) and (d)). Such highly porous structure determines the high BET specific surface area of 92 m^2/g.

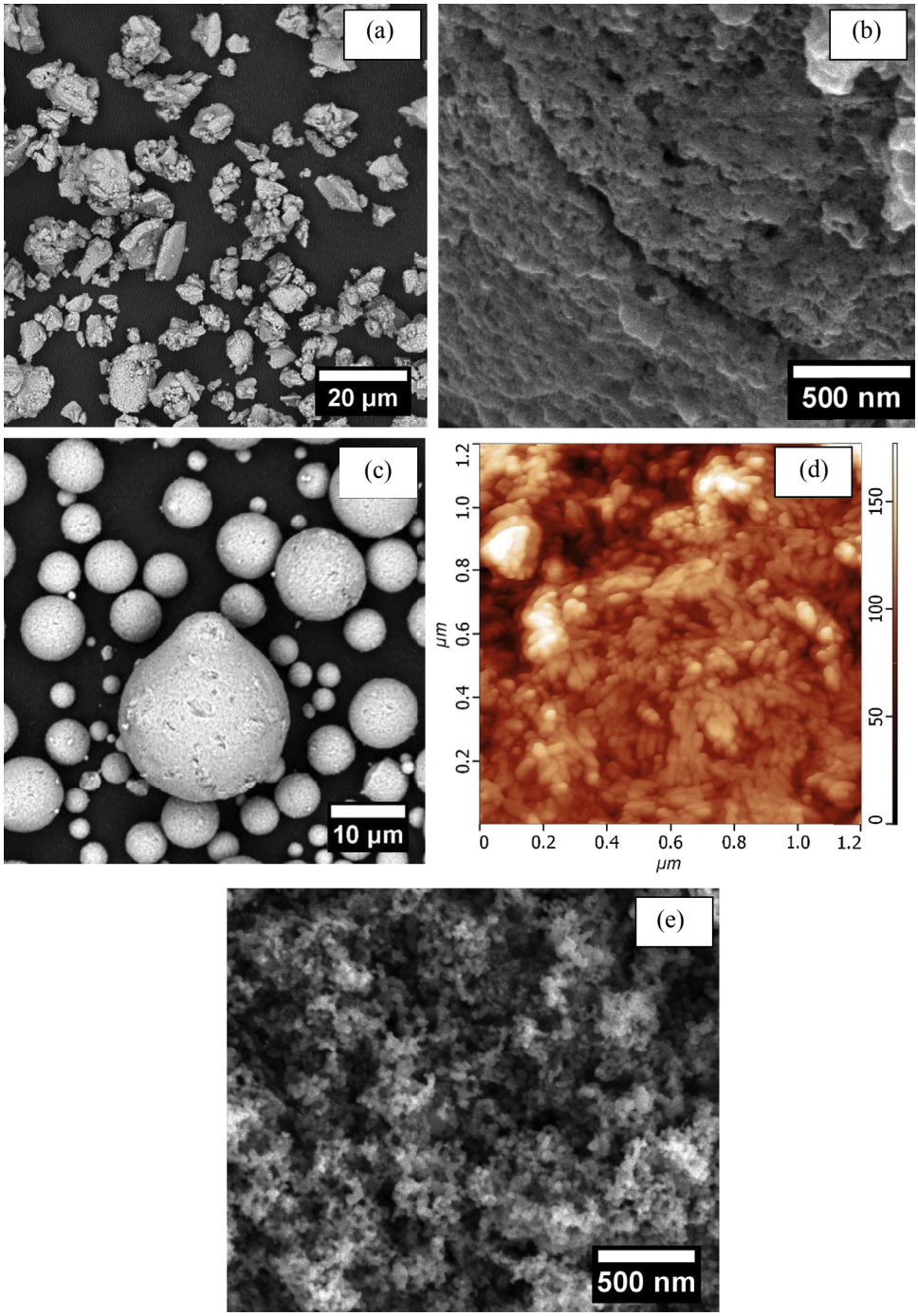

Figure 3 SEM and AFM (d) images of mesoporous TiO_2 (a,b); Hombitan Rutile, micron-sized agglomerates (c) with the magnified view of its surface (d); Degussa P25 powder (e).

Degussa P25 titanium oxide represents the mixture of two crystal phases, i.e., anatase and rutile in the mass ratio 85:15. Powder comprises nanoparticles with diameter less than 50 nm (Figure 3(e)).

Between available titania powders the highest specific surface area (227 m^2/g) has been found for sample Hombitan Anatas, therefore this powder was investigated further in more detail. Powder consists of nanoparticles (<50 nm) having crystal edges (Figure 4(a)). The XRD pattern confirms the sample to be pure anatase—tetragonal crystal phase of TiO_2 with the size of coherent scattering region less than 10 nm. X-ray elemental analysis, coupled with SEM, reveals the presence of Ti and O elements only.

XPS analysis reveals three elements presented on the surface of titanium oxide: Ti, O, and C. Spectra Ti 2p was approximated with doublet of the peaks 2p3/2 and 2p1/2 (spin-orbit splitting of 2p state) with binding energy of the Ti 2p3/2 equal to 458.8 eV corresponding to Ti^{4+} in TiO_2 (Figure 5(a)). The oxygen spectra consist of peak 1 at 530.1 eV resulting from oxygen in oxide and peak 2 at 531.4 eV corresponding to the

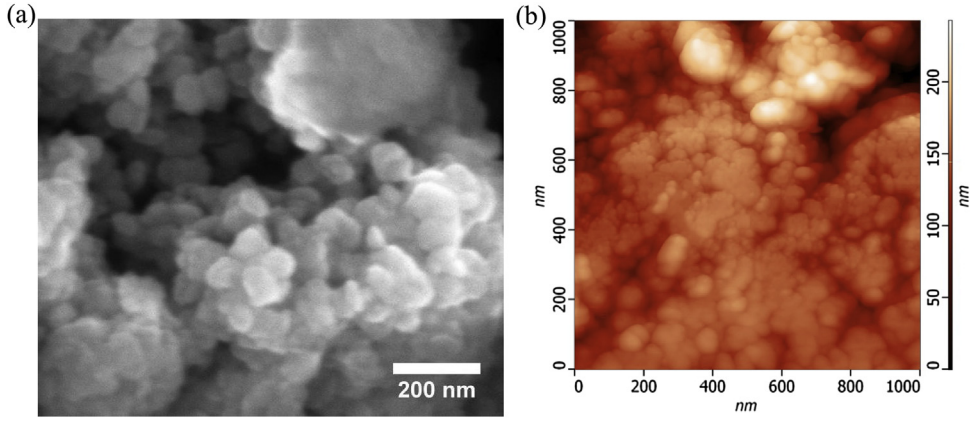

Figure 4 SEM (a) and AFM (b) images of Hombitan Anatas sample.

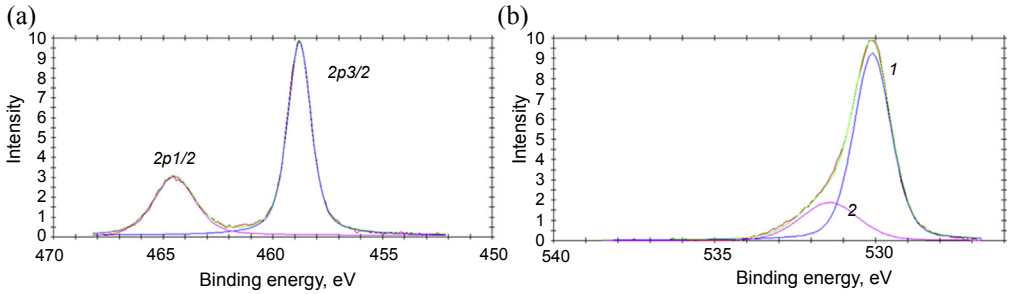

Figure 5 XPS spectra of the surface of Hombitan Anatas particles: Ti 2p (a) and O 1s (b) signals.

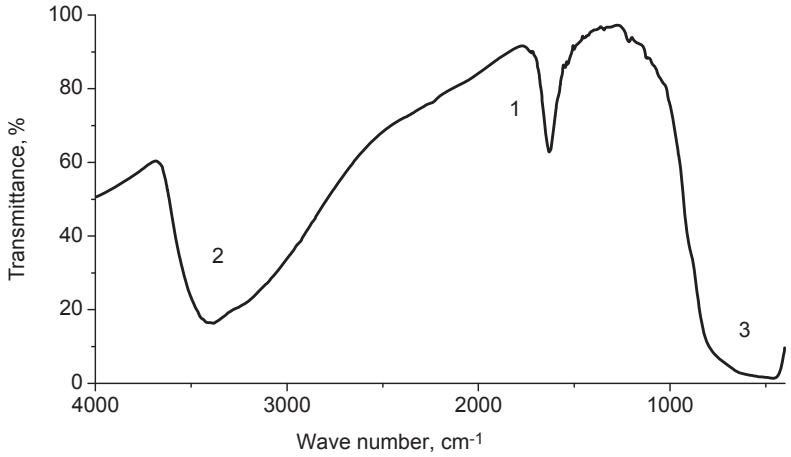

Figure 6 FTIR pattern: the presence of adsorbed OH groups and water on the nano-TiO_2 surface (peak numbers are explained in text).

absorbed oxygen (Figure 5(b)). Proportion of oxide oxygen in total oxygen in the sample is 77%. The ratio of oxygen concentration in oxide to concentration of titanium is close to 2, which agrees with the chemical formula TiO_2. The carbon spectra were also registered, corresponding to the absorbed carbon dioxide.

FTIR pattern of the powder consists of three main peaks, as shown in Figure 6. The narrow peak around 1630 cm^{-1} (peak 1) corresponds to absorbed water; the broad peak near 3400 cm^{-1} (peak 2) accounts for weakly bonded water molecules and hydroxyl groups [42], whereas the sharp drop of the signal in 500–750 cm^{-1} (peak 3) is assigned to Ti—O vibrations in titanium oxide. Weak peak near 2300 cm^{-1} gives evidence of C═O bond oscillations caused by the adsorbed carbon dioxide [42].

The gases evolved from TiO_2 sample under heating to 800 °C were registered with a mass spectrometer. The change was observed only for lines $m/e = 12$, 17, 18, and 44. Temporal behavior and intensities of these lines indicate that signals correspond to H_2O ($m/e = 17$, 18) and CO_2 (12, 44). The concentration of water is two orders of magnitude higher than that of carbon dioxide. Water evolution is caused by superposition of two processes: dehydration (molecular H_2O loss) and dehydroxylation (removal of surface-bounded OH groups).

Thus, nanosized TiO_2 (Hombitan Anatas) consists of nanoparticles in anatase crystal form, has a high amount of adsorbed water and surface-bounded hydroxyl groups, and has a small quantity of carbon dioxide at the surface. During heating, firstly, at temperature below 120 °C, H_2O is evolving from the sample in a form of molecular water, whereas at higher temperature desorption of hydroxyl groups is observed.

3.2 Effect of Nanosized Oxides on HMX Decomposition

3.2.1 Thermogravimetric Data

The results of thermogravimetric analysis of the HMX thermolysis with various additives are summarized in Figure 7. The content of each additive was equal to 3 wt% above 100% HMX. It is evident that the addition of materials decreases the nitramine's thermal stability in different extents. Specific surface area values for additives are presented on the plot in brackets. Some of the additives have specific surface much higher than that of Hombitan Anatas (227 m^2/g), nevertheless, among studied materials the nanosized titanium oxide Hombitan Anatas exhibits the highest catalytic efficiency. Apparently, the S_{BET} value is not the only parameter responsible for the catalytic effect in HMX thermal decomposition.

The influence of the amount of additive (C_a) on catalytic efficiency was studied for nano-titania in detail (Figure 8). With the increase in nano-oxide content up to 12 wt%, parameter α_{275} reaches the maximum, meaning that nitramine is fully decomposed below 275 °C. At the same time, the onset point of the HMX decomposition is almost unaffected by the C_a increase.

Thus, nanosized titanium oxide is found to be the most efficient catalyst of the HMX thermal decomposition. The onset temperature of the nitramine thermolysis decreased from 280 °C to ~160 °C with the addition of nano-TiO_2. Comparing some of the studied nano-oxides, the following order of their catalytic efficiency in HMX thermolysis was obtained:

$$TiO_2 > Fe_2O_3 \approx Al_2O_3 > SiO_2$$

The higher the nanosized titanium oxide content, the stronger the effect on the HMX thermal decomposition.

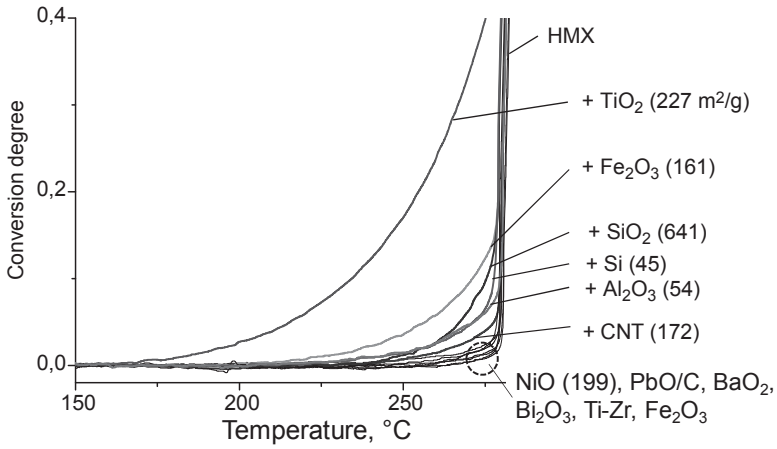

Figure 7 Dependency of the HMX conversion degree on temperature with 3 wt% of various additives (in brackets the S_{BET} values are shown in (m^2/g)).

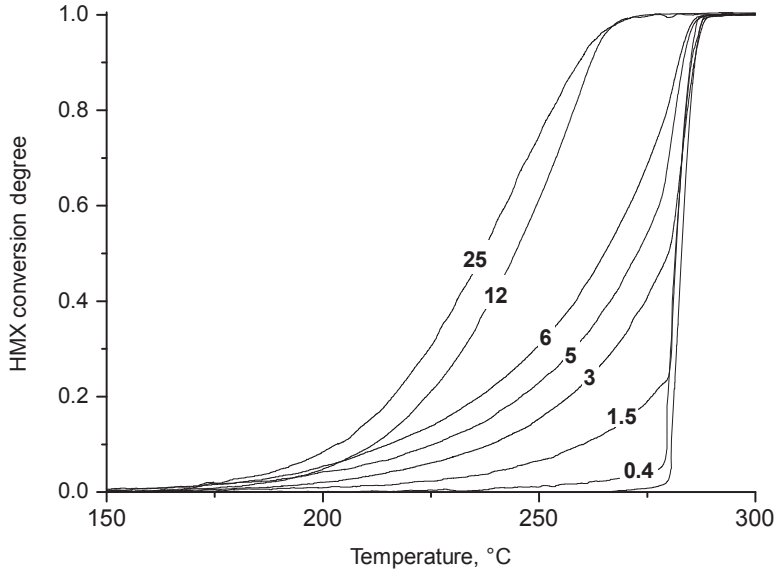

Figure 8 HMX conversion degree against temperature for various amount of nano-TiO_2 above 100% of HMX (shown on the curves in %).

3.2.2 Evolved Gases During Decomposition

Main signals, detected by MS during the neat HMX decomposition, arise from N_2, NO, NO_2, N_2O, CH_2O, HCN, CO, CO_2, and H_2O gaseous products. The addition of nanosized oxides doesn't change the composition of evolved gases, but the temporal behavior for species becomes different. Evolutions of specific products for the neat HMX, nitramine with nano-TiO_2, and nano-Fe_2O_3 thermolysis are shown in Figure 9.

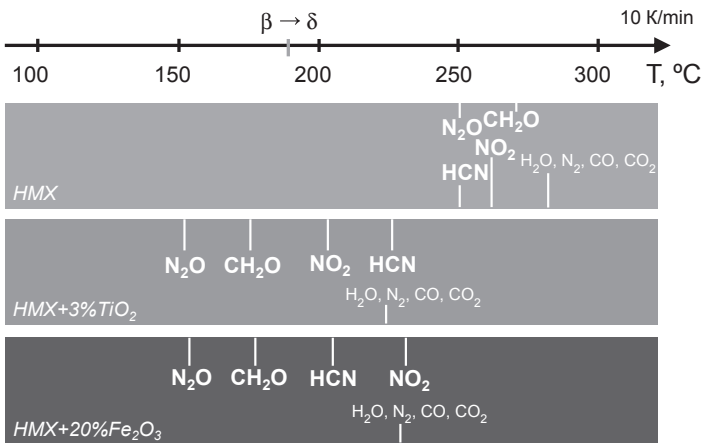

Figure 9 Evolution of gaseous products for HMX and HMX with nano-oxides.

Nanosized iron oxide has specific surface $S_{BET} = 161 \pm 3\ m^2/g$, which is comparable with Hombitan Anatas titania (227 m^2/g). However, to reach the same efficiency as of 3 wt% nano-TiO_2 ($\alpha_{275} \approx 0.4$), the nano-Fe_2O_3 content must be as high as 20 wt%.

For neat HMX the evolution of gaseous products was observed in the temperature range 250–300 °C, whereas the addition of nano-oxides expands this range to 150–300 °C.

Closer observation of obtained data allows understanding the time (temperature) history of decomposition process. For HMX with nano-titania at temperature about 150 °C, line 44 began to increase due to N_2O evolution. At $T \approx 164$ °C signal $m/e = 29$ appears, corresponding to formaldehyde CH_2O release. After the appearance of NO_2 (46) at 200 °C, heat flow (DSC) curve began to grow, along with evolution of products with $m/e = 12$, 28, and 18, according to reaction:

$$CH_2O + NO_2 \rightarrow NO + CO + CO_2 + H_2O \tag{4}$$

The main heat generation during HMX thermolysis is provided by the reaction (4) [55]. After 220 °C the signal of HCN (27) arises, which is caused by N—NO_2 bond breakage as a product of amide intermediates thermolysis. The last group of products, evolved at about 250 °C, correspond to $C_3H_3N_3$ (lines 81, 54, 53), C_2H_4N or N_2CH_2 (42 and 41), and C_2N_2 (52).

The addition of nanosized iron oxide also leads to substantial lowering of the onset temperature of the gaseous evolution, and the temporal behavior of main species is similar to one observed for HMX with nano-TiO_2.

Thus, nano-oxides decrease the onset temperature of the gas products evolution during HMX thermolysis from 250 °C for neat nitramine to 150 °C for mixtures of HMX with nano-TiO_2 and nano-Fe_2O_3. The first registered product for mixtures of HMX with nano-oxides is N_2O. Considering the overall scheme of HMX thermolysis, which assumes two simultaneous reaction paths [55], we can conclude that with the nanosized catalyst this reaction scheme is changed, i.e., firstly appear the products of decomposition pathway (5), and secondly, of the reaction (6):

$$C_4H_8N_8O_8 \rightarrow N_2O + CH_2O, \tag{5}$$

$$C_4H_8N_8O_8 \rightarrow NO_2 + HCN \tag{6}$$

The molar ratio between intensities of CH_2O and N_2O signals (Figure 10(a)) lies in between 4/3 and 3/3, that is close to predicted by reaction (5) ratio 1:1. The amount of NO_2 is significantly lower for HMX with TiO_2 than for HMX with Fe_2O_3 (Figure 10(b), line 46).

3.2.3 Heat Effect of Decomposition with Additives

To investigate the influence of the interface area between the nanoadditive and nitramine on the catalytic effect, the TGA/DSC experiments were performed in three different

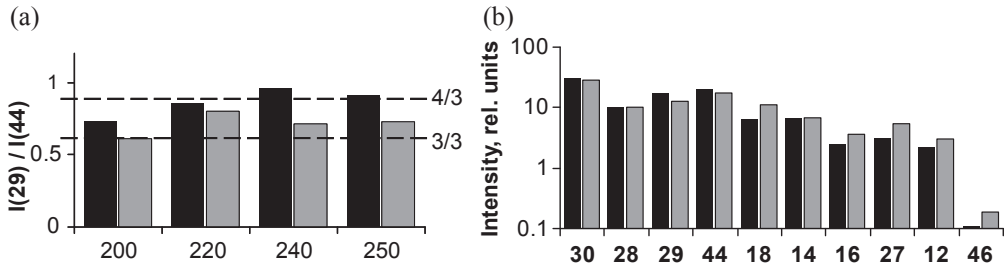

Figure 10 Mass spectrometry results: (a) ratio of intensities of lines 29 and 44 as function of temperature; (b) intensities of registered lines at 250 °C (black bars—HMX with nano-TiO_2, gray—with nano-Fe_2O_3).

configurations: (1) the mechanical mixture of two powders, (2) loose HMX powder covered with a pressed pellet of the nanosized TiO_2, and (3) separate spots of powders of HMX and additive without direct contact between them within the pan.

In the first-type experiment, the onset decomposition temperature was lowered and simultaneously the measured heat effect was reduced as compared to pure HMX. For the second-type experiment, the onset decomposition temperature was also decreased, whereas the heat effect was close to that one for pure HMX. Thus, to lower the onset temperature of the nitramine decomposition, HMX particles need to be in direct contact with nano-TiO_2 particles. In the third configuration, the onset temperature was the same as for pure HMX, but the heat effect was significantly higher than that one for pure HMX (Table 3). Apparently, the presence of nanosized titania influences the exothermic reaction between primary HMX decomposition products, Eqn (4).

The data for SiO_2 and Fe_2O_3 nano-oxides are also presented in Table 3. These powders have high specific surface area values, but the heat effect of the HMX thermolysis is increased only with the TiO_2 addition. To estimate sintering influence during heating, S_{BET} values were obtained under outgassing temperatures $T_{out} = 120$ °C and 300 °C. It was observed that the nano-oxides retain high S_{BET} values.

Thus, in the presence of nanosized TiO_2 the heat effect measured by differential scanning calorimetry technique is higher than that for pure HMX, apparently due to the exothermic reaction (4) on the surface of TiO_2 nanocatalyst.

Table 3 The surface area changes and the heat effect for HMX decomposition in the third configuration with additives (50% HMX/50% nano-oxide).

Additive	S_{BET}, m^2/g ($T_{out} = 120$ °C)	S_{BET}, m^2/g ($T_{out} = 300$ °C)	Heat effect, J/(g of HMX)
Pure HMX	—	—	1500 ± 100
Nano-TiO_2	227 ± 5	181 ± 4	2500 ± 200
Nano-Fe_2O_3	161 ± 3	113 ± 2	1500 ± 200
Nano-SiO_2	249 ± 5	262 ± 5	1400 ± 200

3.3 Influence of Nanosized Oxides on HMX Combustion

3.3.1 HMX Monopropellant Combustion

Prior to determination of the efficiency of additives, the combustion parameters for HMX monopropellant were tested and analyzed. The burning rate of HMX monopropellant has been measured under pressure from 2 to 12 MPa. Density of samples was varied in the range of 1.81–1.89 g/cm^3. Experimentally defined values were approximated by the Vieille law:

$$U(\mathrm{mm/s}) = B \cdot P(\mathrm{MPa})^{\nu}. \tag{7}$$

For HMX monopropellant the following parameters were obtained: $\mathbf{B} = 2.3 \pm 0.1$, $\nu = 0.82 \pm 0.01$, which agrees well with the literature data [56–62], as presented in Figure 11.

3.3.2 Catalytic Influence of Nano-TiO_2 on HMX Combustion

Addition of nano- and micro-sized Fe_2O_3, Al_2O_3, and SiO_2 powders to HMX did not result in the burning rate increase. The only nano-TiO_2 powder being added to HMX enhanced its burning rate. The maximal effect was obtained at titania concentration range 0.8–3% (Figure 12(a)), and the maximal burning rate gain approached was 53% (at 2 MPa) for HMX with 1.5% of nano-TiO_2. The minimal pressure exponent (0.65) was reached with 3% of titania (Figure 12(b)). For decomposition process, the increase of the nano-TiO_2 content up to 25% enhances the catalytic effect (Figure 8). Combustion

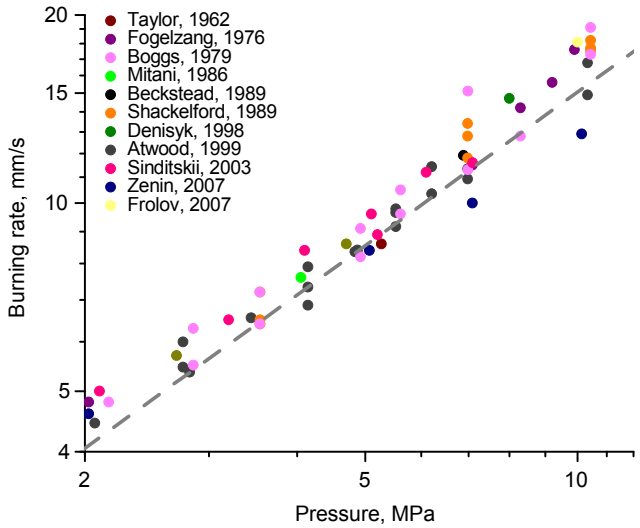

Figure 11 Burning rate versus pressure dependency for HMX monopropellant: present work (gray dotted line) and literature data [56–62].

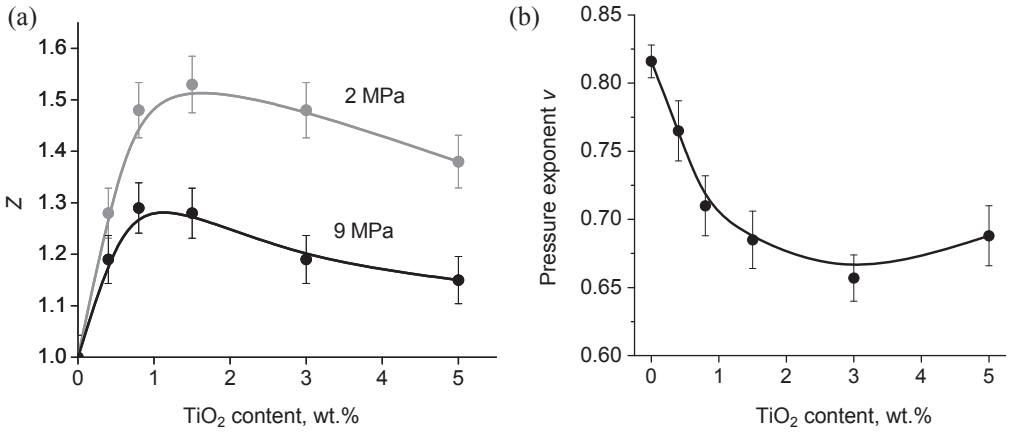

Figure 12 Catalyst content influence on relative burning rate increase (a) and on pressure exponent (b).

results revealed the increase of nano-TiO_2 content has more complex influence because at a certain point inert and highly stable oxide decreases combustion temperature. Thus, the burning rate dependency on additive content (C_a) achieves "saturation," followed by the decreasing region.

Results of decomposition and combustion studies of the HMX formulations with additives revealed two factors that play a key role in catalysis: specific surface area and concentration of nano-oxide. Figure 13 represents the similarities between the influence of TiO_2 specific surface area on catalytic efficiency in both processes, i.e., thermolysis and combustion. Noticeable effect on the U_b (or Z) increase and the pressure exponent decrease is observed for nanosized titanium oxide with $S_{BET} > 50\ m^2/g$ only. This result

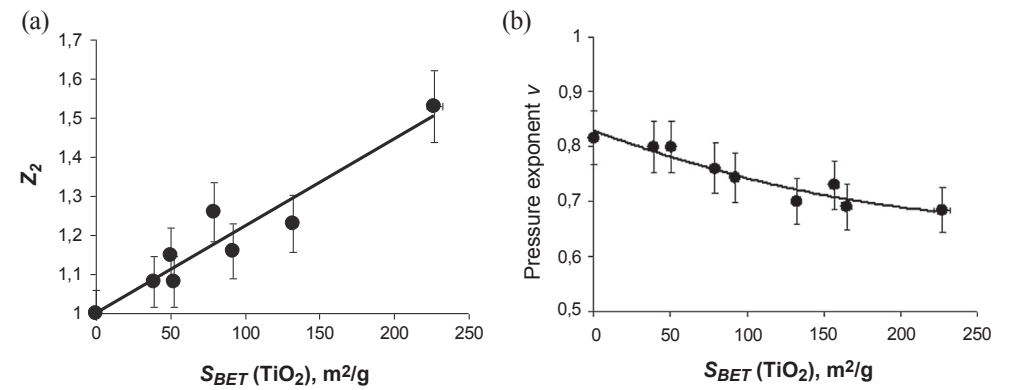

Figure 13 Specific surface area influence of the catalytic efficiency of nano-titania on HMX combustion: burning rate increase (a) at 2 MPa and pressure exponent (b) function of S_{BET}.

explains the earlier accepted statement that TiO_2 has no impact on HMX combustion [19]: micron-sized powder doesn't affect the burning rate. As demonstrated in Figure 13, dependencies correspond to 1.5% of the Hombitan Anatas content. For the titania content of 0.8% and 3%, similar results were obtained.

Thus, the nano-TiO_2 exerts similar influence on both combustion and thermolysis of nitramine—the higher specific surface and catalyst content (up to 1 wt%), the higher catalytic efficiency.

3.3.3 Kinetic Parameters of HMX Thermolysis with TiO_2

Since the model with the leading reaction in the condensed phase can adequately represent the HMX combustion process [37], the impact on HMX thermal decomposition will influence the burning parameters of HMX. Therefore, it is important to study the kinetic parameters for HMX with nano-TiO_2 decomposition to observe whether the change in activation energy is the reason for the burning rate enhancement.

Experimental mass loss curves (TGA) at low heating rates (0.5–2 K/min) were processed with software Thermokinetics™ (Netzsch) using model-free (Kissinger, Ozawa-Flynn-Wall, Friedman) and formal kinetic methods. The idea of the thermokinetic approach is to describe the conversion rate by matching particular functions, i.e., Arrhenius rate $k(T)$ and reaction model $f(\alpha)$:

$$\frac{d\alpha}{dt} = -Ae^{-\frac{E_a}{RT}}f(\alpha), \tag{8}$$

where α is the conversion degree, E_a is the activation energy, A is the preexponential factor. Both kinetic parameters (E_a and A) are considered to have "effective" values calculated for the overall decomposition process.

Analysis of experimental data of the neat HMX thermolysis revealed that at maximum conversion rate the conversion degree values are not constant but different; therefore, the Kissinger method (ASTM E628) cannot be applied. Friedman analysis established the autocatalytic behavior of decomposition process, which is in line with the formal kinetic results revealing that the most appropriate model is the first-order autocatalytic reaction. Obtained using ASTM E1641 method and formal kinetic technique kinetic parameters for neat nitramine decomposition are close to value $E_a = 144$ kJ/mol, which was proposed by Brill for reaction (5), i.e., for heterocycle breakage with formation of CH_2O and N_2O [55].

Predictions of the mass loss, calculated according to model of first-order autocatalysis, were compared with directly measured values during isothermal aging at 180 °C. Results revealed deviation less than 7% between the calculated data and the directly measured ones, proving the correctness of calculated kinetic parameters and model type, i.e., $k(T)$ and $f(\alpha)$.

Table 4 Activation energy values (kJ/mol) for decomposition of HMX with and without catalyst.

Sample	ASTM E1641	Formal kinetics (A → B), $\alpha < 0.3$
HMX	146 ± 8	143 ± 7
HMX + 3% nano-TiO_2	120 ± 20	127 ± 6

Analysis of TGA data for HMX with nanosized titania using formal kinetics revealed the best model to be Avrami–Erofeev reaction, which is often used to describe the energetic materials thermolysis with catalysts [63]. Value $E_a = 127$ kJ/mol, obtained for thermolysis of HMX with nano-TiO_2, is lower than that for the neat HMX decomposition, as presented in Table 4, and lower than estimated bond energies in nitramine molecule [64]. The same result was obtained by isoconversional Friedman analysis (Figure 14), i.e., addition of nanosized titania lowers the activation energy of HMX decomposition.

Apparently, obtained activation energy lowering for the decomposition process is induced by removal of surface-bounded hydroxyl groups on nano-oxide, which is the only process taking place under heating of titania to temperature of the catalytic HMX thermolysis (Section 3.1). It is known from the literature that the nitramine decomposition can be accelerated by OH radicals [64]. The activation energy for hydroxyls removal from the surface of nano-TiO_2 is 65 kJ/mol and with the increase of specific surface area it slightly decreases [65]. When the transport step precedes the chemical decomposition, the effective activation energy of the overall process lies in between E_a values for both processes [66]. The exact value of this effective activation energy (E_{eff}) could be determined as follows, using the reaction constants (k_1, k_2) for different steps:

$$E_{\text{eff}} = \left(k_1 \cdot E_{a,1} + k_2 \cdot E_{a,2}\right) / (k_1 + k_2). \tag{9}$$

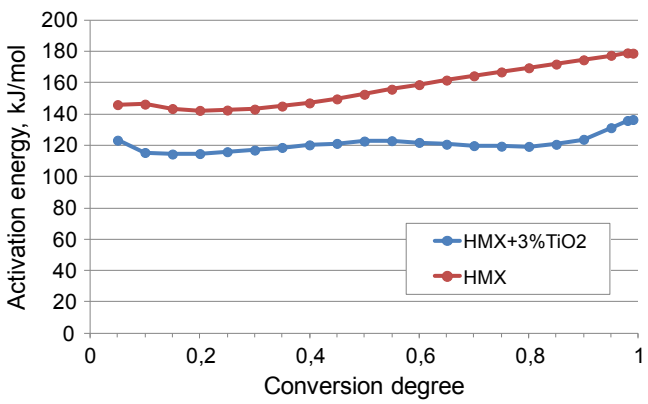

Figure 14 Isoconversional Friedman analysis for HMX and HMX + 3% TiO_2.

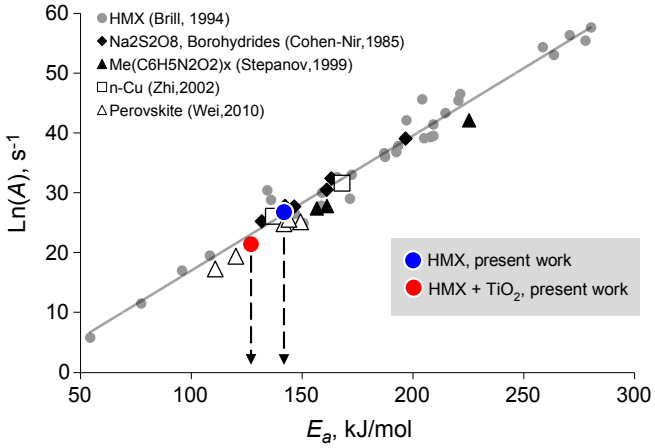

Figure 15 Kinetic parameters for thermolysis of neat HMX and HMX with additives: literature [16,29,31,55,67] and present work data.

Apparently, obtained activation energy for HMX with nanocatalyst is lowered by dehydroxylation of titania (and appearance of active agents), whereas decomposition process is the same as for neat HMX, via C—N bond breakage in heterocycle.

Figure 15 represents a comparison of obtained kinetic parameters with literature data: gray points depict values for neat HMX from Brill's review [55]. Brill showed that nitramine (without additives) exhibits so-called "kinetic compensation effect"—linear correlation between logarithm A and E_a. After addition of the literature data [16,29,31,67] to this plot, it is evident that kinetic parameters for HMX thermolysis with additives also lie on the common compensation line. One of the probable explanations of this fact is the above-mentioned superposition of two registered processes: transport step and thermal decomposition of HMX. When such superposition occurs, the calculated effective activation energy changes from $E_{a,1}$ to $E_{a,2}$, whereas preexponential factor also changes to compensate this variation, which results in the kinetic compensation.

Thus, kinetic studies revealed the activation energy lowering for HMX with nano-TiO_2 thermolysis. Considering the limiting step of HMX combustion to be located in the condensed phase, the burning rate increase for the combustion of these formulations is logical. Nevertheless, answers to the question of which factors are the most important for the HMX catalysis are still unclear.

3.4 Searching the Key Factors of Nano-oxide Effect on HMX Thermolysis

The influence of the amount of additive and its specific surface on the efficiency parameter (α_{275}) for various titania powders was studied in more detail. It was found that α_{275} depends linearly on S_{BET} (Figure 16(a)). At the same time, the mass fraction of

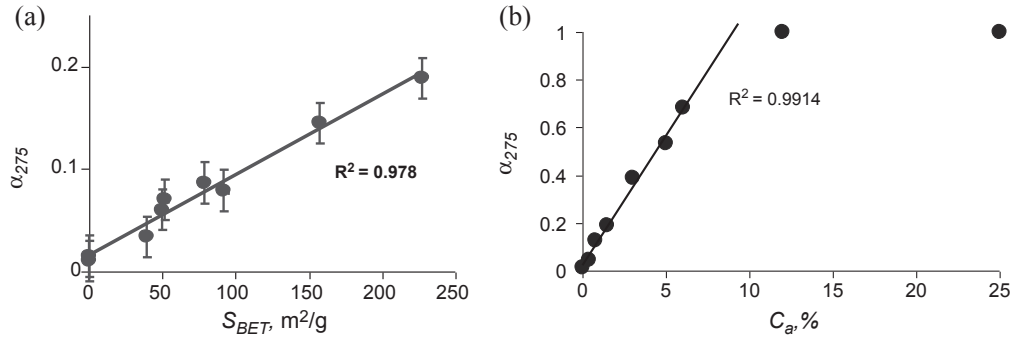

Figure 16 Catalytic efficiency in HMX thermolysis versus S_{BET} values (a) and the amount of additive (b).

hydroxyl groups' M_{OH} is linearly correlated with S_{BET}. Therefore, dependency of α_{275} on specific surface comprises the influence of OH groups.

The dependency of the catalyst efficiency on the amount of the additive is close to linear at additive content less than 6 wt% (Figure 16(b)), and at higher content of nano-TiO_2 this relationship becomes "saturated." The slope of these dependencies for different nano-TiO_2 powders is a function of specific surface area—the higher S_{BET}, the more pronounced catalytic effect is at the same content of catalyst.

Obtained results show that the conversion degree parameter characterizing the nano-oxide efficiency in the nitramine thermal decomposition is proportional to specific surface area and to the content of additive:

$$\alpha_{275} = K_a \cdot S_{BET} \cdot C_a + \alpha_{HMX}, \tag{10}$$

where $\alpha_{HMX} = 0.03$ is the conversion degree of neat HMX at 275 °C, K_a is the coefficient of proportionality, which supposed to be characteristic of the oxide type.

Table 5 represents the results of calculation of coefficient K_a for different nano-TiO_2 powders. Within the accuracy limits, the mean K_a value can be estimated as 59×10^{-5}.

Similar dependencies $\alpha_{275}(S_{BET}, C_a)$ were obtained for other studied oxides. Values of K_a for nano-oxides are presented in diagram (Figure 17) along with the data for ultrafine

Table 5 Coefficient K_a values for different titania powders.

Nano-TiO_2	S_{BET}, m^2/g	C_a, %	K_a*10^5
Degussa P25	52 ± 1	3	68 ± 10
Hombitan Rutile	92 ± 2	3	64 ± 6
Hombitan Anatas	227 ± 5	1.5	54 ± 3
		3	55 ± 3
		5	63 ± 3

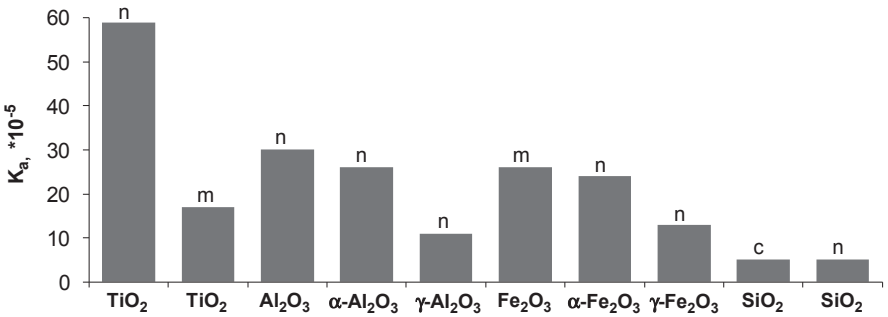

Figure 17 Comparative diagram of the oxide efficiency on the HMX thermolysis (notation the same as in Table 1).

and micron-sized oxides. The efficiency of the oxide influence on the HMX thermolysis decreases in the row:

$$TiO_2 > Al_2O_3 \approx Fe_2O_3 > SiO_2.$$

Thus, analysis of the obtained experimental data revealed that the key factors affecting the efficiency of oxide influence on the HMX thermal decomposition are specific surface and the additive content. Conversion degree is linearly proportional to both factors. The efficiency of nano-TiO_2 is more than twice higher than that one of other oxides. To understand the nature of the observed outstanding catalytic activity of nano-TiO_2, we applied a defect chemistry approach.

3.5 Does the "Strength" of the OH Groups Bonding to the Surface Affect the Catalytic Effect?

We assume the "strength" of the surface-bounded OH groups is affecting the catalytic activity of oxides in HMX thermolysis. To evaluate this parameter, we study the electronegativity of the metal cation χ_i, which characterizes the ability of the metal atom to shift the electron pair [68]:

$$\chi_i = \chi_0 \cdot (1 + 2n), \tag{11}$$

where χ_0 is the electronegativity of the metal element, n is the metal charge in the oxide. The oxides with low χ_i have the base properties, whereas oxides with high χ_i values have acid properties. The K_a dependencies on electronegativity of the metal ion for different micron- and nanosized oxides are plotted in Figure 18(a). Most of investigated oxides have close mean values of the catalytic efficiency, but with the increase in χ_i the value of K_a is lowered. The efficiency of the nano-TiO_2 is two times higher than that of other oxides, including micro-TiO_2, which indicates a complex mechanism of the influence.

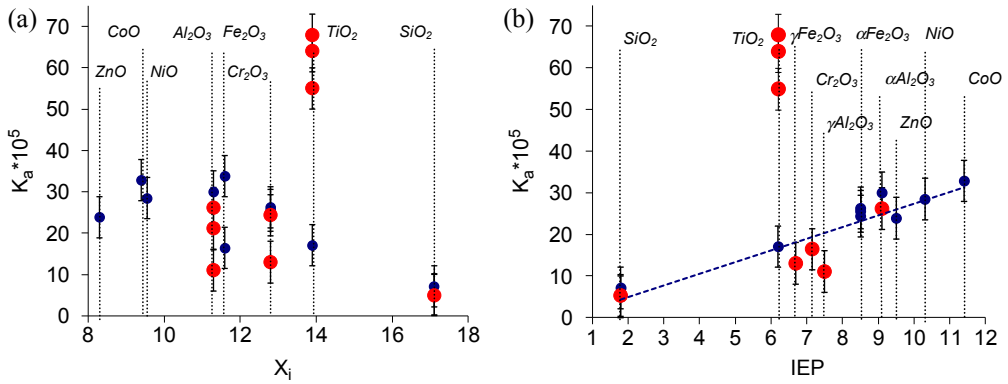

Figure 18 Dependencies of experimentally obtained catalytic efficiency of different oxides in HMX decomposition on cation electronegativity (a) and on isoelectric point (b) of nano- (red (gray in print versions)) and micron-sized (blue (black in print versions) points) oxides.

The oxide point of zero charge (isoelectric point, IEP) characterizes the acidity of the surface and is equal to the acidity value of the medium in which the oxide's surface has no electric charge. The higher the pH_{zpc} of the oxide, the more alkaline its surface is. Plotting the catalytic efficiency values versus pH_{zpc} as it is presented in Figure 18(b), the nearly linear relationship was obtained between these parameters for investigated nano- and micron-sized oxides. The only nano-TiO_2 has exceptionally high catalytic activity (K_a about 60×10^{-5}) and does not fit to this dependency.

Thus, we have demonstrated that the metal oxide surface acidity is an important factor that influences the catalytic performance of different oxides in HMX thermal decomposition. Apparently, the metal oxide surface acidity determines the dehydroxylation process dynamics, and the outstanding nano-titania catalytic efficiency is related to the high activity of the Lewis centers exposed after partial dehydroxylation.

3.6 Changing the Surface Acidity

To study the influence of surface charge of nanosized titania on the catalytic effect in HMX thermolysis in detail, the acid/base properties of TiO_2 Hombitan Anatas powder were altered by treatment with 1 M solution of NaOH and H_2SO_4 [69]. Acid treatment increases the acid sites' concentration on the surface of oxide and lowers concentration of base sites, whereas the alkaline treatment acts in opposite manner. The amount of acid sites on the surface of as-received powder (Hombitan Anatas) far exceeds the number of base sites [69], therefore the base treatment has more pronounced impact on the catalytic efficiency than that of acid treatment.

No significant changes of the amount of surface-bounded OH groups on as-received powder and modified samples were observed. However, the catalytic efficiency of thus

Table 6 The catalytic efficiency of acid-base treated TiO_2 Hombitan Anatas powder.

TiO_2 sample	S_{BET}, m^2/g	α_{275}	Z_2	Z_9
Acid treated (10 M solution H_2SO_4)	265 ± 5	0.16	1.52	1.24
Acid treated (1 M solution H_2SO_4)	195 ± 4	0.17	1.5	1.29
As-received	227 ± 5	0.19	1.53	1.28
Base treated (1 M solution NaOH)	189 ± 4	0.24	1.43	1.19
Base treated (10 M solution NaOH)	236 ± 5	0.26	1.18	1.16

modified powders in HMX thermolysis reaction is considerably enhanced with the basicity increase (Table 6).

Reducing the surface acidity of the nano-TiO_2 enhances its influence on the HMX thermolysis, which is in line with the previous result obtained for different metal oxides (Section 3.5). In addition, when comparing the TG curves, one can conclude that the higher the acidity of treated samples, the fewer the amount of OH groups evolved at a given temperature. The catalytic efficiency of thermolysis increases with the TiO_2-surface acidity lowering, whereas the burning rate factors (Z_2 and Z_9) are decreasing. The influence of TiO_2 is complex, indicating several simultaneous processes occurring during combustion and decomposition.

Thus, the surface treatment of nanosized catalyst appears to be a promising approach to increase its catalytic performance. The presence of acidic or basic groups can be determined by the synthesis conditions, and the resulting surface charge of the TiO_2 catalyst particles is a combination of surface chemistry and space charge as is shown. Total surface charge being positive will lead to an increase in the number of basic groups and hence will enhance the catalytic activity.

4. ELABORATION OF THE PHYSICOCHEMICAL MODEL OF CATALYTIC INFLUENCE OF NANO-TIO_2 ON HMX THERMOLYSIS

Experimental data reveal that the surface charges related to space charges in the nanostructured TiO_2 catalytic particles are of paramount importance for its catalytic efficiency. The question then arises, what is the nature of these charges?

Let us consider the possibility of the electron–hole pair generation upon heating for TiO_2. The bandgap energy E_g of TiO_2 is about 3.2 eV:

$$E_g = kT, \tag{12}$$

where k is the Boltzmann constant $k = 1.381 \times 10^{-23}$ J/K and 1 eV $= 1.602 \times 10^{-19}$ J. Thus, at very high temperatures, actually above the melting point of titania, 2116 K, the electron–hole pairs could be thermally excited in TiO_2.

Obviously, we can propose the following mechanism: upon heating, the intrinsic point defects are generated, resulting in formation of subsurface space charges of the

catalyst particles (oxide ion vacancies and Ti^{3+} ions) along with free electrons and regular tetravalent titanium ions. Both the free and the trapped electrons can produce the radical species. The capacity of the free radical formation is dependent on the degree of non-stoichiometry. Details of this mechanism are presented below along with the general defect chemistry approach.

4.1 Introduction to Defect Chemistry of Titanium Dioxide

Titanium dioxide has three crystal forms—rutile, anatase, and brookite—all existing in nature. In catalysis and photocatalysis, usually the anatase form is used, but also the mixtures of rutile and anatase forms are being used. All of them are commercially available. In catalysis, reactions occur at solid–liquid or solid–gas interfaces. For that reason it is necessary to know which point defects are thermally generated in the catalyst material and how their concentrations can also be varied by changing the chemical composition by doping, or by deviations from stoichiometry or from molecularity, i.e., via engineering on an atomic scale.

In general, point defects determine properties of inorganic materials, like optical and electrical properties, and this engineering on an atomic scale is a powerful approach to control such properties. In addition, the point defects at the interface of an inorganic catalyst material are to be considered in the catalysis mechanism. Moreover, if the length scale is decreased to the nanoscale, defect space charges in the interfacial region of an inorganic material need to be taken into account, besides basic or acidic groups present at the surface.

The thermal generation of point defects, referred to as intrinsic point defects, can introduce a combination of a cation and an anion vacancy (Schottky disorder), a combination of an interstitial cation and a cation vacancy (Frenkel disorder), or a combination of an interstitial anion and an anion vacancy (anti-Frenkel disorder). Usually, in closed-packed crystal structures Schottky disorder is thermally generated, for instance, $V_{Mg}'' + V_O^{\cdot\cdot}(MgO)$, while in the silver halides Frenkel disorder occurs, e.g., $Ag_i^{\cdot} + V_{Ag}'(AgX, X = Cl, Br.I)$. Here, the polarizability of the silver ions plays an important role in this defect formation mechanism. In the materials with the fluorite structure, anti-Frenkel disorder occurs, e.g., $F_i' + V_F^{\cdot}(CaF_2)$.

Here the Kröger-Vink notation for the point defects is used [70]. In this defect chemical notation the symbol S stands for the point defect. In addition, the site, *s*, of the point defect in the crystal structure is indicated, along with the effective charge, *c*, of the point defect, i.e., S_s^c.

Here, S can be an atom, an ion, or V for a vacancy; s can be a lattice atom site, a lattice ion site, or i for an interstitial site. The effective charge −q has as symbol ′, the effective charge +q has as symbol, and *x* stands for neutral, 0q.

Point defect examples are given above for the thermally generated intrinsic point defects. The magnesium ion vacancy has an effective charge −2q, and the oxide ion vacancy has an effective charge +2q. The silver ion interstitial has an effective charge +q, and the silver ion vacancy an effective charge −q. The fluoride ion

vacancy has an effective charge +q, and the interstitial fluoride ion has an effective charge −q. Ions on regular lattice sites have no effective charge, i.e., $Mg_{Mg}{}^{x}(Mg^{2+}), O_O{}^{x}(O^{2-}), Ag_{Ag}{}^{x}(Ag^{+})$, and $F_F{}^{x}(F^{-})$. An interstitial site has no effective charge and can be represented by $V_i{}^{x}$.

The point defects can be involved in reactions and these defect reactions require (1) conservation of mass, (2) conservation of lattice site stoichiometry, and (3) conservation of charge.

4.1.1 Intrinsic Point Defects in TiO_2

The thermal generation of point defects is an endothermic process, and at any particular temperature there will be an equilibrium concentration of point defects in a crystal. The formation of point defects produces a commensurate gain in entropy. The enthalpy of formation of the intrinsic point defects is thus balanced by the gain in entropy such that at equilibrium the overall change in the free energy of the crystal due to the point defect formation is zero according to the equation,

$$\Delta G = \Delta H - T\Delta S \tag{13}$$

The temperature dependence of the number of the Schottky defects, n_s, in a crystal of composition MX is given by

$$n_s = N \exp(-\Delta H_s/kT), \tag{14}$$

where n_s is the number of Schottky defects per m^3 at T(K), in a crystal with N cations and N anions per m^3, ΔH_s (eV) is the enthalpy required to form a set of Schottky defects, T is the absolute temperature (K), and k is the Boltzmann constant.

As expected, for an endothermic process increasing the temperature introduces more intrinsic point defects in a material [71].

It is common practice to present the thermal formation of intrinsic point defects in a reaction in which for the perfect lattice the symbol O is used. Here, we present the formal defect chemical reactions for TiO_2 (rutile) and include the formation enthalpy of a set of point defects,

$$\text{Schottky disorder}: O \leftrightarrow V_{Ti}'''' + 2V_O{}^{\cdot\cdot} \quad 5.2\ \text{eV} \tag{15}$$

$$\text{Anti-Frenkel disorder}: O_O{}^{x} + V_i{}^{x} \leftrightarrow O_i'' + V_O{}^{\cdot\cdot} \quad 8.7\ \text{eV} \tag{16}$$

$$\text{Frenkel disorder}: Ti_{Ti}{}^{x} + V_i{}^{x} \leftrightarrow Ti_i{}^{\cdot\cdot\cdot\cdot} + V_{Ti}'''' \quad 12.0\ \text{eV} \tag{17}$$

Based on the values of the defect formation enthalpies, it is concluded that the intrinsic point defects in TiO_2 (rutile) are thermally generated according to the Schottky mechanism [72]. It is further assumed that the intrinsic disorder in anatase TiO_2 is also thermally generated according to the Schottky mechanism.

4.1.2 Extrinsic Point Defects in TiO_2

In order to control the concentration of intrinsic point defects, it is common practice to dope the material with an aliovalent dopant or to create a deviation from stoichiometry in the material. For TiO_2 both cation and anion doping have been investigated in detail because TiO_2 is also being studied as a photocatalyst [73–75]. As examples, here we present the dopants Fe_2O_3 and Nb_2O_5:

$$Fe_2O_3 \rightarrow 2Fe_{Ti}{}' + 3O_O{}^x + V_O{}^{\cdot\cdot} \tag{18}$$

$$Nb_2O_5 \rightarrow 2Nb_{Ti}{}^{\cdot} + 4O_O{}^x + \frac{1}{2}O_2(g) + 2e' \tag{19}$$

Two iron ions on Ti lattice sites are charge compensated by an oxide ion vacancy, and this dopant increases the concentration of the oxide ion vacancies. Doping with the Nb-oxide fixes the electron concentration in TiO_2. These cation dopants lead to localized energy levels in the bandgap of TiO_2; this is relevant for the photo(electro) chemical application of the doped material as the undoped material only absorbs the near ultraviolet spectrum while the doped material also absorbs parts of the visible solar spectrum.

Asahi et al. [76] reported on anion doping of TiO_2, and their quantum chemical calculations revealed that the wave functions of the anion dopants N and C show significant overlap with the oxygen valence band wave functions, which means that the sub-bandgap defect energy levels are less localized than those for the cation dopants.

It should be borne in mind that at high temperatures the point defect concentrations will be determined by the thermally generated intrinsic point defect concentrations and that the material virtually behaves as a pure material. This is especially relevant if in a catalytic process high temperatures will be achieved.

Besides doping, a deviation from stoichiometry will influence the point defect concentrations; an example of this deviation from stoichiometry is presented in the defect chemical reaction

$$O_O{}^x \leftrightarrow V_O{}^{\cdot\cdot} + \frac{1}{2}O_2(g) + 2e' \tag{20}$$

Here, the oxide ion vacancy is charge compensated by two electrons. The equilibrium constant is

$$K_1 = \left[V_O{}^{\cdot\cdot}\right][e']^2 p(O_2)^{1/2} \tag{21}$$

Such an anion-deficient material at high temperatures can become an *n*-type semiconductor. It is also possible to obtain an anion-excess material, which is exemplified by the defect chemical reaction

$$O_2(g) \leftrightarrow 2O_O{}^x + V_{Ti}{}'''' + 4h\cdot \tag{22}$$

The equilibrium constant is

$$K_2 = \left[V_{Ti}''''\right][h\cdot]^4 p(O_2)^{-1} \tag{23}$$

The incorporation of oxygen results in formation of two oxide ion sites, thereby creating a titanium ion vacancy in order to preserve site balance, which is charge compensated by four electron holes, making the anion-excess material a *p*-type semiconductor. Deviations from stoichiometry always lead to mixed ionic-electronic disorder. In binary materials, only deviations from stoichiometry can occur.

In ternary and more complex materials, besides a deviation from stoichiometry, a deviation from molecularity can also occur. As an illustration, the defect chemistry of I-III-VI_2 chalcopyrite-structured materials with $CuInS_2$ has been reported by Perniu et al. [77]. Here, the deviation from molecularity occurs if the material has dissolved a small amount of one of the binary compounds, i.e., Cu_2S or In_2S_3. Deviations from molecularity only influence ionic disorder. If a deviation from stoichiometry occurs also in a ternary material, the electronic disorder is influenced [77].

In order to obtain in-depth information on the influence of a deviation from stoichiometry in a binary material a Brouwer diagram is constructed, i.e., log [defect concentration] versus log $p(O_2)$, which reveals what ionic and electronic point defects dominate in a certain $p(O_2)$ regime. A detailed derivation of the Brouwer diagram requires knowing the expressions for the equilibrium constants of the defect chemical reactions Eqns (20) and (22), i.e., Eqns (21) and (23), the electronic equilibrium constant,

$$K_3 = [e'][h\cdot] \tag{24}$$

the Schottky equilibrium constant,

$$K_S = \left[V_{Ti}''''\right]\left[V_O{}^{\cdot\cdot}\right]^2 \tag{25}$$

and the total electroneutrality condition, i.e.,

$$2\left[V_O{}^{\cdot\cdot}\right] + [h\cdot] = 4\left[V_{Ti}''''\right] + [e'] \tag{26}$$

It can be seen from the defect chemical reactions Eqns (20) and (22) that at low oxygen pressures the material behaves as an *n*-type semiconductor and at high oxygen partial pressures as a *p*-type semiconductor. In an oxygen pressure regime between the anion-deficient and anion-excess material the ionic regime occurs, where for an undoped material the intrinsic ionic point defects predominate and the material is an ionic conductor. In order to derive a detailed expression for the oxygen-partial pressure dependency of the point defects the use of the total electroneutrality condition Eqn (26) is not very practical. Brouwer proposed to use reduced electroneutrality conditions. For example, at low oxygen pressures the reduced electroneutrality condition is evaluated according to the defect chemical reaction Eqn (20)

$$2\left[V_O{}^{\cdot\cdot}\right] = [e'] \tag{27}$$

At high oxygen pressures it is evaluated according to the defect chemical reaction, Eqn (22),

$$4\left[\mathrm{V_{Ti}}''''\right] = [h\cdot] \tag{28}$$

With these reduced electroneutrality conditions the detailed expressions for the oxygen pressure dependency of the individual point defect concentrations can be obtained.

A representative example of a Brouwer diagram for a binary metal oxide (MO) with Schottky disorder is given in Figure 19 [72].

In case of a ternary material, in addition to Brouwer diagrams of log [defect concentration] versus the activity of each binary constituent needs to be constructed and in that case a three-dimensional Brouwer diagram can be drawn [74].

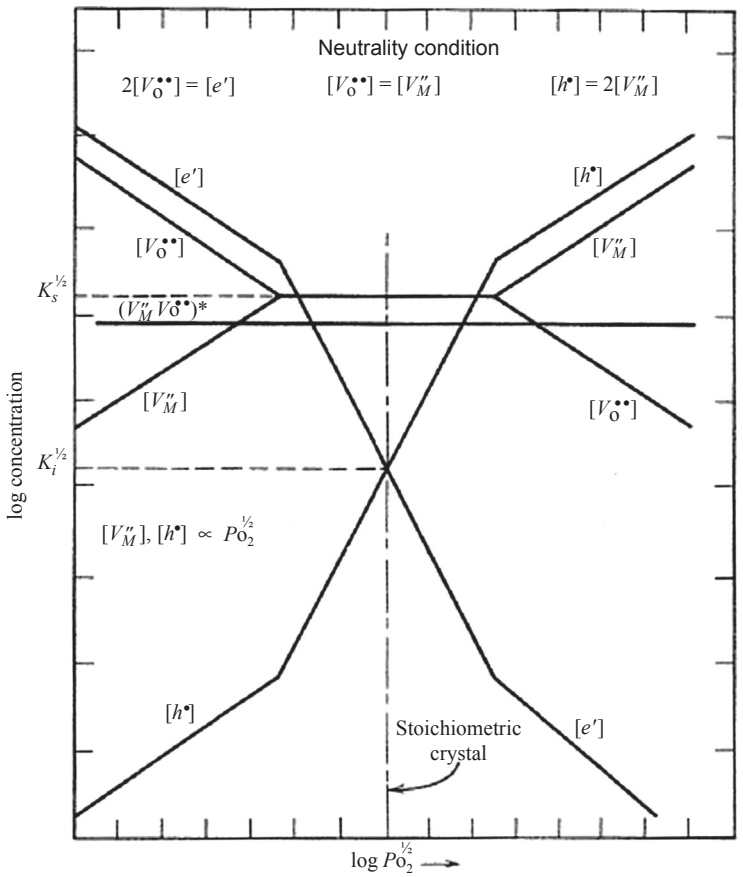

Figure 19 Schematic representation of the log (defect concentration) as a function of the oxygen pressure $p(O_2)^{1/2}$ for an undoped metal oxide MO that forms Schottky disorder at the stoichiometric composition [72].

4.1.3 Ionic Space Charge

The formation enthalpies, ΔH_S and ΔH_F, of intrinsic point defects can be obtained by studying the temperature dependency for diffusion or ionic conductivity of a particular material. In case one cation vacancy and one anion vacancy is formed according to the Schottky mechanism, it is common practice to assign half of the value of the formation enthalpy to each intrinsic point defect. In case of materials that exhibit Frenkel or anti-Frenkel disorder, also half of the formation enthalpy is assigned to the interstitial cation and to the cation vacancy, or to the interstitial anion and to the anion vacancy, respectively.

However, the formation enthalpy of each individual type of intrinsic point defect is different and this leads to a space charge potential difference between the bulk and the surface of the material. The width of this space charge is in ionic materials usually of the order of a few atom layers, much smaller than in semiconductors, and goes, therefore, unnoticed for measurements on bulk ionic materials. If the length scale goes down to the nanoscale, the space charge and its effect on materials properties can no longer be ignored and that is especially important for phenomena occurring at interfaces, like in (photo)catalysis.

For TiO_2, exhibiting Schottky disorder, the surface will be positively charged if the formation enthalpy of the titanium ion vacancies is smaller than the formation enthalpy of the oxide ion vacancies. Within nanostructured TiO_2 the positive surface charge by titanium ions is charge compensated by a space charge of titanium ion vacancies. In order to obtain the position-dependent concentration of the oxide ion vacancies the Schottky defect equilibrium constant, Eqn (25), is used. At some distance from the surface the intrinsic electroneutrality condition, Eqn (29), holds

$$2\left[V_{Ti}^{''''}\right] = \left[V_O^{\cdot\cdot}\right] \tag{29}$$

Figure 20 presents schematically the position-dependent concentrations of the cation and the anion vacancies in the space charge region, along with the position-dependent electrical potential. Here the individual formation enthalpies are presented as g_V, and the Kröger-Vink defect chemical notation is also used for the surface ions.

The surface defect chemistry can be influenced by doping. Ikeda and Chiang [78] studied the influence of doping on the space charge of nanostructured TiO_2. Doping with Nb_2O_5, as presented in the lattice reaction, Eqn (19), leads to a space charge distribution at high temperatures of the Nb dopant ions with an effective positive charge, a minor distribution of electrons, and no titanium ion vacancies. Codoping of TiO_2 with aluminum and niobium ions was studied as well and provided insight into the role of aliovalent dopants on catalytic behavior at high temperatures.

Upon further decreasing, the dimensions of sample space charges will start to overlap [79,80] and then, for example, the intrinsic electroneutrality condition, Eqn (29), will no

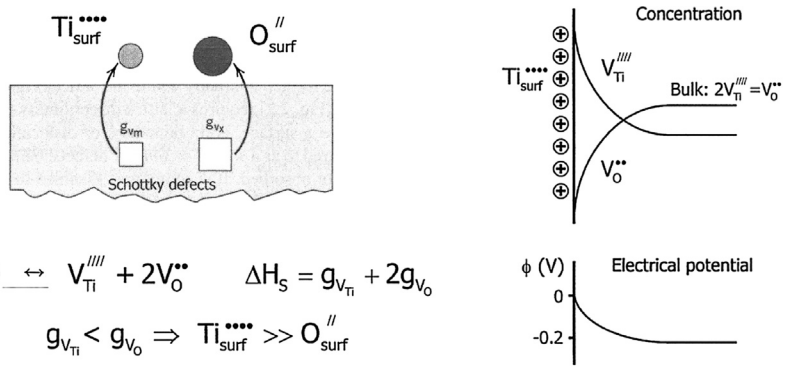

Figure 20 Schottky defects created at the surface with the indicated difference in formation enthalpy of the individual point defects. The ionic space charge potential difference between surface and bulk depends on this difference.

longer be achieved in the bulk of the nanostructured material, i.e., the concentration of one of the intrinsic point defects will be increased beyond the bulk equilibrium value. In order to obtain the concentration of the other intrinsic point defect, the equilibrium constant, Eqn (25), can still be used in this example.

The catalytic properties of TiO_2 have been studied using nonmetal dopants. Deviations from stoichiometry can be used to incorporate H, N, S, and I via the oxide ion vacancies, according to defect chemical reaction, Eqn (20). Doping with nonmetal dopants requires nonstoichiometric TiO_{2-x}, hence large dopant concentrations require large deviations from stoichiometry. Lin et al. [81] have introduced an elegant process for the incorporation of large concentrations of nonmetal dopants in TiO_2, using large deviations from stoichiometry. Oxide ion vacancies can be introduced by thermal treatment in an inert ambient. Lin et al. [81] used molten Al to reduce TiO_2 (Degussa P25) nanocrystals, and as a result the oxygen-deficient amorphous layers surrounding the TiO_2 cores were obtained. The average thickness of the amorphous layers is ~4 nm. The amorphous shells loose lattice ordering with a large number of oxide ion vacancies, charge compensated by electrons, which can convert Ti^{4+} into Ti^{3+}. These core–shell structures $TiO_2@TiO_{2-x}$ were successfully used to dope the material with atoms H, N, S, and I. The nonmetal-doped materials revealed improved photocatalytic behavior. Improved catalytic behavior for other processes might be a challenge as these dopants also influence the point defects comprising the space charge and, therefore, the surface charge. It should also be kept in mind that the density of surface OH groups on anatase TiO_2 is larger than on rutile TiO_2 [82], and this will lead to differences in the nature of the space charges and hence the surface charges.

4.2 Physicochemical Model of the Nano-oxides' Influence on HMX Thermolysis and Combustion

On the basis of the above experimental results we propose the following model of the nano-titania influence on the HMX decomposition (Figure 21). At temperature ~150 °C the surface-bounded OH groups evolve from the nano-oxide surface and attack the nitramine. The nature of the evolved OH groups is not clear—most of the experimental techniques, including one used in present work, observe OH groups as a water vapor. Some authors report about "free OH groups." It is still unclear whether they are OH radicals, because their lifetime is very short, no longer than 10^{-9} s. Apparently, the weakening of the surface OH-groups bonding increases their activity and ability to abstract hydrogen atom from the HMX molecule.

After the hydrogen abstraction, the N—NO_2 bond energy in HMX molecule significantly drops (according to Melius calculations [64]), leading to the nitro-group detachment. The NO_2 group, in turn, can attack an H-atom in another HMX molecule, just like a "cage-effect" (Figure 21, 3a), or absorb on Lewis centers formed after partial dehydroxylation (Figure 21, 3b). The adsorption is the reason for the experimentally observed NO_2 concentration lowering for the system with nano-TiO_2. Adsorption of NO_2 occurs on the titania surface, thus increasing the heat release in condensed phase produced by reaction (Figure 21, 4), which was established in our DSC experiments.

Two main groups of gaseous products are obtained depending on the temperature and heating rate, i.e., at low temperature and/or heating rate the main products are CH_2O and N_2O (Figure 21, 4a), whereas at high rates, HCN and NO_2 (Figure 21, 4b). We detected the greater than unity ratio $[CH_2O]/[N_2O]$, which can be a consequence of the OH interaction with the double bond (Figure 21, 4c).

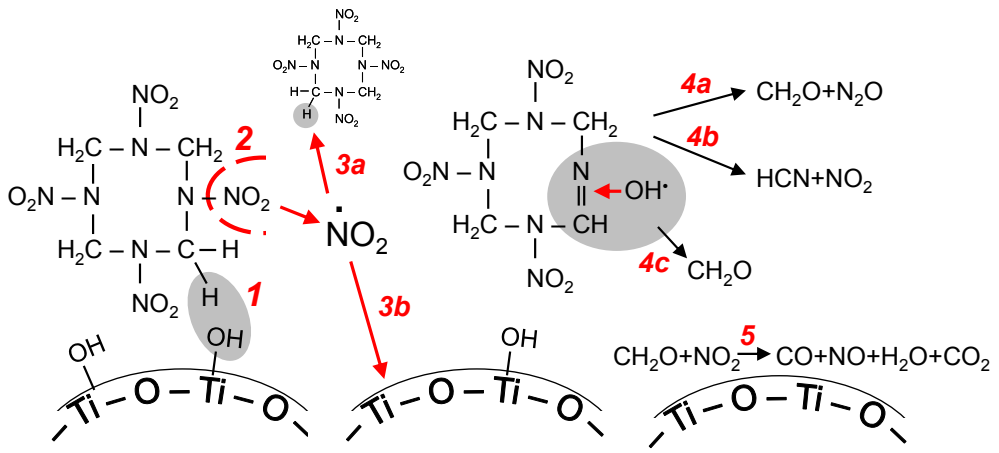

Figure 21 The model of the nanosized titania influence on HMX decomposition and combustion.

At higher temperatures the exothermic reaction $CH_2O + NO_2$ starts, providing the main exothermic effect.

Finally, the main steps of the proposed model are dehydroxylation of the metal oxide nanoparticle surface, followed by the initiation of the nitramine decomposition, and adsorption of liberated NO_2 on the surface of nano-TiO_2 particles. Thus, nano-TiO_2 plays a twofold role in HMX decomposition: (1) being a source of active species (OH groups) initiating the HMX molecule destruction at low temperature (150 °C), and (2) being an adsorption surface to "keep" the NO_2 close to the condensed phase, thus increasing the heat release there. Both indicated processes depend differently on temperature and heating rate, thus defining the catalytic efficiency of the nano-oxide in the HMX decomposition and combustion processes. For other than TiO_2 nano-oxides investigated (Fe_2O_3, Al_2O_3, SiO_2), only the first process was observed, leading to catalysis of the nitramine decomposition and making no impact on HMX combustion.

5. SUMMARY

Experiments reveal nanosized titanium oxide to be the most effective catalyst of the HMX thermal decomposition as compared to Al_2O_3, Fe_2O_3, and SiO_2. The onset temperature of the nitramine thermolysis is considerably decreased with the addition of nano-TiO_2 (from 280 °C to about 160 °C). Comparing studied nano-oxides, the following order of their catalytic efficiency in HMX thermolysis was obtained: $TiO_2 > Fe_2O_3 \approx Al_2O_3 > SiO_2$. The higher the nanosized titanium oxide content, the stronger the effect on the HMX thermal decomposition.

Various thermal analysis techniques were applied to characterize the HMX decomposition: DSC, TGA, in situ mass spectrometry of the gaseous species, and thermokinetic modeling. We have investigated the factors influencing the catalytic efficiency of TiO_2 in HMX-decomposition reactions. The catalytic performance was analyzed, and the key factors were shown to be specific surface area, content, and the properties of the metal oxide surface. The acidity of the surface of nanosized titania was varied to evaluate the subsequent changes in catalytic efficiency during HMX combustion and thermolysis processes. These ionic defects alter the catalytic efficiency—the lower the surface acidity of nanosized metal oxides, the higher the influence on the HMX thermolysis, and vice versa for nitramine combustion.

Results of analysis of gaseous decomposition products show that addition of nano-oxides to HMX lowers the onset temperature of gases evolution from 250 °C to 150 °C. Firstly, the products of decomposition pathway $C_4H_8N_8O_8 \rightarrow N_2O + CH_2O$ appear, and secondly, the products of reaction $C_4H_8N_8O_8 \rightarrow NO_2 + HCN$.

Results of the combustion tests reveal that the burning rate as well as the pressure exponent is affected by the addition of exceptionally nano-TiO_2. Kinetic parameters for

the thermolysis process are decreased with the nano-TiO_2 addition in comparison to pure HMX due to the superposition of the dehydroxylation process from the oxide surface and the nitramine's decomposition.

A physicochemical model of the influence of the nano-oxides on the HMX thermal decomposition and combustion, which involves the dehydroxylation of the nanoparticle's surface, the initiation of the nitramine decomposition, and adsorption of NO_2 on the surface of nano-TiO_2 particles with subsequent exothermic reaction, is proposed.

In the present work, attention was particularly focused on the surface and subsurface conditions of the nanostructured catalyst, and it was shown that alteration of the surface acidity affects the catalytic behavior. In our opinion, the defect chemistry approach to the energetic materials catalysis established here for the first time opens new opportunities in this field of research.

ACKNOWLEDGMENT

Financial support for this work was provided by the Russian Foundation for Basic Research (grant no. 14-03-31528 to N.M.) and by Cranfield University (contract no. 5138841 to N.M., A.P., and K.M.).

REFERENCES

[1] A.I. Atwood, T.L. Boggs, P.O. Curran, et al., Burning rate of solid propellant ingredients, Part 1: pressure and initial temperature effects, J. Propuls. Power 15 (6) (1999) 740–747.
[2] K. Kuo, R. Acharya, Applications of Turbulent and Multi-Phase Combustion, John Wiley & Sons, 2012.
[3] G. Lengelle, J. Duterque, J.F. Trubert, Physicochemical mechanisms of solid propellant combustion, in: V. Yang, T.B. Brill, W.Z. Ren (Eds.), Progress in Astronautics and Aeronautics, Solid Propellant Chemistry, Combustion, and Motor Interior Ballistics, vol. 185, AIAA, Reston, 2000, pp. 287–334.
[4] F.S. Blomshield, Nitramine Composite Solid Propellant Modeling/Report NWC-tp-6992, Naval Air Warfare Center, China. Lake, 1989, 183 p.
[5] A.K. Nandi, M. Ghosh, V.B. Sutar, R.K. Pandey, Surface coating of cyclotetramethylenetetranitramine (HMX) crystals with the insensitive high explosive 1,3,5-triamino-2,4,6-trinitrobenzene (TATB), Cent. Euro. J. Energ. Mater. 9 (2) (2012) 119–130.
[6] J. Sun, H. Huang, Y. Zhang, et al., In-situ coating of TATB on HMX, Energ. Mater. (CHENGDU) 14 (2006) 330–332.
[7] A. Pivkina, N. Muravyev, K. Monogarov, et al., Synergistic effect of ammonium perchlorate on HMX: from thermal analysis to combustion, in: L. De Luca (Ed.), 21st Century Challenges for Chemical Rocket Propulsion, Springer, 2015 in print.
[8] C. An, W. Jingyu, W. Xu, et al., Preparation and properties of HMX coated with a composite of TNT/energetic material, Propell. Explos. Pyrotech. 35 (4) (2010) 365–372.
[9] K.P. McCarty, HMX Propellant Combustion Studies, 1979. Report AFRPL-TR-79-61.
[10] D.A. Flanigan, B.B. Stokes, HMX Deflagration and Flame Characterization, 1980. Report AFRPL-TR-79-94.
[11] S.F. Palopoli, T.B. Brill, Thermal decomposition of energetic materials 52. On the foam zone and surface chemistry of rapidly decomposing HMX, Combust. Flame 87 (1991) 45–60.
[12] N. Kubota, Propellants and Explosives: Thermochemical Aspects of Combustion, Wiley Verlag, 2002, 245 p.
[13] R.S. Stepanov, L.A. Kruglyakova, A.M. Astakhov, et al., Effect of metal formiates and oxalates on HMX decomposition, Combust. Explos. Shock Waves 40 (5) (2004) 576–579.

[14] L.A. Kruglyakova, R.S. Stepanov, K.V. Pekhotin, Potassium and rubidium 3-nitro-1,2,4-triazol-1-il-dinitromethane salts influence on HMX thermolysis, in: Proceedings of the All-Russian Conference "Advantages in Special Chemistry and Chemical Technology". Moscow, 2010, pp. 196–200 (In Russian).
[15] E.V. Sokolov, E.M. Popenko, A.V. Sergyenko, et al., Nitramine propionitrile and its salts influence on HMX thermal decomposition, Polzunov. Vestn. (3) (2007) 130–139 (In Russian).
[16] R.S. Stepanov, L.A. Kruglyakova, K.V. Pekhotin, Kinetics and mechanism of thermal decomposition of HMX with metal cup ferronate additives, Combust. Explos. Shock Waves 35 (3) (1999) 261–265.
[17] A.P. Glazkova, Catalysis of the Combustion of the Explosives, Nauka, Moscow, 1976, 264 p. (In Russian).
[18] K.J. Kraeutle, The thermal decomposition of HMX: effect of experimental conditions and of additives, in: Proc. 18th JANNAF Combustion Meeting, vol. 2, 1981, pp. 383–394.
[19] B.K. Moy, Burning Rate Studies of HMX Propellants at High Pressures, Report AFATL-TR-75-73, 1975, 27 p.
[20] R.A. Fifer, W.F. McBratney, Catalysis of Nitramine Propellants by Metal Borohydrides, Report ARBRL-MR-0330, 1983, 31 p.
[21] R.A. Fifer, J.E. Cole, Catalysts for Nitramine Propellants, US Patent 4379007, 1983.
[22] J. Duterque, G. Lengelle, Combustion mechanisms of nitramine-based propellants with additives, J. Propuls. 6 (6) (1989) 718–726.
[23] E. Kimura, Y. Oyumi, T. Yoshida, Catalytic effects of lead citrate on the HMX azide polymer propellants, J. Energ. Mater. 13 (1) (1995) 1–14.
[24] J. Prakash Agrawal, High Energy Materials: Propellants, Explosives and Pyrotechnics, Wiley-VCH Verlag, Weinheim, 2010, 495 p.
[25] M. Mahinroosta, Catalytic effect of commercial nano-CuO and nano-Fe_2O_3 on thermal decomposition of ammonium perchlorate, J. Nanostruct. Chem. 47 (3) (2013) 1–6.
[26] A. Hong-mei, L. Yun-fei, L. Yu-ping, et al., Study on catalytic combustion of HNIW monopropellant by metal oxide, Chin. J. Explos. Propell. 23 (4) (2000) 1–2.
[27] W. Zhang, L. Jie, L. Xiao-meng, et al., Effect of nano-catalysts on the thermal decomposition of aminonitrobenzodifuroxan, Chin. J. Explos. Propell. 27 (2) (2004) 48–51.
[28] W. Zhi-Xian, X. Yan-Qing, L. Hai-Yan, et al., Preparation and catalytic activities of $LaFeO_3$ and Fe_2O_3 for HMX thermal decomposition, J. Hazard. Mater. 165 (2009) 1056–1061.
[29] W. Zhi-Xian, Y. Wang, Z. Xue-Jun, et al., Combustion synthesis and effect of $LaMnO_3$ and LaOCl powder mixture on HMX thermal decomposition, Thermochim. Acta 499 (2010) 111–116.
[30] V.C. Belessi, P.N. Trikalitis, A.K. Ladavos, et al., Structure and catalytic activity of $La1-xFeO_3$ system ($x = 0.00, 0.05, 0.10, 0.15, 0.20, 0.25, 0.35$) for the NO+ CO reaction, Appl. Catal. A: Gen. 177 (1999) 53–68.
[31] J. Zhi, L. Shu-fen, Z. Feng-qi, et al., Thermal behavior of HMX and metal powders of different grade, J. Energ. Mater. 20 (2) (2002) 165–173.
[32] A. Gromov, Y. Strokova, A. Kabardin, et al., Experimental study of the effect of metal nanopowders on the decomposition of HMX, AP and AN, Propell. Explos. Pyrotech. 34 (6) (2009) 506–512.
[33] C.R. McCulloch, B.K. Moy, Composite Propellants Containing Critical Pressure Increasing Additives, US Patent 3986910, 1976, 4 p.
[34] R.H. Taylor, Controlled Burn Rate, Reduced Smoke, Solid Propellant Formulations, US Patent 5334270, 1994.
[35] V. Rodic, Effect of titanium (IV) oxide on composite solid propellant properties, Sci. Tech. Rev. 62 (3–4) (2012) 21–27.
[36] Muravyev N.V., Pivkina A.N., Frolov YuV., et al. reportA Method of HMX Burning Rate Tailoring. Patent 2441863 Russian Federation. No. 2010126771/05; ann. 01.07.2010; pubd. 10.02.2012, 8 p. (In Russian)
[37] V.P. Sinditskii, V. Yu Egorshev, M.V. Berezin, et al., Mechanism of HMX combustion in a wide range of pressures, Combust. Explos. Shock Waves 45 (4) (2009) 461–477.
[38] C.S. Turchi, D.F. Ollis, Photocatalytic degradation of organic water contaminants: mechanisms involving hydroxyl radical attack, J. Catal. 122 (1990) 178–192.

[39] S. Tojo, T. Tachikawa, M. Fujitsuka, T. Majima, Oxidation processes of aromatic sulfides by hydroxyl radicals in colloidal solution of TiO_2 during pulse radiolysis, Chem. Phys. Lett. 384 (2004) 312–316.
[40] H.A. Schwarz, R.W. Dodson, Equilibrium between hydroxyl radicals and thallium(II) and the oxidation potential of hydroxyl-(aq), J. Phys. Chem. 88 (1984) 3643–3647.
[41] P. Du, J.A. Moulijn, G. Mul, Selective photo(catalytic)-oxidation of cyclohexane: effect of wavelength and TiO_2 structure on product yields, J. Catal. 238 (2) (2006) 342–352.
[42] M.V. Mathieu, M. Primet, P. Pichat, Infrared study of the surface of titanium dioxides. II. Acidic and basic properties, J. Phys. Chem. 75 (9) (1971) 1221–1226.
[43] Y. Jiaguo, Y. Huogen, C. Bei, et al., Enhanced photocatalytic activity of TiO_2 powder (P25) by hydrothermal treatment, J. Mol. Catal. A: Chem. 253 (1–2) (2006) 112–118.
[44] R. Mueller, H.K. Kammler, K. Wegner, et al., OH surface density of SiO_2 and TiO_2 by thermogravimetric analysis, Langmuir 19 (1) (2003) 160–165.
[45] I.V. Kolesnik, Mesoporous Materials Base on Titanium Oxide (PhD thesis), Moscow State University, 2010, 25 p. (In Russian).
[46] I.P. Suzdalev, YuV. Maksimov, V.K. Imschennik, et al., Iron oxides in nano-sized state. Synthesis routes, structure and properties, Russ. Nanotechnol. 2 (5–6) (2007) 73–84 (In Russian).
[47] O.P. Korobeinichev, A.A. Paletsky, A.G. Tereschenko, et al., Combustion Chemistry of Composite Solid Propellants Based on Nitramine and High Energetic Binders, Report DAAD19-02-1-0373, 2005, 58 p.
[48] C.-J. Tang, Y.J. Lee, G. Kudva, et al., A study of the gas-phase chemical structure during CO_2 laser assisted combustion of HMX, Combust. Flame 117 (1–2) (1999) 170–188.
[49] R. Behrens, Thermal decomposition processes of energetic materials in the condensed phase at low and moderate temperatures, in: R.W. Shaw, T.B. Brill, D.L. Thompson (Eds.), Overviews of Recent Research on Energetic Materials, World Scientific Press, 2005, pp. 29–74.
[50] B.B. Goshgarian, The Thermal Decomposition of RDX and HMX, Report AFRPL-TR-78-76, 1978.
[51] NIST/EPA/NIH Mass Spectral Library with Search Program (Data Version: NIST 11, Software Version 2.0g). Available online: http://www.nist.gov/srd/nist1a.cfm#/.
[52] J. Opfermann, Kinetic analysis using multivariate non-linear regression. I. Basic concepts, J. Therm. Anal. Calorim. 60 (2) (2000) 641–658.
[53] G.V. Lisichkin, A.U. Fadeev, A.A. Serdan, et al., Chemistry of Grafted Materials, Phizmatlit, Moscow, 2011, 592 p. (In Russian).
[54] L.T. Zhuravlev, The surface chemistry of amorphous silica. Zhuravlev model, Colloids Surf. A: Physicochem. Eng. Asp. 173 (2000) 1–38.
[55] T.B. Brill, Multiphase chemistry consideration at the surface of burning nitramine monopropellants, J. Propuls. Power 11 (4) (1995) 740–751.
[56] S.A. Shackelford, B.B. Goshgarian, R.D. Chapman, et al., Deuterium isotope effects during HMX combustion: chemical kinetic burn rate control mechanism verified, Propell. Explos. Pyrotech. 14 (1989) 93.
[57] A.E. Fogel'zang, B.S. Svetlov, V.J. Adzhemjan, et al., Combustion of explosives with nitrogen-nitrogen bond, Fiz. Goreniya Vzryva 6 (1976) 827 (In Russian).
[58] I. Atwood, T.L. Boggs, Burning rate of solid propellant ingredients, Part 1: pressure and initial temperature effects, J. Propuls. Power 15 (6) (1999) 740.
[59] A.A. Zenin, S.V. Finjakov, Response functions of HMX and RDX burning rates with allowance for melting, Combust. Explos. Shock Waves 43 (3) (2007) 309.
[60] C.F. Price, T.L. Boggs, R.L. Derr, The steady-state combustion behavior of ammonium perchlorate and HMX, in: 17th Aerospace Sciences Meeting, New Orleans, 1979.
[61] N. Kubota, Propellants and Explosives: Thermochemical Aspects of Combustion, Wiley-VCH, 2002, 117.
[62] V.P. Sinditskii, V. Yu Egorshev, M.V. Berezin, Study on combustion of energetic cyclic nitramines, Zh. Khim. Fiz. 22 (4) (2003) 53 (In Russian).
[63] J.-x. Xu, Thermal decomposition behavior and non-isothermal decomposition reaction kinetics of CL-20 with leads salts as catalyst, Chin. J. Explos. Propell. (5) (2007) 36–41.

[64] C.F. Melius, Thermochemical modelling: I. Application to decomposition of energetic materials, in: S. Bulusu (Ed.), Chemistry and Physics of Molecular Processes in Energetic Materials, Kluwer, Boston, 1990, pp. 21–50.
[65] M. Kang, S.-Y. Lee, C.-H. Chung, Characterization of a TiO_2 photocatalyst synthesized by the solvothermal method and its catalytic performance for $CHCl_3$ decomposition, J. Photochem. Photobiol. A: Chem. 144 (2001) 185–191.
[66] A.A. Khassin, G.A. Filonenko, T.P. Minyukova, Effect of anionic admixtures on the copper-magnesium mixed oxide reduction, React. Kinet. Mech. Catal 101 (1) (2010) 73–83.
[67] E. Cohen-Nir, H. Sannier, A contribution to the study of decomposition and combustion of HMX. influence of some additives, Propell. Explos. Pyrotech. 10 (6) (1985) 163–169.
[68] M. Misono, Heterogeneous Catalysis of Mixed Oxides: Perovskite and Heteropoly Catalysts, in: Studies in Surface Science and Catalysis, vol. 176, Elsevier, 2013.
[69] D.V. Kozlov, A.A. Panchenko, D.V. Bavykin, et al., Influence of humidity and acidity of the titanium dioxide surface on the kinetics of photocatalytic oxidation of volatile organic compounds, Russ. Chem. Bull. 52 (5) (2003) 1100–1105.
[70] F.A. Kröger, The Chemistry of Imperfect Crystals, North-Holland Publishing Co., Amsterdam, 1964.
[71] L. Smart, E. Moore, Solid State Chemistry. An Introduction, Chapman & Hall, London, 1992, ISBN 0-412-40040-5.
[72] Y.-M. Chiang, D. Birnie III, W. David Kingery, Physical Ceramics. Principles for Ceramic Science and Engineering, John Wiley & Sons, Inc., New York, 1997, ISBN 0-471-59873-9.
[73] J. Schoonman, D. Perniu, Ovidius Univ. Ann. Chem. 25 (2014) 32–38.
[74] J. Schoonman, D. Perniu, Z. Anorg, Allg. Chem. 640 (2014) 2903–2907.
[75] J. Schoonman, Production of hydrogen with solar energy, in: R. Boehm, H. Yang (Eds.), Handbook of Clean Energy Systems in: J. Yan (Editor -in-Chief), Renewable Energy Supply, vol. 1. Wiley, 2015, ISBN 978-1-118-38858-7.
[76] R. Asahi, T. Morikawa, T. Ohwaki, K. Aoki, Y. Taga, Science 293 (2001) 269.
[77] D. Perniu, S. Vouwzee, A. Duta, J. Schoonman, J. Optoelec. Adv. Mater. 9 (2007) 1568.
[78] J.A.S. Ikeda, Y.M. Chiang, J. Am. Ceram. Soc. 76 (10) (1993) 2437.
[79] J. Maier, Progr. Solid State Chem. 23 (1995) 171.
[80] N. Sata, J. Maier, Nature 408 (2000) 946.
[81] T. Lin, C. Yang, Z. Wang, H. Yin, X. Lu, F. Huang, J. Lin, X. Xie, M. Jiang, Energy Environ. Sci. 7 (2014) 967–972.
[82] J.T.L.P. Carneiro, Application of TiO_2 Semiconductor Photocatalysis for Organic Synthesis (PhD thesis), Delft University of Technology, 2010, ISBN 978-905335-273-1.

CHAPTER TEN

Preparation, Characterization, and Catalytic Activity of Carbon Nanotubes-Supported Metal or Metal Oxide

Feng-qi Zhao[1], Jian-hua Yi[1], Wei-liang Hong[2], Ting An[1] and Yan-jing Yang[1]
[1]Science and Technology on Combustion and Explosion Laboratory, Xi'an Modern Chemistry Research Institute, Xi'an, China
[2]School of Chemistry and Chemical Engineering, Shenzhen University, Shenzhen, China

1. INTRODUCTION

Since it was discovered that the unique shape, high stability, high mechanical intensity, and high conductivity of carbon nanotubes (CNTs) make them favorable catalyst carriers, more attention has been paid to their potential applications to nano-engineering. The nanoscale catalysts can be prepared for special purpose when CNTs provide support for metals and metal oxides [1–8]. Copper (II) oxide (CuO), as a functional material, can considerably improve the ballistic performance and present the special catalytic properties on solid rocket propellants, i.e., it can increase the burning rate and decrease the burning rate pressure exponent when it is added into the propellant formulations and employed as a combustion catalyst, and the catalytic effects are especially clear for the nanoscale CuO [9–11]. Therefore, CuO/CNTs with CuO nanoparticles supported by CNTs at a high dispersion may exhibit excellent catalytic effects on the propellant combustion.

In the chapter, CNTs-supported metals or metal oxides, such as Pb/CNTs, Ag/CNTs, Pd/CNTs, NiPd/CNTs, PbO/CNTs, CuO/CNTs, Bi_2O_3/CNTs, MnO_2/CNTs, CuO·PbO/CNTs, $Cu_2O·Bi_2O_3$/CNTs, $Bi_2O_3·SnO_2$/CNTs, $Cu_2O·SnO_2$/CNTs, $NiO·SnO_2$/CNTs, and $CuO·SnO_2$/CNTs, were prepared by using CNTs and the metal salts with different methods. The effects of catalysts on the performance of energetic materials, such as nitrocellulose (NC) absorbed nitroglycerin (NG) (NC-NG), hexogen (RDX), ammonium perchlorate (AP), and N-guanylurea-dianitramide (GUDN), were investigated, and the catalytic mechanism was analyzed. Being used as combustion catalyst, CuO/CNTs, Bi_2O_3/CNTs, Pb/CNTs, NiB/CNTs, and NiPd/CNTs were explored in double-base (DB) propellants, whereas

Energetic Nanomaterials
ISBN 978-0-12-802710-3, http://dx.doi.org/10.1016/B978-0-12-802710-3.00010-6

$Bi_2O_3 \cdot SnO_2$/CNTs, CuO·PbO/CNTs, $Cu_2O \cdot Bi_2O_3$/CNTs, $CuO \cdot SnO_2$/CNTs, and $NiO \cdot SnO_2$/CNTs were explored in the composite modified double-base (CMDB) propellants.

The synergistic effect of CNTs and metal oxide nanoparticles on the decomposition reaction and combustion reveals that CuO/CNTs and CuO·PbO/CNTs have potential applications in the solid rocket propellants.

2. PREPARATION AND CHARACTERIZATION

For the preparation of the composite materials of CNTs supported active components, it is very important if there exists efficient bonding between the surface of CNTs and the precursors of the active components. Therefore, the first step is the pretreatment for CNTs, removing the impurities as the residual catalyst for preparation of CNTs, carbon particles, and amorphous carbon; at the same time, the carboxyl groups are introduced to the surface of CNTs, providing a lot of active sites for the reactions. With the high stable structure, CNTs show good resistance to strong acid and base, whereas the impurity with low stable structure possesses bad resistance to them. So, the pretreatment for CNTs is usually conducted using the technology of hydrochloric acid dipping, followed by oxidation.

There are four kinds of composite materials discussed in the chapter: CNT-supported single metal, binary metal, single metal oxide, and binary metal oxide. The first two were prepared mostly by the physical vapor deposition process, the immersion method, and the chemical plating. The latter two were obtained mostly by precipitation method.

Pb/CNTs and NiPd/CNTs were obtained by the chemical plating method. It should be noted that an activation process is required for CNTs before the plating of metal, which is similar to the chemical plating on other nonmetal materials. The chemical plating reduces the metal ions to metal particles, which are then deposited on the surface of the base materials by chemical technology without any electric current provided by the power unit. The activation is achieved by depositing some catalytic metal such as Pd on the surfaces of CNTs. The common course for the preparation of Pd/CNTs is that CNTs are immersed in $SnCl_2$ and $PdCl_2$ acid solutions, and Pd ion is reduced by Sn ion to generate the Pd nucleus. The major drawback of the method is that Sn ion can't be removed completely, thus the reducing and separating of Pd ion are affected.

A new method was developed to reduce Pd ions by polyatomic alcohol to generate Pd nucleis supported by the surface of CNTs, avoiding the intervention of Sn ion and the appearance of byproducts. The newborn Pd particles on the surface of CNTs would be the active sites for the next reaction process, i.e., the chemical plating of Pb and other metals. By using the active CNTs-supported Pd particles, Pb/CNTs and NiPd/CNTs were obtained separately with the reducing agent of $TiCl_3$ and ethylene glycol.

2.1 Pretreatment of CNTs [12,13]

Three procedures for pretreatment of CNTs are as follows:

1. Pretreatment by concentrated nitric acid. A certain amount of CNTs were soaked with HCl solution (30 mass%) for 12 h, washed, and refluxed in concentrated HNO_3 solution at a temperature for 3 h, followed by washing with distilled water until the pH value of the elution was about 7. The filter cake was filtrated, washed with deionized water, and dried in vacuum at 80 °C for several hours, and then the pretreated CNTs were obtained. The oxidation temperatures were: *a*, 100 °C; *b*, 120 °C; *c*, 140 °C.
2. Pretreatment by concentrated sulfuric acid and nitric acid. The soaked CNTs were refluxed in concentrated H_2SO_4 and HNO_3 mixture solution at 70 °C for 3 h. The mixed acid was prepared with the following volume ratios of H_2SO_4 to HNO_3: *a*, 1:1; *b*, 2:1; *c*, 3:1.
3. Pretreatment by $K_2Cr_2O_7$. The soaked CNTs were refluxed in $K_2Cr_2O_7$ solution with a volume ratio at 60 °C for some time. The oxidation durations were: *a*, 1 h; *b*, 2 h; *c*, 3 h.

Fourier transform infrared spectroscopy (FTIR) patterns for CNTs pretreated by concentrated HNO_3 at different oxidation temperatures are shown in Figure 1. From the figure, one can find that the absorbance peak intensities at 1460 cm^{-1} are different for samples with the oxidation temperature of 100, 120, and 140 °C. The intensity is strengthened from 100 to 120 °C, and changed little from 120 to 140 °C. This indicates that more carboxylic groups were created on the surface of CNTs with the increase of temperature, but one thing that should be considered is that the high temperature of

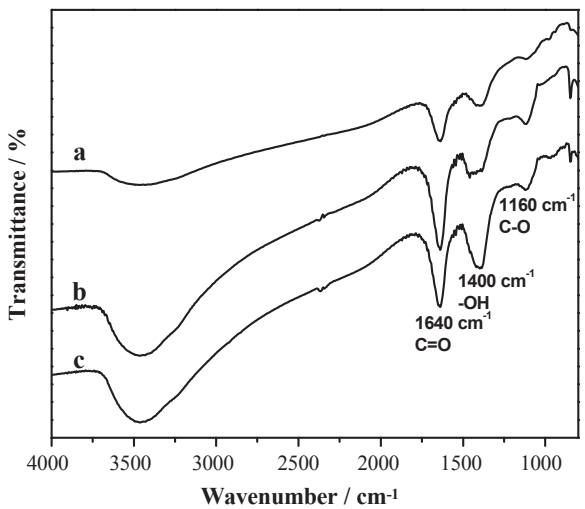

Figure 1 FTIR patterns for CNTs pretreated by concentrated nitric acid. Oxidation temperature (°C): *a*, 100; *b*, 120; *c*, 140.

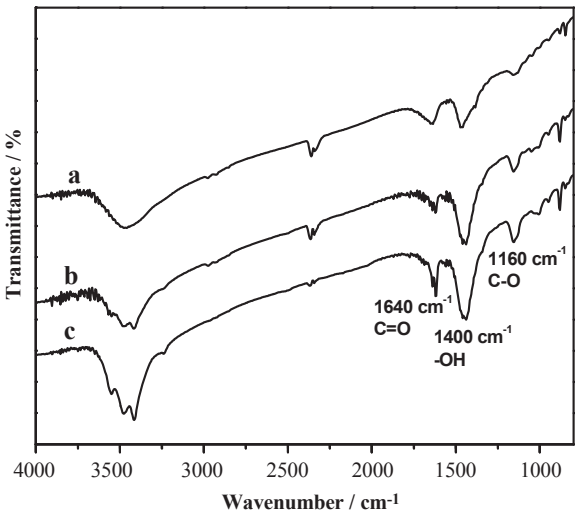

Figure 2 FTIR patterns for CNTs pretreated by concentrated sulfuric and nitric acid. $V_{H_2SO_4}$: V_{HNO_3}: *a*, 1:1; *b*, 2:1; *c*, 3:1.

140 °C will lead to the decomposition of HNO_3, which is not favorable for the oxidation of CNTs. Thus, an oxidation temperature of 120 °C was adopted.

FTIR patterns for CNTs pretreated by concentrated sulfuric and nitric acid with different volume ratios are shown in Figure 2. From it, one can find that the absorbance peak intensities at 1160 and 1640 cm^{-1} are increased remarkably with an increase in the content of sulfuric acid, and this indicates that more carboxylic groups were created on the surface of CNTs with a larger volume of sulfuric acid. Therefore, a ratio of H_2SO_4 to HNO_3 of 3:1 was used.

FTIR patterns for CNTs pretreated by potassium dichromate with a different oxidation time are shown in Figure 3. From it, one can find that the absorbance peak intensities at 1400 and 1640 cm^{-1} are also enhanced remarkably with the increase in oxidation time, and this indicates that more carboxylic groups are created on the surface of CNTs with longer oxidation time. Thus, an oxidation time of 3 h was utilized.

FTIR patterns of original CNTs (*a*) and pretreated CNTs are shown in Figure 4. CNTs were pretreated by (*b*) concentrated nitric acid, (*c*) sulfuric acid and nitric acid, and (*d*) potassium dichromate. The figure shows the appearance of the infrared (IR) bands at 3470 and 1460 cm^{-1} due to −OH stretching and flexural vibration, 1160 cm^{-1} due to C−O stretching vibration, and 1640 cm^{-1}due to C═O stretching vibration after pretreatment, indicating that there are more carboxyl, carbonyl, and hydroxide groups on the surface of CNTs after pretreatment using the three methods mentioned above. But the relative peak intensities at 1400 and 1640 cm^{-1} are distinguished with different pretreatment methods. Figure 4 shows that more carboxyl, carbonyl, and hydroxide groups are found on the

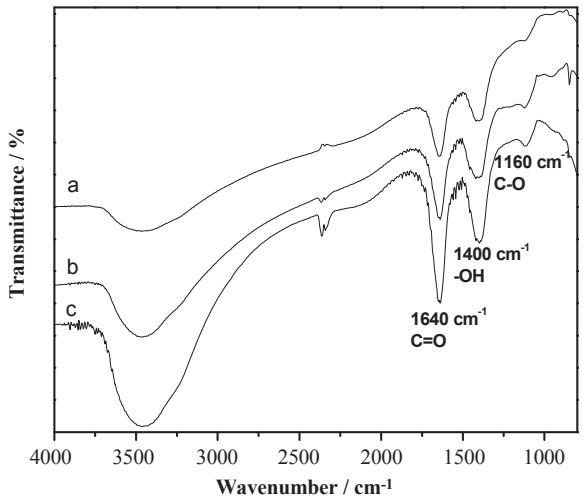

Figure 3 FTIR patterns for CNTs pretreated by potassium dichromate. (Oxidation time (h): *a*, 1; *b*, 2; *c*, 3).

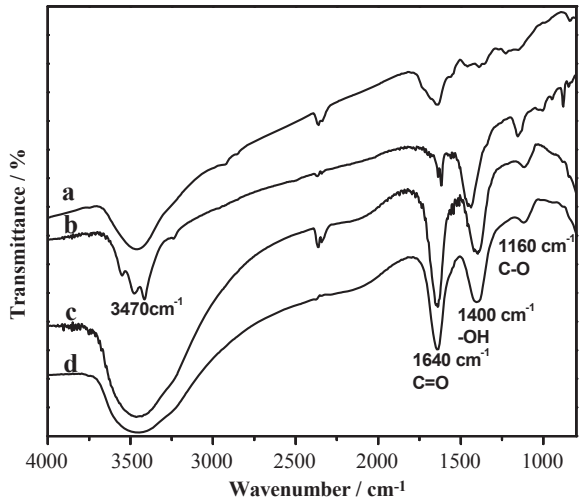

Figure 4 FTIR patterns for original CNTs: *a* and pretreated CNTs. Pretreated method: *b*, concentrated nitric acid; *c*, concentrated sulfuric and nitric acid; *d*, potassium dichromate.

surface of CNTs after pretreatment using procedures 2 and 3. The imported functional groups on the surface of CNTs provide active sites for the reaction process.

Transmission electron microscope (TEM) images for CNTs pretreated by (a) concentrated HNO_3, (b) concentrated H_2SO_4 and HNO_3, and (c) $K_2Cr_2O_7$ are shown in Figure 5. The three samples show similar morphological characteristics, their surfaces were clean and smooth, and no carbon fragments and catalyst particles were found.

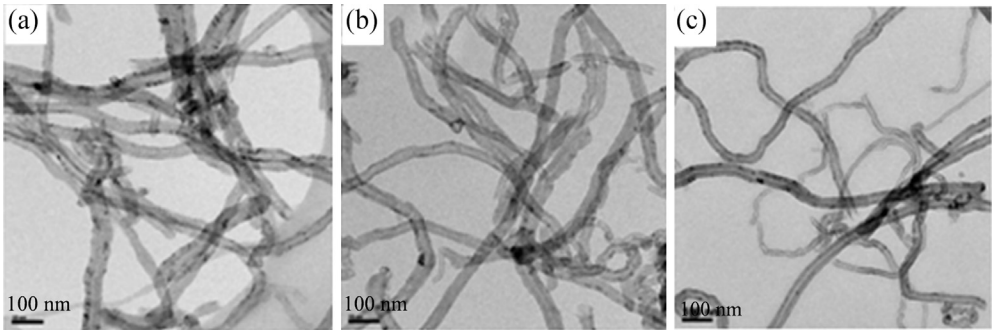

Figure 5 Transmission electron microscope (TEM) images for CNTs pretreated by (a) concentrated HNO_3, (b) concentrated H_2SO_4 and HNO_3, and (c) $K_2Cr_2O_7$.

2.2 CNTs-Supported Metal

As mentioned above, Pb/CNTs and NiPd/CNTs were obtained by the chemical plating method, and an activation process was conducted before chemical plating of CNTs. In this process of preparation, the metal ions were reduced to metal particles and deposited on the surface of the CNT directly. Pd was the suitable active metal obtained by the high-temperature (170–180 °C) reduction reaction with polyatomic alcohol. The activation reactions can be expressed as follows:

$$2CH_2OH{-}CH_2OH \rightarrow 2CH_3CHO + 2H_2O$$

$$2CH_3CHO + Pd(OH)_2 \rightarrow CH_3{-}CO{-}CO{-}CH_3 + 2H_2O + Pd$$

The newly born Pd particles on the surface of CNTs will be the active sites for the chemical plating of Pb. Pb/CNTs were obtained with the reducing agent of $TiCl_3$ and deposited on Pb nucleus. As a poisonous material to catalytic reaction, growth of Pb particles is slow, thus the depositing process on the surface of CNTs was easy to control.

As for the preparation of NiPd/CNTs, the reducing reactions of the two metal ions in the solution are correlated closely with their standard electrode potentials (SEP). For Ni ion and Pd ion, the SEP values are -0.257 and 0.915 V, respectively, therefore Pd ion can be reduced to Pd particles firstly and deposited on the surface of CNTs, providing the active sites for the next process. Ni ion will be reduced subsequently, deposited on the active sites, and then grow up. There is a strong relationship between the particle sizes and the pH values of the solutions, and the nanoparticles of NiPd on the surface of CNTs can be obtained with the suitable pH value.

2.2.1 Pd/CNTs

Palladium chloride ($PdCl_2$) was dissolved in ethylene glycol with ultrasonic treatment. The sodium hydroxide (NaOH) ethylene glycol solution with a concentration of

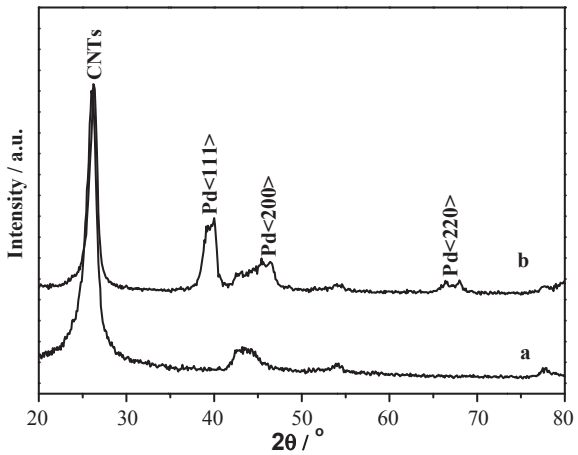

Figure 6 X-ray diffraction (XRD) patterns of *a*: pretreated CNTs and *b*: Pd/CNTs.

0.4 mol/L was added into $PdCl_2$ solution until the pH value was 8; the pretreated CNTs were then added rapidly into the sol at 170 °C and stirred for several hours, and the resultant black material was washed, filtrated, and dried in a vacuum oven at 80 °C to get Pd/CNTs.

X-ray diffraction (XRD) patterns for (*a*) pretreated CNTs and (*b*) Pd/CNTs are shown in Figure 6. The presence of the carbon phase with 2θ at 26.2° reveals the existence of the layer structure of CNTs with Pd on the surface. The strong diffraction peaks with 2θ at 39.9°, 46.4°, and 67.9° were attributed to cubic Pd. As shown in the TEM image of Pd/CNTs (Figure 7), the Pd nanoparticles on the surface of CNTs are mainly spherical with the diameter of 5–9 nm.

2.2.2 Pb/CNTs [14]

A NaOH solution was added into the chemical plating solution containing ethylene diamine tetra acetic acid (EDTA), sodium citrate, lead acetate, and titanium trichloride ($TiCl_3$); the pretreated CNTs were then added rapidly into the sol and kept stirring for 120 min at a certain temperature, and the resultant black material was washed, filtrated, and dried in a vacuum oven at 80 °C, and then Pb/CNTs was obtained.

XRD patterns of (*a*) pretreated CNTs and (*b*) Pb/CNTs are shown in Figure 8. For curve *a*, the strong diffraction peak of CNTs did not appear, but only a diffraction peak at 24.7° was detected. The strong diffraction peaks at 31.3°, 36.3°, 52.2°, and 62.2° are recognized as the characteristic peaks of cubic Pb for Pb/CNTs. The peaks at 28.6°, 31.8°, and 48.5° were recognized as quadrangle phase of PbO. The XRD determination showed that the final product is composed mainly of Pb and CNTs, although a small amount of PbO existed in the final product. Four elements (C, Pb, Pd, and Ti) were

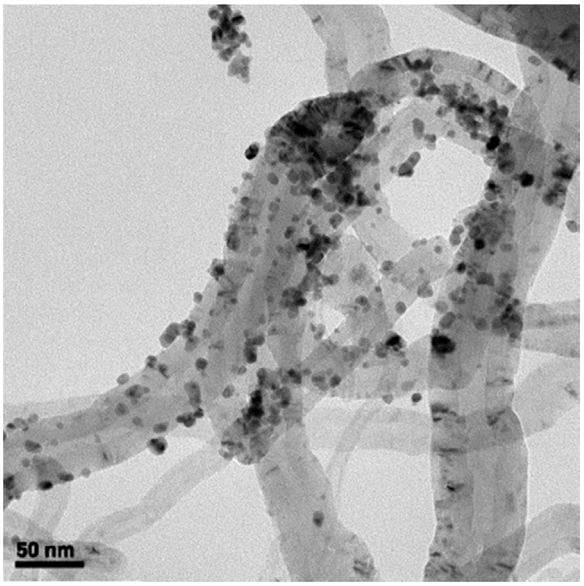

Figure 7 TEM image of Pd/CNTs.

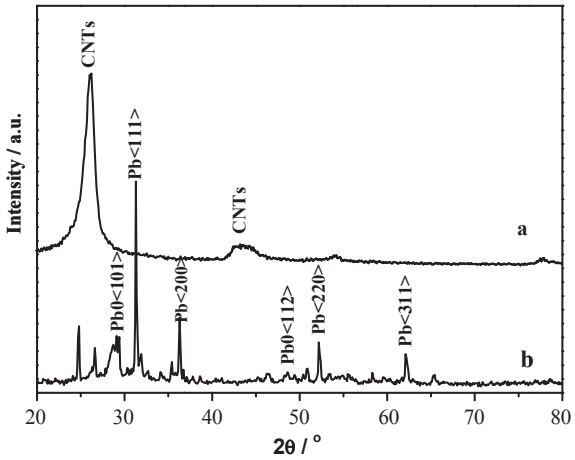

Figure 8 XRD patterns of *a*: pretreated CNTs and *b*: Pb/CNTs.

detected by energy dispersive spectrometry (EDS) analysis. Ti was imported from CNTs chemical plating process using the reducing agent $TiCl_3$.

TEM image of Pb/CNTs is shown in Figure 9. One can find that Pb particles deposited on the surface of CNTs are mainly irregular shape ones with a diameter of about 50 nm.

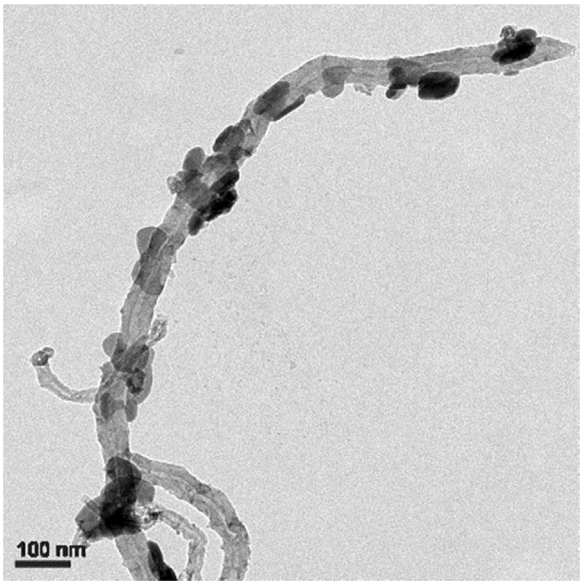

Figure 9 TEM image of Pb/CNTs.

XRD patterns of Pb/CNTs prepared with different plating times are shown in Figure 10. From the curves *a*, *b*, *c*, and *d* it was found that the diffraction peak intensities of Pb became much stronger with the plating time increased from 30 to 120 min, and the diffraction peaks of PbO and Pb_3O_4 were relatively weak. The amounts of plating Pb increased with the increase in plating time. However, the diffraction peaks of Pb became

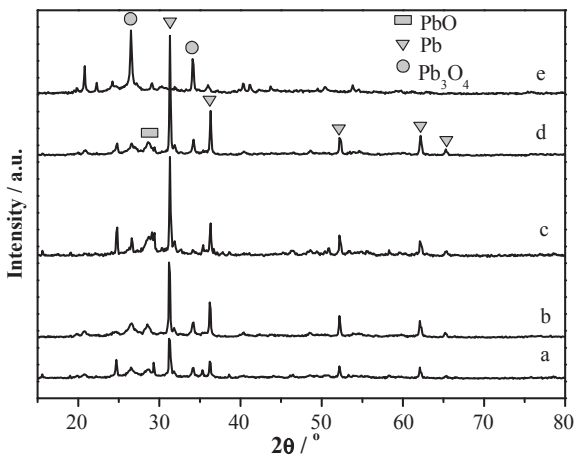

Figure 10 XRD patterns of Pb/CNTs. (Plating time in minutes: *a*, 30; *b*, 60; *c*, 90; *d*, 120; *e*, 150).

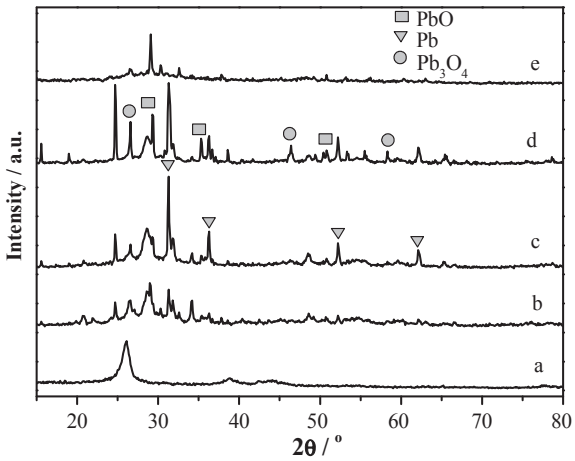

Figure 11 XRD patterns of Pb/CNTs. (pH value: *a*, 8.7; *b*, 8.9; *c*, 9.3; *d*, 9.7; *e*, 10.7).

weak and were replaced by Pb_3O_4 when the plating time was longer than 150 min (see curve *e*). The experiment shows that Pb could be oxidized to the oxide as Pb_3O_4 when the plating time was too long. Therefore, the plating time of 120 min is optimal for Pb plating on the surface of CNTs.

XRD patterns of Pb/CNTs prepared with different pH values are shown in Figure 11. As curve *a* shows, only the diffraction peak of CNTs appeared on the curve when pH value was 8.7, indicating that the plating did not occur. As curve *b* shows, diffraction peaks of Pb, PbO_x (PbO or Pb_3O_4) appeared on the curve when pH value was 8.9. But as curve *c* shows, the major peaks belong to Pb when pH value was 9.3, and the diffraction peaks of PbO_x are very weak. When pH value was higher than 9.7, the peak intensities of Pb would decrease and almost disappeared, and only the peaks of PbO_x existed on the curve. The results indicate that pH value has a strong effect on the plating component. The suitable pH value is near 9 within a narrow range, the optimal plating was carried out when pH value was less than 9 because Pb was easily oxidized at pH value exceeding 9.

XRD patterns of Pb/CNTs prepared with different plating temperatures are shown in Figure 12. From the curves, it was found that the suitable plating temperature was 60 °C, and Pb was easily oxidized to generate PbO on the surface of CNTs when the plating temperature was higher than 60 °C.

2.2.3 NiPd/CNTs

Palladium chloride ($PdCl_2$) and nickel acetate [$Ni(AC)_2 \cdot 4H_2O$] with a molar ratio of 1:1 were dissolved in ethylene glycol. The pretreated CNTs were added rapidly into the solution and dispersed with ultrasonic treatment. NaOH ethylene glycol solution with a concentration of 0.4 mol/L was added into the above solution, which was then stirred at

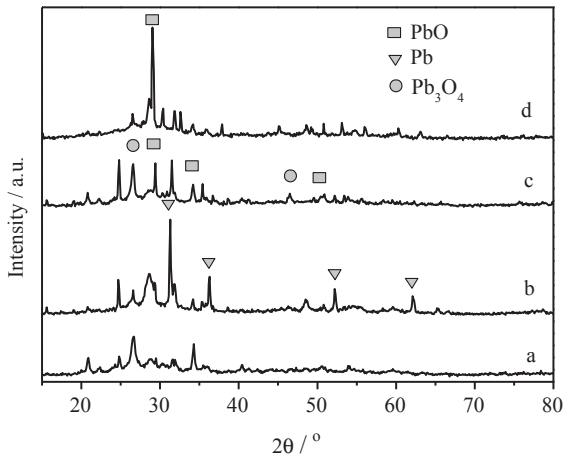

Figure 12 XRD patterns of Pb/CNTs. (Plating temperature in °C: *a*, 55; *b*, 60; *c*, 70; *d*, 90).

170 °C for several hours. The black material in solution was washed, filtrated, and dried in vacuum at 80 °C, and thus NiPd/CNTs were obtained.

TEM results of NiPd/CNTs showed that NiPd alloy on the surface of CNTs are mainly spherical particles with a diameter of 10–20 nm, and the agglomeration of NiPd particles was found. The Ni to Pd atom number ratio in NiPd/CNTs is 30:1, which was determined by electron spectrometer.

XRD patterns of NiPd/CNTs (*a*) and pretreated CNTs (*b*) are shown in Figure 13. The presence of the carbon phase with 2θ at 26.2° reveals the existence of the layer structure of CNTs. The strong diffraction peaks with 2θ at 44.3°, 51.8°, and 76.4° were recognized as the characteristic values of cubic Ni.

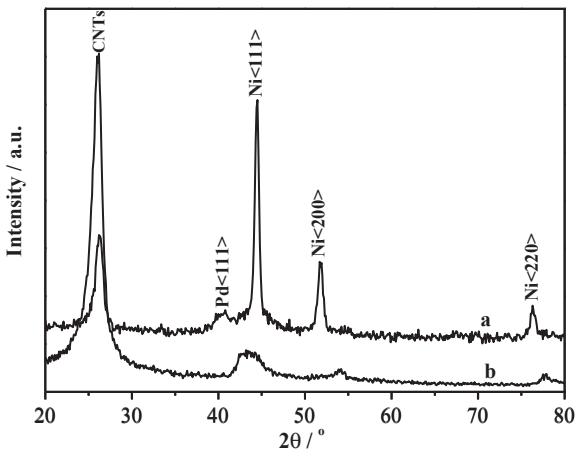

Figure 13 XRD patterns of NiPd/CNTs (a) and pretreated CNTs (b).

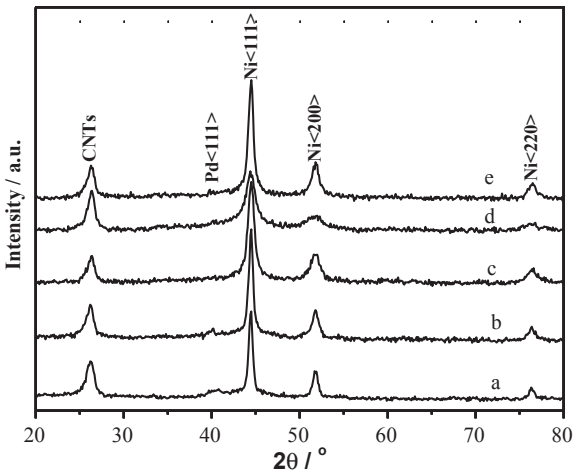

Figure 14 XRD patterns of NiPd/CNTs, pH value: *a*, 5.7; *b*, 7.7; *c*, 8.4; *d*, 10.0; *e*, 10.6.

XRD patterns of NiPd/CNTs prepared with different pH values are shown in Figure 14. From the comparison of the five curves in the figure, a weak peak at 40.1° originating from Pd exists, and its weak intensity was caused by the low content of Pd compared with Ni. The crystallite sizes of Ni particles on the surface of CNTs with different pH values were calculated as (*a*) 17.9, (*b*) 16.5, (*c*) 12.0, (*d*) 10.2, and (*e*) 14.4 nm by applying Scherrer's equation. The particle size of NiPd alloy on the surface of CNTs decreased gradually with the increase in pH value when it was lower than 9, however, an opposite trend was observed when the pH value was higher than 10. The suitable pH value was determined to locate between 9 and 10.

2.2.4 Ag/CNTs

Ag/CNTs [15] can be obtained via two methods, i.e., the silver-mirror method and the hydrothermal method. The details of these two methods are listed as follows.

Silver-mirror method: the pretreated CNTs were added to the Tollen reagent, into which formaldehyde was then introduced. After the reaction ended, filtration was conducted on the solution to get the solid, which was then washed with deionized water until the pH value reached 7. After desiccation of the solid, the final product obtained was a black powder.

Hydrothermal method: the aqueous ammonia was added drop by drop to an $AgNO_3$ solution until it became transparent. Afterwards, both CNTs and a polyvinylpyrrolidone solution were added to it. After being thoroughly ultrasonically dispersed, the solution was loaded into a hydrothermal reactor for 36 h. After completion of the reaction, filtration was conducted on the solution and the resultant solid was washed with deionized water until the pH value became 7. The final product, a black powder, was obtained after desiccation of the solid.

FTIR measurements were conducted on Ag/CNTs samples. The samples prepared by using different methods share have identical IR characteristics. FTIR bands at 3400 and 1630 cm^{-1} originating from the stretching and bending mode of −OH in H_2O as well as the characteristic band of C−O in CO_2 at 2360 cm^{-1} were observed. It was believed that Ag/CNTs prepared by using different methods contained some water. Indeed, the low relative intensity of the characteristic signal of H_2O suggested its low contents, although KBr used for FTIR tests is also hydrophilic.

Actually, the FTIR spectra of Ag/CNTs are similar to those of the pristine CNTs, and the characteristic IR bands of metallic Ag near 400 cm^{-1}, although unlikely to be easily recognizable, also exist. Therefore, the above FTIR results suggest that Ag/CNTs samples are mainly composed of Ag and CNTs.

XRD measurements were also conducted on Ag/CNTs as shown in Figure 15. The diffraction peaks at 25.84° and 44.14° for the sample prepared using silver-mirror method were believed to originate from the (002) and (101) planes of graphite, and the corresponding peaks were detected with 2θ at 25.94° and 44.26° for the sample obtained through the hydrothermal method. These results indicated the existence of layer structure in the composite. However, in comparison with the sample prepared by using the hydrothermal method, these two peaks were broadened for the composite prepared by using the silver-mirror method. This phenomenon is believed to be due to the difference in reaction conditions characterizing these two methods.

Additionally, the diffraction peaks from metallic Ag were detected for both composites. On the composite pattern obtained by using the silver-mirror method, peaks from cubic Ag (04–0783) with 2θ at 37.92°, 44.14°, 64.32°, and 77.24° (corresponding to the (111), (200), (220), and (311) planer, respectively) were observed. As for the

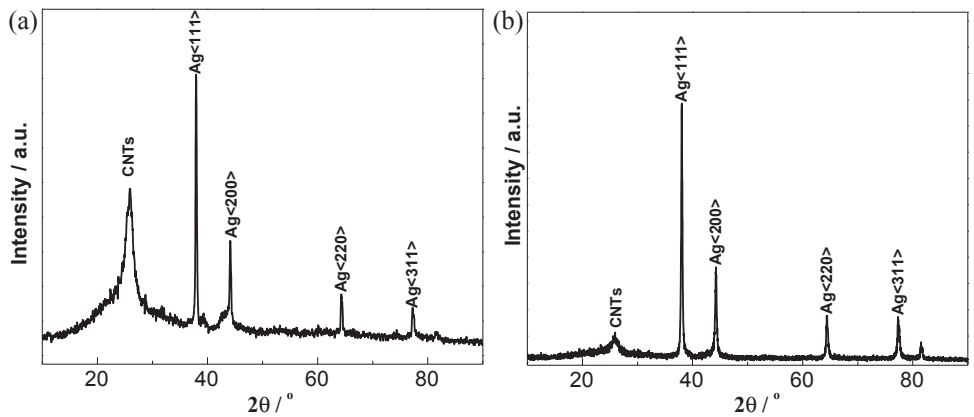

Figure 15 XRD patterns of Ag/CNTs prepared by using different methods: (a) silver-mirror method and (b) hydrothermal method.

Table 1 Phase contents and grain sizes of Ag of Ag/CNTs.

System	PDF No.	Chemical formula	Mineral name	Phase Content, %	Size of nano Ag/nm
A (silver-mirror)	04-0783	Ag	Silver-3C	62.8	29.3
	41-1487	C	Graphite	37.2	
B (hydro-thermal)	04-0783	Ag	Silver-3C	91.9	35.4
	41-1487	C	Graphite	8.1	

sample obtained by using the hydrothermal method, the corresponding peaks were detected with 2θ at 38.04°, 44.26°, 64.38°, and 77.30°. No diffraction peaks from other substances were detected. The above results imply that the Ag/CNTs were composed of CNTs and cubic Ag.

Based on the Scherrer's equation, the crystal sizes of metallic Ag in Ag/CNTs were calculated by using the (111) and (200) diffraction peaks and listed in Table 1. The phase contents of the composites are also provided in Table 1.

Obviously, the grain sizes of metallic Ag are different for the composites prepared by different methods. This is believed to be due to the different reaction conditions for these two methods.

Scanning electron microscope-energy dispersive spectrometry (SEM-EDS) measurements were conducted on Ag/CNTs. Irregular Ag particles with diameters of 10–80 nm are observed on the surfaces of CNTs, thus forming the Ag/CNTs. It should be noted that the Ag particles prepared by using hydrothermal method are larger than the ones obtained by using the silver-mirror method due to the higher temperature and pressure characterizing hydrothermal method.

EDS measurement on the pretreated CNTs showed the absence of element O, suggesting that there was no hydroxyl, carboxyl, and carbonyl on the surfaces of CNTs. As for the Ag/CNTs, only C and Ag were detected. The contents of C and Ag in the composites prepared by using silver-mirror and hydrothermal methods were approximate 88 and 12 wt%, and 61 and 39 wt%, respectively.

Brunnauer–Emmet–Teller (BET) measurements revealed the larger specific surface area of Ag/CNTs than that of the pristine CNTs. This phenomenon is due to the depressed agglomeration of Ag particles in the presence of CNTs as supporter.

2.3 CNTs-Supported Metal Oxides

2.3.1 CuO/CNTs [16,17]

Cupric acetate [$Cu(OAc)_2$] and sodium hydroxide (NaOH) with a molar ratio of 1:2 were dissolved in ethylene glycol, respectively. The NaOH solution was added dropwise into the $Cu(OAc)_2$ solution, and copper (II) hydroxide sol was prepared. Then, the

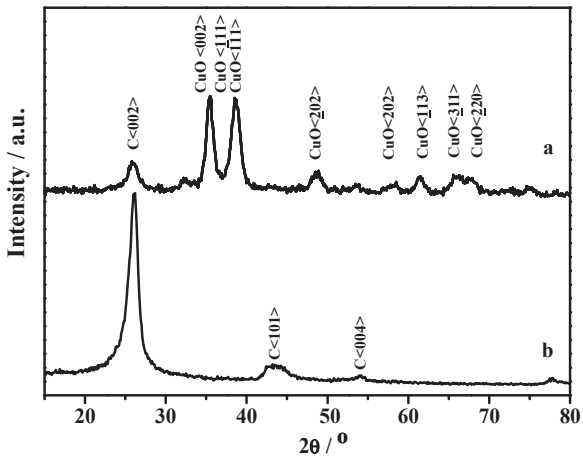

Figure 16 XRD patterns of *a*: pretreated CNTs and *b*: CuO/CNTs.

pretreated CNTs were added rapidly into the sol, which was stirred at 100 °C for several hours, and then the distilled water was dropped into the above mixture, which was refluxed at 100 °C for several hours. Finally, the black material was washed, filtrated, and dried in a vacuum oven at 80 °C, and then CuO/CNTs were obtained.

The XRD patterns of the pretreated CNTs and CuO/CNTs are shown in Figure 16. The diffraction peak at 26.2° indicates the presence of CNTs. The strong diffraction peaks with 2θ at 35.4°, 38.5°, 48.8°, 58.5°, 61.4°, 66.1°, and 68.1° were recognized as the characteristic peaks of orthorhombic CuO. Therefore, CuO/CNTs is a material composed of CNTs and CuO nanoparticles. The crystallite size of CuO supported by the surface of CNTs was calculated to be 9.3 nm by applying Scherrer's equation.

TEM images of the pretreated CNTs are shown in Figure 17(a), which indicate that CNTs pretreated by hydrochloric acid and nitric acid hardly contain any impurity and

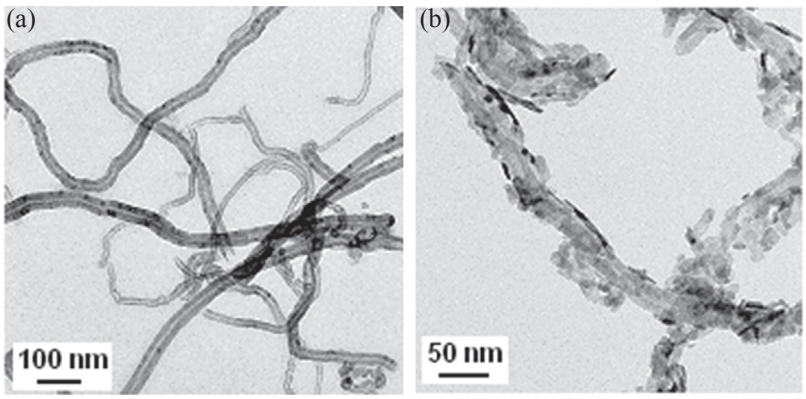

Figure 17 TEM images of (a) pretreated CNTs and (b) CuO/CNTs.

Table 2 Data on the Cu content in catalyst determined by ICP-MS.

Sample	Cu content (mass ratio, %)	Cu conversion (mass ratio, %)
Pretreated CNTs	0.30	–
Cat-1	23.7	95.2
Cat-2	36.9	85.6
Cat-3	41.0	92.4
Cat-4	50.7	89.0

show a smooth appearance. From Figure 17(b), one can clearly see that the CuO nanoparticles supported by the surface of CNTs are mainly oblate with the length of 8–10 nm, and occasionally rod-like with the length of 50 nm and diameter of 5 nm. Thus, the TEM results are in agreement with the values calculated by Scherrer's equation.

The concentration of cupric acetate in precursor solutions was varied in order to investigate the influence of the amount of cupric acetate on formation of CuO on CNTs. CuO/CNTs with different content of CuO were numbered as: Cat-1, Cat-2, Cat-3, and Cat-4, and the corresponding mole ratios of cupric acetate to CNTs were 1.3:1, 2.5:1, 3.8:1, and 5.0:1. All of the samples were treated by incineration–acidolysis process before the copper content in each sample was determined by inductively coupled plasma mass spectrometry (ICP-MS), the results were listed in Table 2. It is shown that the pretreated CNTs still contain 0.3% Cu (mass ratio), because a copper catalyst was employed during the preparation process of CNTs. From Table 2, one can find that the conversion efficiencies of cupric acetate to copper oxide for different CuO/CNTs composites were determined to be of 85.6–95.2%. The mass ratios of CuO can be calculated based on the Cu content as: Cat-1, 26.6%; Cat-2, 39.9%; Cat-3, 47.9%; and Cat-4, 53.3%.

The XRD patterns of Cat-1 ~ Cat-4 are shown in Figure 18. It was found that the intensities of both the CNTs d_{002} diffraction peak located at 26.2° and CuO d_{111} diffraction peak located at 38.5° changed significantly with the increase in cupric acetate concentrations, the former peak was weakened gradually and the latter was strengthened simultaneously, due probably to the increase in the amount of CuO supported by the surface of CNTs from Cat-1 to Cat-4. The crystal sizes of CuO particles were calculated by Scherrer's equation with the half–height width corresponding to the CuO (111) peak: Cat-1, 9.5 nm; Cat-2, 9.5 nm; Cat-3, 9.3 nm; and Cat-4, 8.8 nm. It is seen that the grain size of CuO supported by CNTs hardly changes with the increase in the cupric acetate concentration.

2.3.2 PbO/CNTs

$Pb(OAc)_2 \cdot 3H_2O$ (0.5 g) was dissolved in water to get a transparent solution, and then 0.3 g CNTs was introduced to it [18]. Having been subjected to ultrasonic dispersion, the solution was magnetically stirred at 50 °C for 3 h. Aqueous ammonia was utilized to

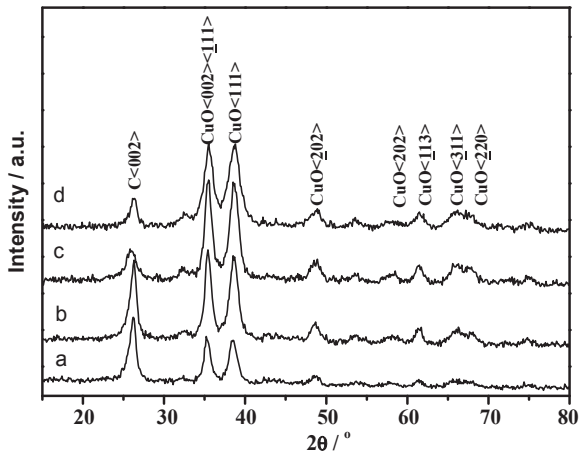

Figure 18 XRD patterns of CuO/CNTs: *a*, Cat-1; *b*, Cat-2; *c*, Cat-3; and *d*, Cat-4.

modify the pH value of the solution to 9.45, followed by stirring for another 4 h. After that, filtration was conducted of the solution to get the solid, which was washed with deionized water and ethanol twice and once, respectively, and then dried at 60 °C. The final product of PbO/CNTs was obtained by heat-treating the dried solid at 250 °C for 2 h under N_2 environment.

Figure 19 shows the XRD pattern of PbO/CNTs, which was heat–treated at 300 °C. A diffraction peak at 26° from CNTs was detected. In addition, diffraction peaks with 2θ at 29.09°, 37.82°, 48.83°, and 68.82° from rhombic PbO and peaks from metallic Pb at 31.31°, 36.27°, 52.23°, 62.12°, and 65.24° were observed. In addition, overlapped peaks of PbO and Pb were also observed near 28.610° and 31.843°.

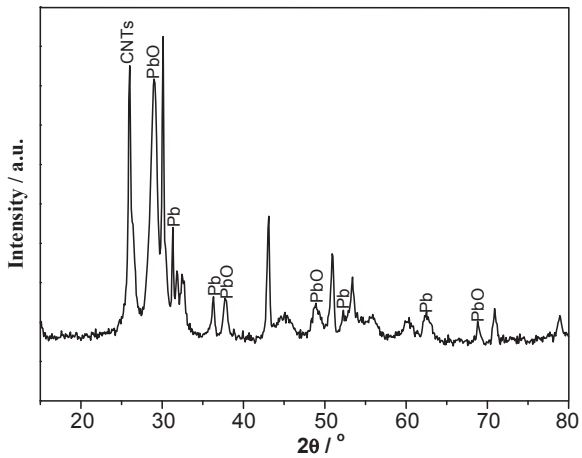

Figure 19 XRD pattern of PbO/CNTs.

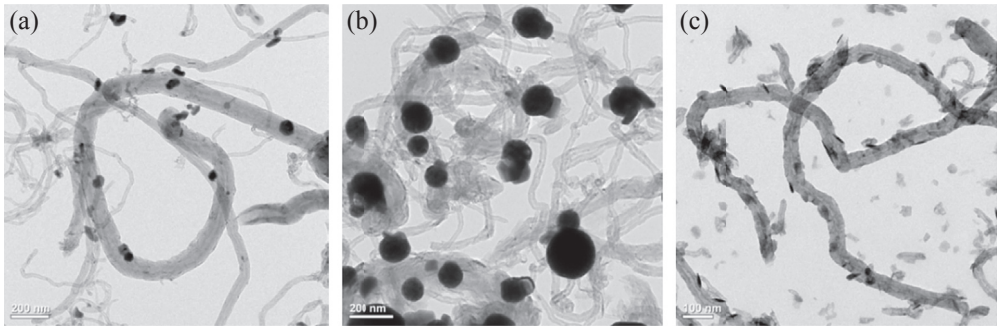

Figure 20 TEM images of PbO/CNTs prepared with different pH value of the solution. (pH value: (a) 8.0; (b) 9.0; (c) 9.45).

The XRD results indicate the existence of Pb in the PbO/CNTs, which is believed to be due to the reduction of PbO to generate metallic Pb on CNTs. It was also found that almost all the PbO could be reduced to form Pb at a heat-treatment temperature of 400 °C. Therefore, the optimal heat-treatment temperature is determined to be 250–300 °C.

The influences of pH on the preparation of PbO/CNTs were also investigated. TEM images of Pb/CNTs prepared by using solutions with different pH value are shown in Figure 20. As exhibited in Figure 20(a), only a few PbO particles with diameters of approximately 45 nm are supported by surfaces of CNTs when pH value is 8.0. As for the sample obtained by using the solution with a pH value of 9.0 (Figure 20(b)), numerous large size (100–200 nm) spherical particles are observed on surfaces of CNTs. Interestingly, when the pH value is further increased to 9.45, plenty of small peg-like particles with sizes of approximately 10 nm are observed to compose with CNTs. Obviously, the pH of solution is critical for the preparation of PbO/CNTs. The pH value of 8.0 is too low for the massive production of $Pb(OH)_3$, which is the precursor for the preparation of PbO. Thus, only a small amount of oxide was obtained when pH was 8.0. On the other hand, a pH value of 9.0 leads to the formation of large size PbO particles. When the pH value of solution is 9.45, $Pb(NO_3)_3$ hydrolyzes to form the $Pb(OH)_3$ gel that covers the surfaces of CNTs evenly. Therefore, the optimal pH value for the preparation of PbO/CNTs is 9.45.

EDS was adopted to further characterize the compositions of PbO/CNTs. The four elements C, O, Pb, and Cu were detected. It should be noted that the signal of Cu originated from the copper network which used for supporting samples. The EDS results confirm that the composite is composed of PbO and CNTs.

2.3.2 Bi_2O_3/CNTs

$Bi(NO_3)_3 \cdot 5H_2O$ (0.21 g) was dissolved in solvent to get a solution, into which 0.1 g of CNTs was then added [19]. After that, the solution was stirred for 30 min, during which

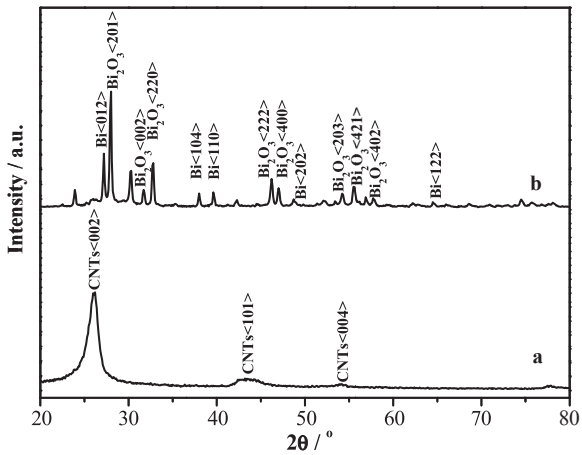

Figure 21 XRD patterns of the pretreated CNTs: *a* and Bi_2O_3/CNTs: *b*.

ammonia solution or NaOH solution was added slowly to get a pH value of 9–10. Finally, the solution was subjected to filtration to get the solid residues, which were then dried and heat-treated at 300 °C to get the resultant product.

Figure 21 shows the XRD patterns of CNTs (a) treated in a mixture of concentrated sulfuric acid and nitric acid and Bi_2O_3/CNTs (b). It is observed that the d_{002} peak from graphite is very weak. On the other hand, diffraction peaks at 27.97°, 31.71°, 32.76°, 46.21°, 47.00°, 54.22°, 55.55°, and 57.77°, which were attributed to the (201), (002), (220), (222), (400), (203), (421), and (402) peaks of tetragonal Bi_2O_3 (65–1209), respectively, were detected. In addition, the diffraction peaks were detected at 27.195°, 37.995°, 39.634°, 48.734°, and 64.559° attributed to the (012), (104), (110), (202), and (122) peaks of the rhombohedral Bi (44–1246), respectively. The above results suggest that the obtained Bi_2O_3/CNTs contain some elemental Bi.

TEM image of Bi_2O_3/CNTs is shown in Figure 22. It is seen that the Bi_2O_3 balls with diameters of 30–50 nm are located on the surfaces of CNTs. Four elements including C, O, Bi, and Cu were detected by using EDS. It should be noted that the signal of Cu element originated from the copper network adopted for TEM tests.

The influence of solvent on the morphologies of Bi_2O_3 nanoparticles was also investigated. It was found that the morphologies and dispersity of Bi_2O_3 nanoparticles supported on the surface of CNTs varied with the solvents used. When ethylene glycol and NaOH were used as the solvent and precipitant, the Bi_2O_3 nanoparticles are rod shaped with the diameter of 10 nm and the length of 50–100 nm. In addition, the distribution of Bi_2O_3 nanoparticles on the surfaces of CNTs is not homogeneous. However, when dimethyl formamide (DMF) was used as the solvent and NaOH as the precipitant, the shapes of the resultant Bi_2O_3 nanoparticles were spherical or spheroidal

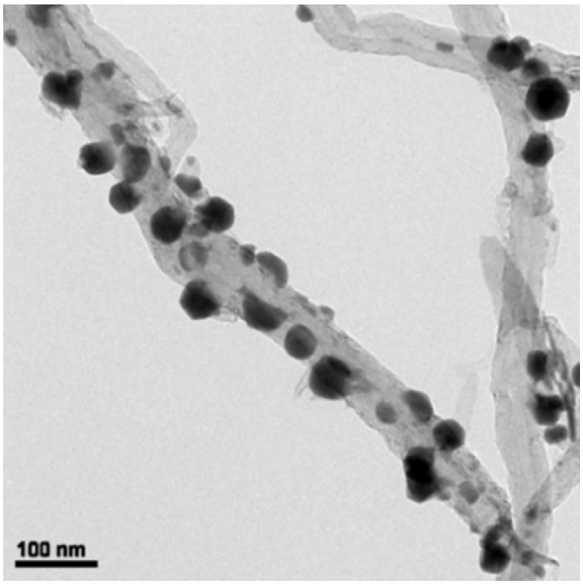

Figure 22 TEM image of Bi_2O_3/CNTs.

with diameters from 10 to dozens nanometers, and agglomeration of the particles was also observed. As for Bi_2O_3/CNTs in the case of using H_2O as the solvent and NaOH as the precipitant, uniformly distributed Bi_2O_3 nanospheres with diameters of 60–100 nm were obtained. Whereas for the sample prepared by using H_2O as the solvent and ammonia solution as the precipitant, 30–50 nm spherical Bi_2O_3 supported by the surfaces of CNTs were produced with uniform distribution and high loading rate. The above results imply that adopting water as the solvent and ammonia water as the precipitant is favorable for obtaining small Bi_2O_3 particles with the uniform distribution of its precursors supported by CNTs.

Figures 23 and 24 show the TEM images and XRD patterns of Bi_2O_3/CNTs prepared with heat treatment under different temperatures, respectively. As shown in Figure 23(a), the Bi_2O_3 particles were spherical with diameters of 20–30 nm after heat treatment at 300 °C. On their XRD pattern (Figure 24), a bump between 25° and 35° was detected, indicating the amorphous nature of Bi_2O_3. As for the product heat-treated at 400 °C, spherical Bi_2O_3 particles were also obtained, although with slightly larger diameter of 30–50 nm. The corresponding XRD test indicates that the Bi_2O_3 nanoparticles are contaminated by some Bi produced by the reduction reaction between Bi_2O_3 and C. When the heat treatment temperature was further increased to 500 °C, the diameters of the nanoparticles were also increased to 50–100 nm. In addition, the particles were determined to be mainly composed of Bi, with a small amount of Bi_2O_3. It is concluded that both the sizes and compositions of the

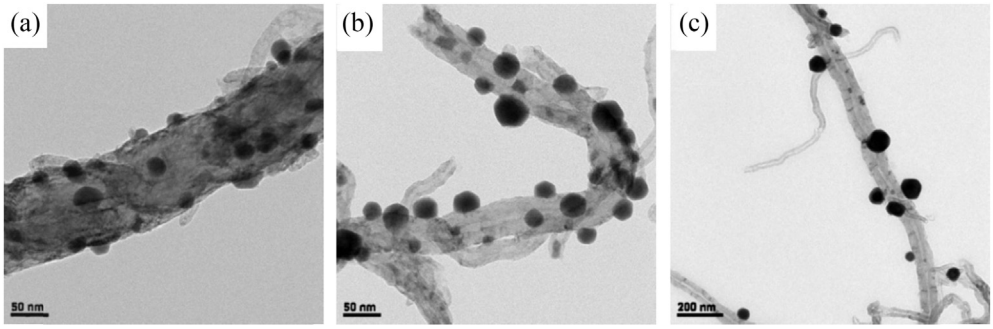

Figure 23 TEM images of Bi_2O_3/CNTs heat-treated at 300 °C (a), 400 °C (b), and 500 °C (c).

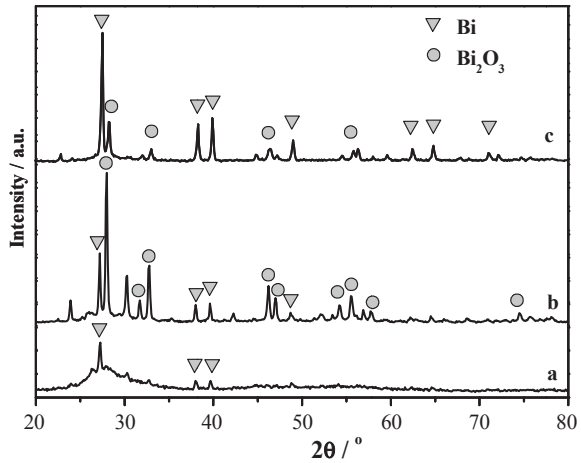

Figure 24 XRD patterns of Bi_2O_3/CNTs heat-treated at 300 °C: *a*, 400 °C: *b*, and 500 °C: *c*.

Bi-containing particles are closely related to the heat treatment temperature. With the increase in the heat treatment temperature, the crystallinity of the particles supported by CNTs improves and their sizes increase. In addition, more Bi_2O_3 could be reduced to be Bi at higher heat treatment temperatures. The best heat treatment temperature is believed to be 400 °C because when the temperature is too high (for example, 500 °C), most of the Bi_2O_3 would be reduced to Bi.

2.3.4 MnO_2/CNTs [20]

The CNTs utilized here were pretreated using a mixture of potassium permanganate and sulfuric acid solutions as described in Section 2.1. It is well known that CNTs are comprised of carbon six-membered rings without unsaturated bonds. However, upon treatment with a mixture of potassium permanganate and sulfuric acid solutions, the

structure of CNTs is changed. It is believed that the following reactions occur during the purification process:

$$3C + 4MnO_4^- + 4H^+ = 4MnO_2 + 3CO_2 + 2H_2O$$

$$Fe + MnO_4^- + 4H^+ = 4MnO_2 + Fe^{3+} + 2H_2O$$

$$3FeS + 7MnO_4^- + 16H^+ = 7MnO_2 + 3Fe^{3+} + 3SO_2 + 8H_2O$$

There are some carbon five- and seven-membered rings on the end caps of CNTs, which are relatively unstable in comparison with the six-membered rings. Therefore, the end caps of CNTs could be opened through oxidation of the mixture of potassium permanganate and sulfuric acid solutions on carbon five- and seven-membered rings. In the meantime, the amorphous carbon, graphite, and catalyst particles were also involved in the oxidation reactions. As a result, upon the treatment of the mixture of potassium permanganate and sulfuric acid solutions, MnO_2/CNTs was obtained.

From the FTIR measurements one can find that a blue shift of the characteristic absorption band of the Mn—O bond from 530 to 551.1 cm^{-1} was observed, originating from the nanosized effect. Moreover, blue shifts for the O—H stretching mode at 3353.4 cm^{-1} and bending mode at 1547.5 cm^{-1} were also observed due to the fact that MnO_2 absorbs moisture.

As shown in Figure 25, XRD measurements were also conducted on MnO_2/CNTs. The diffraction peaks from CNTs with 2θ at 26.52° and 44.66° are observed. In addition, the broadened XRD peaks at 21.38°, 35.64°, 40.87°, and 65.42°, which originate from the orthorhombic γ-MnO_2, are recognizable. In addition, the diffraction peaks from β-MnO_2 are detected at 37.36° and 54.45°. The diffraction peaks from both γ-MnO_2 and β-MnO_2 are relatively weak and broadened indicating small grain

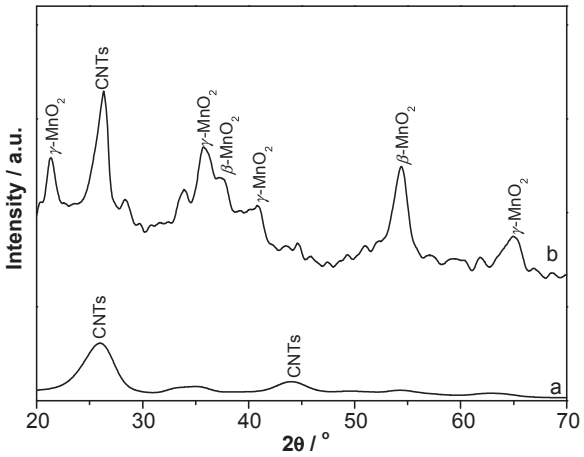

Figure 25 XRD patterns of CNTs: *a* and MnO_2/CNTs: *b*.

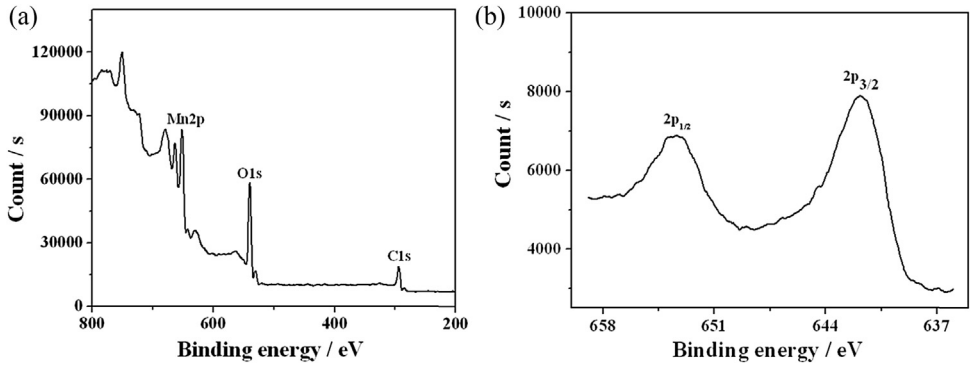

Figure 26 XPS spectra of C 1s, O 1s, and Mn 2p for MnO_2/CNTs (a) and high-resolution spectrum of Mn 2p (b).

sizes of MnO_2 and the existence of many crystal defects in them. The XRD results imply that the MnO_2 particles are mainly composed of γ-MnO_2.

Figure 26(a) shows the X-ray photoelectron spectroscopy (XPS) spectra of MnO_2/CNTs, and the C 1s, O 1s, and Mn 2p peaks were observed confirming the existence of C, O, and Mn. Furthermore, the mass contents of C, O, and Mn were determined to be 29%, 49%, and 22%, respectively, based on the XPS analysis on the surfaces of MnO_2/CNTs. The content of MnO_2 in the composite was evaluated to be 64.44% using an atomic absorption spectrophotometer. Therefore, the content of MnO_2 in the tubes of CNTs is 29%.

Figure 26(b) shows the high-resolution spectrum of Mn 2p for MnO_2/CNTs. Two peaks at 641.7 and 653.47 eV with an energy difference of 11.77 eV were detected and attributed to the Mn $2p_{2/3}$ and Mn $2p_{1/2}$ signals, respectively. The chemical states of Mn 2p indicate that Mn exists in the form of MnO_2. Moreover, the location of Mn $2p_{2/3}$ peak at 641.7 eV suggests that the main phase of MnO_2 is the γ phase, further confirming the XRD results.

TEM was utilized to characterize the morphology of CNTs and MnO_2/CNTs, as shown in Figure 27. It is revealed that the surfaces of CNTs are smooth whereas the

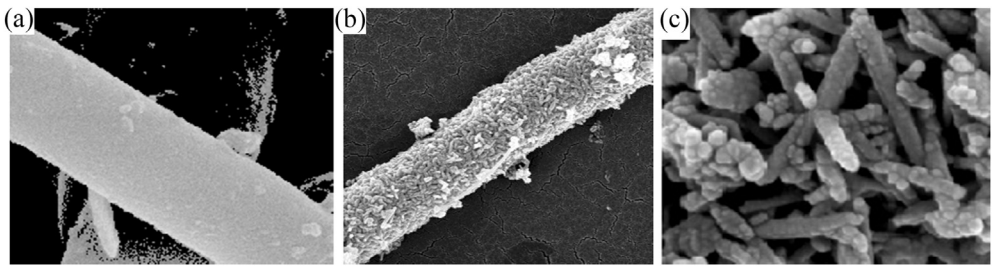

Figure 27 TEM images of CNTs (a) MnO_2/CNTs particles (b), and MnO_2 coated on the surfaces of CNTs (c).

surfaces of CNTs in MnO_2/CNTs are rather rough due to the existence of peg-shaped MnO_2 on their surfaces.

2.4 CNTs-supported Metal Oxide Composite

2.4.1 CuO·PbO/CNTs

$Cu(NO_3)_2 \cdot 3H_2O$ and $Pb(NO_3)_2$ were dissolved in deionized water [21]. The pretreated CNTs were added into the solution, which was then subjected to ultrasonic dispersion for 30 min. After stirring at room temperature for 5 h and standing for another 4 h, the pH value of the solution was modified to be 8.5 using a 2.5 wt% aqueous ammonia followed by standing for another 5 h. Filtration was conducted to get the solid, which was washed with deionized water and ethanol twice and once, respectively, and dried at 60 °C. The dried solid was heat-treated at 280 °C for 2 h to get the final product of CuO·PbO/CNTs.

XRD measurement was conducted on CuO·PbO/CNTs as shown in Figure 28. On the XRD pattern of CuO·PbO/CNTs, the diffraction peaks from monoclinic CuO (45–0937) with 2θ at 35.49°, 38.52°, 48.90°, and 61.49° (originating from the diffraction of the (002), (11̄1), (111), and (202) planes, respectively) are detected and the peaks at 19.27°, 30.74°, 52.61°, and 56.09° are believed to originate from the diffraction of the (001), (101), (112), and (211) planes of PbO, respectively. Note that the diffraction peaks from CNTs in the composite are significantly weakened compared with the pristine CNTs, which is believed to be due to CNTs in the composites being covered by CuO and PbO.

Figure 29 shows the TEM image of CuO·PbO/CNTs. A lot of spherical CuO and PbO particles with diameters of approximately 20 nm are observed. These particles are distributed evenly on the surfaces of CNTs.

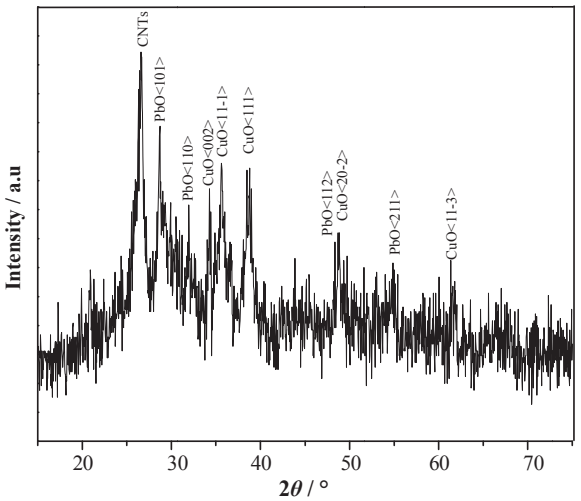

Figure 28 XRD pattern of CuO·PbO/CNTs.

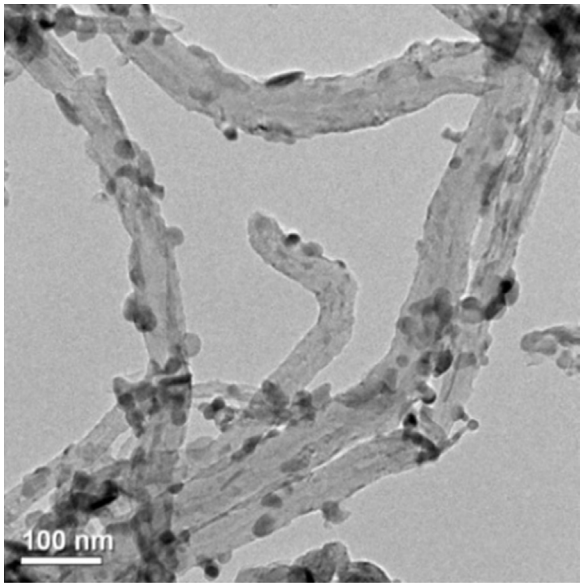

Figure 29 TEM image of CuO·PbO/CNTs.

EDS was utilized to further characterize the composition of CuO·PbO/CNTs. The four elements C, O, Cu, and Pb were detected. This result confirms that the composite is composed of CuO, PbO, and CNTs.

In addition, we investigated the influences of precipitator, pH value of solution, and the heat treatment temperature on the products. Figure 30 shows the XRD pattern of

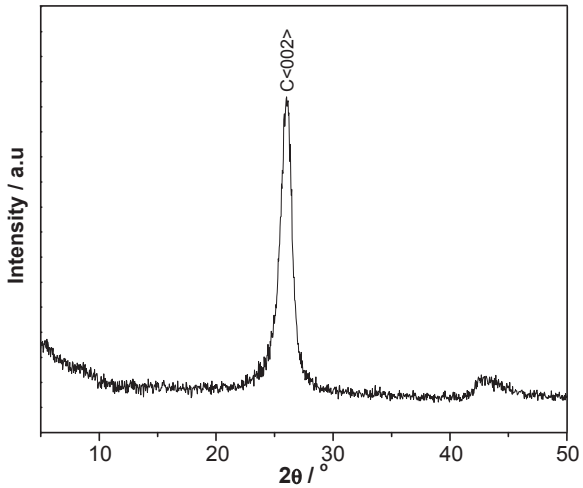

Figure 30 XRD patterns of CuO·PbO/CNTs prepared without precipitator.

composite prepared without the precipitator. The pattern is almost identical to that of pretreated CNTs as only a peak at 25.91° originating from the diffraction of (002) plane of CNTs is observed. On the other hand, besides the peak from CNTs, diffraction peaks from CuO and PbO were detected in the XRD pattern of the composite. Therefore, the introduction of precipitator is critical for the formation of CuO and PbO on the surfaces of CNTs, and the combined impregnation and chemical liquid deposition method is more favorable for the preparation of $CuO \cdot PbO$/CNTs.

It was found that the pH value of the solution is also critical for the formation of $CuO \cdot PbO$ on the surfaces of CNTs. A high pH value would result in the formation of soluble Cu^{2+}-NH_3 complex anions, whereas a low pH is not favorable for the formation of hydroxides. The optimal pH value of the solution was determined to be in the range of 8.4–8.5. The heat treatment temperature is also important for the purity of metal oxides on the surfaces of CNTs. The newly formed CuO would be reduced to metallic Cu at a high temperature, whereas a low temperature would result in the incomplete decomposition of the precursors to CuO and PbO and poor crystallinity of the final products. The optimal heat treatment temperature comprises 280–300 °C.

2.4.2 $Cu_2O \cdot Bi_2O_3$/CNTs [22]

$Bi(NO_3)_3 \cdot 5H_2O$ (0.37 g) was dissolved in 30 mL of 1.0 mol/L sulfuric acid and $CuSO_4 \cdot 3H_2O$ (0.62 g) was dissolved in water. After that, the $Bi(NO_3)_3$ and $CuSO_4$ solutions were mixed evenly and 0.3 g of pretreated CNTs was added to the mixture solution, which was then subjected to ultrasonic dispersion and stirring at room temperature for 5 h. During the stirring, a 1.0 mol/L NaOH solution was added to the mixture drop by drop until obtaining pH = 7.8. The resultant solution was subjected to filtration to get the solid residues, which were washed with water and ethanol twice and once, respectively. Then the solid residues were dried at 60 °C and heat-treated at 350 °C for 2 h to get the final product of $Cu_2O \cdot Bi_2O_3$/CNTs.

The contents of Bi and Cu were determined to be 22.0 and 22.5 mass%, respectively, using atomic spectroscopy. As a consequence, the contents of Bi_2O_3 and Cu_2O were calculated as 24.5 and 25.3 mass%. Figure 31 shows the XRD patterns of pretreated CNTs and $Cu_2O \cdot Bi_2O_3$/CNTs. It is observed that a strong diffraction peak from CNTs at 26° (2θ) with some other weak peaks were detected in the pattern of oxidized CNTs. On the other hand, on the pattern of $Cu_2O \cdot Bi_2O_3$/CNTs, the characteristic diffraction peak of CNTs at 26° (2θ) is weak, suggesting that the surfaces of CNTs are covered with $Cu_2O \cdot Bi_2O_3$. In addition, diffraction peaks from the monoclinic Bi_2O_3 at 27.95°, 31.76°, 32.69°, 46.22°, 46.90°, 54.27°, 55.49°, and 55.66°, as well as the peaks from the monoclinic Cu_2O at 36.50°, 42.20°, 61.52°, and 73.70°, are all recognizable, confirming the successful synthesis of Bi_2O_3 and Cu_2O.

Figure 32 shows the TEM image of $Cu_2O \cdot Bi_2O_3$/CNTs. It is seen that the diameters of CNTs in the composite are larger than those of the pristine CNTs as they

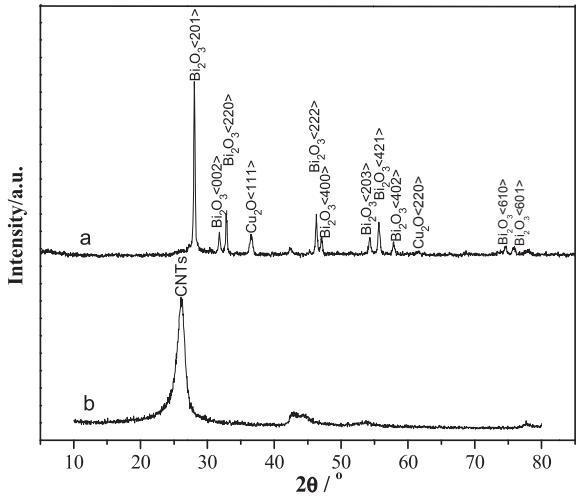

Figure 31 XRD patterns of $Cu_2O \cdot Bi_2O_3$/CNTs (a) and pretreated CNTs (b).

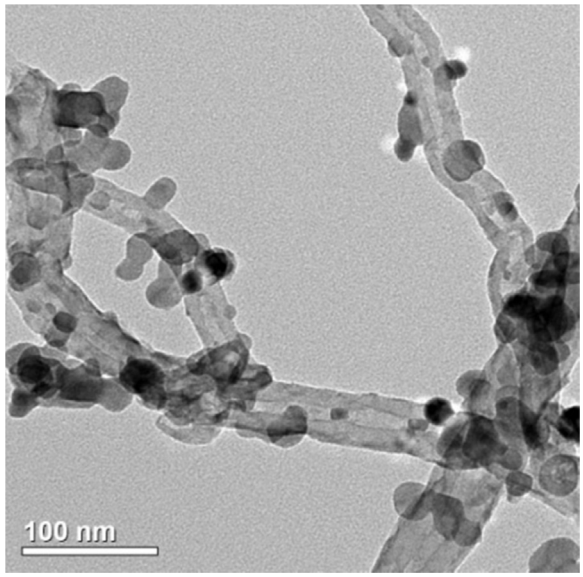

Figure 32 TEM image of $Cu_2O \cdot Bi_2O_3$/CNTs.

are wrapped with 20–25 nm $Cu_2O \cdot Bi_2O_3$ particles. The EDS results of $Cu_2O \cdot Bi_2O_3$/CNTs revealed the existence of the four elements of Cu, Bi, O, and C, confirming the results of XRD measurements.

Figure 33 shows the XRD patterns of the products obtained by using aqueous ammonia to modify the pH of solution to different values. For the sample obtained from the solution with a pH value of 0.5 (no aqueous ammonia was added), only the

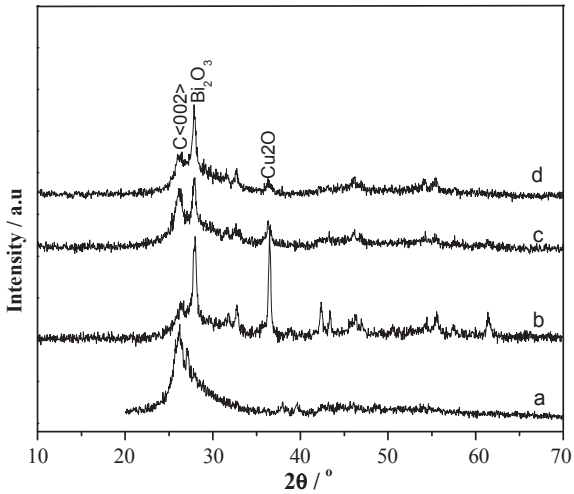

Figure 33 XRD patterns of $Cu_2O \cdot Bi_2O_3$/CNTs obtained from the solution with different pH values. (pH value: *a*, 0.5; *b*, 6.8; *c*, 7.5; *d*, 8.3).

diffraction peaks from CNTs are recognizable, suggesting that the amount of oxides on the surfaces of CNTs is negligible. If the pH value of solution was modified to be 6.8, the diffraction peaks of CNTs on the XRD pattern of resultant composite became weaker, whereas strong peaks with 2θ at 27.52°, 33.12°, 35.12°, 42.44°, and 46.38° emerged. These peaks were attributed to Bi_2O_3. In addition, the diffraction peaks with 2θ at 36.49°, 42.26°, 61.45°, and 73.78° from Cu_2O were also detected. The above results indicate that a lot of $Cu_2O \cdot Bi_2O_3$ is supported by the surface of CNTs. The XRD peaks with lower intensities are observed in the pattern of composite obtained from the solution with a pH value of 7.5, indicating the reduced amount of $Cu_2O \cdot Bi_2O_3$ on the surfaces of CNTs. These peaks are further weakened when the pH value of solution is 8.3, thus suggesting the further reduced oxides amount supported by CNTs. Obviously the amounts of $Cu_2O \cdot Bi_2O_3$ supported by the surface of CNTs are closely related to the pH value of solution. When aqueous ammonia was utilized as a titrant, the optimal pH value of solution for the preparation of $Cu_2O \cdot Bi_2O_3$/CNTs should be 6.5–7.0. The pH value of lower than 6.5 is unfavorable for the formation of hydroxides and thus oxides of Bi and Cu. On the other hand, if the pH value is higher than 7.5, NH_3 would adduct to Cu^{2+} to generate soluble complex cations, which is also unfavorable for the formation of hydroxides and oxides of Bi and Cu. It should be noted that the soluble complex cation can react with NaOH to generate the hydroxide of Cu.

Figure 34 shows the XRD patterns of $Cu_2O \cdot Bi_2O_3$/CNTs prepared with different mass ratios of metal salts to CNTs. It is observed that the peak intensities of Cu_2O and Bi_2O_3 increase with the increase in the mass ratios of metal salts to CNTs, whereas the opposite trend was found for the peak intensities of CNTs. This observation implies that

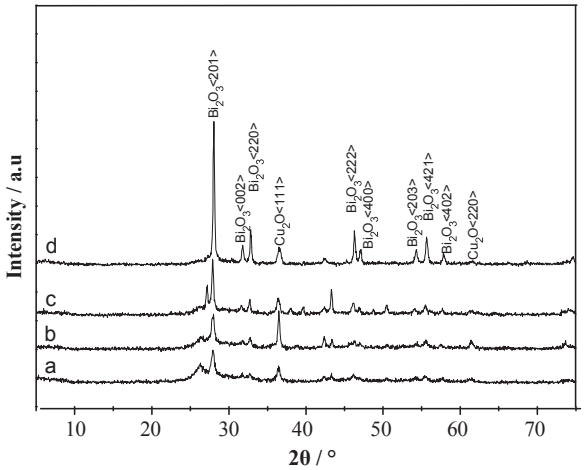

Figure 34 XRD patterns of $Cu_2O \cdot Bi_2O_3$/CNTs prepared by using different mass ratios of metal salts. (Mass ratio (%): *a*, 60; *b*, 100; *c*, 200; *d*, 250).

the amounts of $Cu_2O \cdot Bi_2O_3$ supported by the surfaces of CNTs increase with the increase in the mass ratios of metal salts to CNTs. When a small mass ratio of metal salts to CNTs is adopted, only small amounts of $Cu_2O \cdot Bi_2O_3$ would form on the surfaces of CNTs.

Figure 35 shows the XRD patterns of $Cu_2O \cdot Bi_2O_3$/CNTs heat-treated at different temperatures. For the sample heat-treated at 300 °C, only few weak diffraction peaks can be observed, which suggests the poor crystallinity of sample. When the heat treatment

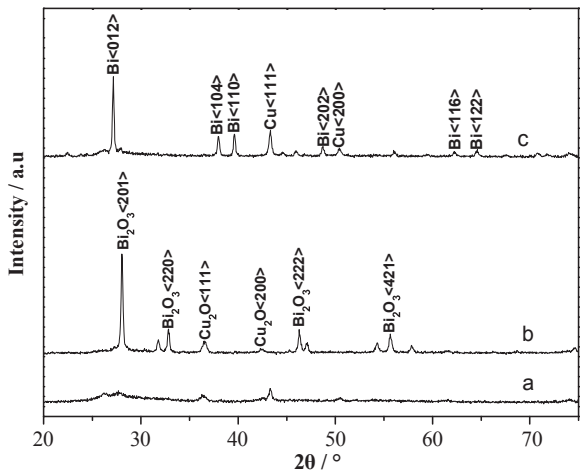

Figure 35 XRD patterns of $Cu_2O \cdot Bi_2O_3$/CNTs heat-treated at different temperatures. (Heat-treated temperature (°C): *a*, 300; *b*, 350; *c*, 400).

temperature was increased to 350 °C, strong diffraction peaks from Bi_2O_3 with 2θ at 27.93°, 32.71°, 46.31°, 55.57°, 57.49°, and 74.46°, as well as the peaks from Cu_2O at 36.56°, 42.46°, 61.56°, and 73.77°, were detected with the weak diffraction peak of CNTs at 26°. After heat treatment at 400 °C, the diffraction peak of CNTs at 26° was recognizable on the XRD pattern of the product, but the peaks from Bi_2O_3 and Cu_2O disappeared completely. Additionally, the diffraction peaks from metallic Bi at 37.27°, 37.67°, 48.68°, 55.95°, 62.15°, and 64.46° and the peaks of Cu at 43.33°, 50.49°, and 74.10° are detected. It is believed that Bi_2O_3 and Cu_2O deposited on the surfaces of CNTs are reduced to generate metallic Bi and Cu at the temperature of 400 °C. Therefore, the heat treatment at 350 °C is optimal for the preparation of $Cu_2O \cdot Bi_2O_3$/CNTs.

2.4.3 $Bi_2O_3 \cdot SnO_2$/CNTs

The solutions of $Bi(NO_3)_3$ and $SnCl_4$, which were prepared by dissolving 0.56 g of $Bi(NO_3)_3 \cdot 5H_2O$ and 0.62 g of $SnCl_4 \cdot 5H_2O$ in 10 mL of 1 mol/L hydrochloric acid, respectively, were mixed thoroughly[23]. Afterward, 0.3 g of pretreated CNTs was introduced into the mixture of $Bi(NO_3)_3$ and $SnCl_4$ solutions, which was then subjected to ultrasonic dispersion followed by stirring for 5 h and then keeping for another 2 h at room temperature.

Aqueous ammonia (2.5 wt%) was added into the solution drop by drop until pH value became equal to 8.8 and then it was left standing for 5 h at room temperature. After that, the solution was filtrated to get the solid residues, which were washed using deionized water and ethanol twice and once, respectively. Then the solid powder was dried at 60 °C and heat-treated at 380 °C for 2 h to get the resultant product of $Bi_2O_3 \cdot SnO_2$/CNTs.

Figure 36 presents the XRD pattern of $Bi_2O_3 \cdot SnO_2$/CNTs. It is observed that, besides the diffraction peaks from graphite, the peaks with 2θ at 24.62°, 27.38°, 33.24°,

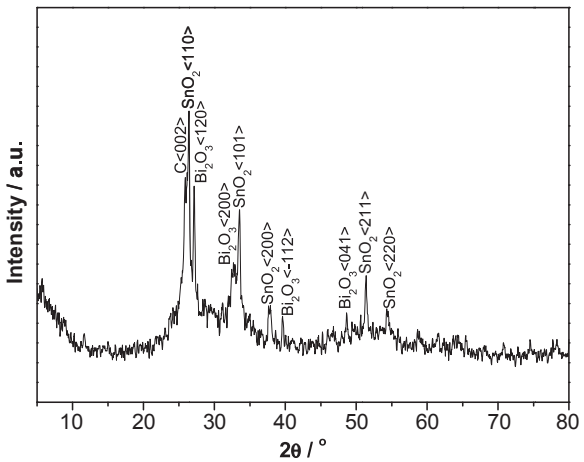

Figure 36 XRD pattern of $Bi_2O_3 \cdot SnO_2$/CNTs.

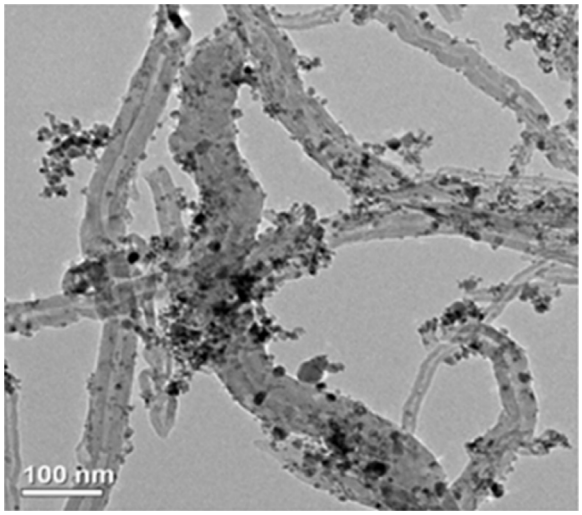

Figure 37 TEM image of $Bi_2O_3 \cdot SnO_2$/CNTs.

37.69°, and 46.31° from cubic Bi_2O_3 (corresponding to the (102), (120), (200), (−112), and (041) planes, respectively) and 26.61°, 33.89°, 37.95°, 51.76°, 53.14°, and 64.72° from cubic SnO_2 (corresponding to the (110), (101), (200), (211), (220), and (112) planes, respectively) were detected, indicative of the existence of cubic Bi_2O_3 and SnO_2.

As shown in the TEM image of $Bi_2O_3 \cdot SnO_2$/CNTs (Figure 37), $Bi_2O_3 \cdot SnO_2$ particles with an average diameter of about 5 nm were found on the surfaces of CNTs, which resulted in the increase in diameters of CNTs. In addition, it should be noted that, after ultrasonic treatment for 30 min, the $Bi_2O_3 \cdot SnO_2$ particles were still located on the surfaces of CNTs.

EDS measurement was conducted to further determine the composition of $Bi_2O_3 \cdot SnO_2$/CNTs. The four elements C, O, Bi, and Sn were detected. In addition, the mass contents of Bi and Sn were determined by using the X-ray fluorescence (XRF) measurements to be 27.3% and 23.1%, respectively. Thus, the contents of Bi_2O_3 and SnO_2 were calculated as 30.4% and 29.3%.

The effects of heat treatment temperature on generation of $Bi_2O_3 \cdot SnO_2$ on the surface of CNTs were investigated by using XRD. After heat treatment at 400 °C, metallic Bi appeared in the product. Upon further increasing the heat treatment temperature to 500 °C, almost all the Bi_2O_3 was reduced to form metallic Bi. When a heat treatment temperature of 380 °C was adopted, only Bi_2O_3 instead of metallic Bi could be detected. However, if the heat treatment temperature is lower than 380 °C, the Bi-containing precursor does not decompose completely to generate Bi_2O_3. Therefore, 380 °C is believed to be the optimal heat treatment temperature.

Moreover, it was found that the pH value of solution is also critical for the formation of $Bi_2O_3 \cdot SnO_2$ on the surfaces of CNTs. If the pH value is too high, the newly formed

Table 3 The productivity of $Bi_2O_3 \cdot SnO_2$/CNTs prepared without the utilization of precipitator.

($Bi_2O_3 \cdot 5H_2O$), g	($SnCl_4 \cdot 5H_2O$), g	CNTs, g	Starting materials, g	($SnO_2 \cdot Bi_2O_3$/CNTs), g	Productivity, %
0.0937	0.1212	0.1044	0.3193	0.0925	46.25
0.0928	0.1135	0.1033	0.3096	0.1049	52.42
0.0927	0.1228	0.1044	0.3199	0.0957	47.85
0.0903	0.1200	0.1013	0.3166	0.0916	45.80
0.0925	0.1223	0.1020	0.3168	0.0945	47.25

Table 4 The productivity of $Bi_2O_3 \cdot SnO_2$/CNTs prepared with the utilization of precipitator.

($Bi_2O_3 \cdot 5H_2O$), g	($SnCl_4 \cdot 5H_2O$), g	CNTs, g	Starting materials, g	($SnO_2 \cdot Bi_2O_3$/CNTs), g	Productivity, %
0.0920	0.1161	0.1000	0.3081	0.1650	82.50
0.0900	0.1162	0.1003	0.3065	0.1635	81.70
0.0912	0.1123	0.1027	0.3062	0.1630	81.50
0.0926	0.1157	0.1057	0.3140	0.1596	79.80
0.0936	0.1227	0.1034	0.3197	0.1523	76.15

$Bi_2O_3 \cdot SnO_2$ would dissolve in the solution, whereas a low pH value is unfavorable for the formation of $Bi_2O_3 \cdot SnO_2$. The optimal pH value for preparation of $Bi_2O_3 \cdot SnO_2$/CNTs was determined to be 8.8.

The influences of precipitator (aqueous ammonia) on the amount of $Bi_2O_3 \cdot SnO_2$ on the surfaces of CNTs were also investigated. Tables 3 and 4 list the amount of $Bi_2O_3 \cdot SnO_2$ prepared without and with the utilization of precipitator (aqueous ammonia), respectively. When aqueous ammonia was not used in the preparation process, the productivity of metal oxides was about 50%, whereas it increased to higher than 80% value when the precipitator was utilized during preparation. Therefore, the utilization of precipitator (aqueous ammonia) is favorable for the formation of $Bi_2O_3 \cdot SnO_2$ on the surfaces of CNTs.

2.4.4 $Cu_2O \cdot SnO_2$/CNTs

The $Cu_2O \cdot SnO_2$/CNTs catalyst was prepared through the combined impregnation and chemical liquid deposition method [24]. A given mass of $SnCl_4 \cdot 5H_2O$ and $CuCl_2 \cdot 2H_2O$ was dissolved in water to generate a solution, into which the pretreated CNTs and dispersant PEG-400 were then added. The solution was then ultrasonically dispersed and stirred at room temperature for several hours. After that, aqueous ammonia was utilized to modify the pH value of solution up to 8.0–8.5. The solution was then subjected to filtration, washing, desiccation, and finally heat treatment to obtain the resultant black $Cu_2O \cdot SnO_2$/CNTs powder.

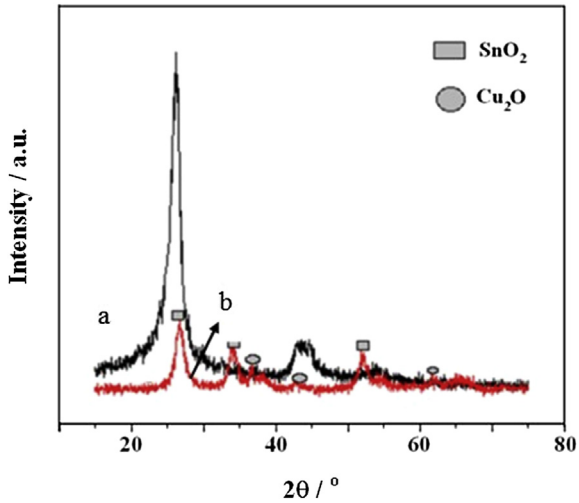

Figure 38 XRD patterns of the pretreated CNTs (a) and $Cu_2O \cdot SnO_2$/CNTs (b)

Figure 38 demonstrates the XRD patterns of pretreated CNTs and $Cu_2O \cdot SnO_2$/CNTs. Diffraction peak with 2θ at 26° originating from the (002) plane of CNTs was detected on the pattern of pretreated CNTs. As for the XRD pattern of $Cu_2O \cdot SnO_2$/CNTs, the peak from CNTs with 2θ at 26° is relatively weaker. However, peaks with 2θ at 26.61°, 33.98°, and 51.78° from SnO_2 (corresponding to the (110), (101), and (211) planes, respectively) and peaks at 36.50°, 42.40°, and 61.52° from Cu_2O (corresponding to the (111), (200), and (220) planes, respectively) are recognizable on this pattern, implying the existence of $Cu_2O \cdot SnO_2$ composites.

Figure 39 shows the TEM image of $Cu_2O \cdot SnO_2$/CNTs. It is revealed that the diameters of CNTs in the composite are larger than those of pristine CNTs due to the existence of $Cu_2O \cdot SnO_2$ balls with a particle size of about 6 nm on their surfaces. This result confirms the successful preparation of $Cu_2O \cdot SnO_2$/CNTs.

XRD measurement was used to investigate the difference in phase compositions of $Cu_2O \cdot SnO_2$/CNTs prepared with (sample *a*) and without (sample *b*) utilization of precipitator (aqueous ammonia), and the results are shown in Figure 40. For the composite prepared without precipitator only the diffraction peak from CNTs with 2θ at 26° ((002) plane) was detected, no peaks from Cu_2O and SnO_2 were discernable. As for $Cu_2O \cdot SnO_2$/CNTs prepared by using aqueous ammonia as precipitator, diffraction peaks from Cu_2O and SnO_2 are observed accompanying the peak from CNTs with 2θ at 26°. Therefore, $Cu_2O \cdot SnO_2$/CNTs can be achieved through the combination of impregnation and chemical liquid deposition methods. It was also found that the optimal pH value of solution should be about 8 as a pH value lower than 8 is unfavorable for the formation of metal hydroxides while pH value higher than 8 would result in the

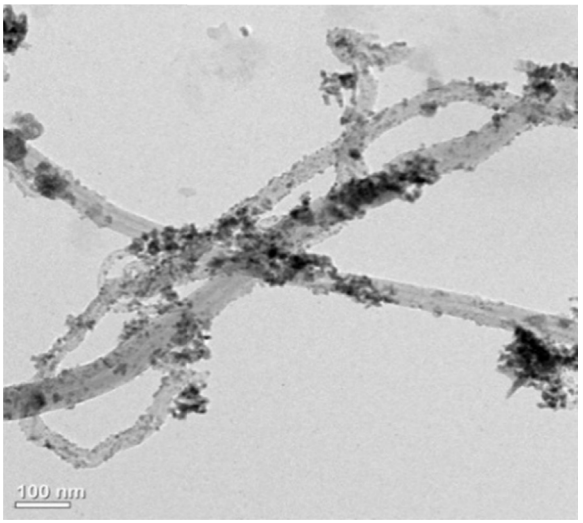

Figure 39 TEM image of $Cu_2O \cdot SnO_2$/CNTs.

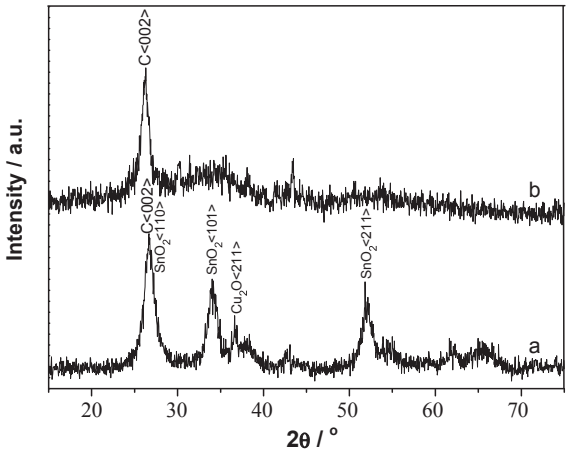

Figure 40 XRD patterns of $Cu_2O \cdot SnO_2$/CNTs prepared with (sample *a*) and without (sample *b*) precipitator.

dissolution of Sn-containing precipitation and formation of soluble Cu-containing complex anions. Moreover, 400 °C is the optimal heat treatment temperature. Heat treatment at temperatures higher than 400 °C may lead to reduction of metal oxides to metals, whereas heat treatment temperatures lower than 400 °C are unfavorable for the crystallization of metal oxides.

2.4.5 $NiO \cdot SnO_2$/CNTs

$SnCl_4$–$NiCl_2$ solution was prepared by dissolving $SnCl_4 \cdot 5H_2O$ and $NiCl_2 \cdot 6H_2O$ in water. The pretreated CNTs were then introduced to the solution and PEG-400 was used as the dispersant. The solution was ultrasonically dispersed and stirred at room temperature for 8 h. NaOH solution (1 mol/L) was utilized as the precipitator to modify the pH value of solution to 8.0 and then the solution was kept for 5 h at room temperature. Filtration was conducted to obtain the solid residue, which was washed with H_2O three times and dried at 60 °C. Finally, the solid was heat-treated at 500 °C for 2 h in N_2 to get the resultant product, $NiO \cdot SnO_2$/CNTs.

Figure 41 shows the XRD pattern of $NiO \cdot SnO_2$/CNTs. It was found that the composite is composed of NiO (47–1049), SnO_2 (41–1445) and CNTs. The TEM image of $NiO \cdot SnO_2$/CNTs is presented in Figure 42. As shown in Figure 42, spherical $NiO \cdot SnO_2$ particles with an average diameter of 5 nm are supported by CNTs.

EDS measurements were also conducted on $NiO \cdot SnO_2$/CNTs. The four elements Ni, Sn, O, and C were detected in the experiment, which confirmed the above XRD results.

2.4.6 $CuO \cdot SnO_2$/CNTs

$SnCl_4 \cdot 5H_2O$ and $CuCl_2 \cdot 2H_2O$ were dissolved in deionized water to get a $SnCl_4$–$CuCl_2$ solution, and the pretreated CNTs were then added to the solution. After being ultrasonically dispersed for 1 h and stirred at 50 °C for 30 min, the solution was kept for 5 h. Aqueous ammonia was utilized as titrant to change the pH value of solution to 8, and then the solution was kept for another 5 h. Filtration was then conducted to obtain the solid, which was washed with water and ethanol twice and once, respectively. After that, the solid residues were dried at 60 °C and heat-treated at 400 °C to achieve the final product of $CuO \cdot SnO_2$/CNTs. The compositions and microstructures of $CuO \cdot SnO_2$/CNTs were similar to those of $NiO \cdot SnO_2$/CNTs.

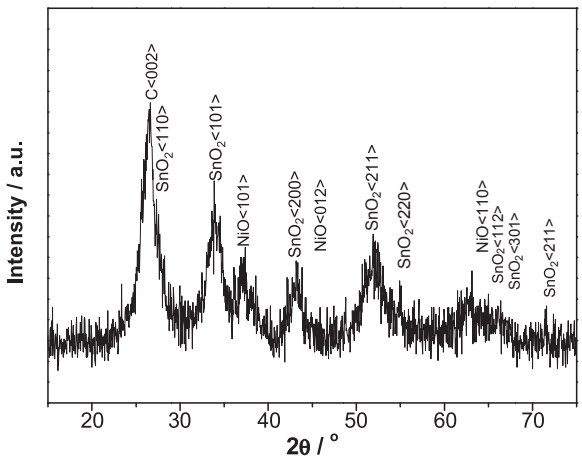

Figure 41 XRD pattern of $NiO \cdot SnO_2$/CNTs.

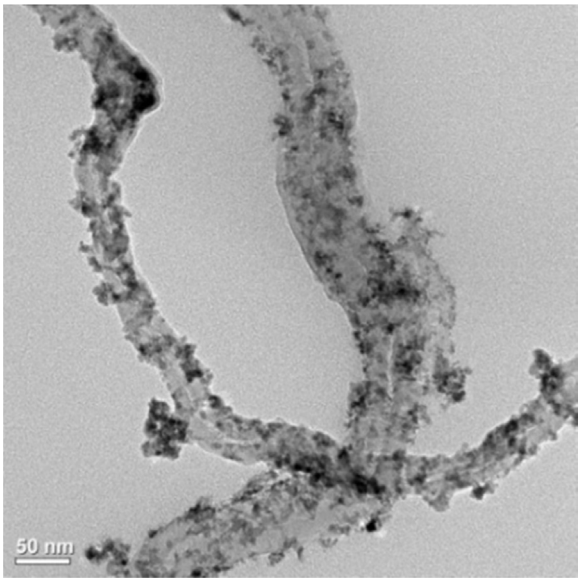

Figure 42 TEM image of $NiO \cdot SnO_2$/CNTs.

3. CATALYTIC ACTIVITY OF CNTs-SUPPORTED CATALYSTS IN THERMAL DECOMPOSITION OF ENERGETIC MATERIALS

CNTs have been proved to be an excellent supporter for burning rate catalysts. This is believed to be closely related to their structural characteristics. The catalyst particles on the surfaces of CNTs are dispersed evenly and their agglomeration is thus hindered. The gaseous decomposition products of propellants can be easily absorbed by the active sites of catalysts, which is favorable for the catalytic reactions. In addition, CNTs are a good conductor of heat, thus favoring the heat transfer during the combustion of propellants.

3.1 Catalytic Effects on the Thermal Decomposition Reaction of Nitrocellulose Absorbed Nitroglycerin

3.1.1 Effects of CNTs, Nano-CuO and CuO/CNTs on the Thermal Decomposition Behavior of Nitrocellulose Absorbed Nitroglycerin [16]

The differential scanning calorimetry (DSC) records with a heating rate of 10 °C/min of different NC-NG/catalyst samples, which were prepared by mixing NC-NG and different catalysts physically, are shown in Figure 43 and the parameters of their thermal decomposition are listed in Table 5 (T_p, peak temperature; Δt, peak width; $\Delta t = t_{end} - t_{start}$; ΔH has been corrected to be the value of 100% NC-NG). Here, it should be noted that Nano-CuO adopted as catalysts was prepared using a sol-gel method similar to the preparation of CuO/CNTs without the introduction of CNTs.

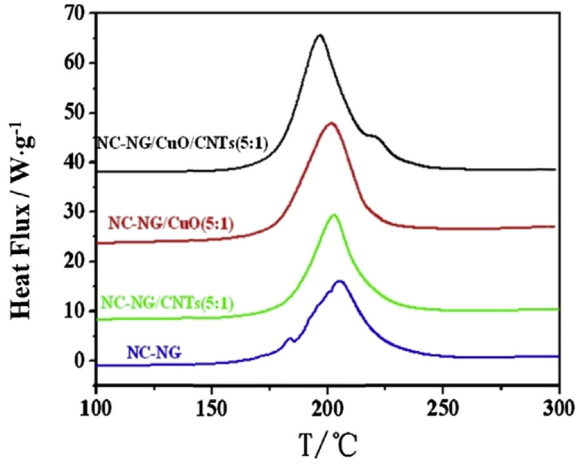

Figure 43 DSC curves of NC-NG, NC-NG/CNTs, NC-NG/CuO, and NC-NG/CuO/CNTs (0.1 MPa, NC-NG: Catalyst = 5:1).

Table 5 Thermal decomposition parameters of NC-NG, NC-NG/CNTs, NC-NG/CuO, and NC-NG/CuO/CNTs.

Sample	T_p, °C	Δt, °C	ΔH, J/g
NC-NG	205.6	98.4	1368
NC-NG/CNTs	202.6	88.7	1440
NC-NG/CuO	201.3	73.6	1596
NC-NG/CuO/CNTs	196.5	83.3	1764

In addition, CuO/CNTs catalyst Cat-4 with a carbon content of 46.7% was utilized, leading to a CNTs content of about 7.8%.

As shown in Figure 43, two exothermic peaks at 183.6 and 205.6 °C were detected by DSC for the pristine NC-NG. All the above-mentioned catalysts promote the decomposition of NC-NG and different catalysts make different catalytic effects. With an NC-NG to catalyst mass ratio of 5:1, CNTs, nano-CuO, and CuO/CNTs decrease the peak temperature of NC-NG by 3.1, 4.3, and 9.2 °C, respectively. At the same time, the decomposition enthalpies were increased by 72, 228, and 396 J/g upon the addition of CNTs, nano-CuO, and CuO/CNTs, respectively. Therefore, it is concluded that catalysts may not only enhance the decomposition reaction rate of NC-NG but also increase the reaction enthalpies. In addition, the CuO/CNTs composite shows better catalytic performances than nano-CuO.

The DSC records of NC-NG/CuO/CNTs samples containing different amounts of CuO/CNTs are shown in Figure 44, and the related parameters are listed in Table 6. It is observed that the DSC peak of NC-NG shifts to lower temperatures with the increase in the content of catalysts. The peak temperature was decreased by 9.2 °C along with an increase in decomposition enthalpy by 396 J/g when the NC-NG to catalyst mass ratio

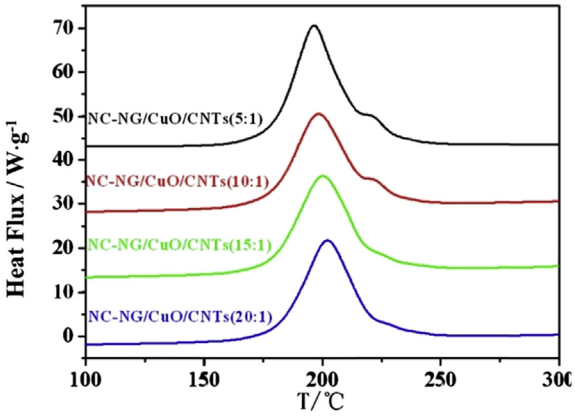

Figure 44 DSC curves of NC-NG mixed with different contents of CuO/CNTs (0.1 MPa).

Table 6 Effect of the content of CuO/CNTs on the thermal decomposition of NC-NG (0.1 MPa).

Sample	T_p, °C	Δ*t*, °C	Δ*H*, J/g
NC-NG/CuO/CNTs (20:1)	202.0	87.1	1680
NC-NG/CuO/CNTs (15:1)	200.2	91.8	1752
NC-NG/CuO/CNTs (10:1)	198.4	89.5	1740
NC-NG/CuO/CNTs (5:1)	196.5	83.3	1764

was 5:1. Additionally, the peak temperatures were decreasing by 7.2, 5.5, and 3.6 °C and the reaction enthalpies were increasing by 372, 384, and 312 J/g when the NC-NG to catalyst mass ratios were 10:1, 15:1, and 20:1, respectively. Therefore, the increase in the content of catalysts is favorable for enhancing the reaction rate and extent of decomposition of NC-NG.

3.1.2 Effect of Other CNTs-Supported Catalysts on the Thermal Decomposition Behavior of NC-NG

The effects of Bi_2O_3/CNTs, Pb/CNTs, NiB/CNTs, and NiPd/CNTs on decomposition of NC-NG are listed in Table 7, and the corresponding DSC traces are shown in Figure 45. Lower temperature decomposition of NC-NG is observed for the samples containing the above-mentioned four catalysts. The NC-NG to catalyst mass ratio of 5:1 was adopted. It is determined that the addition of NiB/CNTs, NiPd/CNTs, Bi_2O_3/CNTs, and Pb/CNTs decreases the decomposition temperature of NC-NG by 5.0, 5.0, 6.3, and 13.2 °C and increases the reaction enthalpy by 264, 252, 312 and 456 J/g, respectively. Therefore, these four catalysts are also effective in enhancing the reaction rates and extents of decomposition of NC-NG, while Pb/CNT was determined to be the most effective catalyst.

Table 7 Effect of different CNTs-supported catalysts on the thermal decomposition of NC-NG (0.1 MPa).

Sample	T_p, °C	Δt, °C	ΔH, J/g
NC-NG/CNTs (5:1)	202.6	88.7	1440
NC-NG/NiB/CNTs (5:1)	200.7	89.4	1632
NC-NG/NiPd/CNTs (5:1)	200.6	82.6	1620
NC-NG/Bi_2O_3/CNTs (5:1)	199.3	91.8	1680
NC-NG/Pb/CNTs (5:1)	192.5	93.9	1824

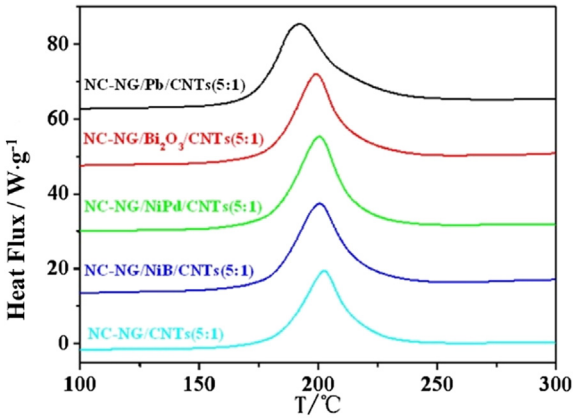

Figure 45 DSC curves of NC-NG mixed with different CNTs catalysts (0.1 MPa).

3.1.3 Nonisothermal Decomposition Reaction Kinetics of Mixture of NC-NG and Catalysts

The effects of CuO/CNTs, Bi_2O_3/CNTs, Pb/CNTs, NiB/CNTs, and NiPd/CNTs on decomposition kinetics of NC-NG were investigated in N_2 environment. The activation energy (E_a) and preexponential factor (A) were evaluated using the Kissinger method, and the reaction rate constant was determined using the Arrhenius equation.

As shown in Table 8, the activation energy for decomposition of NC-NG is 170.20 kJ/mol. Upon addition of 17% of CuO/CNTs, Bi_2O_3/CNTs, Pb/CNTs, Nib/CNTs, and NiPd/CNTs, the values of E_a were decreased by 12.5, 51.8, 13.1, 27.7, and 14.7 kJ mol^{-1}, thus favoring the decomposition of NC-NG. The reaction rate constants of the decomposition of NC-NG are also increased upon the addition of different catalysts.

3.2 Catalytic Effects of Ag/CNTs on the Thermal Decomposition Reaction of Hexogen

In order to evaluate the effects of Ag/CNTs on thermal decomposition of hexogen (RDX), the DSC measurements were conducted on the RDX/Ag/CNTs of different

Table 8 Kinetic parameters of decomposition of the NC-NG/catalyst samples.

Sample	E_a, kJ/mol	A, s^{-1}	k, s^{-1} (200 °C)	Correlation coefficient
NC-NG	170.2	5.831×10^{16}	9.438×10^{-3}	0.9993
NC-NG/CuO/CNTs	157.7	4.283×10^{15}	1.648×10^{-2}	0.9997
NC-NG/Bi_2O_3/CNTs	118.4	1.309×10^{11}	1.103×10^{-2}	0.9997
NC-NG/Pb/CNTs	157.1	4.981×10^{15}	2.250×10^{-2}	0.9979
NC-NG/NiB/CNTs	142.5	6.319×10^{13}	1.158×10^{-2}	0.9980
NC-NG/NiPd/CNTs	155.5	1.980×10^{15}	1.356×10^{-2}	0.9977

compositions as shown in Figure 46. The Ag/CNTs samples adopted were prepared by using two different methods. Figure 46(a) and (b) shows the DSC curves of RDX/Ag/CNTs containing Ag/CNTs prepared by using the silver-mirror method and hydrothermal method, respectively.

As shown in Figure 46, the main exothermic peak at 242.0 °C (515 K) and the shoulder at 253.0 °C (526 K) were detected on the DSC curves of RDX. Upon the addition of Ag/CNTs, the exothermic peaks shifted to higher temperatures, and the peak shapes changed. For the sample with RDX to Ag/CNTs mass ratio of 19:1, the shoulder at 253.0 °C became the main peak whereas the peak at 242.0 °C became a shoulder. With further increase in the content of Ag/CNTs, the main peak became sharper and the shoulder almost disappeared. The result suggests that the introduction of Ag/CNTs modifies the decomposition behavior of RDX. Furthermore, with the increase in the content of Ag/CNTs, the shoulder (secondary reaction) also shifted to lower temperatures. This is believed to be due to the high specific surface area of

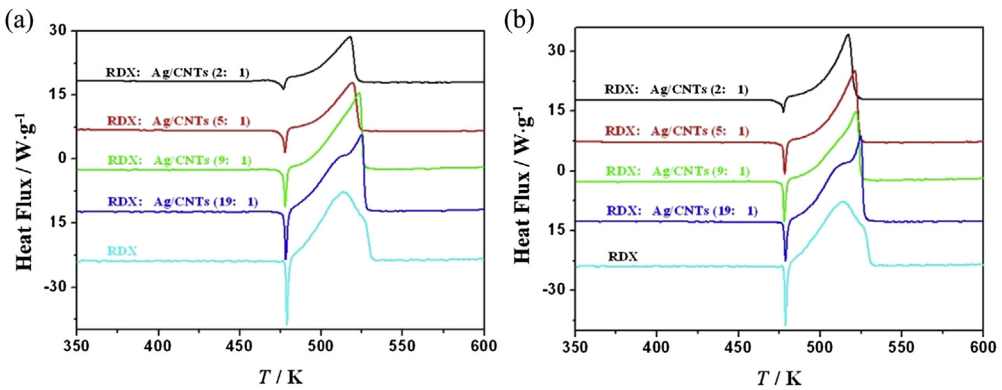

Figure 46 DSC curves of the RDX/Ag/CNTs with different compositions; (a) silver-mirror method, (b) hydrothermal method.

Ag/CNTs, which is apt to absorb the gaseous products and therefore favors the reaction between gaseous species.

The effects of two differently prepared Ag/CNTs on thermal decomposition of RDX are listed in Table 9 and Table 10. It was observed that the melting point of RDX decreased gradually with the increase in the content of Ag/CNTs. Moreover, the decomposition enthalpy of RDX also decreased with the increase in the content of Ag/CNTs. This was ascribed to the high thermal conductivity of CNTs, which was very favorable for heat dissipation, thus reducing the amount of heat detected, although more heat was released during the enhanced secondary decomposition (gaseous reaction). Based on the reaction enthalpies data listed in Tables 9 and 10, the sample of Ag/CNTs prepared by using hydrothermal method exhibits better catalytic performance than the one prepared by using the silver-mirror method.

It is concluded that the thermal decomposition behavior of RDX was modified due to the existence of Ag/CNTs. With the increase in content of Ag/CNTs, the primary decomposition reaction of RDX shifted to higher temperatures whereas the secondary one shifted to lower temperatures. In addition, the DSC peak corresponding to the primary decomposition of RDX disappeared along with sharpening of the secondary decomposition peak when the content of Ag/CNTs was higher than a critical value.

Table 9 Effect of the contents of Ag/CNTs prepared by silver-mirror reaction on the thermal decomposition of RDX.

	T_e, °C	T_m, °C	T_{p1}, °C	T_{p2}, °C	ΔH_s, J/g	$\Delta H_{s(RDX)}$, J/g
RDX	205.1	205.6	240.0	253.1	2546	2546
RDX:Ag/CNTs (19:1)	203.5	205.1	240.8	251.9	2324	2451
RDX:Ag/CNTs (9:1)	203.0	204.7	—	250.3	1911	2120
RDX:Ag/CNTs (5:1)	201.7	204.6	—	246.0	1109	1480
RDX:Ag/CNTs (2:1)	198.4	203.7	—	244.5	1030	1313

Note: RDX:Ag/CNTs, (mass ratio); T_e, onset temperature; T_m, melting peak temperature; T_{p1}, and T_{p2}, decomposition peak temperatures; ΔH_s, enthalpy of the exothermic decomposition reaction of system; $\Delta H_{s(RDX)}$, converted enthalpy of RDX.

Table 10 Effect of the content of Ag/CNTs prepared by hydrothermal method on the thermal decomposition of RDX.

	T_e, °C	T_m, °C	T_{p1}, °C	T_{p2}, °C	ΔH_s, J/g	$\Delta H_{s(RDX)}$, J/g
RDX	205.1	205.6	240.0	253.1	2546	2546
RDX:Ag/CNTs (19:1)	203.6	205.6	241.8	251.7	2410	2499
RDX:Ag/CNTs (9:1)	202.8	205.0	—	249.0	1640	2084
RDX:Ag/CNTs (5:1)	203.4	205.2	—	248.0	1556	1853
RDX:Ag/CNTs (2:1)	201.8	204.4	—	244.1	1357	1632

3.3 Catalytic Effects on the Thermal Decomposition Reaction of Ammonium Perchlorate

DSC measurements were conducted with the samples of the pristine ammonium perchlorate (AP) and the mixtures of AP/CNTs, AP/MnO_2, and AP/MnO_2/CNTs as shown in Figure 47. An endothermic peak and two exothermic peaks were detected on the DTA curve of the pristine AP (Figure 47, curve *a*). The endothermic process at 248.0 °C corresponds to phase transition of AP from orthorhombic to cubic phase. On the other hand, the exothermic peak at 322.3 °C is due to the low-temperature decomposition of AP, during which AP partially decomposes to generate some gaseous products. At higher temperatures, the high-temperature decomposition process peaking at 478.1 °C on the DTA curve occurs resulting in the full conversion of AP to gaseous products. Upon addition of MnO_2 with particle sizes of 60–80 μm and CNTs, the high-temperature decomposition peak was decreased by 143.6 °C and overlapped with the low-temperature peak, suggesting the catalytic effects of MnO_2 and CNTs on decomposition of AP. More interestingly, it was found that introduction of the same amount of MnO_2/CNTs decreases the peak temperature of high-temperature decomposition of AP by 162.2 °C. The resultant peak temperature of high-temperature decomposition was even 4.4 °C lower than the peak temperature of low-temperature decomposition for the pristine AP. In addition, the low-temperature decomposition process of the MnO_2/CNTs-added AP disappeared. Therefore, the MnO_2/CNTs showed better catalytic effect on the decomposition of AP in comparison with the pure MnO_2.

The decomposition enthalpies of the pristine AP, AP + CNTs + MnO_2, and AP + MnO_2/CNTs samples were determined to be 370.5, 948.07, and 1490.22 J/g. The thermal behaviors of these three samples were analyzed, and it was found that the more the high-temperature decomposition shifted to lower temperatures, the higher the decomposition enthalpy became.

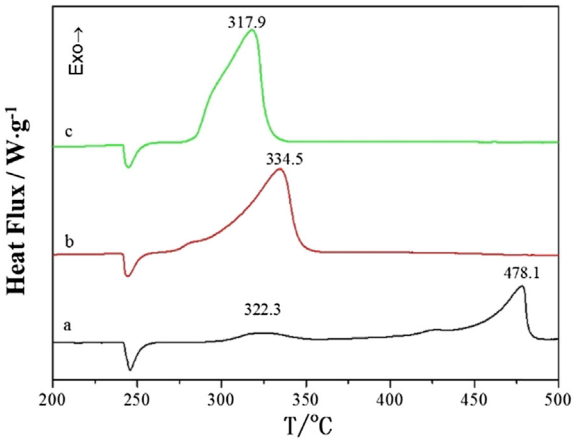

Figure 47 DTA curves of different samples (*a*, AP; *b*, AP + CNTs + MnO_2; *c*, AP + MnO_2/CNTs).

It is well known that the low-temperature decomposition of AP is a solid–gas reaction, in which dissociation and sublimation are involved. The reaction can be expressed as follows:

$$NH_4^+ + ClO_4^- \rightarrow NH_3(s) + HClO_4(s) \rightarrow NH_3(g) + HClO_4(g)$$

The gaseous NH_3 and $HClO_4$ further react with each other to generate N_2O, O_2, Cl_2, and H_2O. The high-temperature decomposition products of AP include NO, O_2, Cl_2, and H_2O. Newman et al. [32] proposed that the rate-determining step of decomposition of AP was electron transfer from ClO_4^- to NH_4^+ and the catalytic effect of transition metal oxides on decomposition of AP was believed to originate from that the oxide acted as a bridge in the electron transfer process. Moreover, the presence of transition metal oxides modified the composition of decomposition products of AP, and more NO was released, which promoted the decomposition of AP. In addition, the gaseous species in decomposition of AP were easily absorbed by active sites on the catalyst particles supported by CNTs, thus resulting in the superior catalytic performance of MnO_2/CNTs in comparison with MnO_2 and CNTs.

3.4 Catalytic Effects on the Thermal Decomposition Reaction of N-guanylurea-dianitramide [17,25]

3.4.1 Effects of CuO Content in CuO/CNTs on the Thermal Behavior of Guanylurea-dianitramide (GUDN)

The DSC curves of the mixtures of GUDN and different CuO/CNT catalysts, abbreviated as GUDN/Cats (the mass ratio of GUDN to Cats is 5:1) obtained at 0.1 MPa are shown in Figure 48 where ΔH (J/g) is the decomposition heat with conversion of

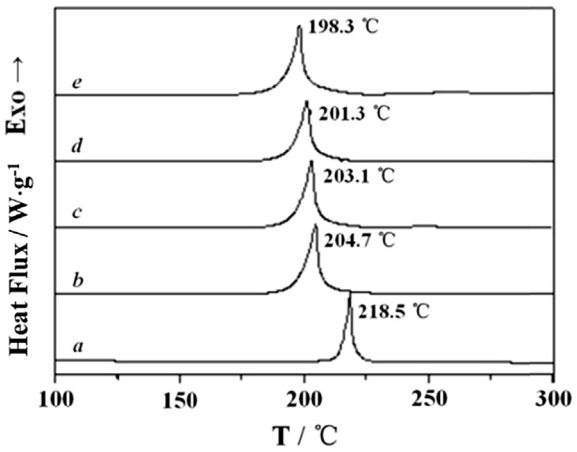

Figure 48 DSC curves of *a*: pure GUDN, *b*: GUDN/Cat-1, *c*: GUDN/Cat-2, *d*: GUDN/Cat-3, and *e*: GUDN/Cat-4 (Cat-1, Cat-2, Cat-3 and Cat-4 are different CuO/CNTs catalysts). ΔH (J/g): *a*, 1.54×10^3; *b*, 1.75×10^3; *c*, 1.78×10^3; *d*, 1.70×10^3; *e*, 1.87×10^3.

GUDN/Cats mixtures into 100% GUDN. It was found that there is only one exothermal decomposition peak (T_p, °C) in each DSC curve, with the peak temperature of the pure GUDN being 218.5 °C. The CuO/CNTs show favorable catalytic effects on the thermal behavior of GUDN. The peak decomposition temperature of GUDN was decreased by 13.8, 15.4, 17.2, and 20.2 °C, in the order from Cat-1 to Cat-4. The converted decomposition heats were increased as compared with pure GUDN by 210, 240, 160, and 330 J/g in the order of Cat-1 to Cat-4. Therefore, it is clear that the peak decomposition temperature of GUDN can be decreased and meanwhile the decomposition heat of GUDN be increased with the increment of CuO content in the CuO/CNTs.

3.4.2 Catalytic Effects of CuO/CNTs with Different Addition Amounts on Thermal Behavior of GUDN

The DSC curves of the GUDN/Cat-4 mixtures with mass ratio of 5:1, 10:1, 15:1, and 20:1 obtained at 0.1 MPa are shown in Figure 49, and ΔH (J/g) is defined the same as in Figure 48. From Figure 49, one can see that the peak temperature of GUDN decreases with the increase in the amount of Cat-4, i.e., when the mass ratio of GUDN to Cat-4 was kept as 5:1, the peak temperature of GUDN decreased by 20.2 °C, and the converted decomposition heat of the GUDN/Cat-4 mixtures increased by 330 J/g; when the mass ratios of GUDN to Cat-4 were kept as 10:1, 15:1, and 20:1, the peak temperatures of GUDN decreased by 18.4, 14.0, and 11.0 °C, respectively, and the converted decomposition heats of the GUDN/Cat-4 mixtures increased by 220, 150, and 70 J/g, respectively. Thus it is clearly seen that the increase in the catalyst amount can improve the decomposition reaction rate of GUDN and the reaction extent. The Cat-4 showed noticeable catalytic effect, even in the case when the mass ratio of the catalyst to

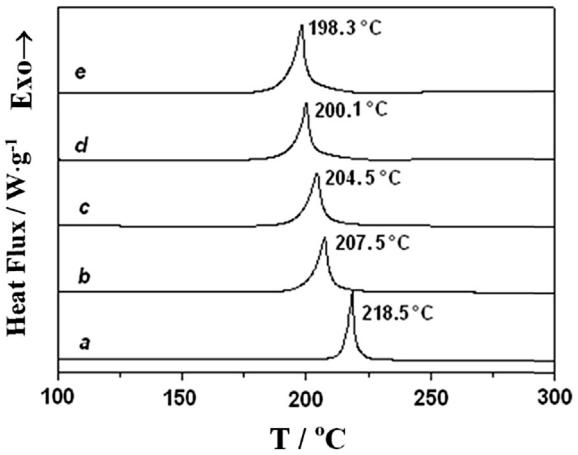

Figure 49 DSC curves of *a*: pure GUDN, *b*: GUDN/Cat-4 (20:1), *c*: GUDN/Cat-4 (15:1), *d*: GUDN/Cat-4 (10:1), and *e*: GUDN/Cat-4 (5:1). (ΔH (J/g): *a*, 1.54×10^3; *b*, 1.61×10^3, *c*: 1.69×10^3; *d*, 1.76×10^3; and *e*, 1.87×10^3.

GUDN was decreased to 1:20, which is close to the usual catalyst content in the propellant formulations.

3.4.3 Nonisothermal Decomposition Reaction Kinetics

To explore the catalytic effect of Cat-4 on the thermal decomposition reaction kinetics of GUDN, and to obtain the corresponding kinetic parameters (apparent activation energy (E_a), preexponential constant (A)) and determine the most probable kinetic model function, the DSC curves of the GUDN/Cat-4 mixture (Cat-4 content was 17%) obtained under 0.1 MPa at the heating rates of 5, 10, 15, and 20 K/min were processed with five integral methods, Eqns (1–5) and one differential method, Eqn (6).The methods are listed in Table 11 [26–29].

In these equations, α is the conversion degree of the exothermic reaction ($\alpha = H_t/H_0$); H_0 is the total heat effect corresponding to the global area under the DSC curve; H_t is the reaction heat at a certain time instant corresponding to the partial area under the DSC curve; T is the temperature (K) at the time instant t; R is the universal gas constant, $f(\alpha)$ and $G(\alpha)$ are the differential model function and the integral model function, respectively, and the meanings of E_a, A, β, and T_p have been mentioned earlier. The data needed for the equations of the integral and differential methods, α_i, β, T_i, T_p, $i = 1, 2, 3,\ldots$ are obtained from the DSC curves, and the $T \sim \alpha$ curves of GUDN/Cat-4 mixture at the heating rates of 5, 10, 15, and 20 K/min are shown in Figure 50. The values of E_a were obtained by Ozawa's method, Eqn (5), with α varying from 0.02 to 1.00, and the $E_a \sim \alpha$ curve of the GUDN/Cat-4 mixture is shown in Figure 51. It is

Table 11 Kinetic analysis methods.

Method	Equation	
General integral	$\ln\left[\frac{G(\alpha)}{T^2}\right] = \ln\left[\left(\frac{AR}{\beta E}\right)\left(1-\frac{2RT}{E}\right)\right] - \frac{E}{RT}$	(1)
MacCallum–Tanner	$\log[G(\alpha)] = \log\left(\frac{AE}{\beta R}\right) - 0.4828E^{0.4357} - \frac{0.449+0.217E}{0.001T}$ (E in kcal/mol)	(2)
Šatava–Šesták	$\log[G(\alpha)] = \log\left(\frac{A_s E_s}{\beta R}\right) - 2.315 - \frac{0.4567E_s}{RT}$	(3)
Agrawal	$\ln\left[\frac{G(\alpha)}{T^2}\right] = \ln\left\{\frac{(AR/\beta E)[1-2(RT/E)]}{1-5(RT/E)^2}\right\} - \frac{E}{RT}$	(4)
Flynn–Wall–Ozawa	$\log\beta = \log\left(\frac{AE}{RG(\alpha)}\right) - 2.315 - \frac{0.4567E}{RT}$	(5)
Kissinger	$\ln\left(\frac{\beta_i}{T_{pi}^2}\right) = \ln\left(\frac{A_k R}{E_k}\right) - \frac{E_K}{RT_{pi}}, \quad i = 1, 2, \ldots, 4$	(6)

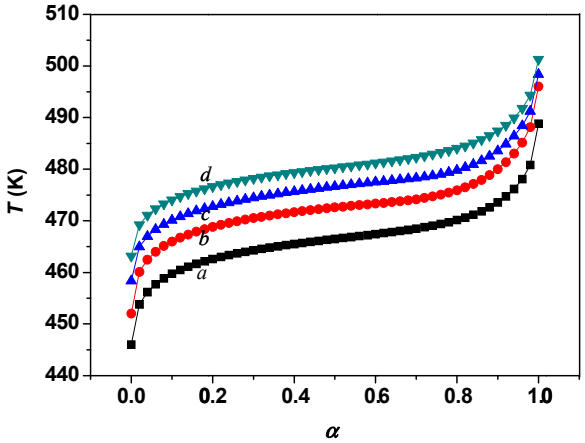

Figure 50 $T \sim \alpha$ curves of GUDN/Cat-4 mixture at the heating rates (K/min) of *a*: 5, *b*: 10, *c*: 15, and *d*: 20.

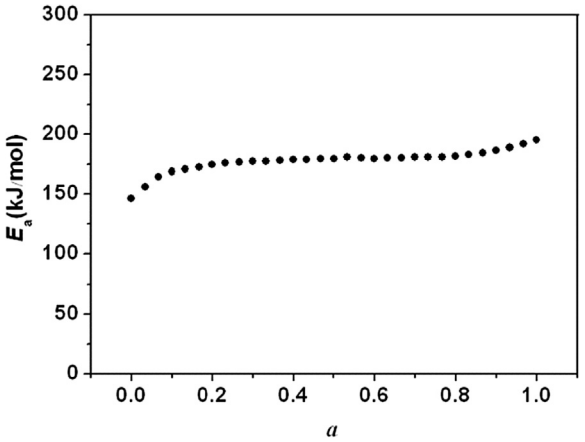

Figure 51 $E_a \sim \alpha$ curve of GUDN/Cat-4 mixture.

obvious that the activation energy changes slightly in the interval of 0.10–0.85 (α). Thus, this interval can be selected to derive the nonisothermal reaction kinetics.

Forty-one types of kinetic model functions and the original data were put into Eqns (1–6) for calculation [26,27]. The values of E_a, log A, linear correlation coefficient (r), and standard mean square deviation (Q) can be calculated by the computer with the linear least-squares and iterative methods at various heating rates of 5, 10, 15, and 20 °C/min. The most probable mechanism function is selected by the best values of r, and Q [26,27]. The results of satisfying the conditions at the same time are the final results as listed in Table 12, and the relevant function is the reaction mechanism function of the exothermic decomposition process of the GUDN/Cat-4 mixture under 0.1 MPa.

Table 12 Kinetic parameters of the decomposition process of GUDN/Cat-4 mixture.

Method	β, °C/min	E_a, kJ/mol	log A, s^{-1}	r	Q
General integral	5	178.0	17.8	0.9914	0.0646
	10	189.3	19.1	0.9850	0.1126
	15	196.8	19.9	0.9907	0.0697
	20	193.3	19.5	0.9880	0.0895
MacCallum–Tanner	5	178.4	17.8	0.9921	0.0122
	10	189.9	19.1	0.9861	0.0212
	15	197.5	19.9	0.9914	0.0131
	20	194.0	19.5	0.9890	0.0168
Šatava–Šesták	5	176.6	17.6	0.9921	0.0122
	10	187.5	18.9	0.9861	0.0212
	15	194.7	19.7	0.9914	0.0131
	20	191.4	19.2	0.9890	0.0168
Agrawal	5	178.0	17.8	0.9914	0.0646
	10	189.3	19.1	0.9850	0.1126
	15	196.8	19.9	0.9907	0.0697
	20	193.3	19.5	0.9880	0.0895
Mean		189.1	19.0		
Flynn–Wall–Ozawa		182.8		0.9988	0.0005
Kissinger		184.4	18.6	0.9987	0.0025

From Table 12, one can find that the values of E_a and log A obtained from the nonisothermal DSC curves are in fairly good agreement with the values calculated by both Kissinger's and Ozawa's methods.

Finally, a conclusion has been drawn that the reaction mechanism of the exothermal decomposition process of the GUDN/Cat-4 mixture under 0.1 MPa is classified as nucleation and growth mechanism, which is described by the Avrami–Erofeev equation $(-\ln(1-\alpha) = (k_3 t)^m)$ with $n = 2/5$, $G(\alpha) = [-\ln(1-\alpha)]^{2/5}$, and $f(\alpha) = (5/2)(1-\alpha)[-\ln(1-\alpha)]^{3/5}$. When substituting $f(\alpha)$ with $(5/2)(1-\alpha)[-\ln(1-\alpha)]^{3/5}$, E_a/(kJ/mol) with 189.1 and A (s^{-1}) with $10^{19.0}$ into Eqn (7):

$$d\alpha/dt = Af(\alpha)\, e^{-E/RT} \tag{7}$$

the corresponding kinetic equation of the decomposition reaction of the GUDN/Cat-4 mixture can be formulated as:

$$d\alpha/dt = 10^{19.4}(1-\alpha)[-\ln(1-\alpha)]^{3/5} e^{-2.27\times10^4/T} \tag{8}$$

Comparing the apparent activation energy of the decomposition reaction of GUDN/Cat-4 mixture with that of pure GUDN, one can find that Cat-4 decreased it by 31.1 kJ/mol [GUDN: E_a (kJ/mol), 220.2; log (A), s^{-1}, 21.2] [30], which means that Cat-4 enhances the rate of decomposition reaction of GUDN effectively.

3.4.4 Catalytic Mechanism Analysis

The violent decomposition reaction of GUDN (pure) occurs between 214.8 °C and 238.5 °C and produces a great deal of gases, with 16.25–18.39% mass remaining, and the rate of mass loss decreases with the increase in temperature [31]. The decomposition reaction of GUDN is a very complicated oxidation–reduction process, and one can speculate about the importance of the gaseous intermediates to the decomposition process when analyzing the reaction rate and the volume of the gases released.

The CuO particles supported by the surface of CNTs with a small grain size and a large specific area possess a large amount of surface active sites and a strong adsorption capacity. Consequently, more gaseous intermediates will be adsorbed on the surface of the nanocatalyst. And the nanocatalyst will therefore accelerate the decomposition of the gases that may result in a real increase in GUDN decomposition reaction rate.

CNTs support the CuO particles, which improves the dispersibility of CuO nanoparticles and increases the specific area, and it is of benefit to the catalytic reaction process. In addition, due to sp^2 hybridized construction of CNTs, electrons can travel along the tube wall and accelerate the electron and heat transfer during the reaction process. Here, CNTs and CuO nanoparticles show synergistic effect on the decomposition reaction of GUDN. Therefore, the composite of CuO/CNTs manifests promising catalytic effect on the thermal decomposition reaction of GUDN.

4. APPLICATION IN SOLID ROCKET PROPELLANTS

In this section, the effects of CNTs-supported catalysts on the combustion of the DB and CMDB propellants are discussed systematically [16,17,20].

4.1 Design and Preparation of Formulations

The double base (DB) propellant samples used were composed of 59% (mass fraction) nitrocellulose (NC), 30% nitroglycerin (NG), 11% diethyl phthalate (DEP), and other auxiliaries. The strand sample of the control propellant DB-1 composed of 500 g ingredients without combustion catalyst was prepared by the solvent-free DB propellant extrusion technique. The propellants DB-2 ~ DB-6 composed of 500 g ingredients with 12.5 g CNTs-supported catalysts as combustion catalyst were mixed physically with other compositions and prepared for the comparison with the control propellant. The catalysts were introduced into the propellants during the slurry mixing processes.

The CMDB propellant samples used were composite modified double-base propellants composed of 38% (mass fraction) nitrocellulose (NC), 28% nitroglycerin

Table 13 Content of CNTs catalysts for DB and CMDB propellants (%).

Type	No.	Content of catalyst, %	
DB propellant	DB-1	None	
	DB-2	CuO/CNTs	2.5
	DB-3	Bi_2O_3/CNTs	2.5
	DB-4	Pb/CNTs	2.5
	DB-5	NiB/CNTs	2.5
	DB-6	NiPd/CNTs	2.5
RDX-CMDB propellant	MB-1	None	
	MB-2	$Bi_2O_3 \cdot SnO_2/CNT_S$	3.4
	MB-3	$CuO \cdot PbO/CNT_S$	3.4
	MB-4	$Cu_2O \cdot Bi_2O_3/CNT_S$	3.4
	MB-5	$CuO \cdot SnO_2/CNT_S$	3.4
	MB-6	$NiO \cdot SnO_2/CNT_S$	3.4

(NG), 26% RDX, 8% N-nitro-dihydroxyethylamine-dinitrate (DINA), and other auxiliaries. The strand sample of the control propellant MB-1 composed of 500 g ingredients without combustion catalyst was prepared by the solvent-free CMDB propellant extrusion technique. The propellants MB-2 ~ MB-6 composed of 500 g ingredients with 17 g CNTs-supported combustion catalysts were prepared for the comparison with the control propellant. The catalysts were also introduced into the slurry during the mixing processes.

The contents of CNTs-supported catalysts for DB and CMDB propellants are listed in Table 13.

4.2 Effect of CNTs-supported Catalysts on Combustion Properties of DB Propellants

CuO/CNTs, Bi_2O_3/CNTs, Pb/CNTs, NiB/CNTs, and NiPd/CNTs were introduced into the DB propellants as the combustion catalysts. The burning rates of the propellants were measured and the pressure exponents were calculated as shown in Figure 52 and Table 14.

For comparison of the catalytic effects of different catalysts, the catalytic efficiency η_r of different catalysts in DB propellant was calculated ($\eta_r = u_c/u_0$, u_c is the burning rate of propellant containing catalyst, u_0 is the burning rate of propellant without catalyst). The results are shown in Table 15.

These results show that all five catalysts enhance the burning rate of DB propellants although only a minor improvement was observed in the NiB/CNTs-added propellant. Under a pressure of 6 MPa, CuO/CNTs exhibited the best catalytic performance as the burning rate of propellant was increased by 115%, from 5.2 to 11.2 mm/s.

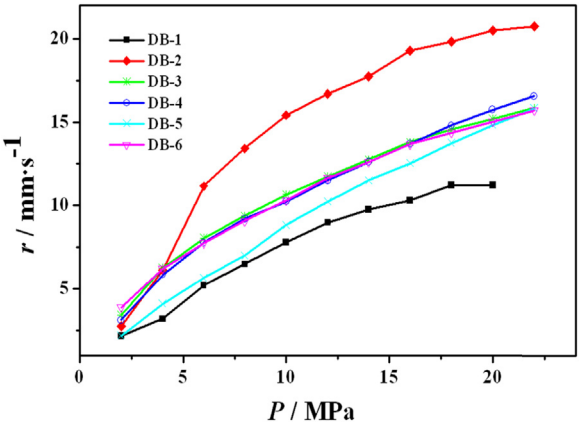

Figure 52 The burning rates of DB propellants containing CNTs-supported catalysts.

Table 14 Pressure exponents of the DB propellants.

No.	*n* (2～22 MPa)	*n* (6～22 MPa)	*n* (16～22 MPa)	*n* (18～22 MPa)
DB-1	0.74	0.72	0.81	0.88
DB-2	0.60	0.42	0.22	0.22
DB-3	0.55	0.50	0.43	0.42
DB-4	0.63	0.58	0.59	0.55
DB-5	0.79	0.77	0.73	0.71
DB-6	0.54	0.52	0.44	0.44

Table 15 The catalytic efficiency of different catalysts in DB propellant.

	η_r at different pressures (MPa)										
No.	2	4	6	8	10	12	14	16	18	20	22
DB-1	1.0	1.0	1.0	1.0	1.0	1.0	1.0	1.0	1.0	1.0	1.0
DB-2	1.3	1.7	2.2	2.1	2.0	1.9	1.8	1.9	1.8	1.7	1.6
DB-3	1.6	1.8	1.6	1.5	1.4	1.3	1.3	1.3	1.3	1.2	1.2
DB-4	1.4	1.6	1.5	1.4	1.3	1.3	1.3	1.3	1.3	1.3	1.2
DB-5	1.0	1.1	1.1	1.1	1.1	1.1	1.2	1.2	1.2	1.2	1.2
DB-6	1.8	1.7	1.5	1.4	1.3	1.3	1.3	1.3	1.3	1.2	1.2

In the pressure range of 6–22 MPa, the pressure exponents of DB propellants decreased from 0.72 to 0.42, 0.50, and 0.52 upon the addition of CuO/CNTs, Bi_2O_3/CNTs, and NiPd/CNTs, respectively. Again, CuO/CNTs were found to be the most effective agent in improving the pressure exponent of DB propellant as the exponent was decreased by 31% upon addition of 2.5 wt% CuO/CNTs.

Thus, CuO/CNTs, Bi_2O_3/CNTs, Pb/CNTs, and NiPd/CNTs composites showed noticeable catalytic performances in improving the burning properties of DB propellant and CuO/CNTs was the best burning catalyst.

4.3 Effect of CNTs-Supported Catalysts on Combustion Properties of CMDB Propellants

$Bi_2O_3 \cdot SnO_2$/CNTs, $CuO \cdot PbO$/CNTs, $Cu_2O \cdot Bi_2O_3$/CNTs, $CuO \cdot SnO_2$/CNTs, and $NiO \cdot SnO_2$/CNTs composites were added to the RDX-CMDB propellants and their burning rates were measured. The combustion parameters of catalyzed RDX-CMDB propellants are shown in Table 16, Figure 53, and Table 17.

For the comparison of the catalytic effect of different catalysts, the catalytic efficiencies η_r of different catalysts in CMDB propellant combustion were calculated. The results are presented in Table 17.

As shown in Tables 16 and 17, almost all the catalysts are able to increase the burning rates of RDX-CMDB propellants. The best catalyst $CuO \cdot PbO$/CNTs increases the burning rate by nearly 100% and decreases the pressure exponent by 50%.

Table 16 Pressure exponent of the RDX-CMDB propellants.

No.	*n* (2～22 MPa)	*n* (4～14 MPa)	*n* (10～14 MPa)	*n* (14～18 MPa)	*n* (16～20 MPa)
MB-1	0.79	0.86	0.83	0.79	0.79
MB-2	0.72	0.69	—	—	—
MB-3	0.43	0.39	0.44	0.41	0.44
MB-4	0.52	0.48	0.51	0.48	—
MB-5	0.60	0.58	0.48	—	0.46
MB-6	0.82	0.77	0.57	—	—

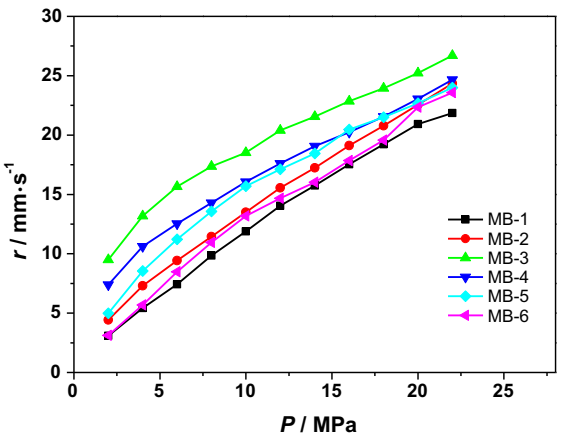

Figure 53 The burning rates of RDX-CMDB propellants containing CNTs-supported catalysts.

Table 17 The catalytic efficiency of different catalysts in CMDB propellant.

	η_r upon the different pressure (MPa)										
No.	**2**	**4**	**6**	**8**	**10**	**12**	**14**	**16**	**18**	**20**	**22**
MB-1	1.0	1.0	1.0	1.0	1.0	1.0	1.0	1.0	1.0	1.0	1.0
MB-2	1.4	1.4	1.3	1.2	1.1	1.1	1.1	1.1	1.1	1.1	1.1
MB-3	3.1	2.5	2.1	1.8	1.6	1.5	1.4	1.3	1.3	1.2	1.2
MB-4	2.4	2.0	1.7	1.5	1.4	1.3	1.2	1.2	1.1	1.1	1.1
MB-5	1.6	1.6	1.6	1.4	1.3	1.2	1.2	1.2	1.1	1.1	1.1
MB-6	1.0	1.1	1.1	1.1	1.1	1.1	1.0	1.0	1.0	1.1	1.1

5. CONCLUSIONS

Several carbon nanotubes-supported metal or metal oxide composites were prepared and characterized as combustion catalysts. These catalysts were found to be effective in enhancing the decomposition rate of the nitrocellulose absorbed nitroglycerin (NC-NG), hexogen (RDX), ammonium perchlorate (AP), and N-guanylurea-dianitramide (GUDN). In particular, it was found that the decomposition peak temperature of NC-NG was decreased by 9.2 °C and the decomposition heat was increased by 396 J/g with addition of CuO/CNTs (catalyst to NC-NG mass ratio of 1:5), which demonstrated better catalytic effect than pure CuO nanoparticles. The thermal behavior and decomposition reaction process of RDX were also changed by Ag/CNTs. Upon addition of Ag/CNTs, the secondary exothermic peaks on DSC curves shifted to lower temperatures, accompanying changes in the shape of the DSC curve. With addition of MnO_2/CNTs the high-temperature decomposition peak of AP was decreased by 161.2 °C and the low-temperature decomposition peak disappeared. The decomposition peak temperature of GUDN was decreased by 20.2 °C with addition of CuO/CNTs, and the decomposition heat was increased by 330 J/g. The apparent activation energy decreased by 31.1 kJ/mol, and the kinetic equation of the decomposition reaction of the mixture of GUDN and CuO/CNTs was derived.

The effects of the catalysts on combustion of propellants were also evaluated. CuO/CNTs, Bi_2O_3/CNTs, Pb/CNTs, NiB/CNTs, and NiPd/CNTs were tested as the combustion catalysts in DB propellants. Their catalytic effect on propellant combustion behavior was noticeable, especially in the case of CuO/CNTs. With its application the burning rate of DB propellant under 6 MPa was increased by 115%. $Bi_2O_3 \cdot SnO_2$/CNTs, $CuO \cdot PbO$/CNTs, $Cu_2O \cdot Bi_2O_3$/CNTs, $CuO \cdot SnO_2$/CNTs, and $NiO \cdot SnO_2$/CNTs were found to be able to improve the combustion properties of CMDB propellants, especially in the case of $CuO \cdot PbO$/CNTs. With this catalyst the burning rate of CMDB propellant at 6 MPa was increased by about 110%. The synergistic effect of CNTs and

metal oxide nanoparticles on the decomposition reaction characteristics and the burning rate demonstrates that CuO/CNTs and CuO·PbO/CNTs may find potential applications in the solid rocket propellants.

REFERENCES

[1] R.H. Baughman, A.A. Zakhidov, W.A. de Heer, Carbon nanotubes – the route towards applications, Science 297 (5582) (2002) 787.
[2] A.P. Ramirez, Carbon nanotubes for science and technology, Bell. Labs. Tech. J. 10 (3) (2005) 171.
[3] K. Yang, M. Gu, Y. Guo, X. Pan, G. Mu, Effects of carbon nanotube functionalization on the mechanical and thermal properties of epoxy composites, Carbon 47 (2009) 1723.
[4] F. Peng, J.W. Jiang, H.J. Wang, J.X. Feng, Preparation of carbon nanotubes supported Fe_2O_3 catalysts, Chin. Inorg. Chem. 20 (2) (2004) 231.
[5] W. Chen, J.L. Li, M.H. Zou, W.T. Zhou, The preparation of highly dispersed Ag/carbon nanotube catalyst, J. Cent. China Normal Univ. (Nat. Sci.) 37 (2) (2003) 211.
[6] X.J. Zhang, W. Jiang, D. Song, Y. Liu, J.J. Geng, F.S. Li, Preparation and catalytic activity of Co/CNTs nanocomposites via microwave irradiation, Propell. Explos. Pyrotech. 34 (2009) 151.
[7] P. Cui, F.S. Li, J. Zhou, W. Jiang, Preparation of Cu/CNTs composite particles and catalytic performance on Thermal decomposition of ammonium perchlorate, Propell. Explos. Pyrotech. 31 (2006) 452.
[8] Q.C. Xu, J.D. Lin, J. Li, X.Z. Fu, Y. Liang, D.W. Liao, Microwave–assisted synthesis of MgO–CNTs supported ruthenium catalysts for ammonia synthesis, Catal. Commun. 8 (2007) 1881.
[9] A.S. Chen, F.S. Li, Z.Y. Ma, H.Y. Liu, Research on the preparation and catalytic function of nano CuO/AP composite particles, J. Solid Rocket Tech. 27 (2) (2004) 123.
[10] H.M. An, Y.F. Liu, Y.P. Li, R.J. Yang, H.M. Tan, Study on catalytic combustion of HNIW monopropellant by metal oxide, Chin. J. Explos. Propell. 23 (4) (2000) 27.
[11] J.W. Zhu, W.G. Zhang, H.Z. Wang, X.J. Yang, L.D. Lu, X. Wang, Synthesis and properties of shape–controlled CuO nanocrystals, Chin. Inorg. Chem. 20 (7) (2004) 863.
[12] Z. Hong-wei, W. De-hai, X. Cai-lu, Carbon Nanotubes, Machine Press, Beijing, 2003.
[13] M. Yasutake, Y. Shirakawabe, T. Okawa, S. Mizooka, Y. Nakayama, Performance of the carbon nano-tube assembled tip for surface shape characterization, Ultramicroscopy 91 (1–4) (2002) 57–62.
[14] H. Wei-liang, Z. Feng-qi, L. Jian-hong, et al., Nanocomposite Pb/CNTs and Its Preparation Method, 2007. China, 200710124599.X.
[15] A. Ting, C. Hui-qun, Z. Feng-qi, et al., Preparation and characterization of Ag/CNTs nanocomposite and its effect on thermal decomposition of cyclotrimethylene trinitramine, Acta Phys. Chim. Sin. 28 (9) (2012) 2202–2208.
[16] H. Wei-liang, Z. Xiu-ying, Z. Feng-qi, et al., Preparation of CuO/CNTs and its combustion catalytic activity on double-base propellant, Chin. J. Explos. Propell. 33 (6) (2010) 83–86.
[17] L. Xiang, H. Wei-liang, Z. Feng-qi, et al., Synthesis of CuO/CNTs composites and its catalysis on thermal decomposition of FOX-12, J. Solid Rocket Technol. 31 (5) (2008) 508–511, 526.
[18] H. Wei-liang, L. Jian-hong, Z. Feng-qi, et al., Nanocomposite PbO/CNTs and Its Preparation Method, 2007. China, 200710124597.0.
[19] H. Wei-liang, L. Xiang, Z. Feng-qi, et al., Nanocomposite Bi_2O_3/CNTs and Its Preparation Method, 2007. China, 200710124598.5.
[20] L. Jian-xun, Preparation of Carbon Nanotubes Combustion Catalysts and Its Application in Solid Propellants, Nanjing University of Science and Technology, Nanjing, 2007.
[21] H. Wei-liang, Z. Feng-qi, L. Jian-hong, et al., Nanocomposite CuO-PbO/CNTs and its Preparation Method, 2008. China, 200810142779.5.
[22] H. Wei-liang, Z. Feng-qi, Z. Jin-xia, et al., Nanocomposite Cu2O-Bi_2O_3/CNTs and Its Preparation Method, 2011. China, ZL 200810142777.6.
[23] H. Wei-liang, Z. Jin-xia, Z. Feng-qi, et al., Nanocomposite Bi_2O_3-SnO_2/CNTs and its Preparation Method, 2011. China, ZL 200810142778.0.

[24] Z. Jin-xia, H. Wei-liang, Z. Feng-qi, et al., Synthesis of SnO_2-Cu_2O/CNTs catalyst and its catalytic effect on Thermal decomposition of FOX-12, Chin. J. Explos. Propell 34 (2) (2011) 47–51.
[25] J. Yi, F. Zhao, S. Xu, et al., Preparation and characterization of carbon nanotubes supported copper (II) oxide catalysts and catalytic effects on thermal behavior of N-guanylurea dianitramide, in: 42th International Annual Conference of ICT, 2011.
[26] R.Z. Hu, S.L. Gao, F.Q. Zhao, Q.Z. Shi, T.L. Zhang, J.J. Zhang, Thermal Analysis Kinetics, second ed., Science Press, Beijing, 2008.
[27] F.Q. Zhao, R.Z. Hu, H.X. Gao, H.X. Ma, Thermochemical properties, non-isothermal decomposition reaction kinetics and quantum chemical investigation of 2,6-diamino-3,5-dinitropyrazine-1-oxide (LLM-105), in: O.E. Bronza (Ed.), New Developments in Hazardous Materials Research, Nova Science Publishers, Inc., New York, 2006.
[28] J.H. Yi, F.Q. Zhao, H.X. Gao, S.Y. Xu, M.C. Wang, R.Z. Hu, Preparation, characterization, nonisothermal reaction kinetics, thermodynamic properties, and safety performances of high nitrogen compound: hydrazine 3-nitro-1,2,4-triazol-5-one complex, J. Hazard. Mater. 153 (2008) 261.
[29] G. Singh, I.P.S. Kapoor, S. Dubey, P.F. Siril, Kinetics of Thermal decomposition of ammonium perchlorate with nanocrystals of binary transition metal ferrites, Propell. Explos. Pyrotech. 34 (2009) 72.
[30] F.Q. Zhao, P. Chen, H.A. Yuan, S.L. Gao, R.Z. Hu, Q.Z. Shi, Thermochemical properties and non-isothermal decomposition reaction kinetics of n-guanylurea dinitramide (GUDN), Chin. J. Chem. 22 (2004) 136.
[31] B.Z. Wang, Q. Liu, Z.Z. Zhang, Y. P Ji, C.H. Zhu, Study on properties of GUDN, Chin. J. Energ. Mater. 12 (1) (2004) 38.
[32] L.L. Bircumshaw, B.H. Newman, Proc. Roy. SOC. (London), A227 (1954) 115.

CHAPTER ELEVEN

Formation of Nanosized Products in Combustion of Metal Particles

Oleg G. Glotov[1] **and Vladimir E. Zarko**[1,2]
[1]Voevodsky Institute of Chemical Kinetics and Combustion, Siberian Branch of the Russian Academy of Sciences, Novosibirsk, Russia
[2]Tomsk State University, Tomsk, Russia

1. INTRODUCTION

1.1 Aluminum and Its Oxide Al_2O_3

The idea of using metals of high caloric value (more than 2 kcal/g), such as beryllium, lithium, magnesium, aluminum (Al), zirconium, and titanium (Ti), as a fuel for rocket propellants was published independently and almost simultaneously by Russian scientists Yu. V. Kondratyuk (1929) and F. A. Tzander (1932) [1]. In the 1950s, the idea of metallized propellants was realized in practice by the Soviet Union (USSR) and the United States (US) and later on, by other countries. Among the metals mentioned, aluminum has been most widely used in solid propellants due to its high caloric value ($\approx$9.8 kcal/g), comparative cheapness, and relative harmlessness of the main combustion product, oxide Al_2O_3.

Introducing aluminum into propellant formulation increases flame temperature and the velocity of combustion products, creating a jet thrust, improves the stability of motor operation by damping the gas oscillations in a combustion chamber, and makes it possible to control the propellant burning rate. At the same time, the presence of aluminum particles causes a great number of problems concerned with their behavior in combustion wave, combustion chamber, nozzle, and motor exhaust plume. Thus, a necessity arises to comprehensively investigate the ignition and combustion of Al particles in oxidizing media [1]. The efficiency of employing aluminum as a metal fuel is determined by the peculiarities of metal transformation into condensed combustion products. The transformation depends mainly on two processes: (1) the agglomeration of the primary particles of metal powder in a combustion wave, and (2) the burning of aluminum in the form of agglomerates or in the form of initial particles, followed by the formation of oxide particles. In the case of rocket motors, the above processes and subsequent evolution of oxide particles in the flow of gaseous combustion products determine the parameters of the size distribution function of oxide particles [2]. The size distribution functions of agglomerates and oxide particles and the data on the completeness of

Energetic Nanomaterials
ISBN 978-0-12-802710-3, http://dx.doi.org/10.1016/B978-0-12-802710-3.00011-8

aluminum combustion represent information that one needs to optimize propellant formulation and to estimate the different effects of the evolution of disperse phase (accumulation of slag in motors, nozzle erosion, two-phase losses of a specific impulse, damping of gas oscillations in combustion chamber). Outside the motor, the characteristics of oxide particles are of interest from two points of view: (1) the detection of rocket start from radiation of an exhaust jet, and (2) the ecological impact of rocket launching. Thus, the formation of aluminum oxide particles is not only of fundamental interest as a part of combustion mechanism but manifests a series of practical important aspects.

Let us discuss the ecological aspect. The life cycle of rocket engineering wares includes the designing, manufacturing, and testing of experimental items, the exploitation of stock-produced items, and their subsequent utilization either because of physical aging or for other reasons (e.g., the disposal of rockets according to international agreements on rocket elimination [3]), Figure 1. The actual ecological problems related to the above stages of the life cycle of rockets have been discussed in many reports, e.g., in Refs [4–15]. The well-known method of rocket disposal via open firing with a removed nozzle block is characterized by the following: (1) the localized release of a great amount of gaseous and solid combustion products and of concomitant substances, and (2) the burning of aluminum agglomerates at relatively low (as compared with the nominal one) pressure and also in the air at atmospheric pressure. These peculiarities give an impetus to the studies on the aerosol systems of oxide particles, especially within a nanosized range.

These particles are almost of no importance from the viewpoint of rocket motor performance but are of great essence for ecology. In particular, upon motor disposal, the concomitant substances, e.g., thermal protection materials, adhesive layer, etc., burn together with a propellant. Generally, combustion products contain toxic compounds,

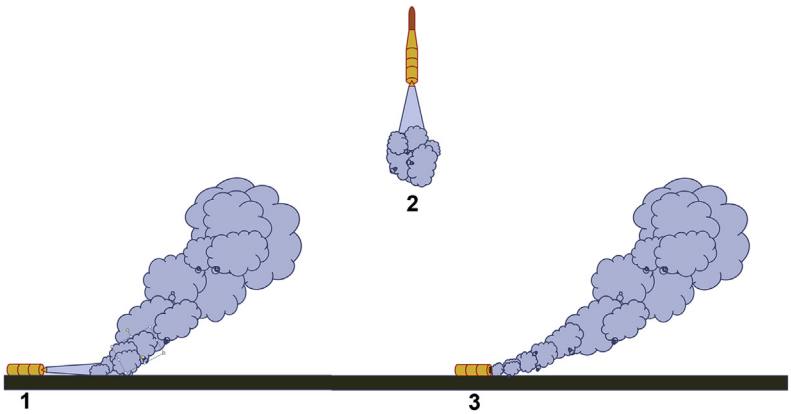

Figure 1 Combustion product emissions in the life cycle of a solid motor, one of the reasons for interest in the parameters of oxide nanoparticles: 1—testing; 2—exploration; 3—incineration (without nozzle).

e.g., dioxins [14]. Harmful substances may be located at the surface of alumina particles, in particular, of nanoparticles, which is favored by their high specific surface area. Therefore, laboratory studies are focused on the size distribution of particles, their concentration, and morphology. These characteristics determine the ability of particles to adsorb and transfer harmful substances in the atmosphere.

Thus, the interest in the characteristics of aluminum oxide nanoparticles is first motivated by the *ecological problems* of tests, exploitation, and utilization of rocket motors based on aluminized propellant. The second reason is related to the problems *of the technological combustion* of metallic fuel. In technological combustion, metal is used as a reagent for producing target products with given properties (oxides, nitrides, carbides, etc.) in various systems, i.e., pressed for self-propagating high-temperature synthesis (SHS), gelatinous (water gel) [16], loosed specimen, aerogel [17,18], aerodisperse [19–21], etc. It seems promising to employ the experience and results of the development of energy-releasing devices based on powdered fuel [19,20] to produce oxide nanoparticles with the given characteristics. In particular, the so-called method of gas-disperse synthesis of oxides has been developed [21]. It involves the burning of metal particles in a specially organized stationary, laminar two-phase flame. The method is characterized by the high purity of a target product (oxide), low manufacturing cost, high productivity, and ecological safety. In addition, the properties of the product may be controlled via variation of flame parameters. In particular, a considerable output of spherical nanoparticles of tens of nanometers can be achieved. Following, we will consider again the characteristics of oxide nanoparticles obtained by this method.

The problems of technological combustion of metal particles in the two-phase flame relate to the general problems of the mechanism of particle burning in a gaseous oxidizer. Knowing the laws of combustion, including the formation of oxide particles, may serve as the basis for understanding the mechanism of combustion and ensure the optimization of combustion process in technical devices.

1.2 Titanium and Its Oxide TiO_2

Titanium, as aluminum, is the "aerospace" metal due to its lightness, strength, refractoriness, and corrosion resistance [22]. The fundamental investigations of Ti burning were carried out in the days of its introduction into technology as a structural material in the 1960–1970s. The goal of the studies was to determine the practical important characteristics (e.g., the burning rate depending on conditions) rather than to consider the combustion mechanism and formation of disperse combustion products. An alternative application of Ti powder as a metallic fuel (e.g., in pyrotechnical compositions, SHS systems, etc.) did not need either detailed understanding of combustion mechanism or information on oxide particles properties. In other words, as compared with Al, the needs of practical work did not stimulate studies on the mechanism of Ti combustion

in a gaseous oxidizer and no corresponding investigations were performed in the past. However, in 2005, it was proposed (probably first in Ref. [23]) to use the combustion of Ti particles in the air to form a cloud of photocatalytically active TiO_2 particles in order to deactivate either harmful or dangerous substances entering the atmosphere after an anthropogenic disaster or a terrorist act (Figure 2).

As a result, there was a revival of interest in Ti burning, confirmed by the appearance of experimental works in France, Germany, Russia, Ukraine, and the US. Studying the mechanism of Ti combustion appeared to be task oriented, i.e., aimed at solution of concrete problems. One of the tasks was to study the influence of burning conditions on the characteristics of resulting TiO_2 particles and to search for ways of controlling those characteristics. As in the case of technological Al burning, it was necessary to study the mechanism of particle combustion in order to develop the schemes of either process organization or technical device development, which provides an effective transformation of metal into oxide with the properties required. The researchers were interested in the size distribution of TiO_2 particles, their concentration (mass yield), and morphology. For Ti, an additional parameter of importance is the phase composition of TiO_2 particles. The latter is related to the photocatalytic activity of TiO_2 particles, which is usually determined in special experiments. Research on the technological combustion of Ti to obtain target products, in particular, oxide nanoparticles, is also underway [21].

Actually, the area of interest of the present work is limited by the combustion products of micron-sized aluminum and titanium particles. In the field of knowledge related to metallic fuels and their technical applications, micron particles are those that vary from units to hundreds of microns, whereas the particles of fractions of microns

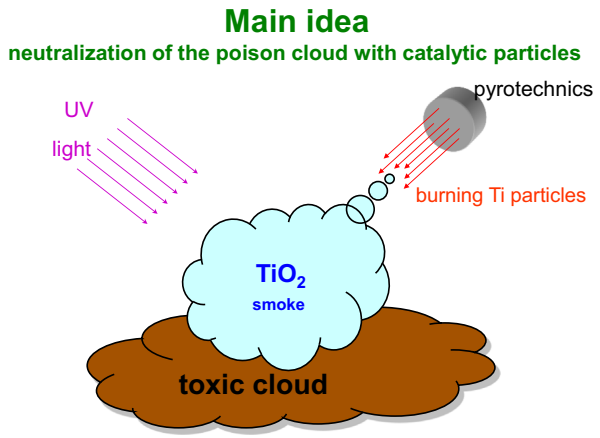

Figure 2 Idea to use a cloud of photocatalytic titanium dioxide nanoparticles to decontaminate atmospheric air, which inspired interest in studying the combustion of titanium microparticles in air.

(e.g., less than 0.1 μm) are commonly called the nanoparticles [24]. The object for analysis here are the nanosized oxide particles formed in combustion of the micron-sized Al and Ti particles. Let us also mention the following.

1. There is a close relation between the examination of the *condensed combustion products* of metallized systems (composite aluminized solid propellants, pyrotechnical compositions with titanium, etc.) and the study of the process of *metal particles combustion* at the level of concepts, techniques, and even objects. On the one hand, the combustion of metallized compositions is characterized by the formation of the disperse phase, including agglomerates (the aggregated particles with a considerable portion of oxide, but containing active metal) and oxide particles with sizes from hundreds of microns to tens of nanometers. The disperse phase parameters of real compositions are necessary for engineering calculations and are measured in routine experiments. On the other hand, special metallized compositions may be used as a source of "mother" particles (i.e., burning particles that generate the oxide particles) in studies under various conditions (e.g., in a high-pressure vessel or in air at atmospheric pressure). This method may be used to produce particles that simulate agglomerates (i.e., comparatively large metal particles resulting from the combination of many small particles), formed in combustion of real composite systems. Thus, the preliminarily characterized "mother" particles of known dimensions, which burn in a specially produced gas medium, may serve as a physical model of the combustion of particle agglomerates in technical devices, e.g., in motor combustion chambers. As for experimental techniques, the essence of most of them reduces to the firing of particles in a vessel and to the sampling of combustion products for further analysis. Besides, one of the typical methods is the forced breaking of particle evolution (extinguishing of mother particles, freezing of oxide particles).
2. The nanosized oxide particles present only one among many types of the condensed combustion products [2]. The nanoparticles may contribute just a minor fraction of all combustion products (on order of units of percent). However, they, as shown above, are of considerable interest but are poorly studied.
3. The nanoparticles usually exist as aerosol systems and these systems are of considerable practical importance. Remember that the main parameters of nanoparticles, determined according to practical needs, are the size distribution of particles, their quantity (concentration, mass output), morphology (regularities of aggregation of primary particles, aggregate shape), and for TiO_2, the phase composition (rutile/anatase/other phases).

The chapter content is as follows. First, the techniques employed (mainly, the aerosol ones) are described. Then the experimental data on Al_2O_3 and TiO_2 nanoparticles, mainly the original data of the authors, are reported. In the conclusions, the actual problems are formulated and future investigations are discussed.

2. EXPERIMENTAL TECHNIQUES FOR PARTICLE SAMPLING

To analyze the disperse phase of burning metallized compositions (the combustion products of metallized particles), and to estimate the parameters of particle combustion macrokinetics, e.g., the combustion time, a series of original techniques have been developed at the Voevodsky Institute of Chemical Kinetics and Combustion, Siberian Branch of the Russian Academy of Sciences (ICKC SB RAS). Not all of the below methods were initially intended for studying nanoparticles. In most cases, the nanoparticles were sampled "among others," i.e., together with larger particles. Particular attention has been paid to the capacity of different techniques to work within the given size range. In Refs [25] and [26], the entire arsenal of techniques was used to study the smoke combustion products of Ti particles. In Ref. [27], all the ICKC SB RAS techniques are presented as well as the main results obtained by these methods. Brief descriptions of them follow.

2.1 Flow-through Bomb for Sampling the Condensed Combustion Products of Metallized Compositions

The essence of sampling methods is to extinguish and to trap particles at various stages of combustion. Further study of sampled particles can be made by different available physical and chemical methods. This may provide a high informational content, and, at the same time, involve the development of corresponding analytical techniques and devices. In particular, for agglomerates and oxide particles, essential are the data on particle size, chemical, and phase composition. Different sampling methods for studying the condensed combustion products (CCPs) are employed in the US, Russia, Germany, Japan, Italy, Taiwan, and other countries. In 1985, at the ICKC SB RAS, an original technique was developed that exhibits a series of advantages as compared with other sampling methods. The various modifications of the technique have been repeatedly described in the Refs [2,25,28–34]. Briefly, a small propellant specimen is fired in a specially designed flow-through bomb pressurized with inert gas (N_2, He, or Ar). The flame of the specimen is directed downward and enclosed in a "protective" tube, where the particles are in the gaseous combustion products of the specimen. Extinction is performed at the exit of the tube by mixing combustion products with a cocurrent flow of inert gas blowing through the bomb. The particles can be frozen at a given distance from the burning surface by varying the length of the protective tube. In the absence of the tube, the particles are extinguished at the shortest distance near the burning surface. Near the exit (inside the bomb), all the particles—combustion products generated by a propellant sample—are trapped by a wire mesh screen stack and by an analytical aerosol filter. The so-called "Petryanov" aerosol filter [35] (e.g., of AFA type) efficiently captures submicron particles. Briefly, the entrapping efficiency of AFA filters amounts to 95% for

the most penetrating particles—the standard oil aerosol with a diameter of 0.1–0.2 μm. Below we will consider the AFA filter characteristics and applications in more detail.

These are the real parameters at which the sampling of CCPs was performed: specimen diameter, 7–20 mm; length, 10–30 mm; and mass up to 5.5 g. When the diameter was 7 mm, the shortest distance of combustion products extinction was about 20 mm (ca. threefold specimen diameter). The maximal length of the protective tube was 190 mm. The maximal pressure was 12 MPa while the minimal one was 0.2 MPa. A low excess pressure is required for gas to flow through the bomb. In Ref. [25], the authors report experiments performed without a strong bomb casing, i.e., actually, at atmospheric pressure. The number of specimens, 1–5, in the series fired under the same conditions (tube length, pressure) depends on specimen size and is determined by the sampled mass needed for analysis. The optimum experimental conditions are provided by the presence of minimal mass, about 1.5 g of the particles sampled. Thus, for a typical metalized propellant, containing 15–25% Al, the total initial mass of specimens is about 5 g. The representativity of sampling, defined as the ratio between the calculated CCP mass and that of the CCP sampled, is not worse than 0.85; usually it equals 0.9–0.95 for aluminized propellants. In Ref. [34], a comparison has been made between the sampling representativity of the ICKC SB RAS technique and the technique of sampling into liquid for the combustion products of the propellant, containing Al-Mg mechanical alloy. In experiments performed at 0.3 and 6 MPa, the sampling representativity of the former technique was 0.57 and 0.80, and that of the latter was 0.27 and 0.61. Note that the Al-Mg alloy is a more "difficult" object than pure aluminum.

It is known that the combustion of metallized propellants results in the formation of particles differing in size by several orders of magnitude, e.g., from 10^{-10} to 10^{-2} m. The maximal size of the particles sampled by the ICKC SB RAS technique is unlimited. In particular, for some propellants we have sampled skeleton fragments of about 20 mm. The lower size limit for the particles analyzed is commonly equal to 0.5 μm. These are the data presented in our papers. However, it is due to the application of a granulometer "Malvern 3600E sizer" for analyzing small particles and is not a methodical limitation. As shown above, the AFA filter is effective in the trapping of nanometric particles. Figure 3(b) of Ref. [36] depicts the nanometric particles from the filter.

The mentioned extremely wide size range of CCP particles requires the application of special methods of particle size analysis to determine a size distribution function of particles. A typical method used by many researchers is either the physical or virtual (as a computational method) division of particles into fractions and the application of specific methods of analysis for each size range (fraction) followed by the computer combination of particular distribution functions and the recovery of a distribution function over the entire range. We have solved this problem using our algorithms and programs, described partly in Refs [28–30]. It is worth noting that the data on the chemical composition of particles (at least, in terms of the metal/oxide ratio) are

needed to evaluate the sampling representativity. The corresponding methods of analytical chemistry were developed and adapted [37–39] for a quantitative determination of both the metallic aluminum (called either active or unburned) content, and the "completeness of combustion" for dual metal fuels such as Al-B and Al-Mg. Obviously, the sampling method, as well as the other methods used to diagnose the disperse phase (e.g., photography/filming/video), face certain difficulties in interpreting the results obtained. For details, see Ref. [40].

2.2 Petryanov Filter

The fibrous filtering materials, Petryanov filters (PFs), are serially manufactured and widely used in Russia [41]. The analytical aerosol Petryanov filter of AFA type was employed in Refs [26] and [27] as a tool for determining the total mass of smoke particles. In this case, a composite propellant specimen or a set of separate metallic particles were burned in a vessel of finite volume (10–20 L), and combustion products pumped through the filter during the time shorter than the sedimentation time of smoke particles in the vessel. If the particles were burned in air, the vessel was initially filled through the filter to prevent atmospheric aerosol from penetration into the vessel.

According to Ref. [35], for the AFA filters, the trapping efficiency, E, determined using a standard oil aerosol, is about 95% for the particles with a diameter of 0.1–0.2 μm. The particles of this size are most penetrating. For other sizes, the efficiency is higher, namely, $E \geq 99\%$, for those with a diameter of 0.3 μm; $E \geq 99.99\%$, for the particles of 1 μm; $E \geq 99\%$, for the particles smaller than 0.1 μm; and $E \geq 99.9\%$ for those of 0.02–0.05 μm. In addition to the high efficiency of particle trapping due to electrostatic charge, the particles can be easily removed from the filters by dissolving the AFA filter in acetone. The resulting suspension of particles can be analyzed using, e.g., an automatic granulometer "Malvern 3600E." The procedure for making the filter optically transparent via impregnation with glycerine is described in Ref. [36]. Thereafter, the particles of tens of microns can be examined and measured under an optical microscope without removing them from the filter.

The Petryanov filters, made of perchlorvinyl fibers, are hydrophobic (the maximal relative humidity of filtered air being 95%), chemically resistant relative to liquid aerosol particles of mineral acids and alkali, but of low thermal resistance (up to 60 °C) and are unstable to oils and organic solvents of the type of plastificators, chlorinated hydrocarbons, etc. The Petryanov filters made of acetylcellulose fibers are hydrophilic and chemically stable to organic solvents of the type of plasificators and oils, but are unstable to acids, alkali, and organic solvents, such as dichloroethane, acetone, etc. Their thermal resistance is limited to 150 °C, the maximal relative humidity of filtered air is 80%. Thus, the main disadvantages of the both types of the Petryanov filters are the limited thermal resistance and the stability to chemically active materials as well as the low filtration rate (about 1 cm/s).

We have tried to estimate the specific surface of filter fibers by the "Sorbi" apparatus, using the BET method. The idea was to measure filter surface prior to experiments and then to sample particles and to measure the surface once again. In this case, the difference in surface values before and after experiment with account for the mass of the particles sampled would provide the specific surface of the particles sampled. Our efforts have failed because it was impossible to correctly measure the filter surface which varied continuously, probably, due to the destruction of filter fibers at cryogenic temperature at which the working gas is adsorbed by the Brunauer–Emmett–Teller (BET) method.

The advantages and disadvantages of the Petryanov filter are presented in detail in Ref. [41].

2.3 Aerosol Impactor

A cascade impactor of Anderson type [42] was employed together with the Petryanov filters [26,27]. The impactor is used to perform the aerodynamic size classification of particles. Each cascade consists of two plates: the first one is with apertures and the second is used to sample particles. The flow of particles moves to the surface of a sampling plate. The cascades differ in diameter, the number of apertures, and the distance between the plates. They are characterized by the size of particles, deposited on a plate at a certain airflow rate. We have used a five-cascade impactor "BP-35/25-4," elaborated and manufactured at the state scientific center of virology and biotechnology "Vector" (Novosibirsk region, Koltsovo). The nominal, characteristic size of particles, d_{50}, trapped by cascade #1 is 17.8 μm, 13.5 μm for cascade #2, 3.65 μm for cascade #3 and 1.27 μm for cascade #4 (calculations were performed for particles of a density of 3.9 g/cm^3). The AFA filter that traps the particles passing through cascades $1 \div 4$, plays a role of the fifth cascade. This impactor allows one to estimate the mass size distribution of smoke particles, including the fraction of those smaller than 1.27 μm. As in the case of the filter, a vacuum pump and a device to control a gas flow rate are needed for the impactor to work.

2.4 Diffusion Aerosol Spectrometer

The diffusion aerosol spectrometer (DSA), developed at the ICKC SB RAS [43], includes diffusion battery, condensation enlarger, and optical counter of particles. It is used to determine the size and concentration of aerosol particles. Such measurements are regulated by a state standard [44], where the working principle of the setup is presented. For description and a block scheme, see Ref. [43]. The basic technical characteristics of the DSA are as follows. The measured particle diameters are 3 nm $\div$ 1 μm, the concentration range of aerosol particles is $10^1 \div 5 \times 10^5$ cm^{-3}, and the measuring cycle lasts 5 min. By the given characteristics, the DSA is either in line with the best foreign aerosol spectrometers [45,46] or even better.

The DSA was employed to study the nanosized oxide smoke TiO_2 aerosol, formed by combustion of tiny specimens of pyrotechnic composition with titanium powder [25]. It was shown that the mean arithmetic size of particles, D_{10}, determined by the DSA, coincides well with that obtained by a laborious detailed treatment of electron-microscopic images (the particles with $D_{10} \sim 20$ nm). Thus, the DSA can be recommended for studying the aerosols of nanoparticles resulting from the combustion of metal particles.

2.5 Vacuum Sampler

A vacuum sampler is a device, similar by its sampling principle, to the probe of molecular-beam mass spectrometry, applied for studying the flame structure of condensed systems [47], and by its deposition principle, to a low-pressure cascade impactor [42]. The vacuum sampler for trapping submicron particles from specimen flame or from vessel volume is of the form of a steel capillary tube. One of its ends is located in the flow of the two-phase medium studied, and the other is in the vacuumized volume that contains a screen with Formvar film that serves as a substrate for inertially deposited particles. This system, screen + film + particles, is the commonly used object for a transmission electron microscope. Other substrates are also possible, e.g., the silicon ones for a scanning electron microscope. The sampler parameters (capillary diameter, the degree of rarefaction, the distance between tube end and a substrate) are to be chosen with regard to the given particle size range. Available are a variant for "cold" aerosols with a conic, Plexiglas tip (Figure 3), and that with a ceramic capillary for sampling from flame (Figure 4). The sampler is calibrated using standard aerosols. The residence time of particles in a working volume of the sampler (from their takeout from flame to deposition on a substrate) varies, depending on sampler parameters, from 1 to 100 ms. In Ref. [25], we have used the vacuum sampler, developed and patented by the researchers

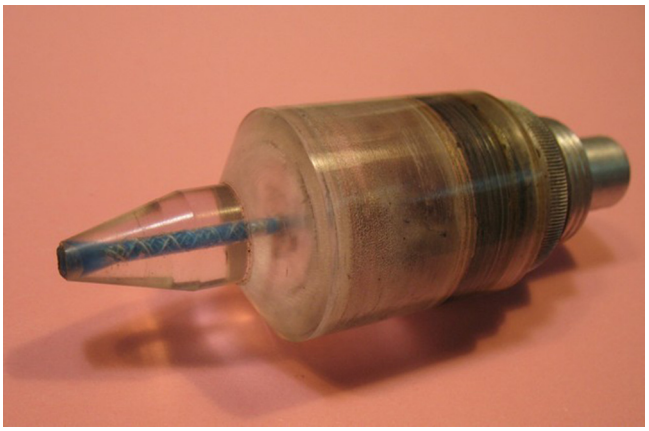

Figure 3 Vacuum sampler—a variant for cold flows with Plexiglas tip (to the left).

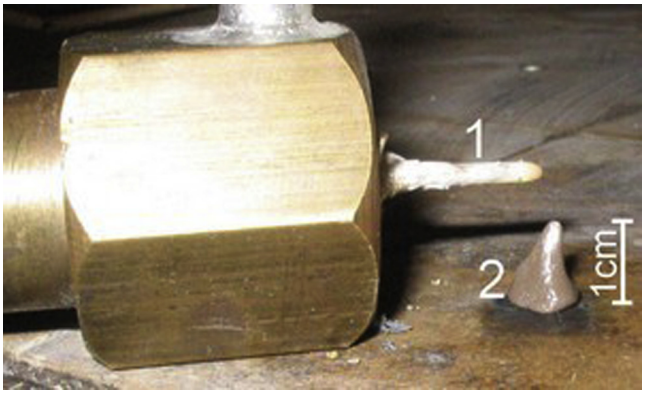

Figure 4 Vacuum sampler—a variant for aerosol sampling from flame. 1—capillary, 2—specimen of pyrotechnical composition.

of the ICKC SB RAS [48,49]. Experiments were performed as follows. A conic specimen of titanium-containing pyrotechnical composition of a height of 1 cm was fired in air at atmospheric pressure. Aerosols were sampled upon combustion from flame through a ceramic capillary 3 cm long with 1 mm inner diameter under relatively small rarefaction (pressure drop of a 20 mm water lift relative to atmospheric pressure) (Figure 4). The aerosol sampled was diluted with purified air at a flow rate of 10 L/min and sent to a 20-L buffer vessel from which it was directed to the diffusion aerosol spectrometer, DSA. It is assumed then that a fast dilution allows us to avoid the formation of aerosol aggregates. A typical aerosol concentration in the buffer vessel was 10^4–10^5 cm^{-3}. In the previous section, it was recommended to use the DSA for studying the aerosols of nanoparticles, formed in combustion of metal particles. This section demonstrates the application of a vacuum sampler for collecting aerosol particles from flame. In this case, the following considerations should be taken into account. If aerosol particles are of complex structure, e.g., in the form of fractal aggregates consisting of primary nanoparticles, it is likely that these aggregates will be destroyed upon sampling and transportation through a capillary under the action of aerodynamic forces. In other words, information on aggregate structure will be lost upon sampling. If a researcher is interested only in the parameters of the primary particles, the use of the vacuum sampler together with the DSA is a good combination. However, when the researcher takes so much interest in aggregate structure (as shown in the introduction, it plays a key role upon aerosol propagation in the atmosphere), then he should use more "delicate" methods of sampling, e.g., a thermophoretic precipitator that is described below.

2.6 Thermophoretic Precipitator

In all our works, the data on the morphology of oxide aerosols were extracted from particle sampling with a thermophoretic precipitator, developed and produced at the

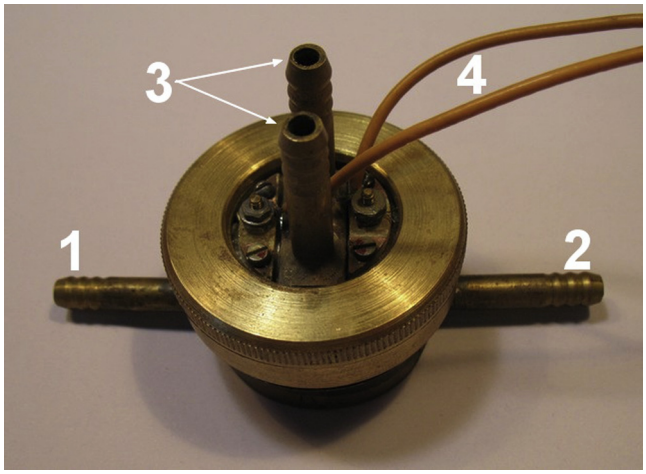

Figure 5 Thermophoretic precipitator. 1,2—inlet and outlet water sockets for cooling the lower wall of the channel; 3—inlet and outlet aerosol sockets; 4—wires for electric heating of the upper wall of the channel.

ICKC SB RAS. The setup is shown in Figure 5; for details see Ref. [50]. The apparatus provides a nonselective sampling of particles with an efficiency close to 100% over a size range of 3 nm–10 μm on the screen with Formvar film, used for subsequent examination under transmission electron microscope. The principle of operation is the following. There is a channel of rectangular cross-section 5 mm wide and 100 μm high. The temperature gradients of 2200–2400 K/cm were set by heating the upper wall of the channel with electric current and by cooling the bottom wall with running water. The walls of the channel are made of bronze. The set of screens with Formvar film are fixed on the lower wall. Aerosol moves slowly through the channel (mass flow rate being below 15 sccm—standard cubic centimeter per minute). The molecules of carrier gas, which move more vigorously near the heated plate, gradually push away the aerosol particles toward the cold plate until their deposition on the screen. After the experiment, the screens are removed and studied by electron microscope. The electron-microscopic images are treated using original software [28–30,51].

3. ORIGINAL EXPERIMENTAL APPROACHES

3.1 Preparation of Monodisperse Agglomerate Particles

The development of special laboratory technologies for producing the burning monodisperse particles of agglomerate origin (i.e., resulting from joining many small particles) has two main motives.

First, the identical particles are the most convenient objects for studying combustion mechanism in general and oxide particle formation, in particular. Particle polydispersity causes the well-known difficulties in interpreting sampling results [40]. The particles of various sizes exhibit different behaviors in gas flows. They are characterized by individual temporal parameters, e.g., the time required to cover distance up to extinction in extinguishing and sampling techniques. Moreover, the macrokinetics of the combustion of various sized particles is different in the general case, probably due to distinctions in the structure and morphology of particles, in particular, due to the metal/oxide ratio. Thus, performing experiments on the particles of a given size and of the same structure provides the most accurate and reliable data.

Second, in most of the cases (except for technological particle combustion in a dust jet, see the introduction), researchers deal with the combustion of agglomerates rather than of single monolithic particles. The regularities of agglomerate combustion should be examined because of their practical importance. In the general case, the combustion of solid particles and agglomerates is different. For example, the formation of burning 500 μm aluminum agglomerates in combustion of composite solid propellants is a common practice [52]. At the same time, a 500 μm solid aluminum particle can be ignited only when using a powerful CO_2 laser. Therefore, the relevance of the application of a solid particle as a physical model of an agglomerate needs to be proved. For aluminum particles, it can be assumed that the smaller the particle or the agglomerate, the smaller are the distinctions in their combustion parameters (the time of complete combustion, i.e., burning time; a fraction of formed highly disperse oxide, etc.). To orient someone, remember a diameter value of 100 μm. It is shown [54] that the combustion behavior of agglomerates and particles of this diameter is almost the same. Similar information is unavailable for titanium particles.

We have developed an original approach to produce monodisperse burning agglomerates of aluminum and titanium just during experiment. The details of its realization for aluminum and titanium are different, but, in both of the cases, the approach is based on the transformation of dosed microquantities of highly metallized composition into individual burning particles. The transformation is performed in a combustion wave of nonmetallized composition in which the above microquantities of metallized composition are contained as inclusions. The mass, size, and composition of inclusions determine the parameters of burning particle agglomerates. The main experimental difficulty in realizing this approach is that the inclusions should be identical. Nevertheless, we have managed to produce the particles with a variation coefficient K_{var} in the range $0.07 \div 0.14$. Notice, that in granulometry, the set of particles with variation coefficients $K_{var} < 0.15$ ([53], p. 212), is assumed to be monodisperse. Here $K_{var} = \sigma/D_{10}$, and $\sigma = \sqrt{D_{20}^2 - D_{10}^2}$ is the mean-square deviation (standard deviation).

Using this approach, we have already produced and studied the burning agglomerates of aluminum 100, 340, and 480 μm in diameter, and those of titanium 300, 390, and 480 μm in diameter. The technology of producing inclusions and specimens as well as the results are fully presented in Refs [36,40,54,55–57] for aluminum agglomerates and in Refs [58–64] for the titanium ones.

3.2 Chamber with Nozzle for Particle Acceleration

Analyzing the literature and our own data on titanium particle combustion, we assumed that the combustion parameters (including the characteristics of nanosized oxide) depend on the velocity of burning particles in a gaseous oxidizing medium [26]. To verify this assumption, we have constructed a setup in the form of a small chamber with a nozzle (Figure 6).

In the chamber, a specimen burns to generate monodisperse burning particles, which are ejected through the nozzle. Firstly, the particles are transported mainly by a jet of gaseous combustion products. Then, the jet is decelerated and dissipated in the ambient air, and the particles move under their own momentum, the Stokes drag force, and the gravity force. The regularities of particle movement in each case (particle diameter, nozzle diameter, up/down direction, etc.) should be studied in detail and generalized statistically for a set of particles of the given nominal size. Note that the influence on the combustion process is related not to the absolute value of particle velocity but to the velocity of movement relative to the ambient air, i.e., the relative flow velocity [63,64].

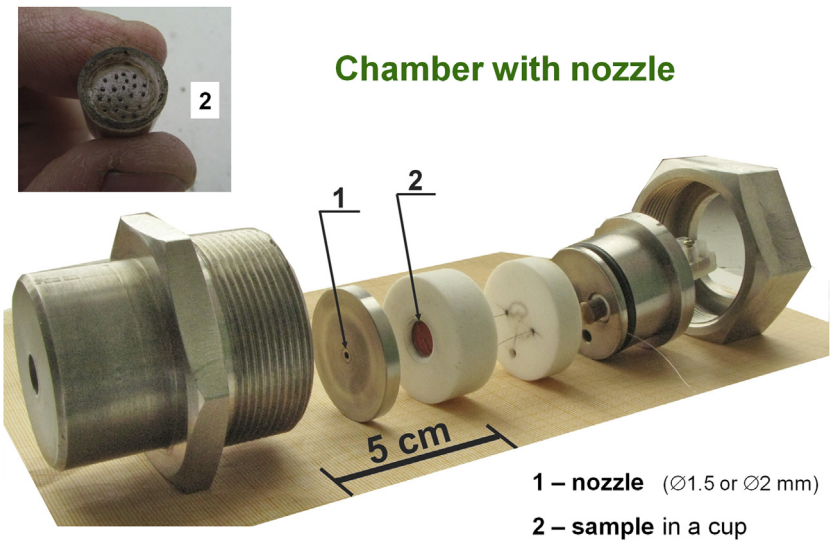

Figure 6 Knocked-down chamber with nozzle. At the top left, there is a specimen of "nonmetalized matrix + metalized inclusions" type upon preparation. The preparation involves a gradual filling of a small cup by successive formation of matrix and particle layers.

In this case, the smaller particles acquire the velocity of either the jet or the ambient gas more quickly so that a blow velocity becomes zero. When the nozzle is 1.5 mm (the minimal value in our experiments) for particles with a diameter of 320 μm, a relative blow velocity, averaged along the entire trajectory, reaches 7.9 m/s. To increase the mean blow velocity one should solve the optimization problem, taking into account the parameters that determine particle motion and burning. The main parameters are: burning rate, temperature, specimen geometry, nozzle diameter, determining the outlet jet characteristics, the diameter and aerodynamic drag force coefficient of burning particles that determine particle acceleration/deceleration ratio, and burning time. The last one determines the time range for averaging. Usually, the motion of particles is recorded using a video camera. Thus, in Refs [63] and [64], the shooting was performed at the rate of 300 fps.

3.3 Video Microscopy in Aerosol Optical Cell of Millikan Type

The setup is schematically depicted in Figure 7 (taken from Ref. [65] by authority of the author of the method). The optically accessible aerosol cell (similar to those of Millikan, Fuchs, Petryanov) has two windows for a laser beam to pass and one window to record particle images, resulting from light scattering at an angle of 90°, with the help of a video camera. The visualized field is located between metallic, parallel electrodes to which a voltage is supplied. The pump is used to inject an aerosol sample into the cell. The valve is then turned off and the behavior of the aerosol sample is recorded.

Specifications of the setup are as follows. The power of helium–neon laser amounts to 2.5 mW. Focusing optical instruments allow one to get an effective beam diameter in a bottleneck within the range 150–350 μm. The gap between the electrodes is 2.5 mm;

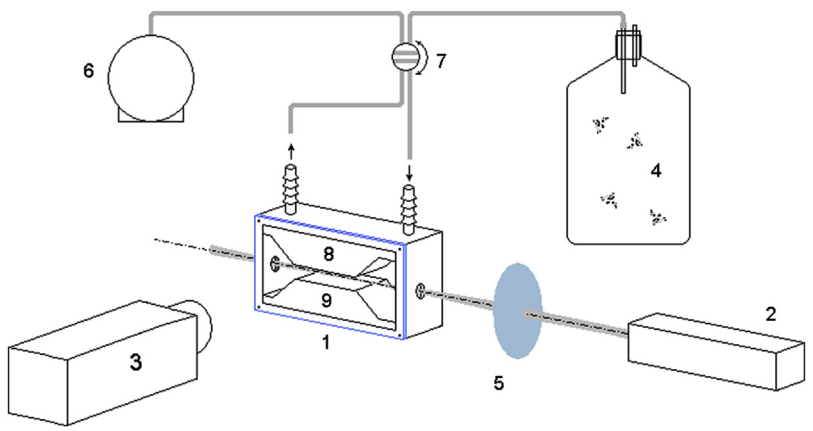

Figure 7 Block-scheme of the system of videomicroscope and aerosol cell [65]: 1—cell; 2—laser; 3—CCD camera with microscope lens; 4—vessel in which the samples, generating aerosol, were burned; 5—lens; 6—pump; 7—double valve; 8,9—electrodes in the cell.

the strength of homogeneous electric field is 160–360 V/cm. A black-and-white camera with a microscope lens provides observation of the working volume region of the cell with $\approx 15\times$ magnification on the camera charged-coupled device (CCD) matrix. The spatial resolution of the system (lens + CCD matrix) is about 3 μm, the focal depth is about 50 μm, and the visualized field of vision in the working volume of the cell is about $300 \times 400\ \mu m^2$. The lower limit to the size of the particles recorded amounts to about 0.1 μm and is limited to the sensitivity of the CCD matrix and the density of laser radiation flux in the volume visualized. The particles smaller than 3 μm are observed as light spots, which makes it possible to follow their movement. The shape of the particles exceeding 3 μm in size can be distinguished, which allows one to observe their rotational motion (e.g., under the action of electric field).

Thus, this technique may be used to follow the motion of aerosol particles with or without electric field and to determine the velocities of photophoresis and Brownian motion, the electric charge, and charge-dipole moment, and the other parameters of single aerosol particles using an ultra-low mass aerosol sample (ten-hundreds of picograms, tens of particles).

4. CHARACTERISTICS OF OXIDE NANOPARTICLES

4.1 Aluminum Oxide Al_2O_3

The literature data on aluminum oxide nanoparticles, formed in combustion of aluminum microparticles, are rather scarce. The method of gas-disperse synthesis of metal oxide nanopowders in a laminar aerodisperse flame was developed at the Odessa National University (Ukraine). It was referenced in the introduction as an example of technological combustion. For technological purposes, the laminar flame is usually used. In this case, the reaction zone is narrow, of almost permanent thickness over the flame surface, with high temperature gradients in preflame and postflame zones, and without recirculation of combustion products. As a result, metal burning and the condensation of combustion products occur along the entire height of the flame zone (conically shaped) almost under the same conditions. The influence of particle coagulation on the size distribution of combustion products is negligible, which favors the production of the narrow fractions of combustion products. The attempt to increase the output of the setup at the expense of turbulization leads to the polydispersity of condensed combustion products.

Reference [21] summarizes the main results of experimental and theoretical studies on the effect of the parameters of the aerodisperse diffusion flame of metal particles (Al, Fe, Ti, Zr) on the dispersity of the combustion products of these metals in oxygen-containing media. The authors [21] have varied the mass concentrations of fuel and oxidizer, the nature of carrier gas, and the method for flame organizing: laminar diffusion flame (LDF) or premixed laminar flame (PLF). These results [21] are presented in Tables 1 and 2.

Table 1 The parameters of aluminum oxide particle size distribution. Effect of initial oxygen concentration C_{O_2}. Initial aluminum particles: mass concentration $C_f = 0.4$ kg/m^3, size $d_{10}^{Al} = 4.8$ μm.

C_{O_2}, %	Carrier gas	d_{10}, nm	d_{20}, nm	d_{30}, nm	Sd, nm	σ	d_{50}, nm	d_m, nm	S_c, 10^4 m^2/kg
0	N_2	103	126	150	73	0.62	77	62	2.4
6.4		83	94	104	44	0.47	75	64	2.3
11.6		69	76	83	32	0.38	66	60	2.7
14.0		61	65	70	22	0.53	58	54	2.8
27.0		63	69	78	28	0.35	59	55	2.7
20.0	He	53	57	60	21	0.31	52	51	3.1

Table 2 The parameters of aluminum oxide particle size distribution obtained in premixed laminar flame (PLF) regime. Effect of initial aluminum size d_{10}^{Al} and concentration C_f.

C_f, kg/m^3	d_{10}^{Al}, micron	d_{10}, nm	d_{20}, nm	d_{30}, nm	Sd, nm	σ	d_{50}, nm	d_m, nm	S_c, 10^4 m^2/kg
0.22	4.8	83	100	119	56	0.57	66	51	2.7
0.40		103	126	150	73	0.62	77	62	2.1
0.62		107	127	152	68	0.63	91	69	1.9
0.7	14.6	71	81	92	39	0.50	63	49	2.7

The parameters used in Tables 1 and 2 are denoted as follows: C_f and C_{O_2} are the mass concentrations of metal fuel and oxygen in the carrier gas, and d_{10}, d_{20}, d_{30} are the arithmetic mean, surface mean, and volumetric mean diameters, correspondingly. These diameters are determined by the formula $d_{mn} = \sqrt[m-n]{(\sum_{i=1}^{k} d_i^m \cdot N_i)/(\sum_{i=1}^{k} d_i^n \cdot N_i)}$, where m, and n are the integers setting the order of the mean diameter, k is the total number of size intervals in histogram, N_i is the number of particles in the i-th interval, and d_i is the middle of the i-th interval. The parameter Sd is the standard deviation determined by the formula $Sd = \sqrt{d_{20}^2 - d_{10}^2}$, σ and d_{50} are the parameters of the lognormal distribution function of oxide particles in the form $\phi(d) = \frac{1}{\sqrt{2\pi}\, d\sigma} \exp\left[-\frac{(\ln d - \ln d_{50})^2}{2\sigma^2}\right]$. For the distribution formula of this type, the parameter σ is called "width" and the parameter d_{50} is called "median." These parameters may be used to calculate "mode" d_m, "specific surface" S_c, and other useful parameters. For instance, $d_m = d_{50} \exp(-\sigma^2)$, $S_c = 6/(\rho d_{32})$, where ρ is the oxide particles density, and $d_{32} = (d_{30})^3/(d_{20})^2$. The mean diameters d_{20} and d_{30} can be calculated using the lognormal size distribution parameter from the common formula $(d_{r0})^r = (d_{50})^r \exp(r^2\sigma^2/2)$, where r is the integer.

As follows from Tables 1 and 2, the mean diameter d_{10} varies from 53 to 103 nm. The position of a maximum of the lognormal distribution of oxide particles, mode d_m, varies slightly ($d_m = 49-69$ nm) within the experimental conditions range studied by

the authors [21]. The influence of experimental conditions on the dispersity of Al combustion products reduces mainly to the variation of the width σ of the particle size distribution function ($0.31 < \sigma < 0.63$).

To control the dispersity of oxide nanoparticles, the authors [21] suggested introducing admixtures into the primary metallic fuel to affect oxide nucleation in flame via ionization. The ions are assumed to be the centers of condensation. Increasing their concentration leads to an increase in combustion products dispersion. This assumption was verified experimentally [21]. Thus, adding 5% carbon (mechanical mixture of 95% Al and 5% C) causes the decrease in d_{10} from 103 nm to 34 nm and in d_m from 62 nm to 30 nm.

As compared with Ref. [21], in our works [57,65–67,69–75], the oxide particles were characterized by several techniques. When performing "delicate" sampling of aerosol particles with a thermophoretic precipitator followed by the analysis of samples by means of transmission electron microscope (TEM), we have managed to study not only the distribution functions of the primary nanoparticles but also the aggregates, consisting of nanoparticles, to obtain information on their morphology, phase composition, etc. The video microscopy made it possible to investigate the charge (and dipole) properties of the aggregates, their mobility, coagulation, and other characteristics. As mentioned in the introduction, the morphology of aggregates determines their transport properties (diffusion coefficient, sedimentation and velocity of photophoresis, etc.), optical characteristics, specific surface, and the ability to adsorb and transfer harmful substances. As is known, the charge properties of nanoparticles and of their aggregates have a substantial effect on aggregate formation and evolution. The typical features of evolution are the change in size due to the merging of the aggregates and single particles (coagulation) owing to the Coulomb interaction, and the restructuring (swerving) of the aggregates.

Consider now the main results from experiments [67] on the combustion of model aluminized composite propellant, containing 20% Al, 25% AP, 35% HMX, and 20% binder (the same as in Ref. [57]). The specimens in the form of a parallelepiped 20–25 mm long and with a cross-section of $1 \times 1.5\ \text{mm}^2$ were burned in a 20-L vessel in the aerosol-free air at atmospheric pressure. The aluminum mass of the specimen was $\approx$6 mg. The burning surface generated aluminum agglomerates with a wide size distribution. They burned upon their fall in the vessel for less than 5 s. Six minutes after propellant burning, the aerosol was sampled from the vessel and its disperse, morphological, and charge characteristics were analyzed. The time value of 6 min can be called the "age" of the aggregates.

Figure 8 shows a typical TEM image of the aluminum oxide aggregate. As follows, the aggregate is chain branched and consists of the primary spherical particles from units to hundreds of nanometers. These particles are called *spherules*. The images were processed to determine the conventional aggregate size R, the number of spherules, and

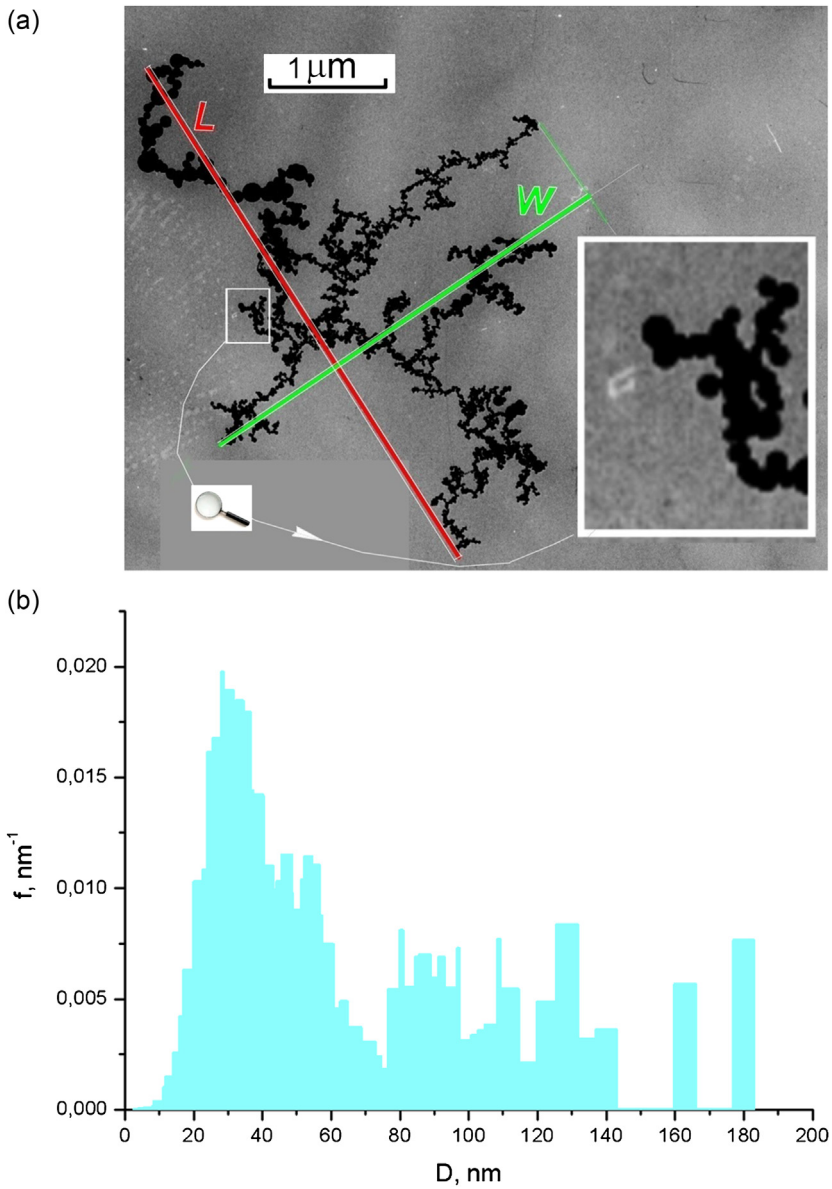

Figure 8 (a) A typical view of aluminum oxide aggregate. (b) Mass size distribution function for spherules of which this aggregate is composed.

their size distribution, see Figure 8. Taking into account particle density, on the basis of these data one can readily calculate the aggregate mass M. The structural characteristics of similar aggregates are usually characterized in terms of the fractal dimension D_f. According to Ref. [68], D_f may be defined as an exponent in the power relationship

$M \propto R^{D_f}$ between the aggregate mass M and its size R. Actually, this approach is based on the assumption of a minor "overlap" of spherules in the image, so that the aggregate projection onto the plane corresponds to the volumetric distribution of spherules in the aggregate. If $D_f < 2$, the fractal dimension of two-dimensional projection is equivalent to that of the three-dimensional object [76]. In Ref. [67], the fractal dimension D_f was found for a set of aggregates, "on average." In this case, a mathematical procedure reduces to the determination of the slope of the straight line, which approximates the size dependency of the mass in logarithmic coordinates $\log(M)$ versus $\log(R)$. Note that there are the alternative ways of estimating the fractal dimension and the size of aggregates. Some of these are discussed in Ref. [51]. In Ref. [67], the authors plotted $\log(M)$ versus $\log(R)$ and got $D_f = 1.60 \pm 0.04$. A total of 52 aggregates at age of 6 min were processed. The convention size R varies from 0.09 to 2.31 μm, and the number of spherules varies from 20 to 3280.

In Figure 8, the fragment in the white frame and its enlarged image demonstrate that the aggregate consists of spherules. It is worth noting that the aggregate contains "clusters," i.e., the regions with particles of visibly different size range. This aggregate was treated using three different magnifications for the different parts of the aggregate. The aggregate includes totally 3217 spherules. Plot (b) presents the mass size distribution function $f(D)$ of aggregate spherules. The value f, a relative spherule mass within the histogram size interval, divided by interval width, is plotted on the ordinate. Figure 8(a) illustrates one of the ways to determine a conventional aggregate size or "radius" from the expression $R = 0.5\sqrt{LW}$, where L is the maximal length, and W is the width, the maximal aggregate size in the direction perpendicular to L. For this aggregate, we get $L = 4.96$ μm, $W = 3.79$ μm, and $R = 2.17$ μm. For comparison: the nominal radius of the sphere with a volume equal to the total one of spherules in the aggregate is 0.256 μm.

For the above-mentioned model propellant, there are different statistics [57], supplemented with the data on 18 aggregates at an age of 12 min. In this case, we have $D_f = 1.64 \pm 0.09$. Besides, in Ref. [57], another technique has been used to estimate the conventional aggregate size. Nevertheless, the derived values of fractal dimension $D_f = 1.60 \pm 0.04$ and $D_f = 1.64 \pm 0.09$ coincide to within experimental error and are noticeably lower than 1.80, which corresponds to the DLCCA model (diffusion-limited cluster–cluster aggregation) [76]. For this model it is assumed that the aggregates merge exclusively due to the Brownian diffusion without long-range interactions between them. As shown below, the process of coagulation of the aerosol particles under study involves electrostatic forces, i.e., those of the Coulomb interaction, determined by the presence of electric charges. Distributed charges promote the formation of "chain" fragments (clusters) in the aggregate structure. The greater the number of such fragments in the aggregate, the closer to 1 is D_f (for a linear chain of spherules $M \propto R$). We may say that the value of D_f deviation from 1.80 characterizes the role and significance of the Coulomb interaction in aggregate formation and evolution.

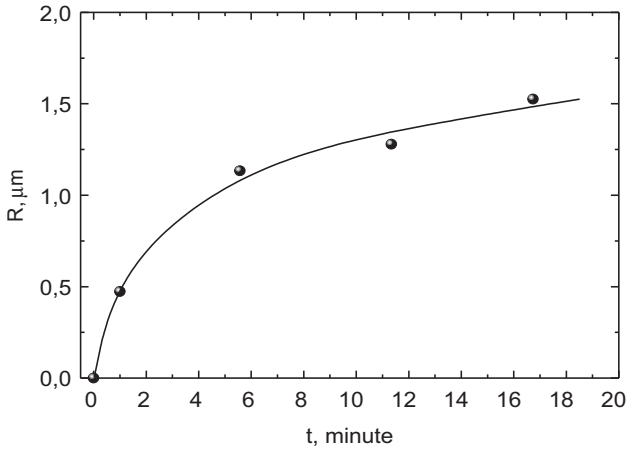

Figure 9 Arithmetic mean radius of aggregates versus coagulation time.

The dependency of aggregate size on age (coagulation time) was revealed in Ref. [69] (Figure 9). The observed asymptotic character of the dependency, is, probably, determined by a limited number of aggregates in a vessel. The greater the number of the aggregates that have already merged, the less is the probability of the subsequent collisions.

The presence of clusters, in which the difference in spherule size is rather small, but at the same time, the difference in spherule size from cluster to cluster is essential (Figure 8), may be explained as follows. The clusters with spherules within a certain comparatively narrow range were first formed by various mother particles. Then these merged into an aggregate via coagulation. This assumption is based on the hypothesis that the size of spherules depends on the size of a burning original particle. The hypothesis was later verified by experiments on monodisperse burning particles [57]. Indeed, the greater the diameter of the mother particle, the larger are the spherules formed, see Figure 10 and Table 3.

Figure 10 shows the joint functions of the normalized density of the size distribution of a number of spherules obtained by combining histograms for the set of aggregates. Numbers near the curves denote the diameter of burning particles. The curve "Polydisp." corresponds to the population of particles-agglomerates, generated by combustion of composite propellants. In this case, the efficient diameter of the burning particles is estimated as $\approx$ 10 μm, which corresponds to the mean arithmetic diameter of aluminum particles used to manufacture the propellant. The insert plots the arithmetic mean spherule diameter versus that of the burning particles.

The data in Figure 10 and Table 3 indicate that the spherules, formed by combustion of a polydisperse system, exhibit a wider size distribution ($K_{var} = 0.58$, whereas for

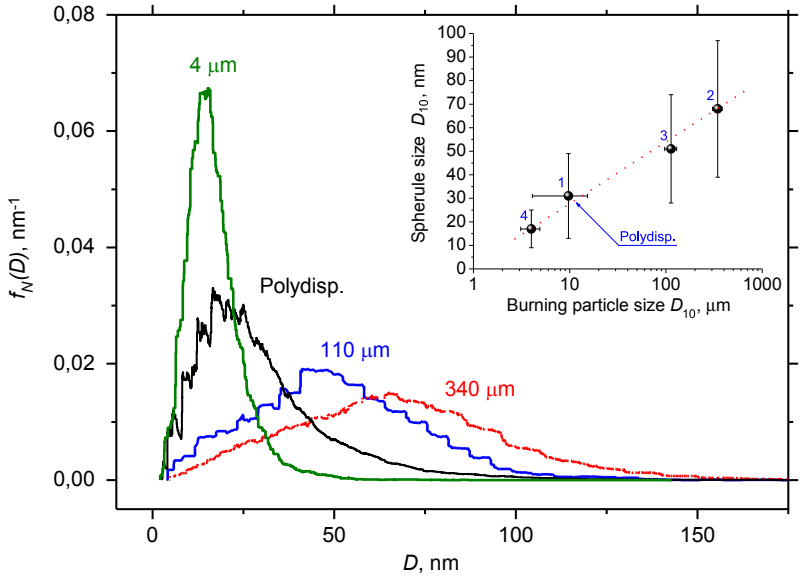

Figure 10 Effect of the size of burning particles on the size distribution of formed oxide nanoparticles. Here, 4 μm, 110 μm, 340 μm and "Polydisp." are the sizes of burning particles.

Table 3 Dependency of the parameters of oxide spherules dispersity on the size of burning particles [57].

Point no. in Figure 10 insert	Size of burning particle, micron	Number of treated spherules	D_{10}, nm	D_{20}, nm	D_{30}, nm	D_{43}, nm	σ, nm	K_{var}
1	Polydisperse	44,843	31	36	43	80	18	0.58
2	340	14,348	68	74	80	107	29	0.43
3	110	14,296	51	56	61	80	23	0.45
4	4	48,885	17	19	21	34	8	0.50

monodisperse particles, $K_{var} = 0.43-0.50$). According to the results of determining the fractal dimension of the aggregates, the values of D_f vary from 1.62 to 1.65 in the case of 10–340 μm burning particles. For the burning particles of 4 μm, $D_f = 1.80$, which corresponds to the DLCCA model and indicates the reduced role of the Coulomb interaction as compared to the Brownian diffusion with decreasing sizes of spherules and/or burning particles. It is interesting that the value of the fractal dimension is actually independent of coagulation time within the range studied (up to 17 min).

Our data (Table 3) on the sizes of Al_2O_3 spherules and those of Ref. [21] (Tables 1 and 2) are mutually complementary. In particular, our data were used in Ref. [21] to construct the dependency of spherule size on the mass concentration of metals (see Figure 6 in Ref. [21]).

Video microscopy makes it possible to observe a series of phenomena to be interpreted quite plainly.

1. The movement of charged (negative or positive) aggregates in a homogeneous electric field of 160 V/cm. The motion direction changes with changing field polarity. A minor part of aggregates does not respond to field switching. Thus, many aggregates carry an electric charge, which can be either positive or negative.
2. The rotation of some aggregates by 180 degree when switching the electric field polarity. Interpretation: such aggregates have a distributed electric charge and a rotating moment appears in the electric field. The (+) and (−) charges may be compensated for by some aggregates. These aggregates are, as a whole, electroneutral and do not make a forward motion in the electric field.
3. The acts of the coagulation (approach and sticking) of various objects: aggregate with aggregate; aggregate with particle; aggregate with wall covered by previously deposited aggregates and resulting "tendrils." In all cases, there occur both the accelerated movement of a fever massive object and the sticking of a given orientation. Interpretation: the accelerated movement is due to the Coulomb force; orientation is provided by distributed charges.

The above phenomena have been repeatedly illustrated by video record frames [65–67, 69,70], omitted here.

A quantitative treatment of the characteristics of aggregate movement in electric field allowed us to estimate the electric charges of the aggregates. Most of the particles-aggregates have a charge with the number of positively and negatively charged particles being almost the same. The distribution of particles by charge may be approximated in terms of the Gaussian function, which is symmetric relative to a zero charge. The characteristic charge of the aggregate composes several elementary units. It is worth noting that the charge values are estimated using an average size determined by electron microscopy ($R \approx 1.13$ μm at aggregate age of 6 min, see Figure 9), and assuming the Stokes drag force law.

The X-ray phase analysis indicates that the crystal structure of the spherules, formed in combustion of aluminum particles, is the α and γ phases of Al_2O_3. For analysis we used: (a) the samples collected by means of a thermophoretic precipitator, and the electron microscope, operating in electronogram recording mode; (b) the samples collected by a vacuum sampler on substrates, and a powder XRD analyzer; and (c) the samples collected on the Petryanov filters. In this case, a filter fragment, cut out with scissors, was used "as is" in the XRD analyzer.

4.2 Titanium Oxide TiO_2

Let us first specify the terminology. In the literature, the nanosized particles, produced by decomposition of a titanium-containing precursor (e.g., $TiCl_4$) with a subsequent oxidation of Ti clusters in the flame of a gas burner, are usually called the TiO_2 particles,

synthesized by combustion [77]. There is a large body of work, see review [78], devoted to the traditional methods of synthesis of photocatalytic TiO_2, including the above synthesis in a burner. These works commonly describe the authorized method of synthesis (reagents, process organization), the properties of produced TiO_2 particles (size, the specific surface and morphology of particles, the size of crystallites and the regions of coherent scattering, the phase composition, photocatalytic activity), and compare the activities of the resulting particles with the commercial catalysts Degussa P25 or Hombikat.

In the present work, when discussing the TiO_2 particles produced in combustion, we imply the combustion products of *metallic* titanium microparticles.

As shown in the introduction, of particular interest are the photocatalytically active TiO_2 particles of nanometric size range and their ability to decompose organic substances. Therefore, we first present general information on the properties of the particles, obtained by conventional methods, to compare them with the particles-products of metallic titanium combustion.

The TiO_2 nanoparticles are spherical (less often, polyhedral or cubic [79]) and like the primary Al_2O_3 nanoparticles, they are called *spherules*. Their diameter does not usually exceed 100 nm. This size is not the size "natural limit," but results from the striving of researchers for producing particles as small as possible to obtain the largest specific photocatalytic surface. It is readily proved that on the surface of TiO_2, any organic substances, including live cells, bacteria, and viruses, may be oxidized to CO_2, H_2O, and inorganic residues. The crystal structure of TiO_2 nanoparticles (the main forms, rutile and anatase) has affects the photocatalytic properties, but the data on this influence are rather contradictory. Numerous studies (see reviews [80,81]) are devoted to the doping of particle surface by various metals and nonmetals to increase the quantum yield of decomposition (i.e., photocatalysis efficiency) by broadening the functioning range for the wavelengths of solar light (it is desirable to shift the edge of absorption band to the visible region).

Let us discuss the characteristics of the combustion products of metallic titanium microparticles. The condensed combustion products are the residues of burning particles, fragmentation products, oxide particles-products of fragment burning mainly in the heterogeneous regime, as well as the highly disperse oxide particles that are either the products of burning in the vapor-phase regime or the condensation products (in particular, spherules). The listed types of the particles-products have been studied in Refs [25,58–65,74,75] (our works) and in Refs [21] and [82] (other authors).

The evolution of Ti particles of a mean size of ≈ 4 μm, moving in a plasmotron chamber for tens of milliseconds, was first studied in Ref. [82]. The residual particles were treated according to their morphology as metallic and oxide particles. Besides, the oxide particles (anatase) smaller than 100 nm were revealed, which allowed the authors [82] to assume a combined heterogeneous plus vapor-phase regime of Ti particles combustion.

In Ref. [21], devoted to the synthesis of oxide particles upon combustion of metal microparticles in a gas-disperse jet, the data on Al_2O_3 are presented along with those on the TiO_2 spherules formed in combustion of Ti. The synthesis conditions are as follows: primary Ti particles of ≈ 5 μm; oxygen concentration, 40%; particles concentration, 10^{12} $m^{-3;}$ and temperature in the jet, 3000–3100 K. The characteristics of synthesized oxide are the following: mean arithmetic diameter, 40 nm; and standard deviation, 16 nm. The size distribution of particles is lognormal with the following parameters: median, 38 nm; mode, 35 nm; and width, 0.38. For parameter definitions, see Section 4.1. The oxide parameters are observed to depend slightly on input conditions (concentration and initial particle size) upon realization of a stable aerodysperse flame. The authors [21] assert that an increase in oxygen concentration above 40% (with a constant concentration of Ti particles of $10^{12}m^{-3}$) causes a substantial increase in the yield of TiO_2 nanoparticles, which reaches tens of percent by weight due to the change in combustion regime from heterogeneous to gas phase with a heterogeneous formation of suboxides and their subsequent, additional oxidation in the vicinity of the particle surface. Thus, in this case, the intensification of combustion process favors the formation of nanoparticles. For the general case, this leads to higher temperatures in the reaction zone and the size and properties of the resulting particles-products depend considerably on subsequent cooling.

Consider now our data on the combustion products of metallic titanium particles, first of all, on the particle size, structural, crystal, and electrophysical characteristics of oxide TiO_2 nanoparticles.

Various experiments were performed using both the different methods of "generation" of burning titanium particles and the different sampling techniques. We present the main experimental techniques.

1. The burning of 1-g specimens of chlorine-free compositions, containing 15–29% metallic titanium, ammonium nitrate, and an energetic matrix binder [25,75] in a 20-L vessel, filled with aerosol-free air. The primary titanium particles were of irregular, "spongy" form with sizes less than 100 μm (the particles smaller than 63 μm contribute 88% of the mass). The composition of plasticine consistency was used either to fill small cups or to obtain specimens of specific form (e.g., conic). The initial titanium particles agglomerated in the combustion wave of the composition. The set of burning particles manifests a wide size distribution, i.e., from the size of the primary particles, introduced in the composition, to the agglomerates of several tens of microns. The size distribution of particles changes with varying fraction of titanium in the composition. Upon combustion of the composition inserted in a small cup 1 cm in diameter, the smallest particles burn out in the flame of the composition while the large ones burn in the air. A certain time after sample combustion (within 0–10 min), the smoke-like aerosol is collected from the vessel onto the thermoprecipitator. The information obtained concerns

aggregate morphology and spherule size. The aerosol is also injected in the video microscopy cell to study the motion, coagulation, and charge properties of the aggregates.

2. The burning of the gram specimens of the same compositions having the conic form with a base of 1 cm in air. The aerosol is sampled just from the specimen flame with a vacuum sampler (Figure 4). We obtain information on spherule sizes.
3. The burning of the gram specimens of the same composition in small cups 1 cm in diameter in a blow-through vessel [30] in the air stream. The particles are sampled on the stack of metallic sieve screens, the Petryanov filter, and the lining covering the surface of the vessel. The time of particle movement from specimen to extinction/sampling location is less than 1 min. We get information on particle distribution within the entire size range, including the smoke fractions with particles smaller than 5 μm.
4. The ejection of single burning particles of 100–350 μm from a horizontal quartz capillary with an inner diameter of 2.5 mm [71]. Before experiments, the capillary is loaded with a mixture of ammonium perchlorate (AP) and polymer binder with Ti particles. The particles fly out from the capillary at a speed of 1.5–2 m/s. The glass plate, covered with Formvar film on which the oxide aerosol, formed in combustion, is deposited thermophoretically, is installed at a small angle to the trajectory of particle movement. The deposited particles are then studied under the electron microscope. The method provides information on spherules at the early stage of their growth (at age of 0.1 ms).
5. The combustion of monodisperse particles in a vertical 10-L vessel 84 mm in diameter and about 2.4 m in height. The particles used were of two types: (1) A narrow-sieved fraction of spongy-shaped particles with a characteristic size of 38 μm. The fraction was extracted using precision sieve screens with a mesh aperture of 36 and 40 μm. (2) The agglomerates formed of tiny inclusions. The diameter of the agglomerates was 320 μm. A mixture for agglomerate formation consisted of 69% titanium powder (Russian commercial sort "PTM," 85% of the mass included particles smaller than 50 μm) and polymeric, active binder based on methylpolyvinyl-tetrazole. To realize the ignition and ejection of agglomerates, we used a nonmetalized composition matrix, consisting of 23% AP, 50% HMX (all particles smaller than 10 μm), and 27% binder [61]. This composition was of plasticine consistency. The specimens were in the form of small cylinders, filled either with a metal-free matrix with inserted metalized inclusions, agglomerate "seeds" (Figure 6, position 2), or single 38-μm particles. In experiments, the latter were placed in the nonmetalized matrix in an amount of less than 0.1% and carefully separated from each other. The combustion of 38-μm particles was completed just in the flame of the specimen. The combustion of 320-μm agglomerates continued upon their movement in the air. Experiments on the 38-μm particles and 320-μm

agglomerates were carried out both under ordinary conditions (sample combustion in a small cup in air, combustion of agglomerates in free fall mode) and using a chamber with a nozzle (Figure 6). In the last case, the maximal trajectory–mean velocity of particle movement relative to gas reached 7.9 m/s. These experiments are discussed below. Earlier experiments [23,60], using a chamber with a nozzle, were performed on the specimens of compositions, consisting of 14% Ti powder, that generated polydisperse agglomerates.

In all the cases, the smoke aerosol was sampled from the vessel with a thermoprecipitator, and the data were obtained on aggregate morphology and spherule size.

The experimental results indicate the following.

The aerosol particles of oxide TiO_2 smoke, like the Al_2O_3 particles, are the chain-branched fractal aggregates of 0.1–10 μm, consisting of spherules of 5–150 nm. Most of the aggregates have either a positive or a negative charge (Figure 11).

It has been established that the charge distribution of the TiO_2 particles is wider than the equilibrium Boltzmann one at room temperature by a factor of 1.4–3 (the so-called "over equilibrium" one). When the polarity of external electric field is switched, some large-size aggregates of titanium oxide rotate through 180° as the aluminum oxide aggregates. These are the dipoles, i.e., they carry the distributed charges.

The X-ray phase analysis indicates that the smoke particles represent TiO_2 in the crystal forms of rutile, anatase, and brukite.

Despite the similarities between the Ti and Al combustion products in the characteristic size of spherules and aggregate morphology, there is a significant distinction in the combustion behavior of these metals. For Al, the size of Al_2O_3 spherules depends on the

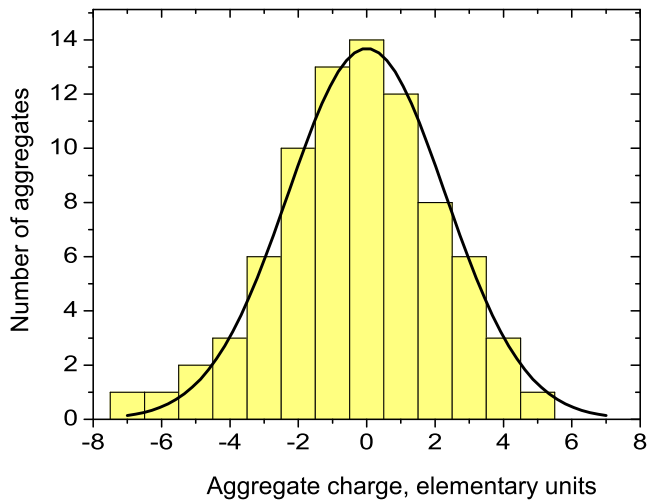

Figure 11 Distribution of TiO_2 aggregates by values of electric charges [74].

diameter of the burning mother particle. The arithmetic mean diameter, D_{10}, of spherules increases with the size of burning particles and amounts to 17, 51, and 68 nm, respectively, for Al particles of 4, 110, and 340 μm, see Figure 10 and Ref. [57]. This actually allows one to control the size of spherules, which is practically impossible for Ti because the size of spherules is almost independent of the size and burning conditions of Ti particles. Thus, in all our experiments, except for the chamber with a nozzle, the same diameter of the TiO_2 spherules was determined, $D_{10} \approx 23$ nm. We have varied the formulation of gasifying pyrotechnical compositions (in particular, we used the solid oxidizers of four types—ammonium perchlorate, ammonium nitrate, hydrazine mononitrate, and HMX), the size, shape and "origin" of burning particles sizes (sizes from <20 μm to 300 μm; spongy irregular particles and spherical agglomerates, including monodisperse particles of ≈38 μm and monodisperse agglomerates 320 μm in diameter, the polydisperse agglomerates of a size up to 1000 μm), and combustion environment (typically small particles burn in the gaseous products of either pyrotechnical composition, solid propellant, or nonmetalized matrix, and the large ones burn in the air beyond the flame). The fractal dimension of the TiO_2 aggregates was constant, $D_f \approx 1.55$.

A conservative character of the TiO_2 smoke properties makes it actual to search for the ways to control the parameters of the resulting oxide nanoparticles. These include the effect on the processes of nucleation and condensation via introduction of admixtures (experimentally confirmed for Al_2O_3 in Ref. [21]) as well as the intensification of particle burning. The latter can be realized either by increasing oxygen concentration [21] or by blowing the burning particles. In Ref. [26], we have assumed that the size of spherules depends on the velocity of the burning Ti particle, moving relative to a gaseous medium (the same as blowing the motionless particle). A tiny chamber with a nozzle has been proposed (Figure 6) for imposing high velocities to the burning particles. The effect of blowing was registered at the qualitative level, but its quantitative description was difficult. In particular, the particle's velocity for actually polydisperse population was estimated very roughly. Therefore, there was a need to carry out more correct experiments on monodisperse particles. In Refs [60,63,64], quantitative experiments were performed on the monodisperse Ti particles of agglomeration origin of a diameter of 320 μm and with a narrow-sieved particle fraction of about 38 μm. Processing the TEM images of sampled smoke particles provided the size distribution functions of nanometric particles-spherules (Figure 12). It has been established that an increase in the velocity of particle movement relative to gas leads to a decrease in spherule size. This effect was observed only with the highest (in our experiments) particle blowing velocity, which indicates its threshold character. For the particles 320 μm in diameter, an increase in the trajectory-averaged particle-gas relative velocity from 0.9 to 7.9 m/s causes a decrease in the spherule diameter D_{10} from 28–30 nm to 19 nm; see the table within the legends to Figure 12.

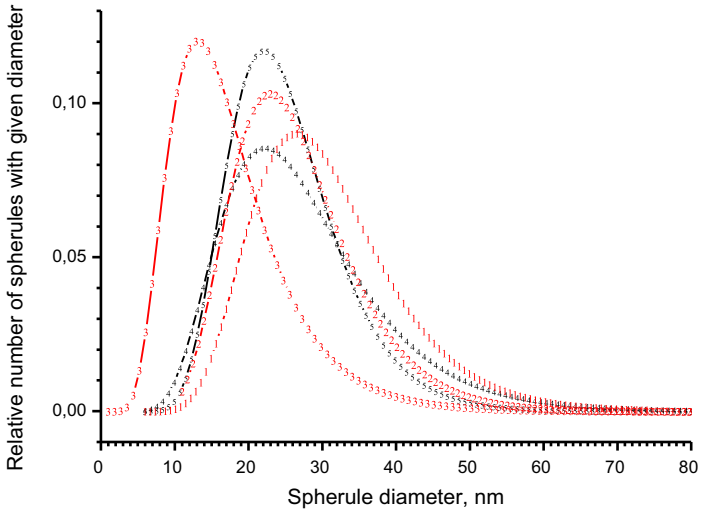

Figure 12 Comparison of approximating size distribution functions of spherules [60,63,64].

Curve labels	1	2	3	4	5
Initial size of burning particles, micron	320	320	320	38	38
Nozzle, diameter in mm	No nozzle	2	1.5	No nozzle	2
Average (over the burning time) velocity of particle movement relative to gas, cm/s	92	568	789	17	7.5
Statistical parameters of spherules size distribution calculated via treating histograms					
Arithmetic mean diameter D_{10}, nm	30	28	19	29	25
Sd—standard deviation	Sd = 9	Sd = 10	Sd = 10	Sd = 12	Sd = 7
Se—standard deviation of the mean	Se = 0.3	Se = 0.3	Se = 0.1	Se = 0.2	Se = 0.1
The number of measured particles N	860	1458	6056	2743	2687

The movement of the burning Ti particles affects the morphological parameters of oxide aerosol, in particular, causes an increase in the fractal dimension of aggregates up to $D_f = 1.79$, Figure 13. The plot reproduced from Ref. [26] illustrates the procedure for determining the fractal dimension from the slope of the $M\left(D_{\text{gaba}}^{D_f}\right)$ line graph. Here, D_{gaba} is the "conventional diameter" of aggregates equal to the doubled "conventional radius" $R = 0.5\sqrt{LW}$, i.e., $D_{\text{gaba}} = 2R$. The hollow circles are the data [26], obtained with blowing; the solid circles are the data [25,74], obtained without blowing. The evaluated maximal blowing velocity is about 10–15 m/s. This rough estimate was obtained from a video record as the length of visible particle tracks divided by frame

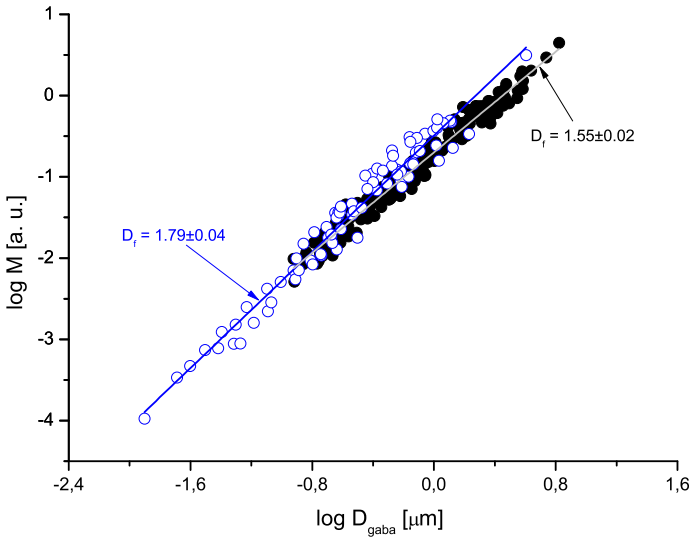

Figure 13 The effect of particle-gas relative motion of burning particles on the fractal dimension of aggregates [26]. ●—data [25,74] without blowing, ○—data [26] with blowing.

exposure time. It is difficult to present an exact value due to the essential polydispersity of the burning agglomerate set in experiments [26].The other morphological peculiarities of combustion products for the particles under blowing are the presence of comparatively large particles (up to 300 nm) and mainly rectilinear chains of spherules in aggregate structure. The presence of large particles in the aggregates is, probably, due to the fact that the blowing may lead to a strong fragmentation of burning particles. The fragments burn rapidly in the heterogeneous regime to give comparatively large particles-products (residues). In addition, the burning time of 320-μm agglomerates was recorded to decrease from 0.45 to 0.26 s with increasing blow velocity from 0.9 to 7.9 m/s [64]. The rectilinear spherule chains appear owing to the charge effects and Coulomb interaction. The "high compactness" of the aggregates formed under blowing (verified by higher fractal dimension) is imposed by the presence of large particles whose mass may amount to 0.8 of the aggregate mass [26].

Thus, the blowing of the burning Ti particles may be considered as a method for intensifying combustion process and for affecting the burning parameters and the characteristics of the nanoparticles formed. It is important to note that the method is of purely physical nature and needs no admixtures.

Finally, we discuss the data of X-ray phase analysis. The crystal structure of TiO_2 spherules sampled by thermoprecipitator is anatase (60% wt) and rutile (40% wt). The smoke particles sampled on the AFA filter are predominantly of crystal rutile form, and the size of crystallites is 60–80 nm. There are also unidentified reflexes.

The meagre experimental data [83,84] on the photocatalytic activity of the TiO_2 particles, formed in combustion of metallic Ti, suggest that the TiO_2 aerosol cloud may be used as countermeasures against the local emission of contaminants.

5. CONCLUSIONS AND FUTURE WORK

The data available show that the charging of particles due to thermoelectron emission plays a key role in oxide particles formation. The generality of the mechanism accounts for structure similarity and for the closeness of many parameters, describing the properties of aerosol Al_2O_3 and TiO_2 systems. Schematically, the evolution of oxide aerosol may be presented as follows. First, a spherule forms and starts growing due to nucleation and condensation at some distance from the burning particle. Within the condensation zone, the growth of oxide particles proceeds through coalescence. The temperature of spherules decreases with distance from the particle. When it drops below the temperature of oxide melting, the spherules crystallize. The coalescence of liquid particles is replaced by the merging of solid particles into aggregates. Later, already far away from the burning particle, the aggregates may combine and change their structure (e.g., to roll in more compact unit). The forces of electrostatic interaction take part in spherule aggregation, coagulation, and restructuring.

Finally, we can state that in studies on oxide nanoparticles formation in combustion of Al and Ti particles, progress was made toward the characterization of particle size and morphology. Some problems, however, remain unresolved.

Note that the formation of nanoparticles is one of the essential features of the mechanism of metal particles combustion. This mechanism includes the transport of reagents to the reaction zone, i.e., oxidizer from the environment, and/or particle substances (primary metal vapor, suboxides or oxides). A concrete realization of these processes greatly affects the number and properties of nanoparticles. The interaction between the macrokinetics of the initial metal consumption and the formation of dispersed oxide may be considered as the major task for future investigations. For nanosized oxide particles, the following particular problems can be formulated. At what stage of mother particle combustion are they formed? What is the actual mechanism? How can it be intensified?

For aluminum, there are the answers to the first two questions. The nano-oxide particles form from either the vapor-phase oxidation of metals or the oxidation of suboxides, evaporated from the burning particle and delivered into the reaction zone above the burning particle surface. Unsolved is the problem of the intensification of Al_2O_3 nanoparticles formation. In particular, it is of interest to explore whether the blowing of Al particle may have any effect. What will happen after a decrease in the size of burning particles, e.g., down to the size of submicron particles?

For titanium, the first two questions have not yet been answered. As for the third question, it has been established that the formation of nanoparticles may be intensified via air blowing (in particular, the spherule size may be reduced). An intense evaporation may occur at an early stage with oxidation reaction proceeding in the kinetic regime. Of interest is a further increase in particle-gas velocity, i.e., the existence of blowing effect "scale". An important problem of the mechanism of titanium particles combustion is the particles fragmentation, and its feasible application for intensifying combustion and for increasing the yield of nanoparticles. Of interest may also be the search for admixtures (e.g., other metals) that may favor the destruction of the oxide layer. Finally, further study of the photocatalytic properties of nanoparticles formed in Ti particles combustion is also needed.

ACKNOWLEDGMENTS

The authors are grateful to all the coauthors and colleagues of the ICKC SB RAS with whom they had fruitful discussions for a number of years. V.E.Z. thanks the Ministry of Education and Science of the Russian Federation for partial financial support within the framework of the Federal Target Program. Agreement No. 14.578.21.0034 (RFMEFI57814X0034).

REFERENCES

[1] P.F. Pokhil, A.F. Belyayev, Y.V. Frolov, V.S. Logachev, A.I. Korotkov, Combustion of Powdered Metals in Active Media, Nauka, Moscow, 1972 (in Russian). Also available in English: FTD-MT-24-551-73, translated by National Technical Information Service, 1973, pp. 1–395.
[2] V.E. Zarko, O.G. Glotov, Formation of Al oxide particles in combustion of aluminized condensed systems (review), Sci. Technol. Energ. Mater. 74 (6) (2013) 139–143.
[3] The Treaty between the United States of America and the Union of Soviet Socialist Republics on the Elimination of Their Intermediate-range and Shorter-range Missiles, December 8, 1987.
[4] V.V. Adushkin, S.I. Kozlov, A.V. Petrov (Eds.), Environmental problems and risks of impact of the missile and space equipment on environment. Handbook, Ankil, Moscow, 2000, 640 pages (in Russian).
[5] A.S. Zharkov, M.G. Potapov, G.A. Demidov, G.V. Leonov, Bench Tests of the Solid Propellant Energetic Devices, Altai State Technical University Press, Barnaul, 2001, 281 pages (in Russian).
[6] L.V. Zabelin, R.B. Gafiyatullin, L.R. Guseva, Environmental aspects of problem of utilization of charges of solid-propellant rockets, Chemistry in Russia 2 (1999) 4–7 (in Russian).
[7] D.P. Samsonov, V.P. Kiryukhin, N.P. Zhiryukhina, R.I. Pervunina, Determining polychlorinated dibenzo-n-dioxins, dibenzofurans, biphenils, and polynuclear aromatic substances in combustion products of solid rocket propellant, J. Anal. Chem. 51 (1996) 1218–1221 (in Russian).
[8] A.M. Lipanov, M.A. Korepanov, Z.A. Tuhvatullin, Experimental and theoretical study of formation of toxic compounds in the process of utilization of complex chemical substances, Bull. Izhevsk State Tech. Univ. (2) (2003) 51–54 (in Russian).
[9] S.E. Pashchenko, V.E. Zarko, B.D. Oleinikov, S.M. Utkin, T.B. Tihomirova, S.P. Vlasova, Qualitative Analysis of Basic Processes Taking Place in Formation and Propagation of the Superfine Aluminium Oxides Aerosols from Open and Bench Firing the Large-size Solid Propellant Motors and Methods of Their Study/Problem Questions of Methodology of Utilization of Solid Rocket Propellants, Wastes and Remainders of Liquid Rocket Propellants in the Elements of Missile and Space Equipment, Joint Stock Company Federal Research and Production Center "Altai" Press, Biysk, 2000 (in Russian) p. 133–143.

[10] V.I. Romanov, Accident of the solid propellant rocket on a launching site, Cosmic Res. 34 (12) (1996) 102–105 (in Russian).
[11] A.M. Lipanov, M.A. Korepanov, Z.A. Tuhvatullin, Study of formation of the polychlorinated aromatic hydrocarbons upon the solid rocket propellant utilization, Chem. Phys. Mesoscopy 9 (1) (2007) 15–26 (in Russian).
[12] S.I. Burdyugov, M.A. Korepanov, N.P. Kuznetsov, Utilization of Solid Propellant Rocket Motors. Rocket Production Series, Space Research Institute Press, Moscow, 2008, ISBN 978-5-93972-657-3 (in Russian).
[13] V.I. Romanov, Applied Aspects of Accidental Atmospheric Emissions. Handbook, Fizmatkniga, Moscow, 2006, 368 pages (in Russian).
[14] L.A. Fedorov, Dioxines as Ecological Hazard: Retrospectives and Perspectives, Nauka, Moscow, 1993 (in Russian).
[15] B.I. Vorozhtsov, A. Galenko Yu, V.P. Lushev, V.I. Mar'yash, B.D. Oleinikov, A.A. Pavlenko, M.G. Potapov, Yu V. Khrustalev, B.M. Bashunov, Experimental investigations of the spread of products from industrial explosive combustion, Atmos. Oceanic Opt. 10 (6) (1997) 425–431, 681–686.
[16] V.G. Ivanov, S.N. Leonov, G.L. Savinov, O.V. Gavriluk, O.V. Glazkov, Combustion of mixtures of ultradisperse aluminum and gel-like water, Combust. Explos. Shock Waves 30 (4) (1994) 569–570.
[17] A.A. Gromov, T.A. Habas, A.P. Il'in, et al., Combustion of Nano-sized Metal Powders, Deltaplan Press, Tomsk, 2008, 382 pages (in Russian).
[18] A.P. Il'in, A.A. Gromov, Combustion of Ultra-fine Aluminum and Boron, Tomsk State University Publ, Tomsk, 2002, 154 pages (in Russian).
[19] D.A. Yagodnikov, Ignition and Combustion of Powder Metals, The Bauman University Publishing House, Moscow, 2009, ISBN 978-5-7038-3195-3 (in Russian).
[20] A.Yu. Kryukov, Adaptation of the Inside-chamber Processes and Elements of the Energetic Installation Utilizing Powder Fuel to Technologies for Obtaining Ultra- and Nanodispersed Materials, Perm national research polytechnic university Press, Perm, 2012, ISBN 978-5-398-00725-1, 236 pages (in Russian).
[21] N.I. Poletaev, A.N. Zolotko, Y.A. Doroshenko, Degree of dispersion of metal combustion products in a laminar dust flame, Combust. Explos. Shock Waves 47 (2) (2011) 153–165.
[22] L.B. Zubkov, Space Metal. All About Titanium, Nauka, Moscow, 1987, 129 pages. (in Russian).
[23] V. Weiser, J. Neutz, N. Eisenreich, E. Roth, H. Schneider, S. Kelzenberg, Development and characterization of pyrotechnic compositions as counter measures against toxic clouds, in: Energetic Materials: Performance and Safety. 36th Int. Annual Conf. of ICT & 32nd Int. Pyrotechnics Seminar, June 28–July 1, 2005, ICT, Karlsruhe, Germany, 2005, pp. 102-1–102-12.
[24] L.T. DeLuca, L. Galfetti, F. Severini, L. Meda, G. Marra, A.B. Vorozhtsov, V.S. Sedoi, V.A. Babuk, Burning of nano-aluminized composite rocket propellants, Combust. Explos. Shock Waves 41 (6) (2005) 680–692.
[25] O.G. Glotov, V.N. Simonenko, R.S. Zakharov, V.E. Zarko, Combustion characteristics of pyrotechnic mixtures containing titanium, energetic materials, in: Characterisation and Performance of Advanced Systems. 38th Int. Annual Conference on Energetic Materials – Characterization and Performance of Advanced Systems, Karlsruhe, Germany June 26–29, 2007, pp. 87-1–87-15. Also Available in Russian: R.S. Zakharov, O.G. Glotov, Combustion characteristics of pyrotechnic compositions containing powdered Ti//Bulletin of Novosibirsk State University, Physics Series, 2 (3) (2007) 32–40, http://www.phys.nsu.ru/vestnik/catalogue/2007/03/Vestnik_NSU_07T2V3_p1-103.pdf.
[26] O.G. Glotov, V.E. Zarko, V.N. Simonenko, A.A. Onischuk, A.M. Baklanov, S.A. Gus'kov, A.V. Dushkin, In search of effective ways for generation of TiO_2 nanoparticles by means of firing Ti-containing pyrotechnic composition, in: EUCASS 2009, 3rd European Conference for Aerospace Sciences, France, Paris, July 6–9, 2009, ISBN 978-2-930389-47-8. M.L. Riethmuller, Editor-in-Chief. CD Copyright 2009 by the von Karman Institute for Fluid Dynamics.
[27] O.G. Glotov, V.E. Zarko, V.N. Simonenko, A.A. Onischuk, A.M. Baklanov, Size and morphology of the nanooxide aerosol formed in combustion of aluminum and titanium particles in air, in: Combustion of Solid Fuel, Proceedings of VII All-Russian Conf. Novosibirsk, 10–13 November, 2009, vol. 3, Kutateladze Institute of Thermophysics Press, Novosibirsk, 2009, pp. 184–190 (in Russian).

[28] O.G. Glotov, S.E. Pashchenko, V.V. Karasev, Z.V. Ya, V.M. Bolvanenko, Methods for sampling and particle-size analysis of condensed combustion products, in: Physics of Aerodisperse Systems, N 30, Vishcha shkola, Kiev-Odessa, 1986, pp. 43–50 (in Russian).
[29] O.G. Glotov, V.У. Zyryanov, The effect of pressure on characteristics of condensed combustion products of aluminized solid propellants, Arch. Combust. 11 (3–4) (1991) 251–262.
[30] O.G. Glotov, V.У. Zyryanov, Condensed combustion products of aluminized propellants. I. A technique for investigating the evolution of disperse-phase particles, Combust. Explos. Shock Waves 31 (1) (1995) 72–78.
[31] O.G. Glotov, V.E. Zarko, V.V. Karasev, M.W. Beckstead, Aluminum agglomeration in solid propellants: formulation effects, in: Propellants, Explosives, Rockets, and Guns. Proceedings of the Second International High Energy Materials Conference and Exhibit, December 8–10, 1998, IIT Madras, Chennai, India, 1998, pp. 131–137.
[32] O.G. Glotov, V.E. Zarko, Agglomeration in combustion of aluminized solid propellants with varied formulation, in: Proc. of 2nd European Conference on Launcher Technology – Space Solid Propulsion, Italy, Rome, 2000, 14 pages.
[33] O.G. Glotov, V.E. Zarko, Condensed combustion products of aluminized propellants, Trans. Aeronautical and Astronautical Society Republic of China 34 (3) (2002) 247–256.
[34] K. Hori, O.G. Glotov, V.E. Zarko, H. Habu, A.M.M. Faisal, T.D. Fedotova, Study of the combustion residues for Mg/Al solid propellant, in: Energetic Materials: Synthesis, Production and Application. 33th Int. Annual Conference of ICT, Karlsruhe, Germany, 2002, pp. 71-1–71-14.
[35] I.V. Petryanov, V.I. Kozlov, P.I. Basmanov, et al., Fibrous Filtering Materials FP, Znanie, Moscow, 1968 (in Russian).
[36] O.G. Glotov, V.A. Zhukov, Evolution of 100-μm aluminum agglomerates and initially continuous aluminum particles in the flame of a model solid propellant. Part I. Experimental approach, Combust. Explos. Shock Waves 44 (6) (2008) 662–670.
[37] T.D. Fedotova, O.G. Glotov, V.E. Zarko, Chemical analysis of aluminum as a propellant ingredient and determination of aluminum and aluminum nitride in condensed combustion products, Propell. Explos. Pyrotech. 25 (6) (2000) 325–332.
[38] T.D. Fedotova, O.G. Glotov, V.E. Zarko, Peculiarities of chemical analysis of ultra fine aluminum powders, in: Energetic Materials. Performance and Safety, 36th International Annual Conference of ICT & 32nd International Pyrotechnics Seminar. Karlsruhe, Germany. June 28–July 1, 2005, pp. 147-1–147-14.
[39] T.D. Fedotova, O.G. Glotov, V.E. Zarko, Application of cerimetric methods for determining the metallic aluminum content in ultrafine aluminum powders, Propell. Explos. Pyrotech. 32 (2) (2007) 160–164.
[40] O.G. Glotov, V.E. Zarko, V.V. Karasev, Problems and prospects of investigating the formation and evolution of agglomerates by the sampling method, Combust. Explos. Shock Waves 36 (1) (2000) 146–156.
[41] P.I. Basmanov, V.N. Kirichenko, N. Filatov Yu, Yu L. Yurov, Highly Effective Purification of Gases of Aerosols with Petryanov Filters, Moscow, 2002, 193 pages (in Russian), http://www.electrospinning.ru/userfiles/ufiles/vysokoeffektivnaya_ochistka_gazov_ot_aerozoley._p.i.basmanov_i_dr..pdf.
[42] J.P. Lodge Jr., T.L. Chan (Eds.), Cascade Impactor Sampling and Data Analysis, American Industrial Hygiene Association, Akron, Ohio, 1986.
[43] Diffusion Aerosol Spectrometer "DSA". http://www.kinetics.nsc.ru/results/paper44.html (in Russian).
[44] State standard specification of Russia GOST R 8.755-2011. Disperse composition of gas environments. Determination of the sizes of nanoparticles by method of diffusion spectrometry (in Russian).
[45] A. Ankilov, A. Baklanov, R. Mavliev, S. Eremenko, Comparison of the Novosibirsk diffusion battery with the Vienna electromobility spectrometer, J. Aer. Sci. 22 (1991) S325.
[46] A. Ankilov, A. Baklanov, M. Colhoun, K.-H. Enderle, J. Gras, et al., Intercomparison of number concentration measurements by various aerosol particle counters, Atmos. Res. 62 (2002) 177–207, http://aeronanotechnology.com/d/54311/d/intercalibration.pdf.

[47] A.A. Paletsky, A.G. Tereshenko, E.N. Volkov, et al., Study of the CL-20 flame structure using probing molecular beam mass spectrometry, Combust. Explos. Shock Waves 45 (3) (2009) 286–292.
[48] S.E. Pashchenko, V.V. Karasev, Method of sampling of aerosol from flame or nozzle. USSR inventors certificate no. 1186994, Bull. Invention (396) (1985) (in Russian).
[49] E.A. Ershov, S.A. Kambalin, V.V. Karasev, S.E. Pashchenko, Sampling of aerosols for electron-probe analysis by vacuum sampler, Zavodsk. Lab. (6) (1992) 31–34 (in Russian).
[50] D. Gonzalez, A.G. Nasibulin, A.M. Baklanov, S.D. Shandakov, et al., A new thermophoretic precipitator for collection of nanometer-sized aerosol particles, Aerosol Sci. Technol. 39 (2005) 1064–1071, http://dx.doi.org/10.1080/02786820500385569.
[51] O.G. Glotov, Image processing of the fractal aggregates composed of nanoparticles, Russ. J. Phys. Chem. A 82 (13) (2008) 49–54.
[52] O.G. Glotov, Condensed combustion products of aluminized propellants. IV. Effect of the nature of nitramines on aluminum agglomeration and combustion efficiency, Combust. Explos. Shock Waves 42 (4) (2006) 436–449.
[53] O.G. Glotov, V.A. Zhukov, The evolution of 100-μm aluminum agglomerates and initially continuous aluminum particles in the flame of a model solid propellant. II. Results, Combust. Explos. Shock Waves 44 (6) (2008) 671–680.
[54] L.Ya. Gradus, Guide to the Dispersion Analysis with a Microscopy Method, Chemistry, Moscow, 1979 (in Russian).
[55] O.G. Glotov, V.V. Karasev, V.E. Zarko, T.D. Fedotova, M.W. Beckstead, Evolution of aluminum agglomerates moving in combustion products of model solid propellant, in: K.K. Kuo, L.T. De Luca (Eds.), Combust. Energ. Mater., Begell House, New York, 2002, pp. 397–406. Also Available in: O.G. Glotov, V.V. Karasev, V.E. Zarko, T.D. Fedotova, M.W. Beckstead, Evolution of aluminum agglomerates moving in combustion products of model solid propellant, Int. J. Energ. Mater. Chem. Propuls. 5 (1–6) (2002) 397–406.
[56] O.G. Glotov, V.E. Zarko, V.V. Karasev, T.D. Fedotova, A.D. Rychkov, Macrokinetics of combustion of monodisperse agglomerates in the flame of a model solid propellant, Combust. Explos. Shock Waves 39 (5) (2003) 552–562.
[57] O.G. Glotov, A.A. Onischuk, V.V. Karasev, V.E. Zarko, A.M. Baklanov, Size and morphology of the nanooxide aerosol generated by combustion of an aluminum droplet, Doklady Phys. Chem. 413 (Part 1) (2007) 59–62, http://dx.doi.org/10.1134/S0012501607030050.
[58] O.G. Glotov, V.N. Simonenko, V.E. Zarko, G.S. Surodin, Combustion of monodisperse titanium particles in air, in: Energetic Materials for High Performance, Insensitive Munitions and Zero Pollution. 41st Int. Annual Conference of ICT, Karlsruhe, Germany, June 29–July 02, 2010, 2010, pp. 30-1–330-14.
[59] O.G. Glotov, V.E. Zarko, V.N. Simonenko, Combustion of monodisperse titanium particles free falling in air, in: Energetic Materials: Modelling, Simulation and Characterisation of Pyrotechnics, Propellants and Explosives. 42nd International Annual Conference of the Fraunhofer ICT, June 28–July 01, 2011. Karlsruhe, Germany, 2011, pp. 45-1–45-12.
[60] O.G. Glotov, Combustion of titanium particles in air, in: Proceedings of the International Conference "Modern Problems of Applied Mathematics and Mechanics: The Theory, Experiment and Practice", Devoted to the 90 Anniversary since the Birth of the Academician N. N. Yanenko (Novosibirsk, Russia, May 30-June 4, 2011), 2011 (in Russian), http://conf.nsc.ru/files/conferences/niknik-90/fulltext/37173/46861/Glotov_Ti_6pages.pdf.
[61] O.G. Glotov, Combustion of spherical titanium agglomerates in air. I. Experimental approach, Combust. Explos. Shock Waves 49 (3) (2013) 299–306.
[62] O.G. Glotov, Combustion of spherical titanium agglomerates in air. II. Experimental results, Combust. Explos. Shock Waves 49 (3) (2013) 307–319.
[63] O.G. Glotov, V.N. Simonenko, A.M. Baklanov, O.N. Zhitnitsky, G.S. Surodin, Effect of size and velocity of moving titanium particles on nano-sized aerosol particle characteristics, in: Combustion of Solid Fuel. Proceedings of VIII All-Russian Conf., Novosibirsk, 13–16 November 2012, Kutateladze Institute of Thermophysics Press, Novosibirsk, 2012, ISBN 978-5-89017-032-3, pp. 32.1–32.8 (in Russian), http://www.itp.nsc.ru/conferences/gtt8/files/32Glotov.pdf.

[64] O.G. Glotov, Combustion characteristics of monodisperse titanium particles fast moving in air, in: Energetic Materials: Characterization and Modeling of Ignition Process, Reaction Behavior and Performance. 44th Int. Annual Conference of the Fraunhofer ICT, June 25–28, 2013. Karlsruhe, Germany, 2013, pp. 61-1–61-14.
[65] V.V. Karasev, Formation of Nanoaerosol of Oxides of Metal, Silicon and Soot in Processes of Combustion and Pyrolysis, 2006. Abstract of Cand. Sci. thesis (Physics and Mathematics, 01.04.17), Novosibirsk (in Russian).
[66] V.V. Karasev, S. di Stasio, A.A. Onischuk, A.M. Baklanov, O.G. Glotov, V.E. Zarko, V.N. Panfilov, Synthesis of charged agglomerates of Al_2O_3 particles in a combustion reactor, J. Aerosol Sci. 32 (S1) (2001) 593–594.
[67] V.V. Karasev, A.A. Onishchuk, O.G. Glotov, A.M. Baklanov, V.E. Zarko, V.N. Panfilov, Charges and fractal properties of nanoparticles – combustion products of aluminum agglomerates, Combust. Explos. Shock Waves 37 (6) (2001) 734–736.
[68] B.M. Smirnov, Physics of Fractal Clusters, Nauka, Moscow, 1991 (in Russian).
[69] V.V. Karasev, O.G. Glotov, A.M. Baklanov, A.A. Onischuk, V.E. Zarko, Alumina nanoparticle formation under combustion of solid propellant, in: Energetic Materials. Synthesis, Production and Application, 33 International Annual Conference of ICT. June 25–June 28, 2002. Karlsruhe, Germany, 2002, pp. 14-1–14-13.
[70] V.V. Karasev, A.A. Onischuk, O.G. Glotov, A.M. Baklanov, A.G. Maryasov, V.E. Zarko, V.N. Panfilov, A.I. Levykin, K.K. Sabelfeld, Formation of charged aggregates of Al_2O_3 nanoparticles by combustion of aluminum droplets in Air, Combust. Flame 138 (2004) 40–54.
[71] S.A. Khromova, V.V. Karasev, A.A. Onischuk, O.G. Glotov, V.E. Zarko, Formation of nanoparticles of TiO_2 and Al_2O_3 at combustion of metal droplets, in: G. Roy, S. Frolov, A. Starik (Eds.), Nonequilibrium Processes, Plasma, Aerosols, and Atmospheric Phenomena, vol. 2, Torus Press, Ltd., Moscow, 2005, ISBN 5-94588-034-5, pp. 225–234.
[72] V.V. Karasev, O.G. Glotov, A.M. Baklanov, N.I. Ivanova, A.R. Sadykova, A.A. Onischuk, Formation of soot and metal oxide charged aggregates of nanoparticles by combustion and pyrolysis, in: G. Roy, S. Frolov, A. Starik (Eds.), Combustion and Pollution: Environmental Impact, Torus press, Moscow, 2005, ISBN 5-94588-030-2, pp. 207–228.
[73] V.V. Karasev, A.A. Onischuk, S.A. Khromova, O.G. Glotov, V.E. Zarko, E.A. Pilyugina, C.-J. Tsai, P.K. Hopke, Peculiarities of oxide nanoparticle formation during metal droplet combustion, in: Energetic Materials. Insensitivity, Ageing, Monitoring. 37th International Annual Conference of ICT. Karlsruhe, Germany, 2006, pp. 124-1–124-12.
[74] V.V. Karasev, A.A. Onischuk, S.A. Khromova, O.G. Glotov, V.E. Zarko, et al., Formation of metal oxide nanoparticles in combustion of titanium and aluminum droplets, Combust. Explos. Shock Waves 42 (6) (2006) 649–662.
[75] O.G. Glotov, V.N. Simonenko, A.M. Baklanov, V.E. Zarko, et al., Formation of nano-particles of titanium dioxide by combustion of pyrotechnical composition on basis of mechanoactivated composition of titanium with mono-nitrate of hydrazine, in: High Energy Materials: Demilitarization, Antiterrorism and Civil Application. Abstracts of IV International Workshop HEMs-2008 (September 3–5, 2008, Belokurikha), FSUE FR&PC ALTAI, Biysk, 2008, pp. 120–124 (in Russian), http://frpc.secna.ru/hems/docs/hems-2008.rar.
[76] S.K. Friedlander, Smoke, Dust, and Haze, Oxford Univ. Press, New York-Oxford, 2000.
[77] N.K. Memon, D.H. Anju, S.H. Chung, Multiple-diffusion flame synthesis of pure anatase and carbon-coated titanium dioxide nanoparticles, Combust. Flame 160 (2013) 1848–1856.
[78] I.F. Myronyuk, V.L. Chelyadyn, Obtaining methods of titanium dioxide (Review), Phys. Chem. Solid State 11 (4) (2010) 815–831 (in Ukrainian), http://www.nbuv.gov.ua/portal/natural/Phkhtt/2010_4/1104-03.pdf.
[79] S. Jõks, D. Klauson, M. Krichevskaya, S. Preis, et al., Gas-phase photocatalytic activity of nanostructured titanium dioxide from flame aerosol synthesis, Appl. Catal. B: Environ. 111–112 (2012) 1–9.
[80] Y.-C. Nah, I. Paramasivam, P. Schmuki, Doped TiO_2 and TiO_2 nanotubes: synthesis and applications, ChemPhysChem 11 (2010) 2698–2713, http://dx.doi.org/10.1002/cphc.201000276.

[81] H. Sun, S. Wang, H. Ming Ang, M.O. Tadé, et al., Halogen element modified titanium dioxide for visible light photocatalysis (Review), Chem. Eng. J. 162 (2010) 437–447.
[82] A.P. Dolganov, V.N. Kovalev, V.E. Liepinya, E.I. Shipin, Investigation of the regularities of titanium burning particles in gas streams. Proceedings of the Academy of Sciences of Latvian the Soviet Socialist Republic, Ser. Phys. Tech. Sci. (Latvijas PSR Zinatnu Akademijas Vestis, Fiz. Tehnisko Zinatnu Ser.) 2 (1990) 106–113 (in Russian).
[83] Y. Kitamura, N. Okinaka, T. Shibayama, et al., Combustion synthesis of TiO_2 nanoparticles as photocatalyst, Powder Technol. 176 (2007) 93–98.
[84] V.S. Zakharenko, V.N. Parmon, S.A. Khromova, Chemical and optical properties of the titanium dioxide produced from combustion of titanium microparticles in air, Atmos. Oceanic Opt. 20 (6) (2007) 486–491.

CHAPTER TWELVE

Encapsulated Nanoscale Particles and Inclusions in Solid Propellant Ingredients

S.F. Son[1], B.C. Terry[1], S. Isert[1], T.R. Sippel[2], I.E. Gunduz[1] and L.J. Groven[3]
[1]Purdue University, West Lafayette, IN, USA
[2]Iowa State University, Ames, IA, USA
[3]South Dakota School of Mines & Technology, Rapid City, SD, USA

1. ENCAPSULATED NANOSCALE CATALYSTS

Catalyst efficacy generally scales with surface area [1]. However, the addition of nanoscale particles, such as high-surface-area catalysts, can result in high-processing viscosities, and ultimately brittle composite propellants. This could be alleviated with the use of additional binder; however, performance would be decreased. A possible solution to this dilemma is to encapsulate the catalysts within the crystalline oxidizer particles [2–4]. Since the high-surface-area components remain within the crystal, rheology and ultimate mechanical properties are unaffected. In addition, the catalyst could be expected to be more effective within an oxidizer crystal than mixed directly into the binder.

The approach taken by Reese et al. [3] and Isert et al. [4] to encapsulate nanoscale iron oxide into ammonium perchlorate (AP) is shown schematically in Figure 1, and the reader is referred to the references for full details. Briefly, a fast-crash solvent–antisolvent approach is used with the nanoscale particles acting as nucleation sites for the crystallization process. Importantly, a fast-crystallization process results in preferential nucleation rather than crystal growth, producing catalyst particles that are captured within or physically bonded to crystal surfaces. A slower crystallization process is less effective at capturing particles since crystallization tends to be a purification process. Fortunately, the size produced using this process is appropriate for replacing typical finer AP crystals, which are nominally 25 μm in size.

Reese et al. [3] also showed that capture is dependent on antisolvent-to-solvent ratio. Specifically, increased quantities of antisolvent yielded faster nucleation rates, smaller crystals, and improved capture. Sonication of the synthesized materials in a hexane bath also showed that well-captured materials could not be easily displaced from the AP crystals. Inductively coupled plasma emission spectroscopy was used to quantify the level of catalyst captured (up to 92% capture rate was demonstrated). This high level of capture

Energetic Nanomaterials
ISBN 978-0-12-802710-3, http://dx.doi.org/10.1016/B978-0-12-802710-3.00012-X

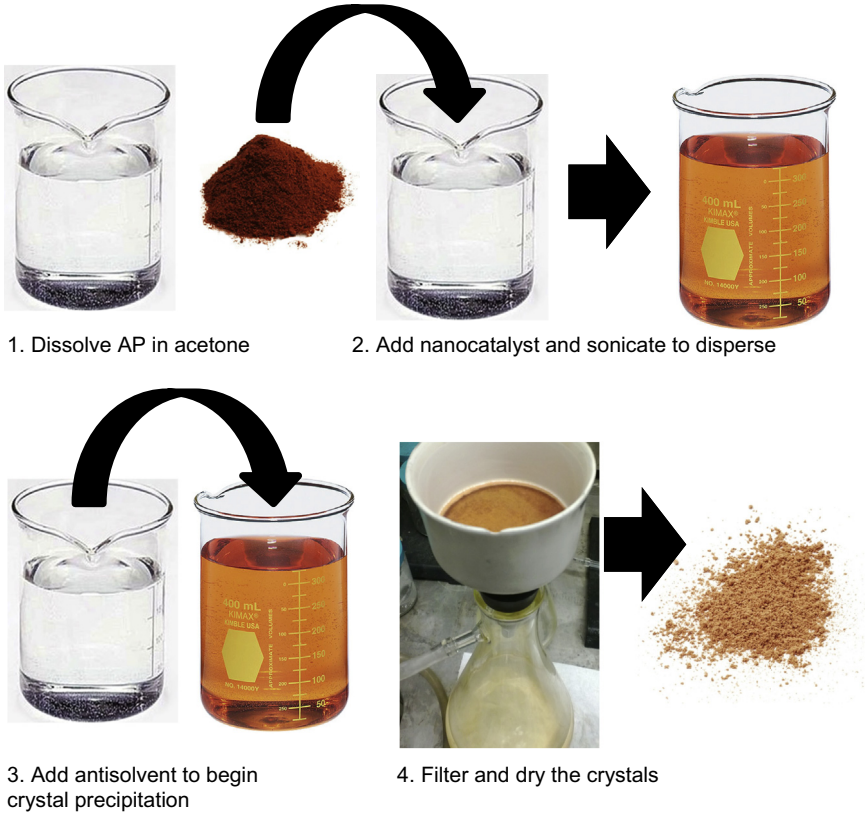

Figure 1 Schematic of process to encapsulate nanoscale particles into ammonium perchlorate.

indicates that the nanoscale particles are effective at nucleating crystal growth. Thermogravimetric analysis showed that decomposition was accelerated with encapsulated catalysts over the physical mixtures, as one might expect with more intimate contact.

Reese et al. [3] also showed that capturing the catalysts inside the crystals yielded a significant decrease in particle surface area compared to a physical mix. Again, this would be expected to result in better propellant rheology and final mechanical properties. Initial encapsulation results were also promising for nanoaluminum with ammonium perchlorate and nanoaluminum with cyclotrimethylenetrinitramine (RDX) systems, but more work is needed to optimize and characterize those results. These latter systems may be particularly interesting for explosives applications, but should be carefully explored because sensitivity and compatibility may prove to be unacceptable.

Isert et al. [4] recently explored the effect of the composite particles (fine AP with encapsulated nano-iron oxide catalyst) on the burning rate and flame structure of an AP-based composite propellant. The coarse AP powders used remained the same (with no encapsulated catalyst). The propellant containing the encapsulated catalyst particles

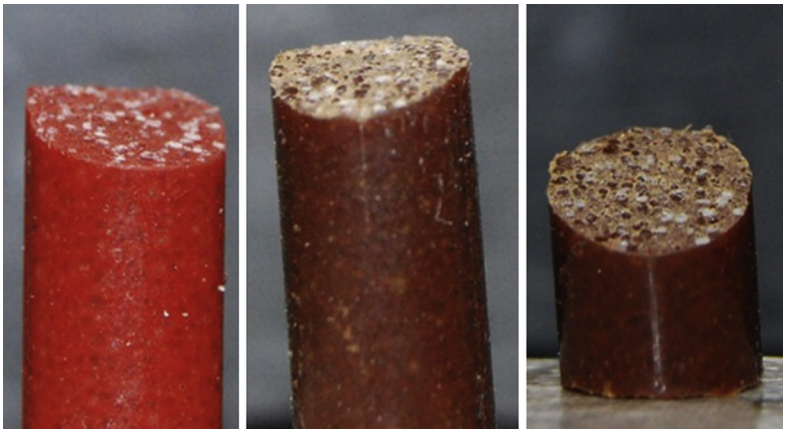

Figure 2 Images of the catalyzed propellant strands (5.8 mm diameter) used by Isert et al. [4]. From left to right, 53 μm catalysts mixed in directly, 3 nm catalyst mixed in directly, and 3 nm catalysts encapsulated (inside AP fines only).

was compared to a baseline propellant without a catalyst, a propellant formulated with micrometer-sized catalyst, and a propellant with the same nanosized catalyst mixed directly. The catalyst loading was held constant. Images of the catalyzed propellants are shown in Figure 2. The measured burning rates (Figure 3) showed that the encapsulated fine AP yielded the highest burning rate, followed by nanoscale catalyst mixed in directly.

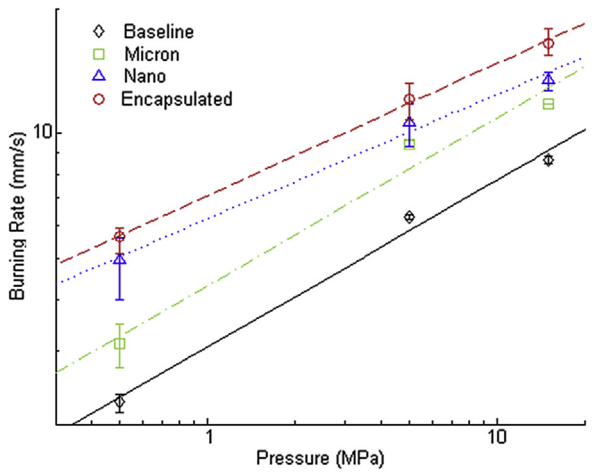

Figure 3 Measured global propellant burning rates. The burning rates for the baseline propellant (Baseline), propellant with micrometer-sized catalyst (Micron), propellant with nanosized catalyst (Nano), and propellant with the encapsulated catalyst (Encapsulated) are shown. Modified from Ref. [4].

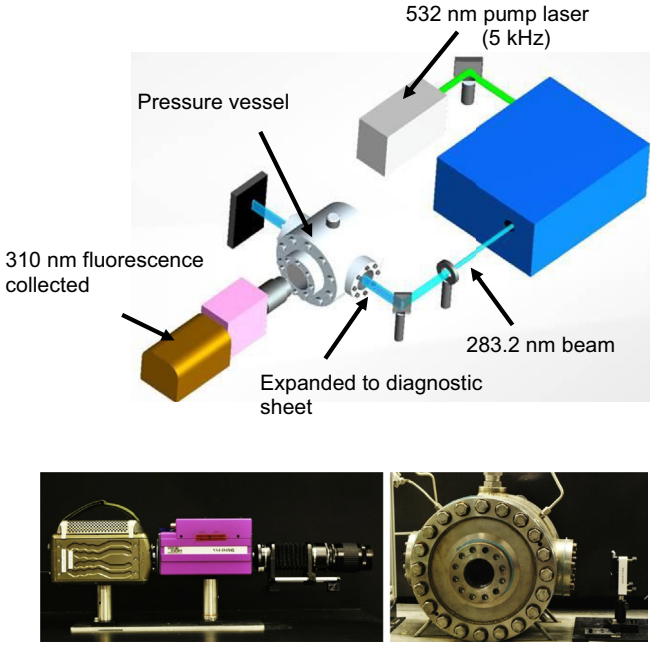

Figure 4 Schematic of the high-speed PLIF system used and images of the camera system and combustion vessel used.

Overall burning rates are useful in evaluating the effectiveness of the encapsulated catalysts in comparison to other formulations but do not explain why encapsulation dramatically improves burning rate. To understand why this enhancement occurs, direct imaging of the solid propellant flame structure can be done in situ using OH planar laser-induced fluorescence (PLIF) [4–8]. Isert et al. [4] employed high-speed (5 kHz) OH PLIF to investigate microscale flame structure and single coarse crystal combustion properties (ignition delay and burning time/rate) for the different formulated composite propellants. Since the AP crystals fluoresce in the UV laser sheet, the coarse crystals are visualized clearly. A schematic is shown in Figure 4, along with images of the camera with intensifier and lens that were used. At higher pressures, adequate signal to noise could not be achieved. Propellants were burned in air at 1 atm, and experiments at pressure were performed in a combustion bomb pressurized with nitrogen at pressures of up to 0.72 MPa.

An example of the kind of imaging obtainable is shown in Figure 5. The dashed line shows the propellant surface location of the fine AP and binder. For the baseline propellant at elevated pressures, very few coarse particles can be observed protruding above the surrounding fine AP and binder. With the addition of micrometer-sized catalyst, the coarse crystals protrude due to the relatively accelerated burning of the

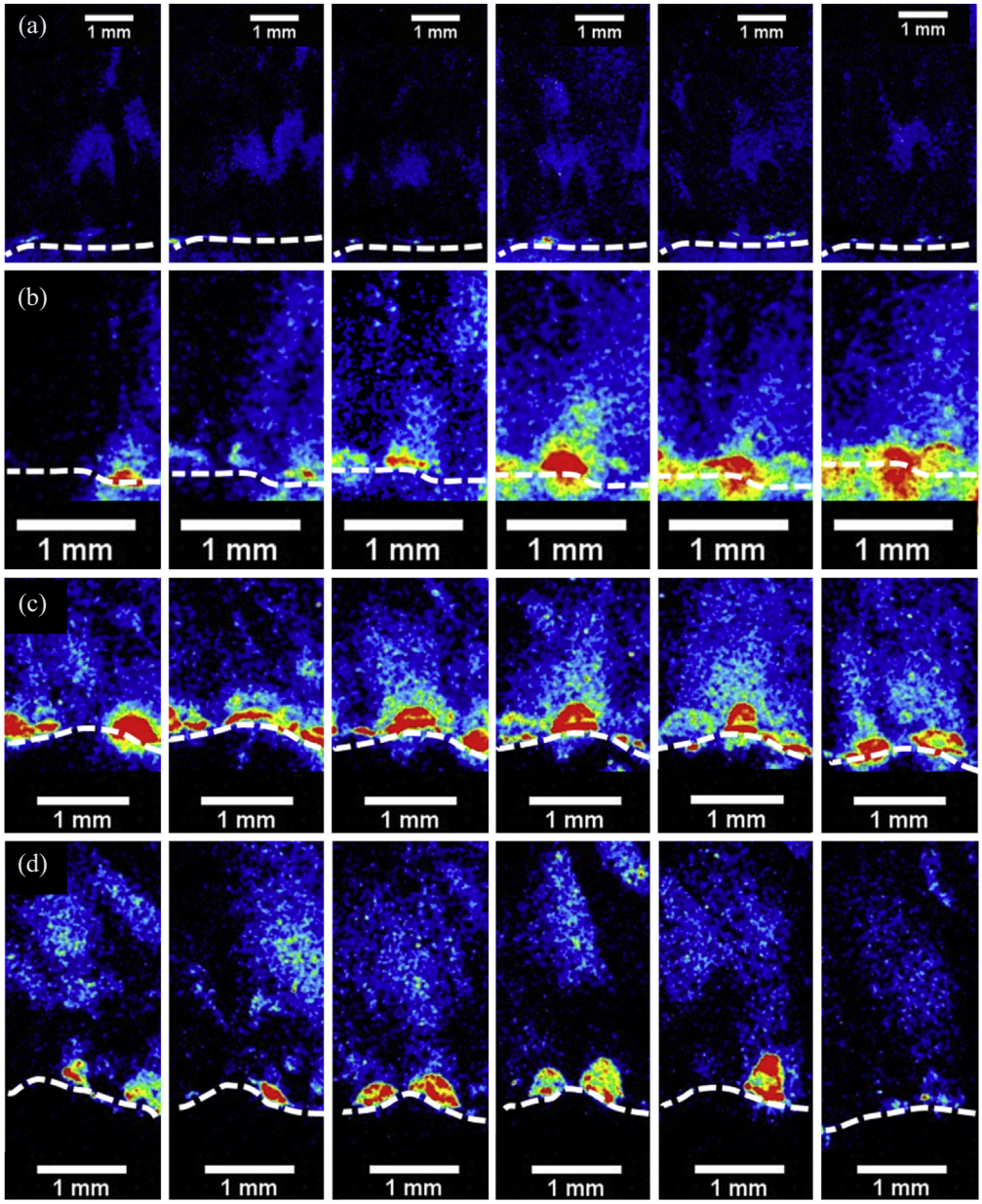

Figure 5 An example of the OH PLIF imaging obtained for baseline propellant (a), propellant with micrometer-sized catalyst (b), propellant with nanosized catalyst (c), and propellant with the encapsulated catalyst (d). Images were taken at 0.7 MPa and the time intervals are 40, 30.8, 25.3, and 35.4 ms for a, b, c, and d, respectively.

fine AP and binder matrix with respect to the coarse AP. As expected, nanoscale catalysts are more effective, especially if encapsulated, and this is clearly seen by even more protrusion. As the fine AP/binder matrix in the encapsulated catalyst propellant burns away more rapidly, the coarse crystals are exposed to high temperatures sooner, increasing coarse crystal burning rate. In addition, the rapid matrix combustion occurring from encapsulation can cause the coarse crystals to be ejected from the propellant surface [4].

Additionally, dynamic OH PLIF can also be used to quantify the ignition delay of the coarse AP crystals, flame structure, and flame heights [4]. The burning rate enhancement of coarse AP crystals is due in part to the shortening of the coarse AP crystal ignition delay, but this is significant only at very low pressures. Direct catalyst addition was observed to have some effect on coarse AP burning rate/lifetime. However, comparing the nanocatalyzed and encapsulated catalyst propellants, the differences in global burning rate are not primarily a function of coarse crystal burning rate. The main differences are due to the rate at which the fine AP/binder matrix burns. Interestingly, encapsulated catalyst had no effect on coarse crystal burning rate as compared to nanocatalyzed propellants, as evidenced by no observed statistical difference in the local coarse crystal burning rates [4].

Current work is focusing on other higher surface area catalysts, including the encapsulation of decorated graphene-based catalysts. Graphene-based catalysts have ultrahigh surface areas and have been shown to increase low pressure neat nitromethane combustion significantly with only low (<1 wt%) addition [9]. Such materials might also be able to be encapsulated within AP. It is also clear that high-speed OH PLIF is proving to be a very useful tool in gaining a more fundamental understanding of how changes in the propellant composition affect the flame structure and surface dynamics. Consequently, we can gain a much more fundamental understanding of what is causing the change in burning rate. This technique could be extended to other species, which may give further insight into the combustion process.

2. ENGINEERED METALLIC FUELS AND ALLOYS

In addition to considering nanoscale catalyst particles, nanoscale metal fuels offer potential advantages, including faster burning rates and more complete combustion. Motivated by this, replacing micrometer-scale aluminum in energetic materials with nanoscale aluminum has been studied for more than a decade [10]. However, simply substituting micrometer-scale particles with nanoscale particles in propellants can lead to drawbacks including unfavorable rheology and final mechanical properties. Nanoscale aluminum also has a relatively thick oxide layer that reduces the performance. Indeed, examples of fielded propellants containing nanoscale aluminum are not currently found. A key question is how one can obtain the advantages of nanoscale fuels without the

drawbacks. Recently, efforts have focused on micrometer-scale aluminum particles with an intraparticle nanoscale structure [13,19–21]. The ideal solution may be a micrometer-sized composite particle that has significantly lower ignition temperature, and when ignited, produces much smaller particles/droplets.

In multiphase liquid combustion, microexplosions can occur for some miscible liquids and also in emulsions [11]. The first observation of this appears to be by Ivanov and Nefedov [12] studying emulsions. A key requirement for this to occur is for one of the constituents to be more volatile than the other. For miscible liquids, a disparity between the liquid-phase mass and thermal diffusion is necessary in establishing droplet dynamics. Mass diffusion in a droplet is one to two orders of magnitude slower than thermal diffusion [11], and this disparity in diffusivities holds for a metal droplet (e.g., a very large Lewis number). As a droplet gasifies, the concentration of the more volatile component in the surface region decreases relative to the core. This is because near the surface, the diffusion scale is small so that the volatile component can diffuse out quickly. However, liquid near the center remains relatively unchanged with a higher concentration of the more volatile, lower-boiling-point component. With continued heating, it is possible that the liquid in the interior can be heated beyond the local boiling temperature and become superheated. If this occurs, the interior liquid can suddenly nucleate and gasify once it exceeds the superheat limit (empirically found to be about 90% of the critical temperature for some liquids by Blander and Katz [14]).

For nucleation, the concentration of the more volatile component must be sufficiently high. Again, this nucleation can result in significant internal pressures and result in fragmentation or breakup of the droplet, as has been observed by many researchers [11]. This has often been termed *droplet microexplosion*. Importantly, for microexplosion to occur, the volatilities of the components must be sufficiently different. Microexplosion is also more likely with increasing pressure [11], but one could expect that at very high pressures it may become inhibited. With the surface relatively devoid of the more volatile component, vaporization can occur just under this surface region, causing "eruptions" and subsequent ejections of smaller droplets. Here we term this phenomenon *dispersive boiling*. This has been observed in other systems such as gelled fuels [15], although the mechanism there is driven by a surface buildup of the gelling agent rather than the accumulation of a less-volatile component. However, the concept is similar.

In contrast to miscible liquids that are a single-liquid phase of two or more liquids mixed on the molecular level, emulsions are multiple-phase mixtures of liquids that are not mixed molecularly. Water-in-oil emulsions are the most common systems considered in combustion studies, with water droplets dispersed within an oil fuel. A small amount of surfactant is used to stabilize the system. Again, the embedded, more volatile component (often water) can be heated to its limit of superheat and violently disperse the droplet. Microexplosion of emulsions are reported to occur more readily, more often, and with more intensity than miscible mixtures [11]. The reason for this is that the more

volatile component may not be as inhibited from nucleating by the less-volatile component in emulsions.

Shattering microexplosions and dispersive boiling of metal fuels, such as aluminum in propellants or other energetic material applications, would clearly be beneficial. For example, droplet breakup in a rocket motor could decrease the size of the burning aluminum droplets and therefore improve combustion efficiency and decrease two-phase flow losses that can be up to about 10% [16–18]. In addition, injection of droplets cannot be directly controlled in solid propellants, as with liquid systems with injector design, so shattering microexplosion and dispersive boiling of engineered aluminum droplets is of significant practical interest.

In a clear analogy to liquid fuels, metal alloys are like miscible liquid fuels in that the atoms or molecules are mixed intimately to form a single phase, eutectic, or solid solution. Likewise, inclusions of more volatile materials within a metal fuel (e.g., a polymer in aluminum) are the equivalent to an emulsion where multiple phases are intertwined together but not atomically or molecularly mixed. The intertwining of phases in a metal can be achieved using milling processes, which can result in lower particle ignition temperatures and dispersive dynamics [13,19–21]. This method is also inexpensive and readily scalable. Another approach to achieve a similar outcome could be the direct bottom-up fabrication of nanoscale fuel particles held together with a more volatile binder [22]. These composite particles also exhibit lower ignition temperatures and dispersive dynamics. To date very little research has been directed toward these modified fuel particles, and much more research is needed. In the following, we review some recent efforts.

3. COMPOSITES OF NANOSCALE ALUMINUM PARTICLES

As discussed above, one approach to obtain a micrometer-sized particle with nanoscale features is to assemble a particle composed of nanoscale metal (e.g., aluminum) with a binder. An example of this is recent work by Wang et al. [22] that considered the fabrication of a composite particle composed of nanoaluminum (oxide passivated) and a nitrocellulose binder using an electrospray technique. In addition to being gas producing, nitrocellulose is an energetic material itself. Additionally, nitrocellulose produces water as it reacts, which can then subsequently react with the aluminum. The microsphere composites showed enhanced combustion behavior when ignited by rapid wire heating compared to micrometer-sized aluminum and nanoaluminum alone. Recently, Young et al. [23] also formulated a solid propellant with these aluminum mesoparticles. In comparison with micrometer-scale aluminum particles, the burning rate was 35 wt% higher, and high-speed imaging qualitatively showed less agglomeration.

This bottom-up approach, and others, shows significant promise. However, some drawbacks are evident. First, the composite fuel particle is composed of passivated

nanoscale aluminum. This means that a significant amount of the 50 nm aluminum particles used is oxide; in this example, likely over 35 wt% of the aluminum particle weight is oxide. In addition, the composite particles have significant voids making the theoretical maximum density less than roughly 60%. These drawbacks make this material unlikely to be adopted into fielded propellants because the higher burning rate and smaller agglomerate size will not likely compensate for the propellant density and energy loss. However, these materials could possibly be useful in some pyrotechnic or other applications where energy and density are not as critical. Also, improved high-density- and low-oxide-containing composite particles, perhaps even aluminum clusters, may be developed in the future and would be of significant interest.

4. MICROMETER-SIZED ALUMINUM PARTICLES WITH INCLUSIONS

An alternative approach to fabricating macroscale composites composed of nanoscale particles is to engineer composite particles by beginning with micrometer-sized aluminum and introducing nanoscale inclusions of another, more volatile material, again analogous to a liquid emulsion. One approach is using mechanical activation (MA), which is the process of milling an inclusion material into a parent material (e.g., a polymer into aluminum). This process with proper choice of milling conditions can result in micrometer-scale particles with nanoscale intraparticle features [13,19–21]. This approach is illustrated conceptually in Figure 6, along with a scanning electron microscopic (SEM) image of an engineered composite particle. Mechanical activation is a scalable approach and can yield high-density, nanostructured particles with high-energy (aluminum) content, as shown by Sippel et al. [13]. Due to the lower quantity of oxide present on particles, their combustion enthalpy can be as much as 60% higher than similar mixtures of nanoaluminum and nano-oxidizers. Most importantly, the presence of polymer inclusions with low-volatilization temperature can result in microexplosions and enhanced particle breakup, earlier particle ignition, and faster combustion.

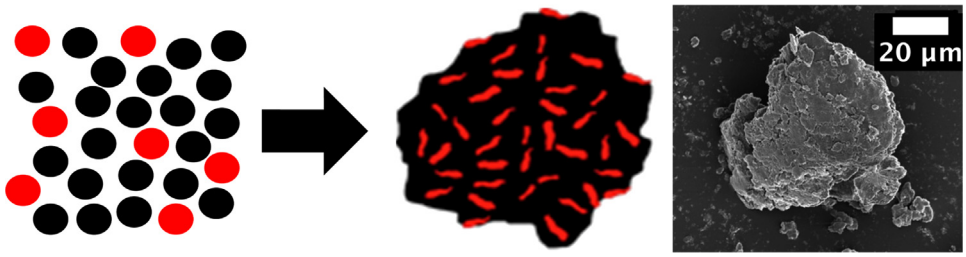

Figure 6 A schematic of the concept of producing a fuel particle with inclusions (left) where initial particles are milled to produce a micrometer-scale particle with inclusions. An SEM image of an Al/PTFE particle is shown on the right.

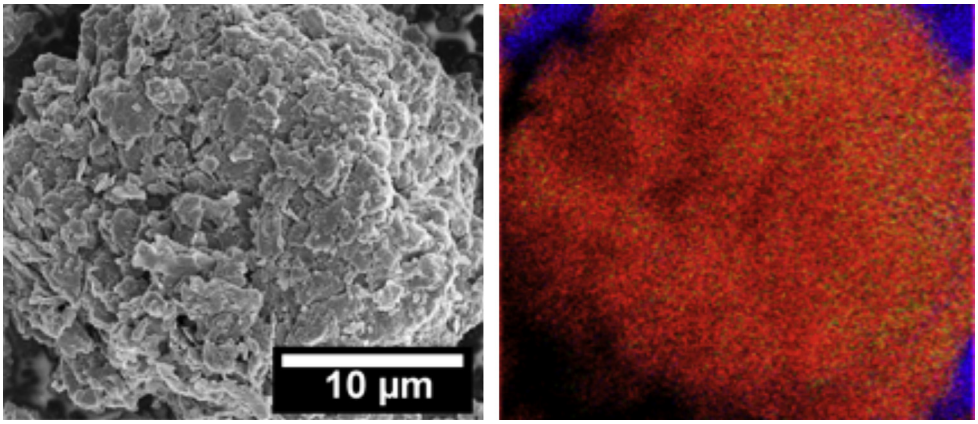

Figure 7 Left: Election micrograph of a MA-fabricated aluminum particle containing inclusions of poly(carbon monofluoride) (PMF) fluorocarbon. Right: Energy dispersive X-ray spectroscopy composite color overlay image of the same showing intraparticle mixing via presence of atomic aluminum (red), fluorine (green), and carbon (blue) [19].

In addition to inclusion materials that simply have a higher volatility (but are nominally noninteracting with aluminum), some inclusion materials can react directly with aluminum such as oxidizing and fluorinating inclusion materials. Materials that have been considered include poly(carbonmonofluoride) (PMF) and polytetrafluoroethylene (PTFE). PMF is also commonly referred to as graphite fluoride. Due to its graphitic nature, a composite of very finely divided layers of PMF and aluminum results. Figure 7 shows an SEM image of such a composite particle and also the corresponding energy dispersive X-ray spectroscopy (EDS) atomic map. This shows a very uniform distribution of PMF, as indicated by the fluorine (green dots distributed in the image). These composite particles can be fabricated to be very electrostatic-discharge sensitive, as well as optically sensitive (camera flash ignition has been demonstrated) [19]. Both of these characteristics are shared with nanoscale aluminum, though Al/PMF particles are nearly 400 times larger in diameter.

Sippel et al. [13,20] also considered inclusions of PTFE with aluminum in composite particles. These particles were thoroughly characterized and were used in a composite propellant. Using microscopic imaging, it was observed that the tailored particles promptly ignite at the burning surface and break into smaller particles, which can increase the heat feedback to the burning surface and improve combustion efficiency. Figure 8 shows two images from high-speed-microscopic imaging of a baseline spherical aluminized AP composite propellant and a similar propellant with aluminum replaced by the same amount of 70/30 wt% Al/PTFE composite particles. It is clear that although the initial sizes are very nearly the same, particles ignite much more readily, as evidenced by the higher surface luminosity. Additionally, Al/PTFE results in much smaller burning particles that leave the burning surface with higher velocity. This is indicated by many

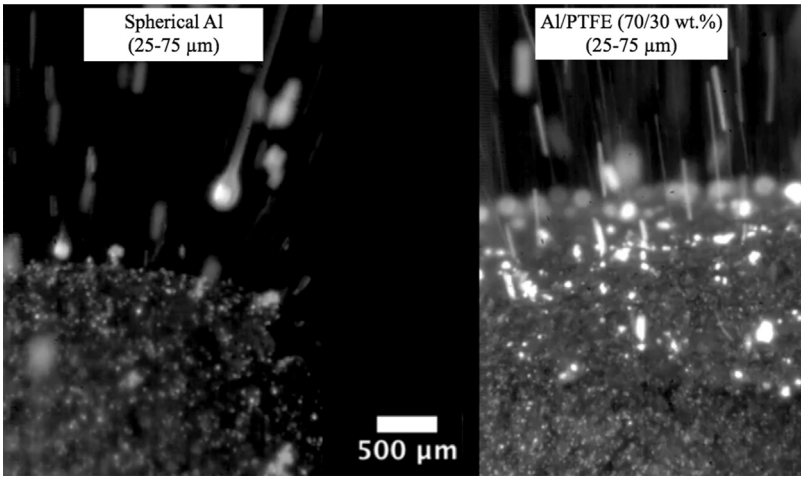

Figure 8 The left image is from a high-speed microscopic video of baseline spherical aluminized AP composite propellant. The right image is for a Al/PTFE 70/30 wt%-based propellant. Images were captured with the same exposure duration.

more longer luminous streaks observed above the propellant surface. Since aluminum and Al/PTFE particles were sieved to similar sizes prior to use, this also indicates that smaller burning fragments are produced from breakup of Al/PTFE particles during combustion.

To quantify the size of the product droplets formed, combustion products were collected using a plume traversing collection plate and were subsequently analyzed microscopically. Figure 9 shows particles collected from both the baseline spherical aluminized and the 70/30 wt% Al/PTFE-containing propellants. The differences are seen to be dramatic. The baseline propellant product sizes are much larger than the 70/30 wt% Al/PTFE-based propellant. From analysis of the captured condensed phase products, it is clear that the propellant with modified aluminum particles results in faster, more complete aluminum combustion. Both Al/PTFE 90/10 and 70/30 wt% composite particles were observed to reduce the coarse product fraction and diameter. The most significant reduction occurs for the 70/30 wt%-based propellant, where average coarse product diameter is 25 μm, which is smaller than the original Al/PTFE particle size and also smaller than the 76 μm average coarse products size collected from baseline spherical aluminized propellant. Some unreacted crystalline aluminum and AP was observed in the X-ray diffraction of the spherical baseline propellant, compared to none for the modified aluminum composite-based propellants. The enhanced aluminum combustion observed with use of modified aluminum also results in a 25% increase in propellant burning rate at 6.89 MPa due to improved heat feedback to the propellant surface as aluminum droplets burn closer to the surface.

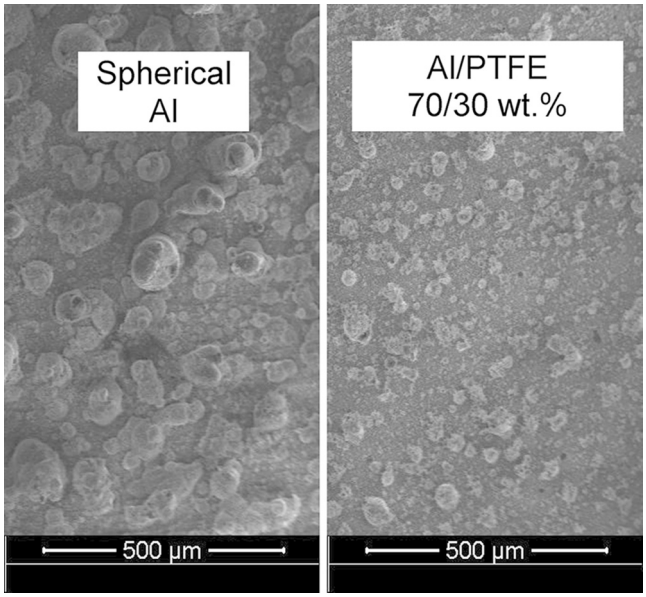

Figure 9 The left image is of particles collected from a baseline spherical aluminized propellant. The right image is for Al/PTFE 70/30 wt%-based propellant.

Though the incorporation of reactive polymer inclusions (e.g., fluoropolymers) within aluminum can significantly enhance combustion, it is unclear whether inclusion-aluminum reactivity is requisite to ignition and combustion enhancement. To investigate this question, aluminum modified with low-density polyethylene (LDPE) inclusions were considered recently in propellants [21]. Unlike fluorocarbons, LDPE is not expected to have significant chemical reactivity with the aluminum. In a solid propellant formulation, the results are qualitatively similar to those found with use of PTFE inclusions, and product size was significantly reduced for the Al/LDPE particles as well. The similar results indicate that the gasification properties are likely the most important in regards to breakup of particles and droplets in propellant configurations. An advantage of LDPE inclusions is that they could be scaled with much less concern for safety because little reaction can occur between the Al and LDPE directly.

Current work in this area includes laser ignition of single particles to elucidate the dynamics and heating rate thresholds needed for disruptive ignition. For example, if the heating is slow, gas buildup caused by inclusion decomposition within the particles will simply vent and no breakup will be observed. In addition, work is proceeding to consider other inclusion materials and also other metals or alloys.

It is clear with the ubiquitous use of metals, especially aluminum, in energetic materials that there are likely other applications of these modified particles, such as use in explosives and pyrotechnics. These other applications are currently being explored.

The current milling approach is low cost, scalable, and results in high-density particles that are roughly the same size as frequently used metal particles (could be considered as drop-in replacements). Open questions include: (1) what inclusion materials would be optimal for specific applications, and (2) precisely what determines the particle microexplosion dynamics?

5. MICROEXPLODING ALLOY FUEL PARTICLES

We argue here that alloys are the metallic analog of miscible hydrocarbon fuels, and we have begun exploring aluminum-lithium alloys as a replacement for aluminum in propellants, in part because of the possibility for droplet dispersion. As discussed previously, for microexplosive droplet shattering or dispersive boiling to occur, a large difference in constituent volatility is required. The boiling points of aluminum (2519 °C) and lithium (1342 °C) adequately meet the volatility requirement [11]. The results of thermochemical equilibrium calculations show that aluminum–lithium alloys can be formulated in AP composite propellants to have good specific impulse and also greatly reduced hydrochloric acid (HCl) is predicted in the products. Significant lithium chloride, LiCl (a gas at these temperatures), forms in the place of HCl because of the halophilic nature of lithium. The details and results of this study will be reported in a future publication, but here we will present a few initial results.

Figure 10 shows the combustion of a baseline aluminized AP composite (26.80/61.48/11.72 wt% Al/AP/HTPB) and a propellant where the aluminum has been replaced with 80/20 wt% Al/Li intermetallic compound. The magenta color of the flame is due to lithium chloride in the products. Figure 11 shows images from backlit high-speed microscopic videos of the same two propellants. The left image shows the

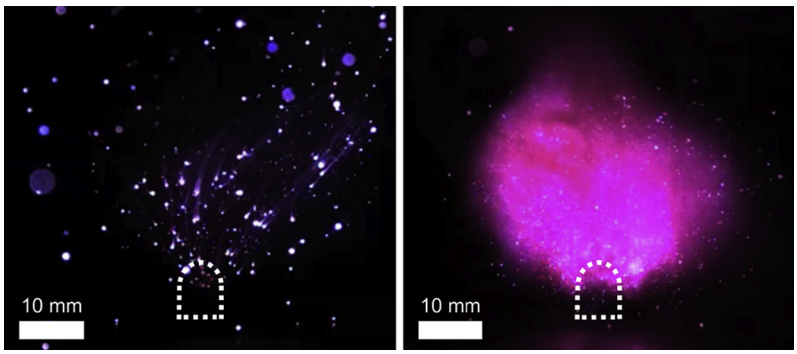

Figure 10 The left image is of a metalized AP propellant burning at 1 atm. The right image is the same propellant, but with aluminum replaced with 80/20 wt% Al/Li alloy (one-to-one atomic alloy). The dashed line is the propellant strand.

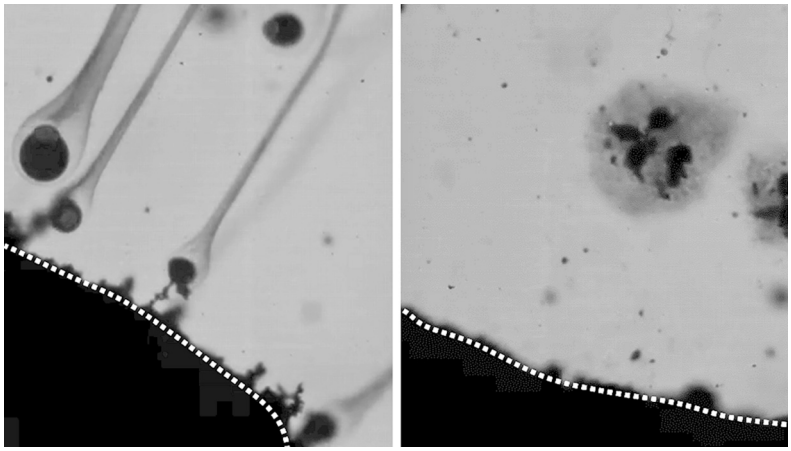

Figure 11 The left image is of a metalized AP propellant burning at 1 atm. The right image is the same propellant, but with aluminum replaced with 80/20 wt% Al/Li alloy (one-to-one atomic alloy). Note the shattering droplet seen in the right image. The dashed line is the propellant strand. All exposures are 1 μs.

baseline aluminized propellant combustion with large agglomerates forming at the surface. The burning droplets form an alumina cap on the otherwise spherical droplet as they leave the propellant surface, and alumina smoke appears above the droplet surface, forming a long tail. In contrast, the Al/Li alloy propellant surface can be seen to erupt from dispersive boiling, propelling droplets off the surface. Above the surface, larger droplets can also be seen ejecting smaller droplets in a dispersive boiling mode. This is similar to what is observed in gelled droplets (e.g., see Ref. [15]). Other droplets (typically smaller droplets) can also be seen to expand quickly and micro-explode (shattering the droplet) presumably due to superheated lithium in the droplet core suddenly gasifying and reacting with chlorine. An example of this shattering explosion can clearly be seen in Figure 11. Alumina smoke above burning droplets and oxide caps on droplet surfaces are rarely observed. Since the flame temperature for the burning droplets is well above the boiling temperature of both lithium and aluminum, homogeneous gas-phase reactions are expected to occur in gases away from the surface. The LiCl produced is also gaseous at these temperatures, and the alumina product formed appears to be much smaller than in the baseline propellant. This could reduce two-phase flow losses in rocket motors, resulting in further performance improvements.

Figure 12 shows schematically the dynamics of metal combustion. In the top case, a homogeneous metal melts and then burns in a normal fashion. The initial solid particle may or may not be spherical. The middle case shows an alloy system that also melts first, followed by preferential gasification of the more volatile component from the surface and

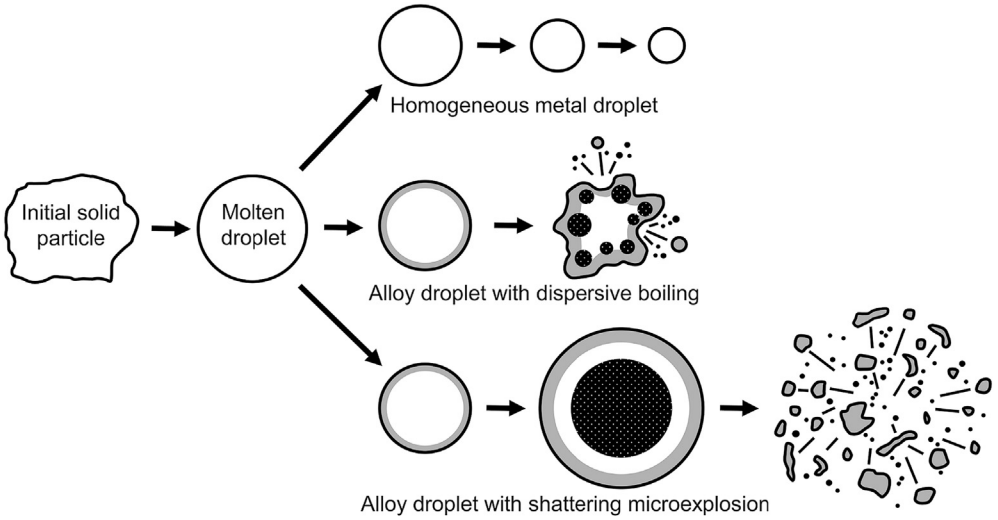

Figure 12 A schematic of homogeneous droplet evaporation, dispersive boiling, and shattering microexplosion due to superheating and flashing to vapor. The gray surface regions indicate the presence of a volatile component concentration gradient, and the dark regions indicate vapor nucleation.

then dispersive boiling that ejects smaller droplets. The bottom case proceeds similarly, but the core has a higher concentration of the volatile component and the conditions are just right so it can superheat and then suddenly flash to vapor resulting in a shattering microexplosion. Both of these alloy combustion/evaporation modes are observed in the Al/Li-based propellant.

In Figure 13 the temperature and the more volatile species concentration, [V], in an alloy droplet that is evaporating or burning is shown schematically. The surface region lies between diffusion radius (r_d) and the surface radius (r_s), and shows a drop in [V]. Here T_{SH} and $T_{BP,v}$ are the superheating limit temperature and the boiling point of the more volatile component, respectively. If the entire core is superheated, then a shattering microexplosion would be expected. However, if only part of the core is superheated, or nucleation is induced near the boiling temperature, then dispersive boiling would be expected that can eject droplets but does not entirely shatter the droplet. A shattering microexplosion would be expected more often for smaller droplets, and this is observed experimentally for this system.

Much work remains to be done with Al/Li-based propellants, but initial experiments and calculations appear promising. The Al/Li alloy will react in the presence of water, so stability will need to be addressed and further characterization is needed. Similar to the inclusion materials, other energetic material applications of this alloy are possible and are being explored. Other alloy systems could also be of interest.

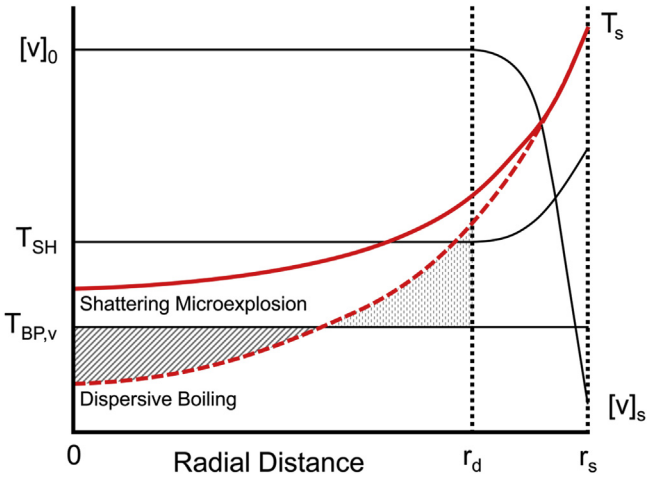

Figure 13 A schematic representation of temperature and more volatile species concentration, [V], in an alloy that is evaporating or burning. Conditions for shattering microexplosions and dispersive boiling are shown schematically.

6. CONCLUSIONS

Conventionally, composite propellant formulators could only change constituents and their size distributions. Nanoscale ingredients have promised to improve performance; however, the high surface area brings unintended consequences such as poor rheology and ultimately unacceptable mechanical properties, making adoption unlikely. In this chapter we reviewed some recent efforts to tailor particles to achieve improved performance.

One approach explored is to encapsulate nanoscale materials into crystalline particles. This can be accomplished by using a fast-crash process, for example. Encapsulated nanoscale catalysts have shown improved performance over direct physical mixing into an AP composite propellant. Additionally, since most of the high-surface-area components are within the crystals and not in direct contact with the binder, higher solid loadings than with conventional nanocatalysts can be potentially considered. Other crystal systems and nanoscale fuels could also be explored.

The other dominant solid component in many composite propellants is aluminum powder. As Bob Geisler [24] said, "When God created aluminum powder he realized rocket scientists would over-use it unless he gave it some undesirable characteristics… He made it agglomerate to droplet sizes of up to several hundred micrometers at the surface of solid propellants as it begins to burn… He also provided condensed phase products which accumulate in motor re-circulation zones as useless unexpended slag weight. These products also give rise to two-phase-flow velocity and thermal lag losses which

reduce the delivered performance…" The conventional approach of just replacing micrometer-sized aluminum with nanoscale aluminum has not proven to be a viable approach. An alternative is to engineer or tailor the intraparticle structure of micrometer-sized particles to have nanoscale features. The proper choice of inclusion materials can lead to dispersive dynamics that produce smaller droplets for combustion and ultimately smaller condensed-phase products.

Milling of inclusion materials into metals, like aluminum, has been shown to be an effective approach and shows promise in overcoming some of the vexing problems of using aluminum in solid propellants. The nanoscale intraparticle features of the composite particle leads to much easier ignition, and smaller products are typically formed since the particles fragment when heated. We argue here that metal particles with inclusion materials are analogous to emulsions (e.g., water and fuel oils) studied in hydrocarbon combustion.

Another analogy to hydrocarbon combustion is miscible fuels and metal alloys. It is well known that miscible fuels with disparate volatility can lead to droplet microexplosions (breakup of the droplet by phase change). An example was presented here of initial results from an aluminum–lithium alloy-based solid propellant. The burning surface was observed to eject drops from the surface. Some of these droplets, especially the larger ones, continue to boil in a dispersive manner, launching smaller droplets from the mother droplet (termed dispersive boiling here). In others, much of the droplet core can be superheated up to a limit, and then suddenly vaporize due to intraparticle boiling, causing inflation of the aluminum-rich surface layer leading to the dramatic shattering of the drop. Further work is needed to fully characterize the aluminum–lithium alloy system (and perhaps others), and other applications should also be explored.

Much work lies ahead in developing each of these approaches to the level that full implementation can occur, but results appear promising. Eventually, high-density/energy particles may be fabricated precisely by high-throughput, bottom-up processes, but even today, scalable approaches that yield viable high-density composite particles can be engineered for a variety of applications using milling processes.

ACKNOWLEDGMENTS

This research was conducted with funding through NSF GRFP Grant No. 1147384, the National Defense Science and Engineering Graduate (NDSEG) Fellowship, 32 CFR 168a, and through AFOSR MURI contract #FA9550-13-1-0004 with Mitat Birkan as program manager.

REFERENCES

[1] S. Chaturvedi, P.N. Dave, Nano-metal oxide: potential catalyst on thermal decomposition of ammonium perchlorate, J. Exp. Nanosci. 7 (2) (2012) 205–231.

[2] Z. Ma, F. Li, H. Bai, Effect of Fe_2O_3 in Fe_2O_3/AP composite particles on thermal decomposition of AP and on burning rate of the composite propellant, Propell. Explos. Pyrotech. 31 (2006) 447–451.

[3] D.A. Reese, S.F. Son, L.J. Groven, Composite propellant based on a new nitrate ester, Propell. Explos. Pyrotech. 39 (5) (2014) 684–688.
[4] S. Isert, L.J. Groven, R.P. Lucht, S.F. Son, The effect of encapsulated nanosized catalysts on the combustion of composite solid propellants, Combust. Flame 162 (5) (2015) 1821–1828.
[5] T.D. Hedman, K.Y. Cho, A. Satija, L.J. Groven, R.P. Lucht, S.F. Son, Experimental observation of the flame structure of a bimodal ammonium perchlorate composite propellant using 5 kHz PLIF, Combust. Flame 159 (1) (2012) 427–437.
[6] T.D. Hedman, D.A. Reese, K.Y. Cho, L.J. Groven, R.P. Lucht, S.F. Son, An experimental study of the effect of catalysts on an ammonium perchlorate based composite propellant, Combust. Flame 159 (4) (2012) 1748–1758.
[7] T.D. Hedman, L.J. Groven, R.P. Lucht, S.F. Son, The effect of polymeric binder on composite propellant flame structure investigated with 5 kHz OH PLIF, Combust. Flame 160 (8) (2013) 1531–1540.
[8] T.D. Hedman, K.Y. Cho, L.J. Groven, R.P. Lucht, S.F. Son, The diffusion flame structure of an ammonium perchlorate based composite propellant at elevated pressures, Proc. Combust. Inst. 34 (1) (2013) 649–656.
[9] J.L. Sabourin, D.M. Dabbs, R.A. Yetter, F.L. Dryer, I.A. Aksay, Functionalized graphene sheet colloids for enhanced fuel/propellant combustion, ACS Nano 3 (12) (2009) 3945–3954.
[10] R.A. Yetter, G.A. Risha, S.F. Son, Metal particle combustion and nanotechnology, Proc. Combust. Inst. 32 (2) (2009) 1819–1838.
[11] C.K. Law, Combustion Physics, Cambridge University Press, New York, 2006.
[12] V.M. Ivanov, P.I. Nefedov, Experimental Investigation of the Combustion Process in Nature and Emulsified Fuels, vol. 19, NASA Scientific and Technical Publications from Trudy Instituta Goryacikh Ishkopayemykh, 1965 p.25–45.
[13] T.R. Sippel, S.F. Son, L.J. Groven, Altering reactivity of aluminum with selective inclusion of polytetrafluoroethylene through mechanical activation, Propell. Explos. Pyrotech. 38 (2) (2013) 286–295.
[14] M. Blander, J.L. Katz, Bubble nucleation in liquids, AIChE J. 21 (5) (1975) 1547–1556.
[15] K.Y. Cho, T.L. Pourpoint, S.F. Son, R.P. Lucht, Microexplosion investigation of monomethylhydrazine gelled droplet with OH planar laser-induced fluorescence, J. Propuls. Power 29 (6) (2013) 1303–1310.
[16] H. Cheung, N.S. Cohen, Performance of solid propellants containing metal additives, AIAA J. 3 (2) (1965) 250–257.
[17] G.P. Sutton, O. Biblarz, Rocket Propulsion Elements, eighth ed., Wiley, 2011.
[18] Y.M. Timnat, Advanced Chemical Rocket Propulsion, Academic Press, Orlando, FL, 1987.
[19] T.R. Sippel, S.F. Son, L.J. Groven, Modifying aluminum reactivity with poly (carbon monofluoride) via mechanical activation, Propell. Explos. Pyrotech. 38 (3) (2013) 321–326.
[20] T.R. Sippel, S.F. Son, L.J. Groven, Aluminum agglomeration reduction in a composite propellant using tailored Al/PTFE particles, Combust. Flame 161 (1) (2014) 311–321.
[21] T.R. Sippel, S.F. Son, L.J. Groven, S. Zhang, E.L. Dreizin, Exploring mechanisms for agglomerate reduction in composite solid propellants with polyethylene inclusion modified aluminum, Combust. Flame 162 (3) (2015) 846–854.
[22] H. Wang, G. Jian, S. Yan, J.B. DeLisio, C. Huang, M.R. Zachariah, Electrospray formation of gelled nano-aluminum microspheres with Superior reactivity, ACS Appl. Mater. Interfaces 5 (15) (2013) 6797–6801.
[23] G. Young, H. Wang, M.R. Zachariah, Application of nano-aluminum/nitrocellulose mesoparticles in composite solid rocket propellants, Propell. Explos. Pyrotech. 40 (3) (June 2015) 413–418, http://dx.doi.org/10.1002/prep.201500020. Online Version.
[24] R.L. Geisler, A global view of the use of aluminum fuel in solid rocket motors, in: AIAA 2002-3748, 38th Joint Propulsion Conference, 7–10 July, Indianapolis, Indiana, 2002.

CHAPTER THIRTEEN

Pre-burning Characterization of Nanosized Aluminum in Condensed Energetic Systems

Christian Paravan[1], Filippo Maggi[1], Stefano Dossi[1], Gianluigi Marra[2], Giovanni Colombo[1] and Luciano Galfetti[1]

[1]Space Propulsion Laboratory, Department of Aerospace Science and Technology, Politecnico di Milano, Milan, Italy
[2]Centro Ricerche ENI per le Energie Rinnovabili e l'Ambiente – Istituto ENI Donegani, Novara, Italy

NOMENCLATURE

a_s	S_{SA}-derived particle diameter, $a_s = 6/(S_{SA}\,\rho_{Al})$, nm
a_{SR}	Fitting parameter (see Table 12)
ADN	Ammonium dinitramide
Al30	μAl with nominal particle size of 30 μm
ALEX	Aluminum exploded (nAl produced by EEW, usually air-passivated)
AP	Ammonium perchlorate
BET	Brunauer–Emmett–Teller
C_{Al}	Active aluminum content, % (wrt overall powder mass)
C-ALEX	Catechol-coated air-passivated ALEX
CH-ALEX	HTPB-coated air-passivated ALEX (catechol as coupling agent)
D_{43}	Volume mean diameter, μm
DOA	Dioctyl adipate
DSC	Differential scanning calorimetry
DTA	Differential thermal analysis
EEW	Electrical explosion of wire
Fluorel™	Fluoroelastomer, vinylidenefluoride hexafluoropropylene (70:30)
GAP	Glycidyl azide polymer
HTPB	Hydroxyl-terminated polybutadiene
IPDI	Isophorone diisocyanate
k_η	Fitting parameter [see Eqn (1)]
L-ALEX	Stearic acid passivated ALEX
n_{SR}	Fitting parameter (see Table 12)
nAl	Nanosized Al
R	Universal gas constant (8.314 J/mol-K)
R^2	Coefficient of determination

(*Continued*)

Energetic Nanomaterials
ISBN 978-0-12-802710-3, http://dx.doi.org/10.1016/B978-0-12-802710-3.00013-1

—cont'd

r_b	Solid propellant burning rate, mm/s
r_f	Solid fuel regression rate, mm/s
SEM	Scanning electron microscopy
S_{SA}	Specific surface area, m^2/g
SPLab	Space Propulsion Laboratory
SR	Shear rate, s^{-1}
SR*	Slippage limiting shear rate, s^{-1}
STA	Simultaneous thermal analysis
T	Temperature, K
T_{ign}	Ignition temperature, K
$T_{on,1}$ ($T_{on,2}$)	1st (2nd) intense oxidation onset temperature, K
TED	Transmission electron detector
TEM	Transmission electron microscopy
TG	Thermogravimetry
VF-ALEX	Fluorohydrocarbon-coated air-passivated ALEX
XRD	X-ray diffraction
$\alpha(\overline{T})$	$Al \rightarrow Al_2O_3$ conversion factor (at an indicated temperature $\overline{T}$), % $\alpha(\overline{T}) = C_{Al}/[\Delta m(\overline{T}) \cdot 0.89]$
ΔH_1, (ΔH_2)	1st (2nd) intense oxidation enthalpy release, J/g
Δm_0	Maximum mass loss (TG), wt%
$\Delta m(\overline{T})$	Mass change at the temperature$\overline{T}$(TG), wt%
η, η^*	Viscosity, complex viscosity, Pa·s
η'	η^* in-phase component, Pa·s
η''	η^* out-of-phase component, Pa·s
μAl	Micron-sized Al
ρ_{Al}	Al density, kg/m^3

CHEMICALS COMMON NAMES AND IUPAC NOMENCLATURE

Catechol ($C_6H_6O_2$)	Benzene-1,2-diol
Dioctyl adipate ($C_{22}H_{42}O_4$)	Dioctyl hexanedioate
FTOH 10:1, telomer alcohol	(2,2,3,3,4,4,5,5,6,6,7,7,8,8,9,9,10,10,11,11) eicosafluoro-undecan-1-ol or (1,1,11)trihydroperfluoro-undecan-1-ol
Maleic anhydride ($C_4H_2O_3$)	Furan-2,5-dione
Stearic acid ($C_{18}H_{36}O_2$)	Octadecanoic acid

1. INTRODUCTION

Metal powders are high-density fuels commonly used in energetic systems such as pyrotechnics, propellants, and explosives. Metal fuels yield high ideal gravimetric and

volume oxidation enthalpies (see Figure 1). Considering the reaction with O_2 as the oxidizer, the highest higher heating value is achieved by H_2. Nevertheless, metals outperform with respect to both H_2 and hydrocarbons on volumetric basis, thanks to their high density. Moreover, metals can supply an amount of enthalpy per available O_2 unit mass that is higher than that of other fuels [1]. In rocket propellants, metals are used to increase both gravimetric and volumetric specific impulse. Missions of trans-atmospheric vehicles or embarked systems can take advantage of augmented thrust density to obtain higher volumetric propulsive force [2,3]. Reactive metals find application in air-blast and underwater explosives to increase the formulation performance when enhanced energy releases are pursued [4,5]. In addition, thermites, which are pyrotechnic compositions based on a redox reaction between a metal and a metal/non-metal oxide [6], can release high energy per unit mass thanks to the metal energy density (e.g., the enthalpy of reaction for the $Al + MoO_3$ thermite is 4705 kJ/kg).

Aluminum offers several appealing features that suggest its use in energetic formulations, in particular, in rocket propellant applications: availability (yielding low raw material costs), low toxicity, high handling safety (for conventional micron-sized systems [7,8]), and low oxygen demand. Some substances such as Be and B offer higher combustion enthalpies than Al (see Figure 1). Nevertheless these materials exhibit high toxicity (for Be and its oxides) or difficult ignition/poor combustion efficiency (for B), hindering the exploitation of their potential. Moreover, the use of micron-sized Al powders can suppress combustion instabilities arising in solid rocket motors [2].

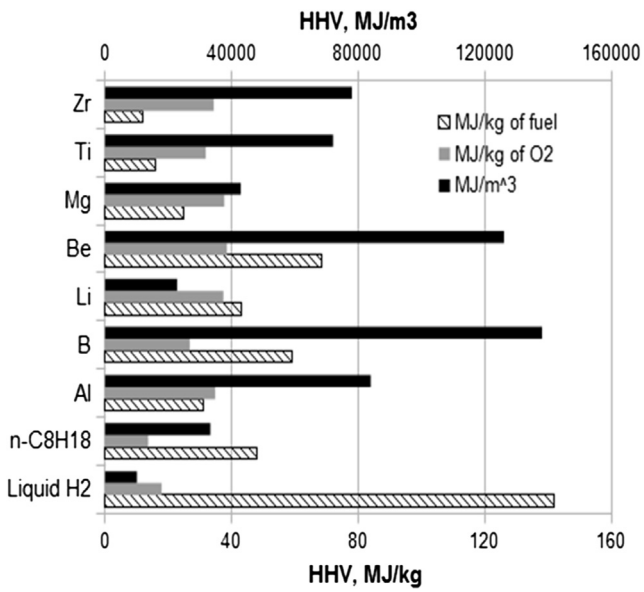

Figure 1 Enthalpy of combustion (higher heating value, HHV) of different substances in oxygen.

Aluminum powders are usually passivated by exposure to dry air, unless different strategies are implemented [9]. Air passivation leads to the formation of an amorphous alumina shell surrounding the metal core of the particle. Under ambient conditions the Al_2O_3 shell exhibits a thickness in the range 3–5 nm. According to the available open-literature results [10–13] the shell thickness is almost independent from the particle size. Considering conventional micron-sized particles ($S_{SA} < 1$ m^2/g), the limited specific surface area results in relatively high ignition temperature [14] and low reaction rate [15]. Experimental data suggest that a temperature of ~2300 K is needed to ignite particles having diameter ~10 μm in air [16]. This value progressively lowers when the particle size is reduced [14]. In particular, nAl particles ($S_{SA} >= 10$ m^2/g) exhibit ignition temperature below 1000 K [6,14,17]. The combustion of Al particles in air follows a diffusion-limited regime, which turns to be kinetically controlled only for powder sizes below 10–20 μm [15,16].

High ignition temperature and diffusion-limited reaction rate cause a delay in the release of combustion enthalpy for micron-sized metal particles. Popenko and co-authors observed that μAl + nAl blends burn in air with a peculiar behavior: the finer particles lead the reaction process while the micron-sized fraction requires longer ignition and combustion times [18]. Under the operating conditions investigated in Ref. [18], mixture ignition cannot be achieved for nAl content <10 wt%, and blends burn with a staged process: in a first part of the combustion T ~1500 K, while in the second part the reaction temperatures of the order of 2700 K are reached. In particular, μAl powders with different S_{SA} were tested observing an influence of this parameter on the duration of the low-temperature stage (i.e., the larger the S_{SA}, the shorter the combustion time). Experiments on deflagration to detonation transition underline the role of particle size for the reaction of metal powder suspensions. Data from Ingignoli et al. [19] referring to experiments performed in both confined and open environments underline that the transition is achieved only for fine particles with diameter below 1–5 μm. Studies on the effects of Al on the ballistic response of solid rocket propellants show that the burning rate and the generation of condensed combustion products benefit from a reduction of the initial metal particle diameter [6]. Published results aiming at the increment of the regression rate of solid fuels for hybrid rocket propulsion show the positive effects of using metal additives and, in particular, nAl in HTPB-based formulations [6]. Recent works [6,17,20–22] report the use of improved μAl- and nAl-based composites obtained by dedicated processes (i.e., mechanical and chemical activation) to tailor the additive reactivity, thus opening interesting possibilities in the perspective of solid propellants/fuels performance enhancement. The higher reactivity of nAl yields increased sensitivity to ageing problems. According to the limited number of open literature studies on the nAl ageing [23,24], the high S_{SA} facilitates nanosized powders degradation during storage due to particle interactions with the surrounding environment. Ageing tests reported in Ref. [25] testify the fast C_{Al} loss of ALEX in a purposely

created environment with 90% humidity. Under the investigated conditions, the $Al \rightarrow Al(OH)_3$ conversion of air-passivated nAl is higher than 90% in 18 days due to the slow reaction with H_2O [25].

Both μAl and its nanosized counterpart are usually passivated by air, though some non-conventional passivation technique can be implemented (especially for ultradisperse systems [13]). The different C_{Al} effects on the energetic system performance must be considered when comparing μAl and nAl. For air-passivated systems, the Al_2O_3 shell thickness does not depend on the particle size and the nAl offers reduced C_{Al} with respect to the μAl. Typically, an air-passivated nAl with $a_s \sim 220$ nm ($S_{SA} \sim 10$ m^2/g) exhibits $C_{Al} \sim 89\%$, while for a 15 μm spherical powder the active metal content is >98%. Due to the limited metal content, nAl powders finer than 50–100 nm size become progressively less suitable from the energetic viewpoint (see Figure 2), though interest can arise from the consideration of kinetic effects. These considerations on the impact of the passivation process on the final product C_{Al} are valid also for non-air passivated powders treated by different substances. It is important to acknowledge that the reduction of the metal content can feature different effects in various applications. Figure 3 shows that GAP-ADN propellants are less sensitive on metal reduction than AP-HTPB ones. Results reported in Ref. [6] evidence that the specific impulse decrease due to reduced metal content is almost negligible in Al-loaded fuels for hybrid rocket propulsion. Moreover, for finer particle sizes (i.e., higher S_{SA}) the effects of the increased reactivity on the additive reaction rate (and energy conversion effectiveness) should be considered in a trade-off process along with all of the nanosized system

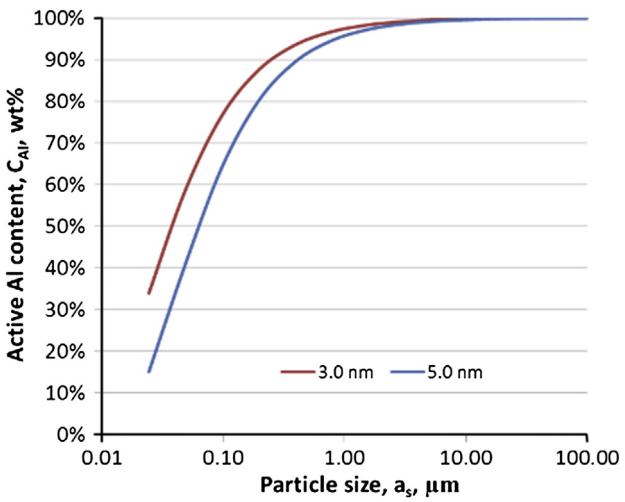

Figure 2 Calculated C_{Al} for an air-passivated Al particle with spherical shape and uniform oxide layer thickness of 3 and 5 nm. Steep metal content decrease is visible for $a_s \leq 0.1$ μm.

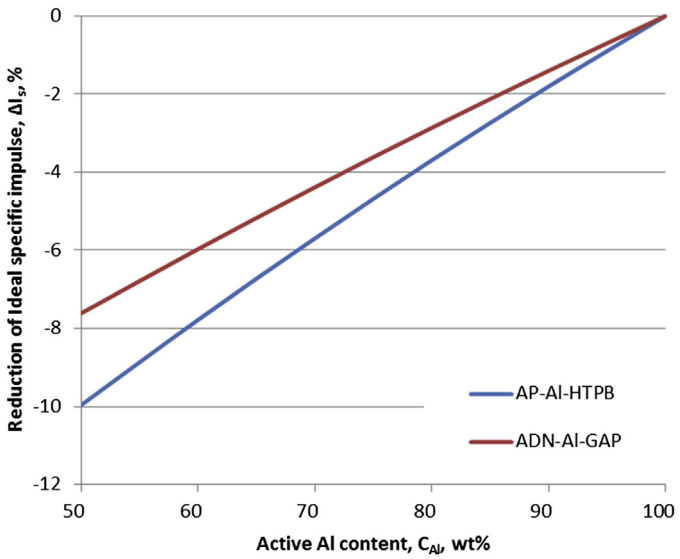

Figure 3 Reduction of calculated gravimetric specific impulse as a function of C_{Al} (combustion chamber pressure 7.0 MPa, exhaust-to-throat area ratio of 40, vacuum expansion). Comparison between AP-HTPB-Al (nominal mass ratio: 68-14-18) and ADN-GAP-Al (nominal mass ratio: 72-20-18) formulations.

characteristics. In this respect, the role of experimentation is crucial. Despite the reduced C_{Al}, nAl-based additives can promote significant solid fuel r_f enhancement and tailoring possibilities [17,20,26]. The implementation of nAl in solid propellant formulations is reported to provide r_b increase by a factor of two and to modify agglomeration process producing agglomerates of reduced size [27,28]. At the same time, a reduction of the Vieille's law ballistic exponent can be observed for nAl-loaded propellants. The outcomes of nanosized powder use in explosives are ambiguous. For example, whereas in plastic-bonded explosives the effects are negligible, detonation velocity and enthalpy of detonation in TNT-Al energetic materials are improved as the size of metal particles is progressively reduced, still remaining below the thermodynamic value [29].

The reduced size and the increased S_{SA} of nanosized systems yield undesired effects of marked particle–particle interactions (i.e., cluster formation and difficult additive dispersion [30,31]) and enhanced viscosity of loaded slurries/suspensions. As a consequence, the use of nAl increases the complexity level for the handling and preparation of the energetic compounds. The nanosized Al has a lower apparent density than μAl and is more prone to be accidentally suspended in the surrounding environment. This leads to safety concerns since the minimum ignition energy of the resulting dust cloud drops when the combustion regime of the particle switches from diffusion to kinetics limited.

However, it seems that the minimum explosive concentration features a plateau for particle size smaller than 50 μm [32]. Concerning the manufacturing of nAl-loaded propellants/fuels, the increase of additive S_{SA} is related to higher hydrodynamic component of the particle-suspending medium interaction [33]. Thus, the compounding viscosity in solid fuels and solid propellants rises as the amount of nanomaterials in the slurry is incremented. The effect is particularly evident for high solid loadings (i.e., aluminized propellants) for which the literature data by Popenko and co-authors show a viscosity ramp-up as the nAl content in the slurry overcomes 5 wt% [34]. In this respect, purposely developed particle coatings are expected to improve the ease of additive dispersion down to the nanoscale while granting protection against further environmental degradation (i.e., nAl ageing during storage) [25,35]. Also in this case a trade-off analysis is required in order to evaluate the possible effects of the coating on the overall powder characteristics (i.e., C_{Al}, reactivity) [20,25].

The SPLab research team is active in the development and characterization of innovative metal additives for space propulsion applications [20,21]. The present work focuses on a preburning characterization of different nAl powders for rocket propulsion applications. The investigated additives differ due to the implemented passivation technique and the particle structure. Air-passivated nAl is compared to a fatty acid passivated variant of the same powder. The effects of possible powder surface treatments (i.e., particle coatings) are discussed, evaluating their effects on solid propellant slurry rheology and pot life. The objective of the work is to relate the nAl characteristics to the resulting effects on the solid fuel/propellant development and manufacturing.

2. TESTED ALUMINUM POWDERS: PRODUCTION, PASSIVATION, AND COATING

The powders tested in this study range from the micron-size to the nanosize. The reference powder (Al30) is a commercial, air-passivated 30 μm Al produced by AMG Alpoco, UK [36]. The actual Al30 volume mean diameter (resulting from a dry measurement by Malvern Mastersizer 2000 [37]) is $D_{43} = 48.2$ μm while the surface mean diameter is 29.4 μm. The tested nAl powders were produced by EEW technique by Advanced Powder Technology LLC, Tomsk, Russia [38]. The hardware for the nAl production was a UDP-5 machine [39]. For all of the tested powders the EEW process was performed in an Ar environment with operating parameters granting a nominal particle size of 100 nm (declared by the supplier). Details on the operating EEW circuit and powders production parameters are reported in [40,41]. After the wire explosion, the condensed nanosized particles were collected and passivated by either Ar + 0.1 vol% air, or stearic acid. Passivation reduces the extreme reactivity of as-produced nAl powder [30] shielding the metal from intense reactions

with the surrounding environment (i.e., the powder ignition as exposed to oxidizing environment). The powder metal content is partially reduced because of the presence of the passivation layer. Nevertheless, thanks to the barrier to the diffusion of oxidizing species toward the metal, C_{Al} stabilization in time during storage is achieved (ageing resistance of the powder being affected by the kind and mass fraction of the passivation layer [9,25]). Passivation by air reduces the powder C_{Al} due to the controlled $Al \rightarrow Al_2O_3$ reaction. On the other hand, the decrease in C_{Al} after passivation by fatty acid (or other substances) is caused by the addition of a layer over the bare metal surface. Passivated nAl powders can be further coated with different substances for the tailoring of characteristics such as reactivity, ageing behavior, and compatibility with other ingredients in complex formulations. Table 1 summarizes the surface treatments of the investigated powders, including those coated after the air passivation. The C-ALEX was coated by catechol (0.2% of the powder mass) dissolved in ethyl acetate. The VF-ALEX was coated by a fluorohydrocarbon composition based on Fluorel™ [42] and ester from esterification of 1H,1H-perfluoro-1-undecanol with furan-2,5-dione. The VF-ALEX coating was solved in an isopropyl alcohol bath and its concentration was selected to provide a mass fraction over the final powder mass of 5–10% [30]. The C-ALEX was further tretated by 1 wt% HTPB, resulting in the HC-ALEX [31]. The VF-ALEX coating was selected in light of the fluoropolymer effects on powder ageing and combustion behavior [13,17]. On the other hand, the HTPB coating was selected to improve the ageing characteristics and the ease of manufacturing of HTPB-based fuel formulations. In particular, the use of the same polymer for coating and solid fuel/propellant manufacturing is a possible strategy to limit the impact of the disperse system on the viscosity of HTPB + HC-ALEX slurries. All of the investigated powders except for L-ALEX were manufactured at lab-scale level, starting from the air-passivated, uncoated nAl. Details of the ballistic response of HTPB-based solid fuel formulations loaded with VF-ALEX and

Table 1 Passivation and coating details of the tested nAl powders.

Powder ID	Passivation	Coating
ALEX	Air	–
C-ALEX	Air	Catechol (0.2 wt%) solved in ethyl acetate
HC-ALEX	Air	Catechol (0.2 wt%) and HTPB (1 wt%) solved in ethyl acetate
L-ALEX	Stearic acid solved in saturated hydrocarbon (5–10 wt%)	–
VF-ALEX	Air	Fluorel™ and ester from esterification of telomer alcohol with maleic anhydride (5–10 wt%)

HC-ALEX are described in Refs [17,41], while the combustion behaviors of solid propellants loaded with the considered nAl powders are discussed in Refs [43,44].

3. MORPHOLOGY, STRUCTURE, AND METAL CONTENT OF NANOSIZED ALUMINUM POWDERS

In this section the results of the morphological characterization of nAl are discussed. Data for a conventional μAl are introduced first, in order to provide a convenient reference for the definition of the nAl peculiar features. The investigated powders were characterized by SEM-TED (JSM-7600F), TEM (JEOL JEM-2010), S_{SA} from nitrogen adsorption (BET approach), and C_{Al}. The active Al content was determined by a volumetric technique exploiting the Al + H_2O reaction in a basic environment (10 wt% $NaOH_{(aq)}$) [45].

The SEM image presented in Figure 4 shows micron-sized particles of nearly spherical shape, with the presence of few non-spherical particles. The finer cut presents round edges and apparently smooth surfaces. The larger and nonspherical objects exhibit a more irregular texture. Thanks to the low dispersity of the powder, particle-particle interactions are limited, and so are the clustering phenomena. Being in the micron-sized range, the powder specific surface area is lower than the minimum value achievable under the investigated conditions by the BET approach (see Table 1). Micrographs of the ALEX powder are reported in Figure 5. The air-passivated and uncoated nAl shows spherical/spheroid particles (Figure 5(a)) with apparent smooth texture and a marked

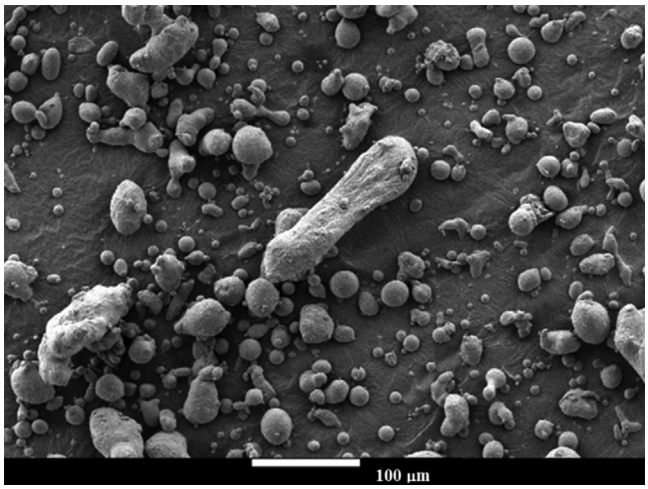

Figure 4 SEM image of Al30 powder. Spherical particles are accompanied by relatively large objects. The smaller particles exhibit smooth texture and spherical shapes. The larger particles show irregular texture and shapes.

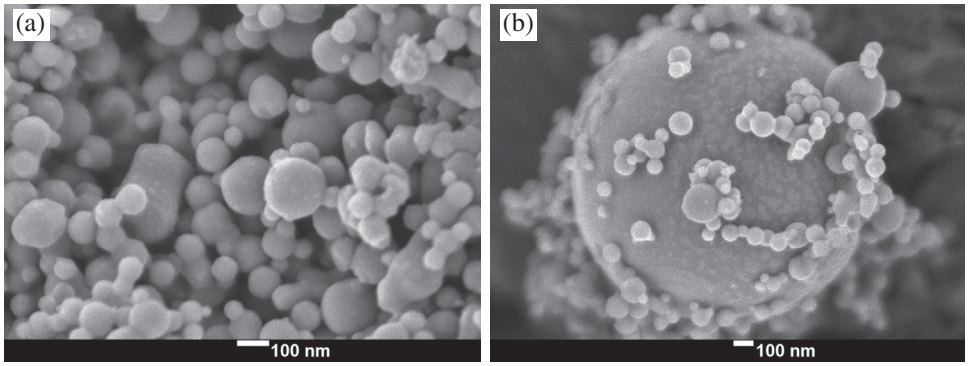

Figure 5 SEM images of the ALEX powder: (a) particles from EEW exhibit a spherical/spheroid shape, and a marked clustering tendency, (b) detail of nanosized particles clustered on a micrometric granule.

clustering tendency. Powders produced by EEW present a bi- or tri-modal size distribution [46], yielding the rare (but possible) occurrence of micron-sized particles in the final powder, as visible in Figure 5(b). The S_{SA} of the ALEX powder (Table 2) yields $a_s = 188$ nm, while the powder metal content is 89 wt%. The TED and TEM images of the investigated powders are presented in Figures 6 and 7 respectively. Transmission images show the effects of the air passivation of the ALEX particles exhibiting a core–shell structure. As shown in Figure 6(a), an external Al_2O_3 shell surrounds the Al core. This structure is common for air-passivated μAl and nAl, independently from the particle size. Under ambient conditions, the alumina of the shell is amorphous. A model developed by Trunov et al. [12] highlights the effects of Al_2O_3 polymorph phase transitions on the μAl particle ignition during heating. Recently, experimental data by Rufino et al. [47] showed how this alumina crystal phase transition could affect the nonisothermal oxidation of nAl. Considering the ALEX a_s and neglecting the presence of surface adsorbed gases, the Al_2O_3 shell thickness calculated from C_{Al} is 3.2 nm.

Table 2 Specific surface area from N_2 desorption (BET model), surface-based particle diameter (a_s), and active aluminum content (C_{Al}). The coatings of particles promote their clustering, thus reducing the S_{SA}.

Powder ID	S_{SA} (BET), m^2/g	a_s, nm	C_{Al}, wt%
Al30	< 0.1	> 22000	99.6 ± 0.1
ALEX	11.8 ± 0.4	188	89 ± 0.2
C-ALEX	11.3 ± 0.1	192	88 ± 1.5
CH-ALEX	Not available	Not available	89 ± 1.0
L-ALEX	Not available	Not available	79[a]
VF-ALEX	6.9 ± 0.2	322	78 ± 1.5

[a]Confidence interval not available.

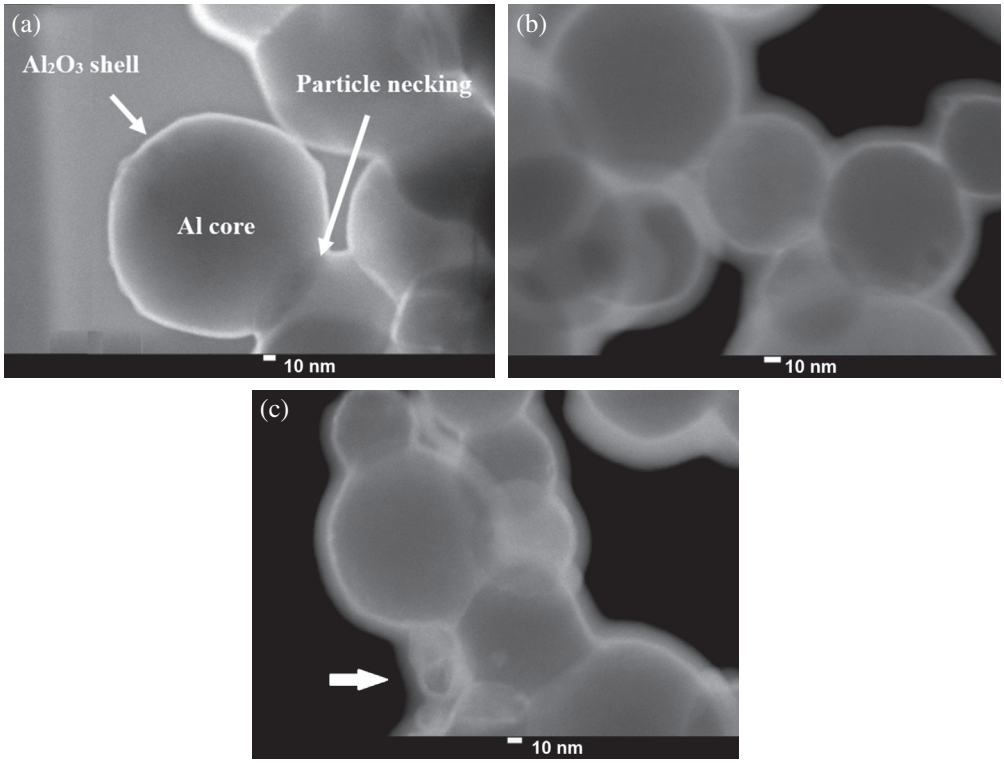

Figure 6 TED images of (a) ALEX, (b) L-ALEX, and (c) VF-ALEX. Note the Al_2O_3 shell surrounding the Al core in (a), and the layered structures of both L-ALEX and VF-ALEX visible in (b) and (c). Particle clustering induced by the fluorohydrocarbon coating is visible in (c).

This value is in agreement with the open literature data reporting maximum amorphous Al_2O_3 layer thicknesses in the range 3–5 nm [10,13]. The TED/TEM images enable identification of details of the structure of the tested particles that cannot be captured by SEM, such as the presence of nonspherical elements due to aggregation of molten aluminum droplets during the wire explosion (see Figure 6(a)).

The TED images of the L-ALEX and of the VF-ALEX (Figure 6(b) and (c), respectively) show a layered structure with a core surrounded by two shells. For the powder passivated by octadecanoic acid (i.e., without direct Al consumption due to conversion in Al_2O_3 during passivation) this is possibly due to two mechanisms: the formation of aluminum stearate because of the Al core interaction with the fatty acid [30] or the ageing of the powder after passivation [13]. Considering the relatively high thickness of the observed layer ($\sim$5 nm according to Figure 6(b)), the birth and growth of an alumina shell between the octadecanoic acid layer and the aluminum core due to powder aging during storage is the most likely explanation for genesis of the observed structure [13]. The presence of aluminum stearate cannot be excluded, considering

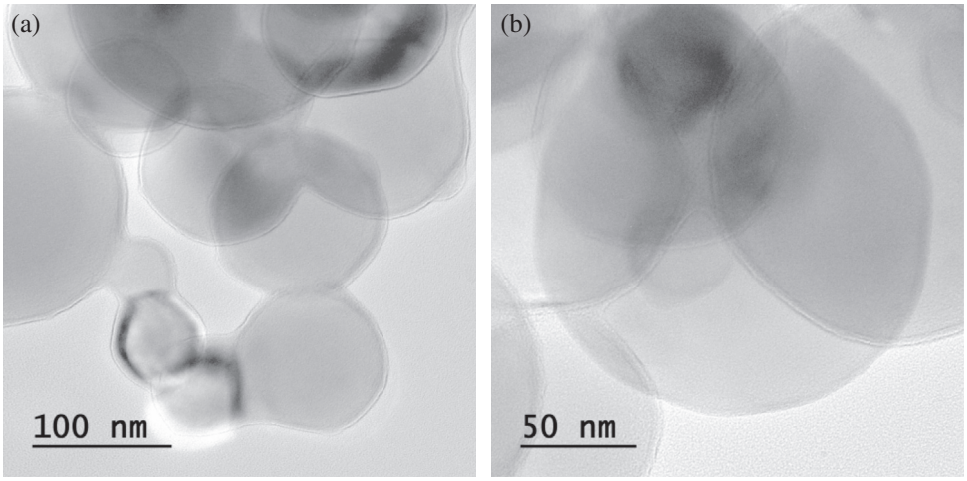

Figure 7 TEM images of (a) C-ALEX and (b) CH-ALEX. C-ALEX exhibits a layered structure with the catechol coating over the Al_2O_3 shell that surrounds the Al core. The CH-ALEX presents a uniform polymeric coating layer around the particles. Details on the HTPB coating and its selection are reported in Ref. [25].

experimental evidence reported in the open literature [13]. X-ray diffraction analyses performed on the investigated L-ALEX batch identified Al as the only crystalline phase existing in the sample. The same holds for all of the investigated nAl powders considered in this study. The reader should remember that XRD technique can identify only crystalline phases. The application of a coating layer promotes particle clustering, as testified by Figure 6(c) and by powder S_{SA} reduction with respect to the starting ALEX (see Table 2). The passivation by octadecanoic acid yields a consistent C_{Al} reduction with respect to the use of air. Considering the nominal coating mass fraction (5–10 wt% of the starting powder), this reduction is possible proof of the powder ageing, with oxygen diffusion through the fatty acid layer, yielding the Al_2O_3 shell formation and growth. For the VF-ALEX, the relatively low metal content is due to the coating application over an already air-passivated powder.

4. NANOSIZED Al POWDER REACTIVITY

The reactivity in air of the nAl powders was characterized by non-isothermal oxidation (DSC and/or TG) and ignition temperature investigations. These tests aim at providing a relative grading of the powder reactivity in an oxidizing environment at different heating rates. The heating history, the morphology, and the structure of the particles can influence their reactivity thus enabling an identification of the features influencing the powder behavior (i.e., ignition temperature, combustion regime, etc.).

4.1 Non-isothermal Oxidation: Low-Heating Rate

Slow non-isothermal oxidation runs were performed in air, with a heating rate of 10 K/min, by DSC-TG (Netzsch STA 449 F3 Jupiter) and by a DTA-TG (Seiko Instruments 6200). The reference pan for the differential analysis was α-Al_2O_3. The calorimetric and gravimetric traces of the performed tests were analyzed by the reactivity parameters identified by Ilyin et al. [48]. Table 3 presents the relevant TG data for all of the investigated powders, while a typical DSC-TG trace of nAl under the investigated conditions is reported in Figure 8. The nAl TG trace presents three main events during the low-rate heating [29,49]: an initial mass loss and a two-stage oxidation. The initial mass loss is due to different reasons, depending on the nature of powder passivation/coating layer. For air-passivated powders, the $\Delta m_0 < 0$ is related to the adsorbed gas desorption thanks to heating. This is a first difference between nAl and Al30—the lower S_{SA} of the latter limits the phenomenon that is clearly recognizable for the former

Table 3 Thermogravimetry data for the investigated powders (air, 10 K/min). Data for the L-ALEX are not available.

Powder ID	Δm_0, wt%	Δm ($T = 933$ K), wt%	Δm ($T = 1273$ K), wt%
Al30	0	0.9	1.5
ALEX	−1.3	29.5	66.0
C-ALEX	−1.3	27.1	60.8[a]
CH-ALEX	−1.4	27.9	66.1
VF-ALEX	−5.8	22.7	53.5

[a]Evaluated for the limiting temperature of 1200 K.

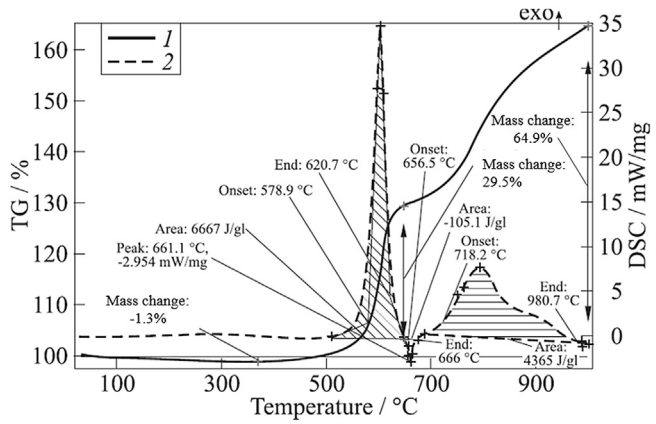

Figure 8 Typical nonisothermal oxidation trace of nAl in air at 10 K/min with (1) TG and (2) DSC traces. Staged Al oxidation, with a first intense reaction before Al melting and a second step involving the liquid metal [49].

(see ALEX vs Al30 data in Table 3). For powders passivated/coated by a reactant deposed on their surface, the initial mass loss is due to the degradation of the applied layer. The data reported in Table 3 show that the C-ALEX initial mass loss exceeds the mass fraction of the applied catechol coating. This is due to the small particle size of the powder featuring a high S_{SA} (see Table 2), with possible adsorption of environmental gaseous species during storage. On the other hand, the VF-ALEX exhibits $\Delta m_0 = -5.8\%$, implying that the mass loss is mainly due to the coating decomposition. Moreover, since the applied coating mass fraction is in the range of 5–10%, it is possible that the fluoropolymer is not completely degraded during the oxidation, thus leaving carbonaceous residuals on the surface of the particles. This explains the different TG behaviors of the nAl powders having low or high coating mass fractions (respectively, HC-ALEX and VF-ALEX): the lower coating fraction, the smaller the presence of residuals on the particle surfaces and, therefore, the higher the powder mass gain thanks to a more complete Al oxidation.

Under the investigated conditions, two intense oxidation processes follow the initial mass loss of the powders. This staged oxidation of the nAl powders is due to the following reasons:

- EEW-produced nAl exhibits relatively wide particle size distribution (see Figures 5 and 6 and Ref. [46]), thus the finer powder fraction reacts at lower temperatures than the coarser one;
- During the powder oxidation the Al_2O_3 shell surrounding the Al exhibits complex phenomena such as polymorph phase transitions [12,47] and possible cracking (due to Al melting at $T = 933$ K), influencing the core oxidation;
- $Al + N_2$ reactions followed by the possible after-oxidation of the products by interaction with O_2 [18,30].

The first nAl intense oxidation starts at temperatures below the Al melting and yields significant mass increases for the ultradisperse powders thanks to their high S_{SA} (see Table 3). ALEX and the variants with catechol-based coatings achieve similar Δm ($T = 933$ K), while the VF-ALEX performance is influenced by the higher coating mass fraction. This behavior is maintained also for the second oxidation stage. At the limiting temperature considered in the study, all of the investigated powders except for VF-ALEX show similar overall mass increases of nearly 66%. A detailed comparison between the nonisothermal oxidation behavior of ALEX and VF-ALEX is reported in Table 4. In this analysis, the first and the second intense oxidation onset temperatures ($T_{on,1}$ and $T_{on,2}$, respectively), are defined by the tangent method [50]. The sole air passivation yields a more reactive powder with respect to the VF-ALEX case. This is testified by the lower $T_{on,1}$ of the ALEX that is 36 K lower than the corresponding value for the fluorohydrocarbon-coated powder (see Table 4). Moreover, VF-ALEX exhibits $\Delta H_1 = 4171$ J/g, while for ALEX the first enthalpy release is 6667 J/g. Similar

Table 4 Nonisothermal oxidation data (DSC-TG) for selected investigated powders (air, 10 K/min).

Powder ID	$T_{on,1}$, K	ΔH_1, J/g	α ($T = 933$ K)[a]	$T_{on,2}$, K	$\Delta H_1 + \Delta H_2$, J/g	α ($T = 1273$ K)[a]
ALEX	852	6667	37.2	991	11032	83.3
VF-ALEX	888	4171	32.7	1065	8090	77.1

[a]Conversion factor for the Al → Al_2O_3 reaction: $\alpha(T) = C_{Al}/[\Delta m(T) \cdot 0.89]$, [48].

considerations are valid for the second intense oxidations of the powders, where the onset delay of the VF-ALEX reaches 74 K. The fluorohydrocarbon-coated powder exhibits a reduced overall enthalpy release with respect to the ALEX: $\Delta H_1 + \Delta H_2 = 11032$ J/g for the air-passivated nAl, while, for the given liming temperature of 1273 K, VF-ALEX delivers 8090 J/g. The oxidation onset delay of the fluorohydrocarbon-coated powder can be explained by considering that, under low-heating rates, the coating decomposition and the powder oxidation occur at different temperatures and times. Consequently, possible interactions between the two phenomena are not possible, while incomplete coating degradation can leave carbonaceous residuals on the aluminum particles. These fluoropolymer-degradation residuals can hinder the particle oxidation, thus justifying the achieved results. It is worth noting that according to literature results, the second oxidation stage is merged with the first one for tests conducted in O_2 with heating rates >30 K/min [51].

4.2 Non-isothermal Oxidation: High-Heating Rate

Ignition temperature of the considered powders was investigated by a hot-wire technique. The test rig developed at SPLab exploits the Joule effect heating a purposely shaped Kanthal™ wire where the powders are accommodated and are directly warmed. Powder temperature history is measured by an S-type (Pt–Pt/10% Rh) microthermocouple (50 μm junction). An infrared photodiode aids in the determination of the T_{ign}. Fine control of the powder heating rate can be obtained by adjusting the electric power input to the wire achieving up to 350 K/s with high degree of reproducibility. The T_{ign} of the tested powders is evaluated by the marked temperature rise during heating, and the photodiode signal provides a confirmation of the ignition occurrence by detecting a steep increase in the radiation emitted by the sample. Complete descriptions of the experimental setup and of the data reduction technique are reported in Ref. [6]. The hot-wire approach offers the possibility to compare the data from low-heating rates of the DSC-TG with the results of faster-heating rate tests. The data presented in Table 5 are obtained in air, at 0.1 MPa pressure, with heating rates of (300 ± 50) K/s.

The results for T_{ign} show different (and opposite) trends with respect to the DSC-TG runs (see $T_{on,1}$ in Table 4). In particular, under the investigated conditions, the VF-ALEX exhibits an enhanced reactivity with respect to the air-passivated ALEX. A T_{ign} reduction

Table 5 Ignition temperature results for the tested powders (air, pressure 0.1 MPa, heating rate [300 ± 50] K/s). Confidence interval is evaluated considering 95% Student's *t*-distribution. The reported T_{ign} is the result of at least 10 single valid tests.

Powder ID	T_{ign}, K
Al30	Not available[a]
ALEX	820 ± 12
L-ALEX	771 ± 16
VF-ALEX	713 ± 20

[a] T_{ign} above the limiting thermocouple temperature (1873 K).

of nearly 110 K testifies a more prompt ignition of the fluorohydrocarbon-coated powder. A similar trend is testified by the stearic acid–coated powder, whose ignition temperature is intermediate with respect to the limiting cases of ALEX and VF-ALEX. Under the investigated conditions, the coating degradation triggers the ignition process of the powders, thus explaining the observed trend of the results [17,40]. The available data do not enable to identify if the L-ALEX and the VF-ALEX ignition is triggered by aerobic reactions between environmental air and coating decomposition products or by heterogeneous anaerobic processes between the solid particle and the coating decomposition products. Literature data from Refs [52] and [53] suggest that an interaction of the second type is likely. Test rig limitations impair testing in low-O_2 (or inert) environments to evaluate the detailed effects of coating decomposition on particle ignition, which are addressed for future works. In any case, the results obtained testify the heating rate effects on the powder ignition phenomena, as discussed in Ref. [54]. The same effect is highlighted by the differences between results for low- and high-heating rates with fluoropolymer-containing Al-based composites [20,22]. The possible interactions between coating degradation products and nAl combustion can be the cause of the peculiar ballistic behavior of HTPB + VF-ALEX fuel burnt at lab-scale level [17,40]. In particular, the presence of a fluorinated coating possibly reduces the aggregation phenomena affecting the ALEX combustion in solid fuels [17,52,53,55]. Under the investigated conditions, the ignition temperature of ALEX occurs on the temperature range identified by Trunov et al. for the amorphous-to-γ transition of the Al_2O_3 that could be the driving mechanism for the particle ignition [12]. However, other effects as the dehydration of Al hydroxides (eventually present on the particle surface as a consequence of exposure to moisture) must be considered as the possible causes of the ALEX marked reactivity, as discussed in Ref. [56].

5. RHEOLOGY OF NANOSIZED ALUMINUM-LOADED SOLID FUELS AND PROPELLANT SLURRIES

In this section the rheological behavior of uncured solid fuels and solid propellant formulations is presented and discussed. The study of the slurry viscosity enables evaluation of the effects of the metal powder S_{SA}, morphology and dispersion on the compound manufacturing, and final characteristics.

The dispersion of nanosized additives in a polymeric matrix requires purposely implemented procedures in order to prevent or limit the particle clustering, thus granting the additive dispersion down to the nanoscale. The commonly implemented methods for effective nAl dispersion are based on ultrasound treatment of the mixtures [25,57]. The fuel and propellant formulations considered in this section are manufactured according to an operating protocol developed at SPLab [58,59] and based on the use of an acoustic mixer (Resodyn™ LabRAM mixer [60]). In particular, during the fuel/propellant slurry manufacturing the compound temperature was controlled by a dedicated setup [61] in order to prevent undesired curing reactions due to the self-heating induced by the intense mixing. The results concerning the rheological behavior of solid fuel formulations are introduced first, and then the focus is moved to evaluation of propellant slurry viscosity.

5.1 Rheological Behavior of Uncured Solid Fuel Slurries

In this section the rheological behavior of uncured HTPB-based fuel slurries is discussed. The experimental investigation was performed on a TA AR2000ex rheometer with the plate–plate configuration. The fuel slurries were tested under oscillatory conditions (2% strain, 1 Hz frequency) for the evaluation of $|\eta^*| = (\eta'^2 + \eta''^2)^{1/2}$ [61]. Operating temperature was set to 333 K, and the test duration was 5 h. Details of the HTPB-binder formulations are presented in Table 6, while composition details of the tested slurries are reported in Table 7. Additive mass fractions were selected referring to the typical values considered in the open literature papers dealing with the hybrid rocket fuel regression rate enhancement studies [17,26,40].

Table 6 Detailed composition of the HTPB-binder considered in the analysis. The curing level (−NCO/−OH) of the formulation is 1.04.

Ingredient	Mass fraction, %
HTPB R-45 HTLO[a]	79.2
DOA	13.1
IPDI	7.7

[a]Hydroxyl functionality 0.83 ± 0.5 meqKOH/g, molecular weight 2800 g/mol, $\eta(T = 303\ \text{K}) = 5\ \text{Pa}\cdot\text{s}$.

Table 7 Detailed composition of the tested uncured fuel slurries. The considered Al powders were ALEX or L-ALEX. The F-OCT fuel formulation is employed to evaluate the effects of the pure stearic acid on the HTPB rheological response.

Fuel slurry ID	nAl type	nAl fraction, wt%
F-HTPB[a]	—	—
F-ALEX − 10%	ALEX	10
F-L-ALEX − 10%	L-ALEX	10
F-OCT[b]	—	—

[a]Nonmetallized fuel formulation (baseline).
[b]HTPB (99.5 wt%) + stearic acid (0.5 wt%).

Table 8 Time evolution of $|\eta^*|$ under isothermal conditions ($T = 333$ K, 2% strain, 1 Hz frequency). Test strain condition is selected to operate in the linear field.

	Time elapsed from the test start, min					
Fuel slurry ID	**0**	**60**	**120**	**180**	**240**	**300**
F-HTPB	0.56	0.78	1.1	1.5	2.0	2.7
F-ALEX − 10%	0.85	0.94	1.1	1.4	1.7	2.1
F-L-ALEX − 10%	0.85	1.2	1.9	2.9	4.2	6.1
F-OCT	0.82	4.0	19	111	Gelled in 218 min	

An extended discussion of the herein presented results (including data on several micron-sized powders) is reported in Ref. [57], while data concerning the time evolution of the $|\eta^*|$ for the formulations of interest are reported in Table 8.

Under the investigated conditions, the suspensions behave as Newtonian fluids [33]. Due to the high specific surface area, both ALEX and L-ALEX act as semireinforcing fillers, promoting significant $|\eta^*|$ increases at $t = 0$ (i.e., at beginning of the test) due to both hydrodynamic effects and particle–particle interactions. In particular, at the beginning of the runs, the viscosity of F-ALEX-10% and F-L-ALEX-10% is increased by 52% with respect to the F-HTPB case. The F-OCT formulation, which is designed in order to simulate the possible HTPB-isocyanate-stearic acid interactions occurring in P-L-ALEX-10%, presents a marked $|\eta^*|$ initial value. This result is due to fast-curing reactions of the compound during the pre-test phases. The complex viscosity of F-OCT shows a rapid and monotonic increase during the test (see Table 8). The gelation point ($\eta' = \eta''$, Ref. [62]) is reached in less than 4 h, suggesting HTPB-stearic acid interactions in the curing process. This is testified by the F-L-ALEX-10% data reported in Table 8. In spite of the fact that L-ALEX exhibits a S_{SA} reduction over ALEX [61], with a consequent reduction of the hydrodynamic stresses, the F-L-ALEX-10% shows a $|\eta^*|$ increase in time with a higher rate than both F-HTPB and the ALEX-loaded slurry. On the other hand, the F-ALEX-10% exhibits a $|\eta^*|$ buildup slower than the baseline slurry. Moreover, for t in the range of 180–240 min, the ALEX-doped formulation shows a lower $|\eta^*|$ than F-HTPB. The viscosity buildup of the tested formulations is captured by the fitting parameters reported in Table 9, which refer to the following exponential approximation:

$$|\eta^*| = |\eta^*|_{t=0} \exp(k_\eta t) \tag{1}$$

The behavior exhibited by the ALEX-loaded formulation is in agreement with the experimental results of Mahanta and Pathak and MacManus et al., showing a viscosity buildup rate decrease for μAl-loaded formulations with respect to the neat HTPB case [63,64]. Interestingly, α-Al_2O_3 micron-sized particles promote different effects on the $|\eta^*|$ evolution in time [61], so the peculiar behavior caused by ALEX (and μAl) might be

Table 9 Exponential fitting of complex viscosity buildup under isothermal conditions ($T = 333$ K, 2% strain, 1 Hz frequency). See Eqn (1) for details.

Fuel slurry ID	$\lvert\eta^*\rvert_{t=0}$, Pa·s	k_s, min^{-1}	R^2
F-HTPB	0.560	0.00527	0.999
F-ALEX − 10%	0.854	0.00332	0.992
F-L-ALEX − 10%	0.855	0.00665	0.999
F-OCT	0.824	0.02700	0.999

related to the amorphous alumina shell surrounding the particles. Nevertheless, further analyses are required to assess properly the phenomenon that is not reported in the open literature.

5.2 Rheological Behavior of Uncured Solid Propellant Slurries

The rheological behavior of uncured solid propellant slurries was characterized using a Rhemoetrics Dynamic Analyzer RDA II. The slurries were tested in a plate–plate configuration (Al, plate diameter 40 mm) with a gap of 1 ± 0.05 mm. The runs were conducted in a steady rate sweep condition (with shear rate varying from 0.5 to 5 s^{-1} and measurement time of 60 s), at the temperature of 333 K [33,35,65,66].

Tests were performed on propellant formulations whose detailed compositions are reported in Table 10. The tested slurry contains a bimodal AP size distribution and a relatively high mass fraction of plasticizer, since DOA is used to simulate the presence of a liquid curing agent having similar viscosity (not included to prevent from undesired curing). The Al30 was used for the manufacturing of the baseline formulation and was gradually replaced by increasing the nAl mass fraction (from 3 to 18 wt%). Details of the solid propellant manufacturing procedure are reported in Ref. [58] while a list of the tested formulations is given in Table 11.

Under the investigated conditions, an accurate data reduction is necessary to validate the results focusing on both viscosity and applied torque as functions of the shear rate (see

Table 10 Detailed composition of the tested uncured propellant slurries. The considered Al powders were Al30, nAl (ALEX, L-ALEX, and VF-ALEX) or a variable mixture of Al30 and nAl. See Table 11 for further details.

Ingredient	Mass fraction, %
AP − 200 μm	58.0
AP − 10 μm	10.0
HTPB R-45HTLO[a]	11.1
DOA	2.9
Aluminum	18.0

[a]Hydroxyl functionality 0.83 ± 0.5 meqKOH/g, molecular weight 2800 g/mol, $\eta(T = 303\ \text{K}) = 5$ Pa·s.

Table 11 Solid propellant slurries tested for the assessment of the nAl effects on the propellant rheological behavior.

Propellant slurry ID	nAl type	μAl, %	nAl, %
P-Al30	–	18	0
P-Alex – 03%	ALEX	15	3
P-Alex – 06%	ALEX	12	6
P-Alex – 18%	ALEX	0	18
P-L-Alex – 03%	L-ALEX	15	3
P-L-Alex – 06%	L-ALEX	12	6
P-L-Alex – 18%	L-ALEX	0	18
P-V-Alex – 03%	VF-ALEX	15	3
P-V-Alex – 06%	VF-ALEX	12	6
P-V-Alex – 18%	VF-ALEX	0	18

Figure 9). In particular, the correct slurry-plate adhesion is monitored by checking the change of viscosity during shear rate sweep. The adhesion was correlated with the SR variations exceeding a critical limiting value indicated as SR* [58]. The results reported in Figure 9(a) for P-Al30-18% show the trend of a test exhibiting no slippage between the plates and the slurry. In some cases, this adhesion can fail. An example of this event is shown in Figure 9(b) where the results of the P-L-ALEX-18% are shown. From the $SR^* = 1.58\ s^{-1}$ the applied torque evolution exhibits an abrupt fall as a consequence of the slurry-plate detachment. Viscosity values registered after SR* are therefore unreliable and are not considered in the following analysis. The experimental results obtained are presented in Figures 10–12. In order to capture the overall η(SR) behavior, a data fitting based on exponential- or power-law functions is proposed (see Table 12). These exponential

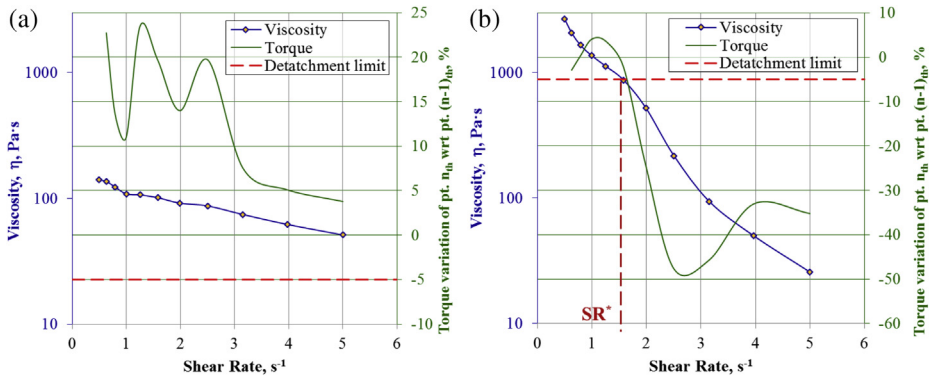

Figure 9 Uncured solid propellant viscosity dependence on torque for (a) P-Al30-18% and (b) P-L-ALEX-18%. It was verified by direct inspection that when the slurry adheres to the plate, the torque variation does not fall below the critical value of −5% (a). The slurry-plate separation produces marked decreases in the torque variation values (b), producing unreliable data from SR* on.

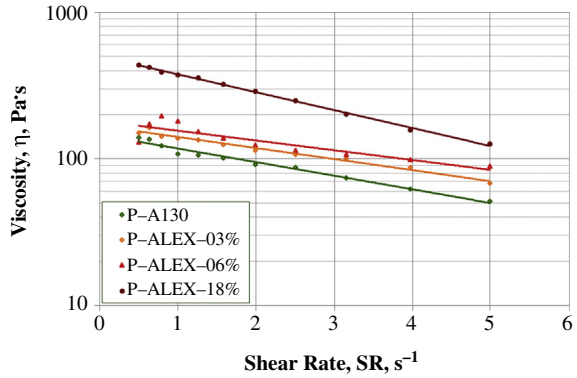

Figure 10 Viscosity of uncured propellants of the P-ALEX series. The solid lines represent the exponential fittings of the experimental data shown in Table 12.

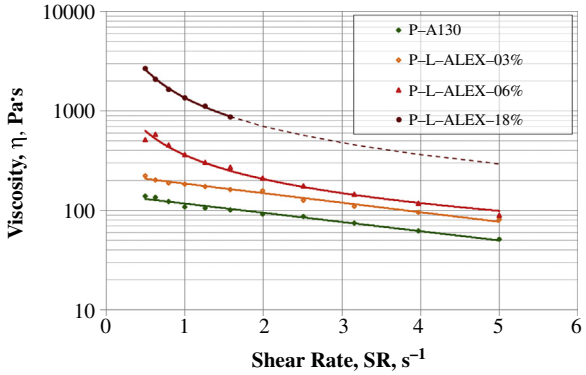

Figure 11 Viscosity of uncured propellants of the P-L-ALEX series. The solid lines represent the exponential fittings of the experimental data shown in Table 12. The dashed line represents the data extrapolated from the trend achieved in the range $SR \leq SR^*$.

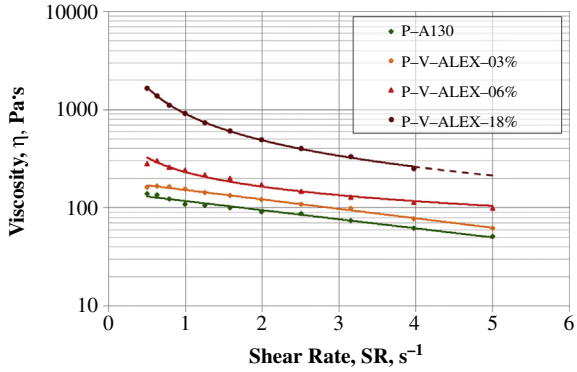

Figure 12 Viscosity of uncured propellants of the P-V-ALEX series. The solid lines represent the exponential fittings of the experimental data shown in Table 12. The dashed line represents the data extrapolated from the trend achieved in the range $SR \leq SR^*$.

Table 12 Fittings of the propellant slurry rheological behavior data. Exponential- or power-law data fitting is selected, depending on the form maximizing the coefficient of correlation (R^2) of the approximation.

Propellant slurry ID	η(SR) approx.[a]	R^2
P-Al30	$(145.52 \pm 3.71)\cdot\exp[(-0.214 \pm 0.010)\mathrm{SR}]$	0.977
P-Alex − 03%	$(167.63 \pm 3.41)\cdot\exp[(-0.174 \pm 0.008)\mathrm{SR}]$	0.978
P-Alex − 06%	$(181.17 \pm 12.4)\cdot\exp[(-0.\ 154 \pm 0.028)\mathrm{SR}]$	0.746
P-Alex − 18%	$(499.48 \pm 5.32)\cdot\exp[(-0.281 \pm 0.004)\mathrm{SR}]$	0.998
P-L-Alex − 03%	$(232.70 \pm 5.39)\cdot\exp[(-0.214 \pm 0.010)\mathrm{SR}]$	0.982
P-L-Alex − 06%	$(361.78 \pm 11.8)\cdot\mathrm{SR}^{(-0.803\pm0.038)}$	0.978
P-L-Alex − 18%	$(1361.4 \pm 14.8)\cdot\mathrm{SR}^{(-0.948\pm0.026)}$	0.996
P-V-Alex − 03%	$(190.33 \pm 2.70)\cdot\exp[(-0.222 \pm 0.006)\mathrm{SR}]$	0.993
P-V-Alex − 06%	$(231.71 \pm 5.56)\cdot\mathrm{SR}^{(-0.493\pm0.028)}$	0.969
P-V-Alex − 18%	$(907.93 \pm 6.93)\cdot\mathrm{SR}^{(-1.051\pm0.089)}$	0.999

[a]Approximating laws are in the form $\eta(\mathrm{SR}) = a_{\mathrm{SR}}\cdot\exp(n_{\mathrm{SR}}\cdot\mathrm{SR})$, or $\eta(\mathrm{SR}) = a_{\mathrm{SR}}\cdot\mathrm{SR}^{n\mathrm{SR}}$.

laws were used for the extrapolation of the slurry viscosity in the range from the (eventual) SR* value until the limiting tested SR of 5 s^{-1}, as shown in (Figures 11 and 12).

Figure 10 reports a comparison between the rheological behaviors of uncured propellants containing a variable amount of ALEX (P-ALEX-series) with the baseline formulation (P-Al30-18%). Under the investigated conditions, the viscosity of the slurries shows a shear thinning behavior, with decreasing viscosity for increasing SR. Due to the higher S_{SA} of the ALEX particles with respect to the Al30, a 3 wt% nAl addition determines a 27% viscosity increase with respect to the baseline at the $\mathrm{SR} = 1\ s^{-1}$. Under the same operating condition, when the ALEX content is incremented up to 6 wt%, the viscosity becomes 181.1 Pa·s (showing a percent increase of 67% with respect to the baseline). For the reported tests the maximum viscosity values are achieved by the P-ALEX-18% featuring $\eta(\mathrm{SR} = 1\ s^{-1}) =$ 1367 Pa·s. This viscosity is one order of magnitude higher than the respective property demonstrated by the baseline. Data presented in Table 12 also capture the highest sensitivity to SR changes of the P-ALEX-18% within the tested slurries. This result is due to the fact that higher nAl mass fractions imply the presence of more clusters. These cold-cohesive groups of particles may be destroyed by the hydrodynamic effects induced by the shear rate, thus generating the observed high SR sensitivity. Viscosity curves for P-L-ALEX series and P-V-ALEX series of slurries are reported in Figures 11 and 12, respectively. The propellants loaded with the stearic acid-treated powder exhibit a trend similar to that of the ALEX-doped slurries. The P-L-ALEX-06% and the P-L-ALEX-18% have a more marked shear thinning behavior than the corresponding ALEX-loaded formulations and, as a consequence, the trend of η as a function of SR is better captured by a power-law approximation (see Table 12). For the $\mathrm{SR} = 1\ s^{-1}$ the viscosity percent difference with respect to the

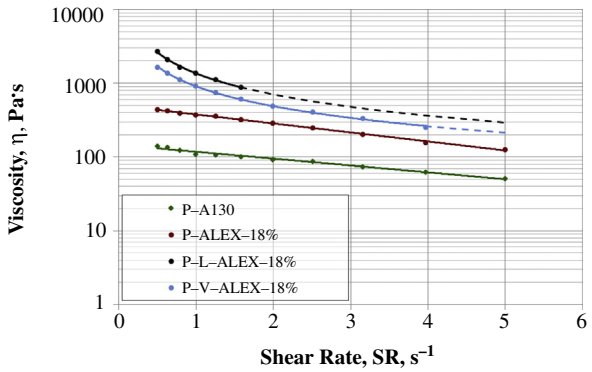

Figure 13 Viscosity diagram of the uncured propellant slurries with 18 wt% load of nAl. Note the shear thinning behavior of the L-ALEX- and VF-ALEX-loaded formulations.

baseline of P-L-ALEX-06% and P-L-ALEX-18% are 234% and 1160%, respectively. According to Ref. [58], the more intense shear thinning behavior of P-L-ALEX slurries with nAl content higher than 3 wt% is due to the presence of a coating that modifies interparticle interactions and is evident only when critical L-ALEX content is reached in the uncured formulation.

In spite of a relatively poor compatibility between fluoropolymer and HTPB, the rheological behavior of the slurries loaded with the VF-ALEX does not present marked differences with respect to the results obtained in the P-L-ALEX series (see Table 12). A comparison between the propellant slurries containing 18 wt% of nAl and the baseline is reported in Figure 13. The collected data testify to the detrimental effect of nAl-loading on the rheological response to the applied shear rate, with increased η over the baseline. The L-ALEX and the VF-ALEX generate slurries with enhanced viscosities with respect to the mix using ALEX. This result is probably due to the wettability of the L-ALEX and of the fluorohydrocarbon-coated powder surfaces with the HTPB + AP compound. Further investigations are needed in order to get a better insight into the observed phenomena.

6. CONCLUSION AND FUTURE DEVELOPMENT

This work is focused on characterization techniques for nanosized aluminum powders used in condensed energetic systems. Both qualitative and quantitative information were retrieved from techniques based on electron microscopy (SEM, TED, and TEM), non-isothermal oxidation (DSC-TG, T_{ign} determination), and viscosimetry. The investigated nAl powders were produced by the EEW method. They differ in the implementation of two passivation processes (air vs stearic acid) and in the eventual coating of the passivated surface (see Table 1).

SEM micrographs revealed no significant differences between the morphology of the tested powders. In spite of their surface treatments (i.e., air or stearic acid passivation, eventual coating of the air-passivated surface), nAl particles generally exhibit spherical shape, with particle size possibly in the sub-micrometric or in the micron-sized range, and smooth texture. Considering air-passivated ALEX particles, a marked clustering behavior yielding the formation of micron-sized assembles is observed (see Figure 5). Cold cohesion is a widely observed phenomenon affecting high-S_{SA} systems due to particle–particle interactions (e.g., electrostatic forces). TED/TEM observations of ALEX enable the identification of interparticle necking and aggregation (effects of the production technique) and particles clustering (a behavior induced by the powder features such as S_{SA}, particle size dispersity, and surface texture characteristics). Transmission images provide effective analysis of the thickness and of the structure of the oxide layer surrounding ALEX particles, in spite of the amorphous nature of the Al_2O_3 preventing its detection by XRD technique. For coated air-passivated powders, TED/TEM data enable direct verification of the layered structure of the particles. At the same time, possible critical points (e.g., clustering promoted by the coating deposition) can be observed by these diagnostics. Moreover, TED and TEM allow monitoring the powders' ageing behavior (e.g., oxide shell thickening, metal core consumption). The observation of L-ALEX double-shell structure that is generated by the oxidizer diffusion through the stearic acid layer after passivation is a clear example of the possibilities of TEM and TED.

The features of the passivation layer (composition, amorphous/crystalline phase) and their evolution during heating are crucial to understand the results of the analyses dedicated to the combustion behavior of the particles [6]. The energy release of the disperse system oxidation depends on the powder reactivity and C_{Al}. For air-passivated powders, the oxidation reaction onset is related to the change in the Al_2O_3 shell characteristics [12,56] and/or integrity [56]. In this respect, the decomposition of coatings applied on the oxide layer can trigger the particle ignition, if some oxidizing species diffuses toward (or is in contact with) the metal fuel after coating degradation [17,20,40,53,54]. The reaction process can be the result of concurring natural oxide cracking and applied coating decomposition. Non-isothermal analysis at low-heating rates is demonstrated to be very effective in the investigation of the basic phenomena occurring as powder temperature is increased, especially in the presence of a coating (see Tables 3 and 4). Coating degradation, particle oxidation, and even oxide polymorphic transformations [12,47] can be recorded, even though sometimes the identification of the single processes can be complex. The TG trace enables to investigate the effectiveness of the coating deposition procedure—since under low-heating rates the coating decomposition occurs over a different temperature range with respect to the oxidation of pure nAl particles, Δm_0 can provide information on the presence of the coating layer on the particle surface (see Table 3). Experimental data demonstrated that high-heating rate

analyses were more informative in the definition of a ranking between the reactivity of different samples, reproducing realistic thermal stresses on the sample (see Table 5). From this point of view, the contrast between ALEX and VF-ALEX DSC-TG and T_{ign} data is very important. While at low-heating rates (10 K/min, see Table 3) the coating degradation and the nAl oxidation occur over well-separated temperature ranges, in the tests performed at (300 ± 50) K/s VF-ALEX ignites at a lower temperature than ALEX. In the case of fluorohydrocarbon coating, it is possible that the main cause of the enhanced particle reactivity is the interaction between fluorine-containing coating degradation products and the particle metal core, as suggested by theoretical and experimental results presented in [17,20,41,53,54].

Due to reduced size and increased S_{SA}, nanosized particles are prone to particle–particle interactions requiring purposely implemented solid fuel/propellant manufacturing procedures, and strongly affecting the rheological behavior of particle-loaded suspensions. Rheological analyses performed under low-amplitude and low-frequency oscillatory conditions reveal the semireinforcing behavior of nAl, yielding augmented slurry viscosity (see Table 8). The detrimental effect on viscosity buildup for curing HTPB suspensions loaded with ALEX is captured by the rheological investigation conducted under oscillatory conditions (see Table 9). The high S_{SA} of ALEX amplifies the behavior observed for μAl-doped compounds in open literature works [63,64]. On the other hand, curing process evolution of HTPB + L-ALEX data show the enhancing effect of the fatty acid layer on the urethane reaction, with a strong and fast viscosity increase in time under the investigated conditions. Investigations of the rheological behavior of uncured solid propellant slurries evidenced the marked η enhancement due to nAl loading. Under the tested conditions, increased η values are achieved for increasing nAl content. For nAl + μAl loads with 6 wt% of nanosized powder, the η increase over the baseline is ∼70%. These results highlight the importance of a rheological characterization of the nAl powder characteristics for an effective manufacturing procedure and for possible industrial, large-scale applications.

Future characterization of nAl powders should be performed by an integrated approach that includes particle morphology, low- and high-heating rate reactivity, and powder-suspending medium interactions. The "high-safety with high-reactivity" requirement of rocket propulsion applications implies a comprehensive understanding of the nanosized system preburning characteristics, directed to the full exploitation of nAl features. Storage, handling, and use of nanopowders in industrial environments should be comprehensively analyzed on the basis of wide experimental screening.

ACKNOWLEDGMENTS

Some of the characterizations presented in this work are performed in the frame of a cooperative action between the Space Propulsion Laboratory (SPLab) and the Advanced Manufacturing Laboratory (AMALA) of Politecnico di Milano.

REFERENCES

[1] A.V. Grosse, J.B. Conway, Combustion of metals in oxygen, Ind. Eng. Chem. 50 (1958) 663–672.
[2] G.P. Sutton, O. Biblarz, Rocket Propulsion Elements, seventh ed., John Wiley & Sons, Hoboken, New Jersey, USA, 2007.
[3] N. Kubota, Propellants and Explosives: Thermochemical Aspects of Combustion, second ed., Wiley-VCH, Weinheim, Germany, 2006.
[4] E.L. Dreizin, Metal-based reactive nanomaterials, Prog. Energy Combust. Sci. 35 (2009) 141–167.
[5] N.H. Yen, L.Y. Wang, Reactive metals in explosives, Propell. Explos. Pyrotech. 37 (2012) 143–155.
[6] L.T. De Luca, L. Galfetti, F. Maggi, G. Colombo, C. Paravan, A. Reina, S. Dossi, M. Fassina, A. Sossi, Characterization and combustion of aluminum nanopowders in energetic systems, in: A.A. Gromov, U. Teipel (Eds.), Metal Nanopowders Production, Characterization, and Energetic Applications, Wiley VCH, Weinheim, Germany, 2014.
[7] A. Vignes, F. Muñoz, J. Bouillard, O. Dufaud, L. Perrin, A. Laurent, D. Thomas, Risk assessment of the ignitability and explosivity of aluminum nanopowders, Process Saf. Environ. Prot. 90 (4) (2012) 304–310.
[8] L.K. Braydich-Stolle, J.L. Speshock, A. Castle, M. Smith, R.C. Murdok, S.M. Hussain, Nanosized aluminum altered immune function, ACS Nano 4 (7) (2010) 3661–3670.
[9] Y.S. Kwon, A.A. Gromov, Y.I. Strokova, Passivation of the surface of aluminum nanopowders by protective coatings of the different chemical origin, Appl. Surf. Sci. 253 (2007) 5558–5564.
[10] L.P.H. Jeurgens, W.G. Sloof, F.D. Tichelaar, E.J. Mittemeijer, Structure and morphology of aluminium oxide films formed by thermal oxidation of aluminium, Thin Solid Films 418 (2002) 89–101.
[11] L.P.H. Jeurgens, W.G. Sloof, F.D. Tichelaar, E.J. Mittemeijer, Composition and chemical state of the ions of aluminium-oxide films formed by thermal oxidation of aluminium, Surf. Sci. 506 (2002) 313–332.
[12] M.A. Trunov, M. Schoenitz, X. Zhu, E.L. Dreizin, Effect of polymorphic phase transformations in Al_2O_3 film on oxidation kinetics of aluminum powders, Combust. Flame 140 (2005) 310–318.
[13] A. Gromov, A. Ilyin, U. Förter-Barth, U. Teipel, Characterization of aluminum Powders: II. Aluminum nanopowders passivated by non-inert coatings, Propell. Explos. Pyrotech. 31 (2006) 401–409.
[14] M.A. Trunov, S.M. Umbrajkar, M. Schoenitz, J.T. Mang, E.L. Dreizin, Oxidation and melting of aluminum nanopowders, J. Phys. Chem. B 110 (2006) 13094–13099.
[15] M.W. Beckstead, A summary of aluminum combustion, in: Internal Aerodynamics in Solid Rocket Propulsion, 2004 (Chapter 5), RTO-EN 023.
[16] Y. Huang, G.A. Risha, V. Yang, R.A. Yetter, Effect of particle size on combustion of aluminum particle dust in air, Combust. Flame 156 (2009) 5–13.
[17] C. Paravan, Ballistics of Innovative Solid Fuel Formulations for Hybrid Rocket Engines (PhD dissertation), Politecnico di Milano, Milan, Italy, 2012.
[18] E.M. Popenko, A.P. Ilyin, A.M. Gromov, S.K. Kondratyuk, V.A. Surgin, A.A. Gromov, Combustion of mixtures of commercial aluminium powders and ultrafine aluminium powders and aluminium oxide in air, Combust. Explos. Shock Waves 38 (2002) 157–162.
[19] W. Ingignoli, B. Veyssiere, B.A. Khasainov, Study of detonation initiation in unconfined aluminium dust clouds, in: G.D. Roy, S.M. Frolov, K. Kailasanath, N.M. Smirnov (Eds.), Gaseous and Heterogeneous Detonaions: Science to Applications, ENAS publishers, Moscow, Russia, 1999, pp. 337–350.
[20] C. Paravan, M. Stocco, S. Penazzo, J. Myzyri, L.T. DeLuca, L. Galfetti, Effects of aluminum composites on the regression rates of solid fuels, Presented at the 6th EuCASS (European Conference for Aeronautics and Space Sciences), Krakow, Poland, 29 June–03 July, 2015.
[21] S. Dossi, C. Paravan, F. Maggi, G. Colombo, L. Galfetti, Enhancing Micrometric Aluminum Reactivity by Mechanical Activation, AIAA Paper No. 2015-4221, 2015.
[22] M. Boiocchi, C. Paravan, S. Dossi, F. Maggi, G. Colombo, L. Galfetti, Paraffin-based Fuels and Energetic Additives for Hybrid Rocket Propulsion, AIAA Paper No. 2015-4042.

[23] M. Cliff, F. Tepper, V. Lisetsky, Ageing Characteristics of ALEX™ Nanosized Aluminum, AIAA Paper 2001-3287, 2001.
[24] S. Cerri, M.A. Bohn, K. Menke, L. Galfetti, Ageing behaviour of HTPB based rocket propellant formulations, Cent. Eur. J. Energ. Mater. 6 (2009) 149–165.
[25] A. Reina, C. Paravan, M. Morlacchi, A. Frosi, F. Maggi, L.T. DeLuca, Rheological and mechanical behavior of coated aluminum loaded nano-composites, in: C. Bonnal, L.T. DeLuca, S.M. Frolov, O. Haidn (Eds), Advances in Propulsion Physics, vol. 5, Torus Press, Moscow, in press
[26] G.A. Risha, B.J. Evans, E. Boyer, K.K. Kuo, Metals, energetic additives and special binders used in solid fuels for hybrid rockets, in: M.J. Chiaverini, K.K. Kuo (Eds.), Fundamentals of Hybrid Rocket Combustion and Propulsion, AIAA Progress in Astronautics and Aeronautics, vol. 218, 2007 (Chapter 10), pp. 413–456.
[27] L.T. DeLuca, L. Galfetti, G. Colombo, F. Maggi, A. Bandera, V.A. Babuk, V.P. Sinditskii, Microstructure effects in aluminized solid rocket propellants, J. Propuls. Power 26 (2010) 724–732.
[28] L.T. De Luca, L. Galfetti, F. Severini, L. Meda, G. Marra, A.B. Vorozhtsov, V.S. Sedoi, V.A. Babuk, Burning of nano-aluminized composite rocket propellants, Combust. Explos. Shock Waves 41 (2005) 680–692.
[29] P. Brousseau, C.J. Anderson, Nanometric aluminum in explosives, Propell. Explos. Pyrotech. 27 (2002) (2002) 300–306.
[30] A. Sossi, E. Duranti, C. Paravan, L.T. DeLuca, A.B. Vorozhtsov, A.A. Gromov, Y.I. Pautova, M.I. Lerner, N.G. Rodkevich, Non-isothermal oxidation of aluminum nanopowder coated by hydrocarbons and fluorohydrocarbons, Appl. Surf. Sci. 271 (2009) 337–343.
[31] A. Reina, Nano-metal Fuels for Hybrid and Solid Propulsion (PhD dissertation), Politecnico di Milano, Milan, Italy, 2013.
[32] J. Bouillard, A. Vignes, O. Dufaud, L. Perrin, D. Thomas, Ignition and explosion risks of nanopowders, J. Hazard. Mater. 181 (2010) 873–880.
[33] U. Teipel, U. Forter-Barth, Rheology of nano-scale aluminum suspensions, Propell. Explos. Pyrotech. 26 (2001) 268–272.
[34] E.M. Popenko, A.A. Gromov, Y.Y. Shamina, A.V. Sergienko, N.I. Popok, Effects of the addition of ultrafine aluminum powders on the rheological properties and burning rate of energetic condensed systems, Combust. Explos. Shock Waves 43 (2007) 46–50.
[35] B. Mary, C. Dubois, P.J. Carreau, P. Brousseau, Rheological properties of suspensions of polyethylene-coated aluminum nanoparticles, Rheol. Acta 45 (2006) 561–573.
[36] AMG Alpoco UK, http://www.amg-s.com/aluminum.html, 2015 (last visited 13.07.15).
[37] Malvern Instruments, http://www.malvern.com/en/support/product-support/mastersizer-range/mastersizer-2000/, 2015 (last visited 13.07.15).
[38] Advanced Powder Technology LLC, http://www.nanosized-powders.com, 2015 (last visited 31.03.15).
[39] Y.S. Kwon, A.P. Ilyin, T.V. Tikhonov, O. Nazarenko, Installation "UDP-5" for nanopowders production by wire electrical explosion. Presented at the 8th Russian–Korean International Symposium on Science and Technology (KORUS), 2004.
[40] A. Sossi, E. Duranti, M. Manzoni, C. Paravan, L.T. DeLuca, A.B. Vorozhtsov, M.I. Lerner, N.G. Rodkevich, A.A. Gromov, N. Savin, Combustion of HTPB-based solid fuels loaded with coated nanoaluminum, Combust. Sci. Technol. 185 (2013) 17–36.
[41] Y.F. Ivanov, M.N. Osmonoliev, V.S. Sedoi, V.A. Arkhipov, S.S. Bondarchuk, A.B. Vorozhtsov, A.G. Korotkikh, V.T. Kuznetsov, Productions of ultra-fine powders and their use in high energetic compositions, Propell. Explos. Pyrotech. 28 (2003) 319–333.
[42] 3M Material Safety Data Sheet FC-2175 Fluorel (TM) Brand Fluoroelastomer, October 13, 2010.
[43] S. Dossi, A. Reina, F. Maggi, L.T. De Luca, Innovative metal fuels for solid rocket propulsion, Int. J. Energ. Mater. Chem. Propuls. 11 (2012) 299–322.
[44] F. Maggi, S. Dossi, A. Reina, M. Fassina, L.T. De Luca, Advanced aluminum powders for solid propellants, Presented at the 5th EuCASS (European Conference for Aerospace Sciences), Munich, Germany, 1–5 July, 2013.

[45] L. Chen, W. Song, J. Lv, X. Chen, C. Xie, Research on the methods to determine metallic aluminum content in aluminum nanoparticles, Mater. Chem. Phys. 120 (2010) 670–675.
[46] Y.S. Kwon, Y. Jung, N.A. Yavorovsky, A.P. Ilyin, J. Kim, Ultra-fine powder by wire explosion method, Scr. Mater. 44 (2001) 2247–2251.
[47] B. Rufino, F. Boulc'h, M.-V. Coulet, G. Lacroix, R. Denoyel, Influence of particles size on thermal properties of aluminium powder, Acta Mater. 55 (2007) 2815–2827.
[48] A.P. Ilyin, A.A. Gromov, V. An, F. Faubert, C. de Izarra, A. Espagnacq, L. Brunet, Characterization of aluminum powders I. Parameters of reactivity of aluminum powders, Propell. Explos. Pyrotech. 27 (2002) 361–364.
[49] C. Paravan, A. Reina, A. Sossi, et al., Time-resolved regression rate of innovative solid fuel formulations, in: C. Bonnal, L.T. DeLuca, S.M. Frolov, O. Haidn (Eds.), Advances in Propulsion Physics, vol. 4, Torus Press, Moscow, 2013.
[50] W.W. Wendlandt, Thermal analysis, third ed., John Wiley & Sons, New York, USA, 1986.
[51] L. Chen, W.L. Song, J. Lv, L. Wang, C.S. Xie, Effect of heating rates on TG-DTA results of aluminum nanopowders prepared by laser heating evaporation, J. Therm. Anal. Calorim. 96 (2009) 141–145.
[52] D.A. Yagodinkov, E.A. Andreev, V.S. Vorob'ev, O.G. Glotov, Ignition, combustion, and agglomeration of encapsulated aluminum particles in composite solid propellant. I. Theoretical study of the ignition and combustion of aluminum with fluorine containing coatings, Combust. Explos. Shock Waves 42 (5) (2006) 534–542.
[53] O.G. Glotov, D.A. Yagodinkov, V.S. Vorob'ev, V.E. Zarko, V.N. Simonenko, Ignition, combustion, and agglomeration of encapsulated aluminum particles in composite solid propellant. II. Experimental studies of agglomeration, Combust. Explos. Shock Waves 43 (3) (2007) 320–333.
[54] V.N. Vilyumov, V.E. Zarko, Ignition of Solids, Elsevier Science Publisher, Amsterdam, 1989.
[55] L.T. DeLuca, C. Paravan, A. Reina, M. Spreafico, E. Marchesi, F. Maggi, A. Bandera, G. Colombo, B. Kosowski, Aggregation and incipient agglomeration in metallized solid propellants and solid fuels for rocket propulsion, in: 46th AIAA/ASME/SAE/ASEE Joint Propulsion Conference & Exhibit. American Institute of Aeronautics and Astronautics, AIAA Paper No. 2010-6752.
[56] A.V. Korshunov, A.P. Iliyin, N.I. Radishevskaya, T.P. Morozova, The kinetics of oxidation of aluminum electroexplosive nanopowders during heating in air, Rus. J. Chem. Phys. 84 (9) (2010) 1728–1736.
[57] A. Gedanken, Doping nanoparticles into polymers and ceramics using ultrasound radiation, Ultrason. Sonochem. 14 (2007) 418–430.
[58] S. Dossi, Mechanically Activated Al Fuels for High Performance Solid Rocket Propellants (PhD dissertation), Politecnico di Milano, Milan, Italy, 2014.
[59] M. Fassina, Effect of Al Particle Shape on Solid Propellants (PhD dissertation), Politecnico di Milano, Milan, Italy, 2014.
[60] Resodyn™ Acoustic Mixtures, LabRAM Mixer, 2015. http://www.resodynmixers.com/products/labram/ (last visit 20 Jun 15).
[61] F. Maggi, Curing viscosity of HTPB-based binder embedding micro- and nano-aluminum particles, Propell. Explos. Pyrotech. 39 (2014) 755–760.
[62] H.H. Winter, Can the gel point of a cross-linking polymer be detected by the G′–G″ crossover? Polym. Eng. Sci. 27 (1987) 1698–1702.
[63] A.K. Mahanta, D.D. Pathak, HTPB-polyurethane: a versatile fuel binder for composite solid propellant, in: F. Zafar, E. Sharmin (Eds.), Polyurethane, InTech, Rijeka, Croatia, 2012.
[64] S.P. McManus, H.S. Bruner, H.D. Coble, Stabilization of Cure Rates of Diisocyanates with Hydroxy-terminated Polybutadiene Binders, Research Report 140, University of Alabama in Huntsville, USA, 1973.
[65] D.M. Kalyon, P. Yaras, B. Aral, U. Yilmazer, Rheological behavior of a concentrated suspension: a solid rocket fuel simulant, J. Rheol. 37 (1993) 35–53.
[66] R. Muthiah, R. Manjari, V.N. Krishnamurthy, B.R. Gupta, Rheology of HTPB propellants: effects of mixing speed and mixing time, Defence Sci. J. 43 (1993) 167–172.

INDEX

'*Note*: Page numbers followed by "f" indicate figures, and "t" indicate tables.'

D

E

F

G

H

I

K

L

M

N